AD-A020 429

WATER ENTRY AND THE CAVITY-RUNNING BEHAVIOR OF MISSILES

Albert May

NAVSEA Hydroballistics Advisory Committee
Silver Spring, Maryland

1975

044214

ADA020429

WATER ENTRY
AND
THE CAVITY-RUNNING
BEHAVIOR OF MISSILES

NAVSEA HYDROBALLISTICS ADVISORY COMMITTEE

D D C

SEP 12 1976

REPORT DOCUMENTATION PAGE		READ INSTRUCTIONS BEFORE COMPLETING FORM
1. REPORT NUMBER SEAHAC/TR 75-2	2. GOVT ACCESSION NO.	3. RECIPIENT'S CATALOG NUMBER
4. TITLE *(and Subtitle)* Water Entry and the Cavity-Running Behavior of Missiles		5. TYPE OF REPORT & PERIOD COVERED Final
		6. PERFORMING ORG. REPORT NUMBER
7. AUTHOR(s) Albert May		8. CONTRACT OR GRANT NUMBER(s)
9. PERFORMING ORGANIZATION NAME AND ADDRESS Naval Surface Weapons Center White Oak Laboratory White Oak, Silver Spring, Maryland 20910		10. PROGRAM ELEMENT, PROJECT, TASK AREA & WORK UNIT NUMBERS SEA-18483/SR023-01-002
11. CONTROLLING OFFICE NAME AND ADDRESS		12. REPORT DATE 1975
		13. NUMBER OF PAGES 450
14. MONITORING AGENCY NAME & ADDRESS*(if different from Controlling Office)*		15. SECURITY CLASS. *(of this report)* Unclassified
		15a. DECLASSIFICATION/DOWNGRADING SCHEDULE

16. DISTRIBUTION STATEMENT *(of this Report)*

Approved for public release; distribution unlimited

17. DISTRIBUTION STATEMENT *(of the abstract entered in Block 20, if different from Report)*

18. SUPPLEMENTARY NOTES

Monitored by Naval Sea Systems Command, Washington, D. C. 20360.

19. KEY WORDS *(Continue on reverse side if necessary and identify by block number)*

Water Entry, Cones, Ogives, Disks, Spheres, Disk Ogives, Cavity-Running Missiles

20. ABSTRACT *(Continue on reverse side if necessary and identify by block number)*

This report contains a comprehensiv compilation of test data and analytical techniques for predicting the behavior of vehicles during water entry and during the cavity-running phase. It contains data to predict the water impact forces on nose shapes such as disks, cones, ogives, spheres, cusps, disk ogives, etc. during vertical and oblique water entry. Cavity development phenomena are discussed and approximate ways of predicting

#20.
cavity size and shape are presented. Stability characteristics
during the early running phase are also discussed. In general,
the report is intended to provide the necessary data for the
design of water-entry ordnance.

ACKNOWLEDGEMENT

ıb

WATER ENTRY AND THE

CAVITY-RUNNING BEHAVIOR OF MISSILES

Compiled by:

Albert May
Naval Surface Weapons Center
White Oak Laboratory

ii

TABLE OF CONTENTS

Chapter 1 - Water Entry

TABLES

ILLUSTRATIONS

CONTENTS (Continued)

CONTENTS (Continued)

Chapter 2 - The Forces Acting on Cavity Running Missiles

CONTENTS (Continued)

TABLES

ILLUSTRATIONS

CONTENTS (Continued)

Figure

Chapter 3 - Cavities

CONTENTS (Continued)

ILLUSTRATIONS

CONTENTS (Continued)

CONTENTS (Continued)

Chapter 4 - Forces at Water Impact

TABLES

ILLUSTRATIONS

CONTENTS (Continued)

CONTENTS (Continued)

CONTENTS (Continued)

ILLUSTRATIONS

CONTENTS (Continued)

Chapter 6 - Optics in Experimental Hydroballistics

ILLUSTRATIONS

CONTENTS (Continued)

Chapter 1

WATER ENTRY

Symbols

A   maximum cross-sectional area of missile;
maximum cross-sectional area of cavity in equation (1-5)

C   parameter in equation (1-5)

c   speed of sound

C_D cavity-running drag coefficient

°C   degrees Celsius

D   distance; for example, D_{dc} is depth of deep closure

d   truncation diameter of missile nose, or maximum
diameter of sphere or other nose having continuous
curvature

F   Froude number = $U_o/\sqrt{gL}$

°F   degrees Fahrenheit

g   acceleration due to gravity

h   depth below water surface

L   a characteristic length, usually d; width of
infinite strip in equation (1-3)

M   effective mass = $m/\rho d^3$
Mach number where so defined

m   mass of missile

P   a point on Figure 1-4

p   pressure; medium denoted by subscript

P_c pressure in the cavity

P_o pressure of freestream or at water depth under
consideration

P_v saturation vapor pressure of water at existing
temperature

R   Reynolds number = U_oL/ν; a distance defined in
Figure 1-5

r   a radius defined in Figure 1-29

s   distance of missile tip from entry point

s	dimensionless distance $= s/d$
t	time after water impact; a parameter in equation (1-3)
T	dimensionless time $= tu_o/d$
U	instantaneous speed
U'	instantaneous missile velocity $= U/U_o$
U_1	velocity of missile when at depth h
U_o	velocity of missile at first water contact
w	Weber number $\rho LU^2/\gamma$
x, y	coordinates along major and minor axes of ellipsoid
y, y_1	measures of sphere depth in Figure 1-4
o	$C_D A/2M$, retardation coefficient
γ	surface-tension coefficient
θ	angle of water entry, measured from horizontal; polar angle defined in Figure 1-50; a coefficient introduced by Mallock
θ_a, θ_b, θ_o	angles defined in Figure 1-28
θ_m	a maximum angle appearing in equation (1-6)
λ, μ	parameters used by Blackwell
ν	kinematic viscosity
ρ	mass density, usually of water (fluid may be identified by subscript)
σ	cavitation number $= (p_\infty - p_c)/(1/2)\rho U^2$
σ_v	vapor cavitation number $= (p_\infty - p_v)/(1/2)\rho U^2$

Subscripts

a	air
w	water
dc	(time or depth of) deep closure of water-entry cavity
pa	(time of) pullaway of cavity from water surface
sc	(time of) surface closure of water-entry cavity

INTRODUCTION

When a missile enters water from the air its behavior comprises a complicated series of events which occur both above and below the original water surface, and depends on the configuration of the missile and on the conditions of the entry. Many details of the missile configuration are important, including nose shape, fineness ratio, size, tail design, weight, and moment of inertia. The experimental conditions of the water entry include missile speed, angle of entry, angles of pitch and yaw, angular velocities, and the atmosphere above the water. The atmosphere is included since its pressure and density are frequently varied for purposes of scaling or research, and the study of behavior under varied atmospheric conditions leads to a better understanding of behavior under normal conditions.

Knowledge in the water-entry field has been developed largely by experiment, since its problems resist theoretical solution. Water-entry studies have been conducted under particular conditions, which are far from spanning the ranges of experimental conditions of importance. Much early research was carried out at vertical entry, most often with spheres and at low-entry speeds. Frequently these speeds were less than 30 feet per second, while others extended to 100 or 200 feet per second. Studies at higher speeds (up to 7000 feet per second) generally yielded little detailed information.

Most of the early oblique-entry research was in support of torpedo development. Accordingly, it was frequently restricted to entries at about 20 degrees and speeds of 400 or 500 feet per second for a 22-inch prototype. Detailed information has usually been obtained from models having diameters up to two inches.

Water-entry behavior involves many interconnected regimes, but in the interest of simplification, various aspects may be treated separately. In the present work, three main divisions will be considered.

1. The phenomenology of water entry (here titled simply "Water Entry").

2. The force systems at water impact and while cavity running, and

3. The trajectory of the missile after water entry.

"Water Entry" will deal especially with the history of the air-water interface (that is, changes of the original water surface and the underwater cavity which is generated) and with the flow behavior of water and air. The force systems and missile trajectories will be discussed in separate chapters.

The sequence of events which follow water entry, including those which occur below the water surface, was first reported near the turn of the century by Worthington (Refs. (1-1), (1-2), and (1-3)), who dropped spheres into water and made observations and photographs from above the water surface and through a glass side wall of the tank, using a high-speed spark. In spite of the limitations of his equipment and the small breadth of his experiments, he established an excellent foundation for later water-entry research.

The generation, growth, and decay of the water-entry cavity has been described in detail in the literature and will be discussed extensively in this report. First, the most usual water-entry behavior will be outlined for the orientation of those who may be unfamiliar with its most common details. Not all behavioral features of water entry will be mentioned in this brief outline, nor does inclusion of details here intimate their presence under all experimental conditions. Later, a detailed discussion will be given of the various components of the water-entry process.

At vertical entry the forward portion of the missile nose is first wetted. The nose gives a velocity, principally transverse, to the water and the flow separates from the missile nose with the generation of a cavity (Fig. 1-1A). Air rushes in from above the water to fill the cavity. Later the splash forms a dome which closes over the entry point of the missile and seals the cavity from the air above (Fig. 1-1B). When this "surface closure" or "surface seal" occurs, the cavity is usually expanding so that the cavity pressure tends to decrease. The pressure above the water is then greater than that in the cavity, and the cavity is pushed down from the water surface (Fig. 1-1C). The separation of the top of the cavity from the water surface has been called "pullaway." The cavity then travels with the missile down into the water. Since the pressure is less than the pressure in the surrounding water, the walls of the cavity accelerate inward. When opposite walls touch at a point, "deep closure" or "deep seal" is said to occur. This closure separates the cavity into two parts (Fig. 1-1D) and lessens the size of the cavity attached to the missile. Often a series of deep closures occur, and the air content of the cavity is continually reduced until, finally, no cavity remains and the missile is fully wetted, unless its velocity is sufficient to maintain a vapor-filled cavity.

When the missile enters the water obliquely rather than vertically, the behavior is similar to that already described, and differs rather in details than in any essential way. In particular, surface closure occurs later after oblique entry, and the cavity grows to a larger size.

THE PHASES OF WATER ENTRY

During the entry of a missile into water, the successive conditions which exist are commonly divided into a number of "phases," given variously by different authors. The following division is frequently made. It should be noted here that the force system which exists during the various phases will be discussed in a separate report and no detailed explanation of the phases will be given in this section.

Shock-Wave Phase

During this phase, which is most significant for the vertical entry of a blunt body, a shock wave is generated in the water. Although large forces which may cause damage to the missile are effective during the phase, the time is extremely short and the phase is usually of small practical importance.

Flow-Forming Phase

During its entry, the missile has to establish a pattern of flow in water which was initially at rest. While this flow is being generated, the missile experiences its greatest deceleration during water entry.

Open-Cavity Phase

During this phase the missile is cavity running, that is, it is generating a cavity as it travels, but the cavity is open to the atmosphere at its upper end (at the water surface).

Closed-Cavity Phase

In this phase the cavity has closed above the water surface (Fig. 1-1C) and envelops the missile (when conditions are suitable).

Collapsing-Cavity Phase

The cavity size decreases and later the rear of the cavity collapses onto the tail of the missile. This phase includes all partial cavity conditions.

Fully Wetted Phase

Finally, the water is in contact with the complete surface of the missile.

There are a number of overlapping phases which can be, and have been named: the nose-riding phase, when the nose alone is in contact with the water; the tail-clipping phase when the tail of the missile strikes the under lip of the water-entry cavity; the tail-riding phase when the missile travels with its tail bearing on the cavity wall; and so forth.

The motion of the missile within the cavity and the impacts of the missile with the cavity wall will be discussed with the trajectory in another report.

DIMENSIONLESS QUANTITIES

The systematic treatment of water entry (or of any dynamic process) requires the consideration of scaling criteria, and of the dimensionless quantities and parameters to which the behavior can in general be related. The principal quantities which have been so used for water entry and are best suited to its analysis, are listed below.

Froude Number

Froude number, which compares the inertial forces with the force of gravity, has special pertinence to problems in which there is a free surface, that is, an air-water interface. In this report it will be defined as

$$F = U_o \sqrt{gL}$$

where U_o is the velocity of the missile at water impact, g is the acceleration of gravity, and L is a characteristic length. For the water entry of axially-symmetric bodies, L is usually taken as the missile diameter d. This choice will be assumed unless another is mentioned. In defining Froude number in past years, engineers used the definition given above, but scientists frequently chose the square of this quantity. The latter usage is rare today, but the definition used must always be verified when older reports are read. Dependence on Froude number is strongest when its value is small, corresponding to greater influence of gravity.

Reynolds Number

Reynolds number,

$$R = U_o L/\nu$$

where ν is the kinematic viscosity, compares inertial and viscous forces. In water entry it may be applied to flows of either air or water, with use of the appropriate value of ν.

Mach Number

Mach number will be used in the form

$$M = U_o/c,$$

the ratio of missile impact velocity to the velocity of sound in either air or water. For air (Ref. (1-4))

$$c_a = (331.5 + 0.607°C) \text{ meters/sec} = (1085 + 1.42°F) \text{ ft/sec}$$

where °F and °C are temperatures on the Fahrenheit and Celsius scales. For air flow into the cavity, it may be important to scale Mach number if the entry speed is of the order of 1000 feet per second.

The speed of sound in water is much higher (Ref. (1-5)). For fresh water

$$c_w = 1403 + 5°C - 0.054°C^2 + 0.0002°C^3 \text{ meters/sec, or}$$

$$c_w = 4603 + 9.1°F - 0.15°F^2 + 0.00055°F^3 \text{ ft/sec}$$

and for salt water about 8 or 9 percent higher than this. Hence, Mach number is less likely to be important for the water flow.

Weber Number

During water entry, surface tension is probably only of importance for small missiles at low speeds. The dimensionless quantity which compares the surface tension forces and inertial forces is the Weber number

$$W = \rho L U^2 / \gamma,$$

where γ is the surface tension coefficient (72 dynes/cm for pure water) and L is a characteristic length (for example, the radius of a bubble).

Cavitation Number

The cavitation number

$$\sigma = (p_\infty - p_c)/(1/2)\rho U^2$$

(where p_∞ is the freestream pressure or the pressure at the depth of the cavity, p_c is the pressure within the cavity, and ρ is the mass density of water) has been discussed in detail in another chapter. Here it is sufficient to remark that it is a most useful parameter for the "steady" cavity (that is, a closed cavity of almost constant size and shape), because the numerator, $p_\infty - p_c$, is the pressure tending to close the cavity and the denominator, $(1/2)\rho U^2$, is the dynamic pressure effective in resisting this closure.

There appears to be little logic in using σ as a parameter for the transient water-entry cavity. It is easily shown that, for this cavity, neither $p_\infty - p_c$ nor $(1/2)\rho U^2$ serves the purpose mentioned above. Actually the vapor cavitation number

$$\sigma_V = (p_\infty - p_V)/(1/2)\rho U^2$$

(where p_v is the saturation vapor pressure of water at the temperature of the cavity's surroundings) has been used as a parameter for the water-entry cavity (Ref. (1-6)). Its application to the main water-entry cavity is questionable since, in addition to the objections mentioned above, the cavity is vented, that is, it is filled with air and water vapor rather than with water vapor alone. On the other hand σ_v is a logical parameter for the treatment of vapor cavities formed during the water-entry process, apart from the main cavity (especially on the underside of the missile nose following oblique entry).

In general, both the pressure p_a and the density ρ_a of the gas above the water must be suitably scaled if the cavity behavior is to be independent of missile size. When the pressure is scaled, the pressure itself is generally a better parameter than the cavitation number for use with the main cavity, and both pressure and density can conveniently be expressed as fractions of the normal pressure and density of the atmosphere.

Other Dimensionless Quantities

The missile speed, time, and distance traveled can be non-dimensionalized by writing

$$U = U/U_o; \quad T = tU_o/d; \quad and \quad S = s/d.$$

A reference length (usually the missile diameter d in this report) is taken as the unit length; unit time is the time d/U_o required for the missile to travel a distance equal to the reference length at the impact speed; and unit speed is the speed at impact. Time is measured from impact, that is, from the first contact of missile and water.

When the effect of missile mass is being considered, dimensionless parameters of several forms can be employed. Ballistic Coefficients are of the form A/m, where A and m are the cross-sectional area and mass of the missile. Or, one can use C_DA/m where the product C_DA is called the drag area. At a given speed, C_DA is proportional to the drag force so that C_DA/m is proportional to the acceleration. Another parameter which has been used (Ref. (1-7)) is the

$$\text{Effective mass} = M = m/\rho d^3,$$

the ratio of the mass of the missile to the mass of a cube of water of edge d.

THE SPLASH

When a missile strikes the water surface, spray and splash appear and a variety of changes occur above the original surface, for example:

a. At the first impact, drops of _spray_ are propelled into the air. This is a phenomenon of impact rather than of flow and the drops do not come off tangent to the surface of the nose, but at least for vertical entry, usually along a line approximately half way between the nose and water surfaces. The formation of spray probably has no importance.

b. The flow becomes established along the nose surface and leaves it at the point of flow separation. At about the time when this separation begins, there is a _piling up_ of water above the original surface, between this surface and the surface of the missile nose. The important impact forces on the nose are strongly affected by the configuration of this portion of the splash, since it must be accelerated out of the path of the missile.

c. As the flow continues to separate, it forms the _splash sheath_. This is the main portion of the splash and it is attached to the water surface at the lip of the cavity where a meniscus appears. After its generation, the splash sheath has no effect on the missile until it causes surface closure, which influences the whole later history of the cavity.

d. The cavity formed below the water surface represents a region from which water has been removed. A portion of this water volume is accounted for by the splash (and later by a jet), but the major part of the displaced volume appears as a uniform _raising of the level_ of the water surface over a large area (Ref. (1-3)). This rise in level is detected only by a careful study.

e. Under some entry conditions, partial collapse of the cavity generates _jets_, one of which may rise to a considerable height above the water surface.

Vertical Entry

As an example of the spray and splash, the vertical impact of a sphere will be considered first. Two series of photographs are included to show the splash generation. Figure 1-2 is a set of four shadowgraphs of the entry of a 2-inch sphere at 22 feet per second (Ref. (1-8)), and Figure 1- (Ref. (1-9)) is part of a high-speed motion picture (frame rate .0 per second) of the entry of a 1-inch sphere at 35 feet per second.

For the impact of a sphere, an almost flat surface hits the water first and this is followed by a surface of increasing, but still small slope. The first two photographs of Figure 1-2 show the splash produced while the angle is very small. Later the increasing slope presented by the nose, together with the establishment of a flow pattern, results in a sheet of splash whose angle increases to a maximum of about 60 degrees. This is shown in Figures 1-2 and 1-3

The curvature of the splash shown in the first photograph of Figure 1-3 does not represent the path followed by the water particles (Ref. (1-3)). The path is almost a straight line, with a slowly increasing drop due to gravity. The apparent curvature in the photograph results from the different angles at which successive contributions to the splash are ejected by the sphere.

The initial speed of the splash measured during the vertical, low-speed entry of spheres was reported to be slightly less than the impact velocity, with an average of about $0.95U_O$ (Ref. (1-9)). Earlier observers reported values of 4 to $5U_O$ (Ref. (1-10)). No data are available on the thickness of the splash sheath or on the amount of water in the splash, but some approach to the latter determination was reported by Ramsauer (Ref. (1-11)).

Splash generation occurs only during the impact and flow-forming phases. There is probably no addition of water to the splash after the nose is completely wetted, and it has been verified experimentally (Ref. (1-12)) that the water in the splash comes from the surface layer of the undisturbed water. After the nose is wetted, the flow continues to leave the nose at the separation angle, but does not leave the body of the liquid. The latter flow causes the cavity wall to be a continuation of the splash sheath. Under usual conditions, surface tension maintains the integrity of the splash sheath, that is, no holes appear in it. Since the splash sheath continues to grow without the addition of water after the missile nose is wetted, the sheath becomes thinner and sometimes, if the experimental conditions preclude surface closure, holes appear after the sheath has become quite large.

While surface tension is responsible for the integrity of the splash sheath, it appears that its effect on the splash is small otherwise, except in the case of small missiles (d < 1/4 inch) or low speeds of entry ($U_O \leq 20$ feet per second). At very low speeds, the splash attains only a bowl shape, and the bowl remains at its maximum height for an appreciable time (as viewed in high-speed motion pictures) during which the splash walls visibly thicken and acquire a beaded rim at the top (Ref. (1-3)). When the vertical entry speed is very low, Worthington (Ref. (1-3)) found that an air-filled cavity is not always formed -- only a little spray and perhaps a few bubbles. May showed (Ref. (1-13)) that this condition may exist up to 20 feet per second for 1-inch steel spheres if they are sufficiently hydrophilic.

Table 1, which was given by Gilbarg (Ref. (1-12)) for the vertical entry of spheres, shows the effect of surface tension on the splash sheath for spheres between 1/4 and 1 inch in diameter. These entries were Froude scaled, that is, the velocities were proportional to the square root of the sphere diameter. The dimensions of the splash when the splash was approximately vertical and at the completion of the dome causing surface closure, are seen to be proportionately somewhat smaller for the smaller spheres, presumably as a result of the inward pressure on the splash sheath due to surface tension.

TABLE 1-1   SPLASH DIMENSIONS FOR VARIOUS ENTRY CONDITIONS

MODEL SIZE	PRESSURE (ATMOSPHERE)	VELOCITY FT/SEC	DIAMETER OF CYLINDRICAL SPLASH IN MODEL DIAMETERS A	DIAMETER OF SPLASH AT SURFACE CLOSURE IN MODEL DIAMETERS B	HEIGHT OF SPLASH AT SURFACE CLOSURE IN MODEL DIAMETERS C
1/4	1/4	35	2.6	2.8	2.6
1/4	1/8	34	3.2	3.6	3.6
1/4	1/16	36	5.0	4.8	5.6
1/2	1/4	49	2.8	3.0	2.6
1/2	1/8	49	3.6	4.0	5.6
1/2	1/16	50	4.6	5.0	8.0
1	1/4	69	3.0	3.6	3.4
1	1/8	72	4.3	4.8	5.7
1	1/16	69	8.0	NO S.C.	NO S.C.

DIAMETER A

DIAMETER B

HEIGHT C
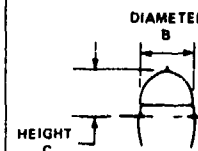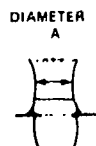
Attempts to calculate the axial force during water impact have led to detailed studies of the configuration of the water surface very near the entering nose (Refs. (1-8), (1-14) and (1-15)). Figure 1-4 is a sketch of this area during the water entry of a sphere (Ref. (1-8)). A thin sheet of water travels up the surface of the sphere and then detaches to form the splash sheath. It is assumed (Ref. (1-15)) that the pressure in the water is high, up to some point P, (Fig. 1-4) and that above this the thin layer of sheath is practically at atmospheric pressure. Hence, the sphere is regarded as effectively at a depth y_1 (measured from P) rather than y, based on the sphere travel alone. The quantity y_1/y is called the Wetting Factor (Ref. (1-15)).

Formulas predicting the value of the wetting factor for the vertical entry of spheres were developed by Shiffman and Spencer (Ref. (1-15)) and by Cooper (Ref. (1-16)), and these were compared with empirical data by White (Ref. (1-8)). The only conclusion which appears justified by the comparison is that the wetting factor for spheres seems to average about 1.38.

The curves which outline the sides of the splash in Figure 1-4 are very close to being parabolas and the oblique line at the left of the figure is the bisector of the parabola.

For the vertical entry of cones, spray is produced in a direction approximately bisecting the angle between the cone surface and the water surface (Ref. (1-7)). The splash and the flow on the cone surface can be seen in Figures 1-5 and 1-6. Figure 1-5 (Ref. (1-17)) shows that the splash forms a very thin layer on the cone. The separation of the splash sheath from the conical surface can be seen in Figure 1-6, but the position at which the flow separates from the surface has not been determined. The thinness of the layer on the cone surface suggests that the pressure within it must be very close to atmospheric.

The splash for the vertical entry of the right cylinder is somewhat anomalous. Instead of a flat saucer as might be expected, the splash sheath forms a cup with a small separation at its sides, from the cylindrical wall. A series of sketches of the splash sheath and cavity wall are shown in Figure 1-7 (Ref. (1-18)). In this figure the ticks external to the outlines denote the height of the undisturbed water surface. In the water entry of Figure 1-7, it is evident that the cavity did not close onto the cylinder since the cavity grew considerably during the period shown.

Splash at Oblique Entry

Little has been published on the splash accompanying oblique water entry. Three studies have been made: a photographic study of spheres, made by White (Ref. (1-8)); and predictions for the broadside entry of two-dimensional plates (Ref. (1-19)),and of cylinders (Ref. (1-20)) by Cooper. For oblique entry there is always a marked forward splash, and for the disk or right cylinder the initial splash is parallel to the entering face.

The nature of the splash can be seen from Figure 1-8, which is copied from White's work (Ref. (1-8)) on spheres. White says "the forward splash is small and thin, the forward surface rise is less than for vertical entry, and there is a relatively large rear surface rise which develops into quite a large hump at low entry angles."

The hump, which may be observed behind the entering sphere in Figure 1-8B, was predicted by Cooper for the oblique entry of plates (Ref. (1-19)).   This hump has a two-fold importance; frequently it is this hump which is struck by the cylindrical afterbody of torpedo-like missiles shortly after entry; and the humps frequently contribute to the formation of blind vapor-filled cavities on the underside of the missile, and furnish the under-pressure which contributes to the whip at entry. This will be discussed in some detail in a description of the force system at impact in another report.

SURFACE CLOSURE

Under most experimental water-entry conditions, the cavity which forms behind a missile closes later above the water surface when the splash domes over. This closure, which prevents further flow of air into the cavity, is called Surface Closure or Surface Seal. It should be noted that not all workers in the water-entry field have meant the same thing by "Surface Closure." At the Naval Ordnance Laboratory (Ref. (1-9)) the term has been used to denote the time at which the cavity becomes completely sealed above the water surface. Birkhoff and Isaacs (Ref. (1-21)) and Waugh and Stubstad (Ref. (1-22)) have specified surface closure as the time at which a visible thickening is observed in the water layer above the cavity, near the original water surface. This is very close to what has been called "pullaway." It will be discussed in the following section.

In this report "Surface Closure" will mean the time when flow into the cavity is completely interrupted. It would appear justifiable to assign a name to this event even if the closure were entirely unmeasurable and of theoretical interest only. Actually some quantitative data on surface closure are available, although there are difficulties in the way of its determination:

a. The closure is gradual and may be partially "effective" before it is actually complete,

b. A considerable randomness is to be expected because of the imprecise manner in which the splash walls converge, and

c. The time at which the closure is complete must be inferred rather than observed.

It does not appear feasible to attempt to determine by measurement the instant at which flow into the cavity stops. Instead, since the closure limits the expansion of the cavity, the completion of the closure is inferred from measurements of cavity volume. This is rather impractical as a measurement criterion, and other bases have been adopted as fixing the time of surface closure, t_{sc}. Gilbarg and Anderson (Ref. (1-12)) took the time at which the dome appeared to be closed. May (Ref. (1-9)) studied the volume history of the water-entry cavity due to the vertical entry of steel spheres and decided that the surface closure was not quite complete when the splash dome first appeared to the eye to be closed. A plot of the volume calculated from measurements of photographs is given in Figure 1-9 (Ref.(1-9)) for the entry of a sphere at 77 feet per second from air whose pressure was one quarter of the normal atmospheric pressure. It will be shown that this reduction of atmospheric pressure slows down surface closure. Along the graph are sketches showing the cavity outline at various times. Observation indicated that the rounded dome occurred too long before the maximum volume was reached for it to represent a completely closed cavity. It was decided that at surface closure the splash had a cusped appearance similar to, but not quite as late as, that shown in Figure 1-10 (Ref. (1-9)). To provide an objective basis (whether accurately defining the time of surface closure or not) the closure was assumed to occur when the spray jet (which can be seen in Figure 1-10) first appears below the roof of the cavity.

Worthington (Ref. (1-3)) believed that surface closure was due to surface tension. Blackwell (Ref. (1-23)) was the first to ascribe the closure to a Bernoulli reduction of pressure in the neck of the splash sheath resulting from the velocity of the inrushing air. This reduction has usually been assumed to be $1/2\rho_a U^2$, based on steady flow conditions. Abelson (Ref. (1-24)) has shown that the actual pressure reduction is somewhat greater than this. It has been well established that the closure depends primarily on the density of the atmosphere and

SEAHAC/TR 75-2

is almost independent of its pressure (Ref. (1-9)). Davies
(Ref. (1-25)) first showed that the effect of surface tension
is not sufficient to account for the closure. On the other hand,
surface tension affects the splash and has some importance in
closing the cavity when other influences are small. Some
evidence of this was given in Table 1, and some will be found
later in Table 2.

While surface closure usually occurs for water entries of
practical importance, it tends not to occur at entries of very
low speed, for missiles of small mass, or for entries from a
low-density atmosphere. The absence of a closure for low speeds
or low-density atmosphere follows from the need for a pressure
reduction within the splash sheath more or less equal to $1/2\rho_a U^2{}_o$.
When the missile mass is small, deceleration is rapid and the
speed of the air entering the cavity decreases. For vertical
entry from a normal atmosphere, it has been said (Ref. (1-10))
that surface closure occurs only if the Froude number is greater
than about 4.5. The question has been raised whether surface
closure occurs for "full-scale" missiles (Ref. (1-10)) (presumably
of 22-inch diameter) or for missiles entering water obliquely
(Ref. (1-26)). These questions would hardly be raised today
in application to usual experimental conditions.

Details of the surface closure following the vertical entry
of spheres can be seen from Figure 1-3. Similar behavior may be
expected for other nose shapes. For the sphere the main splash
is initiated at an angle of about 60 degrees, and is generated
only while the nose is being wetted. The splash then travels
outward and upward under the influence of the force of surface
tension within the splash, which ties the splash sheath to the
meniscus at the water surface, and the drag force which retards
the forward motion of the splash. The air which flows into the
cavity through the tube formed by the splash sheath has a pressure
which is less than that about the splash, so that a pressure is
exerted on the sheath causing it to move inward. This pressure
is aided in the later phases of the closure, by the inrushing
air itself, which entrains drops of spray, and blows them toward
the axis and down toward the closing sheath. Evidently the closure
is not a precise operation and large variations in the time of
closure are to be expected because of random fluctuations.
Gilbarg (Ref. (1-12)) found that ripples on the water surface
could hinder or prevent surface closure.

Time of Surface Closure

Blackwell (Ref. (1-23)) first showed experimentally that
surface closure occurs more rapidly for higher entry velocities.
For the vertical entry of spheres, Gilbarg and Anderson (Ref. (1-12))
found the time of surface closure to be inversely proportional
to U_o, and May (Ref. (1-9)) showed a proportionality to the sphere
diameter. These scaling laws indicate that the dimensionless time
of surface closure is roughly constant, that is

$$T_{sc} = t_{sc}U_o/d = \text{constant},$$

at least for the case of the vertical entry of spheres and, of course, at a fixed atmospheric density. Finally Birkhoff and Isaacs (Ref. (1-21)) proved by a rough theoretical argument that $T_{sc}\rho_a$ should be approximately constant when the atmospheric density is varied.

Times of surface closure determined experimentally for the vertical entry of 1/2-inch steel spheres are given in Figure 1-11 (Ref. (1-9)). The scatter of data is large as might be expected. The four graphs as drawn, show the value of $T_{sc}\rho_a$ to be independent of U_o but there is some evidence that the value is greater at the higher values of U_o. In fact, it is evident that T_{sc} cannot remain independent of U_o when U_o becomes very large. At this time, as the flow into the cavity through the sheath becomes supersonic, the flow will choke, and the speed of flow into the cavity cannot remain proportional to U_o. The graphs of Figure 1-11 would lead roughly to the relation $T_{sc}(\rho_a)^{0.6} = \text{constant}$, but data in Table 2 for a 1-inch sphere give a value of 0.9 for the exponent.

The strong dependence of the time of surface closure on the atmospheric density ρ_a makes the later development of the cavity depend on it also. The dependence of T_{sc} on the pressure of the atmosphere, as distinguished from the density, is small but Waugh and Stubstad (Ref. (1-22)) obtained some evidence that a dependence exists.

Reynolds number seems to have no influence on surface closure except when "smooth" flow separation occurs. Then, on the sphere for example, the separation point can move because of small surface forces. For vertical entry, when the Reynolds number based on length of flow on the sphere is less than about 3×10^5, the time of surface closure is apparently significantly less than at higher Reynolds numbers, since this behavior is found (Ref. (1-18)) in the time of pullaway of the cavity from the water surface.

Table 2 gives mean values of $T_{sc}\rho_a$ for the vertical entry of 1/4- to 1.5-inch steel spheres from air at pressures from 1/32 to one atmosphere (Ref. (1-9)). The dependence on ρ_a can be seen also, at medium and low densities, a faster closure for small spheres, presumably because of surface tension.

Table 2

Average Values of $T_{sc}\rho_a = t_{sc}U_o\rho_a/d$ for Steel Spheres

Sphere Diameter, d, in inches	Pressure of Air in Atmospheres					
	1	1/2	1/4	1/8	1/16	1/32
3/2	4.6	3.2	3.7			
1	4.5	4.1	3.8	4.2		
1/2	4.6	3.5	2.5	2.1	1.9	
1/4	5.3	3.5	2.6	2.0	1.8	1.9

Insofar as T_{sc} is constant for spheres of a specific density, the depth of the spheres at the time of surface closure is the same for all if the drag coefficients are the same. Further, the cavity shapes tend to be the same if C_D is the same (Ref. (1-27)) so that within the approximation considered, all cavities will have the same volume when they close. In particular, changes of missile density and of atmospheric density will destroy the approximate equality.

No quantitative data for the time of surface closure have been published except for spheres at vertical entry. Some estimate of T_{sc} can be made from measured values of the time of pullaway which will be discussed in the next section. Only a few general comments will be included at this point.

The time of surface closure is considerably shorter for the right cylinder at vertical entry than for the sphere because of the small divergence of the splash, which was shown in Figure 1-7. At low speeds the closure frequently occurs on the cylinder, and then the closure time is shorter still.

For cones T_{sc} may be expected to increase with the divergence of the splash, that is, with the cone angle. Abelson observed (Ref. (1-24)) that surface closure after vertical entry is slower for 70-degree half-angle cones than for the sphere, and similar behavior has been shown (Ref. (1-18)) for pullaway with 45-degree cones.

A special comment might be pertinent concerning the "spigot" or "probe" head. This head has a slender cylindrical extension, of perhaps one-quarter the missile diameter, projecting forward usually from a flat nose. The principal reason for this nose is to lessen the impact shock by increasing it gradually. Blackwell (Ref. (1-23)) noted that t_{sc} is smaller when a spigot is added to the nose. Because of its small diameter, it throws a correspondingly small cavity, which commonly closes on the body, and another cavity is generated at the base of the missile, quite slender and little fatter than the cylinder itself.

While no measurements are available for the t_{SC} of oblique entry, it is evident that the closure becomes much slower as the entry becomes flatter. This is generally ascribed to the fact that the opening at the water surface is elliptical rather than circular with a major axis equal to $\csc\theta$ times the transverse axis (where θ is the entry angle measured from the horizontal). The aperature is large and therefore takes longer to cover over. It might be argued, however, that the width of the aperture at the water surface is the same as for vertical entry and should be covered in the same time. Actually the closure is an imprecise process and certainly depends on both axes of the ellipse. It is a fact that the closure is much slower for entries at low angles.

It is not known how t_{SC} varies with nose shape for oblique entry, but it appears probable that the variation is less than for vertical entry.

PULLAWAY

Usually surface closure is followed by "pullaway", a motion of the top of the cavity downward from the water surface. While pullaway does not have the basic importance of surface closure, it is closely related to it and can be measured with precision. In spite of this possible precision, pullaway data exhibit considerable scatter which arises from the large scatter of t_{SC} on which it depends strongly. Apparently data on the time of pullaway are based on only four studies: for the vertical entry of spheres in Reference (1-9), in a comparison of several nose shapes at vertical entry in Reference (1-18), and for oblique entry in References (1-7) and (1-21). Pullaway never occurs without surface closure, but surface closure may occur without pullaway following it.

Waugh and Stubstad defined surface closure (Ref. (1-22)) "as the closure of the water surface itself and not the dome of the splash," and Birkhoff and Isaacs (Ref. (1-21)) defined it as occurring when "the layer of water separating the cavity from the outer air thickens visibly" following the complete blocking of the access of air to the cavity. These definitions are approximately that of pullaway in the present report.

Vertical Entry

In the previous section it was stated that surface closure does not occur for very light missiles, at very low speeds, or with a low-density atmosphere. Similarly, pullaway generally will not occur if the conditions are only just sufficient to permit a surface closure. Under such conditions the closure is late, the cavity is large at the time of the closure, its expansion rate is low, and the cavity pressure does not drop sufficiently to cause pullaway. Some idea as to the minimum speeds at which pullaway will occur for vertical entry can be obtained from the graphs of Figure 1-12 which are based on experimental

data from the vertical entry of steel spheres (Ref. (1-9)). The graphs are only roughly indicated by the sphere data and may be in error by a factor of 2. These graphs show that higher speeds are required to produce pullaway for missiles of larger diameter and for lower atmospheric pressures. Two points should be noted regarding conceivable extrapolations of the data of Figure 1-12. When the atmosphere has a pressure near the vapor pressure of water, no increase of speed will cause pullaway because of the small mass flow available. Further, if pullaway does not occur at moderately high speeds, very high speeds are not likely to cause it because a higher speed is unable to produce a greater drop in the pressure of the air entering the cavity as the pressure approaches zero.

For the data on which Figure 1-12 was based, it was reported (Ref. (1-9)) that when pullaway occurred, the ratio of the time of pullaway to the time of surface closure, t_{pa}/t_{sc}, was always between 1.5 and 3.5. (These "times" are measured from first contact between missile and water.) As with the time of surface closure, the actual time of pullaway, t_{pa}, for these entries decreases with increase of U_O, although the dimensionless time, T_{pa}, increases slowly. At very high speeds, t_{pa} presumably will increase with increase of entry speed. This is indicated by the earlier argument and is verified by data for oblique entry which will be presented later.

Time of pullaway, T_{pa}, is plotted against U_O in Figure 1-13 for small spheres at vertical entry for several atmospheric pressures (Ref. (1-9)). It was found that data for spheres with diameters between 1/4 and 1 inch gave the same graphs within the large scatter of the data. The graph for a pressure of one atmosphere is shown as a broken line with considerably slower pullaway times at low speeds. As was mentioned earlier, this may be ascribed to the presence of a critical Reynolds number (Ref. (1-7)).

In Figure 1-14, times of pullaway for vertical water entry are compared for a number of nose shapes. The data are plotted against Froude number as they were presented in Reference (1-18). The use of Froude number rather than U_O in the treatment of pullaway is questionable. There is no apparent reason why the data should scale with F rather than with U_O, since the process of pullaway is complicated and only slightly dependent on gravity. Since all missiles from which data were used in Figure 1-14 were 1.5 inches in diameter, the abscissa scale can be rewritten with $U_O = 2F$. Three graphs are given for right cylinders, with M values of 9, 18, and 50. Here, M is an Effective Mass, $M = m/\rho d^3$, the mass of the missile divided by the mass of a water cube whose edge is the diameter of the missile. The spheres used for Figure 1-14 were steel and had M = 18.

The times of pullaway plotted in Figure 1-14 show that the relative behavior of the various nose shapes is qualitatively like that for surface closure: the right cylinder has the fastest pullaway, next comes the sphere, while the 45-degree half-angle

cone pulls away somewhat later. While the times of pullaway differ considerably with nose shape, the slopes of the graphs in Figure 1-14 are nearly the same, that is, the rate of increase of the dimensionless time of pullaway with increase of Froude number (or with entry speed) is about the same.

While T_{pa} increases with U_O for all the nose shapes shown, the actual time of pullaway, t_{pa}, does not. Figure 1-14 shows that for the lightest right cylinders (M = 9), t_{pa} is independent of U_O, with a value of about 7.7 milliseconds. For spheres and 45-degree cones, t_{pa} tends to decrease as U_O is increased, while for heavier right cylinders it increases with U_O.

Variation of pullaway time with the Effective Mass of missiles with right-cylinder noses is due to deceleration. The light missiles decelerate most rapidly, the mass flow into the cavity is less, and surface closure and pullaway are slower.

Oblique Entry

Data on the time of pullaway for oblique water entry are principally available from a single source (Ref. (1-7)) and are given in Figure 1-15. These data were obtained from water entries of missiles with diameters of 1 and 1 1/2 inches, at angles to the horizontal of 45 to 70 degrees. The entry speeds were between 300 and 1600 feet per second, much higher than for known studies of vertical entry. Although only a casual study was made of the effect of entry angle, this dependence was evidently small between 45 and 70 degrees, and it was neglected although there is a slight increase of pullaway time as the obliquity is increased.

The characteristic length used in F, T_{pa}, and M requires explanation. Most of the missiles tested were truncated cones or ogives and it was shown that the behavior was that which would have been obtained if the missile were a right cylinder with a diameter equal to the truncation diameter. In the case of hemispherical noses, the "effective diameter" was based on the diameter of a right cylinder with the same drag as the hemisphere. This behavior is at variance with that found for vertical entry, where the angle of the splash is of great importance. In addition, it will be seen that there is very little dependence on M, that is, on the mass of the missile. These differences between oblique and vertical entry result from the much slower surface closure of oblique entry. Since it is slow, the cavity reaches a large size before the closure, and is growing only slowly at that time, the closure (and also pullaway) depends much less on such parameters as missile weight, nose shape, and entry angle.

The graphs of Figure 1-15 are contour lines--lines of constant pullaway time, T_{pa}, on F-M coordinates. The figure shows that T_{pa} is considerably larger than values extrapolated from the vertical-entry data of Figure 1-14. The dimensionless time T_{pa}

increases strongly with U_o, and t_{pa} also increases as U_o increases. This is partly due to the high entry velocities used.

Birkhoff and Isaacs (Ref. (1-21)) have given some approximate data for the time of "surface closure" for oblique entries, at angles of 45 to 75°, of 1 1/2-inch steel spheres. As was mentioned earlier they have used the term "surface closure" very nearly in the sense of the "pullaway" of the present report. Their measurements permit an interesting extrapolation to lower entry speeds of the data in Figure 1-15. All steel spheres have an M value of about 18, and data read from Figure 1-15 at M = 18 and combined with data from Birkhoff and Isaacs, are plotted in Figure 1-16. The dashed lines at higher values of F are from extrapolations from the contours of Figure 1-15 and are only approximate.

DEEP CLOSURE

As a missile travels through the water after water entry, giving each layer of water a velocity which is principally transverse, this transverse component is proportional to the instantaneous missile speed, and the proportionality factor depends on the missile nose shape. The outward transverse flow is decelerated and reversed under the combined action of the hydrostatic pressure due to depth and the reduced cavity pressure resulting from expansion of the cavity after surface closure. In general these influences act on cavity cross sections at all depths, and deep closure occurs at the depth at which the collapse first becomes complete, that is, where the opposite cavity walls come together.

Most influences tend to make the closure occur at greater depths; the "momentum-propelled" missile slows down and gives less transverse velocity to the water as the depth increases; the hydrostatic pressure increases with depth; and pressure reduction within the cavity due to its expansion, occurs late rather than early. On the other hand the portion of the cavity nearest the water surface is generated first and therefore would collapse first if other influences were the same.

The deep closure which is best known occurs clearly at a point on the cavity axis, and has been called a "point closure" (Ref.(1-7)). It is most striking when produced at reduced air pressures. Figure 1-17 shows the development of the cavity due to a 1/4-inch sphere which entered water vertically at 77 ft/sec. from an air atmosphere whose pressure was 1/4 normal (Ref. (1-9)). Because of the reduced air pressure, surface closure and pullaway were very late and the upper cavity moved only a short distance from the water surface. Deep closure, which occurred near the center of the cavity resulted principally from hydrostatic pressure.

The behavior of the cavity due to a very light missile (a 1-inch polystyrene sphere) can be seen in Figure 1-18 (Ref. (1-9)). In the figure the cavity is approaching deep closure which will occur rather near the sphere because the small residual velocity can give little energy to the water.

For the vertical entry of heavy missiles deep closure is usually of the form shown in Figure 1-1D. This is a point closure but the separation is not as clean as it appears in the photograph. It can be seen better in Figure 1-19 where a downward jet is apparent in the upper segment of the cavity (Ref. (1-18)). The cavity narrows at a point rather near its upper end, and the downward jet entirely fills the neck but not the segment above it. Later a few bubbles emerge from the bubble cloud. At higher speeds, depth is acquired more rapidly and the depth of closure increases slightly.

The rapid surface closure which follows the vertical entry of right cylinders, favors still shallower deep closure (Refs. (1-9) and (1-12)). For such entries the closure often moves all the way to the base, or upper end, of the cavity. Hence no deep closure occurs, but instead the upper end of the cavity moves downward, often at a rapid pace, leaving a trail of small bubbles in its wake. This has also been described as "base closure" (Ref. (1-7)).

Similar behavior is very common after oblique entry, with two principal modifications. The fact that depth is acquired more slowly favors collapse at the base of the cavity, a base closure rather than a true deep closure. Under certain conditions the slow increase of depth causes a type of closure which, instead of occurring clearly at a point, occurs along a line, that is, a length of the cavity disappears at almost the same time. This has been called a line closure (Ref. (1-7)). Line closures have not been reported for vertical entry.

Figure 1-20 gives a series of cavity outlines obtained after the oblique entry of a missile with truncated nose, effectively a right cylinder (Ref. (1-7)). The missile was 1-1/2 inches in diameter and entered the water at an angle of 60 degrees with a speed of 1000 ft/sec. The upper line is furnished as a reference from which the point of entry can be measured. It does not represent the water surface since the entry was oblique. Cavity details at the water surface and along the sections shown by dashed lines were not available. High-speed entries are characterized by very uniform cavities, at least if the drag is low and the missile is stable. The missile in Figure 1-20 traveled almost 25 feet before pullaway occurred approximately 30 milliseconds after entry. Cavity expansion after surface closure caused a rapid pressure drop which was followed by a rapid and rather uniform reduction in cavity diameter. When the missile had traveled 32 feet, the upper part of the cavity was reduced to a line and a severe shock was sent into the water.

The types of deep closure observed during a program of oblique entries at angles between 45 and 70 degrees are shown in Figure 1-21 (Ref. (1-7). Most of the noses were truncated ogives and cones but they are here treated as right cylinders of the diameter of the truncation, as was described in the section on pullaway. Each plotted point in Figure 1-21 represents a separate water entry and the points are so placed on F-M coordinate axes as to indicate the value of these quantities for each round. Point closures, base

closures, and line closures are shown by dots, circles and crosses, respectively. A cross in a circle shows that the line closure was at the base of the cavity. The dashed line on the figure roughly divides the area into regions of point closures and of base closures.

Incandescent bulbs immersed in the water for photographic illumination, broke during a number of the tests (including that of Figure 1-20), immediately after cavity collapse. It will be seen from Figure 1-21 that rounds for which lamps broke, indicated by the darker symbols, were predominantly associated with line closures. This indicates that the most destructive pressure wave occurs at intermediate speeds where these rounds were located.

The pattern of cavity development is shown for a large range of experimental parameters in Figure 1-22 (Ref. (1-7)). The study from which these data were taken was made with 1-inch and 1-1/2-inch models at entry speeds from 300 to 1600 ft/sec., and entry angles between 45 and 70 degrees. As has been mentioned, dependence of the behavior on angle of entry was apparently rather small.

In Figure 1-22, series of sketches of cavity outlines are placed on an overall set of F-M coordinate axes, with each series of sketches positioned approximately at the F and M values of the entry. The abscissa of each small set of axes is at the water surface, and the outlines have been drawn as if the missile were traveling vertically upward instead of downward at oblique angles of 45 to 70 degrees. The coordinates of the small axes are the dimensionless distance $S = s/d$ and time $T = tU_O/d$, and the scales are shown in the center of the figure.

At the extreme left of the figure are three rounds of light weight (small M). Because of rapid deceleration these cavities did not pull away from the water surface and the deep closure occurred very near the forward ends of the cavities, as has been described earlier for vertical entry. The cavities become much longer as the value of M is increased. At the top of the figure where F and the entry speed are high, the cavities barely pull away from the surface. This is because the transverse speed given to the water is very high near the water surface and the pressure reduction of the inflowing air is able to cause surface closure only after a considerable time, and the several influences mentioned earlier combine to cause a deep closure near the missile.

At the bottom of Figure 1-22 the entry speed is less (but still rather high); surface closure occurs rapidly with a large pressure drop which causes an early pullaway and a rapid motion of the tail end of the cavity away from the water surface.

A study made with small steel spheres at vertical entry (Ref. (1-9)) showed that if the air pressure above the water is reduced sufficiently to prevent the occurrence of surface closure, then the behavior at deep closure is not affected by the actual value of the air pressure nor the size of the sphere. On Figure 1-23 graphs are

closures, and line closures are shown by dots, circles and crosses, respectively. A cross in a circle shows that the line closure was at the base of the cavity. The dashed line on the figure roughly divides the area into regions of point closures and of base closures.

Incandescent bulbs immersed in the water for photographic illumination, broke during a number of the tests (including that of Figure 1-20), immediately after cavity collapse. It will be seen from Figure 1-21 that rounds for which lamps broke, indicated by the darker symbols, were predominantly associated with line closures. This indicates that the most destructive pressure wave occurs at intermediate speeds where these rounds were located.

The pattern of cavity development is shown for a large range of experimental parameters in Figure 1-22 (Ref. (1-7)). The study from which these data were taken was made with 1-inch and 1-1/2-inch models at entry speeds from 300 to 1600 ft/sec., and entry angles between 45 and 70 degrees. As has been mentioned, dependence of the behavior on angle of entry was apparently rather small.

In Figure 1-22, series of sketches of cavity outlines are placed on an overall set of F-M coordinate axes, with each series of sketches positioned approximately at the F and M values of the entry. The abscissa of each small set of axes is at the water surface, and the outlines have been drawn as if the missile were traveling vertically upward instead of downward at oblique angles of 45 to 70 degrees. The coordinates of the small axes are the dimensionless distance $S = s/d$ and time $T = tU_o/d$, and the scales are shown in the center of the figure.

At the extreme left of the figure are three rounds of light weight (small M). Because of rapid deceleration these cavities did not pull away from the water surface and the deep closure occurred very near the forward ends of the cavities, as has been described earlier for vertical entry. The cavities become much longer as the value of M is increased. At the top of the figure where F and the entry speed are high, the cavities barely pull away from the surface. This is because the transverse speed given to the water is very high near the water surface and the pressure reduction of the inflowing air is able to cause surface closure only after a considerable time, and the several influences mentioned earlier combine to cause a deep closure near the missile.

At the bottom of Figure 1-22 the entry speed is less (but still rather high); surface closure occurs rapidly with a large pressure drop which causes an early pullaway and a rapid motion of the tail end of the cavity away from the water surface.

A study made with small steel spheres at vertical entry (Ref. (1-9)) showed that if the air pressure above the water is reduced sufficiently to prevent the occurrence of surface closure, then the behavior at deep closure is not affected by the actual value of the air pressure nor the size of the sphere. On Figure 1-23 graphs are

given of the dimensionless time of deep closure, $T_{dc} = t_{dc}U_o/d$, against F, obtained from experiments with spheres at vertical entry. The upper straight line in the figure represents the values of T_{dc} observed for entries without surface closure. It has a slope of 1.45.

Similarly, Figure 1-24 shows (Ref. (1-9a)) that the dimensionless depth of deep closure can be approximated by a straight line on log-log coordinates, when no surface closure occurs. The straight line has the equation

$$D_{dc}/d = 1.43F^{0.71}$$ (1-1)

When surface closure occurs, deep closure is sooner and shallower, and varies with missile size and with the time of surface closure (that is, with the pressure of the air above the water). On Figure 1-23 graphs are given of T_{dc} for 1-1/2-inch and 1/2-inch spheres entering from air which has normal and half-normal atmospheric pressure.

Graphs of depth of deep closure, D_{dc}/d, are given for 1 inch and 1/2 inch spheres for vertical entry from air of various pressures, in Figures 1-25 and 1-26; respectively (Ref. (1-9a)).

SHAPE OF THE EARLY WATER-ENTRY CAVITY

In the study of the water-entry cavity it is convenient to relate its development and collapse to several time periods. Considerations of the present section are restricted to the "early" cavity, covering the period over which cavity studies have principally extended: the time when the cavity is open to the atmosphere and the succeeding period during which surface closure seals it from the atmosphere and deep closures detach cavity portions from the missile.

There is a later period about which comparatively little is known, a period during which the cavity is robbed of its air partially by closures and partially by entrainment, so that the size decreases and the cavity eventually disappears. This period will be discussed in a later section.

The shape of the early cavity varies greatly because of the wide range of experimental conditions encountered and the complicated and transient system of forces which acts. For the cavity which is open to the atmosphere, the shape has been studied analytically and experimentally. For the analysis it is generally assumed that the entry is vertical and that the pressure within the cavity is the same as that above the water surface. Experimentally it is attempted to approximate the same pressure conditions by reducing the pressure of the air above the water to a very low value. Although these experimental conditions are not paralleled in the ordinary use of missiles, the results obtained are instructive and furnish a basis on which realistic solutions can be built.

The "Ideal Cavity"

It is useful at the start to consider missile behavior and cavity development under four simplifying assumptions: vertical water entry, constant missile speed, cavity pressure equal to the ambient pressure, and the absence of gravity. It is assumed that there is an "ideal" cavity shape which would be obtained under these conditions and that this shape can be approximated experimentally. Although a gravity-free condition is unrealistic, the effect of gravity (through hydrostatic pressure) does not become observable on a particular cavity cross section during some short time interval. During this time the cavity produced has approximately the ideal shape. For a long cavity, some portion nearest the missile nose may be very close to the ideal shape although further back the cavity will deviate considerably from it. The ideal portion may be of appreciable size if the entry speed is high, but under other conditions it may be very short; the portion which is ideal will be spoken of here as an "ideal cavity".

It has been known for a long time (Ref.(1-11)) that water-entry cavities are approximately paraboloidal, and recent measurements have shown (Ref. (1-18)) that the ideal cavity is almost exactly paraboloidal except near the missile nose. Theoretical arguments and experimental measurements lead to the conclusion that Ideal Cavities are

a. identical when formed by the same missile at different speeds,

b. proportional to the missile size when formed by two missiles identical except for size, and

c. proportional in size to the square root of the drag forces at the same speed, when formed by dissimilar missiles.

An approximation to the universal form of the ideal cavity equation was found experimentally to be (Ref. (1-18))

$$\frac{x}{C_D^{1/2} d} = 1.716 \left(\frac{y}{C_D^{1/2} d} \right)^2 \tag{1-2}$$

where the equation has been written so that the cavity outline passes through the origin of coordinates. The distance between the vertices of the analytical and experimental outlines will be mentioned later.

The assumption that the pressure in the cavity is the same as that of its surroundings means that this axially symmetric cavity has zero cavitation number. The equation of the outline of this cavity has never been derived theoretically, although the equation for the corresponding cavity due to a two-dimensional strip, with $\sigma = 0$, is found by complex variable methods to be (Ref. (1-28))

$$x = \frac{L}{4 + \pi} \left[t \sqrt{t^2 - 1} - \log(t + \sqrt{t^2 - 1}) \right]$$

$$y = \pm \frac{L}{2} \pm \frac{2L}{4 + \pi} (t - 1), \qquad t \geq 1$$

$$(1-3)$$

Here, L is the width of the infinite strip and t is merely a parameter connecting the equations. Equation (1-3) is very close (Ref. (1-18)) to the parabola

$$x/L + 1.00 = 1.588 \ (y/L)^2 \tag{1-4}$$

(within 1.0% for 1.7 < x < 23 and within 2.4% for 1.3 < x < 55).

Figure 1-27 contains cavity outlines produced under various conditions, which approximate the ideal cavity (Ref. (1-29)). The experimental outlines were obtained, because of availability, from cavities due to vertical water entry from atmospheres of reduced pressure. Presumably the shape of these water-entry cavities, insofar as they are ideal, should not differ from corresponding shapes generated during steady cavity running, except that the reduced pressure increases the extent of the ideal portion of the cavity.

The outlines of Figure 1-27, which were scaled in accordance with Equation (1-2), were obtained from the following entries or conditions: A) 1-1/2-inch-sphere at 116 ft/sec, B) plot from Equation (1-2), C) plot from Equation (1-3), D) 1-1/2-inch sphere at 41 ft/sec, E) 1/2-inch sphere at 208 ft/sec, F) 1/4-inch right cylinder at 37 ft/sec, and G) 45° cone at 139 ft/sec. If the outlines are superimposed, with axes and cross lines coinciding, the agreement is very close except near the vertex. Cavities agree in this way, of course, only insofar as they are ideal. For atmospheric pressure the portion of the cavity that would approximate the ideal cavity would be considerably shorter.

The distances in calibers between the vertices of the analytical and experimental outlines were found to be: sphere 0.5; right cylinder 0.4; 45° cone-0.2. A positive value means that the vertex of the computed outline is ahead of the nose tip of the missile.

The ideal cavity represents a maximum envelope within which the actual cavity will lie. The concept should apply as well to oblique entries and to horizontal cavity generation as to vertical entry.

Shape Predictions for the Open Cavity

In 1919 Mallock gave the first quantitative theory (Ref. (1-30)) for the shape of the water-entry cavity in terms of the motion of the

cavity wall. He assumed that the radial velocity of the wall at any depth h is constant and equal to $(\theta U_1 - \sqrt{2gh})$. The first term is proportional to the velocity U_1 of a sphere at depth h. The second term is the Torricelli velocity. This formula gives a constant radial wall speed: outward if above a certain depth, inward if below.

Ramsauer, in 1927 (Ref. (1-11)) experimented with spheres at speeds above 2000 ft/sec, much higher than in other early water-entry studies. He confirmed the fact that the water has a velocity component in the radial direction which is proportional initially to that of the sphere, and concluded that later this speed is inversely proportional to the distance from the trajectory, so that the area of a slice of the cavity increases at a constant rate.

A model proposed by Biot (Ref. (1-31)) was ingenious but based on incorrect premises, and will not be discussed here.

Richardson, in two papers (Refs. (1-32) and (1-33)), attempted to predict the velocity given to the water from the angle of the cone which approximates the water-entry cavity.

Blackwell (Ref. (1-23)) built on Richardson's model. He started with an initial transverse velocity λU_1 proportional to the instantaneous speed of the sphere, and then postulated a constant deceleration $2\mu h/d$, proportional to the distance below the water surface and inversely proportional to the sphere diameter. He applied the method to oblique as well as to vertical entries.

McMillen verified (Ref. (1-34)) that the cross-sectional area of the cavities due to spheres increases at an almost constant rate for most of its growth, and he gave the formula

$$dA/dt = 1.77d^2U - C \qquad (1-5)$$

where C is a function only of the sphere diameter, and all quantities are in cm-sec units. He states (Ref. (1-35)) that the maximum cavity area at a given depth was found to be proportional to the space rate at which the sphere lost energy, and he suggested in unpublished work that, when no surface closure occurs, this rate of energy loss should equal the work done in the expansion of unit length of cavity to the maximum diameter against hydrostatic pressure. This latter idea was investigated by May (Ref. (1-9)) for the vertical entry of 1/2 inch missiles. He and that the ratio (dE/dh)/pA, where p is the hydrostatic pressure, varied from 0.8 at a 4-inch depth to 1.1 at 24 inches. This variation is due to the fact that flow is not restricted to horizontal laminae, but follows flow lines somewhat like those shown in Figure 1-28 (Ref. (1-21)).

Loomis sta   . (Ref. (1-34)) that Blackwell's formula works well for Froude numbers of about 14 and McMillen's for about 3000, but that neither is good between. Birkhoff (Ref. (1-10)) said that Blackwell's formula predicts D_{dc} and T_{dc} well but that it makes plots of cavity diameter against time parabolic while they are nearer to being elliptical.

In 1951 Birkhoff and Isaacs developed (Ref. (1-21)) a superior hydraulic model of cavity formation at vertical entry, and a detailed application of the model to measured cavities was made by Abelson (Ref. 1-36)). The dynamic basis of 'he model can be seen in Figure 1-29 which is taken from (Ref. (1-36)). The model assumes that the missile, when at any depth, generates a flow only in a thin spherical shell centered at the entry point and containing the missile. In Figure 1-2?A is shown the shell of radius r and a sphere which has not yet reached the shell. In sketch b the sphere has reached the shell and has given the water in it motion away from the axis. The energy in the shell is that expended against drag as the sphere travels a distance equal to the width of the shell. The system is assumed to be conservative so that the energy given to the shell remains as the sum of its kinetic and potential energies. Sketch c shows the system at a later time. Within the shell an angle Θ_a about the axis has become empty of water and this water is now within the shell but above the original water level. The upward flow continues until some maximum angle Θ_m is reached, when the energy is all potential, and the angle then begins to decrease. The solution of the problem is straightforward and leads to the result

$$\frac{d\Theta_a}{dt} = \frac{\sqrt{4g}}{\sqrt{r}} \csc \Theta_a \sqrt{\frac{\cos \Theta_a - \cos \Theta_m}{\ln \left[\frac{(2 - \cos \Theta_a)(1 + \cos \Theta_a)}{\cos \Theta_a (1 - \cos \Theta_a)}\right]}} \qquad (1-6)$$

where

$$\cos \Theta_m = (1/2) \left[1 - \frac{\frac{C}{D} \frac{A}{c} v^2 \frac{e-2r\alpha}{p_o}}{2\pi \, gr^3}\right]$$

The agreement between Birkhoff's model and the actual cavity fails near the water surface where the model does not represent the flow. Abelson found that the agreement was otherwise generally good almost to deep closure (Ref. (1-36)), as is seen in Figure 1-29d. The failure of the model near deep closure is due to the considerable depth at which closure occurred and the change of flow pattern as the sphere becomes deeper. From Figure 1-28 it is seen that the flow becomes centered about a point much lower than the water-entry point, so that there is a flow toward the point of deep closure. Figure 1-28e shows that the agreement of the model with experiment is good also for entries from air at normal pressure, up to the time of pullaway.

Birkhoff and Isaacs have discussed also the application of their model to oblique entry where it is generally applicable but more difficult in application.

While the entry cavity approaches a paraboloidal shape, it is nearly conical over much of its length. This was especially observed by early writers (Refs. (1-10), (1-11), (1-23), (1-32), (1-33), and (1-37)) who generally gave the cone angle for the water-entry cavity

due to a spherical nose as 6° half angle, with larger angles for missiles of larger drag coefficients.

Graphs of cavity diameter at various depths are given in Figure 1-30 (Ref. (1-9)) for the cavity due to the vertical entry of a 1-inch sphere. The pressure of the air above the water was low enough to prevent surface closure. Under such conditions the slice of cavity at the water surface never stops expanding until it is filled from below. For the deeper cross sections the cavity expands to a maximum diameter and then contracts. Deep closure occurred at a 24-inch depth. The collapse of the cross sections is seen to be slower than the expansion, and Figure 1-31 gives an acceleration graph from the same data, for a depth of 22 inches.

The Early Cavity After Oblique Entry

Early cavities due to oblique entry differ significantly from those for vertical entry principally because of two influences: the much later occurrence of surface closure and the asymmetry of the flow above and below the nose of the missile. The greater increase of cavity volume resulting from late surface closure is aided by the delay of deep closure, due to the smaller depths attained when the entry is oblique.

The more constrained conditions below the missile might be expected to make the pressure there greater than that above the nose where the escape of the water is easy, but the opposite condition exists. While the flow separates readily above the nose, a slender void tends to form on the under side. At high Reynolds numbers air flows into this region, but at lower values the air's viscosity prevents it. When this happens, the void is filled only with water vapor, and the pressure is the saturation vapor pressure rather than the pressure of the atmosphere. The location of this closed cavity is shown in Figure 1-32 (Ref. (1-38)). The presence of an unvented cavity space causes the well-known "underpressure" below the nose. This may have a large effect on the trajectory at entry as will be described in another section.

Cavity Dimensions

A graph of cavity volume after vertical entry of a sphere was given in Figure 1-9 (Ref. (1-9)) and another is contained in Figure 1-33 (Ref. (1-18)). While these graphs are similar, the volume of the cavity attached to the sphere decreased much more at the first deep closure in the entry of Figure 1-9 because of the reduced density of the atmosphere above the water. After the three deep closures in Figure 1-33 almost a fifth of the maximum volume is still contained in the attached cavity.

Figure 1-34 shows a graph of cavity volume for the vertical entry of a right cylinder. For the sphere the maximum volume was reached very shortly after pullaway; for the right cylinder the cavity

continues to expand for a considerable time. Surface closure for the cylinder occurred very early while the cavity was expanding strongly. Hence a rapid pressure drop occurred which triggered an early pullaway, but could not immediately stop the expansion of the cavity. For vertical entry the dependence on velocity of the maximum cavity volume has not been reported. Corresponding experimental data for oblique entry, which will be discussed later, indicate that the maximum volume may be roughly proportional to the cube of entry speed.

A comparison is made in Figure 1-35 of the cavity development after vertical water entry of a sphere, with and without surface closure (Ref. (1-18)). When the air pressure above the water was reduced sufficiently to prevent surface closure, the cavity grew to a size which was 11 times that produced by an entry from normal air.

For oblique entry it has been shown (Ref. (1-7)) that cavity development seems to depend significantly on only three parameters: the angle of entry, Θ, the Froude number, F, based on truncation diameter, and the dimensionless effective mass, $M = m/\rho d^3$. Further, the effect of angle of entry, for angles between 45° and 70° appears to be small.

In Figures 1-36 to 1-41, graphs are given (Ref. (1-7)) for the size of cavities due to the oblique water entry of missiles with Effective Mass values of 11 and 69, which might be characterized as light and medium-heavy rounds. Figures 1-36 and 1-37 contain graphs of volume against dimensionless time for various Froude numbers, and Figures 1-38 and 1-39, and Figures 1-40 and 1-41 give corresponding data for length and diameter, respectively, for the same cavities.

The volume curves in Figures 1-36 and 1-37 are similar and differ principally in two respects: greater volumes are attained for the heavier missiles because of the smaller deceleration; and at M = 11 all rounds had point closures while at M = 69 "base closures" occurred rather than deep closures. Hence for M = 11 the curves show discontinuous changes of volume at deep closure while at M = 69 the volume varies continuously down to very small values. A slight increase in the maximum volume of the cavity as the obliquity increased from 45 to 70 degrees, was neglected in the preparation of Figures 1-36 and 1-37.

Plots of length and diameter for cavities due to the vertical entries of a sphere and a right cylinder, were contained in Figures 1-33 and 1-34. The behavior is similar for the two nose shapes. Cavity length increases continually until deep closure occurs, although pullaway takes place much earlier for the cylinder. For both noses maximum diameter occurs slightly before the time of maximum volume.

For oblique entry the following details of the length and diameter graphs in Figures 1-38 to 1-41 might be noted in relation to the volume graphs of Figures 1-36 and 1-37. The maximum volume, as has been seen, is greater for the heavier missile (greater M). This behavior is due to the cavity length, since the diameter varies in the

reverse manner, that is, the maximum diameter is greater for M = 11 than for M = 69. This is explained by the greater deceleration at M = 11, which prevents a considerable decrease of the cavity pressure, and permits the diameter to continue increasing. On the other hand, the greater deceleration at M = 11 has a direct effect in lessening the cavity length.

Because, in Figures 1-38 and 1-39, cavity length is plotted against the dimensionless distance traveled by the missile, the early parts of all graphs lie on the same straight line, with a 45-degree slope. Points on this line correspond to cavities which have not pulled away from the water surface.

All of the graphs for volume, length and diameter at M = 11 have vertical sections indicating a (point) deep closure, as is seen in Figure 1-22. At M = 69 "base closures" rather than deep closures generally occur. Figure 1-22 showed, however, that (point) deep closures start to appear at the highest value of F, and there is some indication of this in the volume and length graphs for F = 550.

In Figures 1-42 to 1-44, contours are given on F-M coordinate axes, of the maximum values of the volume, length and diameter. The dependence on M is generally small. For the volume it is only at very low values of M that appreciably higher values of F are required to produce the same maximum volume as for heavier missiles. It is interesting that the maximum diameter is only slightly dependent on M (Figure 1-44) because it occurs near the water surface before the deceleration effect becomes significant.

Some slight numerical inconsistencies are apparent between the contour maps and the families of graphs for various values of F. These result from random variations from test to test and the different effects these have in the smoothing processes used in obtaining the two sets of contours.

If maximum cavity volumes are read from Figure 1-42 for M = 100, it is found that a graph against F on log-log coordinates can be represented by a broken straight line with a change of slope at F = 500. The maximum volume varies as $F^{2.4}$ below F = 500, and as $F^{2.0}$ above.

In general, deep closure is not a suitable event for correlating oblique-entry data because it is often impossible to assign a time and position to its occurrence. Two parameters which might replace it are shown in Figures 1-45 and 1-46; the length of the cavity when it is half the distance that the missile has traveled from first water contact; and the time at which this condition occurs. It generally exists at the time of deep closure when there is one; and when the base of the cavity is traveling rapidly down from the water surface, when there is not.

THE LATER WATER-ENTRY CAVITY AND ITS DISPERSAL

The early water-entry cavity discussed in the previous section, included the cavity while open to the atmosphere and its sealing off by surface or deep closures. The present section will comment on the later cavity - its persistence and its collapse and dispersal. It has been mentioned that comparatively little is known about this later cavity. Its general behavior is understood, but available details do not permit the prediction of cavity size lon, after entry. To provide such information is not easy; observations require a large instrumented facility, it is improbable that data derived from model studies can give reliable information about the collapse of large cavities (Ref. (1-38)). fins and other appendages tend to break up the cavity in unpredictable ways, and statistical analyses are required because of the variation of behavior due to minor differences in experimental conditions.

The size of the closed water-entry cavity depends strongly at any time on the amount of air which it contains, but this amount is not known, especially long after entry. At first the cavity is filled with air at a pressure below atmospheric by an amount depending on the missile speed. A rough estimate of the air loss from the attached cavity during deep closures may be possible from the study of photographs, but usually clouds of small bubbles are left in the wake of the cavity and the estimation of their volume is impracticable.

For vertical entry the cavity development shown for a sphere in Figure 1-33 is probably typical. The three deep closures included in the graph will be followed by others until the cavity has become quite small. At some point the cavity length becomes insufficient to include the tail of the missile, the rear end of the cavity closes on the afterbody, and deep closures cease. Further dissipation of the cavity is due to entrainment of its air in the flow along its walls, especially in the very turbulent region where this flow meets the missile surface. The last remnants of the cavity appear at points of lowest pressure on the missile, such as behind a blunt after-body. Of course the cavity will not disappear completely if the missile speed is sufficient to sustain a vapor-filled cavity. At higher entry speeds the cavity will be larger initially and will persist longer because of the greater mass of air contained and also because of the higher continuing speed of the missile. On the other hand, for the slow vertical entry of a right cylinder usually the small cavity closes initially on the afterbody. The later history of such a cavity is similar to that of a fast-entering missile at a corresponding, much later, cavity stage.

In general, cavity disappearance occurs soonest if the initial cavity is small, and large cavities generated at oblique entry tend to last longer than the vertical cavities generated at the same missile speed. The rate of cavity dispersal increases with the deceleration of he missile. Although a high-drag missile generates a large cavity, its deep closures detach most of the cavity volume from the missile (Fig. 1-18). Bodies which broadside after entry lose

their cavities rapidly. Small cylinders, called spigots or probes, have been used on the front surface of blunt noses to cause a small cavity to close on the missile itself, for rapid dispersal. Wilcox and Waugh reported (Ref. (1-39)) that the cavities due to missiles with artificially roughened noses, were shed very rapidly.

Some interesting points may be observed in the oblique entry of Figure 1-20. When the missile had traveled 30 feet, its speed had dropped from 1000 to about 240 ft/sec. If the cavity were filled only with water vapor, the cavitation number based on this velocity and the pressure above the water or at the cavity midpoint would correspond to a steady cavity length of less than two feet instead of the observed length of 30 feet. The cavity is not steady nor is it only vapor filled. The cavity pressure cannot differ much from that of its surroundings.

For oblique entry several processes are observed by which air is taken from the cavity. When "base closure" occurs and the upper end of the cavity travels rapidly toward the missile, a long, narrow, vortical wake is commonly seen behind the cavity, made visible by a trail of bubbles which are individually too small to be resolved. A greatly increased formation of detached bubbles is often associated with re-entrant jets (to be discussed later) which may alternate with deep closures. Increased entrainment of air occurs in the large turbulence which arises when these jets strike the cavity wall.

With present knowledge it is not possible to predict the variations of the cavity dispersal mechanism, nor the rate of rather steady entrainment from air-filled cavities attached to cavity-running missiles. During cavity running the missile usually slows down and air is lost from the cavity, and both of these facts tend to increase the cavitation number. This means that the steady cavity would have to be smaller and have a smaller L/d_m. The water-entry cavity tends toward such a condition; it never reaches equilibrium but always lags behind.

Studies of artificially vented cavities in the water tunnel have shown that jets are formed at the higher values of σ (Ref. (1-40)). At high ventilation rates where σ is smaller, trailing vortices appear. It is doubtful that the same vortex condition occurs in the natural cavity. From the water-tunnel results it might be possible to predict the steady entrainment rate if cavity and flow conditions were accurately known.

Cavity Added Mass

It is well known that a fully wetted missile traveling through water behaves as if its effective mass (called "virtual mass") were greater than the actual mass of the missile due to the added mass or induced mass. This is the mass of a quantity of water which may be regarded as sharing the velocity of the missile and which must be accelerated when the missile is accelerated. There is added mass for the cavity-running missile also but it is less than for the fully

wetted missile because the wake region has been replaced by a cavity of negligible mass. Estimates of cavity-running added mass appear to have been made only for the sphere. Birkhoff estimated (Refs. (1-21) and (1-41)) the added mass of cavity-running spheres to be about 60 percent that for a fully wetted flow, or about three tenths the displaced mass of water. For oblique entry (Ref. (1-21)) he gave a value nearer four-tenths the displaced mass.

Because of cavity added mass the drag coefficient of a sphere calculated from its deceleration after water entry appears to be decreased, and the coefficient for a sphere of light material such as a plastic is decreased more than that of a steel sphere. May and Woodhull used this idea (Ref. (1-42)) to determine the cavity added mass for the sphere. They obtained a value of about one-tenth the displaced mass of water. Birkhoff pointed out (Refs. (1-21) and (1-41)) that, because of the free surface and the fact that the water does not immediately take the velocity of the sphere but lags behind it, there will be a distortion of the cavity, and the experiment does not measure the full added mass.

The Re-Entrant Jet

The re-entrant jet frequently accompanies both the steady cavity and the water-entry cavity. In the study of the potential flow about an ellipsoidal solid, it is shown that the reverse curvature (convex within) at the rear of the ellipsoid can only occur because of the pressure exerted on the water by the surface of the ellipsoid in the vicinity of the rear stagnation point. When the solid ellipsoid is replaced by an ellipsoidal cavity, this flow becomes impossible because the cavity is unable to exert the required pressure at a rear stagnation point. The pressure in the cavity is substantially constant and less than the ambient pressure so that the flow must continue to be concave within. The flow, instead of being turned away from the ellipsoid at its rear, continues to bend inward to form a "re-entrant jet".

The closures of water-entry cavities are also accompanied by jets. At a deep closure the flow has had an inward component at the region of deep closure, from all sides. The pressure is built up where these flow lines converge, and the water escapes in the only free directions, which are along the axis of the cavity. From momentum considerations it is necessary that an opposing pair be generated. Naturally the intensity of this jet pair will depend on the strength of the flow toward the closure point.

The first "jet" that is observed after a vertical water entry is hardly a jet at all but a column of spray. At the time when surface closure is nearly complete, spray in the region above the cavity is blown down into the cavity by the inflowing air. The resulting column of spray can be seen in Figures 1-1B and 1-10, just after the first appearance, and at a later stage in Figure 1-1C. In Figure 1-1C pullaway has occurred; flow has converged on the entry point and generated upward and downward jets. At this time the spray jet is

followed by a so-called "solid" jet, which can be seen also in Figures 1-17, 1-18, and 1-19. In Figure 1-19 the jet is of sufficient size to fill the restricted cross section where deep closure is occurring, and it has actually completed the closure.

The very flat appearance of the top of the cavity in Figures 1-17 and 1-19 is due to the jet. The top of the cavity is concave because of the flow of the water downward to form the jet. The flat section seen is the rim which appears flat because of its symmetry.

Somewhat different behavior is to be expected for entries with considerable obliquity. The slow surface closure and pullaway denote a slow flow of both air and water toward the entry point, promising little downward jet, if any.

In some vertical entries the jet travels the length of the cavity, often striking the missile, sometimes disturbing it. At other times a cloud of bubbles may appear beside the missile nose as the jet penetrates the cavity wall carrying air with it.

The jets are usually apparent in photographs of deep closure and may range from very weak to very strong, depending on the intensity of the flow. A weak downward jet can be seen in Figure 1-1D. Perhaps the most striking jet formation is the upward jet from deep closure which has been observed after vertical entry of a sphere from an atmosphere of low enough pressure to prevent surface closure. The upward jet starts out very thin but continues to widen until its base or root at the cavity boundary finally reaches the water surface. The jet at that time may have a diameter five or more times that of the sphere diameter. The velocity of the upward jet from deep closure has been reported to be more than twice the speed of the projectile (Ref. (1-25)).

Flow Near the Cavity

Flow in the water near the water-entry cavity was investigated experimentally by Birkhoff and Caywood (Ref. (1-43)). A pattern which they obtained for the flow due to the vertical entry of a sphere has been given in Figure 1-28. There is some flow in advance of the sphere but the main flow is set up within spherical shells centered initially at the point of water entry as was described in connection with the model sketched in Figure 1-29. As the cavity widens, reaches a maximum diameter, and then contracts, the lateral flow at any instant may be outward or inward at various depths. The region where collapse is taking place is a "sink" region, and flow is toward the axis both from above and below, as is seen in Figure 1-28.

Birkhoff and Caywood studied also the oblique entry of spheres. The general features are similar to those for vertical entry and the flow lines were found to be approximately concentric circles centered at the point of impact. On the other hand, velocities above the cavity are considerably higher than below. Observations of imperfections on

the cavity wall after vertical entry shows that there is almost no
flow along the wall until about the time of pullaway. As the downward
jet develops at the top of the cavity, an upward flow is apparent
on the upper wall.

VENTILATION AND PRESSURE IN THE WATER-ENTRY CAVITY

Before surface closure occurs air rushes into the cavity from
above the water surface. During this time the pressure in the cavity
will be less than atmospheric by a pressure difference which is
required to produce the air flow. At first this flow is through an
open tube but the beginning of surface closure causes a restriction
in the opening, with an increased pressure drop. The pressure
difference needed to produce the flow into the open cavity has
generally been taken as $(1/2) \rho U^2_o$ (Refs. (1-9), (1-13) and (1-21)).
This is the drop which would occur if the flow were steady and had
the speed of the missile at impact.

After surface closure the cavity is a closed air container.
Because of the rapidity of volume changes of the early cavity, the
expansion or contraction is presumably adiabatic.

The constant shape of the part of the cavity near the missile
nose leads to an interesting conjecture concerning the ventilating
flow. In Figure 1-3, if the cavity outline in the third photograph
is superimposed on the seventh, it will be found to be exactly the
same in their common portion. It is reasonable that not much change
will take place within this invariant volume as the cavity grows.
The volume may be thought of as a sealed or frozen space which travels
forward in the water. The air within it is not flowing forward into
a converging tube but its trapped air is traveling forward in a container
of constant shape and volume (even though its wall is continually
made up of different surfaces of liquid). Naturally there is some
flow within this volume and it probably changes as the cavity changes,
but primarily it contains almost stagnant air.

Instead of flow into a converging pipe, the flow is closer to
that which follows a piston in a uniform cylinder, retreating downward
from the water surface. Above the water the air flows down through
the surface into an orifice which is continually growing.

In 1970 Abelson described determinations he had made (Ref. (1-24))
of the pressure in water-entry cavities. Prior to that work only two
isolated measurements of this pressure had been reported (Refs. (1-44)
and (1-45)). In most of his work Abelson used two pressure probes
mounted in the water one above the other, and near the vertical line
of fire, so that they became enveloped in the cavity. Figure 1-47
contains sketches of traces from probes 3 and 15 inches below the
water surface for vertical entry of a 3-inch 70° half-angle cone
at 145 ft/sec. Nine outlines from high-speed photographs are shown
for correlation with the pressure traces. Figure 1-48 gives pressure
traces from the two probes and also plots of cavity volume over the

same time period. The solid-line graph shows the volume based on the cavity outline below the water surface, and the dashed graph was corrected for the volume above the water surface before pullaway and the volume occupied by the downward jet as shown by the shaded areas below the water surface in Figure 1-47. It appears doubtful that the whole of the shaded areas represent "solid" water, and the later "true" volumes are probably somewhat too small.

For this water entry, Abelson's measurements showed pressure drops 15 or 20 times as large as the commonly assumed value, $1/2\rho U^2_0$. His values correspond however to the time of surface closure when the drop would be greater than during the time when the cavity is completely open, but his results show the cavity pressure dropping almost linearly with time from water impact almost to the time of surface closure. It is not evident why this variation is so strong.

After both probes are in the cavity (beyond the intersection of the upper graphs) the graphs nearly coincide. This means that no appreciable pressure gradient was present, nor did Abelson find any pressure difference between two probes placed 4 inches above and 2 inches below the water surface, before surface closure. Further he observed no transverse gradient in the cavity. Indications then are that, within experimental error, the pressure is uniform throughout the open cavity, but changes strongly with time.

A study of the volume-pressure variation after surface closure showed reasonable agreement with the assumption of adiabatic expansion.

Pressure graphs for various entry angles are compared in Figure 1-49. Only the portions of the graphs to the right of the circles are significant since the remainder represents pressure in the water. In general the pressures after vertical and 60° entries are closely the same, but those for 45 degrees are somewhat higher. The smaller pressure drop is due to the later surface closure after 45-degree entry.

An interesting result was obtained by plotting against entry velocity, the minimum pressure due to cavity expansion after surface closure, as shown in Figure 1-50. The straight line in Figure 1-50a for vertical entry is well defined by the data points. This graph is repeated without the vertical data in Figure 1-50b. Data for entries at 60 degrees are in good agreement with the vertical data, while data for 45-degree entries define a straight graph at higher cavity pressures.

It has been remarked that flow into the water-entry cavity is not the flow into a converging tube because the front end of the cavity grows to accommodate the air which had formerly occupied an almost identical volume and shape. There are other details of the flow that merit attention, even though they might be regarded as obvious.

The ventilating air flows past the water surfaces which are the cavity walls, and a boundary layer forms on these walls with zero relative velocity at the wall. The boundary layer thickens near the missile nose and this will prevent complete stagnation of the air in this region.

Flow conditions relative to the missile are totally different from those of free flight in air. There is no flow past the missile and hence the "base pressure" is not related to such a flow. Rather the surrounding air is traveling with the missile.

It was mentioned earlier that an "almost steady" cavity is sometimes observed long after water entry, large enough to enclose the missile, and appearing rather like an ellipsoidal body traveling through the water. Within such a cavity the air flow may be expected to approximate that previously discussed for the steady cavity. The pressure in the "almost steady" cavity can be estimated (Ref. (1-7)) by regarding the cavity as steady and applying the relations between cavitation number and fineness ratio found by Reichardt (Ref. (1-48)). Since the cavity long after water entry will probably, if momentum propelled, be traveling at a slow speed, the fact that the cavity is long enough to envelop the missile, requires that the pressure be almost equal to the ambient pressure. Because of the head of water above the missile the cavity pressure may well be above atmospheric pressure.

PRESSURE IN THE WATER AFTER ENTRY

The water entry of a missile is, of course, accompanied by pressure changes in the water near the entry cavity. Since there is no pressure discontinuity at the cavity wall, the water pressure at the wall must equal the cavity pressure. For a vapor-filled cavity evidently the necessary pressure reduction in the water must be effected in accordance with the Bernoulli equation as a result of an increased velocity of flow along the cavity. An interesting case is that of vertical water entry from an atmosphere with a pressure close to the vapor pressure of water. Within the cavity the pressure will be close to vapor pressure. In the neighboring water the static pressure will be that of the head of water. The wall pressure will be brought down to the pressure of the cavity by a gravity-induced flow along the cavity wall. The same behavior must exist at a closed vertical cavity in which the pressure is substantially uniform.

Abelson's measurements (Figures 1-48 and 1-49) include readings of the pressure in the water near the cavity; consisting especially of a rapid increase in pressure as the descending missile approaches the gage. In connection with earlier water-entry pressure measurements, Hoover and Dawson (Ref. (1-45)) used a half-body approximation (a superposition of a single source on a uniform flow) to simulate the cavity free surface, and gave graphs of pressure due to the oncoming missile. This approximation gives at least a qualitative picture of the pressure distribution, although it is known (Ref. (1-47)) that the

approximation to the cavity shape and pressure is not very close. The method leads to the formula

$$\Delta p = 1/2\rho U^2 (2 \cos\theta/R^2 - 1/R^4) \qquad (1-7)$$

where the symbols are explained in Figure 1-51. The figure shows the pressure changes to be expected at two and six radii from the path of the sphere. They are related to the instantaneous values of the sphere's velocity, and are significant only until the cavity wall is reached.

In addition to pressure changes related to the missile velocity there are others of an impulsive nature. Pulses of this type are observed which are due to the impact of the missile on the water surface, but shocks due to cavity collapse may be much more severe. Intense shocks have been reported (Ref. (1-7)) because of "line closures" as was described in connection with Figure 1-21.

For vertical entry at considerably higher speeds, intense shock waves have been reported (Ref. (1-48)) and have been photographed by the shadowgraph technique. These shock waves are attached to the missile (Ref. (1-49)) when the missile speed is supersonic in water, but become detached, with the missile falling behind, as deceleration lowers the speed below the speed of sound.

SURFACE APPEARANCE OF THE WATER-ENTRY CAVITY

The surface appearance of the steady cavity has been discussed elsewhere (Ref. (1-27)) with a description of the principal causes of rough surface texture. These causes are almost identically the same for the water-entry cavity, but the relative importance of various causes differs somewhat.

Longitudinal striations are commonly observed on the water-entry cavity when the entering missile has a nose from which "smooth" separation occurs. The cause of this can be seen in Figure 1-10 where separation has occurred from a sphere along a very ragged line. The striations can be followed along the length of the cavity, past the meniscus onto the splash sheath. When the sheath domes over just before surface closure, strings of drops can often be observed above the dome, evidently representing thick regions of the striations which did not get sucked into the cavity.

When "abrupt" separation occurs from a flat-nosed cylinder or the truncation on an ogive or cone, the cavity surface is commonly quite smooth and transparent but burrs or other imperfections at the edge cause shallow cavity striations. For spinning missiles, striations are deformed into helices and have been used in estimating the spin rate (Ref. (1-50)).

A roughened and opaque cavity surface is most often due to the spray jet which travels down the cavity at about the time of surface closure. In Figure 1-17 this roughening is seen, together with a coating of small bubbles created by drops of spray when they struck the cavity surface.

A transverse pattern of ridges is sometimes generated by vibrations of the missile after its impact on the water surface (Ref. (1-22)). Rather large-scale transverse corrugations may be created on the cavity by a forward-backward oscillation of a part, or all, of the separation line on the missile (Ref. (1-39)).

REFERENCES

1-1. Worthington, A. M. and Cole, R. S., "Impact with a Liquid Surface, Studied by the Aid of Instantaneous Photography." Phil. Trans. Roy. Soc. 189A, pp 137-148, 1897

1-2. Worthington, A. M. and Cole, R. S., "Impact with a Liquid Surface, Studied with the Aid of Instantaneous Photography," Phil. Trans. Roy. Soc. 194A, pp 175-199, 1900

1-3. Worthington, A. M., A Study of Splashes, Longmans, Green and Co., London, 1908; reprinted, The Macmillan Co., New York, 1963

1-4. Kaye, G. W. C. and Laby, T. H., Tables of Physical and Chemical Constants, John Wiley and Sons, Inc., New York, 13th Ed. 1966

1-5. Wilson, W., "Tables for the Speed of Sound in Distilled Water and in Sea Water," NOL NAVORD Report 6747, 1959

1-6. Waugh, J. G. and Stubstad, G. W., "Water-Entry Cavity Modeling, Part 2, Oblique Cavities," NOTS NAVORD Report 5365, 1957

1-7. May, A. and Hoover, W. R., "A Study of the Water-Entry Cavity," NOLTR 63-264, 1965

1-8. White, F. G., "Photographic Studies of Splash in Vertical and Oblique Water Entry of Sphere," NOTS NAVORD Report 1228, 1950

1-9. May, A., a) "On the Entry of Missiles into Water," NOL NAVORD Report 1809, 1951; b) abridged version, "Vertical Entry of Missiles into Water," J. Appl. Phys. 23, pp 1362-1372, 1952

1-10. Summary Technical Report of the National Defense Research Committee, "Mathematical Studies Relating to Military Physical Research," Vol. 1., Washington, D. C., 1946

1-11. Ramsauer, C. and Dobke, G., "Die Bewegungserscheinungen des Wassers beim Durchgang schnell bewegter Kugeln (Water-Motion Phenomena due to the Passage of High-Speed Spheres)," Ann. d. Phys. 4F, 84 pp 697-720, 1927

1-12. Gilbarg, D. and Anderson, R. A., "Influence of Atmospheric Pressure on the Phenomena Accompanying the Entry of Spheres into Water," J. Appl. Phys. 19, pp 127-139, 1948

1-13. May, A., "Effect of Surface Condition of a Sphere on its Water-Entry Cavity," J. Appl. Phys. 22, pp 1219-1222, 1951

1-14. Wagner, H., "Ueber Stoss- und Gleitvorgänge an der Oberfläche von Flussigkeiten (Impact and Planing on the Surface of Liquids)," Z. f. AMM 12, pp 193-215, 1932

1-15. Shiffman, M. and Spencer, D. C., "The Force of Impact of a Sphere Striking a Water Surface (Second Approximation)," National Def. Res. Comm., Appl. Math. Panel Report 42.2R, 1945

1-16. Cooper, E. P., "Splash Contours in Water Entry: 1. Normal Entry of Spheres and Cones," NOTS TM 50-15, 1950

1-17. Mason, M. and Slichter, L. B., "Water Entry and Underwater Ballistics of Projectiles," CIT OSRD Report 2551, 1946

1-18. May, A., "The Cavity After Vertical Water Entry," NOLTR 68-114, 1968

1-19. Cooper, E. P., "Theory of Water Entry of Missiles with Flat Noses," NOTS NAVORD Report 1154

1-20. Cooper, E. P., "Splash Contours in Water Entry. II. The Forward Splash on a Cylinder in Broadside Oblique Entry," NOTS TM 50-16, 1950

1-21. Birkhoff, G. and Isaacs, R., "Transient Cavities in Air-Water Entry," Bureau of Ordnance NAVORD Report 1490, 1951

1-22. Waugh, J. G. and Stubstad, G. W., "Water-Entry Cavity Modeling. Part 1. Vertical Cavities," NOTS NAVORD Report 5365, 1956

1-23. Blackwell, B. D., "Preliminary Remarks on the Cavity made by a Projectile Entering Water," Dept. of Sci. Res. and Exp. Rept S.R.E./U.1./4, 1944

1-24. Abelson, H.I., "Pressure Measurements in the Water-Entry Cavity," J. Fluid Mech. 44, pp 129-144, 1970

1-25. Davies, R. M., "The Influence of Atmospheric Pressure on the Phenomena Accompanying the Fall of Small Scale Projectiles into a Liquid," Cambridge Univ. Eng. Lab. UBRC 23, 1944

1-26. Levy, J. and Kaye, J., "Studies of Water Entry-Effect of Atmospheric Pressure on Entry Behavior of Models of Mark 13-6 Torpedo with Standard Head (Head F) and one Finer Head (Head I)," CIT Hyd. Report N-59, 1949

1-27. May, A., "Cavities and Cavity-Running Behavior of Missiles," Chapter 3 of this report

1-28. Gilbarg, D., "Jets and Cavities," Encyclopedia of Physics (Handbuch der Physik) Vol. IX, Fluid Dynamics III, Springer, 1960

1-29. May, A., "Review of Water-Entry Theory and Data," J. of Hydronautics 4, pp 140-142, 1970

1-30. Mallock, A., "Sounds Produced by Drops Falling in Water," Proc. Roy. Soc. A95, pp 138-143, 1919

1-31. Biot, M. A., "The Mechanism of Water Entry of Projectiles," CIT JPO OSRD Report 13, 1943

1-32. Richardson, E. G., "Scale Effect on Air Cavities Formed when Spheres Enter Water," R.A.E. Tech. Note 116, 1942

1-33. Richardson, E. G., "Further Experiments on Air Cavities Formed when Spheres Enter Liquids," R.A.E., Tech. Note 289, 1944

1-34. Proceedings of Second Conference on Underwater Ballistics, David Taylor Model Basin and NOL, 1/29-31/1945, NORC-AMG

1-35. McMillen, J.H. and Harvey, E. N., "Drag and Cavity of Fast Spheres Shot into Water," Phys. Rev. 71, 475 (A), 1947

1-36. Abelson, H.I., "Cavity Shapes at Vertical Water Entry-- A Comparison of Calculated and Observed Shapes," NOLTR 67-31, 1967

1-37. Birkhoff, G., "Modeling of Entry into Water," OSRD AMP Memo 42.10M, 1945

1-38. Levy, J., "On Modeling the Oblique Entry into Water of Air-Launched Missiles," CIT Hyd. Report E-12.19, 1956

1-39. Wilcox, G. M. and Waugh, J. G., "Water Entry Study of the MK 25 Torpedo with 3.5 Calibre 70-Degree Spherogive Head," CIT Hyd. Report E-12.12, 1953

1-40. Swanson, W. M. and O'Neill, J. P., "The Stability of an Air-Maintained Cavity Behind a Stationary Object in Flowing Water," CIT Hyd. Memo Report M-24.3, 1951

1-41. Birkhoff, G., "Induced Mass with Free Boundaries," Quart. Appl. Math. 10, pp 81-86, 1952

1-42. May, A. and Woodhull, J. C., "The Virtual Mass of a Sphere Entering Water Vertically," J. Appl. Phys. 21, pp 1285-1289, 1950

1-43. Birkhoff, G. and Caywood, T. E., "Fluid Flow Patterns," BuOrd NAVORD Report 447, 1947; also J. Appl. Phys. 20, pp 646-659, 1949

1-44. Richardson, E. G., "The Impact of a Solid on a Liquid Surface," Proc. Roy. Soc. 61, pp 352, 1948

1-45. Hoover, W. R. and Dawson, V. C. D., "Hydrodynamic Pressure Measurements of the Vertical Water Entry of a Sphere," NOLTR 66-70, 1966

1-46. Reichardt, H., "The Laws of Cavitation Bubbles at Axially Symmetrical Bodies in a Flow," Ministry of Aircraft Production Volkenrode, MAP-VG Reports and Translations 766 ONR, 1946

1-47. McMillen, J. H., Kramer, R. L., Allmand, D. E., and March, R. S., "Pressure Fields Surrounding High-Speed Spheres in Water," 1950

1-48. McMillen, J. H. and Harvey, E. N., "A Spark Shadowgraphic Study of Body Waves in Water," J. Appl. Phys. 17, pp 541-555, 1946

1-49. McMillen, J. H. and Kramer, R. L., "Shadowgraphic Investigation of Small Spherical Missiles Entering Water Vertically at 7000 Feet per Second," NOL NAVORD Report 2646, 1952

1-50. Mosteller, G. G., "Spin Rate of Spheres Projected under Water as Determined from the Direction of Striations on the Cavity Formed at Water Entry," NOTS NAVORD Report 1012, 1948

Abbreviations

CIT Hyd.   California Institute of Technology, Hydrodynamics Laboratory

NOL   Naval Surface Weapons Center, White Oak Laboratory, Silver Spring, Maryland (formerly the Naval Ordnance Laboratory)

NOTS   Naval Ordnance Test Station, Pasadena, California

R. A. E.   Royal Aircraft Establishment, Farnborough, England

A   B   C   D
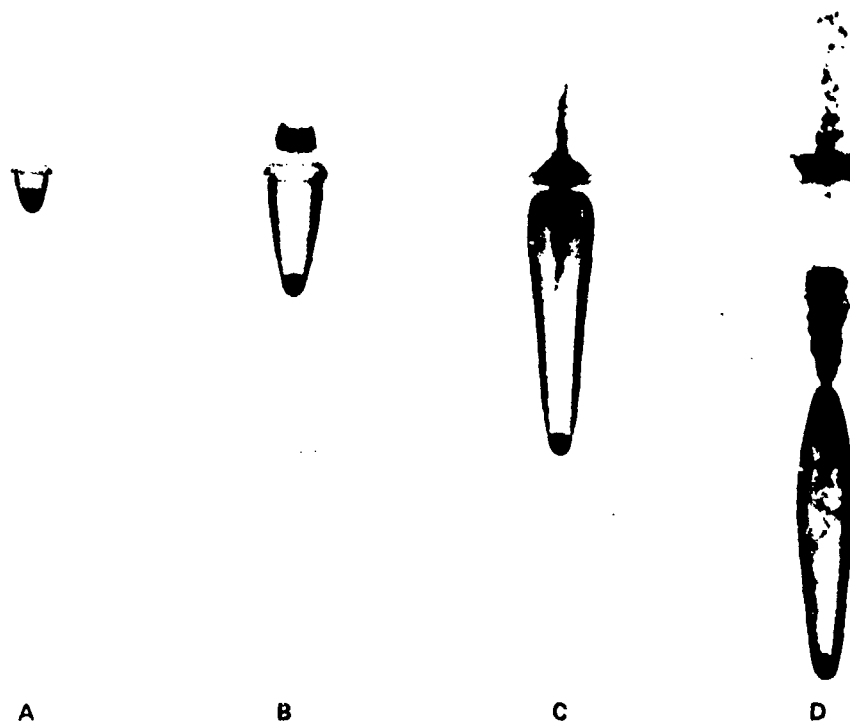
FIG. 1-1 CAVITY DEVELOPMENT AFTER THE VERTICAL WATER ENTRY OF A SPHERE

FIG. 1-2 VERTICAL ENTRY SHADOWGRAPHS; 2-IN. DIAMETER SPHERE, ENTRY VELOCITY 22 FPS AFTER WHITE REF (1-8)
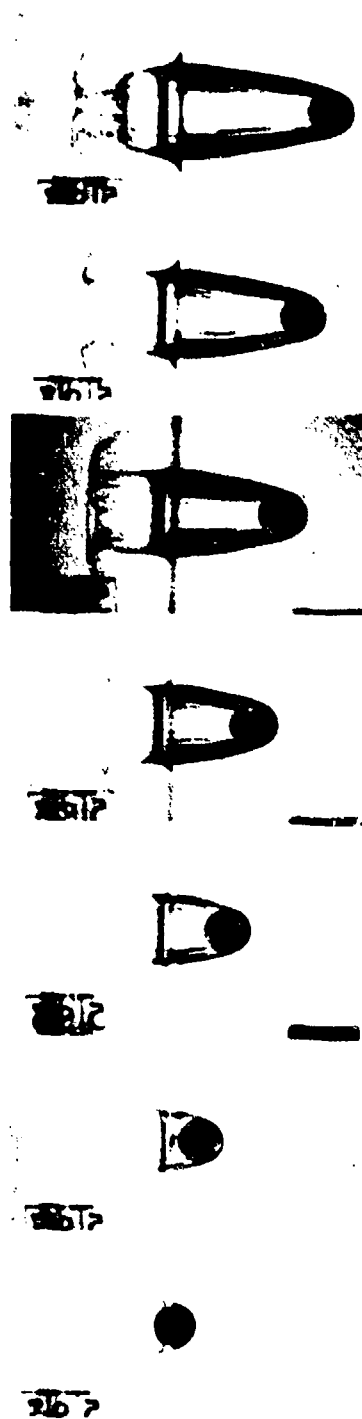
FIG. 1-3 HIGH-SPEED MOTION PICTURES OF 1-INCH STEEL SPHERE ENTERING WATER AT 35 FT/SEC. FROM REF (1-9)
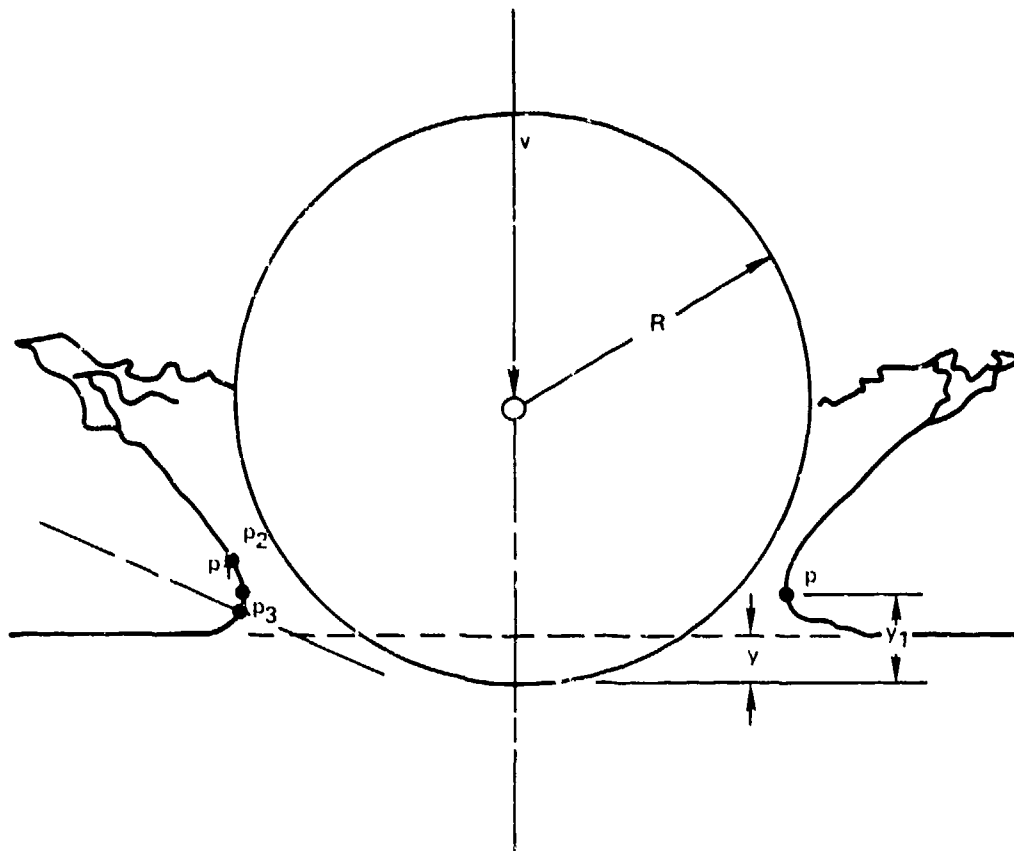
FIG. 1-4 TYPICAL VERTICAL ENTRY SPLASH CONTOUR
AFTER WHITE REF (1-8)

FIG. 1-5 SHADOWGRAPH SHOWING VERTICAL ENTRY OF 90^0 CONE.
DIAMETER, 8 IN.; ENTRY VELOCITY, 24.0 FT/SEC. FROM REF (1-17)

FIG. 1-6 SPLASH DUE TO THE VERTICAL WATER ENTRY OF A CONE
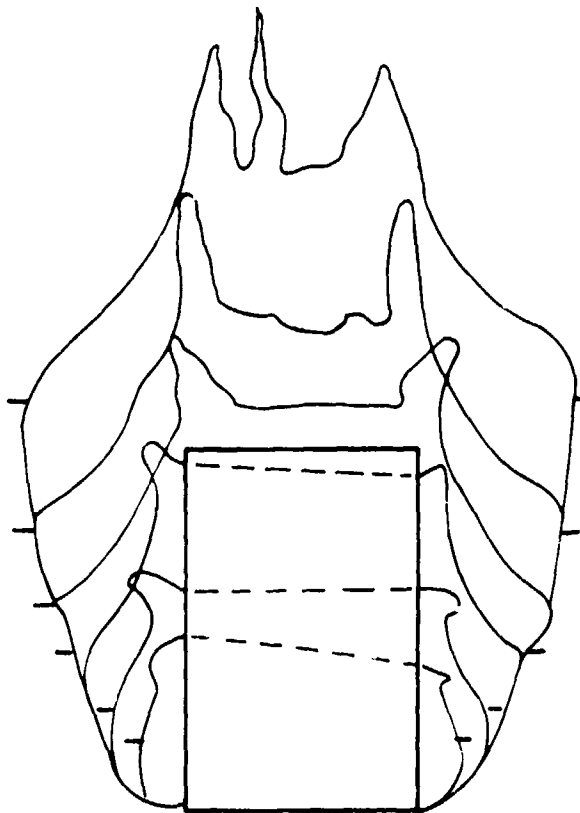
FIG. 1-7 SPLASH CONFIGURATION FOLLOWING THE
VERTICAL WATER IMPACT OF A RIGHT CYLINDER
FROM REF (1-18)

NOTE: TICKS INDICATE THE HEIGHT OF THE
ORIGINAL WATER SURFACE FOR EACH
SPLASH OUTLINE
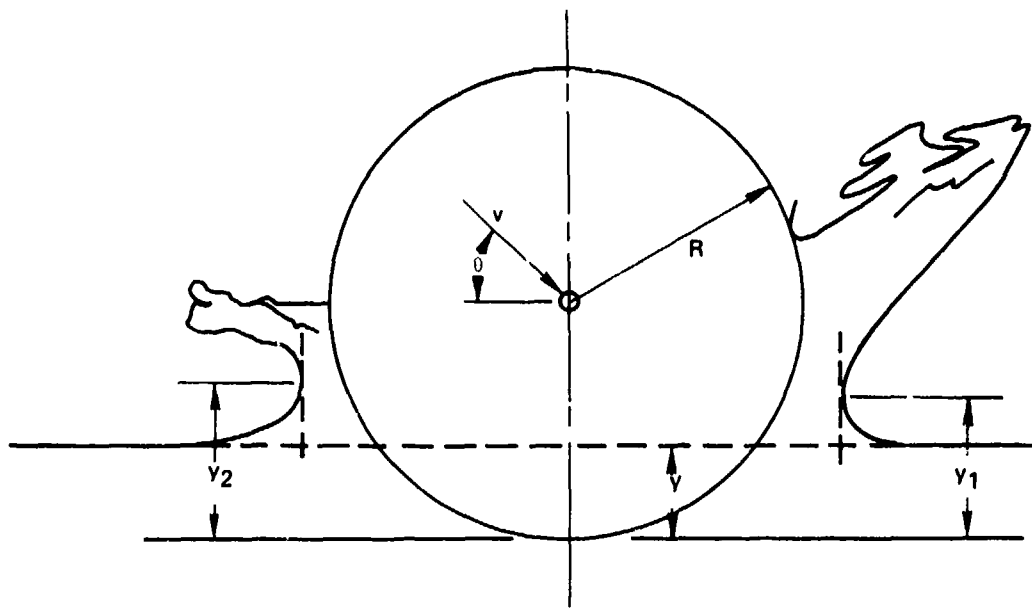
A. TYPICAL SPLASH CONTOUR FOR OBLIQUE ENTRIES AT STEEP ANGLES
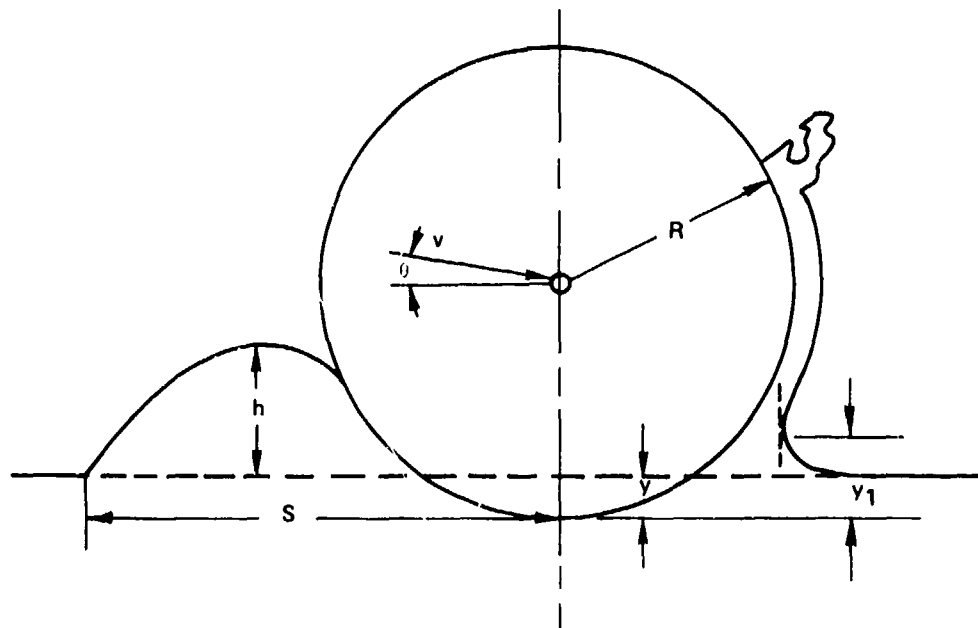
B. TYPICAL SPLASH CONTOUR FOR OBLIQUE ENTRIES AT FLAT ANGLES

FIG. 1-8 TYPICAL SPLASH CONTOUR FOR OBLIQUE ENTRIES
AT STEEP AND FLAT ANGLES. AFTER WHITE REF (1-8)
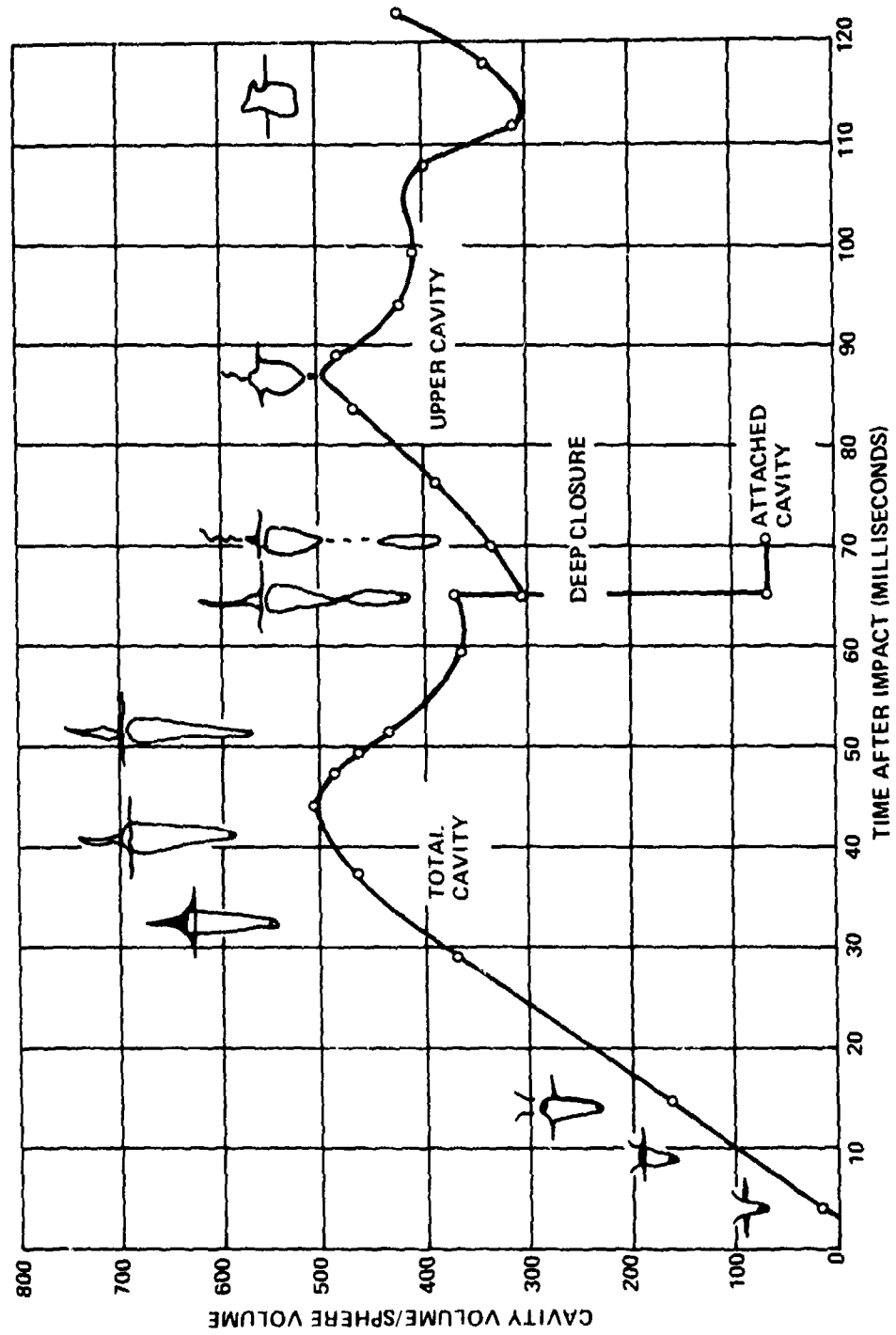
FIG. 1-9   FROM REF (1-9)
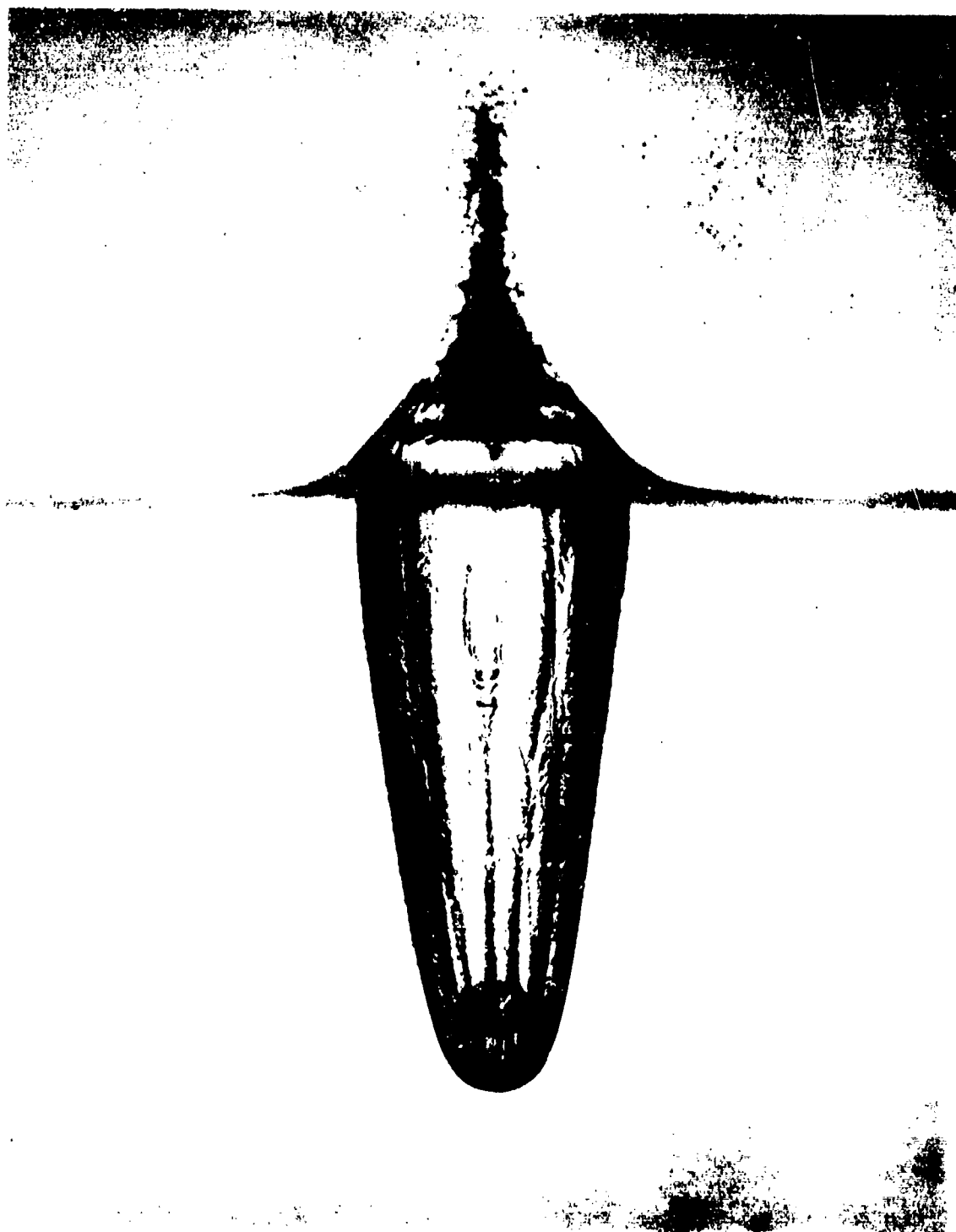
FIG. 1-10 WATER ENTRY OF 1-INCH STEEL SPHERE AT 32 FT/SEC.
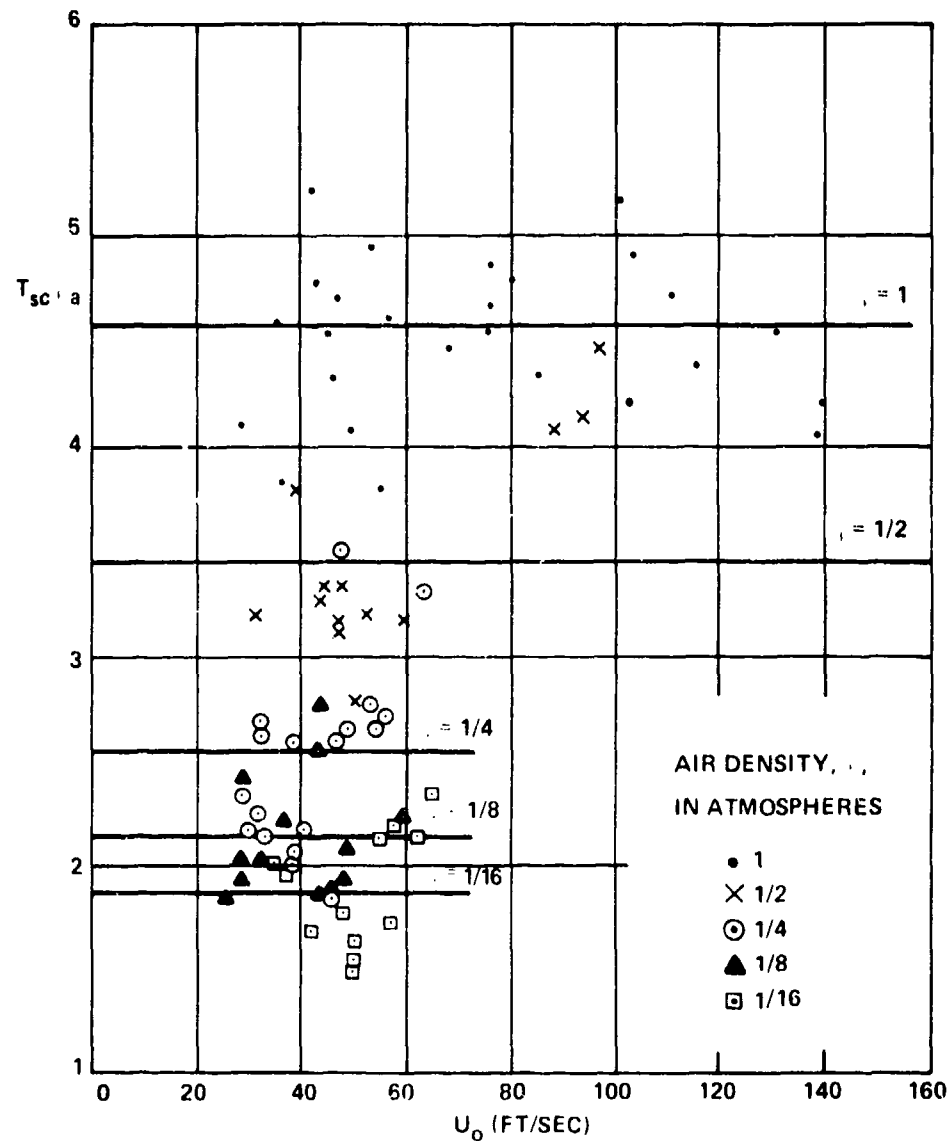
FIG. 1-11 DEPENDENCE OF TIME OF SURFACE SEAL ON ENTRY SPEED AND ON
AIR DENSITY FOR THE CAVITIES FORMED BY 1/2-INCH STEEL SPHERES.
THE LINES SHOW AVERAGE VALUES FOR VARIOUS AIR DENSITIES.
FROM REF (1-9)
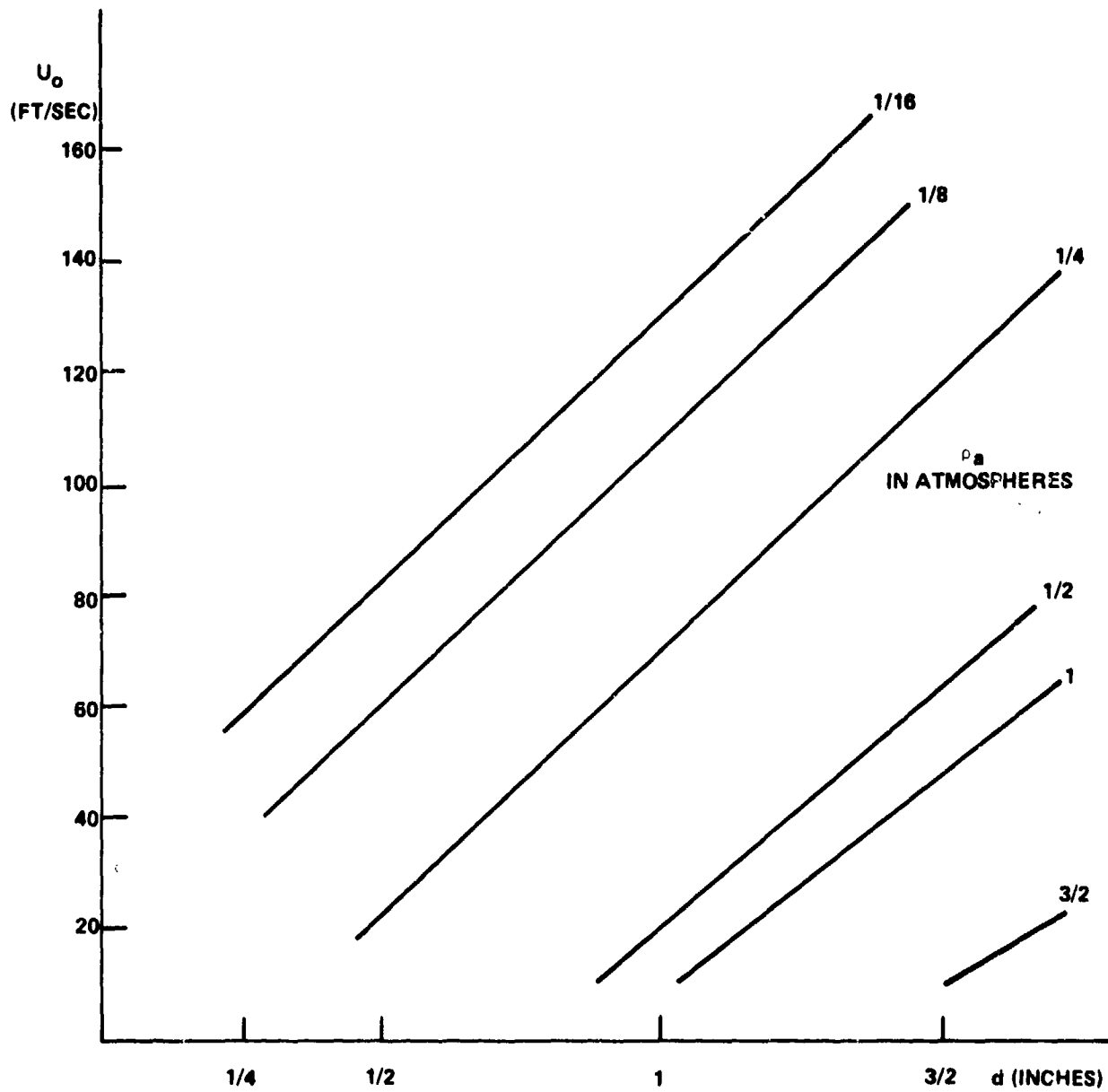
FIG. 1-12 THE SMALLEST VELOCITIES OF VERTICAL WATER ENTRY
OF SMALL SPHERES, FOR WHICH PULLAWAY OCCURS
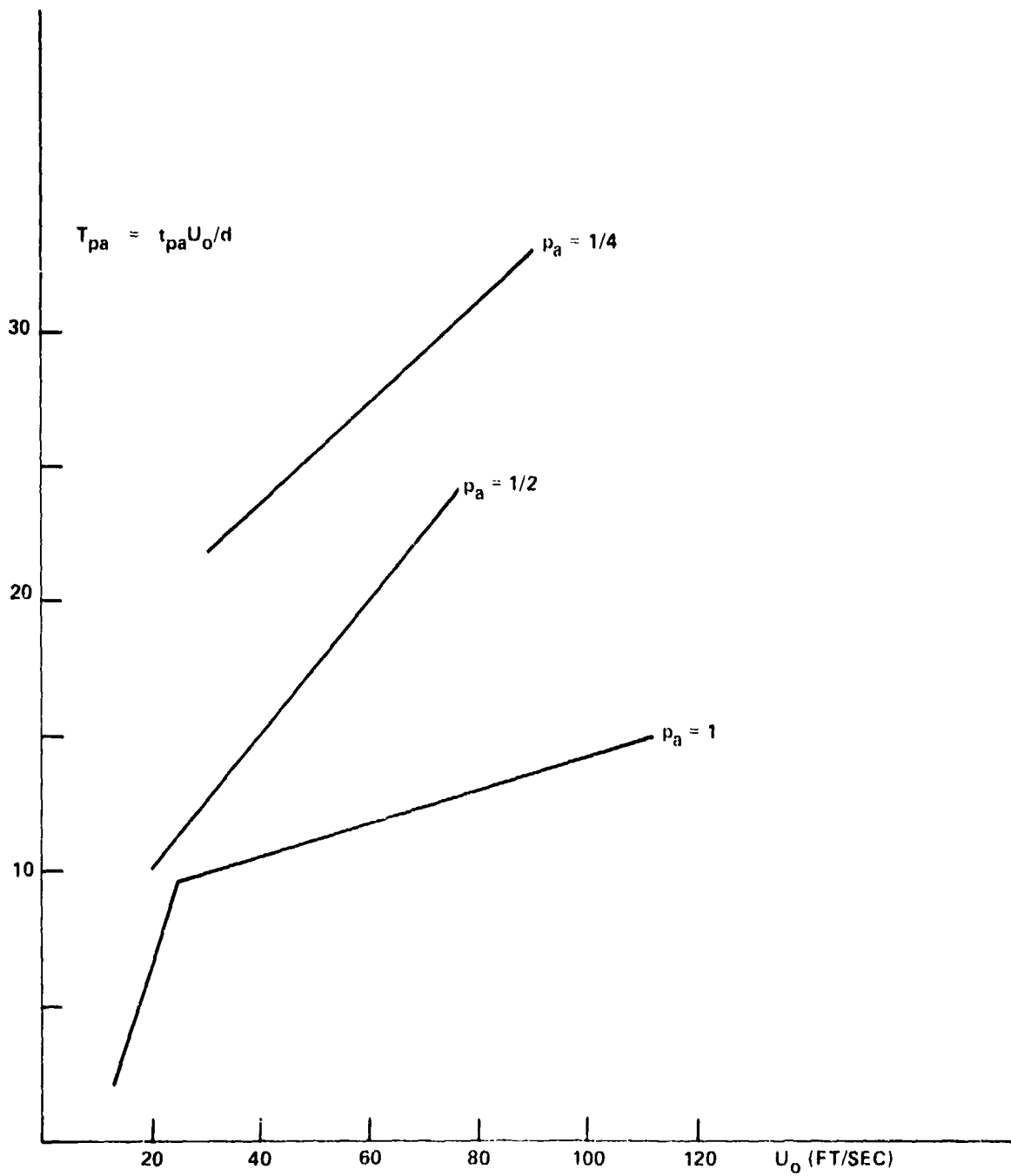
FIG. 1-13 DIMENSIONLESS TIMES OF PULLAWAY FOR SMALL SPHERES AFTER VERTICAL ENTRY
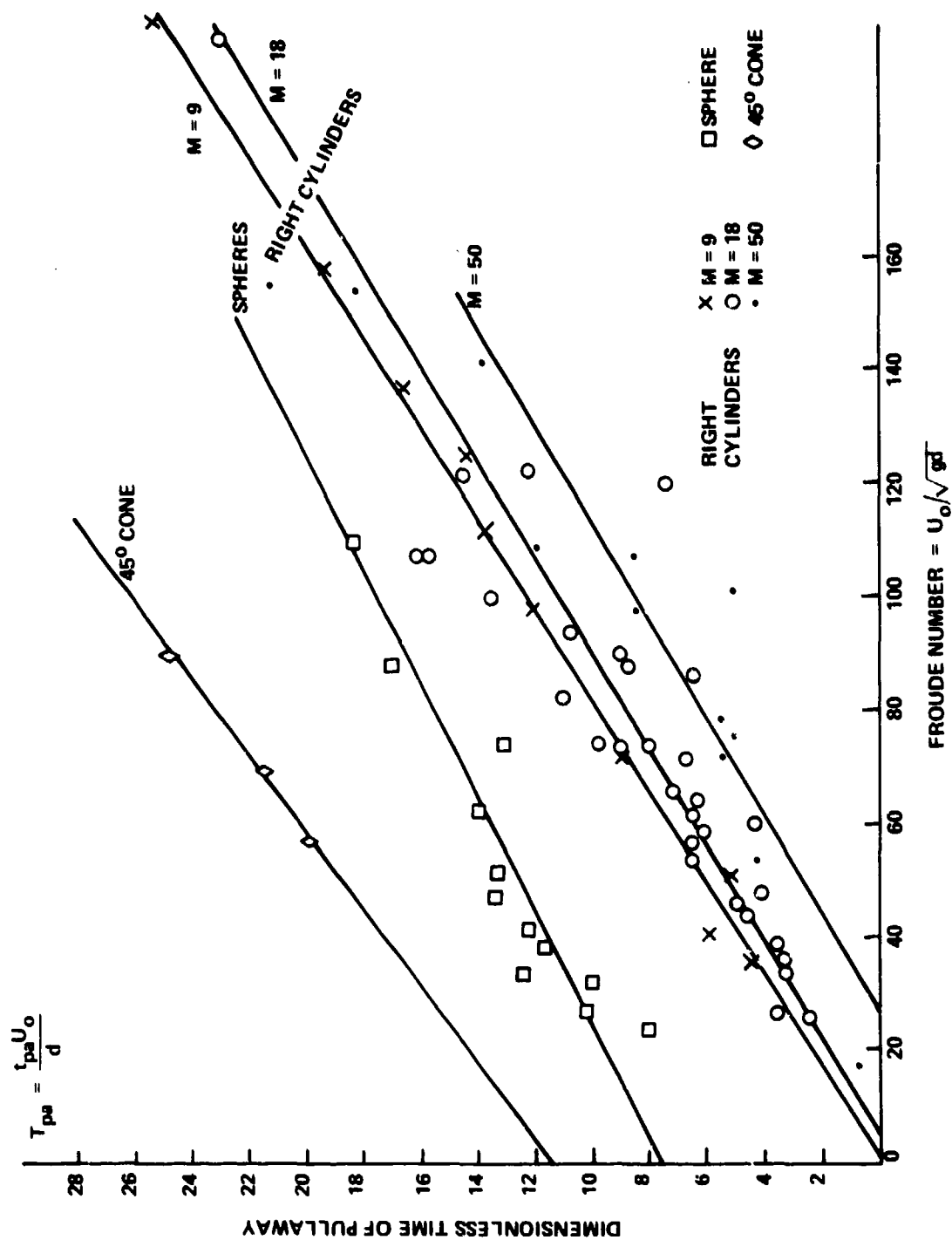
FIG. 1-14 TIME OF PULLAWAY AFTER VERTICAL WATER ENTRY
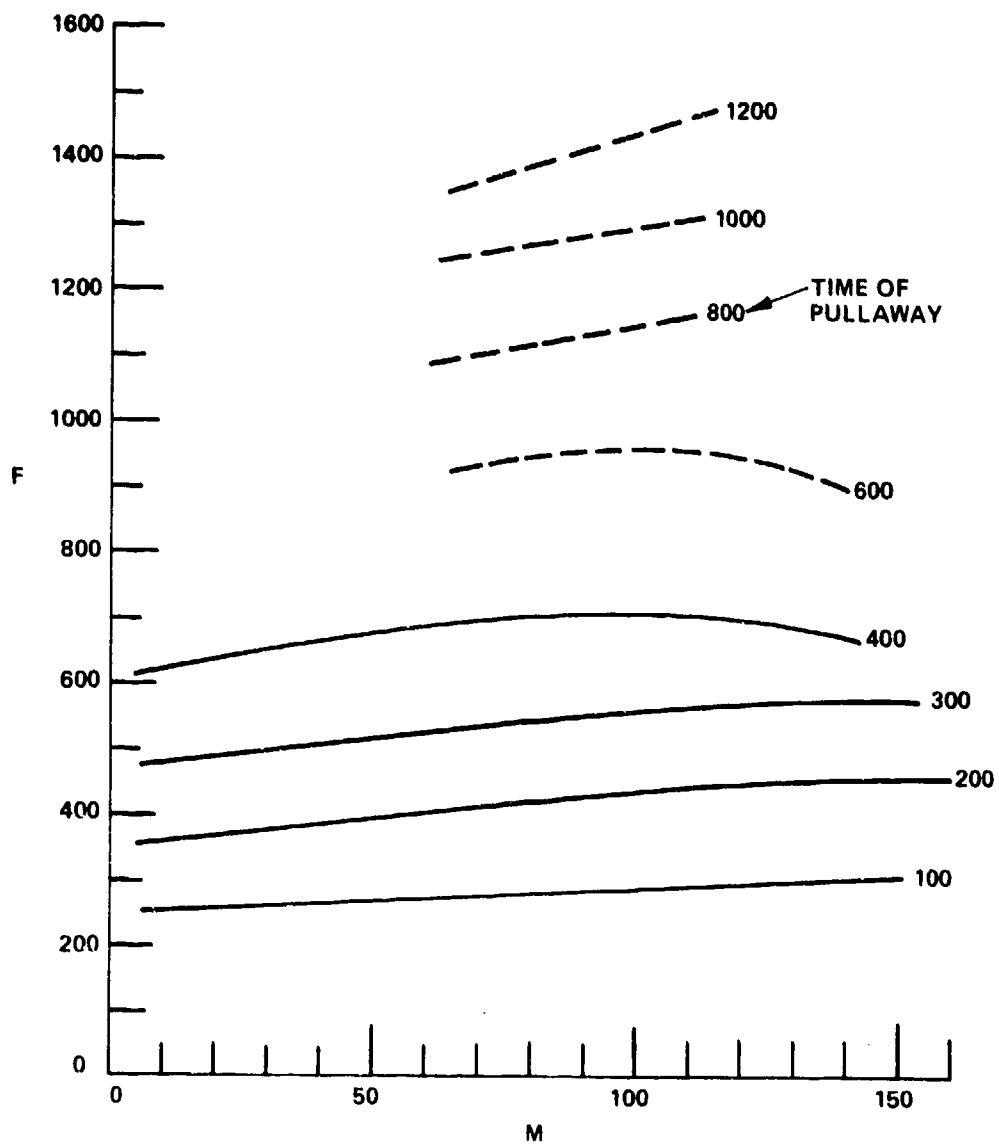
FIG. 1-15 CONTOURS OF TIME OF PULLAWAY OF CAVITY FROM WATER SURFACE
(TIMES ARE MEASURED FROM WATER IMPACT) REF (1-7)
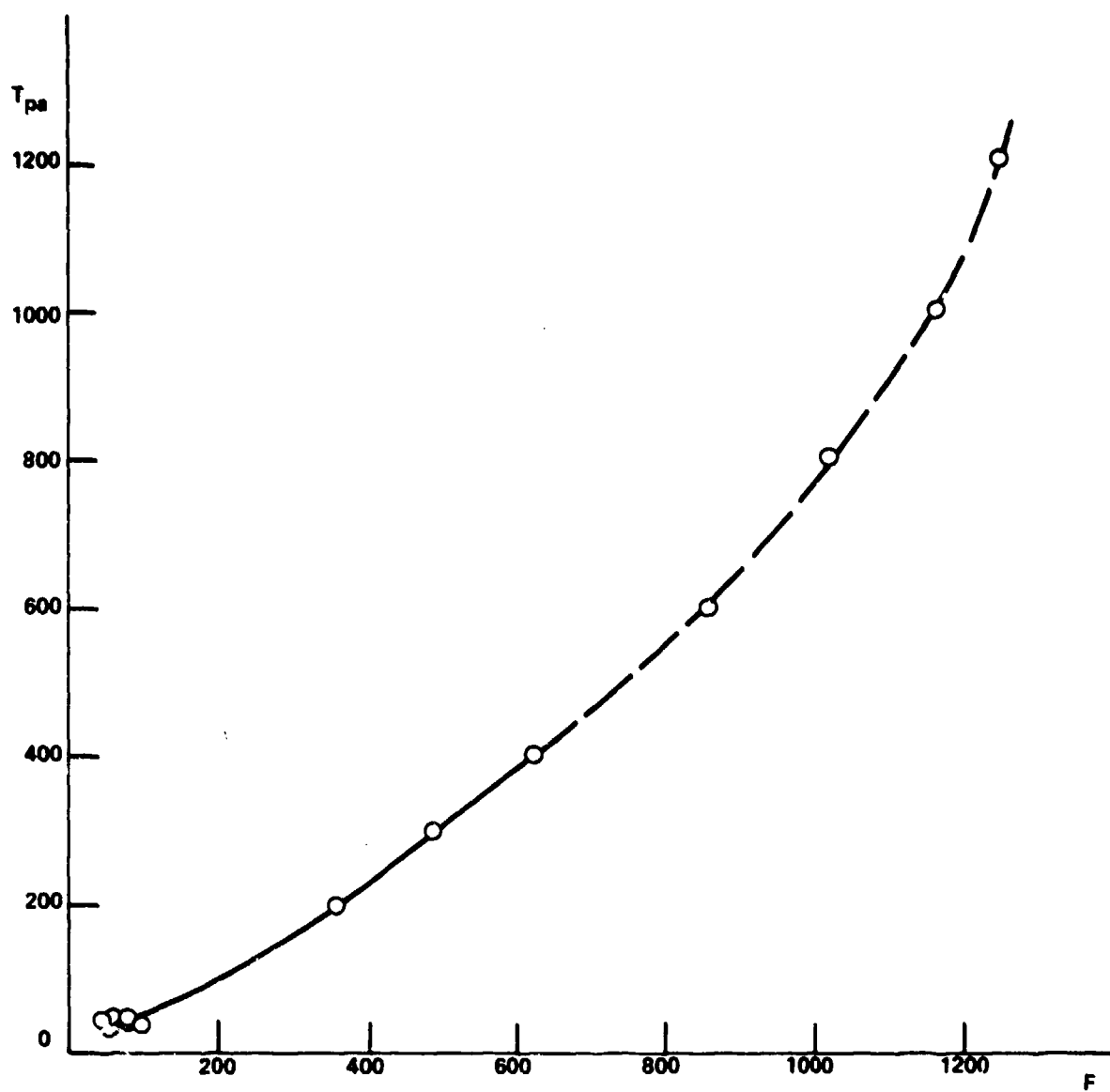
FIG. 1-16 DIMENSIONLESS TIME OF PULLAWAY FOR STEEL SPHERES
AFTER OBLIQUE ENTRY (45 TO 70°)
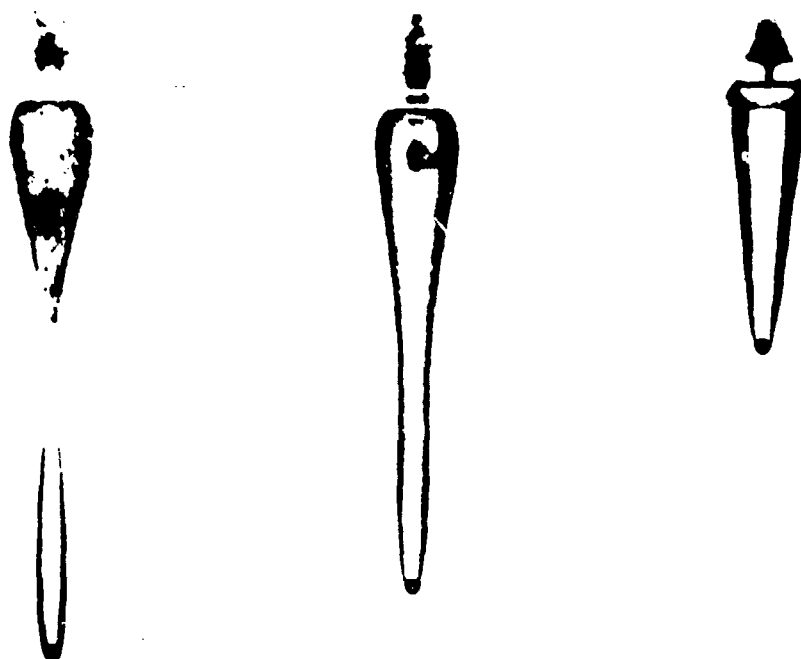
FIG. 1-17 ENTRY OF A 1/4-INCH STEEL SPHERE AT 77 FT/SEC. THE AIR PRESSURE WAS ONE-FOURTH
OF A NORMAL ATMOSPHERE. NOTE THE SYMMETRICAL HOUR-GLASS CONFIGURATION
AT DEEP SEAL REF (1-9)

FIG. 1-18 WATER ENTRY OF 1 INCH POLYSTYRENE SPHERE. THIS CAVITY SHAPE IS CHARACTERISTIC OF LIGHT SPHERES. NOTE THE LARGE DOWNWARD JET REF (1-9)
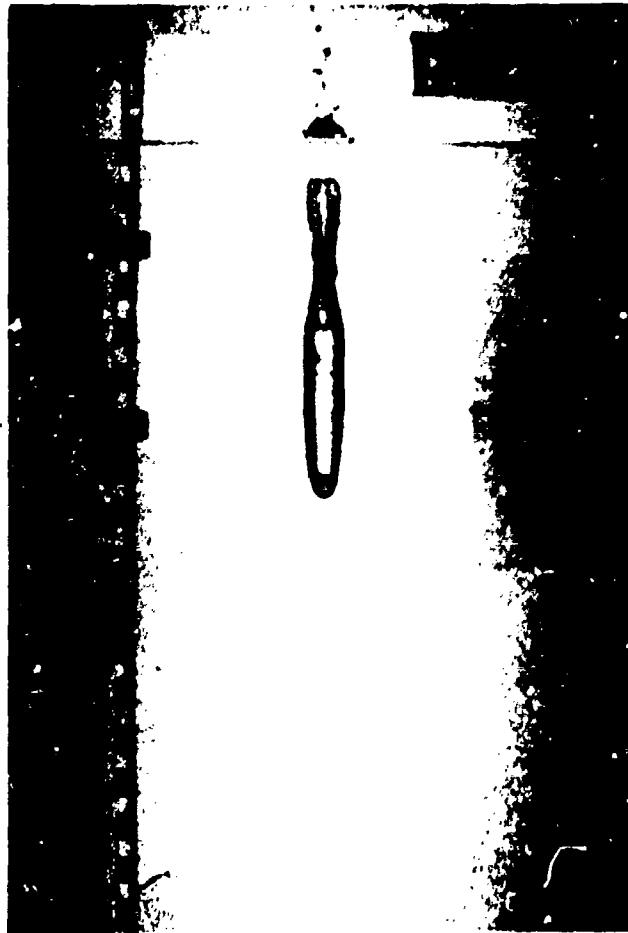
FIG. 1-19 TYPICAL DEEP CLOSURE AFTER VERTICAL WATER ENTRY
FROM REF (1-18)

DISTANCE FROM WATER-ENTRY POINT

10 FT.

20 FT.

30 FT.

λ = 60°; d = 1.5 INCH
U_o = 1000 FT/SEC

DETAIL WAS NOT AVAILABLE
AT WATER SURFACE AND IN
DASHED SECTIONS
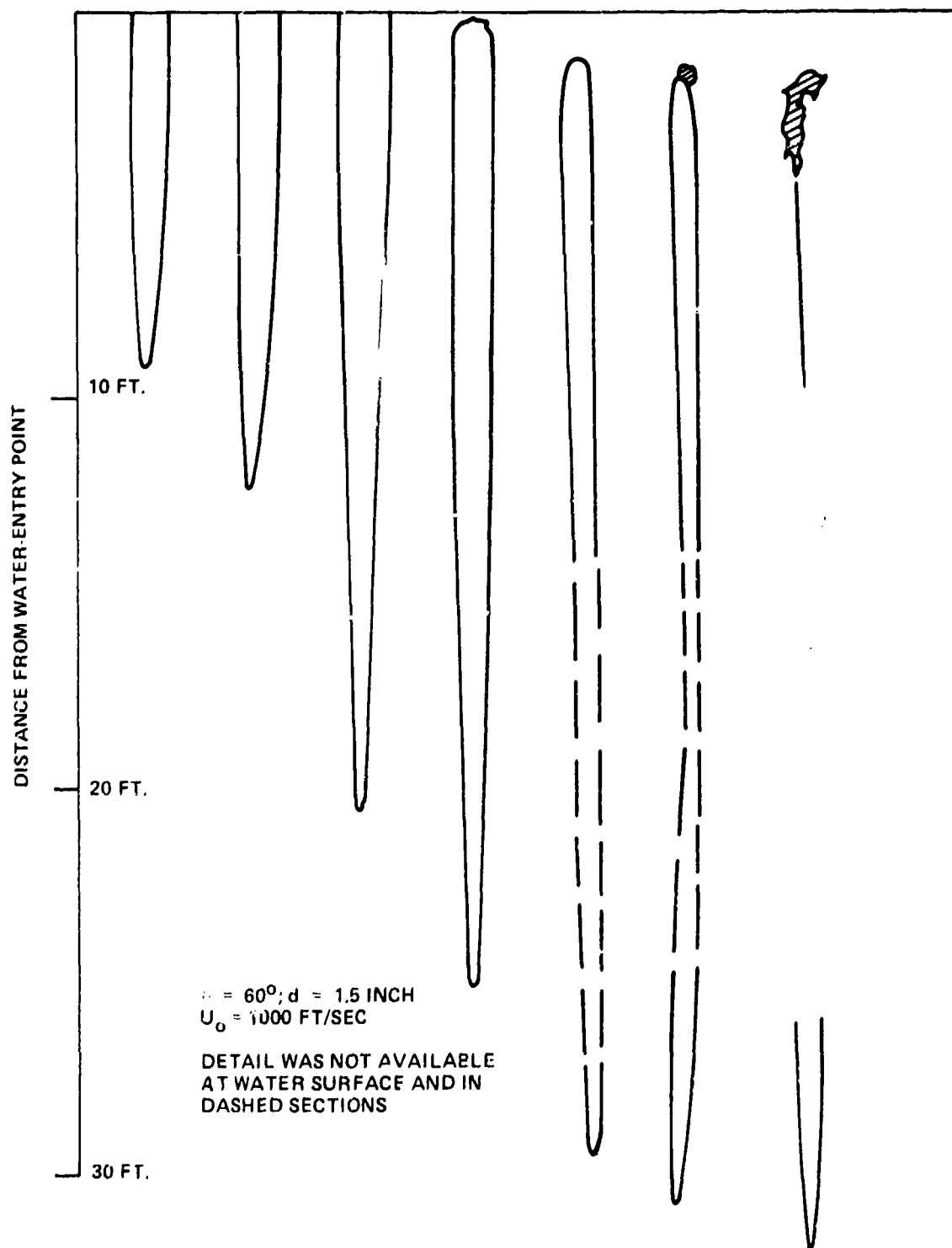
FIG. 1-20 CAVITY DUE TO MISSILE WITH TRUNCATED NOSE
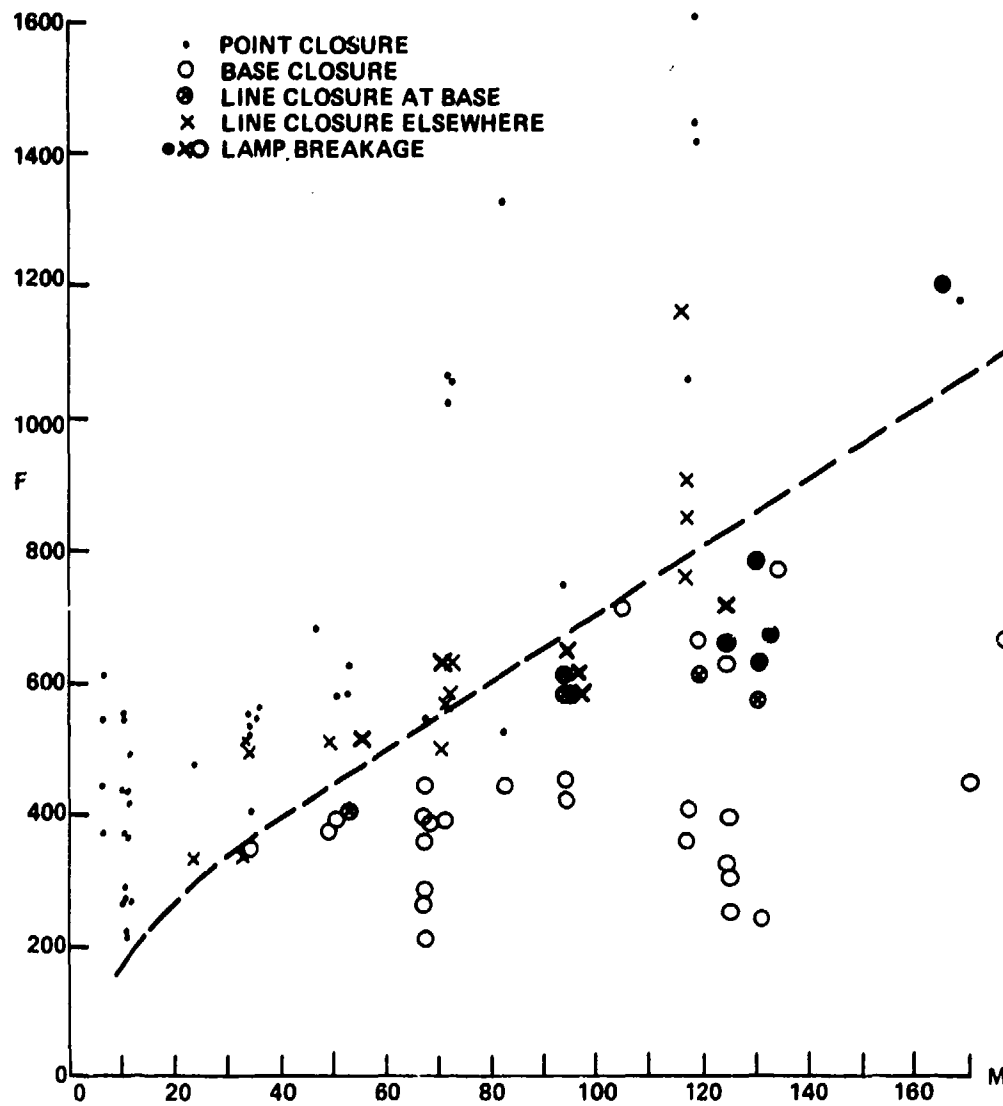
FIG. 1·21 TYPE OF CAVITY COLLAPSE REF (1·7)

Legend:
- · POINT CLOSURE
- O BASE CLOSURE
- ⊗ LINE CLOSURE AT BASE
- × LINE CLOSURE ELSEWHERE
- ●×O LAMP BREAKAGE

Axes: F (vertical), M (horizontal)

ROUND
#131
F = 1380
M = 74.1
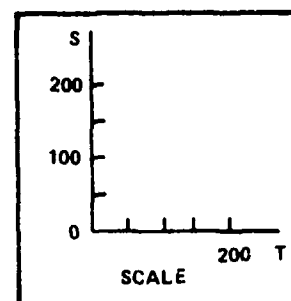
ROUND
#172
F = 548
M = 11.0

ROUND
#159
F = 437
M = 11.0
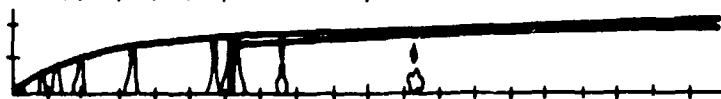
ROUND
#169
F = 290
M = 11.0

ROUND
#189
F = 444
M = 68.7
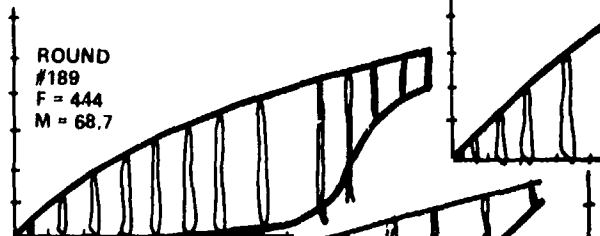
ROUND
#180
F = 397
M = 68.7
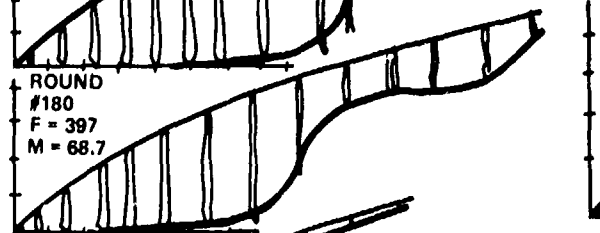
ROUND
#190
F = 211
M = 68.7

S
200
100
0
200   T
SCALE
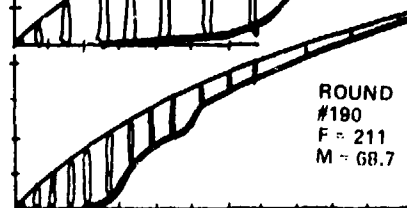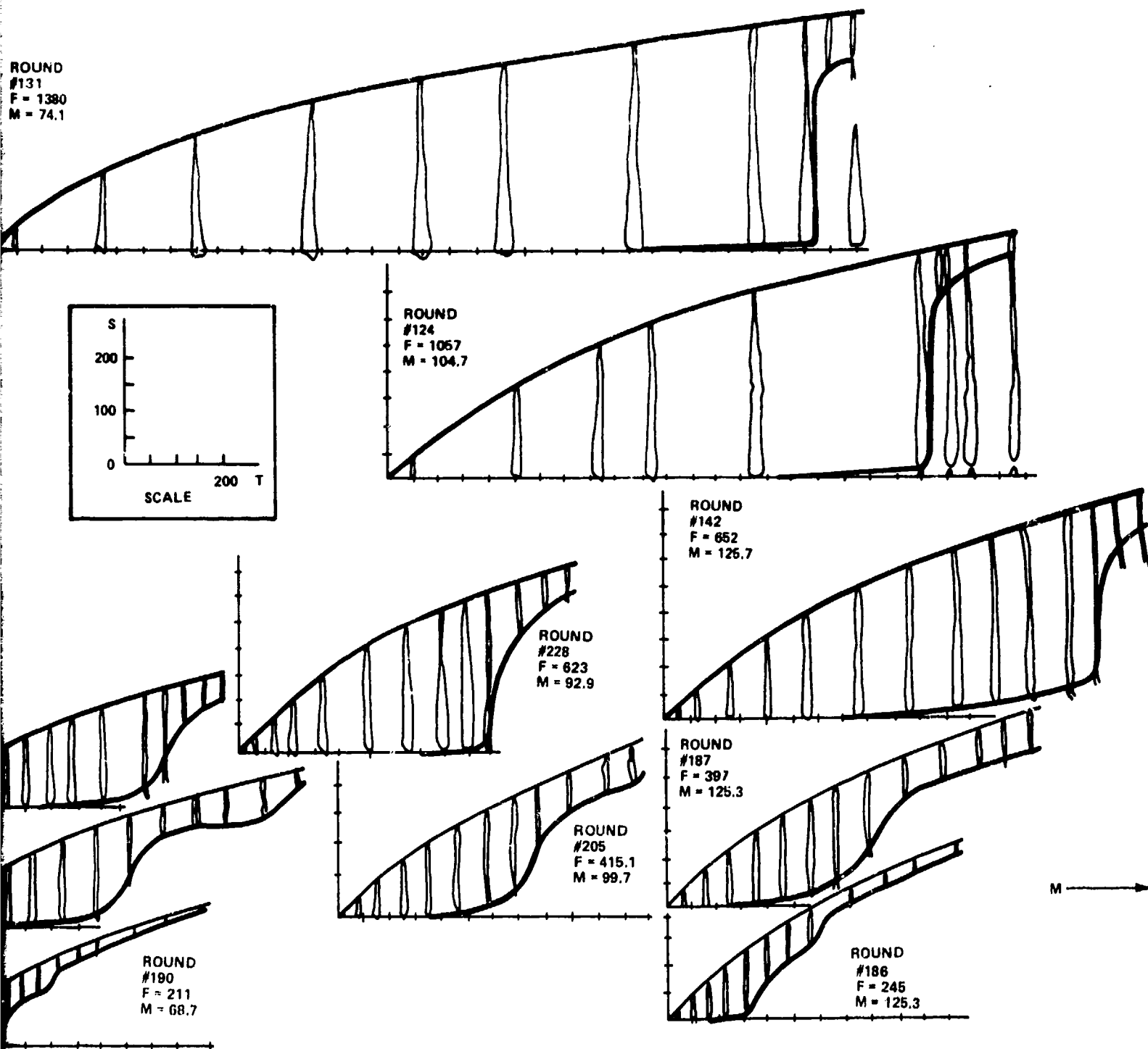
FIG. 1-22 DEPENDENCE OF CAVITY DEVELOPMENT ON
CONDITIONS OF TEST (EACH SET OF CAVITY
SKETCHES IS POSITIONED ROUGHLY AT THE
VALUES OF F AND M USED IN THE TEST)
ENTRIES WERE AT ANGLES OF 45 TO 70°
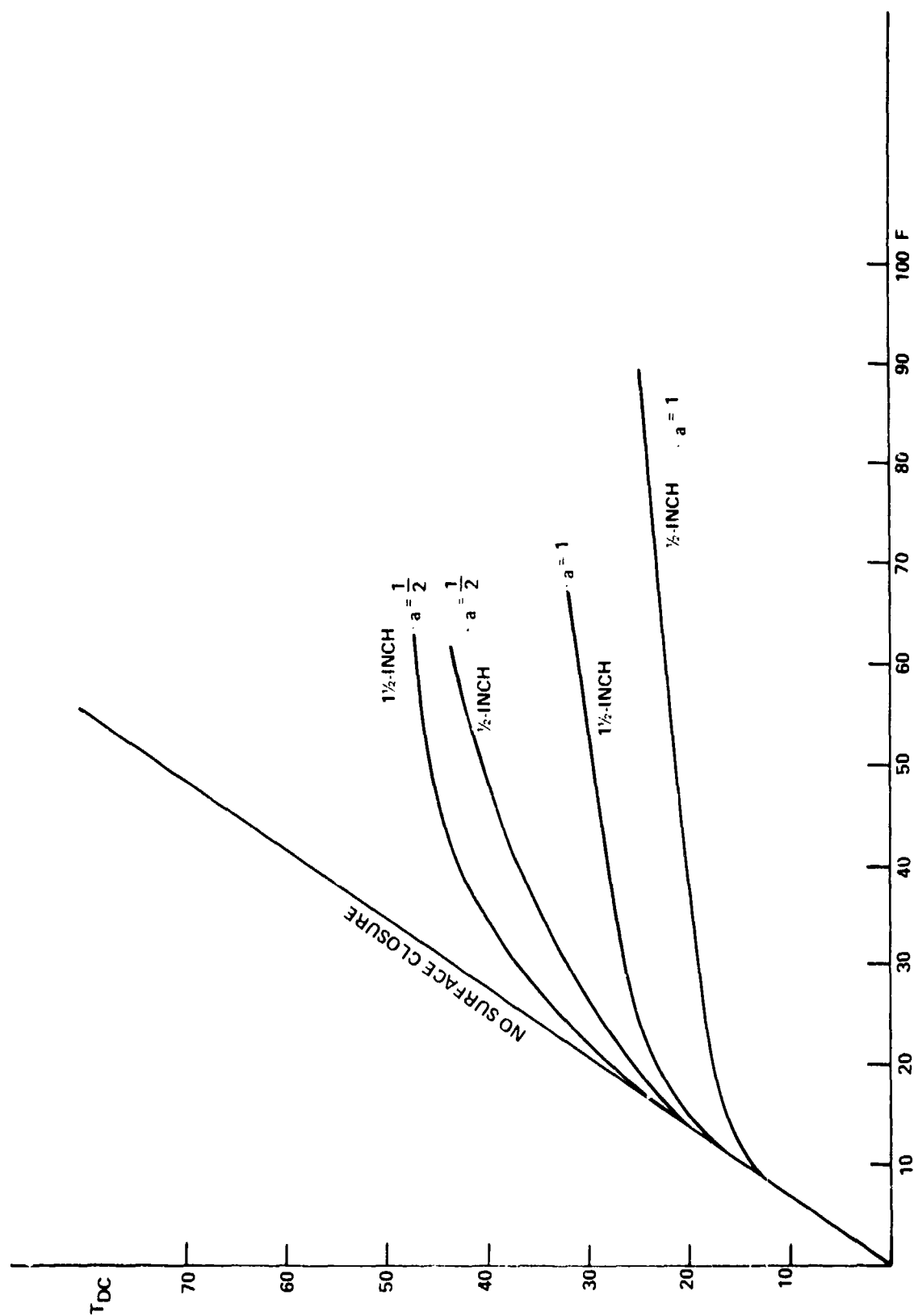
FIG. 1-23 TIME OF DEEP CLOSURE AFTER THE VERTICAL ENTRY OF SPHERES
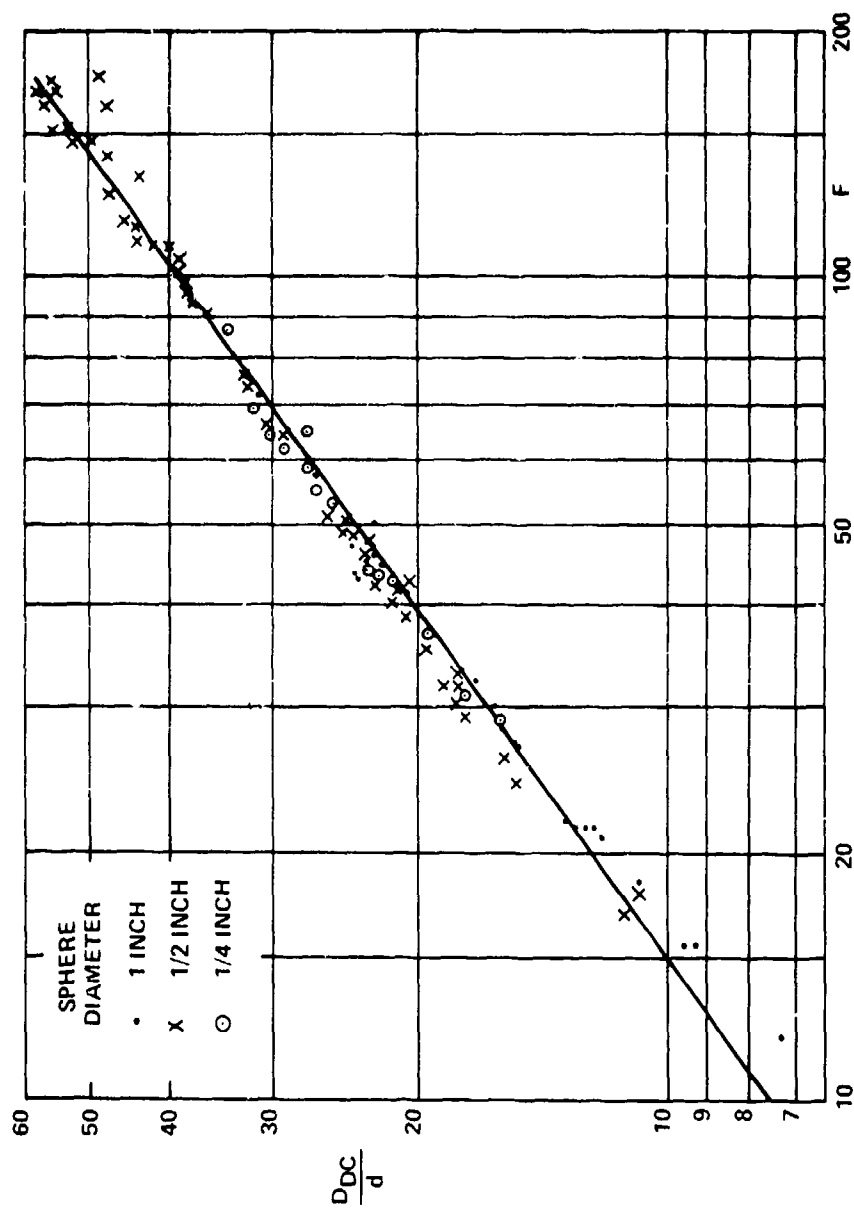
FIG. 1-24 DEPTH OF DEEP CLOSURE AFTER VERTICAL ENTRY OF SPHERE WHEN NO SURFACE CLOSURE OCCURS. EQUATION OF LINE IS $D_{dc}/d = 143F^{0.71}$ REF (1-9a)
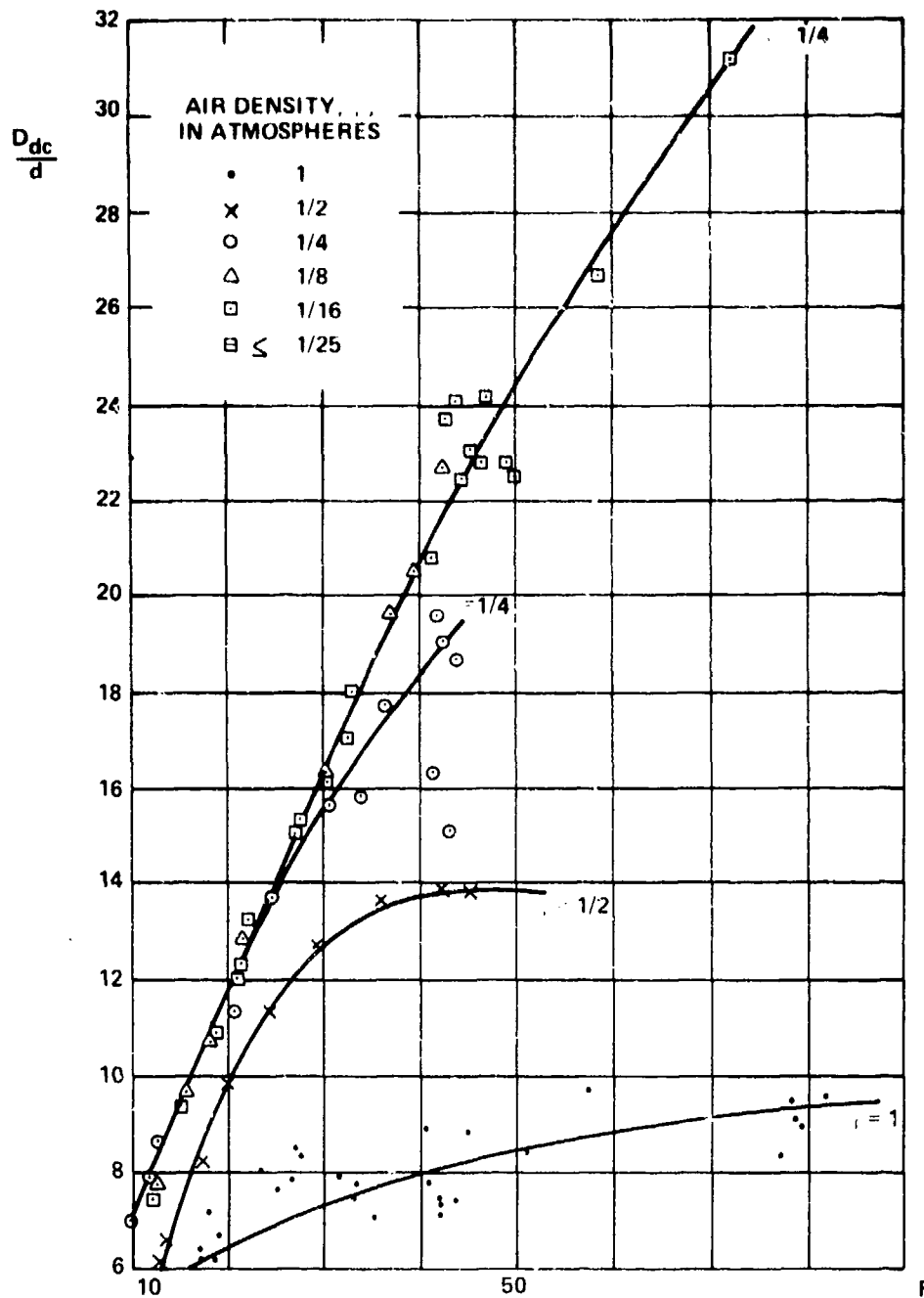
FIG. 1·25 DEPTH OF DEEP CLOSURE FOR VERTICAL ENTRY OF
1·INCH STEEL SPHERES FROM REF (1·9a)
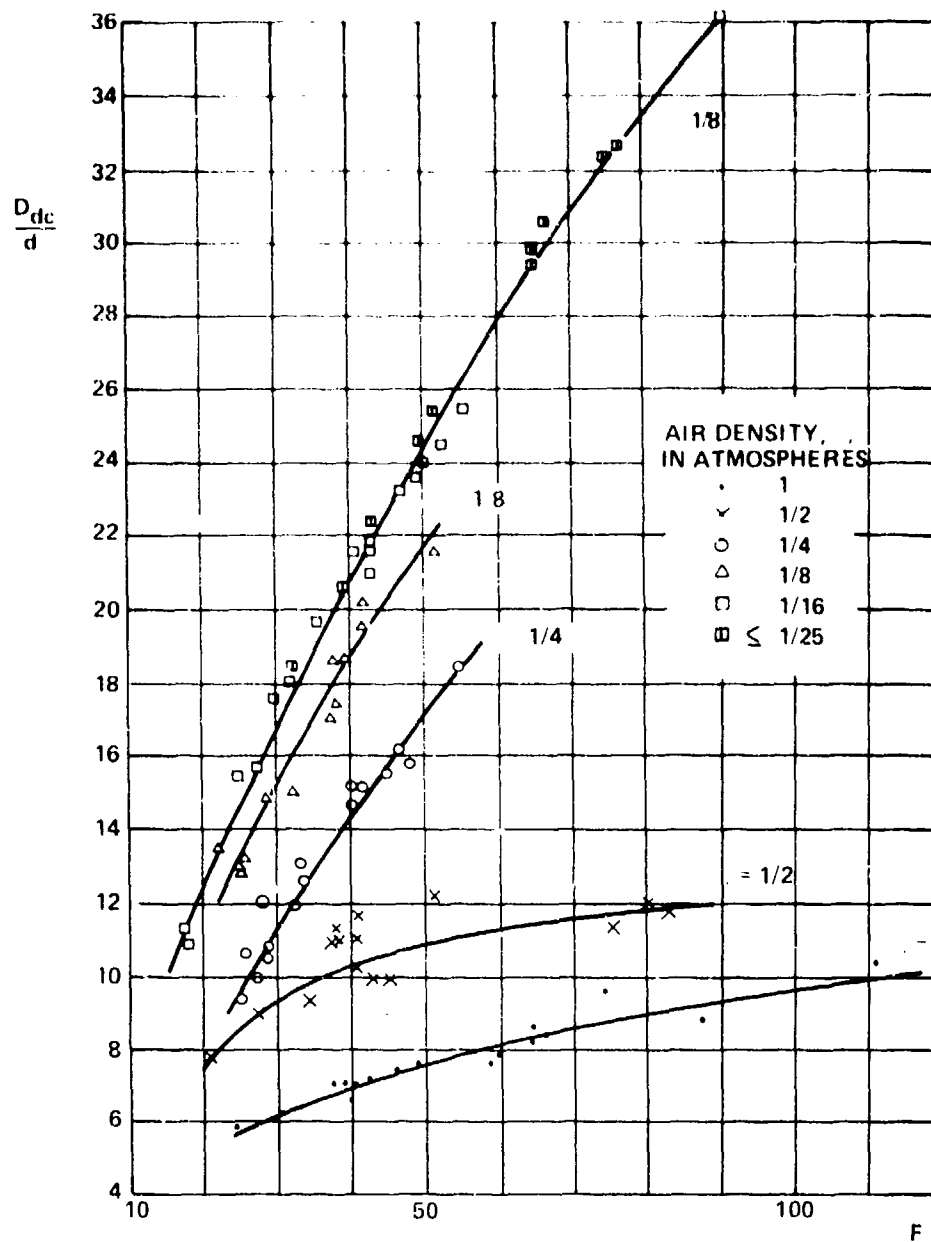
FIG. 1-26 DEPTH OF DEEP CLOSURE FOR VERTICAL ENTRY
OF 1/2-INCH STEEL SPHERES REF (1-9a)
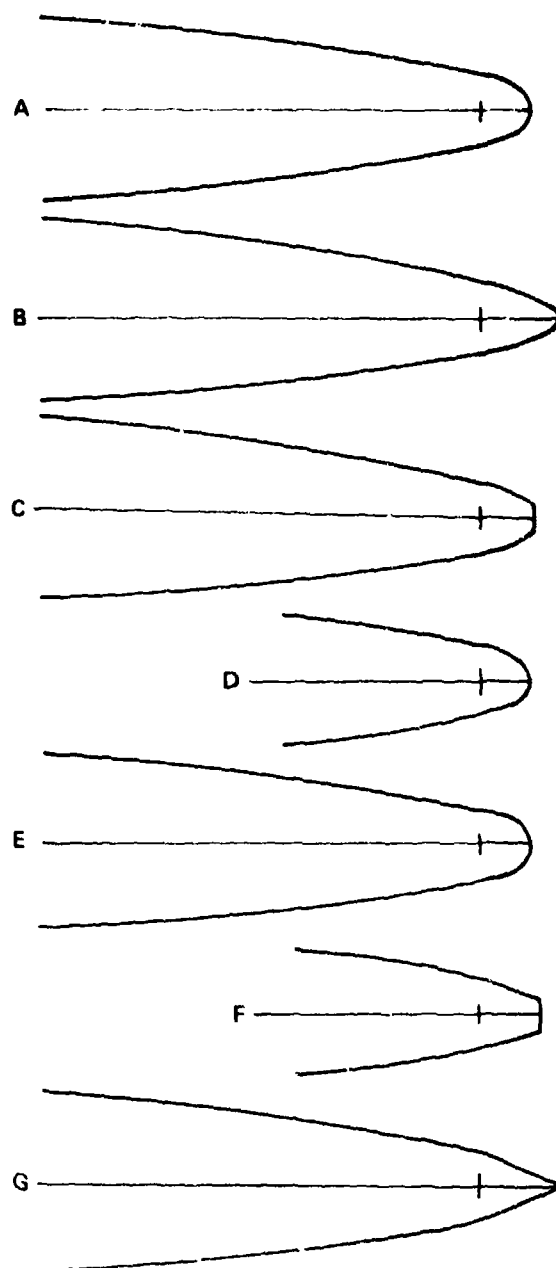
FIG. 1-27 SCALED CAVITIES REF (1-29)
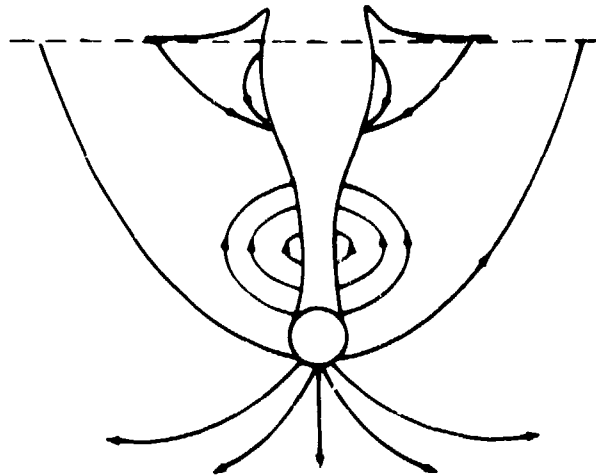
FIG. 1-28 OBSERVED FLOW IN WATER AFTER VERTICAL
ENTRY OF A SPHERE (AFTER BIRKHOFF AND
ISAACS)
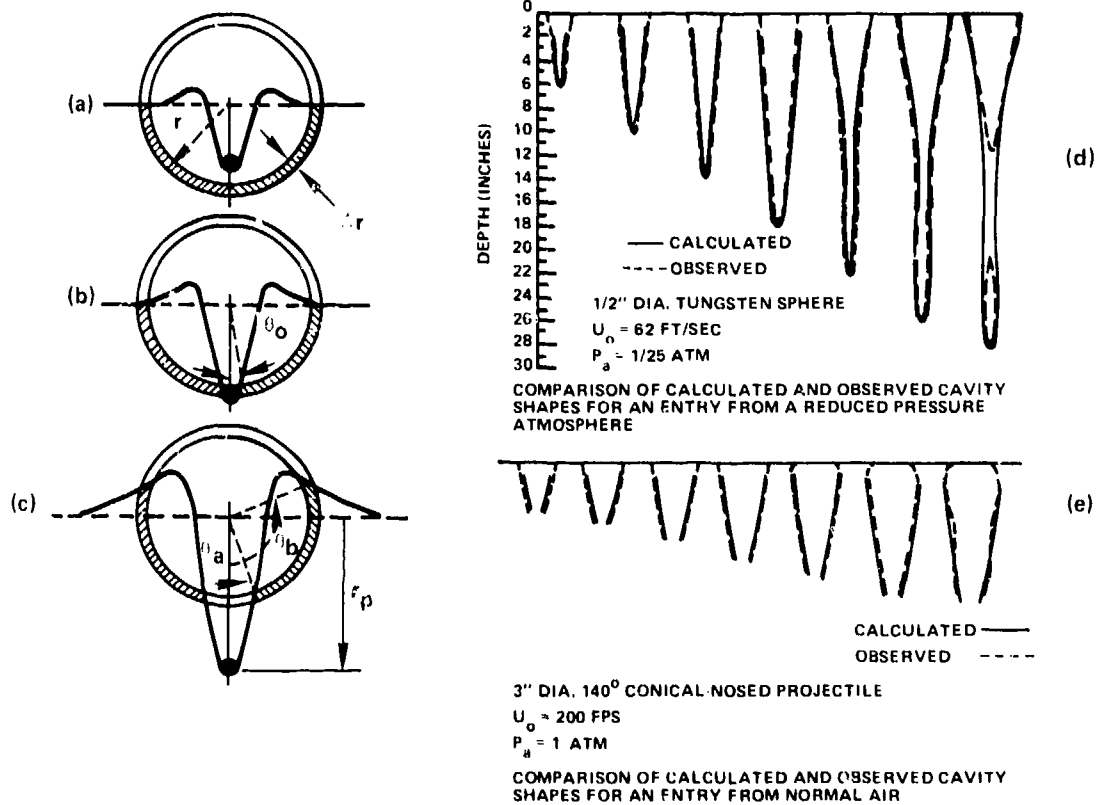
FIG. 1-29 TYPICAL SPHERICAL "SHELL" IN HYDRAULIC FLOW MODEL
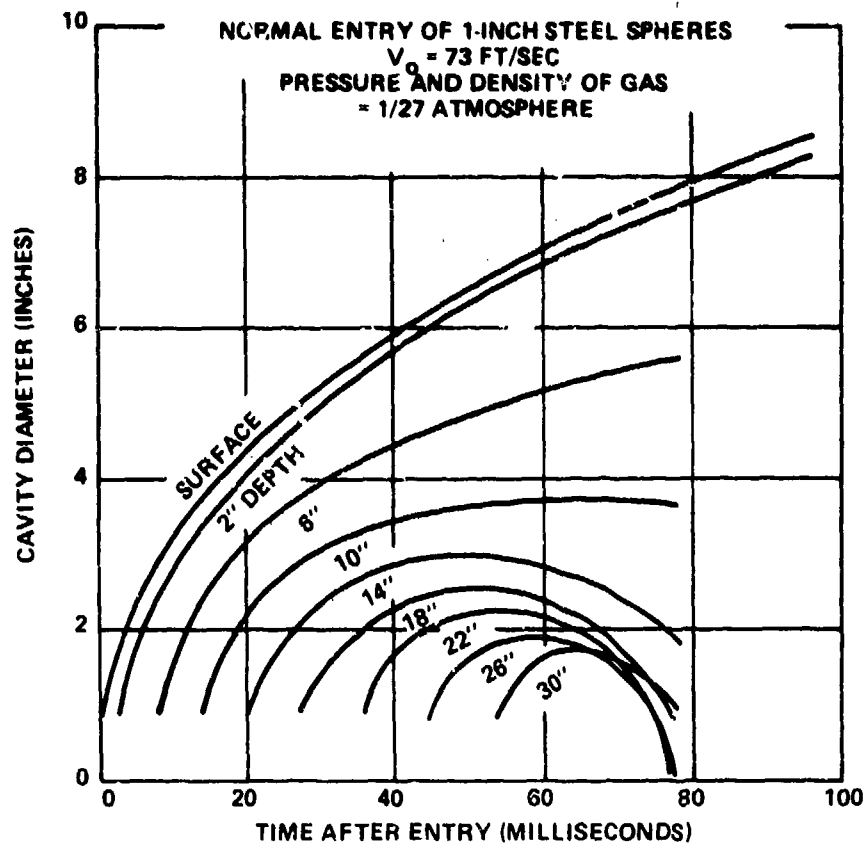
FIG. 1-30 VARIATION OF CAVITY DIAMETER (AT VARIOUS DEPTHS) WITH TIME AFTER ENTRY. REF (1-9)
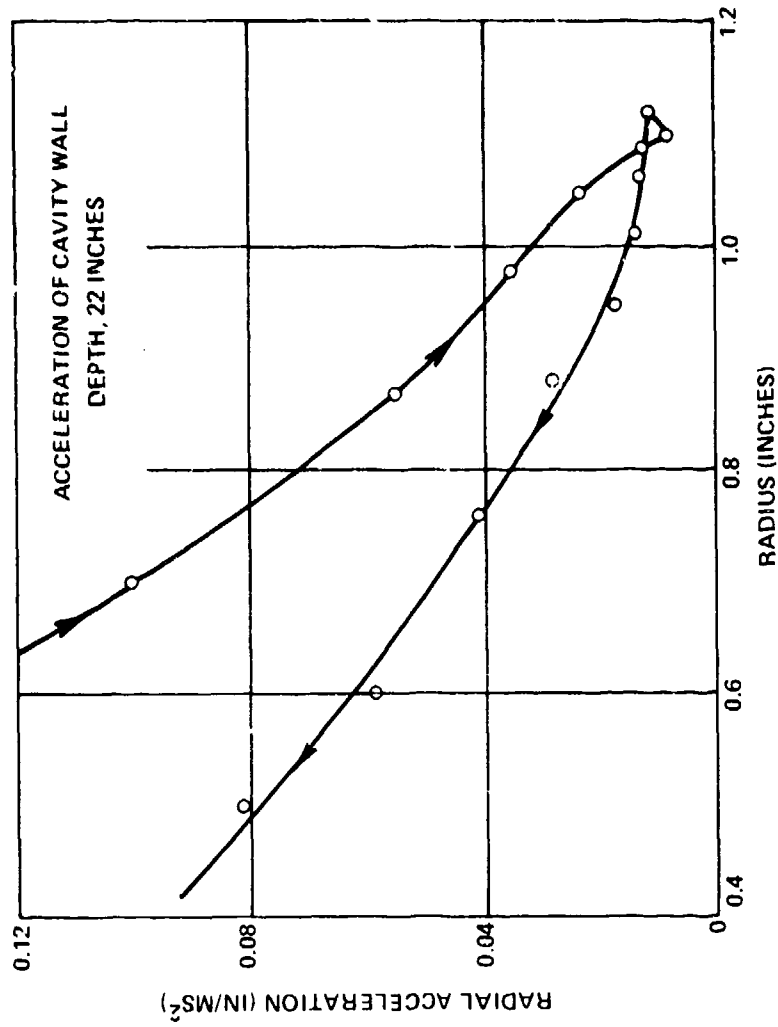
FIG. 1-31 ACCELERATION OF THE CAVITY WALL AS A
FUNCTION OF CAVITY RADIUS REF (1-9)
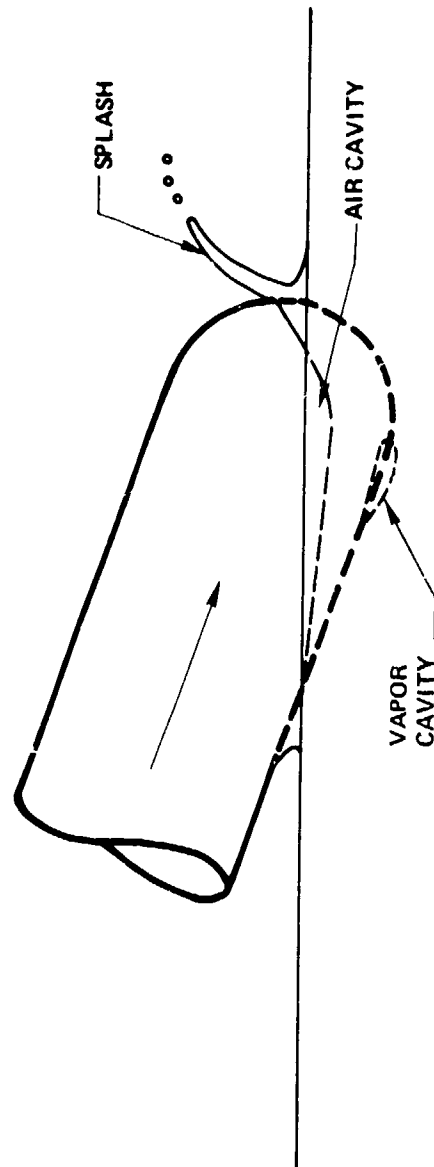
FIG. 1-32 TWO TYPES OF CAVITIES WHICH MAY BE FORMED SIMULTANEOUSLY
SHORTLY AFTER ENTRY. AFTER LEVY REF (1-38)
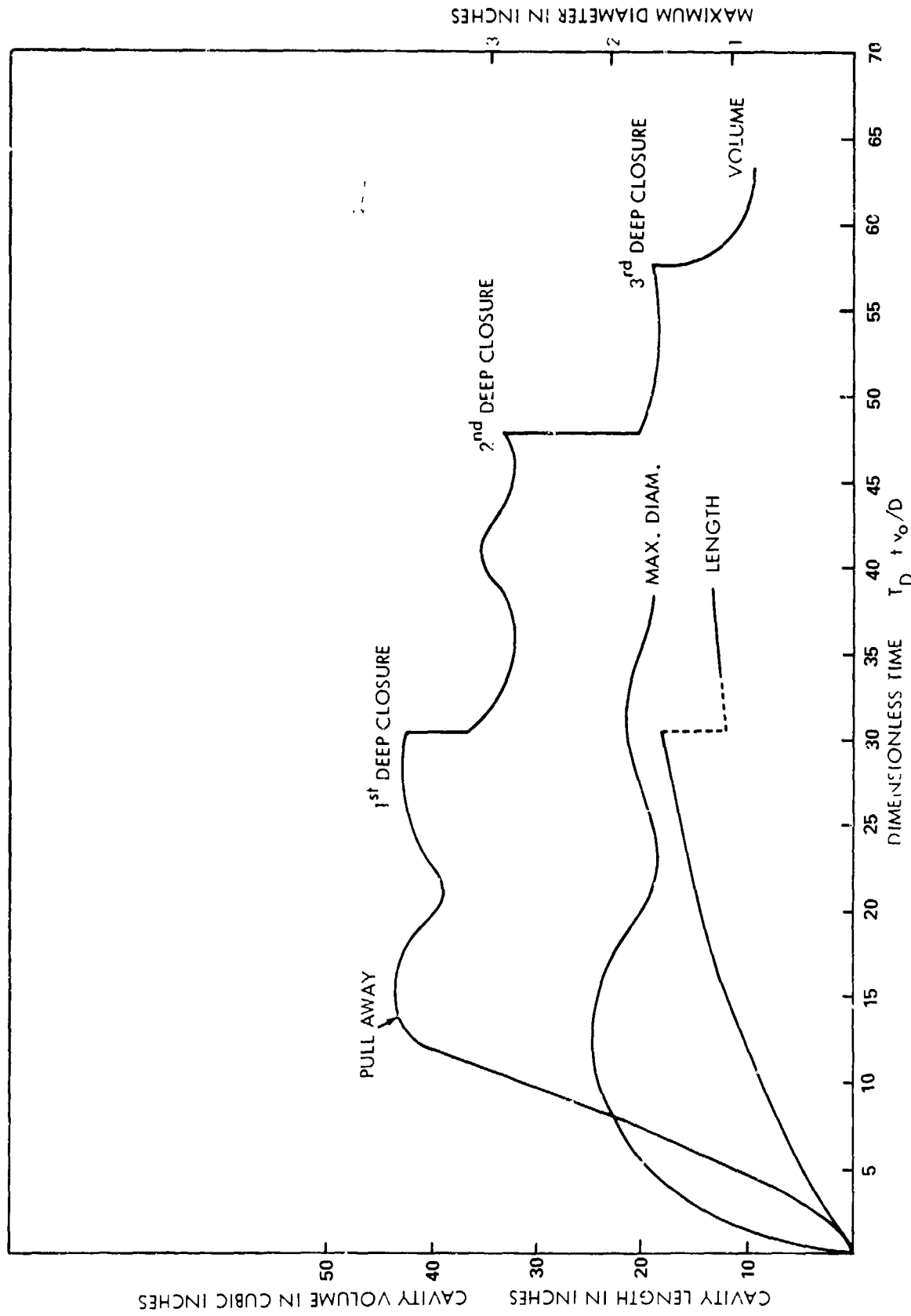
FIG. 1-33 DEVELOPMENT OF THE CAVITY DUE TO WATER ENTRY OF A SPHERE. THE WATER ENTRY OF A 1-INCH SPHERE WAS VERTICAL AT 96 FEET PER SECOND.
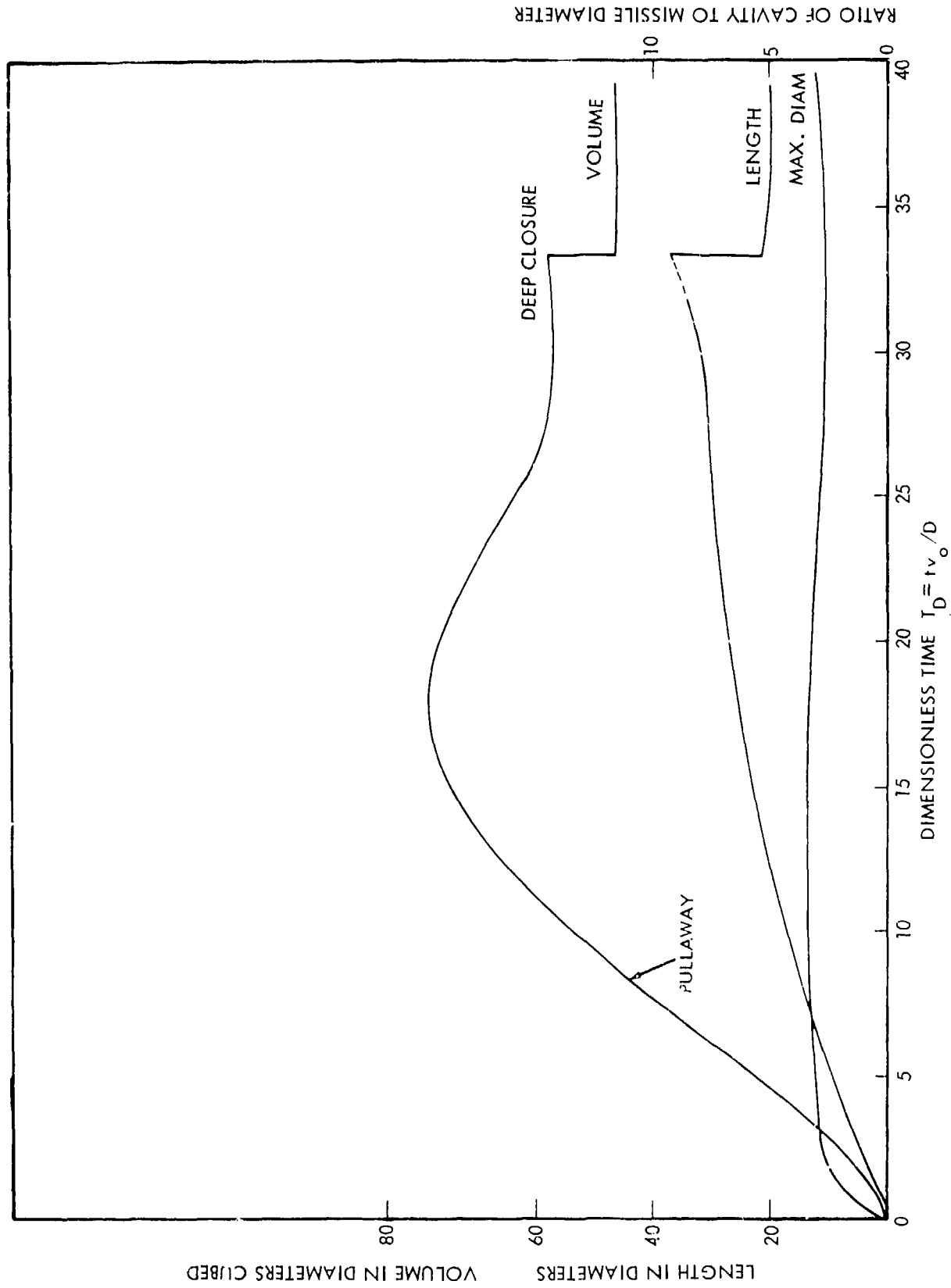
FIG. 1-34 DEVELOPMENT OF THE CAVITY DUE TO THE WATER ENTRY OF A RIGHT CYLINDER. THIS WAS A VERTICAL ENTRY OF A 1-1/2-INCH RIGHT CYLINDER AT 145 FEET PER SECOND. REF (1-18)
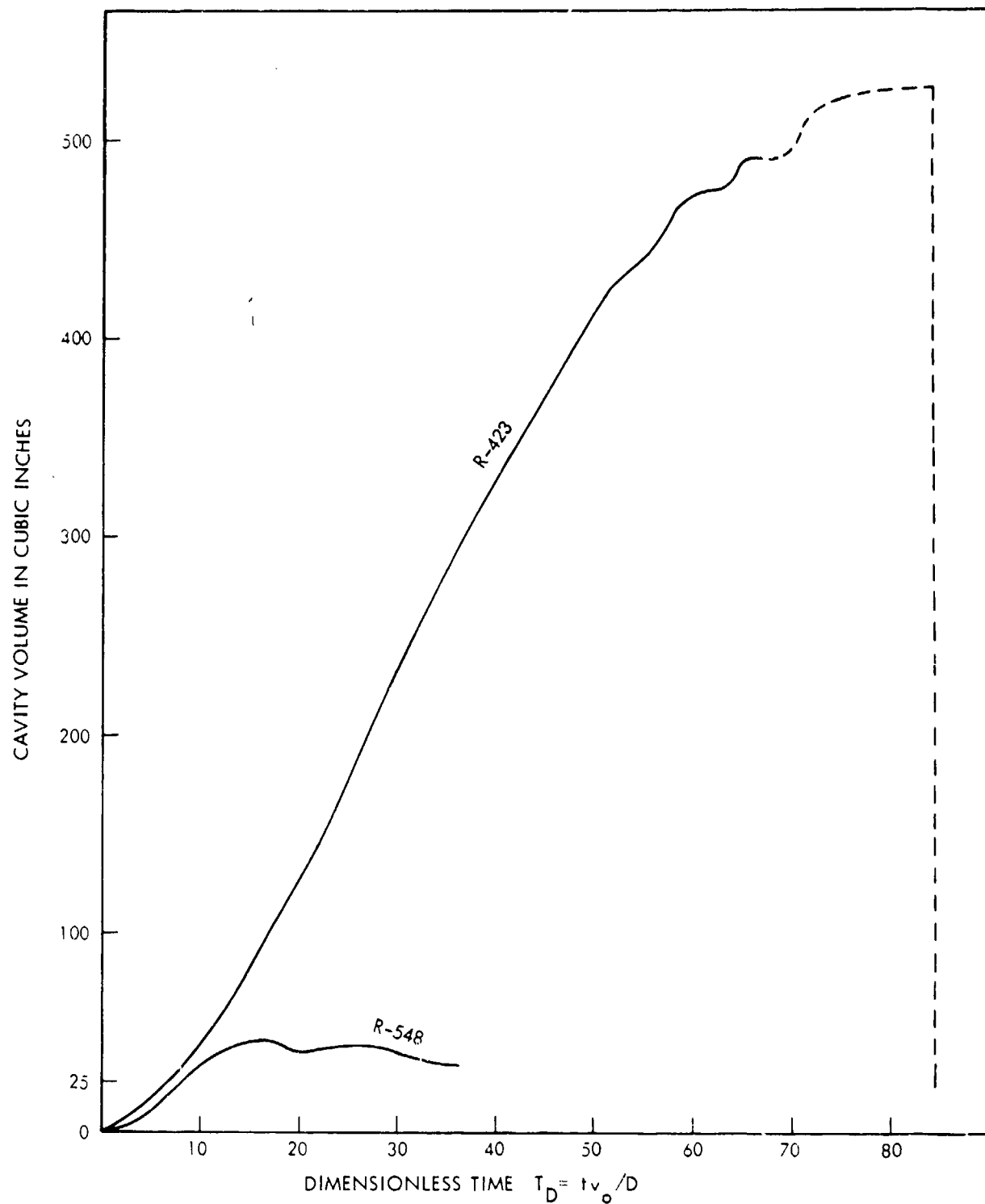
FIG. 1-35 CAVITY VOLUME WITH AND WITHOUT SURFACE CLOSURE
BOTH VERTICAL WATER ENTRIES WERE OF 1-INCH STEEL SPH RES AT 96 FEET PER
SECOND. BECAUSE OF LOW PRESSURE ABOVE THE WATER, ROUND R-423 HAD
NO SURFACE CLOSURE. THE VERTICAL LINE SHOWS THE DECREASE IN VOLUME
OF THE ATTACHED CAVITY AT DEEP CLOSURE. REF (1-18)

FIG. 1-37 VARIATION OF CAVITY VOLUME AFTER ENTRY (M=69)

FIG. 1-36 VARIATION OF CAVITY VOLUME AFTER ENTRY (M=11)

FIG. 1-39 VARIATION OF CAVITY LENGTH AFTER ENTRY (M=69)

FIG. 1-38 VARIATION OF CAVITY LENGTH AFTER ENTRY (M=11)
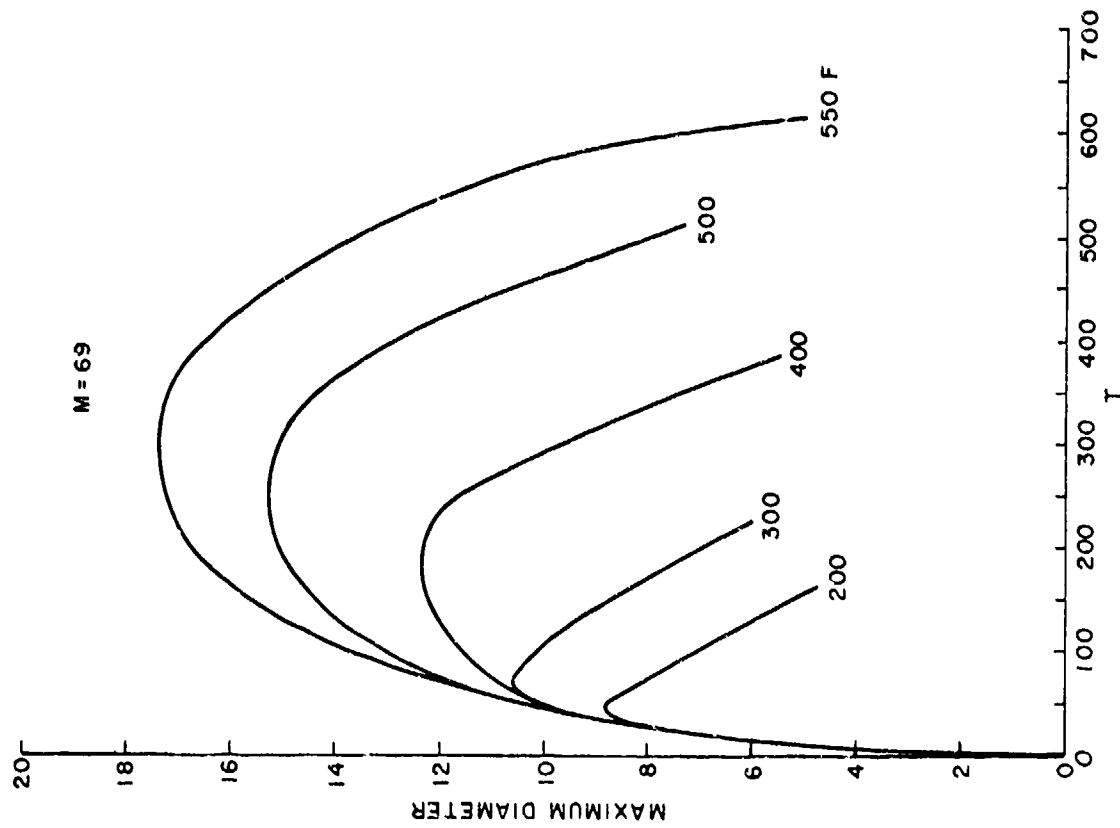
FIG. 1-41 VARIATION OF CAVITY DIAMETER AFTER ENTRY (M=69)
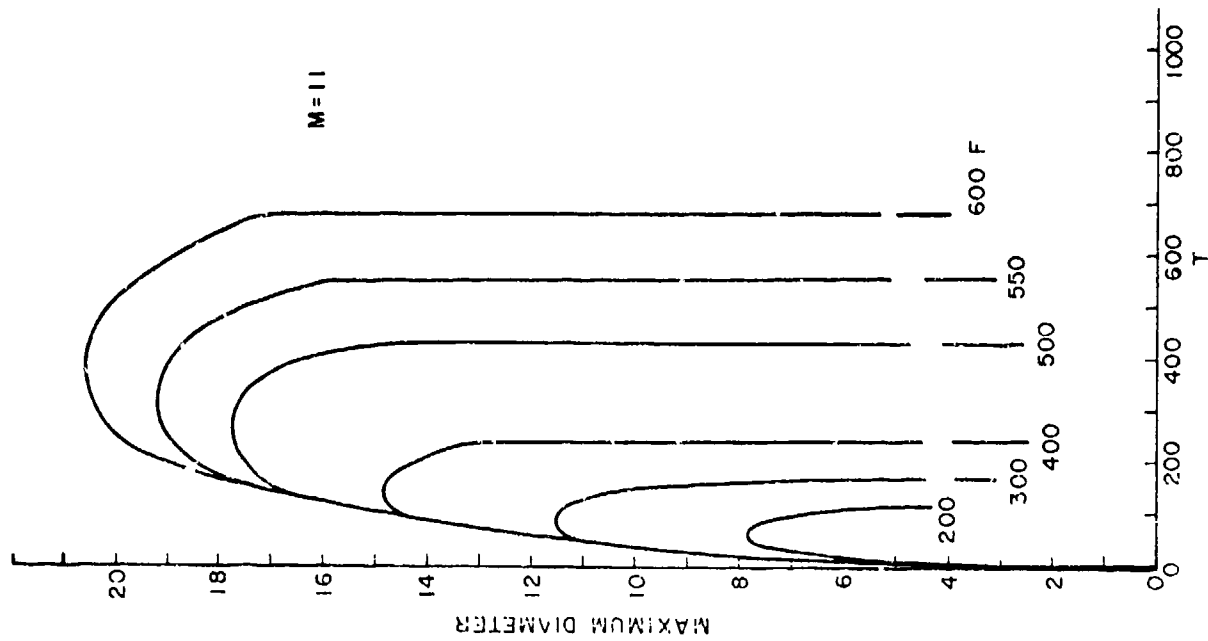
FIG. 1-40 VARIATION OF CAVITY DIAMETER AFTER ENTRY (M=11) REF (1-7)
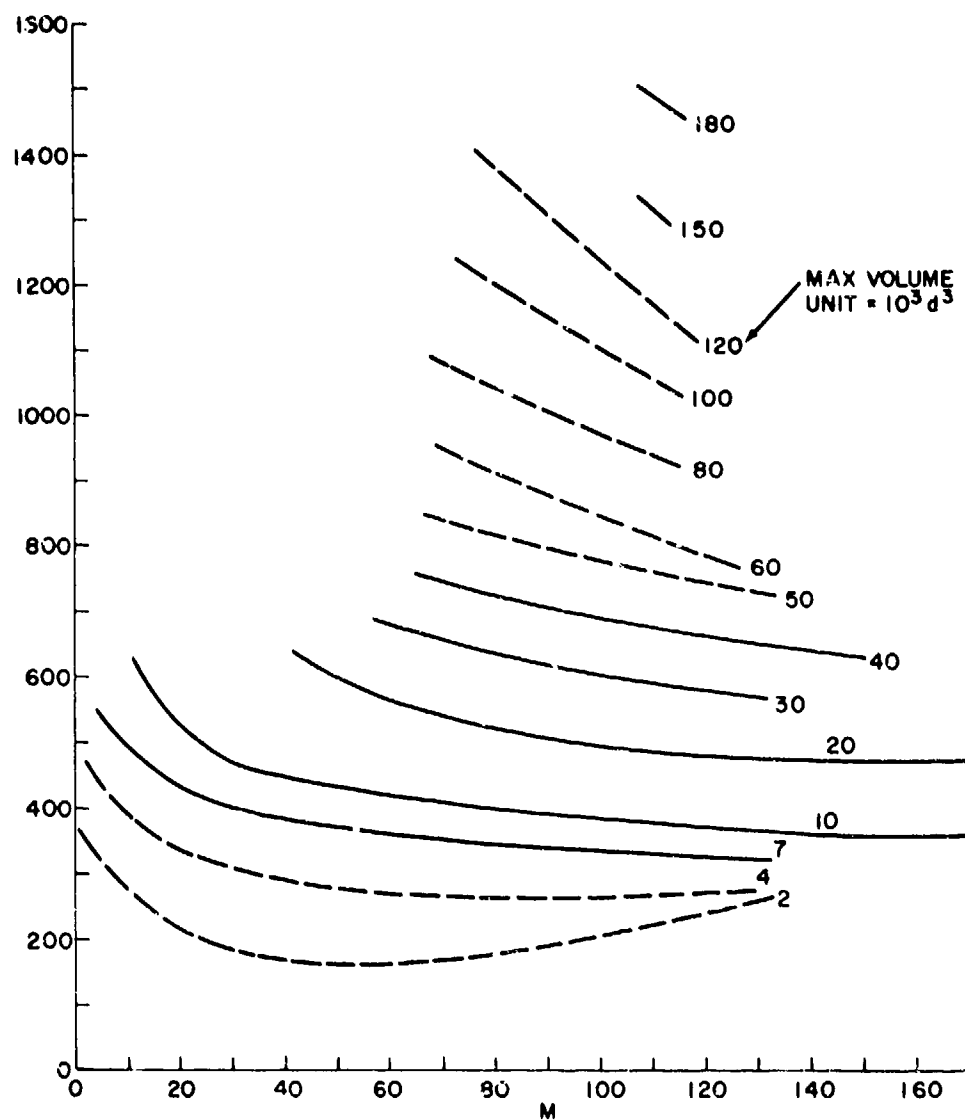
FIG. 1-42 CONTOURS OF MAXIMUM CAVITY VOLUME REF (1-7)
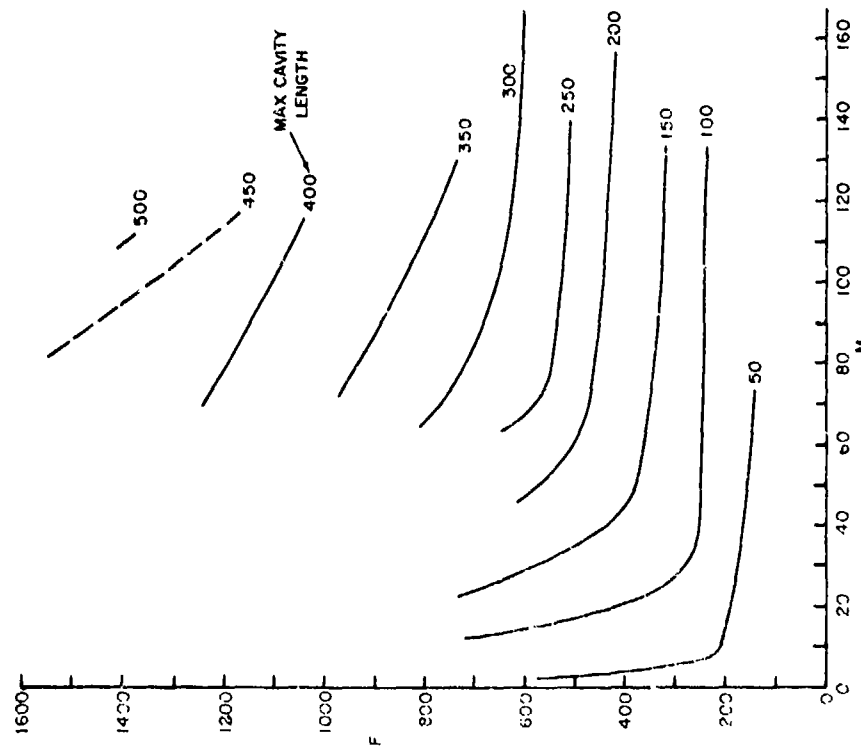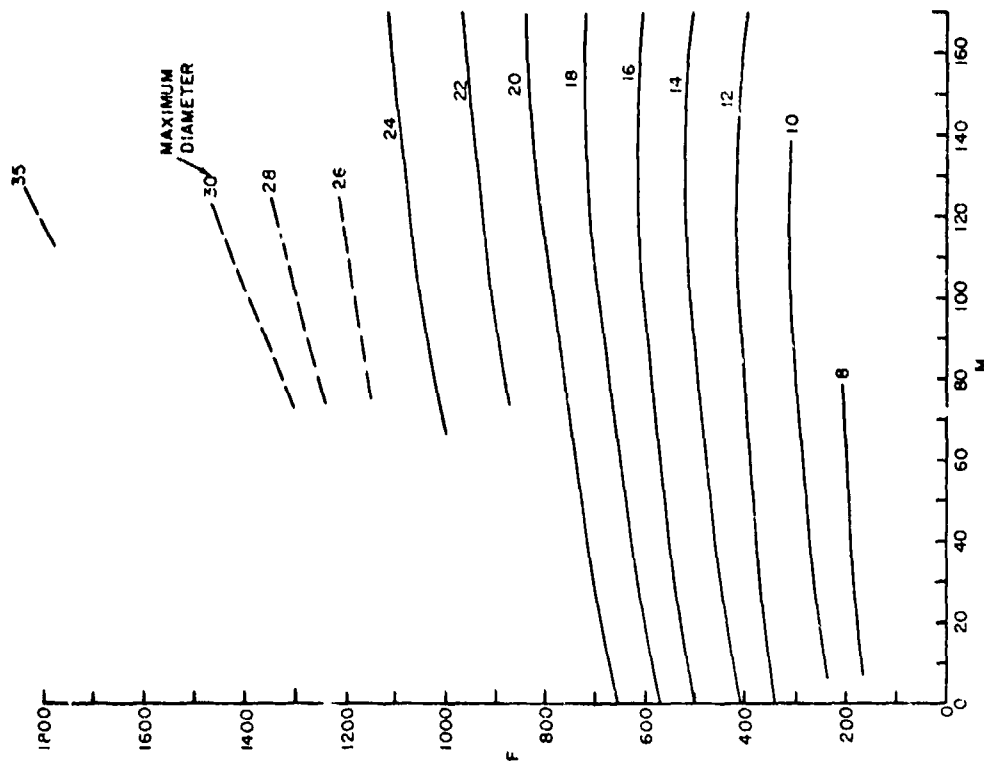
FIG. 1-44 CONTOURS OF MAXIMUM CAVITY DIAMETER

FIG. 1-43 CONTOURS OF MAXIMUM CAVITY LENGTH FROM REF (1-7)

FIG. 1-46 CONTOURS OF TIME AFTER ENTRY WHEN CAVITY
LENGTH IS HALF THE DISTANCE TRAVELED
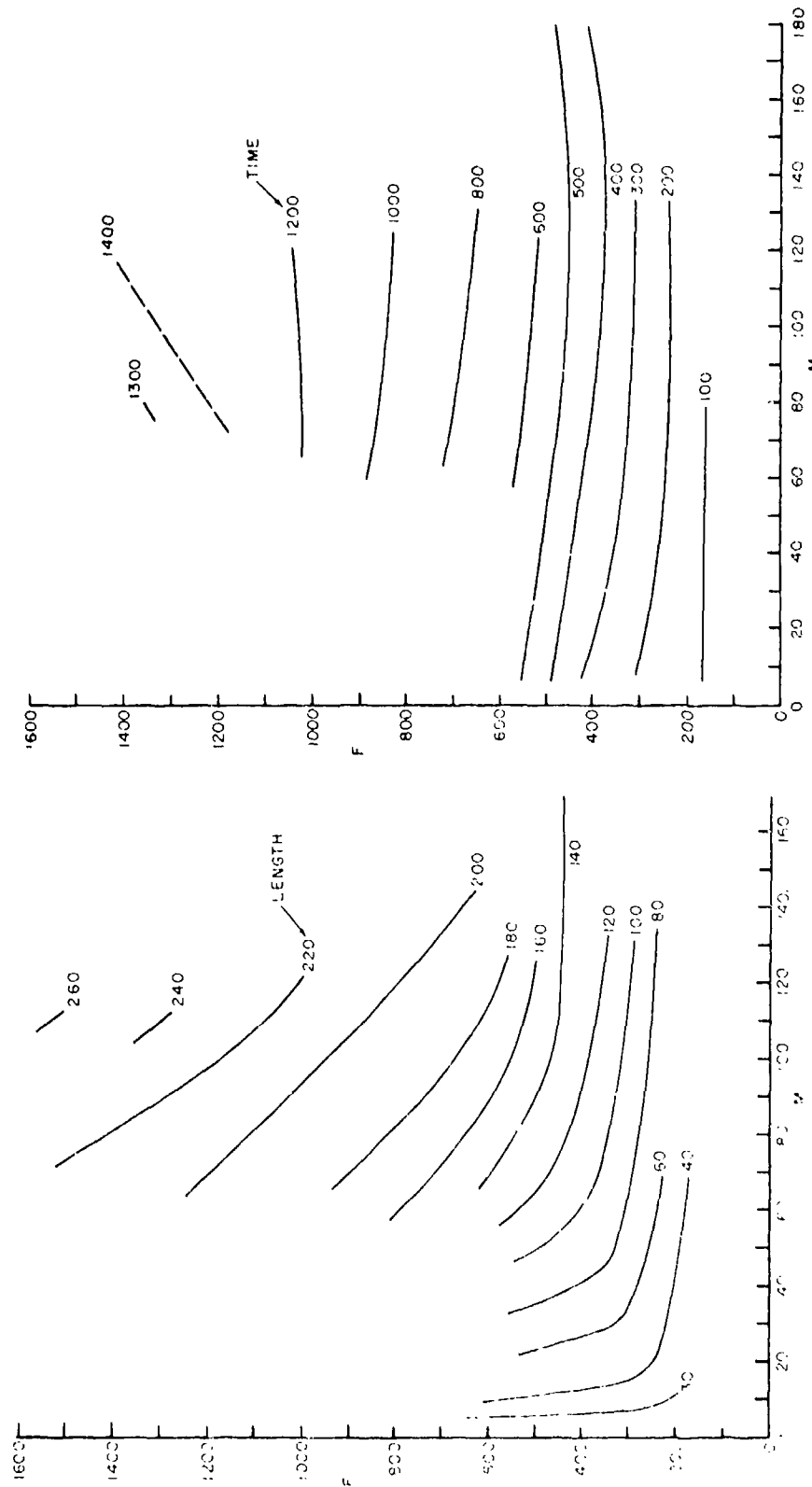
FIG. 1-45 CONTOURS OF CAVITY LENGTH WHICH IS
HALF THE DISTANCE TRAVELED REF (1-7)
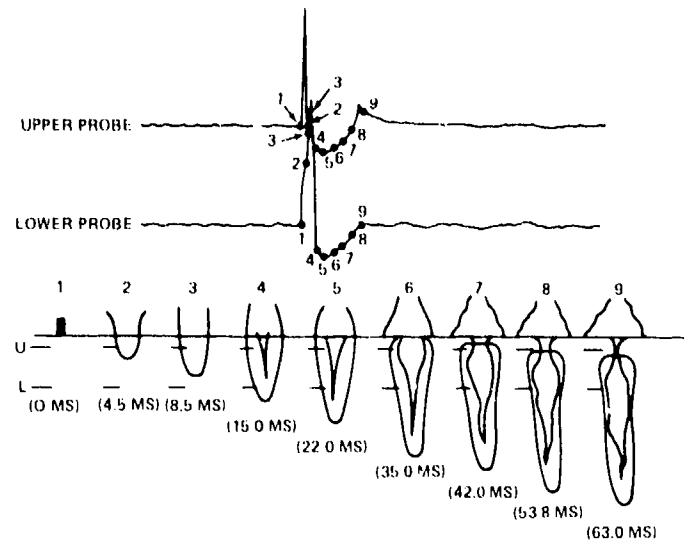
FIG. 1-47 CORRELATION OF PRESSURE DATA WITH PHOTOGRAPHICALLY OBSERVED CAVITY BEHAVIOR
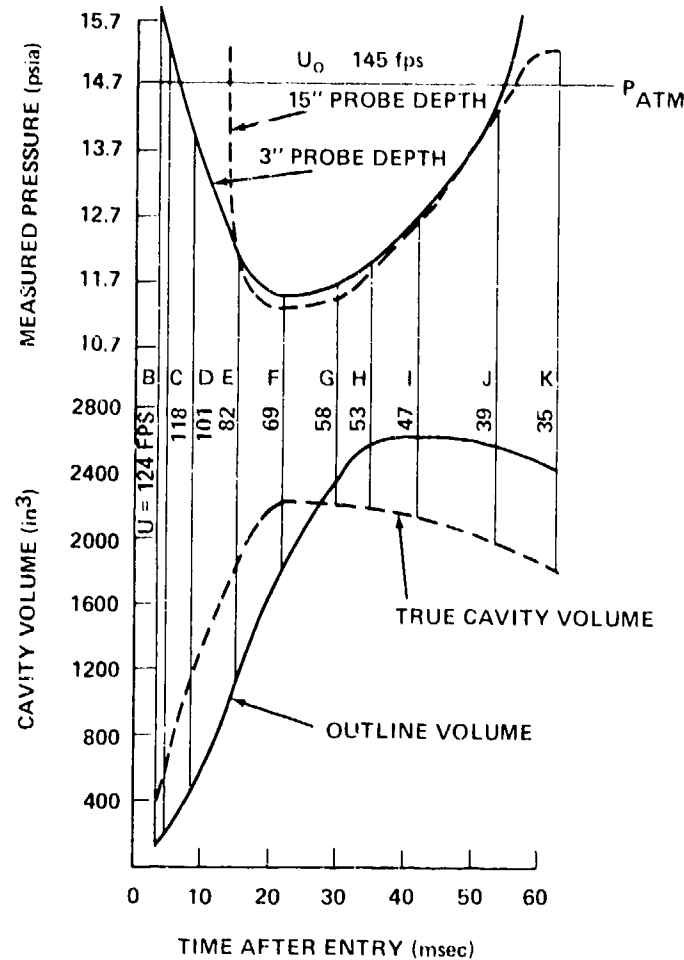
FIG. 1-48 CAVITY PRESSURE-CAVITY VOLUME CORRELATION
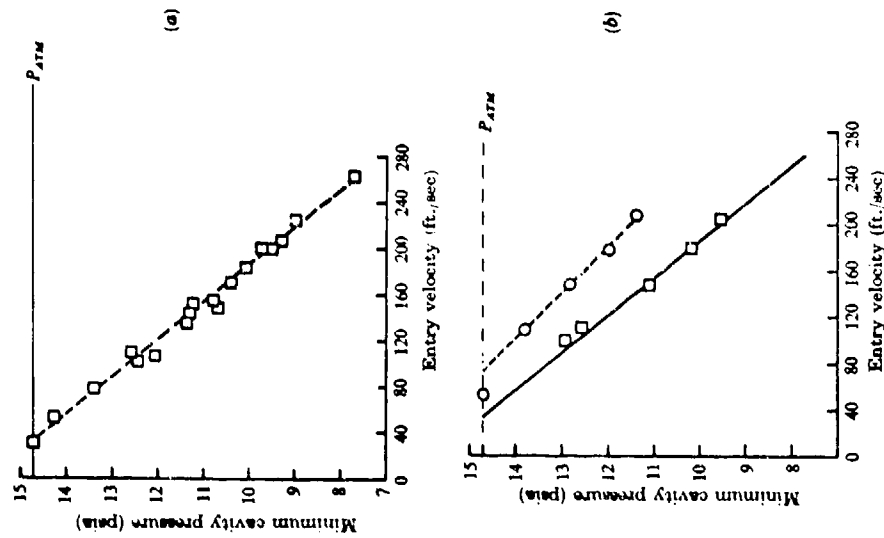
FIG. 1-50 MINIMUM CAVITY PRESSURE VS. ENTRY VELOCITY FOR VERTICAL AND OBLIQUE ENTRIES. —, VERTICAL; (a) □ , VERTICAL. (b) □ , 60°; ○ , 45°.
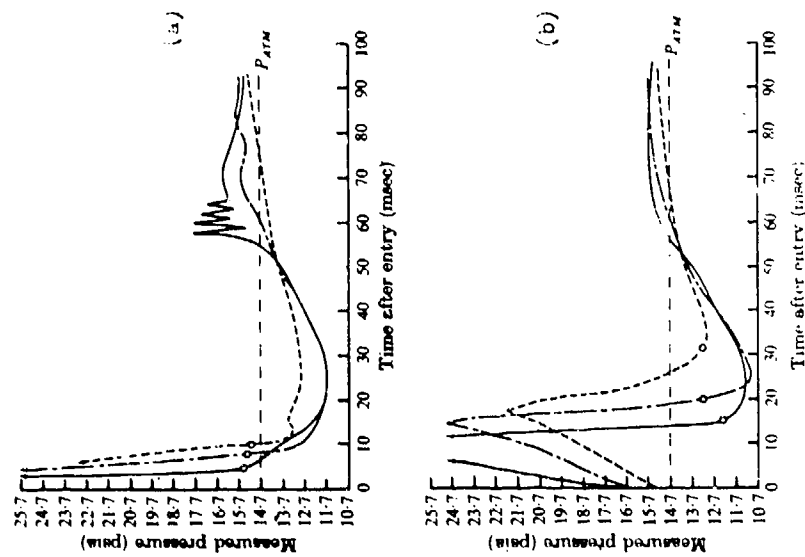
FIG. 1-49 COMPARISON OF PRESSURE DATA FOR VERTICAL AND OBLIQUE ENTRIES. U_o = 145 FT./SEC. PROBE DEPTH (IN.): (a) 3; (b) 15. —, VERTICAL; — — OBLIQUE (60°); - - - -, OBLIQUE (45°).
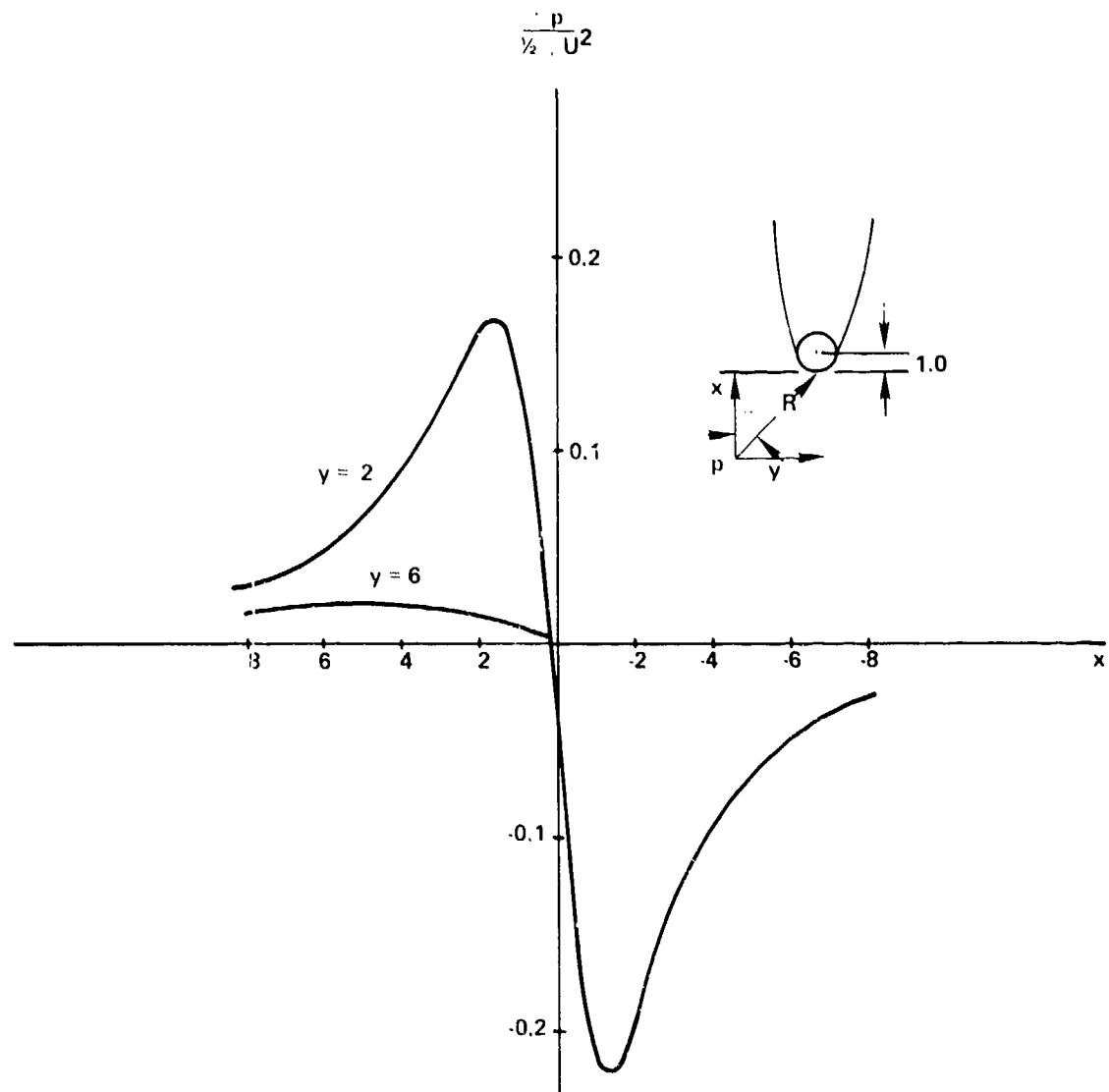
FIG. 1-51 APPROXIMATE PRESSURE CHANGE IN WATER
DUE TO APPROACH OF WATER-ENTRANT SPHERE

Chapter 2

THE FORCES ACTING ON CAVITY-RUNNING MISSILES

Symbols

a	a parameter in equation (2-4)
A	maximum cross-sectional area of missile
A_n	area of nose truncation
C_D	drag coefficient = $2D/\rho U^2 A$
C_{Do}	drag coefficient for $\sigma=0$
C_L	lift coefficient = $2L/\rho U^2 A$
C_{Lo}	lift coefficient for $\sigma=0$
$C_{L\alpha}$	lift coefficient derivative = $dC_L/d\alpha$ at $\alpha = 0$
C_M	moment coefficient = $2M/\rho U^2\ Ad$
C_p	pressure coefficient = $(p - p_o)/q$
C_{po}	pressure coefficient for $\sigma = 0$
C. G.	center of gravity
C. P.	center of pressure of hydrodynamic forces
d	maximum diameter of missile
D	drag force; also cavity diameter at planing tail
f	fineness ratio = L/d for nose
Fr	Froude number = $U/\sqrt{gd}$
g	acceleration of gravity
k	a parameter in equation (2-16)
L	lift force; also missile or nose length
L_1	distance of C.P. from center for M
M	hydrodynamic moment
p	local pressure on missile nose
p_c	cavity pressure
p_∞	freestream pressure
p_v	saturation vapor pressure of water

q	dynamic pressure $= (1/2)\rho U^2$
Q	correlation parameter for disk ogives $= 1/(1 + 2R_O)$
r_O	ogive radius
R	Reynolds number
R_O	ogive radius in calibers $= r_O/d$
U	freestream or missile velocity
α	angle of attack (see Fig. 2-42)
α_p	angle of attack of disk (see Fig. 2-38)
β	half angle of cone or wedge
δ	depth of submergence of tail tip of missile (Fig. 2-47)
θ	flow-separation angle, measured from stagnation point; or angle of spherical surface on spherogive; or surface angle of attack (Fig. 2-46)
ρ	mass density of water
σ	cavitation number
σ_V	vapor cavitation number

iii

INTRODUCTION

When a missile travels through water at a sufficiently high speed, the flow along the nose usually separates from the missile surface and a cavity is generated which may envelop a portion or the whole of the missile (Fig. 2-1). The relative motion between solid body and water may be due to motion of the body or to the flow of water past a body which is mounted in a water tunnel. It is well known that the cavity shape depends principally on the cavitation number

$$\sigma = \frac{p_\infty - p_C}{(1/2)\rho U^2} \tag{2-1}$$

where p_∞ is the freestream pressure, p_C the gas or vapor pressure within the cavity, ρ the liquid density, and U the speed of the freestream or of the missile. Equation (2-1) is discussed in detail in Reference (2-1). The missiles in Figure 2-1 are said to be cavity running.

The forces which the water exerts on the missile nose may be resolved into a drag force, a lift force, and a moment above a transverse axis, or equivalently an axial force, a normal force and moment. The drag and axial forces are parallel respectively to the trajectory and to the missile axis, and the other forces are perpendicular to these.

For a fully wetted missile it is customary to take the moment about an axis through the center of gravity or the center of buoyancy. For the cavity-running missile, especially when the nose alone is in contact with the water (and the missile is said to be "riding on its nose"), the moment may not depend on the unwetted afterbody of the missile and it is more useful to use a center for the moment which is associated with the nose, usually at the center of the base of the nose, that is, the center of a hemispherical nose or the center of the base of a cone. In the present report the center used for the moment will be specified when values are given.

Hydrodynamic coefficients are defined as follows:

the DRAG COEFFICIENT

$$C_D = D/(1/2)\rho U^2 A$$

where D is the drag force and $A = \pi d^2/4$ is the maximum cross-sectional area of the missile nose;

the LIFT COEFFICIENT

$$C_L = L/(1/2)\rho U^2 A$$

where L is the lift force, and

the MOMENT COEFFICIENT

$$C_M = M/(1/2)\rho U^2 \, Ad$$

where M is the moment of the force on the nose. Because C_L is frequently almost proportional to the angle of attack, α, for small angles, the lift-coefficient derivative is frequently used. This is defined as the slope at $\alpha = 0$ of the graph of C_L against α, or

$$C_{L\alpha} = C_L/\alpha.$$

Usually the instantaneous force or the integrated impulse can be regarded as acting at a specific point on the axis of the missile, the <u>center of pressure</u>. In some cases, especially when the moment is large, the center of pressure may not be within the nose, and in an extreme case, when the force system is a pure couple, it may go to infinity in front or behind the missile.

In the discussion of forces during cavity running, the situation where the missile is "riding on its nose" is of special interest, but impulsive or steady forces act on the tail or afterbody when the tail strikes or leans against the cavity wall. It is generally practical and useful to regard the overall forces as due to independent force systems acting on the nose and tail of the missile. They will be treated separately in this report.

Under fully wetted flow conditions the drag force is less than the total force acting on the nose (form and skin-friction drag) because of the pressure (due to "pressure recovery") on the aft end of the missile. During steady cavity running in an enveloping cavity the flow pattern on the forward part of the nose usually differs little from the flow when fully wetted but the aft end of the missile is subjected to cavity pressure, which may have any value from the ambient pressure, p_∞, to the vapor pressure of the water. The force resulting from the cavity pressure is regarded as a part of the nose force system since it does not matter whether this uniform pressure acts on the base of the nose or on an unwetted afterbody. Because of the effect of cavity pressure the drag can be expressed as a function of the cavitation number. Drag always increases with an increase of cavitation number, and the dependence will be discussed in detail later.

For bluff shapes which have a relatively large form drag and a short wetted path, the friction drag may be less than one percent of the total drag. The evaluation of the bluffness or "fullness" of the nose shape is not always simple. It might be mentioned for example that cone and paraboloid noses, both of fineness ratio (L/d = length/diameter) of 3.33 differ by less than one percent in their friction drag, but the form drag of the cone (half angle 8.5°) is almost three times that of the paraboloid. The friction drag of bodies of revolution can generally be evaluated adequately by use of the formula for the flat plate (Refs. (2-2) and (2-3)).

Many investigators have contributed to the knowledge of cavity-running drag by means of theoretical predictions and experimental measurements and both will be studied in this report. The larger part of their work is related to the drag force and to the symmetric cavity conditions which exist when the missile is traveling at zero angle of attack, that is, when the missile axis is parallel to the trajectory. For this reason the first and major part of this report is devoted to drag and zero angle of attack.

Nose shapes may be divided into two classes (Ref. (2-4)) depending on whether the flow separation occurs at a shoulder or other line at which the tangent to the surface changes suddenly; separation has been called smooth when the nose has moderate curvature near the line of separation. The importance of the distinction is the fact that abrupt separation presumably occurs always at the same position, independent of Reynolds number and cavitation number. In smooth separation, on the other hand, small influences (especially Reynolds number) are able to vary the position of separation. Because of this the surface of the cavity which follows "smooth separation" is generally far from smooth. The actual mechanism of separation behavior is treated elsewhere (Ref. (2-1)) and will not be discussed in this report.

It will be noted from Figure 2-1 that the separation from an ogive may be smooth or abrupt, depending on whether the separation occurs before the end of the curved surface or at its end. The same types of behavior may be observed with a spherical surface consisting of a spherical segment which subtends an angle which may be more or less than the angle of the surface normally wetted by the flow. When the sphere is generating a cavity, the flow normally separates from the windward hemisphere; hence the behavior is the same for a hemisphere as for a full sphere.

THE DRAG EQUATION

Experimental cavity-running drag data are obtained either from the water tunnel (or towing basin) or from free flight (usually during water entry). Free-flight measurements are subject to serious objections: the cavitation number is not known with accuracy (for water entry it may generally be assumed that it is near zero while the cavity is open to the atmosphere), and the determination is made over a travel distance for which the speed is not quite constant and the force varies because of the transient conditions of water entry. As a consequence drag values obtained during free flight will be given little weight compared to those observed in the steady flow of the water tunnel.

On the surface of a disk during cavity running the pressure should have a maximum (stagnation) value of $p_\infty + q$, the ambient pressure plus the dynamic pressure $q = (1/2)\rho U^2$. The pressure will fall off toward the edges, presumably to p_c. For the cup shown in Figure 2-2 it may be expected that the pressure will be very close to $p_\infty + q$ over the

whole inner surface of the cup since steady flow will not be set up there. This nose is usually called a "stagnation cup", but is referred to as a "scoop ring" in the translation of Reference (2-5).

From Figure 2-2 the effective force on the cylinder with stagnation-cup nose should be

$$(p_\infty + q - p_c)A.$$

From the definition of the drag coefficient C_D then, the drag force

$$D = (p_\infty + q - p_c)A = qAC_D,$$

so that

$$C_D = 1 + \sigma \tag{2-2}$$

From this, C_{Do} (C_D at $\sigma = 0$) should equal unity for the stagnation cup and the equation can be written

$$C_D = C_{Do} + \sigma \tag{2-3}$$

Reports state (Refs. (2-6) and (2-7)) that equation (2-3) is approximately correct also for slender cones. This will be investigated later in this section. Actually this equation should hold whenever the pressure over the wetted part of the missile does not vary with the cavitation number. In general the form

$$C_D = C_{Do} + \frac{dC_D\sigma}{d\sigma} = C_{Do} (1 + a\sigma) \tag{2-4}$$

is required. For the stagnation cup where $C_{Do} = 1$, equation (2-3) can also be written

$$C_D = C_{Do} (1 + \sigma) \tag{2-5}$$

Equation (2-5) has been predicted for other shapes as well (Refs. (2-6), (2-8), (2-9) and (2-10)). Reichardt (Ref. (2-5)) gave a derivation of equation (2-5) which is substantially as follows. Figure 2-3 shows plots of the quantity $1 - C_p$ on the cavity-generating nose against position across the missile diameter: the shallow graph for zero cavitation number and the other for a positive cavitation number σ. Here

$$C_p = (p - p_\infty)/q$$

is the well-known pressure coefficient and p is the local pressure on the nose. At the center of the nose the pressure will equal the stagnation pressure $p_\infty + q$; and $1 - C_p = 0$. At the rear end of the nose where the nose meets the cylindrical body and the radius is d/2, the pressure presumably drops to the cavity pressure p_c. For $\sigma = 0$ this pressure will be p_∞ and $1 - C_p = 1$. When the cavitation number is greater than zero

$$1 - C_p = 1 + \sigma$$

at the outside of the nose. Reichardt made the assumption that the value of $1 - C_p$ at each distance from the missile axis is $1 + \sigma$ times as large when the cavitation number is σ, as when it is zero. In general the drag force on a missile, cavity running as in Figure 2-2, is

$$D = \int (p - p_c) dA \qquad (2-6)$$

where dA is the projection in a transverse plane of an element of nose area. The drag coefficient is then

$$C_D = D/qA = \frac{1}{A} \int \frac{p - p_\infty}{q} + \frac{p_\infty - p_c}{q} \ dA$$

or

$$C_D = \frac{1}{A} \int (C_p + \sigma) \ dA \qquad (2-7)$$

with

$$C_{Do} = \frac{1}{A} \int C_{po} dA \qquad (2-8)$$

where C_{po} is the value of the pressure coefficient when $\sigma = 0$. Since the ordinates of the curves in Figure 2-3 are in the ratio $(1 + \sigma)/1$,

$$1 - C_p = (1 + \sigma)(1 - C_{po}).$$

Hence

$$(1 + \sigma) C_{po} = 1 + \sigma - 1 + C_p = C_p + \sigma \qquad (2-9)$$

When equation (2-9) is used with equation (2-7)

$$C_D = \frac{1 + \sigma}{A} \int C_{po} dA$$

is obtained. Hence from equation (2-8)

$$C_D = C_{Do} (1 + \sigma) \qquad (2-5)$$

From equation (2-7)

$$C_D = \frac{1}{A} \int (C_p + \sigma) dA = \overline{C}_p + \sigma,$$

where $\overline{C}_p$ is the average pressure coefficient on the nose of the missile. Dawson and Seigel (Ref. (2-11) noted that when

$$C_D = C_{Do} (1 + \sigma), \qquad (2-5)$$

$$C_D = C_{Do} + C_{Do}\sigma = \overline{C}_p + \sigma,$$

leads to

$$\overline{C}_p = C_{Do} - \sigma(1 - C_{Do}). \qquad (2-10)$$

Equation (2-10) shows that the average pressure coefficient on the missile nose decreases linearly with σ if equation (2-5) is obeyed.

Various claims have been made as to the validity of equation (2-5). Gilbarg (Ref. (2-10)) stated that it is generally valid for both plane and axially symmetric cavities having fixed separation points. The experimental data of the present report show the agreement to be good for rather blunt bodies with fixed separation points.

DRAG OF AXIALLY-SYMMETRIC BODIES

The Disk

The disk (or right cylinder) is perhaps the simplest nose shape. Numerous attempts have been made to predict its cavity-running drag coefficient theoretically (principally at $\sigma = 0$) and many experimental drag measurements have been reported.

Garabedian calculated (Refs. (2-9) and (2-12)) the drag coefficient of the disk theoretically and obtained $C_{Do} = 0.827$ (Ref. (2-9)) and $C_D = 1.058$ at $\sigma = 0.2235$ (Ref. (2-12)). From these values, $a = 1.25$ in equation (2-4). Plesset and Shaffer (Ref. (2-13)), by assuming the same pressure distribution on the disk as on an infinite strip, obtained drag values which can be written (Ref. (2-14))

$$C_D = 0.8053 \ (1 + \sigma + 0.028\sigma^2),$$

and Armstrong, in a modification of that method (Ref. (2-15)), found $C_{Do} = 0.823$. Fisher (Ref. (2-16)) gave two predicted values for C_{Do} for the disk: 0.805 and 0.824, with the latter being presumably more accurate, in excellent agreement with Garabedian (Ref. (2-9)) and Armstrong.

Numerous values of C_D have been reported for the cavity phase of the water entry of disks. Reference (2-17) shows that for such water entries σ should lie between 0 and 0.05, but this range will depend somewhat on how the value of the coefficient is derived. A few of the more reliable water-entry values of C_{Do} for disks are 0.83 (Ref. (2-17)); 0.84 to 0.85 (Ref. 2-18); 0.82 (Ref. (2-19)).

Values obtained from water-tunnel or towing tests should be most accurate although the possibility that the value of the drag coefficient is influenced by the finite width of the tunnel should be considered. This report includes data for disks from the references shown on Table 1. Values of σ for these tests ranged from 0. to 1.6. The greatest data density is in the region $\sigma < 0.3$, and this range is considered separately in Figures 2-4a and 2-4b, where values of drag coefficient and $C_D/(1 + \sigma)$ are plotted against σ.

It is evident from these graphs that the large differences in drag value at given values of σ are not so much dependent on random variations as on differences between various experimenters. In many cases the data points for different experiments can be completely separated by a straight line, that is, there is often no overlapping of data, and where overlapping does occur the data for different tests define quite different graphs. For example it will be seen in Figure 2-4a that Reichardt's data (Ref. (2-5)) lie consistently below the least-square straight line by an average of about $\Delta C_D = 0.02$. One, or both, of two reasons are presumably responsible for these differences:

1) systematic errors due to instrumentation (such as inaccurately calibrated drag balances), the effect of tunnel size, or incorrect evaluation of σ, and

2) true differences in drag coefficient caused by different experimental conditions. These include the effect of Reynolds number (through model size or flow velocity) or other dimensionless numbers, air content of the water, etc.

The reason why various experiments obtained different numerical results is not determined in this report, in part because the information reported was generally insufficient to permit this evaluation. The evaluator of the data has two alternatives: to assume all data of equal probable accuracy and to obtain graphs from the mean of all data; or to weight the data on the basis of some knowledge of the tests. Evidertly neither assumption is superior a priori.

Experimental conditions for various tests of disks and cones are given in Table 2-1. Oversmith (Ref. (2-21)) made his tests in a towing basin while the others used water tunnels of various types. The listed ratios of tunnel width to model diameter are based on the lowest value of this ratio for each test, except that the distance to a solid wall rather than the distance to a free surface was used when both were involved. Most reports express the belief that no significant choking occurred in the experiments and this has been assumed in the evaluation of data. It is a matter which would merit further study especially since it is the width of the cavity rather than the diameter of the model which is of prime significance. Some of the experimenters used vapor-filled cavities, some air-filled, and some used both. Some cavitation was enveloping and some was not. Here obviously one might look for differences, but no evidence was seen of the effect of cavity pressure apart from cavitation number.

The equation of the least-square straight line for the disk on Figure 2-4a is

$$C_D = 0.807 + 0.891\sigma = 0.807 (1 + 1.104\sigma). \qquad (2-11)$$

This graph differs little from others reported for accumulated experimental data (Refs. (2-7), (2-20), (2-22), and (2-27)). The

Table 2-1

TEST DATA COMPARISON FOR DISKS AND CONES

Ref.	Vel. max or range ft/sec	Reyn. No. max or range x 10^{-5}	Model Diam. (in.)	Air or Vapor Cavity	σ	Tunnel Width / Model Diameter
DISKS						
(2-5)			.08-.59	V	.02-.12	6
(2-7)	38	.7-1.3	1/4-1/2		.001-.07	
(2-20)	25			A	.07-.16	21
(2-21)	108	A.6-20	1	A		
		V18-22	1	V	.03-.31	84
(2-22)	50	5	1, 1.5	V	.4-1.6	24
(2-23)	27-32	4.0-4.8	2 1/4	V	.5-1.2	3.0
	18-24	3.9-5.2	3 1/4	A	.6-1.3	3.0
	14-19	4.4-6.0	4-3/4	A&V	?	3.0
(2-24)	45?	9.0	3		.2-.7	13
(2-25)	17.5	1.2	1	A		21
(2-11,2-26)	8-35	.5-5.0	1	V	.3-.6	12
CONES						
5° (2-7)	38	1.9	3/4		.01-.10	
	38	1.3	1/2		.01-.10	
10° (2-7)	38	1.9	3/4		.01-.09	
	38	1.3	1/2		.01-.08	
14° (2-5)			.08-.59	V	.02-.07	6
15° (2-7)	38	1.9	3/4		.01-.08	
	38	1.3	1/2		.01-.10	
(2-20)	25			A	.04-.19	21
	100?	5.0	1/4-1/2	V	.10-.25	14
(2-25)	17.5	2.3	2	A	.07-.15	21
26.6° (2-5)			.08-.59	V	.02-.09	6
30° (2-7)	38		5/8		.02-.09	
45° (2-5)			.08-.59	V	.02-.12	6
(2-7)	38				.007-.09	
(2-20)	25			A	.05-.16	21
	100?		1/4-1/2	V	.18-.20	14
(2-21)	108	6-20	1	A	.01-.15	84
(2-25)	17.5	1.6	1.41	A	.09-.16	21
(2-11,2-26)	8-35	.5-5.0	1	V	.3-1.2	12
63.5° (2-5)			.08-.59	V	.03-.13	6
67.5° (2-11,2-26)	8-35	.5-5.0	1	V	.2-.8	
STAGNATION CUP						
(2-5)			.08-.59	V	.02-.12	6
(2-20)	25			A	.06-.14	21
	100?		1/4-1/2	V	.04-.12	14

C_{Do} values from all of these comparisons are probably contained in the range

$$C_{DO} = 0.082 \pm 0.013$$

While equation (2-11) appeared to be a satisfactory representation of the data, the nearness of this equation to

$$_D = C_{DO} (1 + \sigma) \tag{2-5}$$

led to a plotting of $C_D/(1 + \sigma)$ against σ as shown in Figure 2-4b. It is immediately evident that a constant value of $C_D/(1 + \sigma)$, as indicated by equation (2-5) is within experimental error. Further, data of individual experimenters generally show a reasonably constant value of $C_D/(1 + \sigma)$, as is apparent from Figure 2-4b. Table 2-2 lists the average values of $C_D/(1 + \sigma)$ found by each experimenter, given separately for the regions below and above $\sigma = 0.4$. For the lower range of σ, four of the experimenters reported data leading to almost identical values of the average, namely 0.815 $\pm$ 0.001. One of these tests (that of Oversmith) extended beyond $\sigma = 0.4$, and it showed good agreement in the two regions. The higher range is shown in Figure 2-5. The average C_D of Klose-Acosta, in the higher range, is hardly significant because of the large scatter at $\sigma > 1.2$, as will be seen in Figure 2-5.

From Table 2-2, Reichardt's data lie well below those of other tests, while the data of Brennan and Kermeen lie far above. Each of these is self consistent.

While the representation of the data by the straight line in Figure 2-4a appeared satisfactory, the substantiation of theory, by agreement with equation (2-5), seems to make the graphs of Figures 2-4b and 2-5 more acceptable, especially since equation (2-11) gives values which are too high at large values of σ. Hence, based on present information, the drag equation for the cavity-running disk can best be written

$$C_D = 0.815 (1 + \sigma) \tag{2-12}$$

Table 2-2

ANALYSIS OF DRAG DATA FOR THE CAVITY-RUNNING DISK

Reference	Average Value of $C_D/(1 + \sigma)$	
	$\sigma \leq 0.4$	$\sigma > 0.4$
Reichardt (2-5)	0.792	
O'Neill (2-20)	0.814	
Kiceniuk (2-25)	0.814	
Oversmith (2-21)	0.815	0.812
A.R.D.E. (2-7)	0.816	
Brennan (2-24)	0.833	0.840
Kermeen (2-20)	0.837	0.836
Eisenberg-Pond (2-22)		0.809
Klose-Acosta (2-23)		0.814

Stagnation Cup

The stagnation cup was described earlier and was sketched in Figure 2-2. Because of the small amount of flow along the inner base of the cup the pressure over this surface should be very close to the stagnation pressure $p_\infty + q$. Hence it is expected that

$$C_D = 1.0 + \sigma \qquad (2-2)$$

and

$$C_D = C_{Do} (1 + \sigma) \qquad (2-5)$$

Actually, it is necessary that the cup be sufficiently deep for this result to be obtained. Perry, (Refs. (2-20) and (2-29)) calculated the pressure distribution across the bottom of a two-dimensional slot for various ratios of depth to width; and pressures for the three-dimensional cup were computed from these by the Plesset-Shaffer method (Ref. (2-13)). A plot of C_{Lo} based on this pressure distribution is given in Figure 2-6 together with values from measurements (Ref. 2-20)) for several cup configurations. It is seen that experimental C_D values obtained for shallow cups were lower than those predicted. Values have been calculated also by Wu and Wang (Ref. (2-14)).

Reichardt measured (Ref. (2-5) the drag coefficient of the stagnation cup but did not state the depth of the cup used. O'Neill (Ref. 2-20)) reported measurements by himself and by Kermeen with a stagnation cup having a depth/diameter = 1. The results of these experiments are plotted in Figure 2-7. The data from the three series of tests are completely separate. The two straight lines were computed by least squares separately from Reichardt's and O'Neill's data. The separation of the lines is only about $\Delta C_D = 0.02$, and is

remarkably constant. Kermeen's data were obtained over a very small range of cavitation numbers and lie between the lines representing the other data.

A least-square straight line was calculated for all of the data on Figure 2-7, but the result evidently was not a proper representation of the data because of the distribution of the data points within the individual experiments: the greater concentration of data at larger values for O'Neill and at lower values for Reichardt. Moreover the scatter of the data is obviously not random. It is probably due to errors either in the determination of σ or in the measurement of force. The data bracket the theoretical prediction

$$C_D = 1 + \sigma \qquad (2-2)$$

Using all of the data, a least-square calculation was made to determine the best slope with an assumed value of the intercept C_{D_0} = 1.0. The slope was found to be 1.010 in very good agreement with the predicted value.

It appears that equation (2-2) is the best representation of C_D for the stagnation cup. Because of confidence in the correctness of this equation it has been suggested (Ref. (2-20)) that the stagnation cup be used as a calibrating device for cavity measurements.

Cones

Drag-coefficient measurements have been reported for cones of various angles and the disk may be added to these as the limiting case of the cone with a half angle of 90°. (The half angle β will be used throughout in describing cones). Table 2-1 lists six references to drag measurements of cones and shows the cone angles tested. As with the disk, Oversmith (Ref. (2-21)) conducted tests in a towing basin while others used various types of water tunnels. The table shows that all six tests obtained data on 45° cones, three on 15° cones, while single tests were reported for other angles.

Drag-coefficient data for various cone angles are plotted against σ in Figures 2-8 to 2-15 and least-square straight lines, computed for these data, are shown. The straight line seems to be quite adequate in the presentation of drag curves up at least to $\sigma = 0.2$ or 0.3. Data for the various cone angles will be compared in Table 2-3 and Figure 2-16.

Figure 2-8 gives data for the 5° cone from tests at the Armament Research and Development Establishment at Fort Halstead, England (Ref. (2-7)). Data for 1/2-inch and 3/4-inch diameter cones are shown with least-square lines for each size and for the combined tests. The 1/2-inch data are slightly higher than those for the 3/4-inch, with little overlapping. Similar data for 10° cones in Figure 2-9 display much the same behavior except that the two sizes are interchanged, that is, the 3/4-inch shows a higher drag than the 1/2-inch. Reference (2-7) further shows that 15° cones behave like

those of 10°, with the 3/4-inch curve above the 1/2-inch. The reversal between the 5° cone and the larger angles makes it improbable that the data separation is due to such causes as Reynolds number.

Data for the 15° cone are given in Figure 2-11. Results of the three contributing reports (Refs. (2-7), (2-20) and (2-25)) are split into five groups: the measurements of O'Neill and Kermeen (Ref. 2-20)) were separated, as were the 3/4-inch and 1/2-inch data in Reference (2-7). With this breakdown it is found that Kermeen's data (Ref. (2-20)) and the 1/2-inch data (Ref. (2-7)) contribute to a lower graph and the other three to an upper one, with no overlapping of the areas occupied by the data points. The separate and combined graphs are shown in Figure 2-11.

Reichardt's data (Ref. (2-5)) for 14° and 26.6° cones and A.R.D.E. data for 30° cones are given in Figures 2-10, 2-12, and 2-13, respectively.

Data from five sources are given in Figure 2-14a for the 45° cone. There is considerable separation of the data from different sources in certain regions of σ, but with overlapping in other areas. The single least-square straight line appears to be a good average, but a great deal of systematic variation is evident. The only data for $\sigma > 0.2$ for the 45° cone were reported by Dawson and Seigel (Ref. 2-11)) based on integration of the pressure measurements of Rouse and McNown (Ref. (2-26)), and their two data points provide an extension of the 45° cone graph to higher values of σ in Figure 2-14b.

In Figure 2-15a, Reichardt's data for the 63.5° cone are given, together with a least-square straight regression line. An extension is made to this graph in Figure 2-15b by using two data points obtained by Dawson and Seigel by integration of pressures for a 67.5° cone. The data were adjusted to 63.5° by use of the results of overall cone comparisons to be described.

On Figure 2-16 values of C_D for $\sigma = 0$ and 0.1 are plotted against cone angle. The smooth curves approximate the data well for C_{D_O} and fairly well for C_D (0.1). The errors in C_D which may have been made in choosing the individual regression graphs are presumably of the order of 0.005 to 0.01.

The differences between the C_{D_O} graph of Figure 2-16 and those previously reported in the literature on the basis of experimental data, are small. The equation $C_{D_O} \cong 0.01\beta$ (with β in degrees) may be useful as a rough rule-of-thumb for cones. Based on Figure 2-16, it has a maximum error of 0.2 and the error is not greater than 0.05 up to 77 degrees.

Since no mention has generally been made of skin friction in reporting drag measurements on cones, it is assumed that experimental data will usually include friction, whereas theoretical results will not. If skin friction is present C_{D_O} should increase as the cone angle approaches zero.

In the best analytical predictions of C_D for cones (Refs. (2-13) and (2-15)) pressures on the cone faces are estimated from values calculated theoretically for the wedge. The agreement with experimental data is fairly good. It has been discussed in the references cited.

In Table 2-3, values are given for the least-square regression lines for the various cone angles, and for the quantities C_{Do}, $dC_D/d\sigma$, and $a = (1/C_{Do})dC_{Do}\sigma$. The quantity $dC_D/d\sigma$ is the coefficient of σ in the expression

$$C_D = C_{Do} + (dC_D/d\sigma)\sigma$$

It was assumed to be unity in

$$C_D = C_{Do} + \sigma, \tag{2-3}$$

and equal to C_{Do} in

$$C_D = C_{Do} (1 + \sigma). \tag{2-5}$$

The values in Table 2-3 are intermediate between these two. In any case the predicted values are significant only for small values of σ.

The last three columns of Table 2-3 give data obtained by reading values from the curves of Figure 2-16 where the curves deviated somewhat from the experimental points.

Figure 2-17 is a plot of $dC_D/d\sigma$ against cone angle, using the smoothed values of the ordinate where they are given in Table 2-3. It is seen that only for the needle does $dC_D/d\sigma$ approach a value of unity, so that equation (2-3) is roughly valid. Table 2-3 shows also that the data satisfy the equation

$$C_D = C_{Do} (1 + \sigma) \tag{2-5}$$

only for the disk.

The Sphere

Thus far only noses for which the flow separation is abrupt have been considered. The sphere is the simplest axially-symmetric example of smooth separation. Because drag varies with the separation angle, theoretical predictions of drag are poor when smooth separation occurs. There are two principal contributions on this subject: the predictions of Armstrong and Tadman (Ref. (2-29)), and the calculations and comparisons of Brennan (Ref. (2-24)).

Most experimental drag values for spheres have been based on free-flight and zero cavitation number. Only two were found which give drag data over a range of values of σ (Refs. (2-22) and (2-30)). Hsu and Perry (Ref. (2-30)) reported tests with spheres of three diameters (1, 1.5, and 2 inches), and the data given permit calculation of the Reynolds number, which was in the critical region where the flow changes from laminar to turbulent. Values of σ ranged from 0.03 to

Table 2-3

DRAG DATA FOR CONES

Cone Half-Angle	Data from Straight-Line Least-Square Reduction				Data Smoothed by Graphs of Figure 2-16		
	C_{Do}	$dC_D/d\sigma$	$a = (1/C_{Do})dC_D/d\sigma$	$C_D(\sigma = .1)$	C_{Do}	$dC_D/d\sigma$	$(1/C_{Do})dC_D/d\sigma=a$
5°	.0362	.900	27.6	.1262			
10°	.0765	.822	10.75	.1587			
14°	.142	.398	2.80	.182	.140	.550	3.93
15°	.151	.587	2.57	.210			
26.6°	.319	.434	1.36	.362	.312	.500	1.60
30°	.347	.510	1.47	.398	.351	.570	1.62
45°	.498	.663	1.33	.564			
63.5°	.637	.549	0.86	.692	.637	.750	1.18
90°	.815	.815	1.00	.896			

0.14. The tests of Eisenberg and Pond (Ref. (2-22)) were made with a single sphere diameter of 1 inch and values of σ between 0.17 and 0.38. Since the velocity is not known, precise values of Reynolds number cannot be calculated, but it is probable that all tests were made at Reynolds numbers of about 3×10^5.

Figure 2-18 gives a plot of C_D against σ for all the data reported by Hsu and Perry (Ref. (2-30)). The data involve five values of Reynolds number (1.2, 1.7, 2.1, 2.5 and 3.3×10^5) and different symbols are used for each. An attempt was made to obtain a set of independent least-square straight lines, one for each Reynolds number. There was an evident trend toward higher C_D at higher Reynolds number but the scatter in both C_{Do} and $dC_D/d\sigma$ was enough to confuse the analysis.

A basic difficulty of the analysis is worth mentioning. The quantities which are usually specified are C_{Do} and the slope, $dC_D/d\sigma$. In spite of the importance of C_{Do}, measurements are not made at $\sigma=0$. As a result the analysis yields less accuracy for the value at $\sigma=0$ than it does at the values of σ used in the tests. Too low (or too high) a value of C_{Lo} will be associated with too high (or too low) a value of $dC_D/d\sigma$, so related as to give the experimental value of C_D at the σ of measurement.

Because of the unsatisfactory results due to scatter in the values of intercept and slope a least-square analysis was carried out to yield a straight line for each Reynolds number, but with the same slope for all lines. The basis for this was a feeling that one might expect the slope to vary little with Reynolds number even though the drag might change. The results of the analysis are given in Table 2-4 and in Figure 2-18.

Table 2-4

SPHERE REGRESSION DATA

Reynolds Number	C_{Do}	$dC_D/d\sigma$
1.2×10^5	0.2553	
1.7	0.2576	
2.1	0 8	0.357
2.5	0.2053	
3.3	0.2663	

It will be seen that C_D increases monotonically with increase of R, for the straight graphs of Figure 2-18, except in the case of $R = 2.1 \times 10^5$. The set of data for $R = 2.1 \times 10^5$ contains only data points that are at higher values of σ ($0.09 \leq \sigma \leq 0.14$).

In Figure 2-19 the graphs just considered for R-values of 1.7 and 2.5×10^5 are redrawn, and data from Eisenberg and Pond (Ref. (2-22)) have been added, together with the least-square straight line

$$C_D = 0.241 + 0.488\sigma \qquad (2-13)$$

determined from their data (Ref. (2-31)). This line is seen to form a reasonable continuation of the upper graph at higher Reynolds numbers.

Reference (2-30) contains information also regarding the angular position at which the flow separates from the cavity-running sphere. These data are plotted in Figure 2-20 together with two least-square straight lines determined by them. The data surrounding the upper graph had $R \le 3.4 \times 10^5$, and for the lower graph $R \ge 4.0 \times 10^5$. The separation of the data points is striking and unmistakable, and presumably due to the onset of turbulence. Figure 2-20 is included here only to facilitate the discussion of the changes in C_D. One is certainly tempted to relate the two effects although the jump in C_D was noted at about $R = 2.0 \times 10^5$ and the shifting of the point of separation at $R \ge 3.4 \times 10^5$. Small shifting of the separation may occur about $R = 2.0 \times 10^5$ but the accuracy of the data was not adequate to permit so fine an analysis.

On Figure 2-19 the drag prediction of Armstrong and Tadman (Ref. (2-29)) has been graphed for comparison with the experimental data. The predicted values are approximately 20 percent higher than the experimental.

It is interesting to compare the results of the present study with experimental values in the early literature. The most frequently quoted value for the sphere has been $C_D = 0.30$. A principal exception was the Eisenberg-Pond result in equation (2-13).

Most other data were taken from free flight and usually from water entry where for a time the cavitation number is near zero. One early paper (Ref. (2-32)) reported results at least qualitatively similar to those of the present study. In that work, force data from deceleration measurements on spheres at vertical water entry were modified to remove the effect of forces other than drag. In particular low air pressures were used to prevent the closure of the water-entry cavities at the water surface. It was found that

$$C_D = 0.0174 \log_e (RFr). \qquad (2-14)$$

where Fr is the Froude number based on sphere diameter and redefined here as $Fr = U/\sqrt{gd}$. This result would be related to the small cavitation number of the water-entry cavity.

A most interesting comparison is possible between equation (2-14) and the results of Hsu and Perry (Ref. (2-30)). The latter include two groups of spheres with $R = 1.7 \times 10^5$: 6 items for a 1-inch sphere and 7 for a 1 and 1/2-inch sphere. These are identified on Figure 2-18. For all of these readings, Table 2-4 shows a C_{D_0} value of 0.2576. If C_D reductions are carried out separately for the two sets, assuming the same slope as the overall slope (0.357) of Figure 2-18, regression

lines are obtained with C_{D_0} = 0.259 for the 1-inch spheres and
0.256 for the 1 and 1/2-inch. If C_{D_0} is calculated for the two sets
from equation (2-14), the respective values are 0.262 and 0.253. The
scatter of these data is comparable with the differences found, but
the general agreement between water-tunnel and water-entry results
is most gratifying. Moreover the idea that the value of C_D may depend
on Fr should not be ignored. This effect would be related to
separation which is discussed in more detail in another report (Ref.
(2-1)).

Disk Ogives

Disk ogives form a family of nose shapes which was conceived with
the purpose of coordinating and comparing coefficients throughout a
broad range of shapes. Typical members of the family are shown in
Figure 2-21. Starting with the right cylinder the edge may be rounded
by a radius of any value desired. The disk ogive is identified by the
radius of the arc expressed in calibers, i.e., missile diameters. If
the radius is small, the arc is drawn so that it is tangent to both
the cylindrical wall of the missile and the flat surface on the front
of the nose. In the figure, B and C are typical disk ogives. If the
radius of the circular arc is half the body diameter (a half-caliber
ogive) the nose is a hemisphere. For greater radii the arc does not
become tangent to the front surface but the arcs meet to form a
typical pointed ogive tip. If the arc is still tangent to the
cylindrical body the shape is a tangent ogive; otherwise it is a
secant ogive. Sketches E and F are typical of pure tangent ogives.
Usual ogive calibers run from one to six or more.

Finally, in the limit, the radius is infinite and the body becomes
a geometrical line. This configuration is of little value even as a
limit since it has zero diameter.

A point to be kept in mind when the disk ogives are used as a
family for cavity-running drag, is that the flow separation for some
of its members is abrupt and for others it is smooth. The importance
of this difference is not known but it is probably not significant
today because the overall accuracy of drag information is not high.

Two members of the family, the disk and hemisphere, have been
discussed already. Data for pure ogives and pure disk ogives are
given in Table 2-5.

Table 2-5

DRAG DATA FOR OGIVES AND DISK OGIVES

Drag Coefficient $C_{DO} + (dC_D/d\sigma)$	Ogive Caliber, R_O	Reference
$0.195 + 0.209\sigma$	1	(2-21)
$0.114 + 0.416\sigma$	2	(2-22)
$0.1515 + 0.595\sigma$	1	(2-33)
$0.0716 + 0.626\sigma$	3	
$0.056 + 0.54\sigma$	5	
$0.040 + 0.55\sigma$	7	
0.70	0.1	(2-34)
0.41	0.2	
0.44	0.25	(2-17)
0.14	1.5	
0.62	0.1	
0.09	3.5	
0.11	2.7	(2-18)
0.22	1	(2-35)
0.13	3	

A plot of C_{DO} for the disk-ogive family is given in Figure 2-22. The values indicated by circles are regarded as relatively undependable. Most of these were derived from water entry.

An equivalent plot is given in Figure 2-23, where C_{DO} is plotted in calibers against $Q = 1/(1 + 2R_O) = 1/(1 + 2r_O/d)$, and R_O is the ogive radius in calibers. The quantity Q has frequently been used in the treatment of data for the disk-ogive family. It was invented to improve the presentation of data for the family.

Figure 2-24 is a logarithmic plot of the disk-ogive data. Excluding the value for the disk (which would lie at minus infinity) it will be seen that the data, within the existing scatter, can reasonably be presented by the straight line

$$C_{DO} = 0.171 \; R_O^{-0.60} \qquad\qquad (2-15)$$

Since the graph must reach the value $C_D = 0.8$ (the coefficient for the disk) at an infinite distance, the left end of the graph is almost certainly too high.

In Figure 2-25 the curve for C_{DO} has been copied from Figure 2-22 in the ogive region (ogive calibers one to seven), and a graph of C_D at

$\sigma = 0.1$ has been added. Values for this graph were obtained from Table 2-5. It will be seen that the slope $dC_D/d\sigma$, in the region $0 \leq \sigma \leq 0.1$, has a mean value of about 0.170 at one caliber, and rises rapidly to a value of about 0.55 which remains substantially constant up to 7 calibers.

Paraboloids

Paraboloids or parabolic bodies of revolution are shapes of particular interest although apparently only a single test has been reported (Ref. (2-36)) for them. The front portion of the cavity generated by a cavity-running missile (but excluding the portion very near the nose) is almost exactly parabolic (Refs. (2-1) and 2-37)). Since the pressure within the cavity is reasonably uniform, the cavity wall approximately, at least, is a constant pressure surface. A missile nose which is almost exactly the shape of this cav ty should have very small pressures on its surface and a very low drag.

Reference (2-36) derives formulas for the computation of the force on the wetted portion of ellipsoidal noses. Further it is shown that when the eccentricity of the ellipsoid is very large, a forward portion of this nose (a small fraction of the major axis) is very nearly a paraboloid, and hence the forces on this wetted portion are close to those on the paraboloid.

Further, such a parabolic nose will almost exactly match the liptical nose up to the point at which the pressure coefficient ops to zero. Calculated values of the total force on the positive essure region of the elliptical nose of large eccentricity (Ref. 36)) are plotted in Figure 2-26 against the reciprocal of the fineness ratio $(1/f = d/L)$ of the nose. The method of calculation is given in Reference (2-36).

Tests were performed (Ref. (2-36)) on paraboloidal noses of fine- ne ratios 3.33 and 1.0. The drag coefficients measured for these noses while cavity running, less the calculated friction drag, are plotted as circles in Figure 2-26. The experimental values, 0.025 for $f = 3.33$ and 0.125 for $f = 1.0$, lie very close to the curve.

The form drag of the paraboloid is much less than that of the cone of the same fineness ratio, although the friction drags are almost the same.

Ellipsoids

Experimental data on the cavity-running drag of ellipsoidal noses is scant. A start can be made with two shapes that have already been considered: the hemisphere for which the ratio of longitudinal to transverse axes is 1:1, and the disk with a ratio of 1:00.

Data are available from two other sources: for the ratio 2:1 from measurements of Eisenberg and Pond (Ref. (2-22)), and for the ratio 1:2 by integration of the pressure measurements of Rouse and McNown (Ref. (2-26)). All data are collected in Table 2-6, and Figure 2-27 gives a plot of C_{DO} and of $dC_D/d\sigma$.

Table 2-6

DRAG DATA FOR CAVITY-RUNNING ELLIPSOIDS

Longitudinal Axis
Transverse Axis

(a/b)	C_{Do}	$dC_D/d\sigma$	Source
1:00 (disk)	0.815	0.815	this report
1:2	0.40		(2-26)
1:1 (sphere)	0.265	0.357	this report
2:1	0.126	0.367	(2-22)

The drag of ellipsoids has also been treated analytically (Ref. (2-29)) but numerical evaluations are available only for the sphere.

Other Nose Shapes

In addition to the simple geometrical shapes that have been discussed as missiles noses in this report, many variations have been used. Both theoretical and experimental drag information are generally lacking on any but the simplest of these, and the best one can do is to approximate the drag by comparison with shapes for which coefficients are known. The most important nose variations are created by combining two simple geometrical shapes. They may be formed by truncating cones or ogives as shown in sketches A and B of Figure 2-28, or by inscribing a spherical surface within a cone, an ogive (spherogive), or even an ellipsoid, as in sketches C, D, and E. The noses with spherical tips are specified by giving the angle θ of the spherical surface and the caliber of the ogive, the angle of the cone, etc.

It is of primary importance to know where the flow separates from the nose (without later contact with the missile surface). The form drag will depend principally on the nature of the surface in the vicinity of the separation. For example, if the separation from a spherogive is from the ogival surface, the drag will depend rather little on the spherical surface and will be fairly close to that of a pure ogive. On the other hand if a truncated cone (sketch A) is used and the flow reattaches after a separation at the plane of the truncation, the drag will be considerably higher than for the cone.

In the case of the spherogive the separation may be from the spherical surface at some Reynolds numbers and from the ogive at others, as may be surmised from the separation angles of Figure 2-20. The

separation position is also influenced by the cavitation number. As was mentioned earlier in this report, a chopped-off spherical surface such as that of Figure 2-28F will behave like a sphere if separation occurs before the outside of the surface is reached. If abrupt separation occurs at the edge of the nose, the drag will be between that of a disk and a sphere.

Truncated noses are important especially because of their better behavior at water entry. For the disk it was found that $C_{Do} = 0.815$. This value was based on the area of the disk; for the truncated cone the area would be that of the truncation. If in Figure 2-28A the truncation has only half the diameter of the cylindrical body, then the drag coefficient based on the cross section area of the missile will be only $0.815/4 = 0.204$ (assuming that the flow does not again strike the body). Because of this arbitrariness in the choice of the area used in the definition of C_D, frequently the drag area is used instead of the drag coefficient. For the truncated nose the drag area (for $\sigma = 0$) is $C_D A_n = 0.815 A_n$, where A_n is the area of the truncation. Evidently the drag area is independent of the maximum diameter, or caliber, of the missile (assuming that the flow does not reattach). Since $D = qAC_D$, the drag area is D/q.

THE DRAG OF TWO-DIMENSIONAL SHAPES

It is bodies of revolution, such as those discussed so far, which have greatest interest for the hydroballistician and the missile designer, but two-dimensional shapes cannot be ignored. A torpedo-like vehicle approximates a two-dimensional body if it happens to travel sideways through the water, and knowledge regarding the two-dimensional problem has permitted approximations for bodies of revolution as was mentioned earlier. Analytical predictions for two-dimensional shapes are commonly more accurate than those for bodies of revolution because of the availability of complex-variable methods for their solution. Most of the shapes that were discussed as bodies of revolution have analogs in two dimensions but measurement of two-dimensional drag has been infrequent. Recent literature has shown increased interest in the flow past two-dimensional bodies largely because of application to the struts of hydrofoils.

Since the length of a two-dimensional body is infinite or at least indefinite, the drag coefficient is defined for unit length and the cross-sectional area is numerically equal to the width of the body.

The Flat Plate

The flat plate (or infinite two-dimensional strip) has been much studied since the days of Kirchhoff. Theoretical treatments will not be discussed in this report and the reader is referred to the list of references, especially (2-8), (2-13) and (2-38). The drag predictions in these three reports agree well and a graph based on them is shown in Figure 2-29. The quantity $C_D/(1 + \sigma)$ is plotted rather than C_D, since the predicted behavior approximates the relation

$$C_D = C_{DO} (1 + \sigma). \qquad\qquad (2-5)$$

Two series of experimental measurements have been reported for the flat plate (Refs. (2-39) and (2-40)) and the data points for these are plotted on Figure 2-29. The experimental data is seen to average almost two percent lower than the theoretical. The best mean of both is probably about

$$C_D/(1 + \sigma) = 0.870$$

with no dependence on σ.

Figure 2-30 shows the same data replotted as C_D instead of $C_D/(1 + \sigma)$. The theoretical predictions can be approximated closely by the straight line

$$C_D = 0.880 + 0.894\sigma$$

The least-square straight line through the experimental data is

$$C_D = 0.875 + 0.849\sigma$$

The close agreement between theoretical and experimental values of C_{DO} may be misleading. The data of Cox-Clayden (Ref. (2-40)) which are at small values of σ, separately give $C_{DO} = 0.848$. The value of C_{DO} for the combined experimental data is three percent above this because of the influence of the larger number of data points at the higher values of σ (Ref. (2-39)).

Stagnation Channel

The stagnation channel is the two-dimensional analog of the stagnation cup which was discussed earlier. It is a channel with rectangular cross section in which the pressure presumably is everywhere close to the stagnation value $p_\infty + q$. Based on the same argument as for the stagnation cup the drag coefficient should be

$$C_D = 1 + \sigma \qquad\qquad (2-2)$$

Two series of measurements have been reported for stagnation channels (Refs. (2-39) and (2-41)) and values of $C_D - \sigma$ from these tests are plotted on Figure 2-31. For each experiment the mean value of $C_D - \sigma$ is 1.02, and there is no evidence of a dependence on σ.

Probably equation (2-2) gives the best prediction for this shape.

The Wedge

The drag of wedges has been discussed frequently and the accuracy of prediction, as for the flat plate, appears to be good. In Figure 2-32 graphs based on the calculations of Wu and Wang (Ref. (2-14)) are given for the drag coefficient of wedges with half angles between 5 and 90 degrees (flat plate). For the larger angles the

graphs are nearly straight. The curvature increases and starts at smaller values of σ as the wedge angle becomes less. Other graphs were given earlier by Plesset and Shaffer (Ref. (2-13)) and Tulin (Ref. (2-15)) but those of Wu and Wang appear in slightly better agreement with experiment. Data from the experimental reports of Silberman (Ref. (2-41)), Waid (Ref. (2-39)) and Cox and Clayden (Ref. (2-40)) are also shown in Figure 2-32.

On Figure 2-33 the same data are plotted as $C_D/(1 + \sigma)$ against σ. The graphs for wedges of large angle are very close to the equation

$$C_D = C_{Do} \, (1 + \sigma) \qquad\qquad (2-5)$$

The Circular Cylinder

In discussing the drag of spheres it was mentioned that prediction is difficult because the point where smooth separation occurs is not known with accuracy. The situation is similar for the circular cylinder.

In Figure 2-34 two theoretical graphs are given for $C_D/(1 + \sigma)$ based on smooth detachment (Refs. (2-29) and (2-38)), together with experimental data points due to Waid (Ref. (2-39)) and Silberman (Ref. (2-41)), and a broken line from experiments of Daily (Ref. (2-42)). The scatter in C_D values is exaggerated by the expanded ordinate scale. There is strong indication that the data points lie on two or more graphs which depend on the condition of the boundary layer and the resultant separation angles (Ref. (2-1)). It should be mentioned also that Silberman obtained his data in a vertical open-jet tunnel while Waid and Daily used closed horizontal tunnels.

Elliptic Cylinders

Theoretical studies have been made of cavity flow about the elliptic cylinder with smooth detachment (Refs. (2-43) and (2-44)) but no experimental tests have been reported. Brodetsky (Ref. (2-43)) calculated the drag coefficient for a large range of axis ratios, but only for zero cavitation number. In Figure 2-35 Brodetsky's data are given with modifications which were made by Tulin (Ref. (2-6)).

An evaluation and extension of the data of Figure 2-35 might be made somewhat as follows. On the basis of the data of Figures 2-18 and 2-34 for the sphere and circular cylinder, it appears probable that experimental results would lie from three to seven percent below the curve of Figure 2-35 with the higher values applicable to Reynolds numbers above the critical value. The dependence of drag on cavitation number might be obtained from the theoretical graphs of Figure 2-34.

LIFT, MOMENTS, AND NON-ZERO ANGLES OF ATTACK

Axially-Symmetric Bodies

Thus far the force data presented have consisted of drag at zero angle of attack. At non-zero angles of attack the literature has contained data principally for the disk and cone family, and these include drag, lift and moments.

Figure 2-36 contains Kiceniuk's (Ref. (2-25)) much-copied graphs for disks, and 45- and 15-degree half-angle cones at $\sigma = 0.1$. Values of C_D, C_L, and C_M are plotted against negative angles of attack. The drag coefficient for the blunter shapes (the disk and 45° cone) decreases with increasing angle of attack qualitatively somewhat like the decrease of disk width presented to the flow, but more rapidly. Up to $\alpha = 30$ degrees, C_D for the disk decreases approximately as $\cos^2 \alpha$, and for the 45-degree cone, a little more rapidly than this.

The dependence of C_D on σ for various angles of attack, is approximated in Reference (2-25) by a family of straight lines. In Table 2-7, data derived from these graphs are given for C_{Do}, the slope $dC_D/d\sigma$, and the quotient $a = (dC_D/d\sigma)/C_{Do}$, together with corresponding data for lift forces and moments.

Kiceniuk's individual data points for the disk at $\alpha = 0$, were plotted in Figures 2-4a and 2-4b, and it was shown in the discussion of those figures, that his values, within experimental error, obey the relation

$$C_D = C_{Do} (1 + \sigma) \qquad (2-5)$$

and this equation was regarded as a better representation of his data at $\alpha = 0$ than

$$C_D = C_{Do} + (dC_D/d\sigma)\sigma = C_{Do}(1 + a\sigma) \qquad (2-4)$$

with a having a value slightly greater than one.

The data for non-zero angles of attack, as given in Table 2-7, show that equation (2-4) may be used to represent the drag of disks with an approximately constant value of a = 1.06 for $\alpha \leq 20$ degrees. Presumably within the accuracy of the experimental data, equation (2-5) could be used alternatively with rather negligible increases of the values of C_{Do} given in Table 2-7.

The disk has a negative lift coefficient, that is, as the face of the disk is turned slightly downward, the lift force is upward; for the 15-degree cone the behavior is similar but opposite in sign. For the 45-degree cone the lift is quite small. For small angles of attack, the lift force for the disk is nearly equal to sin α times the drag force at $\alpha = 0$.

Table 2-7

DRAG AND LIFT DATA FOR DISKS AND CONES
(From graphs in Ref (2-25)

	α Degrees	C_{Do}	$dC_D/d\sigma$	$\dfrac{dC_D/d\sigma}{C_{Do}}$	C_{Lo}	$dC_{Lo}/d\sigma$
Disk	0	.809	.846	1.05	0	0
	5	.802	.846	1.06	.069	.05
	10	.785	.835	1.06	.127	.17
	20	.725	.765	1.06	.254	.15
	30	.615	.590	0.96	.345	.25
45° Cone	0	.502	.612	1.22	-.012	.095
	5	.494	.617	1.25	.006	.040
	10	.477	.633	1.33	.014	.035
	20	.432	.550	1.27	.010	.095
	30	.356	.483	1.36	-.016	.065
15° Cone	0	.152	.55	3.6	0	.188
	2.5	.160	.55	3.4	-.048	.150
	5	.166	.54	3.3	-.100	.225
	10	.164	.70	4.3	-.190	.212
	15	.184	.70	3.8	-.294	.288
	20				-.368	.275

Within experimental error, Kiceniuk found the moment coefficient
of the disk and 45-degree cone to be zero. The 15-degree cone has
a large destablizing moment because of the forward location of the
center of pressure, and the same behavior is had, for the same reason,
with slender ogives and with "spigot" heads (Ref. (2-35)).

Values of the lift-coefficient derivative $C_{L\alpha}$ are available from the
data of Figure 2-36 and Table 2-7, and from several data points given
by Reichardt (Ref. (2-5)). Values from these sources are plotted
against cone angle in Figure 2-37. The agreement is poor for the
two graphs for $\sigma = 0$. Since the drag data of Kiceniuk in Figures 2-
4 and 2-14 are in better agreement with other experimenters than are
Reichardt's, preference perhaps should be given to Kiceniuk's $C_{L\alpha}$ data.

Lift and moment data, cavity-running, seem not to be reported for
missiles with curved noses. For spherical noses, if the flow separates
from the spherical surface and underpressure forces are not large,
presumably the drag force is independent of α, the lift force is zero,
and the moment, $M = DL_1 \sin \alpha$, where L_1 is the distance from the
center of the sphere to the C.G.

Two-Dimensional Bodies

Drag and lift coefficients have been reported for the flat plate
based on theory and experiment. Figure 2-38 gives plots of $C_D/(1 + \sigma)$
against σ for various angles of attack of the infinitely long flat
plate, based on calculations of Wu (Ref. (2-45)). Experimental data
are also plotted on Figure 2-38 for comparison with theory.

The angle of attack will be designated α_p for the flat plate because
of the method of specification. A right cylinder is said to be
traveling with zero angle of attack when the velocity vector is
normal to the disk which forms the front surface of the cylinder. By
contrast the flat plate is at zero angle of attack when the freestream
velocity is parallel to the surface of the plate. Hence the two
angles α and α_p, used in defining angle of attack, are complementary.
The wedge of 180-degree vertex angle is a flat plate, but α is used
for the angle of attack of the wedge, and α_p for the plate.

In Figure 2-38 the agreement between theory and experiment is
fairly good, but the theoretical values appear to be consistently a
little high compared to those from experiment. Both theory and
experiment show that $C_D/(1 + \sigma)$ is nearly independent of σ, with an
increasing dependence as the angle of attack is made small.

Lift coefficients for the flat plate are shown in Figure 2-39. The
differences between theoretical and experimental values are similar
to, but slightly larger than in the case of C_D. The lift is seen to
be a maximum for an intermediate angle of attack, in the vicinity of
30 degrees. Since the hydrodynamic force is almost normal to the
plate, the force is downward when the plate is tilted upward, as shown
in the sketch on Figure 2-39.

At small cavitation numbers where the plate is fully cavitated, Wu's theory shows (Ref. (2-45)) that

$$C_L/C_D = \cot \alpha_p$$

and the approximation to this relation is sketched in Figure 2-40. At large values of α it will be seen from Figure 2-39 that C_L approaches the relation

$$C_L = C_{Lo} (1 + \sigma),$$

analogous to equation (2-5).

Cox and Clayden (Ref. (2-40)) obtained drag and lift values for symmetrical wedges at angles of attack by theory and experiment. The theoretical bases were obtained only for $\sigma = 0$, and the angles of attack in the tests ranged between $\pm$ 15 degrees. The values of C_D which they reported for zero angle of attack were given in Figure 2-32. Cox and Clayden expressed the dependence on α by a relation of the form

$$C_D = C_{D(\alpha = 0)} (1 + k\alpha^2) \qquad (2\text{-}16)$$

where k is constant for a given vertex angle and α is in degrees. Values of k and expressions for $dC_L/d\sigma$ which they reported are listed in Table 2-8.

Table 2-8

DRAG AND LIFT DATA FOR WEDGES
Ref. (2-40)

β	k	$dC_L/d\sigma$
15°	0.00742	0.116 + 0.093σ
30°	-0.000305	0.0398 + 0.0192σ
45°	-0.000342	0.0097
60°	-0.00032	-0.0052
90°	-0.000170	-0.0171

The dependence of C_D on α is in reasonable agreement with the theory due to Wu in Figure 2-38. Within the accuracy of measurement no dependence of $dC_L/d\sigma$ on σ was found for β values of 45, 60 and 90 degrees.

EFFECT OF GRAVITY ON NOSE FORCES

The effect of gravity on the geometry of the cavity which accompanies a missile was discussed in another report (Ref. (2-1)) and the effect was shown to vary greatly with the direction of the gravity field. In the present section some qualitative remarks will be made about the effects of gravity on the forces on the missile nose.

When the gravity field is transverse, as when a missile is traveling horizontally, the effects have been considered in several theoretical studies based on the flow over the flat plate or the wedge.

For the transverse field one theoretical study (Ref. (2-49)) has discussed the flat plate and three have considered the slender wedge; two from a theoretical viewpoint (Refs. (2-50) and (2-51)), and one based on experiment (Ref. (2-52)). The results are qualitatively the same: the drag and lift coefficients increase with increase of $1/F^2$, where F is the Froude number, that is, with the strength of the gravity field, or inversely with the missile speed, although theory shows (Ref. (2-52)) that the lift force due to gravity is independent of missile speed, for given σ and bubble length.

Two reports (Refs. (2-49) and (2-53)) have given theoretical predictions for the effect of the longitudinal gravity field on the C_D of wedges. One experimental paper reported (Ref. (2-41)) no effect of gravity on the lift and drag of a disk at tunnel speeds between 25 and 48 ft/sec, but found a reduction of C_D for the wedge in a vertical tunnel when the speed dropped from 27.6 to 19.4 ft/sec. They found no gravity effect at high speeds.

EFFECT OF WALLS ON NOSE FORCES

While it is natural to think of missiles as traveling in an infinite fluid, indefinitely far from bounding walls, laboratory experiments are commonly performed in water tunnels where the walls may affect both the geometry of the cavity generated by the missile (Ref. (2-1)) and the forces on the missile nose. Study of wall effects on nose forces has been made principally for drag on the wedge (Refs. (2-54) and (2-55)), although one report (Ref. (2-56)) relates to lift forces on the flat plate. Correction techniques are available in these and earlier references.

The drag and lift at a given cavitation number are less than in unbounded flow, and for the wedge the percent reduction in drag is found to be in inverse relation to the wedge angle, so that the wall effect is especially significant for slender wedges.

Figure 2-41 shows the computed effect of the tunnel walls on the drag of a 15-degree half-angle wedge.

TAIL FORCES

While cavity-running, a missile ordinarily does not "ride on its nose" (with only the nose in contact with the water) for very long. After water entry this condition often exists briefly, but generally, even for truncated noses or right cylinders, the afterbody soon falls against the cavity wall. In some cases the tail bounces away from the wall, but more usually it remains in contact with it and partially submerged in it, as in Figure 2-42. This behavior will be discussed in detail in the treatment of trajectories in another report. The

force acting on the afterbody can be resolved into drag and lift components and, together with the force on the nose, can be used to approximate the subsequent motion of the projectile and the cavity generation.

The angle of the projectile while its afterbody is riding on the cavity wall, will depend on a number of conditions. It may be highly variable; it will increase as the cavity becomes wider and as the missile is made shorter or of smaller diameter in its aft section. Data obtained from experiment will be given here for the tail forces due to several tail shapes, but more detail on these shapes and their evaluation will be reserved for the discussion of trajectories and of missile-design criteria.

A number of experimental factors must be considered in the study of tail forces.

a. The shape of the afterbody will have a large effect on the forces. The shapes generally considered have been: the cylinder, as sketched in Figure 2-42; the cone which has been used to prevent the tail from remaining in contact with the cavity wall (Fig. 2-43); afterbodies containing tail fins, shrouds and other appendages.

b. The cavitation number

$$\sigma = \frac{p_\infty - p_C}{(1/2)\rho\ U^2} \tag{2-1}$$

The cavitation number must be used with some caution in the consideration of tail forces. It was designed to relate dynamic pressure, $q = 1/2\rho U^2$, which is instrumental in opening up the cavity, to the differential pressure $p_\infty - p_C$, which is effective in closing the cavity at its downstream end. In the situation sketched in Figure 2-42, it appears that the tail forces are principally dependent on the geometry existing during the planing operation and on reduced local pressures which may result from the flow, including the "underpressure" discussed earlier, and vapor cavitation which may occur when this underpressure becomes sufficiently large. Evidently the cavitating condition will not depend directly on the cavitation number of the cavity in which the missile travels, but rather on the vapor cavitation number which has the usual definition

$$\sigma_V = \frac{p_\infty - p_V}{q} \tag{2-17}$$

where p_V is the saturation vapor pressure of the water on which the missile is planing. Under the present considerations σ_V might better be expressed as

$$\sigma_V = \frac{p_C - p_V}{q}$$

since the cavity pressure p_C plays the role of the ambient pressure during the planing operation;

c.   Froude number

$$Fr = U/\sqrt{gd}$$

or other dimensionless quantities involving missile speed and size;

d.   The geometry of the tail immersion, relating the submergence depth δ, the angle of attack, etc.

e.   The curvature of the cavity wall, including the curvature shown in Figure 2-42, but also curvature in the transverse direction, which is dependent on the diameter of the cavity at the position of the tail.

Cylinder

The most extensive experiments on the planing cylindrical tail were carried out by Waid and Kermeen (Ref. (2-57)), and typical graphs of lift coefficient against dimensionless immersion depth δ/d, for a missile angle of attack of 16 degrees, are shown in Figure 2-44a. The four curves relate to different values of σ_v, based on the value in the water tunnel in which these graphs were obtained, for planing on a flat water surface.

Since there is a variation of about 40 percent in the value of C_L due to changes in σ_v, some idea of the value of σ_v must be available for proper interpretation and use of the graphs. Since its value must be based on the difference between cavity pressure and the vapor pressure of the water, the graph for $\sigma_v = 3.22$ would be characteristic of the lift behavior when the cavity pressure is high: for example, in the water-entry cavity soon after entry, when the entry speed is not comparable with the speed of sound in air. The other graphs apply when the amount of air in the cavity is small.

Graphs of C_D, C_M, and L_1/d at 16-degree angle of attack are also contained in Figure 2-44. As shown in Figure 2-42, L_1/d is the dimensionless distance of the center of pressure of the planing force from the trailing end of the cylindrical afterbody. The moment has been taken about the base of the cylinder, rather than about the C. G., as shown in Figure 2-42.

The drag coefficient (Fig. 2-44b) and the center of pressure distance (Fig. 2-44d) depend little on the cavity pressure, but the moment (Fig. 2-44c) is considerably less at the high cavity pressure because of the smaller lift.

The dependence of the same quantities on angle of attack is given for $\sigma_v = 3.2$ in Figure 2-45. This figure shows that both C_L and C_D increase strongly with the angle of attack. The increase of drag is due to the change of the flow from longitudinal to transverse about the cylindrical body. In contrast, Figure 2-45C shows that C_M is almost independent of the angle of attack up to 30 degrees. The reason is seen in Figure 2-45D; the variation of C. P. position counteracts the effect of changing lift. The former is due to the changing flow pattern and its effect on separation and cavitation.

The planing tests of Figures 2-44 and 2-45 were made with a flat water surface, but Waid and Kermeen (Ref. (2-57)) conducted tests also on surfaces having lateral curvature. These surfaces were formed either by skimming on a flat water surface or by cavity generation below water using a disk and cavity ventilation.

Although experimentation has been insufficient for the production of precise results, and results are confused by scale effects, the dependence on lateral curvature appears large enough to be important. Details are available in Reference (2-57) where the coefficients are treated as varying linearly with d/D, the ratio of missile to cavity diameter. Results indicate that both C_L and C_M increase with lateral curvature, with a variation of the order of

$$C_{L,M} = C_{L,M}(d/D = 0) \ (1 + (1/2)d/D), \tag{2-18}$$

where $C_{L,M}$ denotes either C_L or C_M. The drag coefficient depends in an irregular fashion on the lateral curvature: for 6-degree angle of attack the dependence is small but inverse, but it becomes positive as α is increased until at $\alpha = 19$ degrees C_D would approximate the relation of equation (2-1ð). The variation of the C. P. position is small, but it generally moves slightly aft with increased curvature.

Kiceniuk showed (Ref. (2-58)) that it is important to use Froude scaling in the consideration of tail forces, but he and Waid and Kermeen observed scale effects which have not been explained.

Cores

Kiceniuk and Greengard (Ref. (2-59)) measured the lift on cones with half angles of 7.5, 15, 22.5, 30 and 45 degrees, while the cones planed on water. In Figure 2-46 representative values from their lift data are plotted not against the angle of attack but against "surface angle of attack", the angle between the cone surface and the water, as shown in the sketch on the figure. Kiceniuk and Greengard found that when plotted against surface angle of attack, lift values for various cone angles and even for the cylinder could be represented by one set of graphs. In any particular region of the graphs they did not vary the cone half angle by more than 15 degrees, but they report that where the data overlap the scatter is not significantly greater than for data from a single model. On the basis of their results they suggest that lift data can be applied to cones of other angles than those studied, including the cylinder, and that this may make possible the use of theoretical results obtained, for example, for the cylinder, in application to other members of the cone family.

Other Tail Configurations

There is some information available for forces on tapered tails, fins and shrouds (Refs. (2-60) and (2-61)) such as the assembly shown in Figure 2-47 (Ref. (2-60)). In Figures 2-48 to 2-50 graphs are given for the lift coefficient, C_L, drag coefficient, C_D, and moment coefficient, C_M, for the bare body (no stabilizing surfaces), and for

fins with convex and concave shrouds. "Convex" and "concave" relate to the outward appearance of the tail. The angle of attack is assumed to be positive as shown in Figure 2-47, but even for a negative depth of submergence of the tail tip, δ/d, the fins and shroud may be in the water and contribute forces and moments. The lift coefficient for the bare (tapered) body is negative, indicating that the tail is pulled toward the cavity wall. When a shroud is provided the lift force is, in general, away from the wall. The fins and shroud add considerably to the drag coefficient (Fig. 2-49). Since the center of pressure of the tail forces is behind the C. G., the signs of the lift and moment coefficients are usually opposed.

REFERENCES

2-1. May, A., "Cavities and the Cavity-Running Behavior of Missiles" Chapter 3 of this report

2-2. Mottard, E. J., and Loposer, J. D., "Average Skin-Friction Coefficients from Tank Tests of a Parabolic Body of Revolution," NACA Report 1161, 1954

2-3. Schoenherr, K. E., "Resistance of Flat Surfaces Moving Through a Fluid," Trans. Soc. Nav. Arch. and Marine Eng., 40, pp 279-313, 1932

2-4. Armstrong, A. H., "Abrupt and Smooth Separation in Plane and Axisymmetric Cavity Flow," ARE Memo 22/53, Dec 1953

2-5. Reichardt, H., "The Laws of Cavitation Bubbles at Axially Symmetric Bodies in a Flow," M.A.P. Volkenrode Ref: MAP-VG, Repts. and Translations No. 766 ONR, 1946

2-6. Eisenberg, P. and Tulin, M. P., "Cavitation", Handbook of Fluid Dynamics, McGraw-Hill, 1961

2-7. Cox, R. N., and Maccoll, J. W., "Recent Contributions to Basic Hydroballistics," Naval Symp., 1956, pp 215-239

2-8. Gilbarg, D. and Rock, D., "On Two Theories of Plane Potential Flows with Finite Cavities," 1946

2-9. Garabedian, P. R., "Calculation of Axially Symmetric Cavities and Jets," Pac. J. Math. 6, pp 611-684, 1956

2-10. Gilbarg, D., "Free-Streamline Theory and Steady-State Cavitation," Naval Symp. pp 281-295, 1956

2-11. Dawson, V. C. D. and Seigel, A. E., "The Steady-State Drag Coefficients of Various Cavitating Head Forms," NOLTR 70-206, 1970

2-12. Garabedian, P. R., "The Mathematical Theory of Three-Dimensional Cavities and Jets," Bull. Am. Math. Soc. 62, pp 219-235, 1956

2-13. Plesset, M. S. and Shaffer, P. A., Jr., "Cavity Drag in Two and Three Dimensions," J. Appl. Phys. 19, pp 934-939, 1948

2-14. Wu, T Y-T, and Wang, D. P., "A Wake Model for Free-Streamline Flow Theory. Part 2. Cavity Flows Past Obstacles of Arbitrary Profile," J. Fluid Mech. 18, pp 65-93, 1964

2-15. Armstrong, A. H., "Drag Coefficients of Wedges and Cones in Cavity Flow," ARE Rept. 21/54, 1954

2-16. Fisher, J. W., "Discontinuous Fluid Flow with Cavity Formation," UBRC, Fairlie, Internal Rept. 217, 1945

2-17. Waugh, J. G. and Ager, R. W., "Water-Entry Whip and Deceleration of Six Full-Scale Torpedo Models with Ogive and Plate-Ogive Heads," NOTS NAVORD Rept. 1308, 1951

2-18. Norman, J. W. and Burden, W. J., "Deceleration at Water Entry-- Some Preliminary Measurements with Strain Gauge Accelerometers," ARL/R2/G/HY/2/3, 1955

2-19. Mosteller, G. G., "Axial Deceleration at Oblique Water Entry of 2-inch Diameter Models with Hemisphere and Disk-Cylinder Noses," NOTS NAVORD Rept. 5424, 1957

2-20. O'Neill, J. P., "Flow Around Bodies with Attached Open Cavities," CIT Hyd. Rept. E-24.7, 1954

2-21. Oversmith, R. H., "Some Observations on Cavitating Flows," Convair Eng. Dept. Rept. ZR-659-015 1959

2-22. Eisenberg, P. and Pond, H. L., "Water Tunnel Investigations of Steady State Cavities," DTMB Rept. 668, 1948

2-23. Klose, J. and Acosta, A. J., "Some New Measurements on the Drag of Cavitating Disks," J. Ship Res. 9, pp 102-104, 1965

2-24. Brennan, C., "A Numerical Solution of Axisymmetric Cavity Flows," J. Fluid Mech. 37, pp 671-688, 1969

2-25. Kiceniuk, T. "An Experimental Study of the Hydrodynamic Forces Acting on a Family of Cavity-Producing Conical Bodies of Revolution Inclined to the Flow," CIT Hyd. Rept. E-12.17 1954

2-26. Rouse, H. and McNown, J. S., "Cavitation and Pressure Distribution Head Forms at Zero Angle of Yaw," State U. Iowa, Studies Eng., Bull 32, 1948

2-27. Anderson, R. F., "The Correlation of Axisymmetric Cavity Data for Design Use," NOTS TM 1288, 1953

2-28. Plesset, M. S., and Perry, B., "On the Application of Free Streamline Theory of Cavity Flows," Memoires sur le mechaniques des fluides... Publ. Scient. et Techniques du Ministere de l'air, 1954

2-29. Armstrong, A. H. and Tadman, K. G., "Axisymmetric Cavity Flow about Ellipsoids," Proc. Joint Adm. USN Mtg. on Hydroball. 1954

2-30. Hsu, E-Y and Perry, B., "Water Tunnel Experiments on Spheres in Cavity Flow," CIT Hyd. Rept. E-24.9, 1954

2-31. Eisenberg, P., "A Brief Survey of Progress on the Mechanics of Cavitation," DTMB Rept. 842, 1953

2-32. May, A. and Woodhull, J. C., "Drag Coefficients of Steel Spheres Entering Water Vertically," J. Appl. Phys. 19, pp 1109 1948

2-33. Shaw, R. A., "Underwater Projectiles, Prediction of Underwater Behavior from Wind Tunnel Measurements," MAEE Helensburgh, Rept. H/ARM/Res 23, 1944

2-34. Norman, J. W., Burden, W. J., and Suter, R. A., "Deceleration at Water Entry V - The Effects of Varying Head Radius," ARL/R6/G/HY/2/3, 1962

2-35. Birkhoff, G., Summary Tech. Rept. of the Nat. Def. Res. Comm., "Mathematical Studies Relating to Military Physical Research," Vol. 1, 1946

2-36. Johnson, V. E. and Rasnick, T. A., "The Drag Coefficient of Parabolic Bodies of Revolution Operating at Zero Cavitation Number and Zero Angle of Yaw," NACA TR R-86, 1960

2-37. May, A., "Review of Water Entry Theory and Data," J. Hydronautics 4, pp 140-142, 1970

2-38. Roshko, A., "A New Hodograph for Free-Streamline Theory," NACA TN 3168, 1954

2-39. Waid, R. L., "Water Tunnel Investigation of Two-Dimensional Cavities," CIT Hyd. Rept. E-73.6, 1958

2-40. Cox, A. D. and Clayden, W. A., "Cavitating Flow about a Wedge at Incidence," J. Fluid Mech, 3, pp 615-637, 1958

2-41. Silberman, E., "Experimental Studies of Supercavitating Flow About Simple Two-Dimensional Bodies in a Jet," J. Fluid Mech. 5, pp 337-354, 1959

2-42.   Daily, J. W., "Hydrodynamic Forms Resulting from Cavitation on Underwater Bodies," CIT Hyd. Rept. ND 31.2, 1945

2-43.   Brodetsky, S., "Discontinuous Fluid Motion Past Circular and Elliptic Cylinders," Proc. Roy. Soc. A102, pp 542-553, 1923

2-44.   Birkhoff, G., Goldstine, H. H. and Zarantonello, E. H., "Calculation of Plane Cavity Flows Past Curved Obstacles," Rend. Seminar. Mat. Turino 13, pp 205-224, 1954

2-45.   Wu, T. Y-T, "A Free Streamline Theory for Two-Dimensional Fully Cavitated Hydrofoils," J. Math and Phys. 35, pp 236-265, 1956

2-46.   Parkin, B. R., "Experiments on Circular-Arc and Flat-Plate Hydrofoils," J. Ship Res. 2, pp 34-67, 1958

2-47.   Wu, T Y-T, "A Wake Model for Free-Streamline Flow Theory. Part 1. Fully and Partially Developed Wake Flows and Cavity Flows Past an Oblique Flat Plate," J. Fluid Mech. 13, pp 161-181, 1962

2-48.   Larock, B. E. and Street, R. L., "A Riemann-Hilbert Problem for Nonlinear, Fully Cavitating Flow," J. Ship Res. 9, pp 170-178, 1965

2-49.   Acosta, A. J., "The Effect of a Longitudinal Gravitational Field on the Supercavitating Flow over a Wedge," J. Appl. Mech. (Transact. ASME) 28, Series E., pp 188-192, 1961 and Discussion by B. R. Parkin. Also CIT Eng. Rept. 79.1, 1958

2-50.   Street, R. L., "Supercavitating Flow about a Slender Wedge in a Transverse Gravity Field," J. Ship Res. 7, pp 14-23, 1963

2-51.   Street, R. L., "A Note on Gravity Effects in Supercavitating Flow," J. Ship Res. 8, pp 39-45, 1965

2-52.   Kiceniuk, T. and Acosta, A. J., "Experiments on Gravity Effects in Supercavitating Flow," J. Ship Res. 10, pp 119-121, 1966

2-53.   Lenau, C. W. and Street, R. L., "A Non-Linear Theory for Symmetric Supercavitating Flow in a Gravity Field," J. Fluid Mech. 21, pp 257-280, 1965

2-54.   Whitney, A. K., Brennan, C., and Wu, T. Y-T, "Experimental Verification of Cavity-Flow Wall Effects and Correction Rules," CIT EAS Rept. E-97A-18, 1970

2-55.   Wu, T. Y-T, Whitney, A. K., and Brennan, C., "Cavity-Flow Wall Effects and Correction Rules," J. Fluid Mech. 49, pp 223-256, 1971

2-56. Cohen, H., Sutherland, C. D. and Tu, Y-O, "Wall Effects in Cavitating Hydrofoil Flow," _J. Ship Res._ 1, 31-39, 1957

2-57. Waid, R. L. and Kermeen, R. W., "Forces on Cylinders Planing on Flat and Curved Surfaces in Cavitating and Noncavitating Flow," CIT Hyd. Rept. E-73.5, 1957

2-58. Kiceniuk, T.,"Experimental Study of Froude Number Modeling for Cylinders Planing on Water," CIT Hyd. Rept. E-24.4, 1952

2-59. Kiceniuk, T. and Greengard, R., "Measurements of Lift Coefficients for a Family of Cones Planing on Water," CIT Hyd. Rept. E-12.3, 1952

2-60. Kiceniuk, T., "Force and Moment Measurements on a Torpedo Afterbody with Three Tail Configurations Planing on a Free Water Surface," CIT Hyd. Rept. E-54, 1953

2-61. Waid, R. L., "Force Coefficients of Six Related Body Configurations in Cavitating Flow," CIT Hyd. Rept. E-51.1, 1954

Abbreviations

ARE   Armament Research Establishment, Fort Halstead, Kent, England

ARL   Admiralty Research Laboratory, Admiralty Hydroballistic Research Establishment, Glen Fruin, Scotland

CIT   California Institute of Technology, Pasadena, California

CIT Hyd.   CIT, Hydrodynamics Laboratory

CIT Eng.   CIT, Engineering Division

CIT EAS   CIT, Engineering and Applied Science Division

DTMB   David Taylor Model Basin, Carderock, Maryland

NACA   National Advisory Committee for Aeronautics

NOL   Naval Surface Weapons Center, White Oak Laboratory, Silver Spring, Maryland (formerly the Naval Ordnance Laboratory)

NOTS   Naval Ordnance Test Station, Pasadena, California

Naval Symp.   Proc. of the (first) Naval Hydrodynamic Symposium, 24-28 September 1956
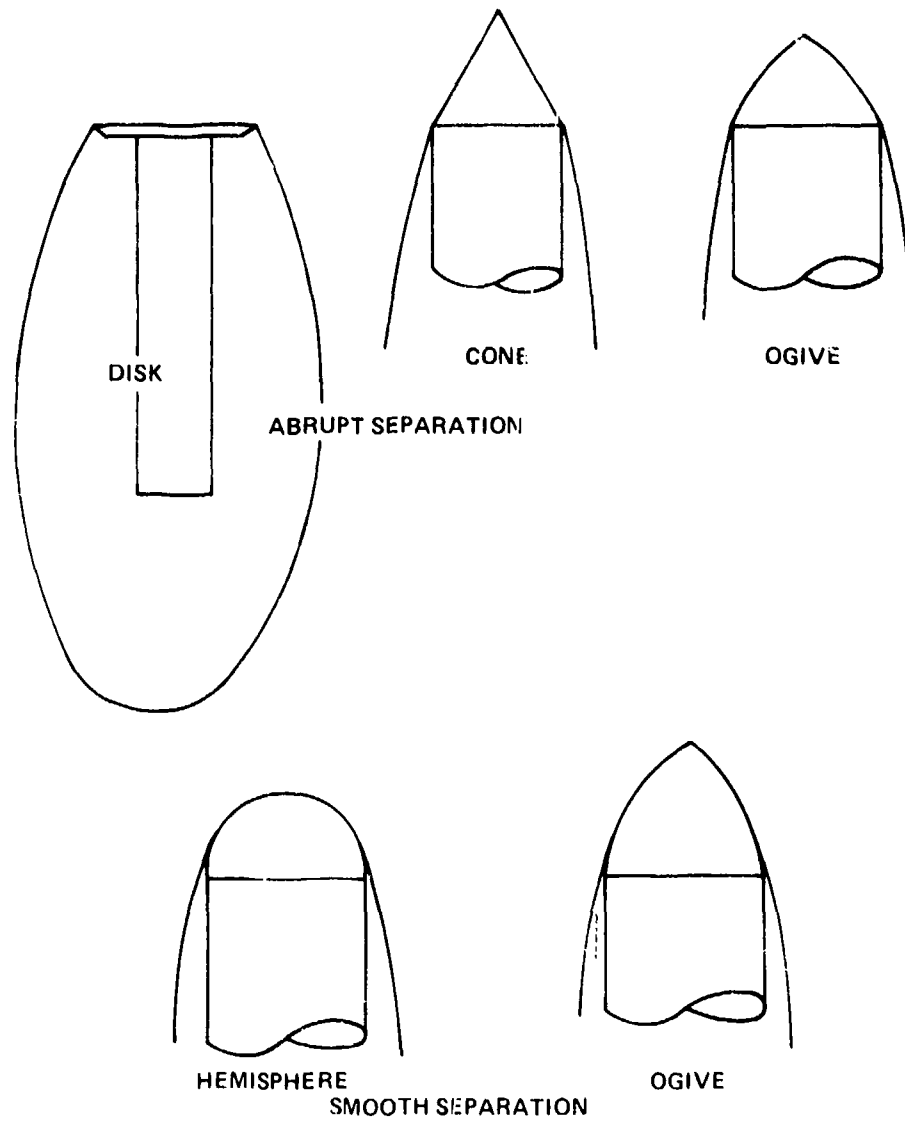
FIG. 2-1 FLOW SEPARATION FROM CAVITY-RUNNING MISSILES
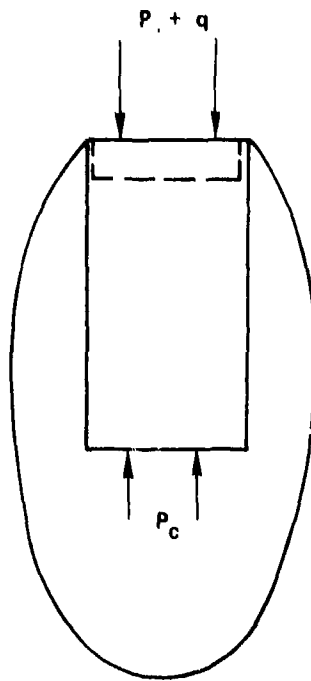
FIG. 2-2 PRESSURES ON MISSILE WITH
STAGNATION-CUP NOSE WHILE
CAVITY RUNNING
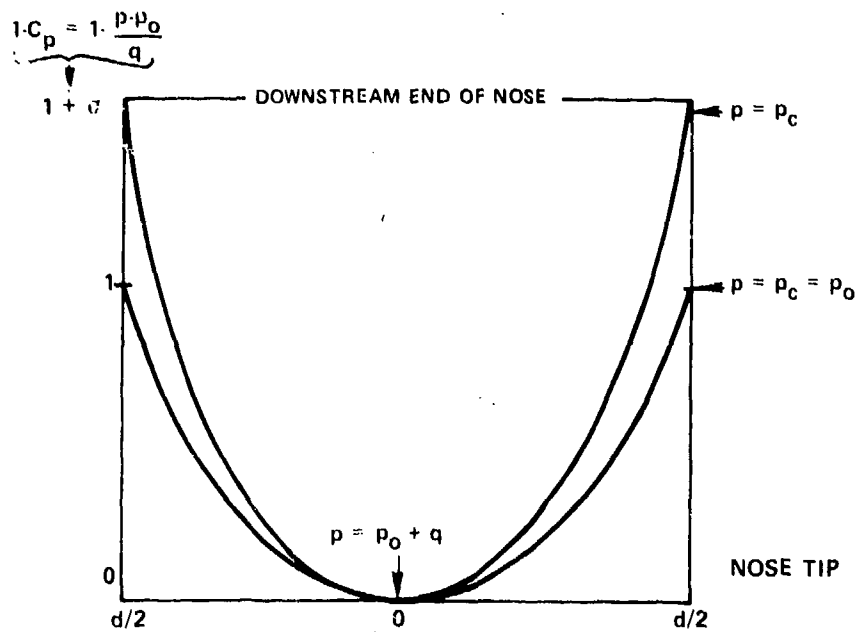
FIG. 2-3 ASSUMED PRESSURE CONDITIONS ON THE NOSE OF A
CAVITY-RUNNING MISSILE. AFTER REICHARDT REF (2-5)

KEY

O OVERSMITH REF (2-21)
X KERMEEN REF (2-20)
▽ O'NEILL REF (2-20)
△ A.R.D.E. REF (2-7)
□ KICENIUK REF (2-25)
+ REICHARDT REF (2-5)
◇ BRENNAN REF (2-24)

THE STRAIGHT LINE HAS THE EQUATION
$C_D = 0.807 + 0.891$
BUT EQN (12) IS PROBABLY TO BE PREFERRED

FIG. 2-4a   DRAG OF CAVITY-RUNNING DISK $\sigma \leqslant 0.32$
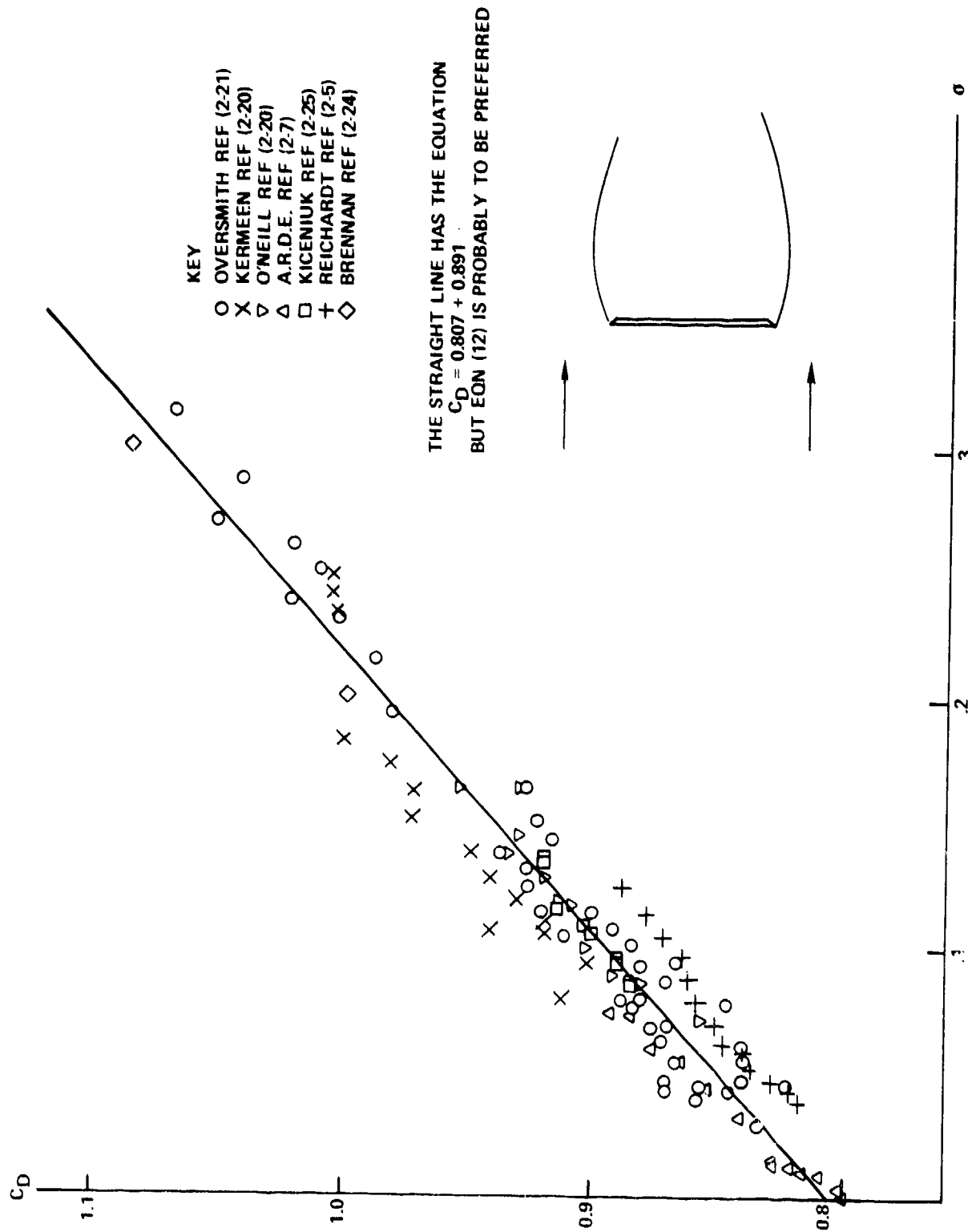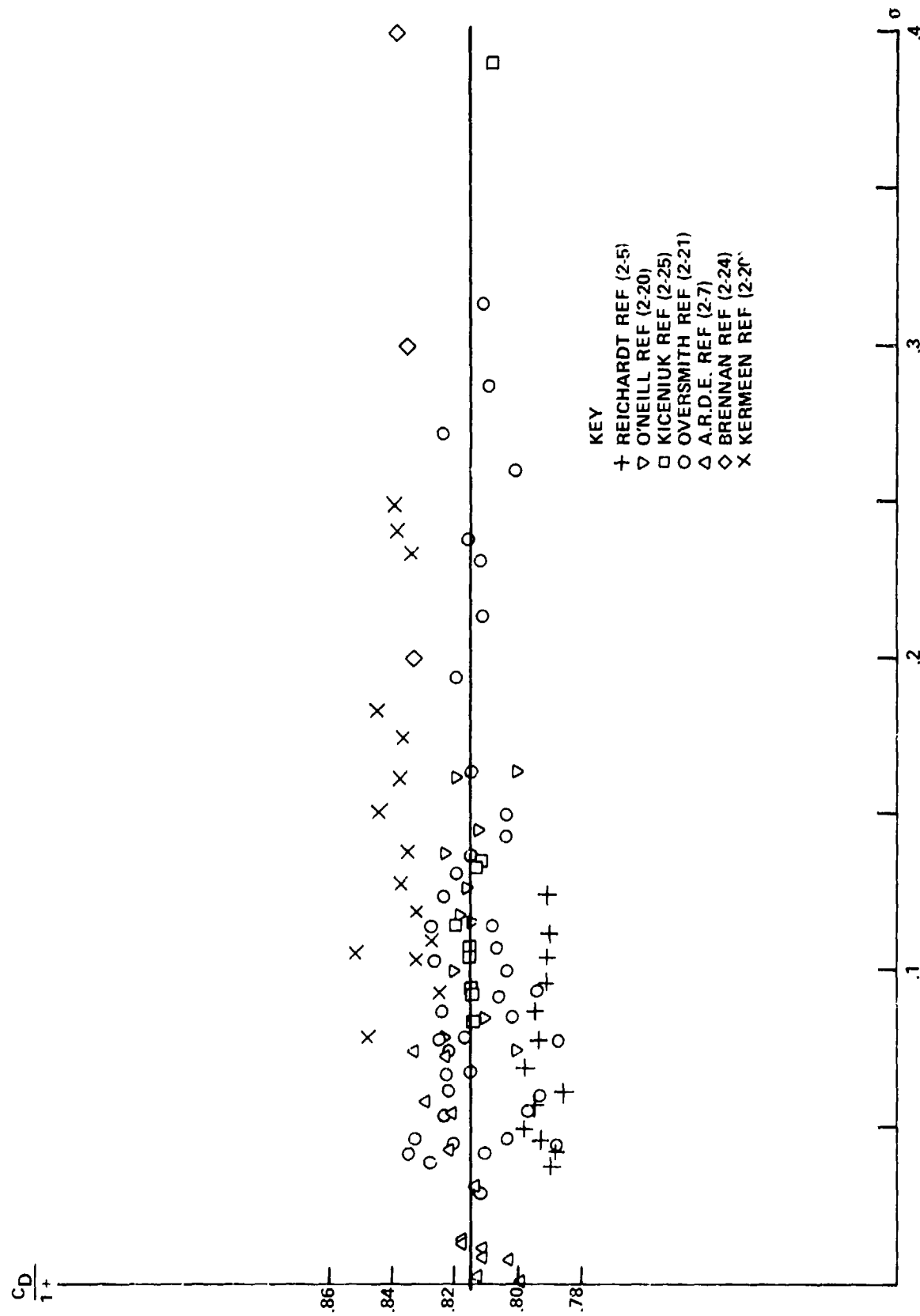
FIG. 2-4b DRAG OF CAVITY-RUNNING DISK · ≤ 0.4

KEY
+ REICHARDT REF (2-5)
∇ O'NEILL REF (2-20)
□ KICENIUK REF (2-25)
○ OVERSMITH REF (2-21)
◁ A.R.D.E. REF (2-7)
◇ BRENNAN REF (2-24)
✕ KERMEEN REF (2-2?`

FIG. 2-5 DRAG OF CAVITY-RUNNING DISK

KEY

O OVERSMITH REF (2-21)
X KERMEEN REF (2-20)
◁ KLOSE-ACOSTA REF (2-23)
◇ BRENNAN REF (2-24)
□ EISENBERG-POND REF (2-22)
▷ DAWSON-SEIGEL REF (2-11)

(O MEASURED VALUES REF (2-20)
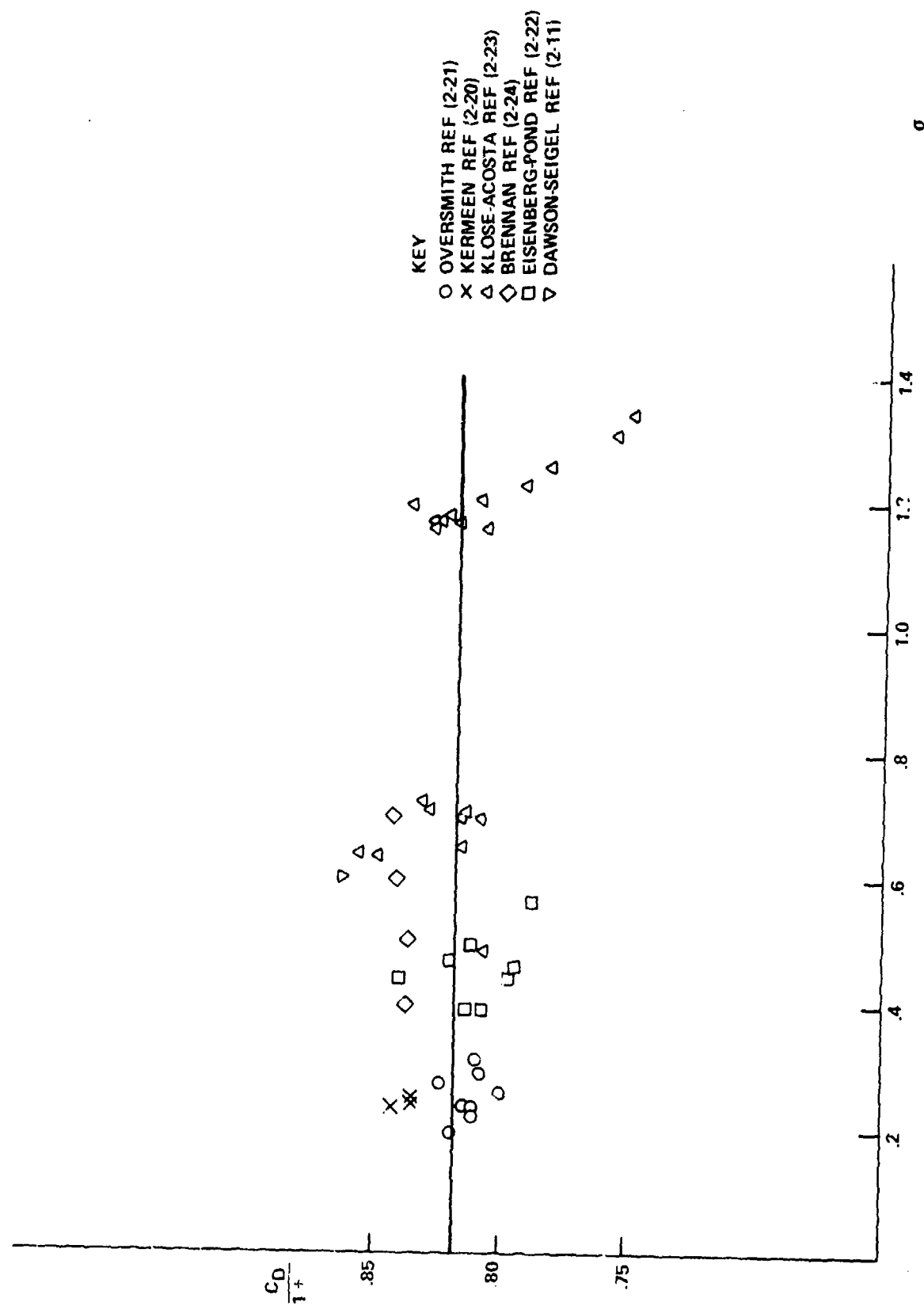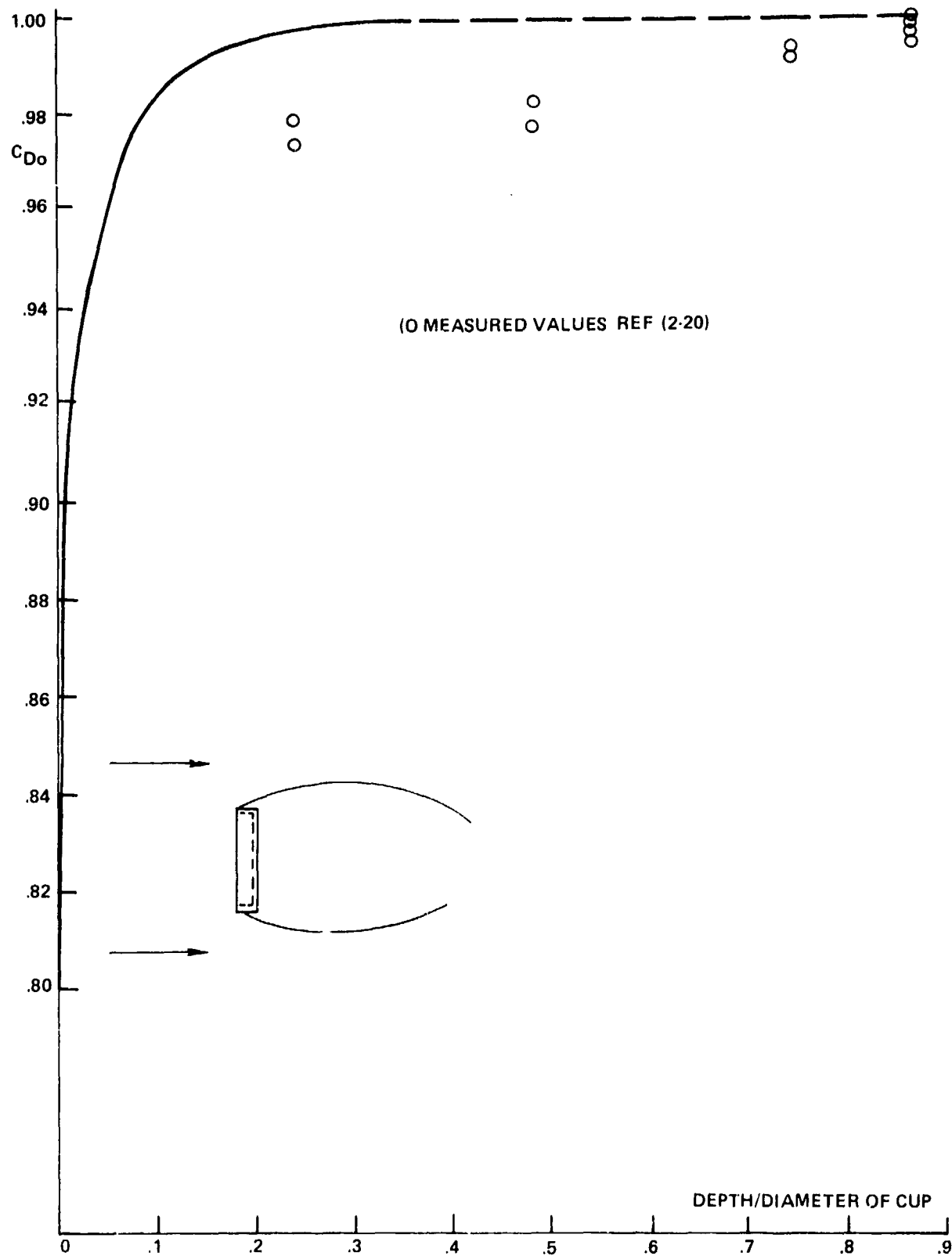
FIG. 2-6 THEORETICAL DRAG COEFFICIENT FOR CAVITY-RUNNING
STAGNATION CUP AS A FUNCTION OF THE DEPTH OF THE CUP REF (2-13)

KEY
○ REICHARDT (1.017 + 0.987 ·) REF (2-5)
✕ O'NEILL (0.996 + 1.003 ·) REF (2-20)
△ KERMEEN REF (2.20)
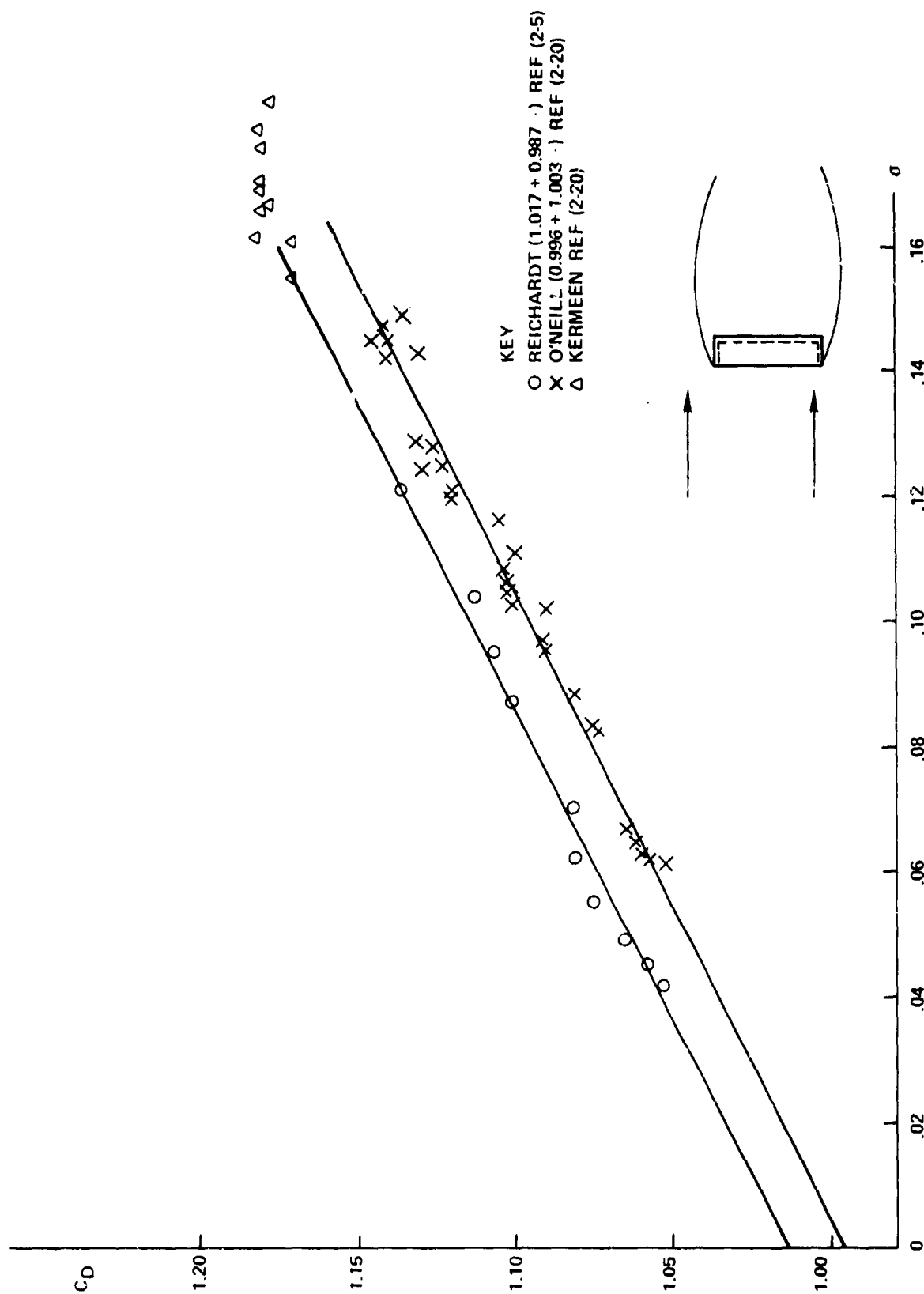
FIG. 2-7 DRAG OF STAGNATION CUP CAVITY RUNNING
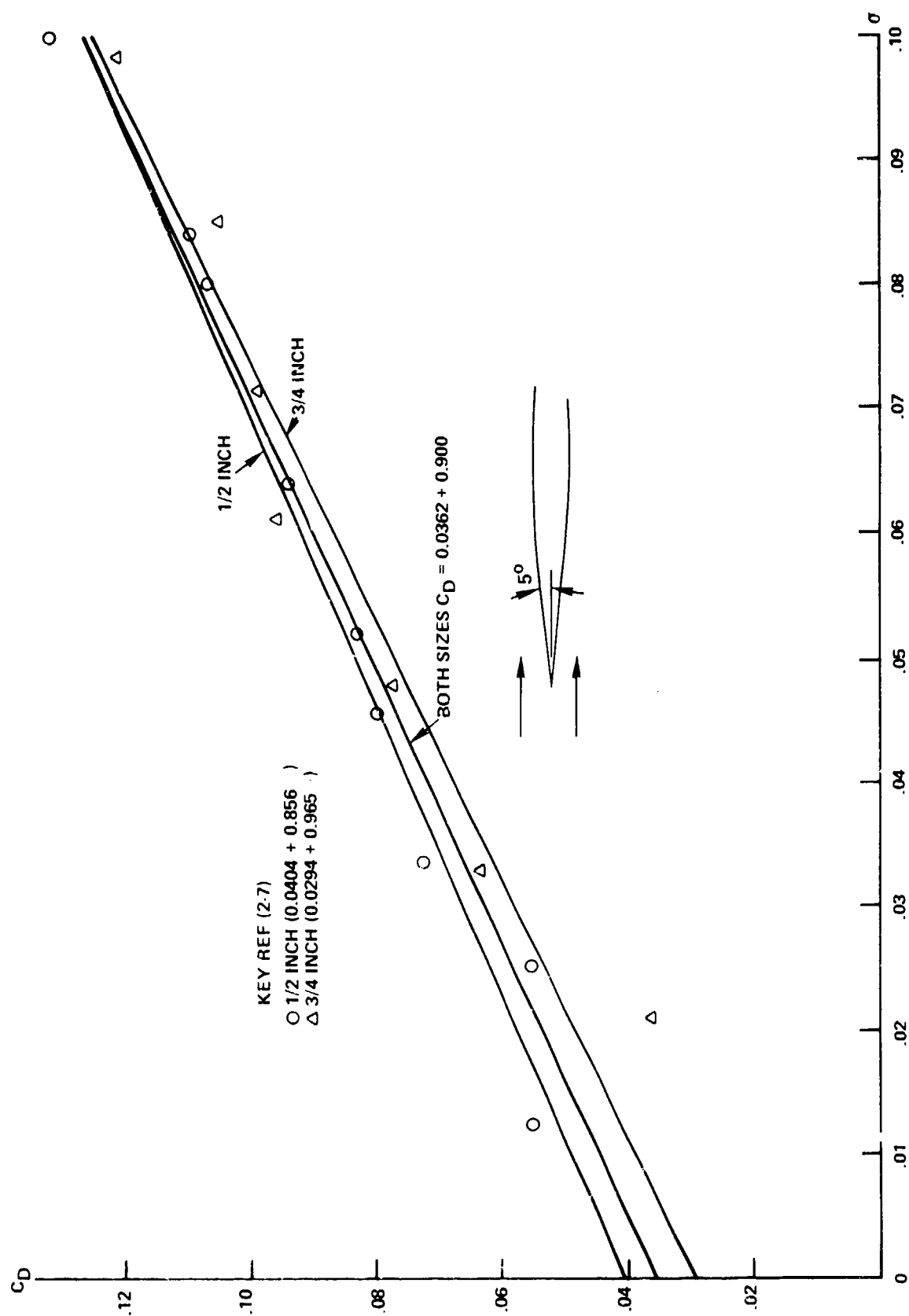
FIG. 2-8 CAVITY-RUNNING DRAG OF 5-DEGREE CONES

KEY REF (2-7)

O 1/2 INCH (0.0404 + 0.856)
△ 3/4 INCH (0.0294 + 0.965)

1/2 INCH

3/4 INCH

BOTH SIZES $C_D = 0.0362 + 0.900$

5°

C_D
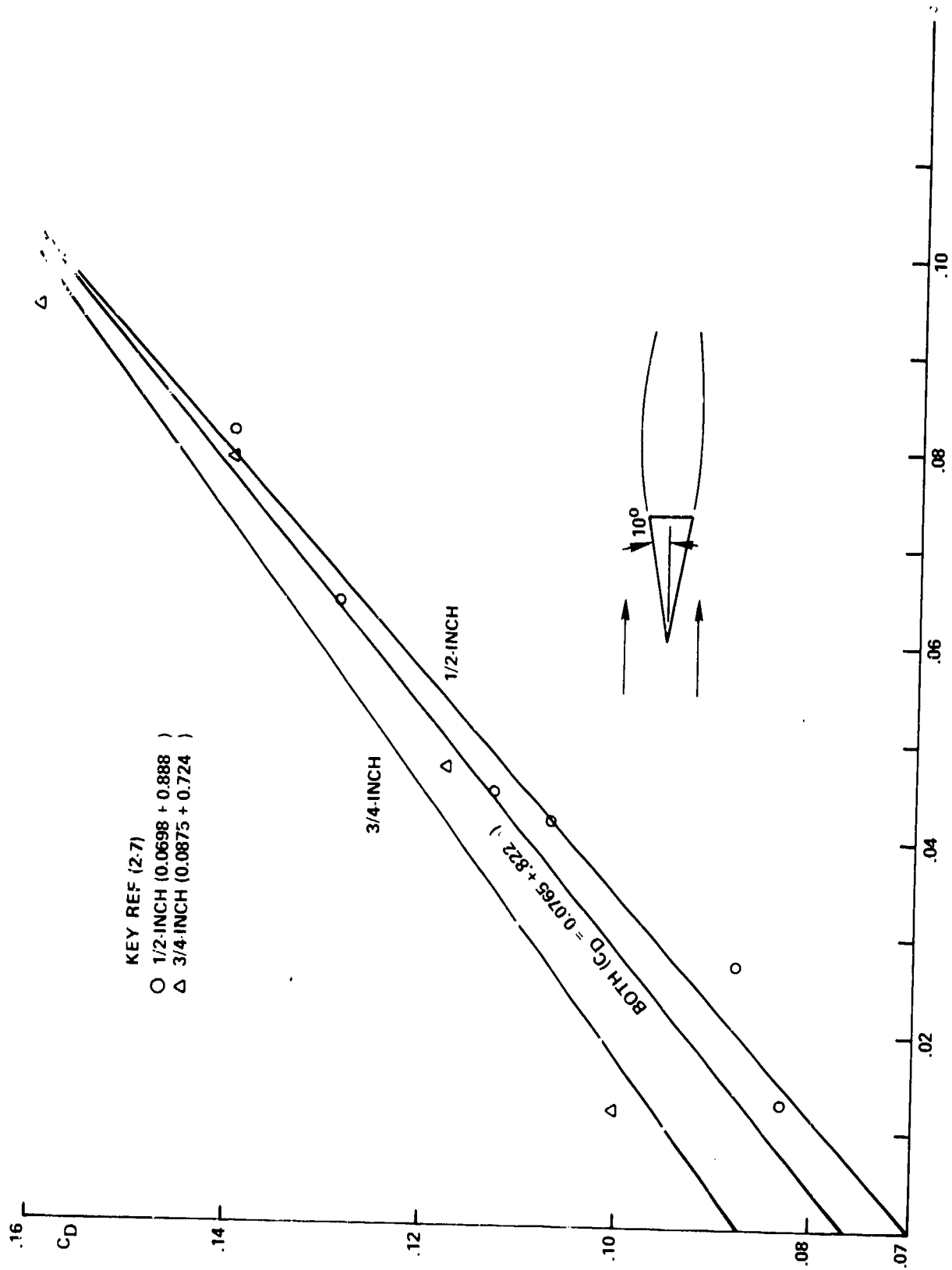
FIG. 2-9 CAVITY-RUNNING DRAG OF 10-DEGREE CONES

KEY REF (2-7)

○ 1/2-INCH (0.0698 + 0.888)
△ 3/4-INCH (0.0875 + 0.724)

1/2-INCH

3/4-INCH

BOTH (CD = 0.0765 + .822)

10°
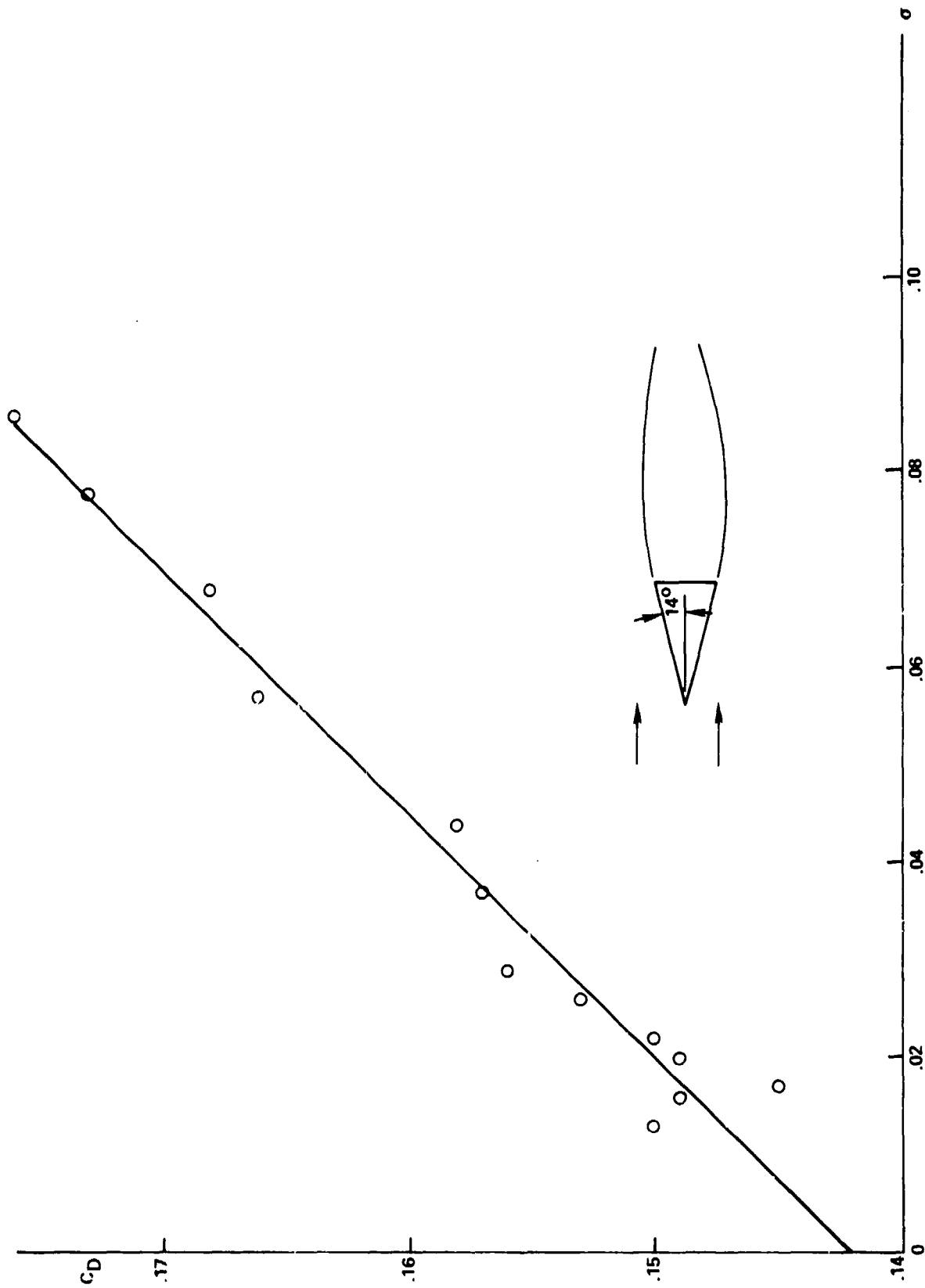
FIG. 2-10 CAVITY-RUNNING DRAG OF 14-DEGREE CONES REF (2-5)

FIG. 2-11 CAVITY-RUNNING DRAG OF 15-DEGREE CONES

KEY REF (2-7)

- KICENIUK REF (2-25)
- O'NEILL REF (2-20)
- KERMEEN REF (2-20)
- X 1/2 INCH REF (2-16)
- + 3/4 INCH REF (2-16)
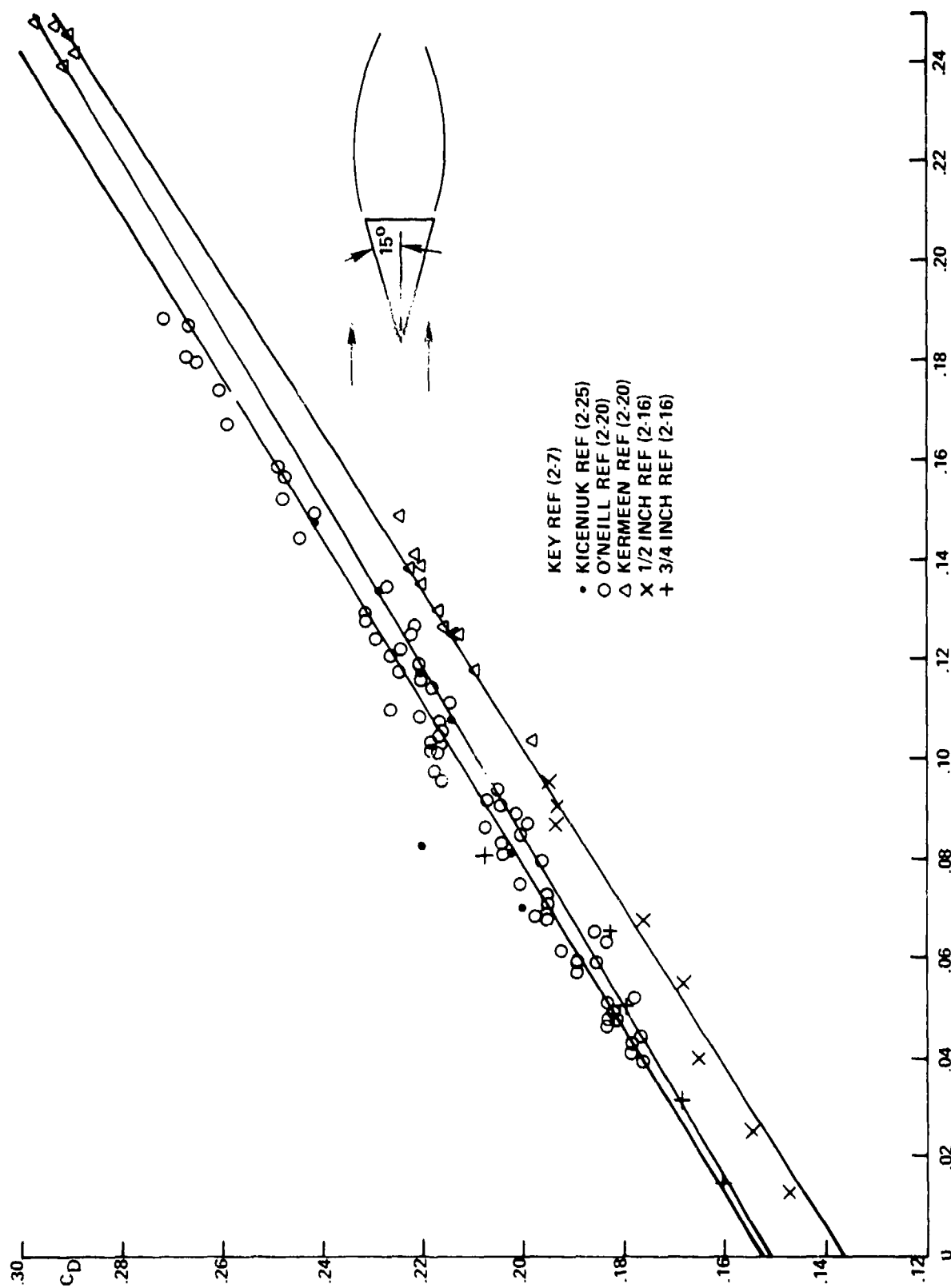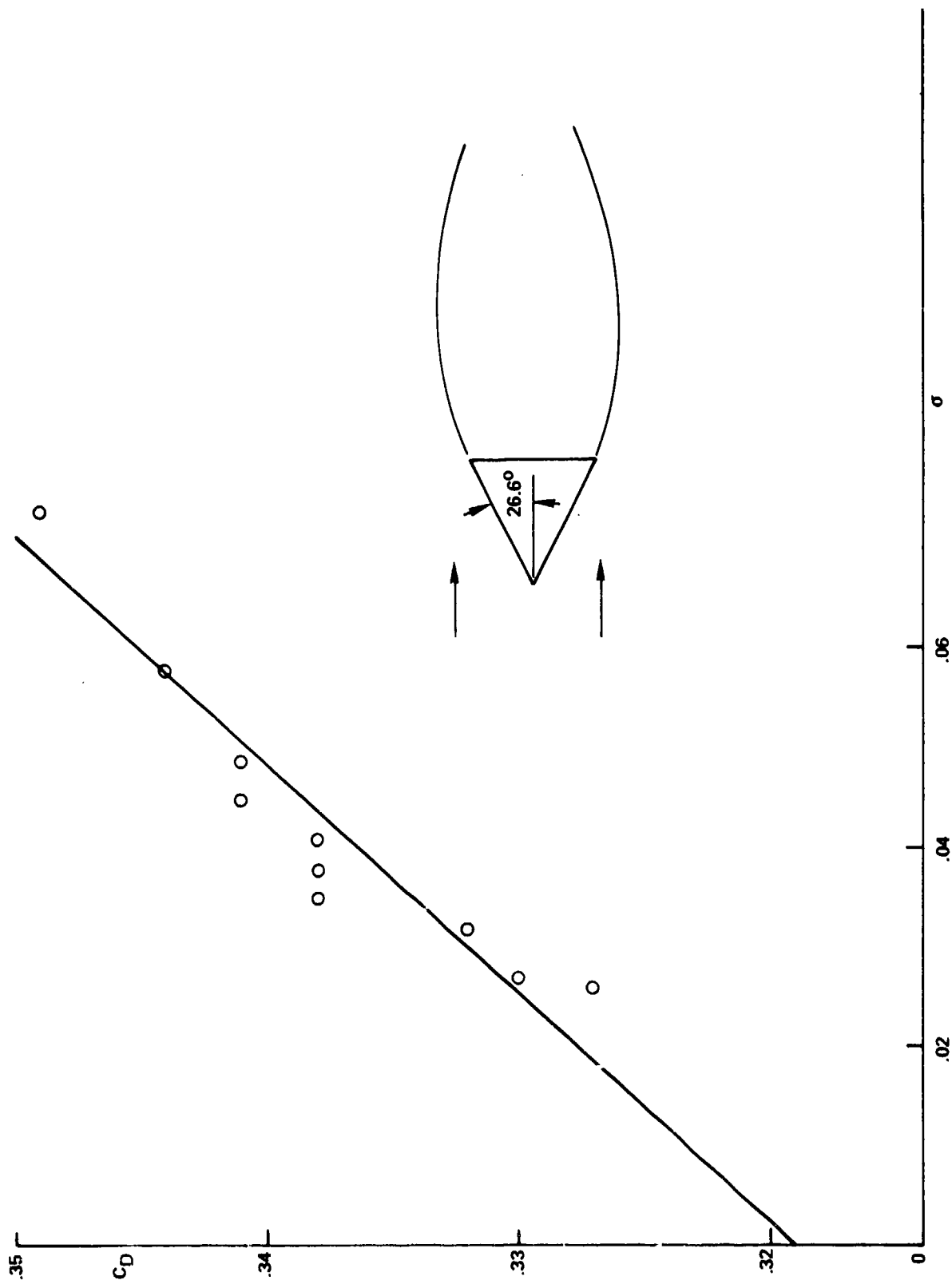
FIG. 2-12 CAVITY-RUNNING DRAG OF 26.6-DEGREE CONES REF (2-5)
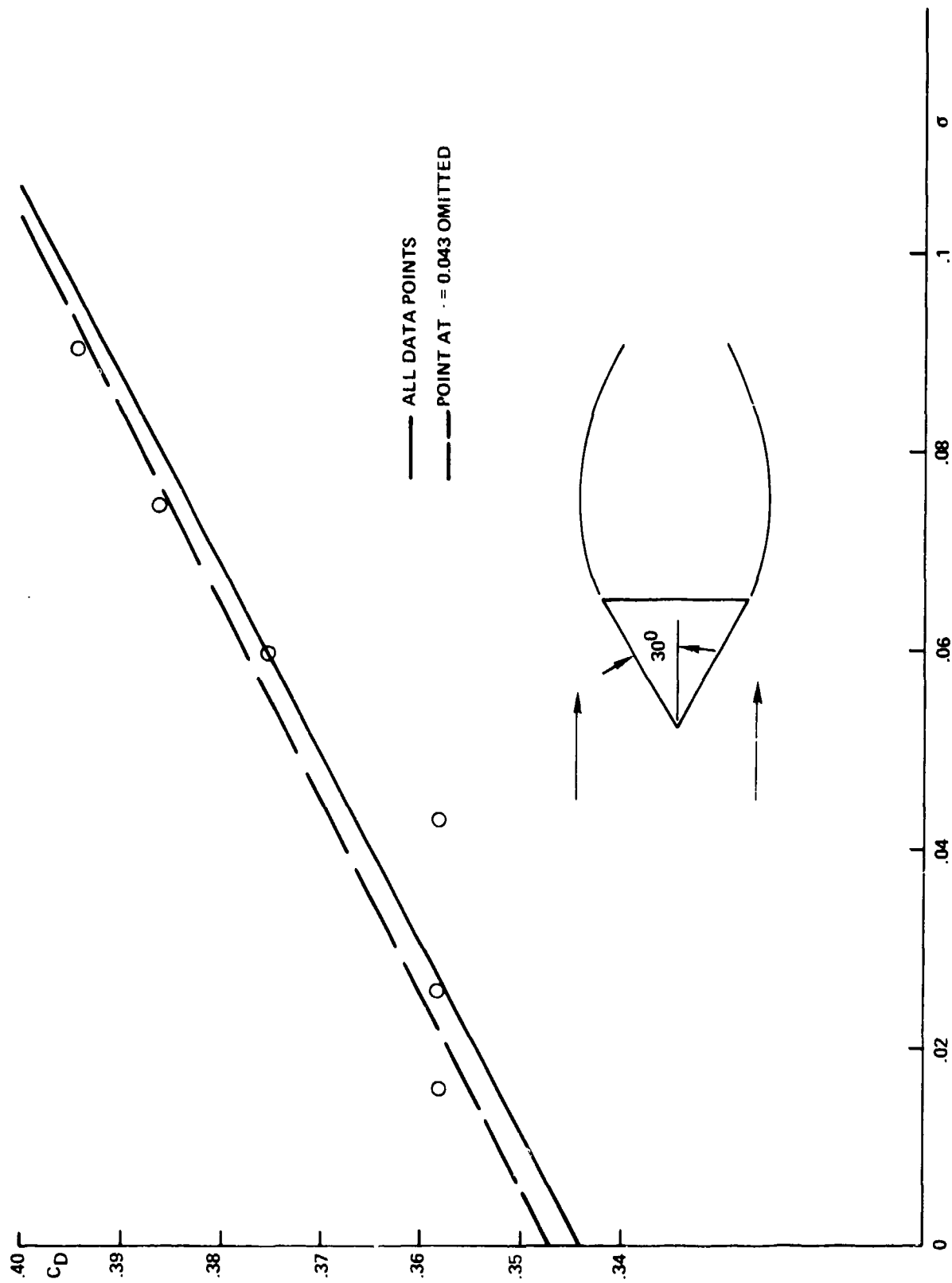
FIG. 2-13 CAVITY-RUNNING DRAG OF 30-DEGREE CONES REF (2-7)

KEY

× REICHARDT REF (2-5)
▽ O'NEILL REF (2-20)
+ KERMEEN REF (2-20)
○ OVERSMITH REF (2-21)
△ COX-MACCOLL REF (2-7)
□ KICENIUK REF (2-25)
◇ DAWSON-SEIGEL REF (2-11)
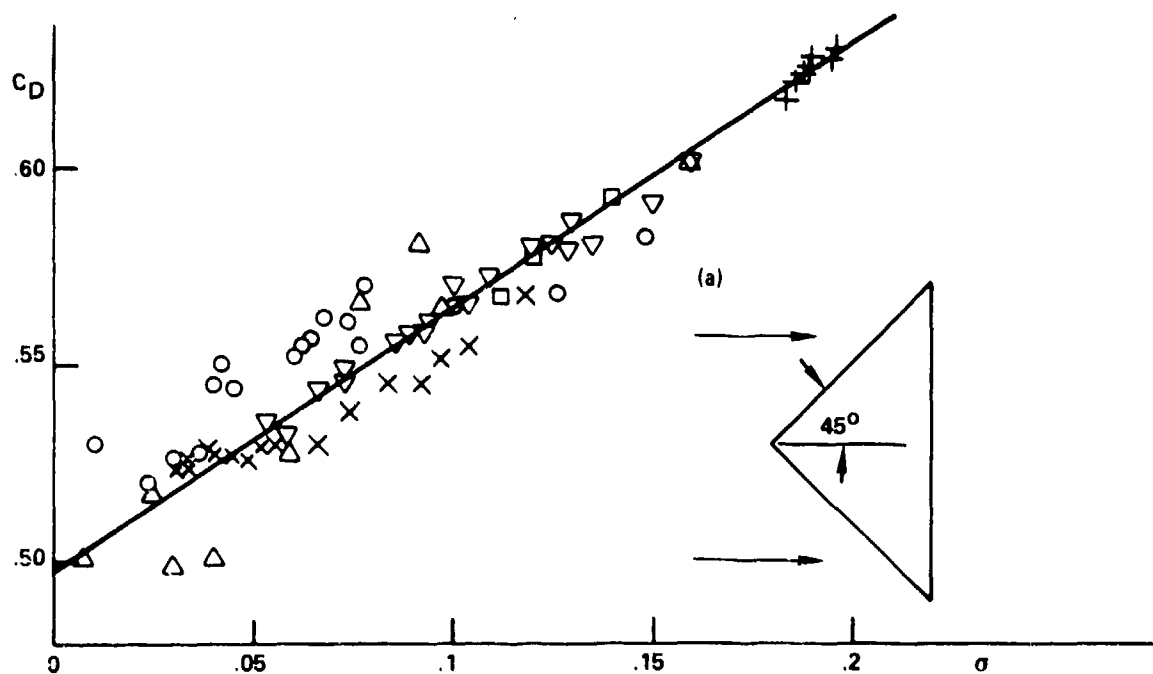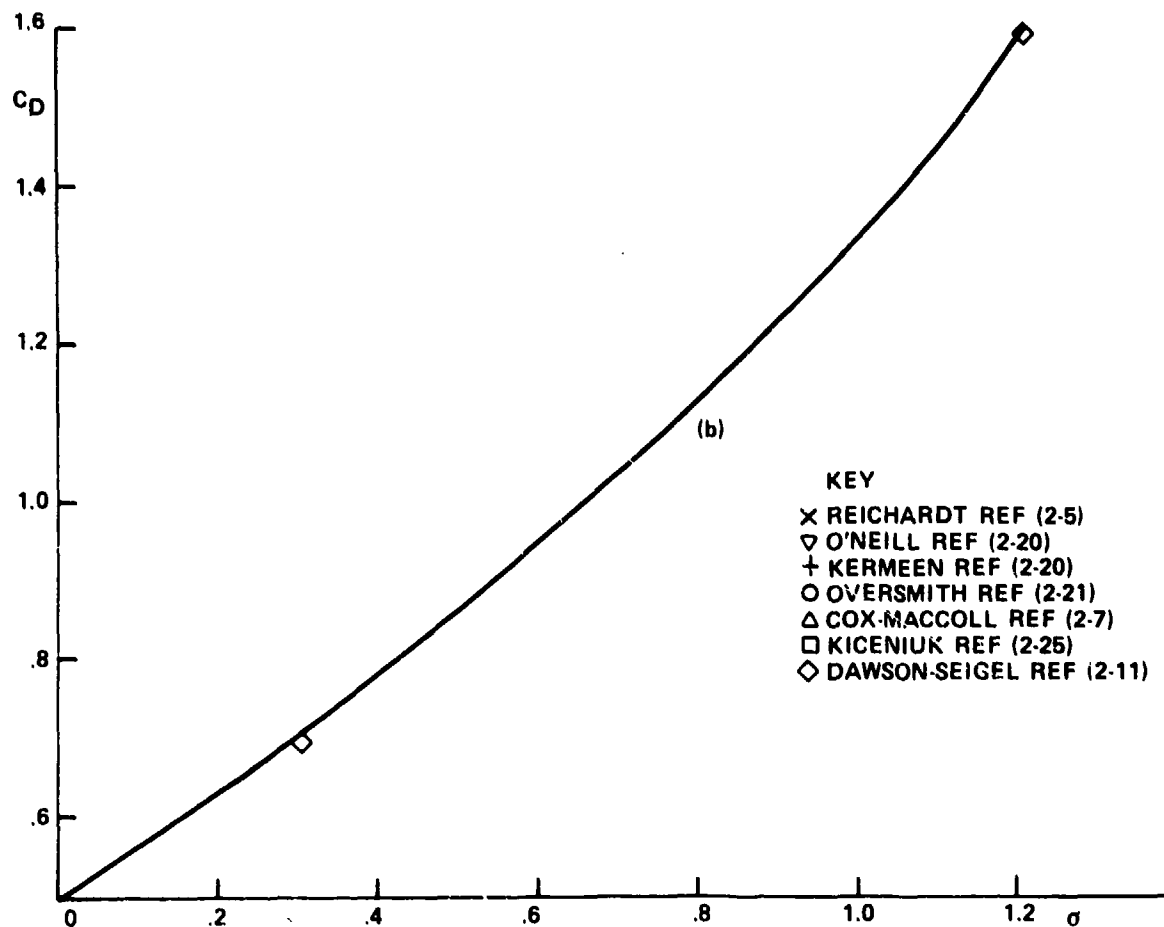
FIG. 2-14 CAVITY-RUNNING DRAG OF 45-DEGREE CONES
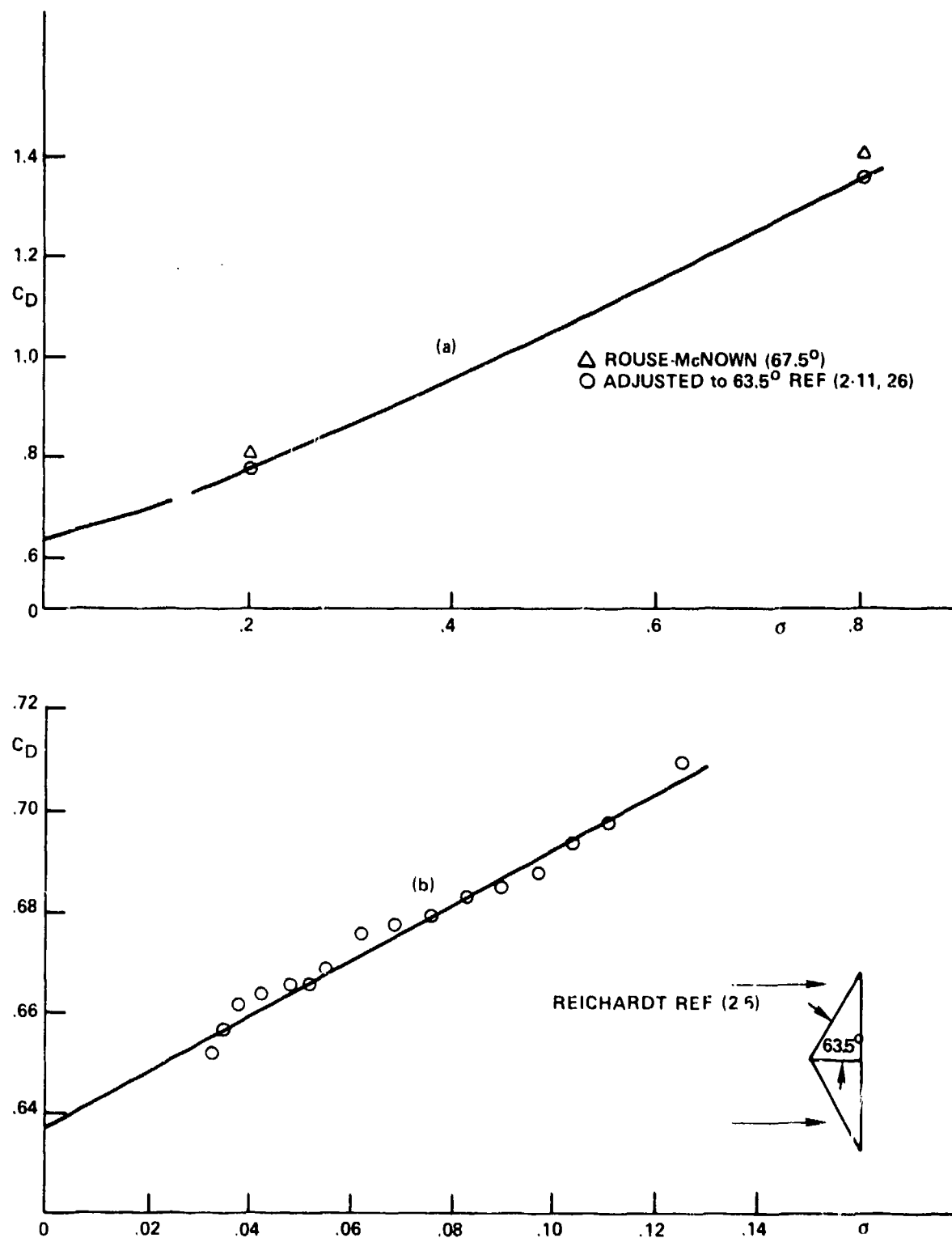
FIG. 2-15 CAVITY-RUNNING DRAG OF 63.5-DEGREE CONES
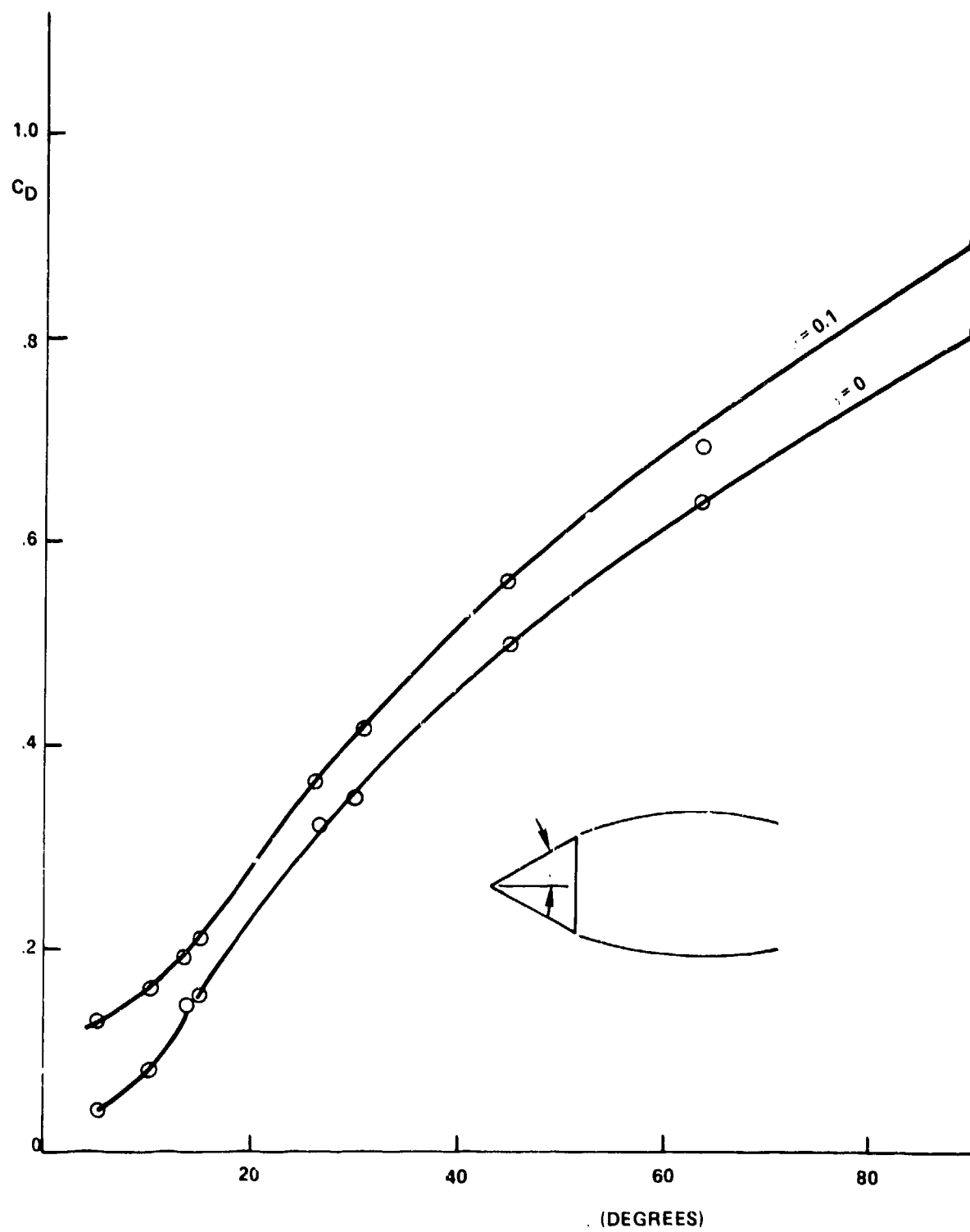
FIG. 2-16 CAVITY-RUNNING DRAG OF CONES
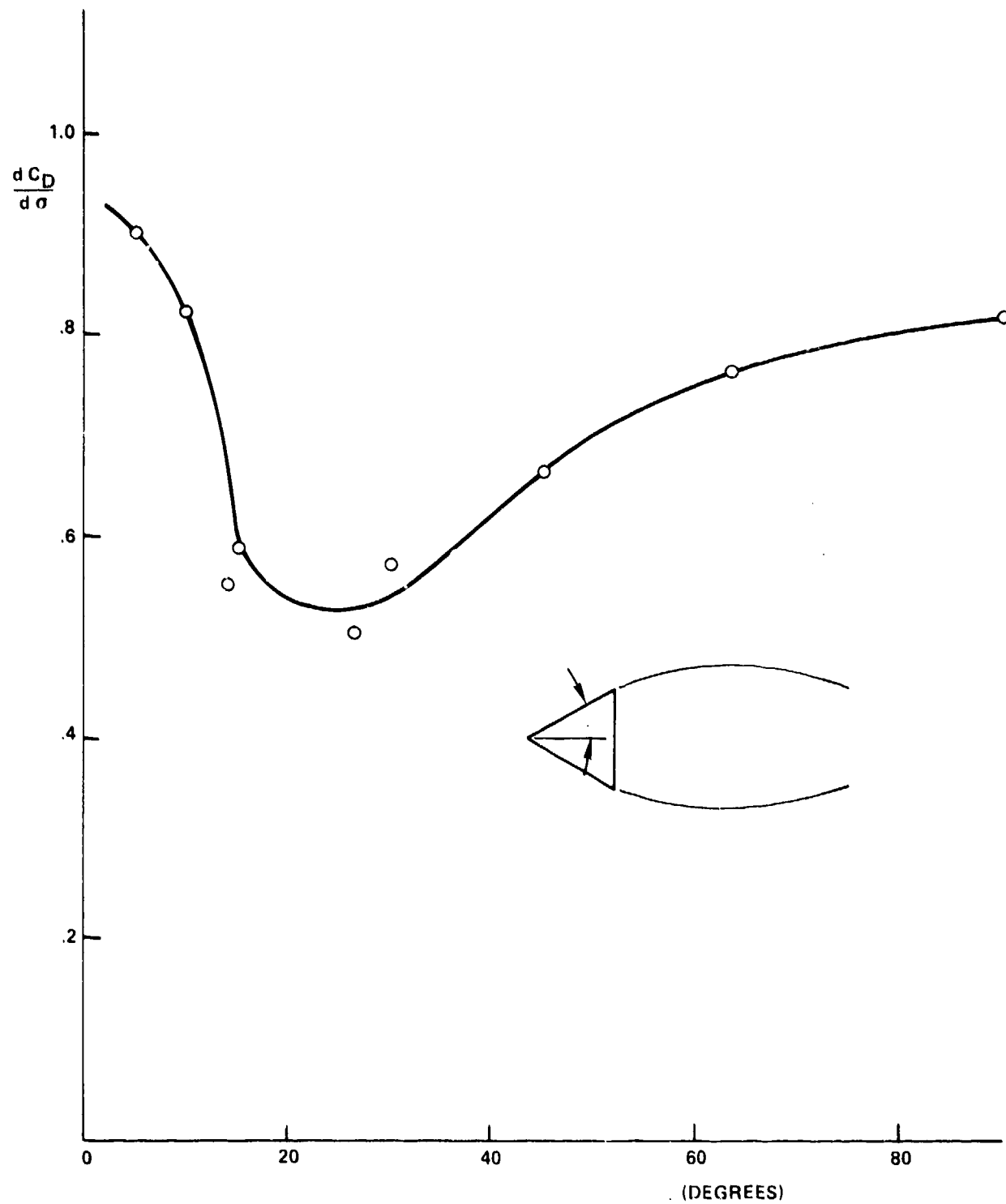
FIG. 2-17 SLOPE OF DRAG CURVES FOR CAVITY-RUNNING CONES
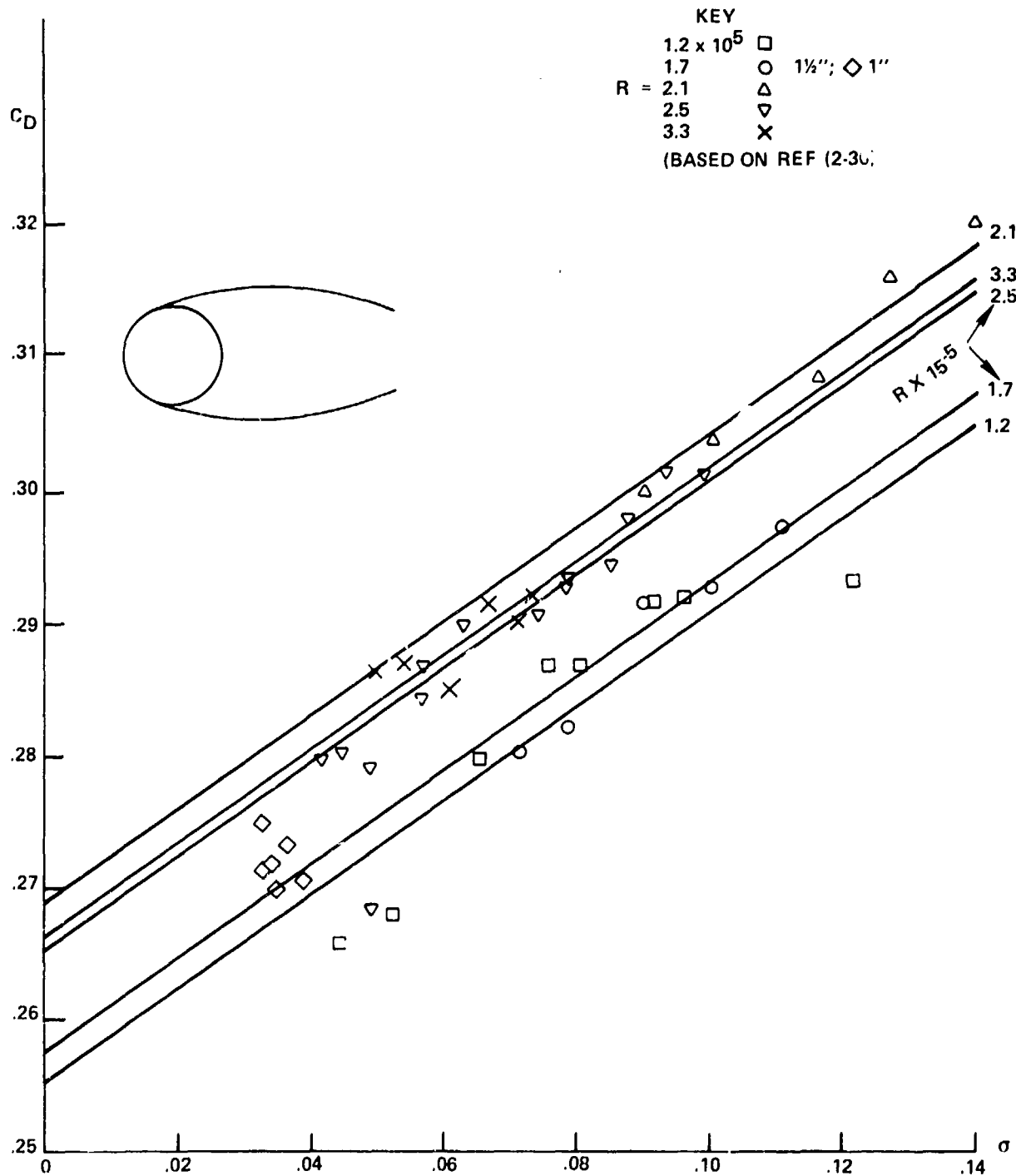
FIG. 2-18 DRAG OF SPHERES CAVITY RUNNING AT VARIOUS REYNOLDS NUMBERS
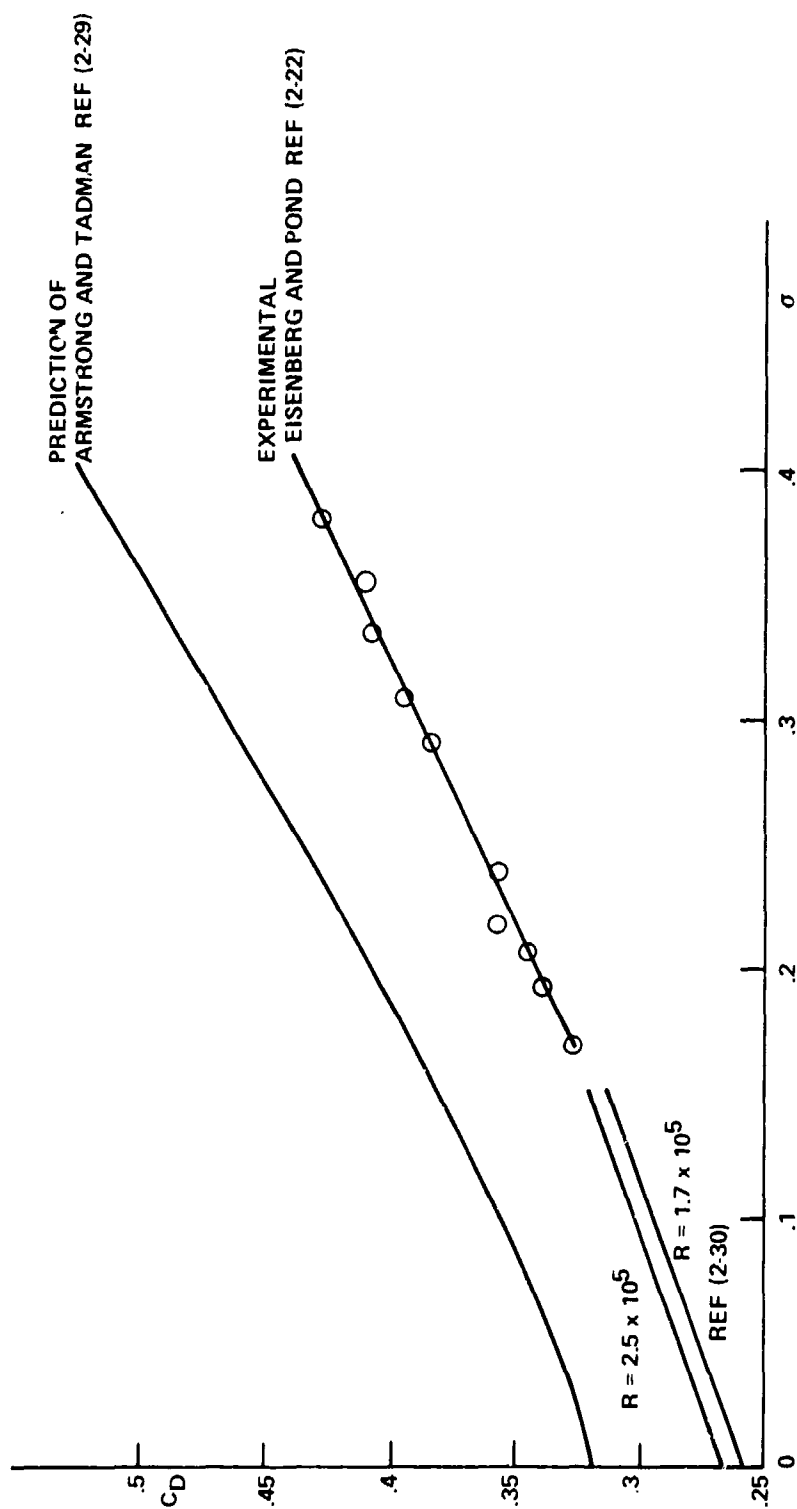
FIG. 2-19 CAVITY-RUNNING DRAG OF SPHERES
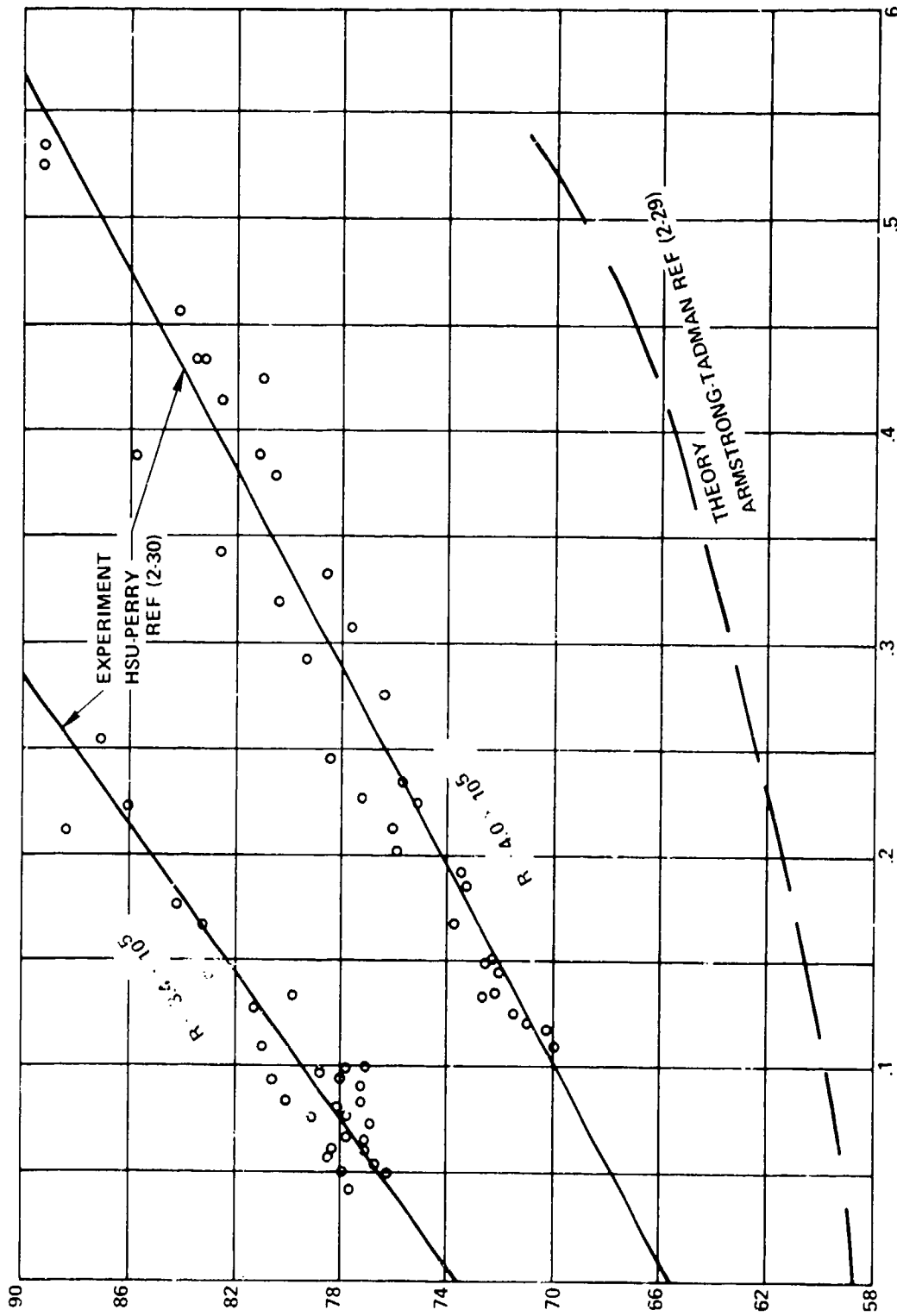
FIG. 2-20 ANGLE OF FLOW SEPARATION FOR SPHERES
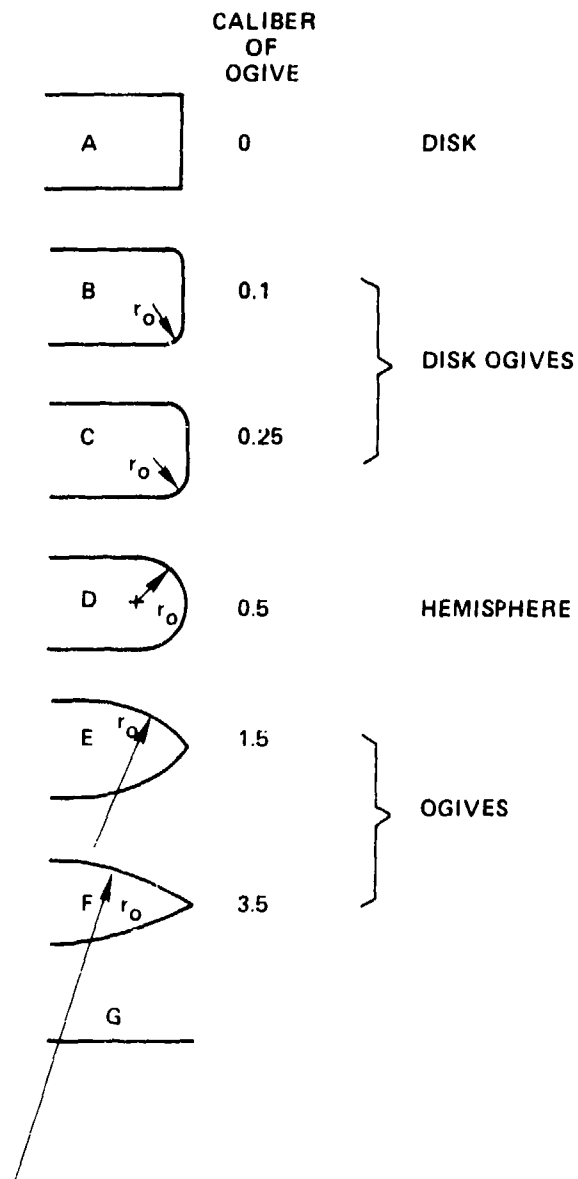
FIG. 2-21 OGIVE AND DISK-OGIVE FAMILIES
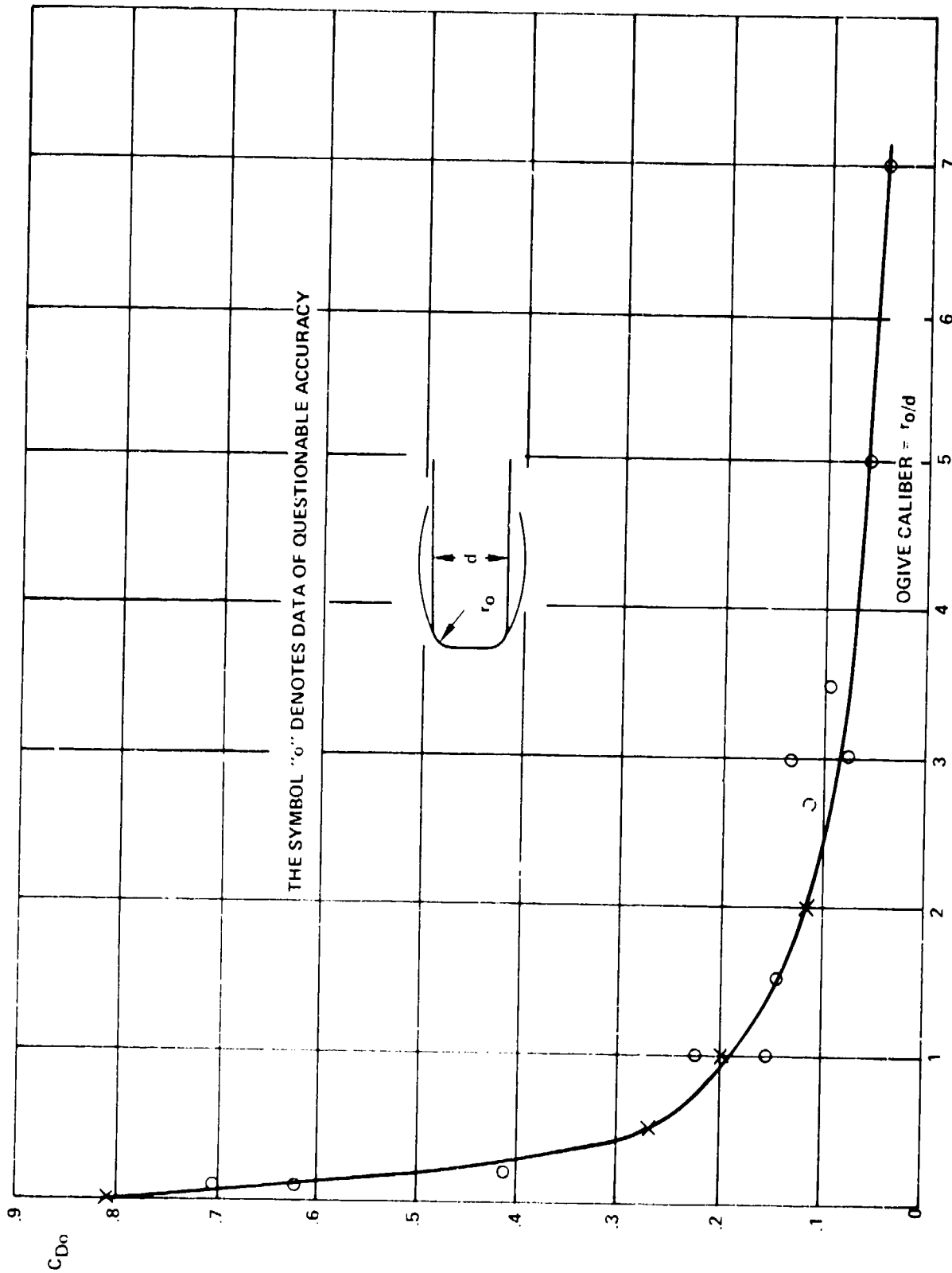
FIG. 2-22 CAVITY-RUNNING DRAG OF DISK OGIVES
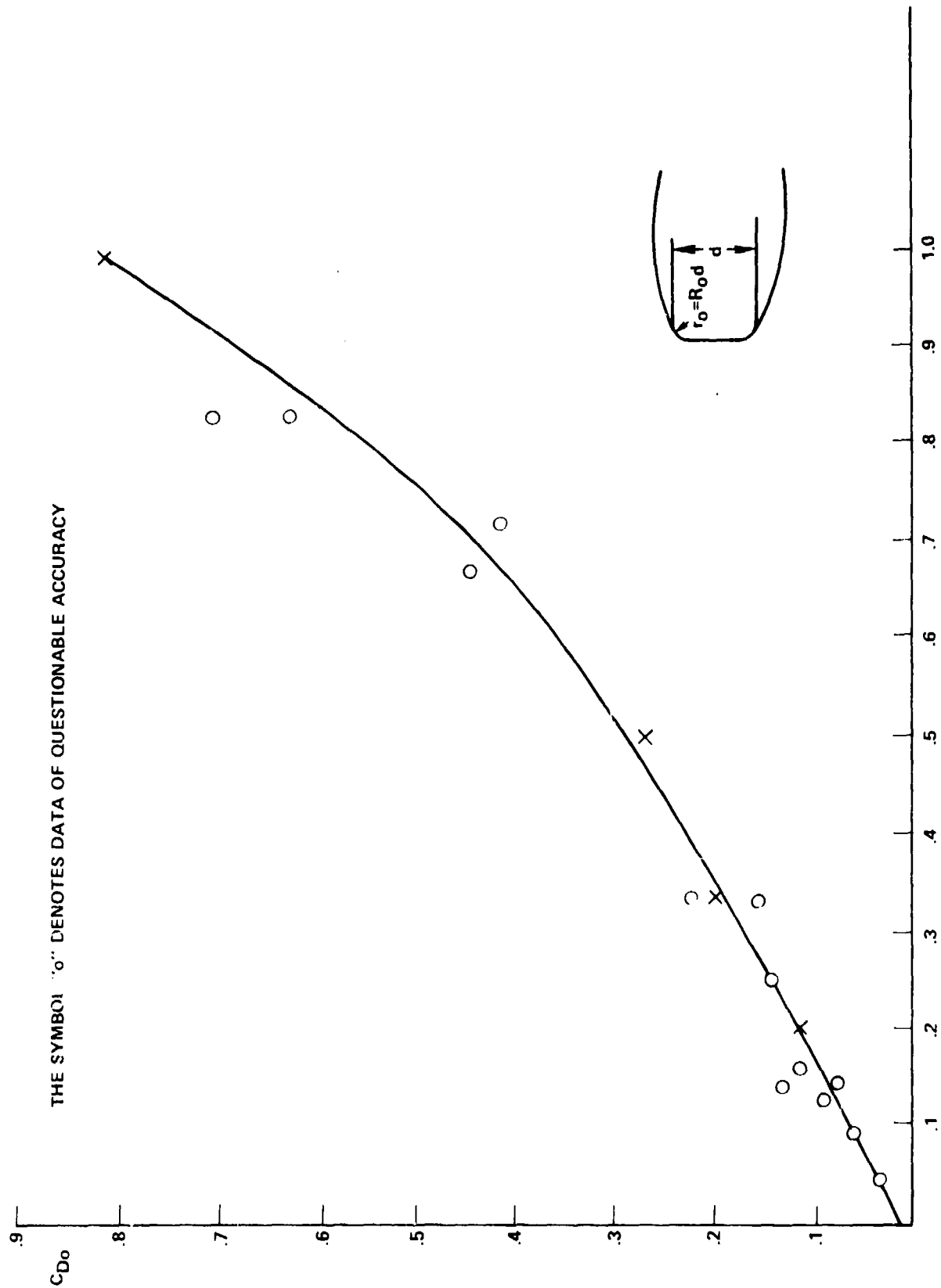
FIG. 2-23 CAVITY-RUNNING DRAG OF DISK OGIVES PLOTTED AGAINST PARAMETER $Q = 1/(1+2R_o) = 1/(1+2r_o/d)$
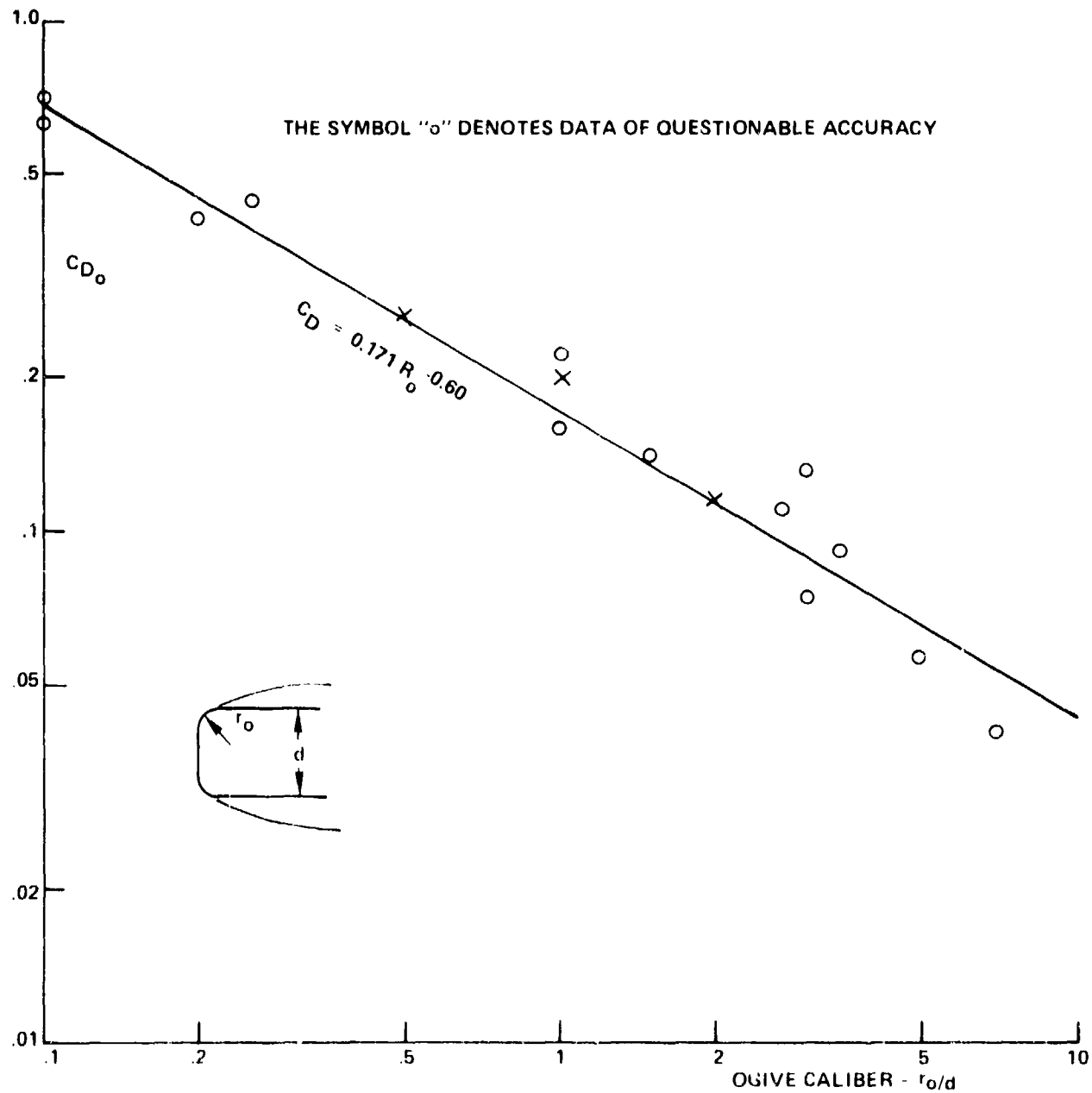
FIG. 2-24 CAVITY RUNNING DRAG OF DISK OGIVES LOGARITHMIC PLOT
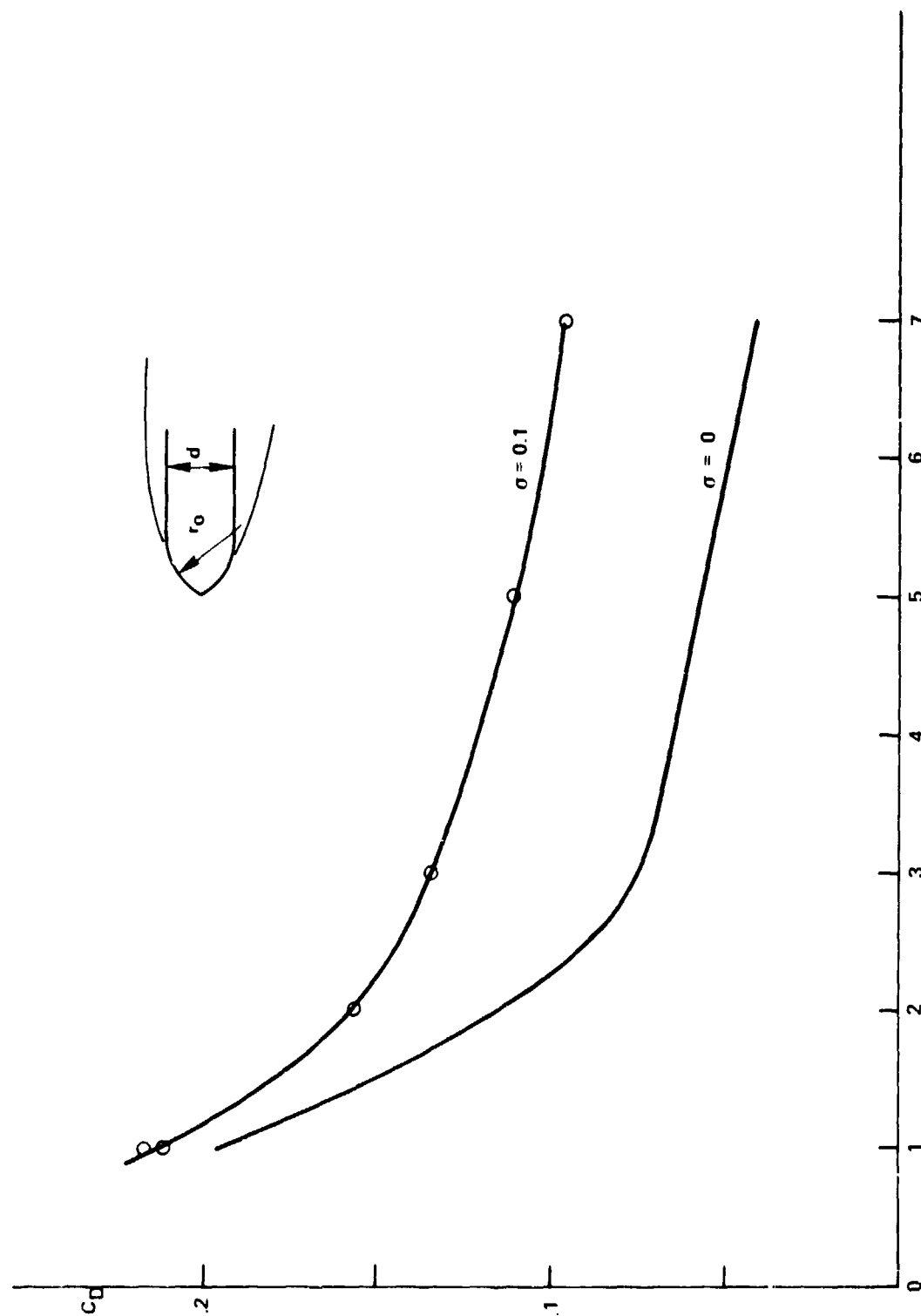
FIG. 2-25 CAVITY-RUNNING DRAG OF OGIVES

C_{Do}

○ EXPERIMENT FROM REF (2·36)
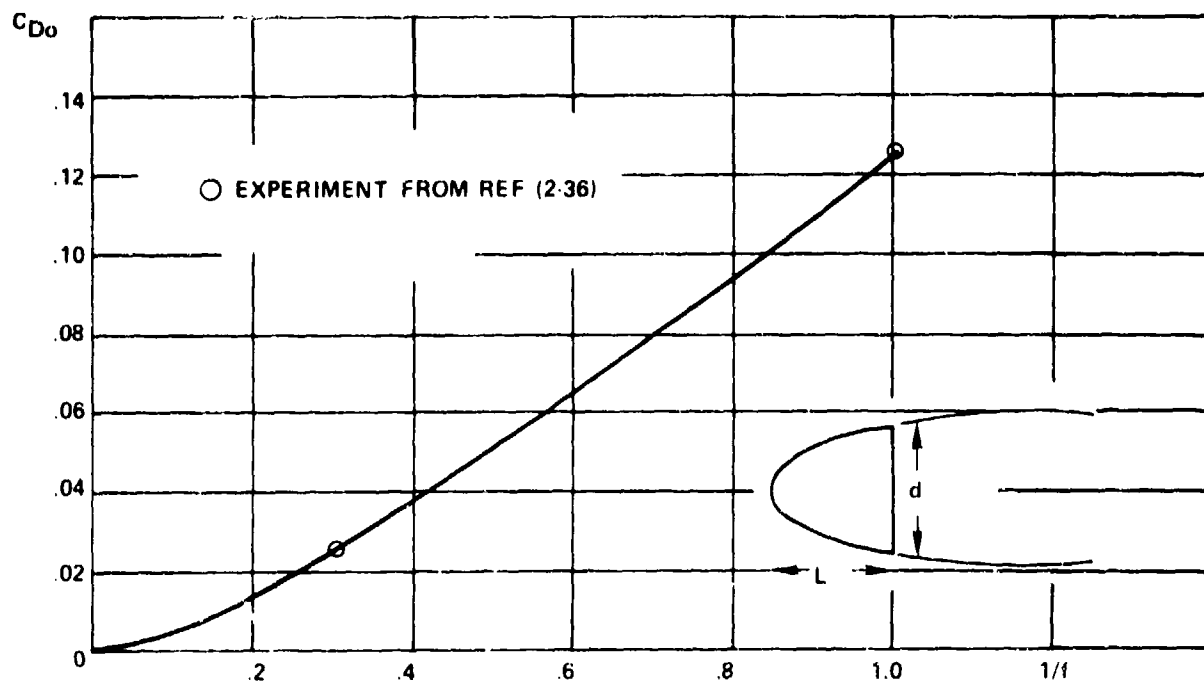
FIG. 2·26 DRAG OF CAVITY-RUNNING PARABOLOIDS OF
VARIOUS FINENESS RATIOS, f = L/d

$\frac{d\,C_D}{d\,\sigma}$

C_{Do}

AXIS RATIO OF ELLIPSE a/b
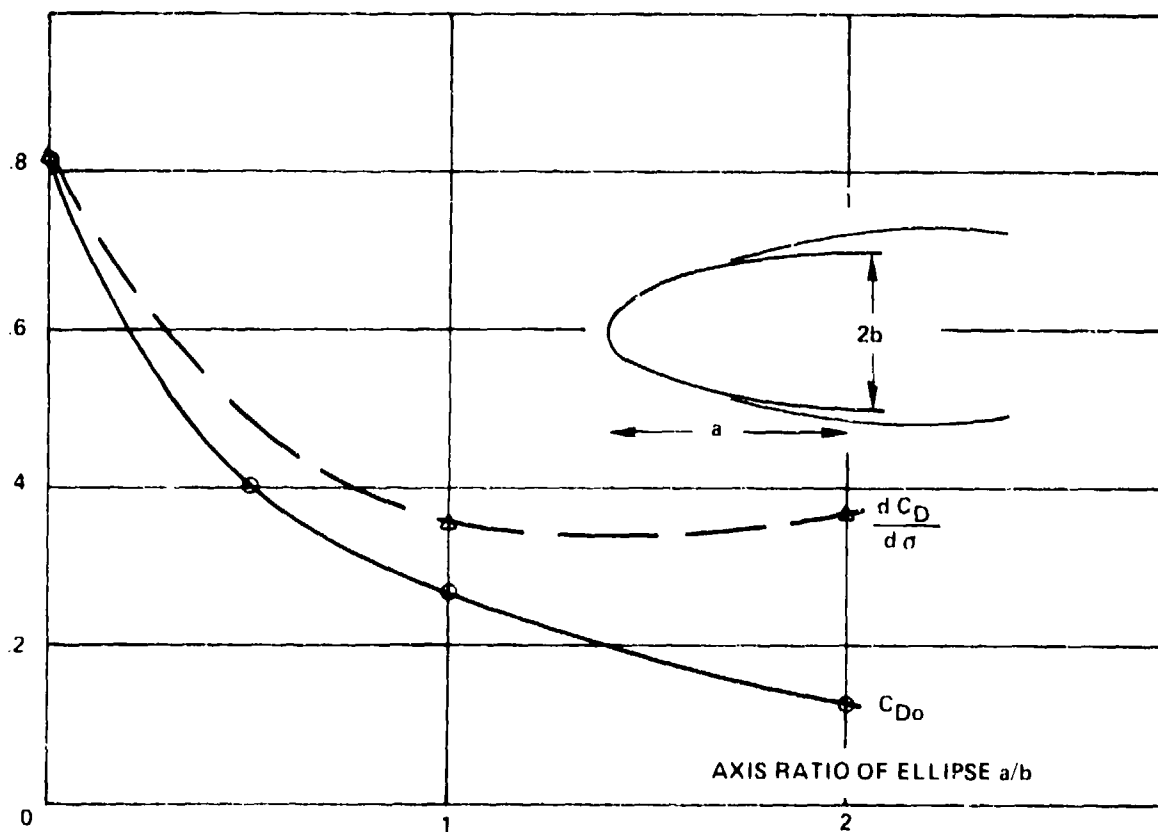
FIG 2 27 CAVITY RUNNING ELLIPSOIDS OF VARIOUS AXIS RATIOS
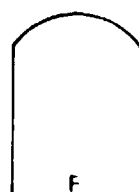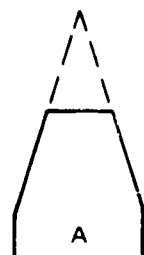
FIG 2 28 MORE COMPLICATED NOSE SHAPES
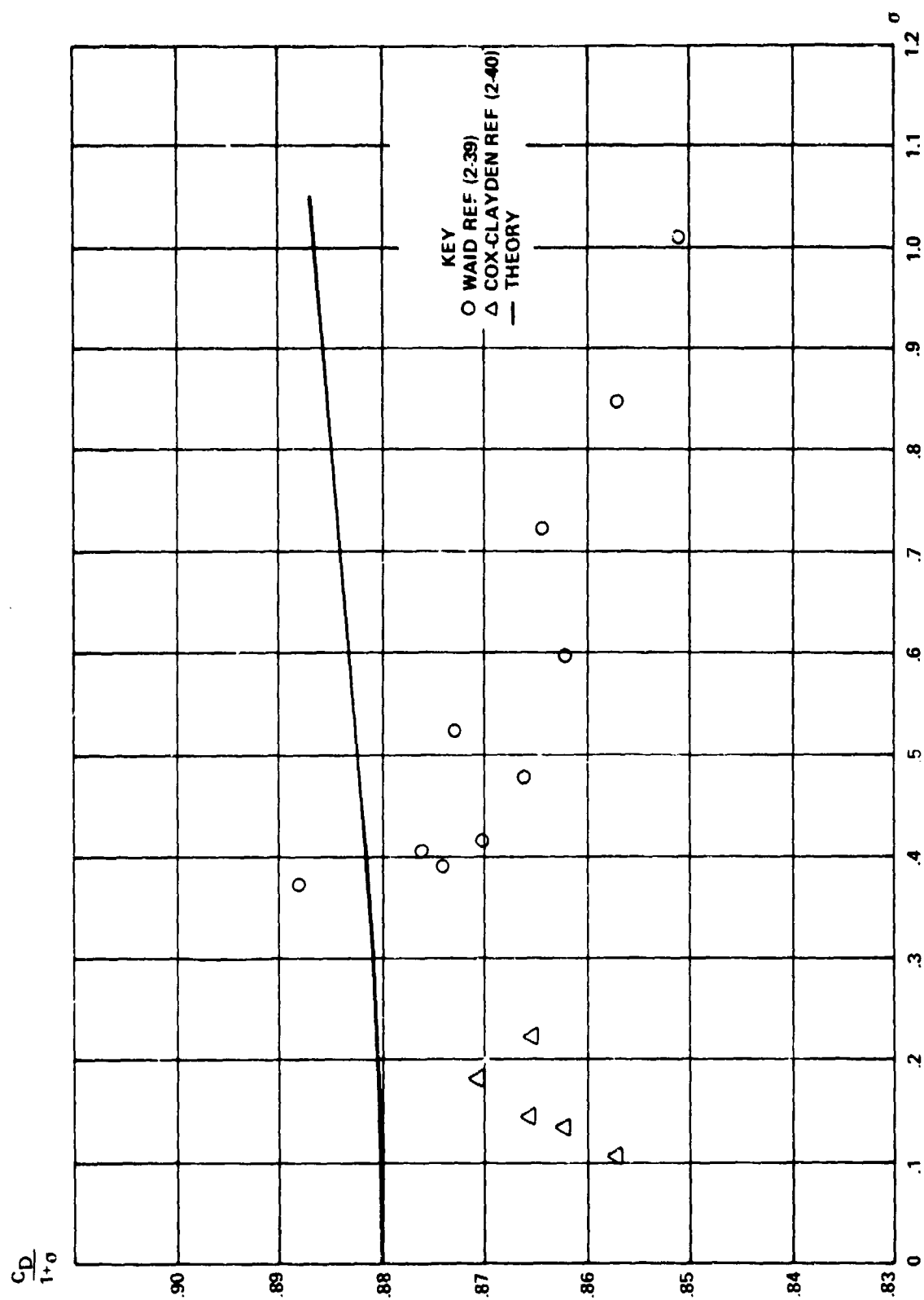
FIG. 2-29 DRAG OF FLAT PLATE WITH CAVITY
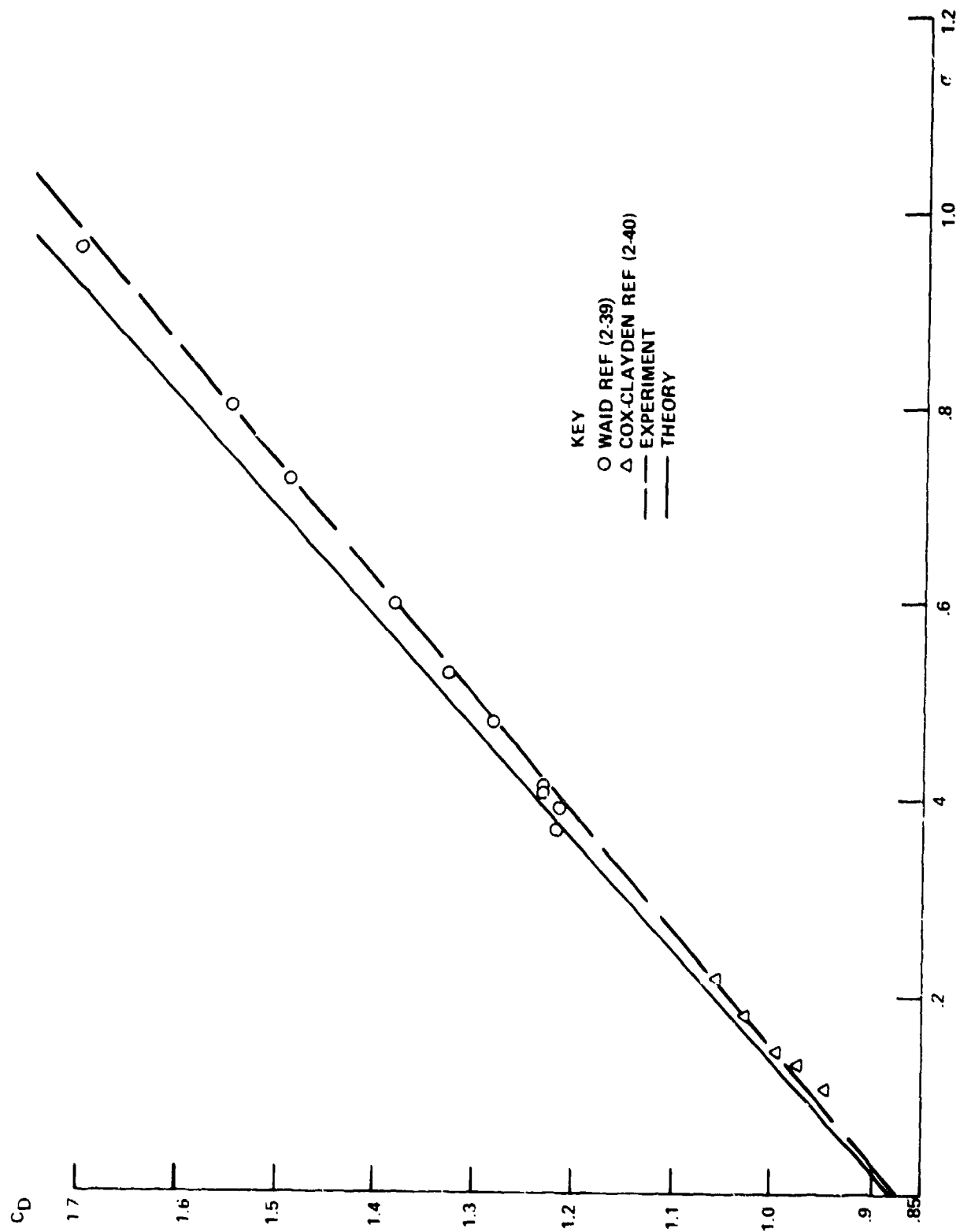
FIG. 2-30 DRAG OF FLAT PLATE WITH CAVITY

KEY

O WAID REF (2-39)
△ COX-CLAYDEN REF (2-40)
—— EXPERIMENT
—— THEORY
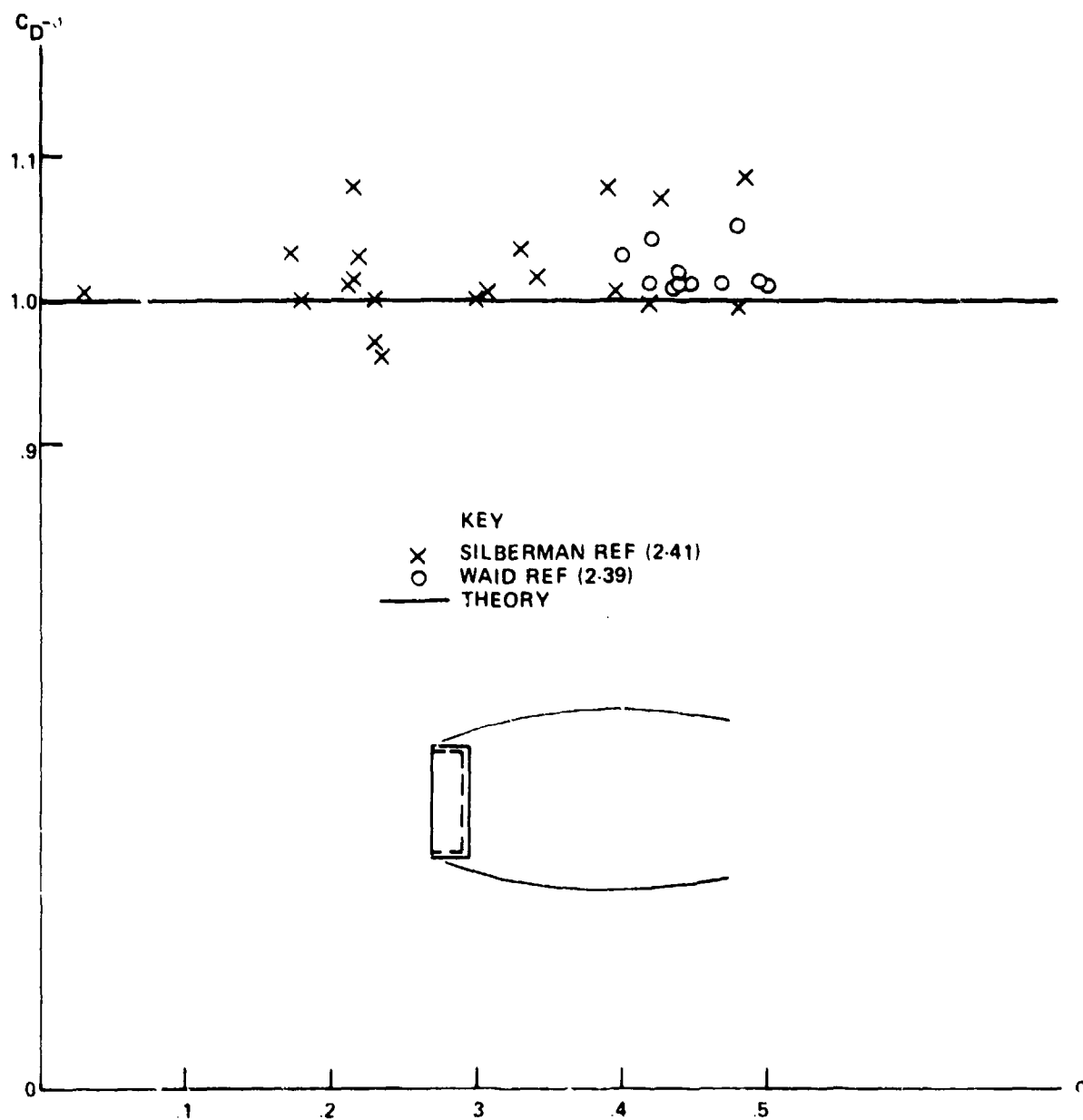
FIG. 2 31 DRAG OF STAGNATION CHANNEL WITH CAVITY
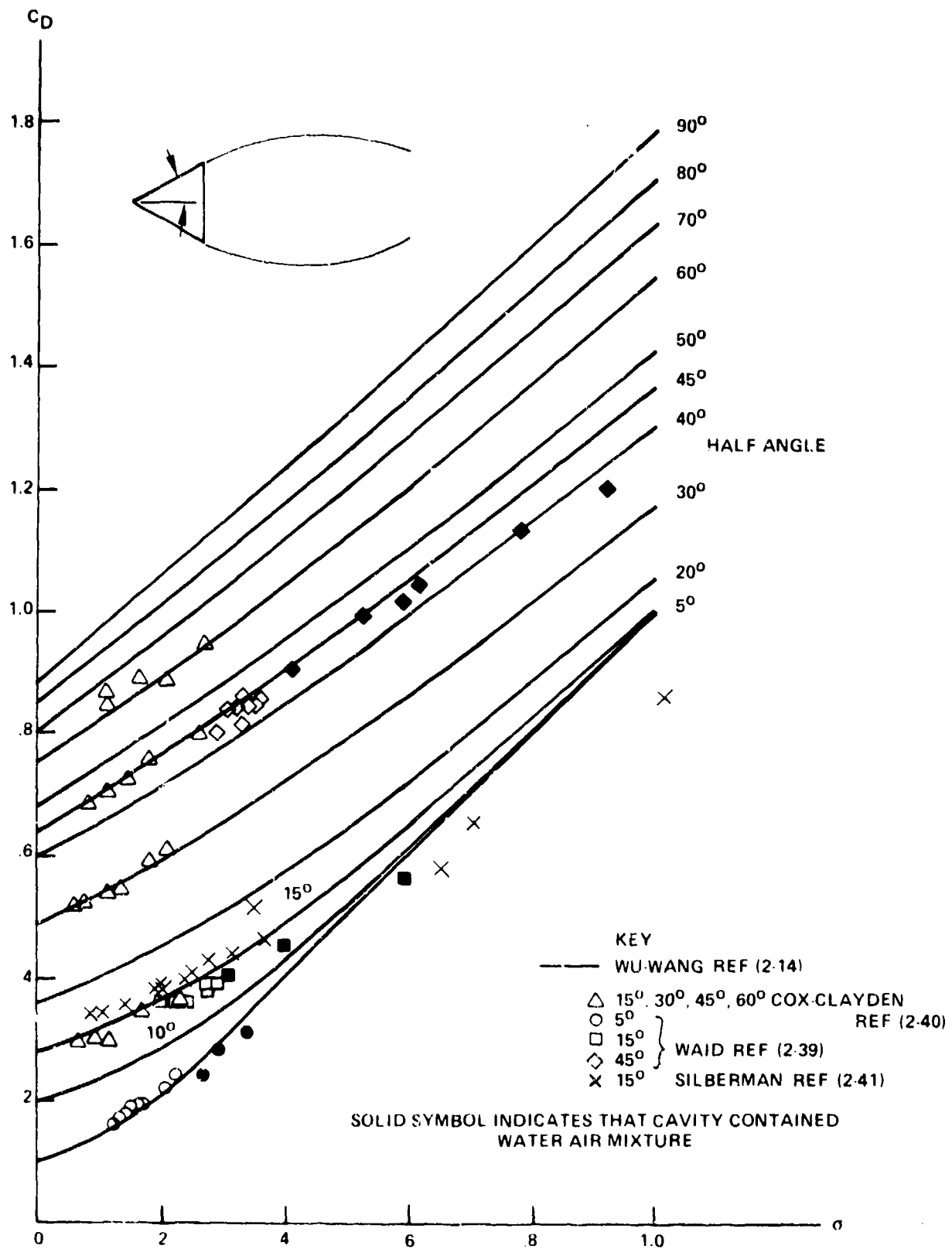
FIG 2.32 DRAG OF CAVITY RUNNING WEDGES

KEY

—— WU-WANG REF (2-14)

△ 15°, 30°, 45°, 60° COX-CLAYDEN
○ 5° } REF (2-40)
□ 15° } WAID REF (2-39)
◇ 45°
✕ 15° SILBERMAN REF (2-41)

SOLID SYMBOL INDICATES THAT CAVITY CONTAINED
WATER AIR MIXTURE
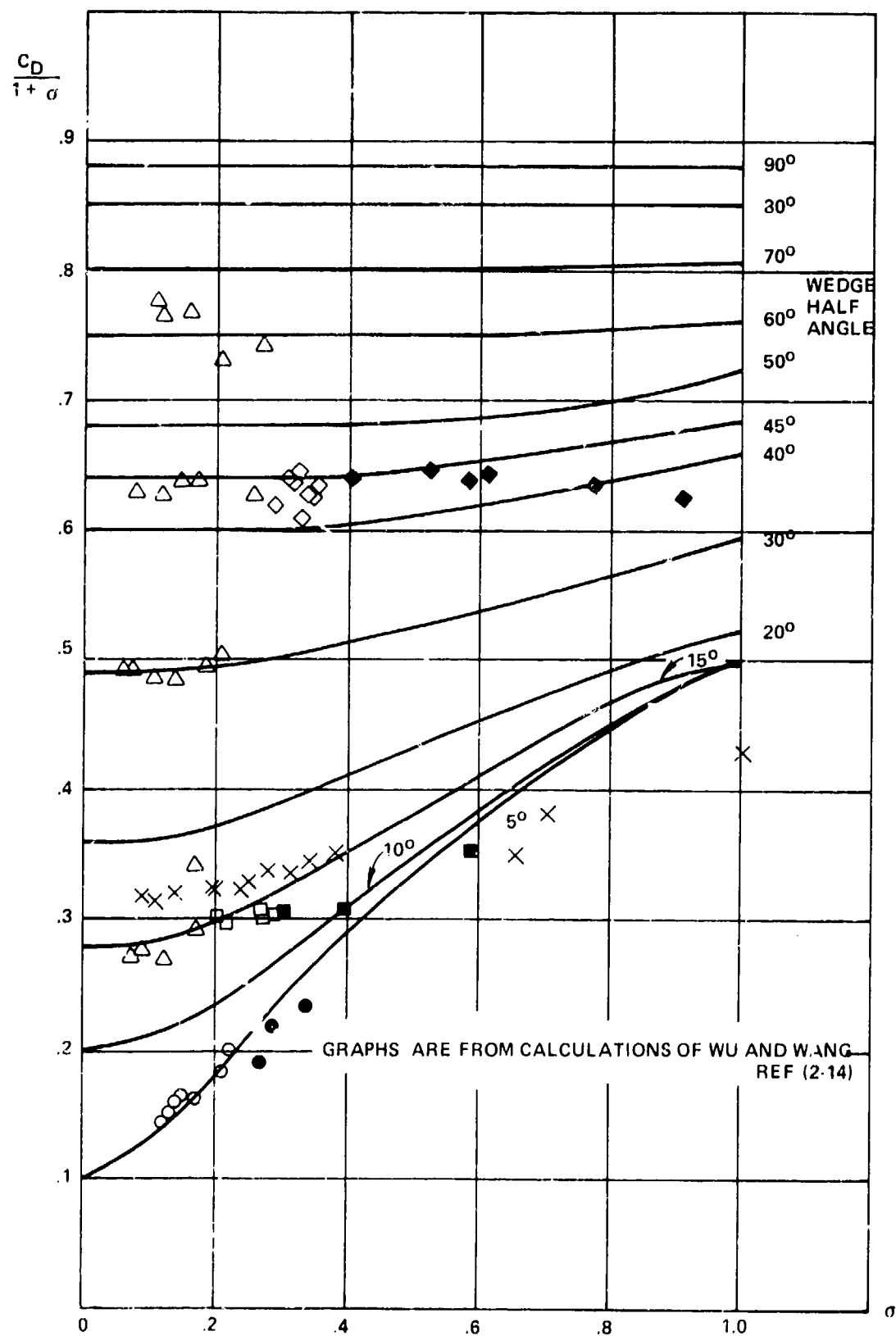
FIG. 2.33 DRAG OF CAVITY RUNNING WEDGES
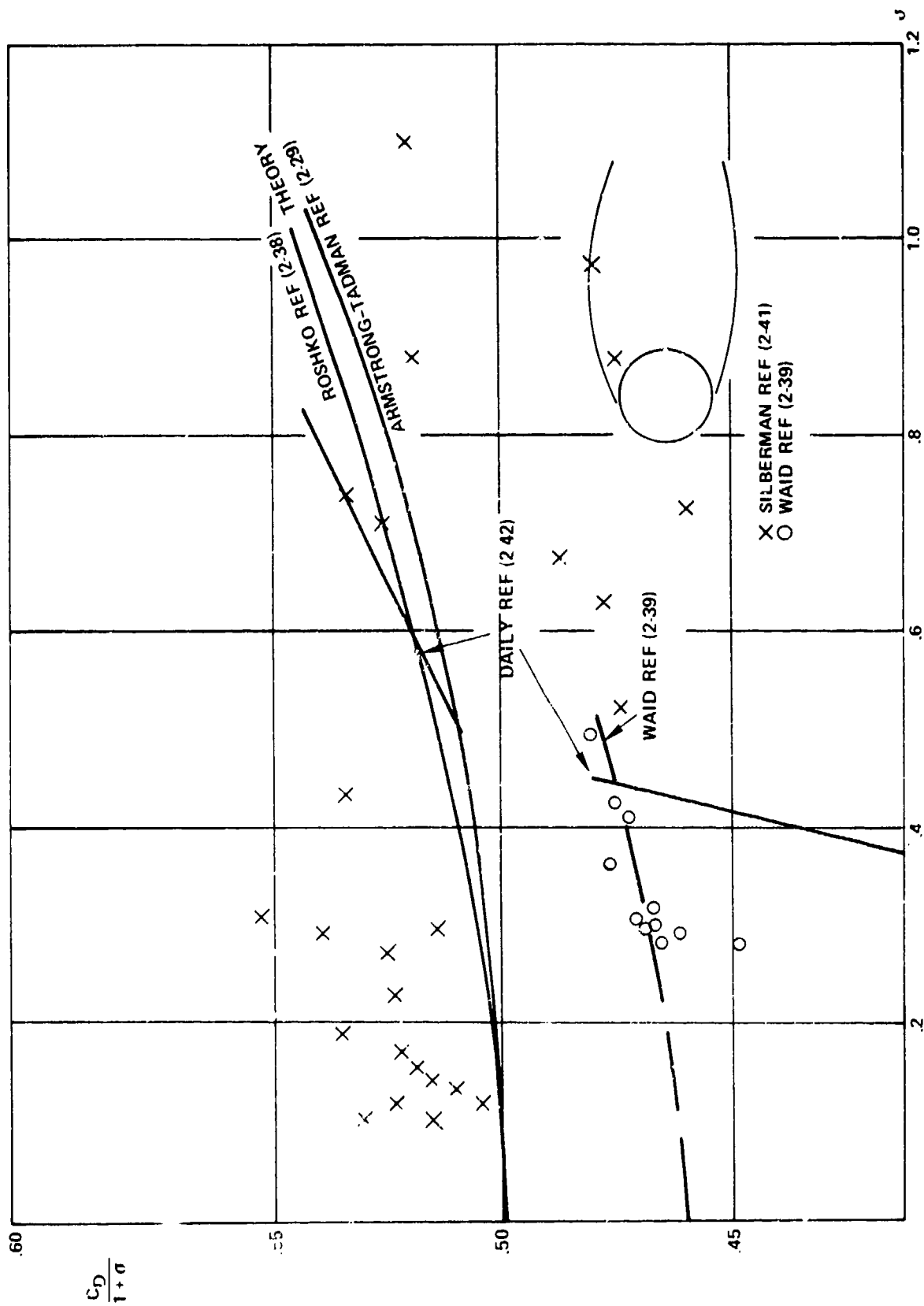
FIG. 2-34 DRAG OF CIRCULAR CYLINDER WITH CAVITY
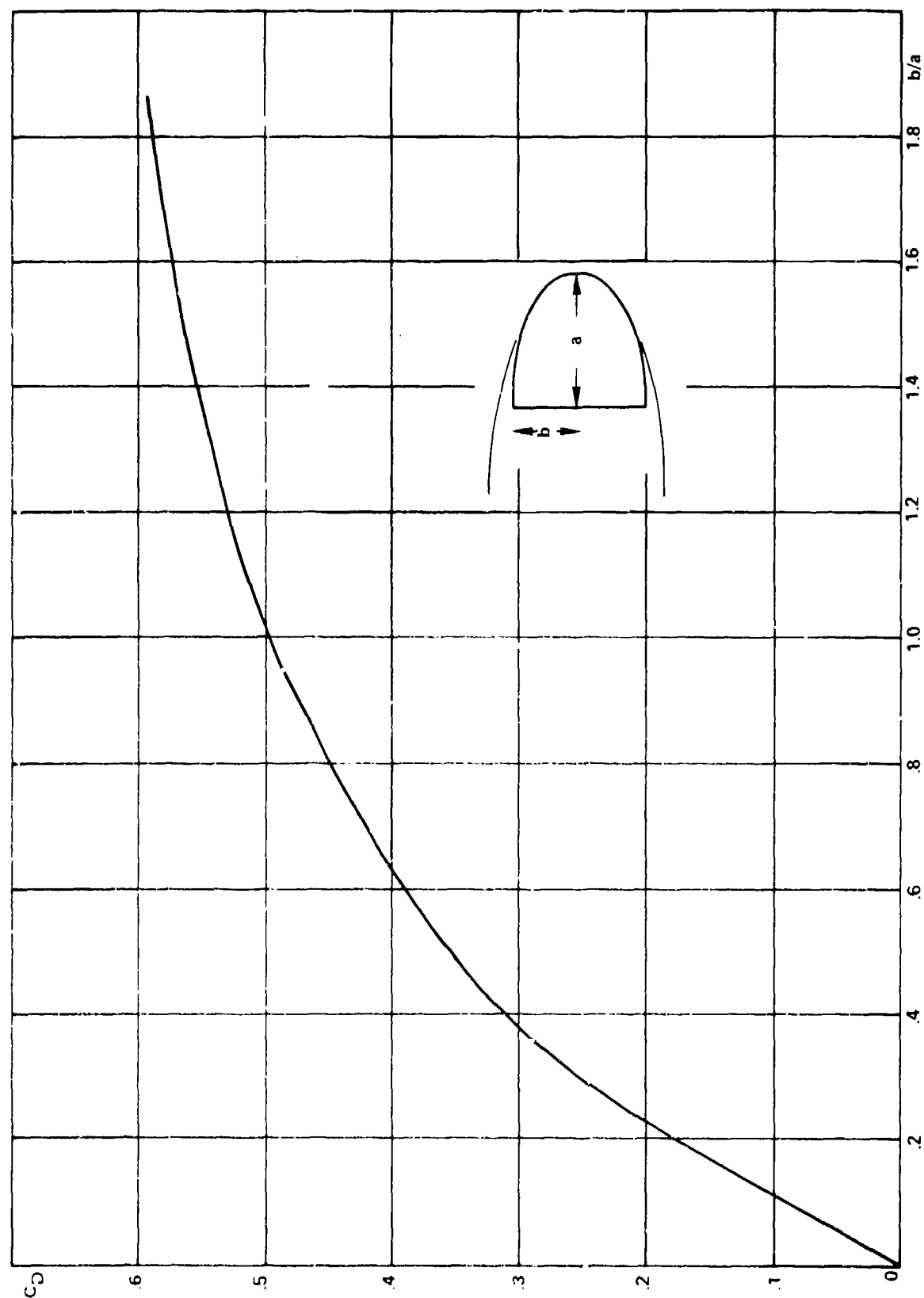
FIG. 2-35 DRAG OF ELLIPTIC CYLINDERS WITH CAVITIES REF (2-43,5)
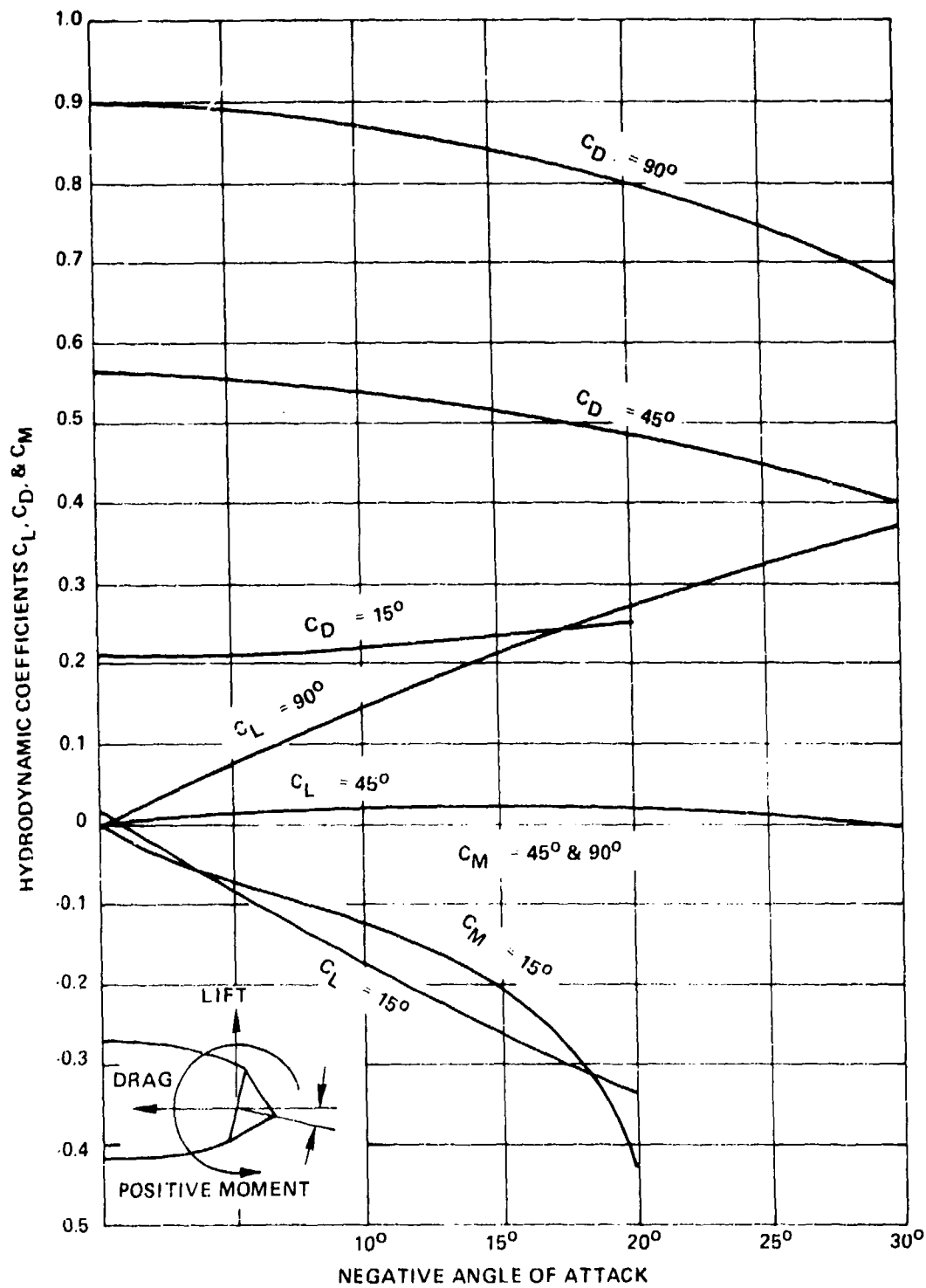
FIG. 2-36 HYDRODYNAMIC COEFFICIENTS OF CONES AT
ANGLES OF ATTACK (= 0.1) (AFTER KICENIUK REF (2-25)
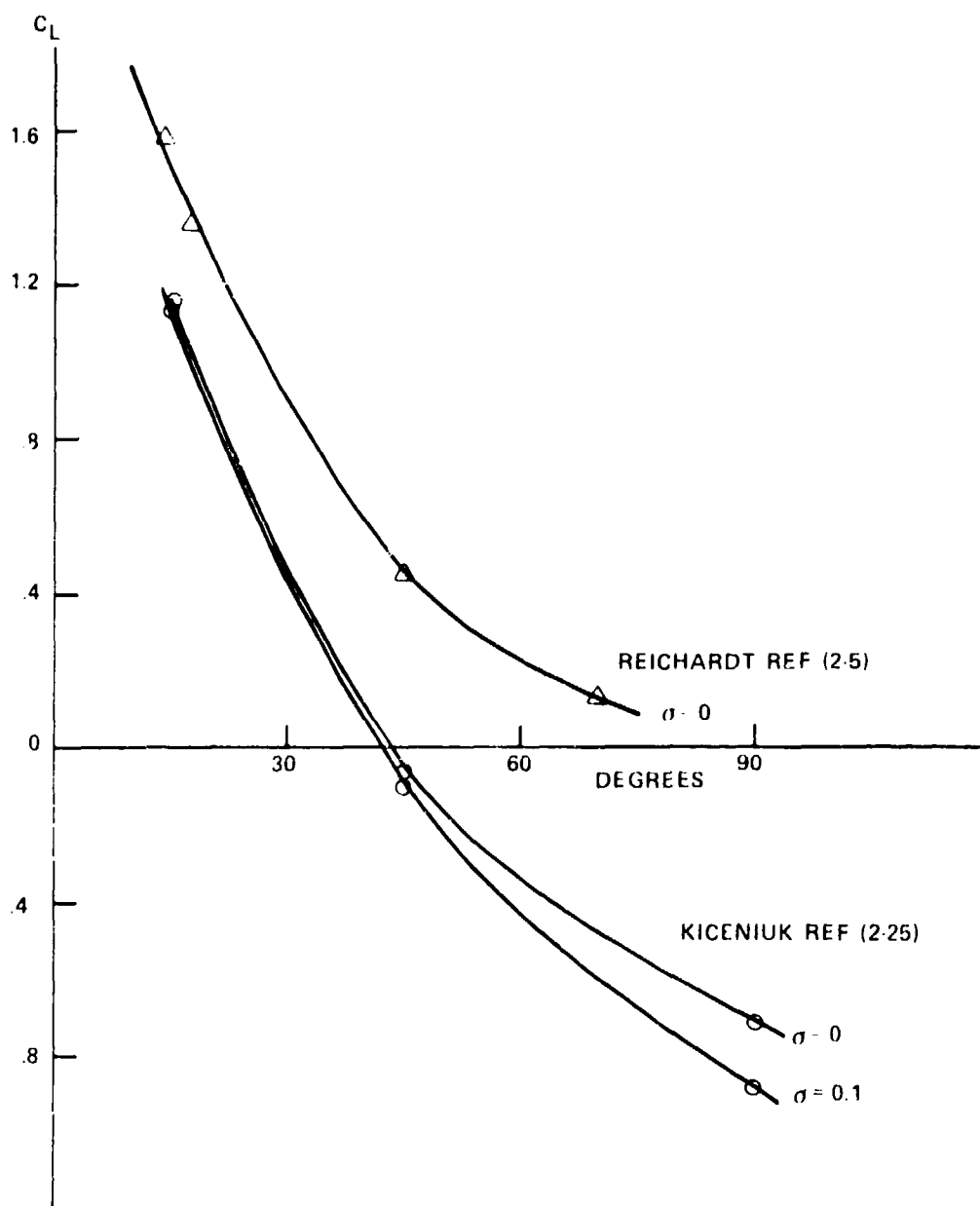
FIG. 2 37 LIFT COEFFICIENT DERIVATIVE FOR CAVITY-RUNNING CONES
(AND DISKS)
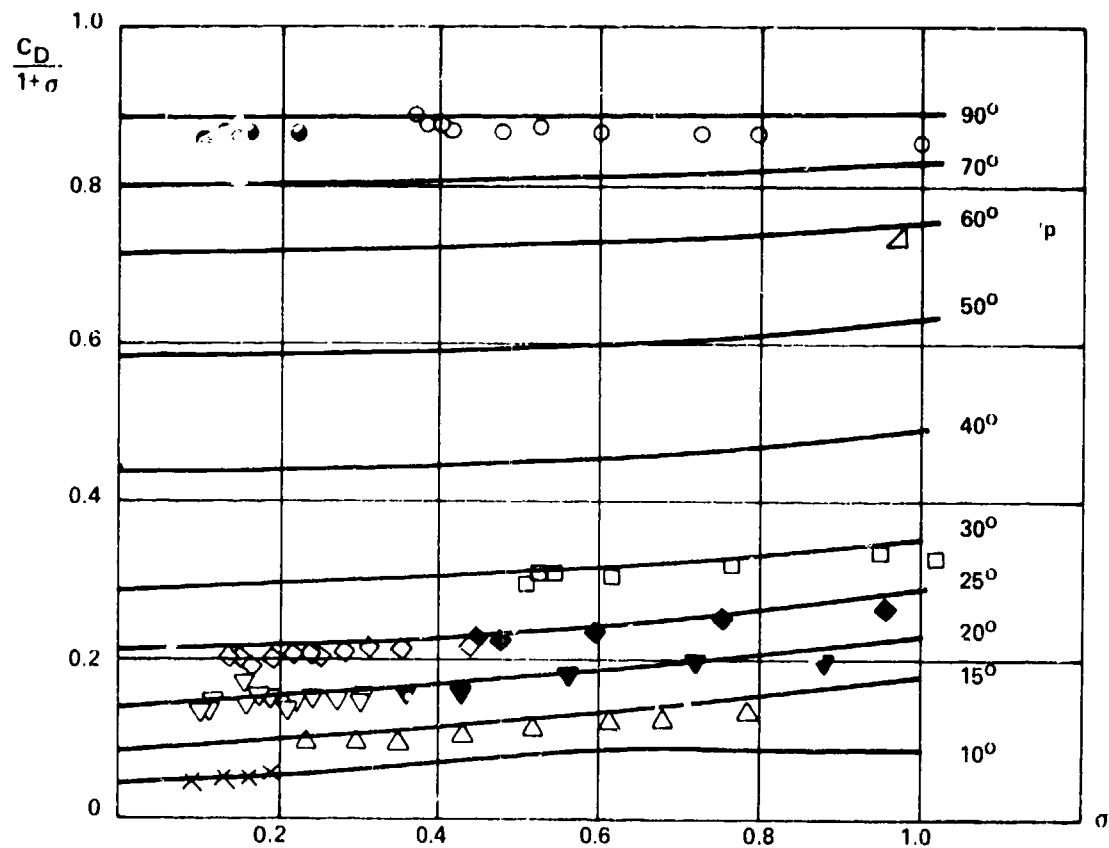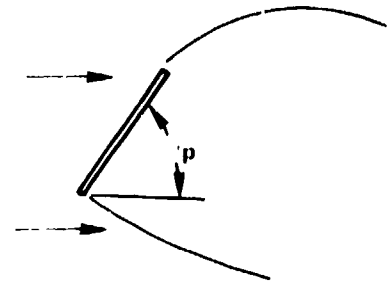
FIG. 2 38 DRAG COEFFICIENT OF FLAT PLATE AT ANGLES OF ATTACK
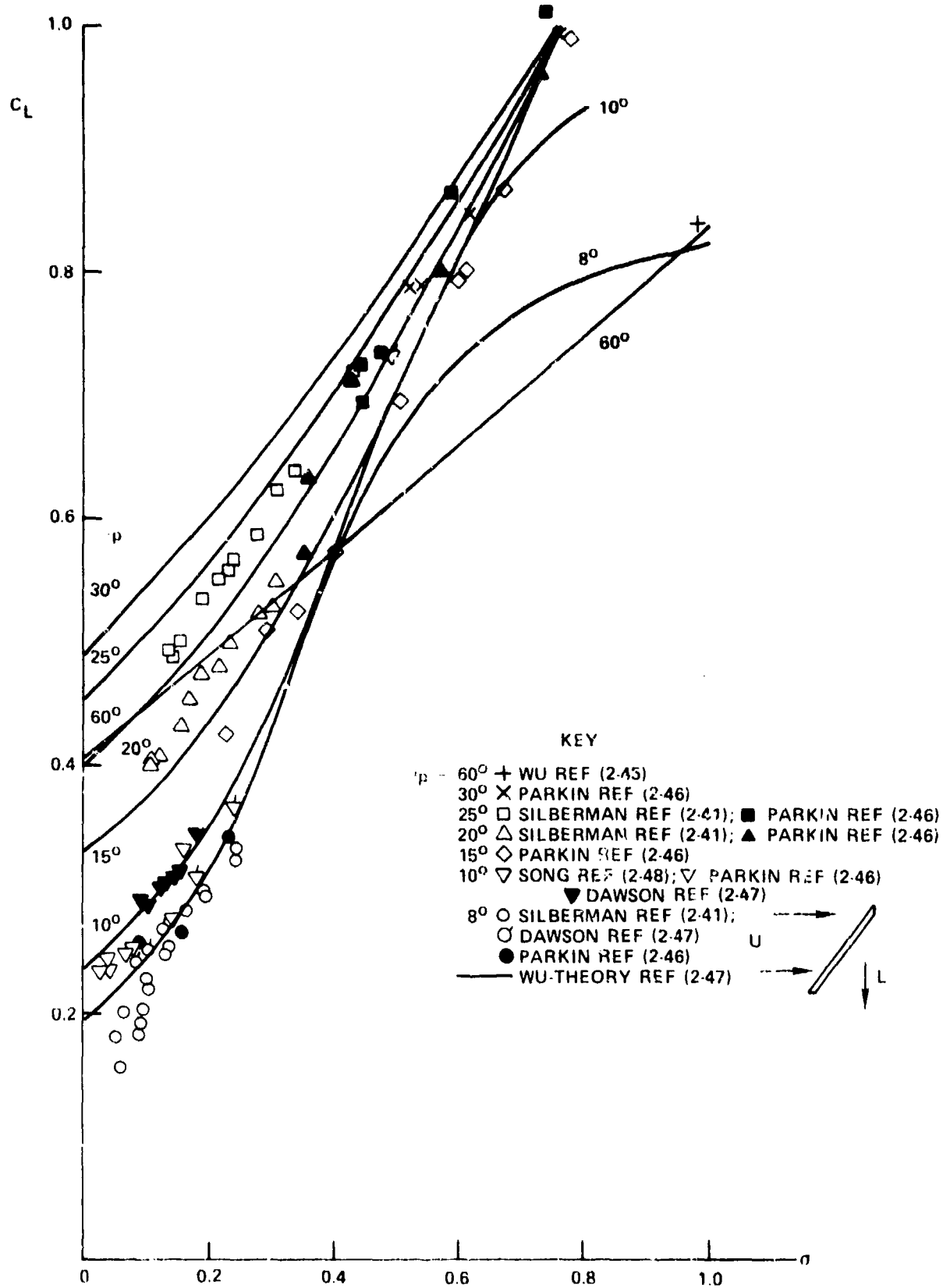
FIG 2 39 LIFT COEFFICIENT OF FLAT PLATE AT ANGLES OF ATTACK
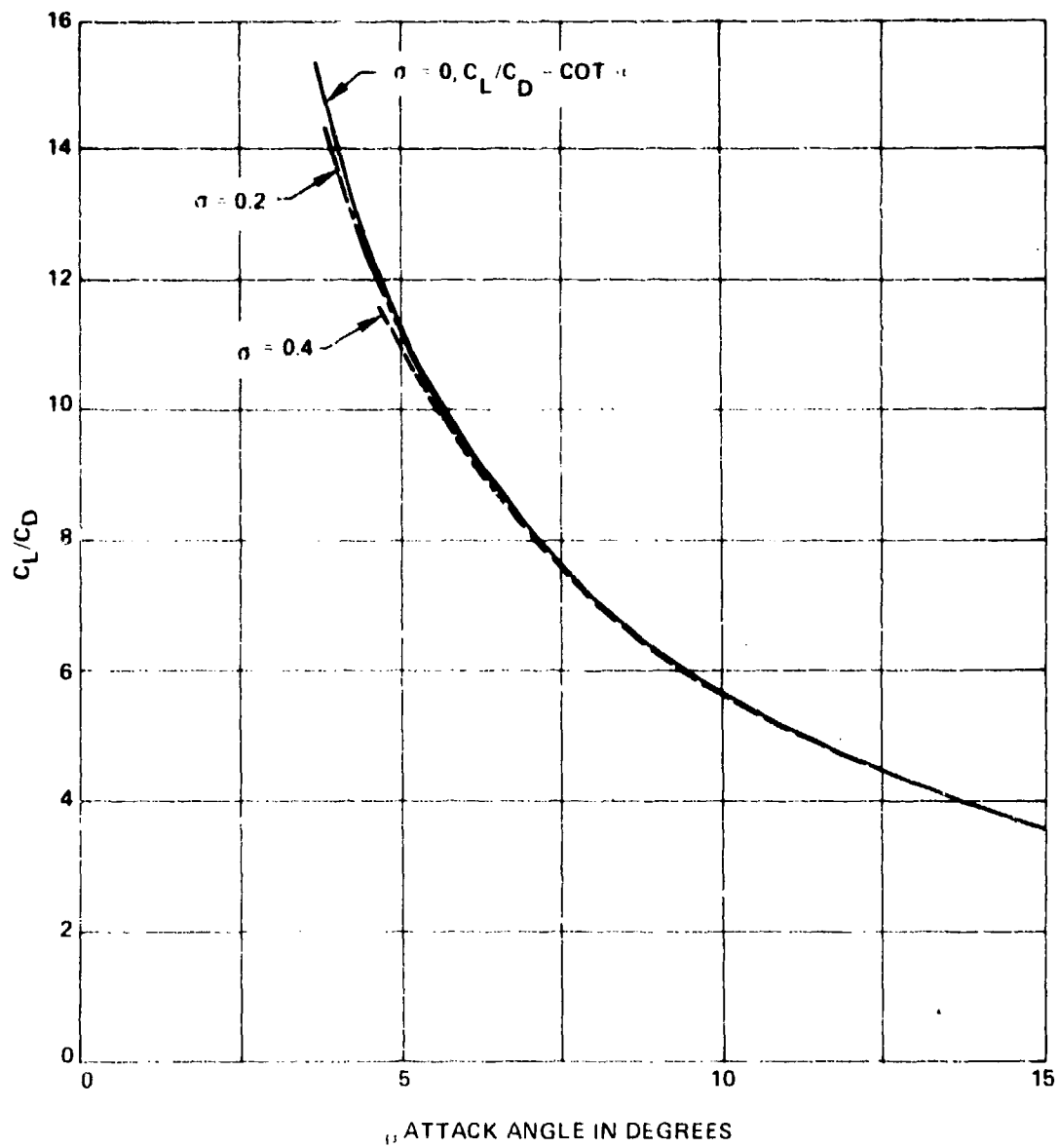
FIG. 2·40 VALUES OF C_L/C_D FOR THE FLAT PLATE FROM REF (2·45)
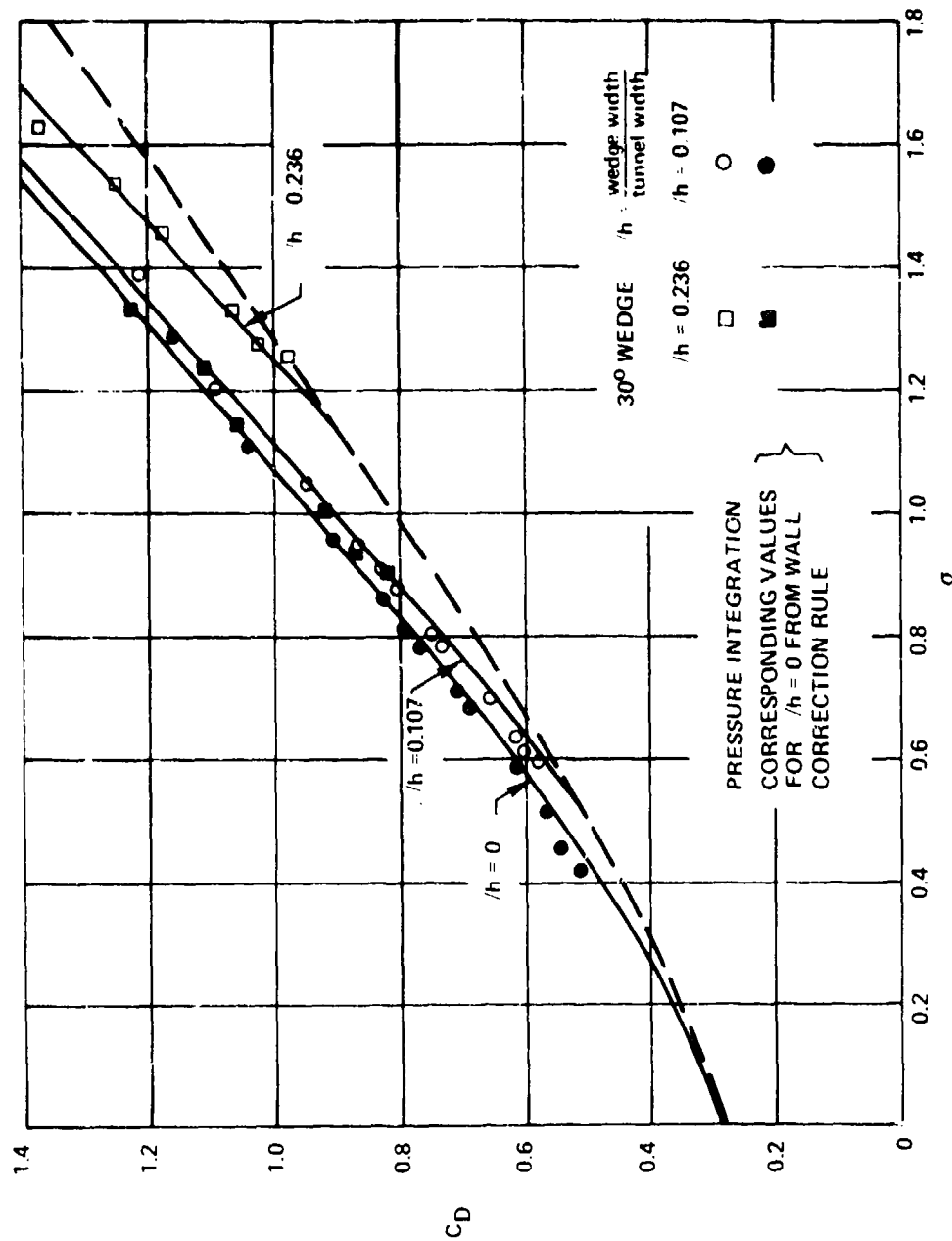
FIG. 2-41 EFFECT OF TUNNEL WALLS ON NOSE FORCES FOR 15° HALF-ANGLE WEDGE (ADAPTED REF (2-54)
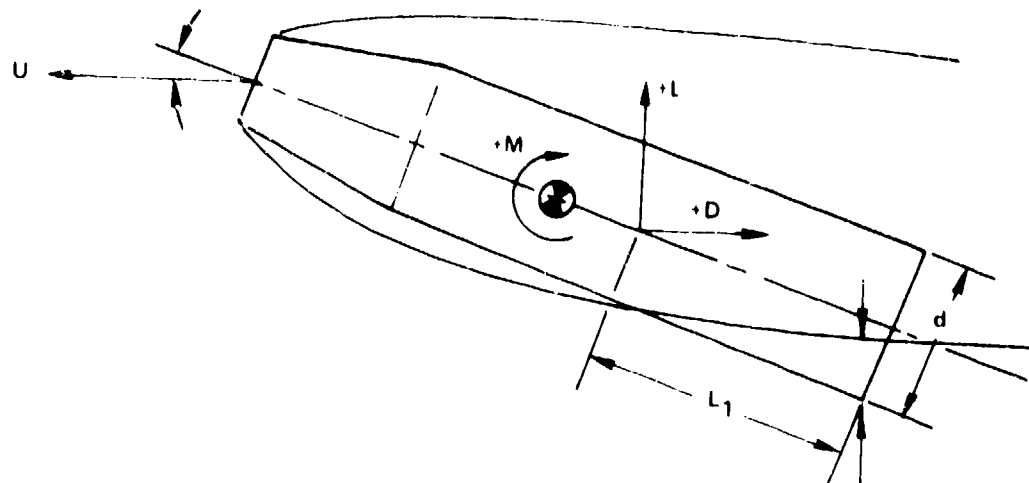
FIG. 2 42 TAIL IMMERSION SCHEMATIC
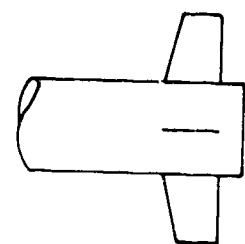
A. FINS
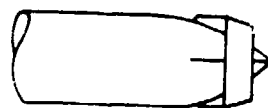
B. FINS AND SHROUD
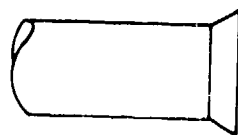
C. CONE TAIL

D. RECESSED FLARE

FIG. 2 43 TAIL CONFIGURATIONS
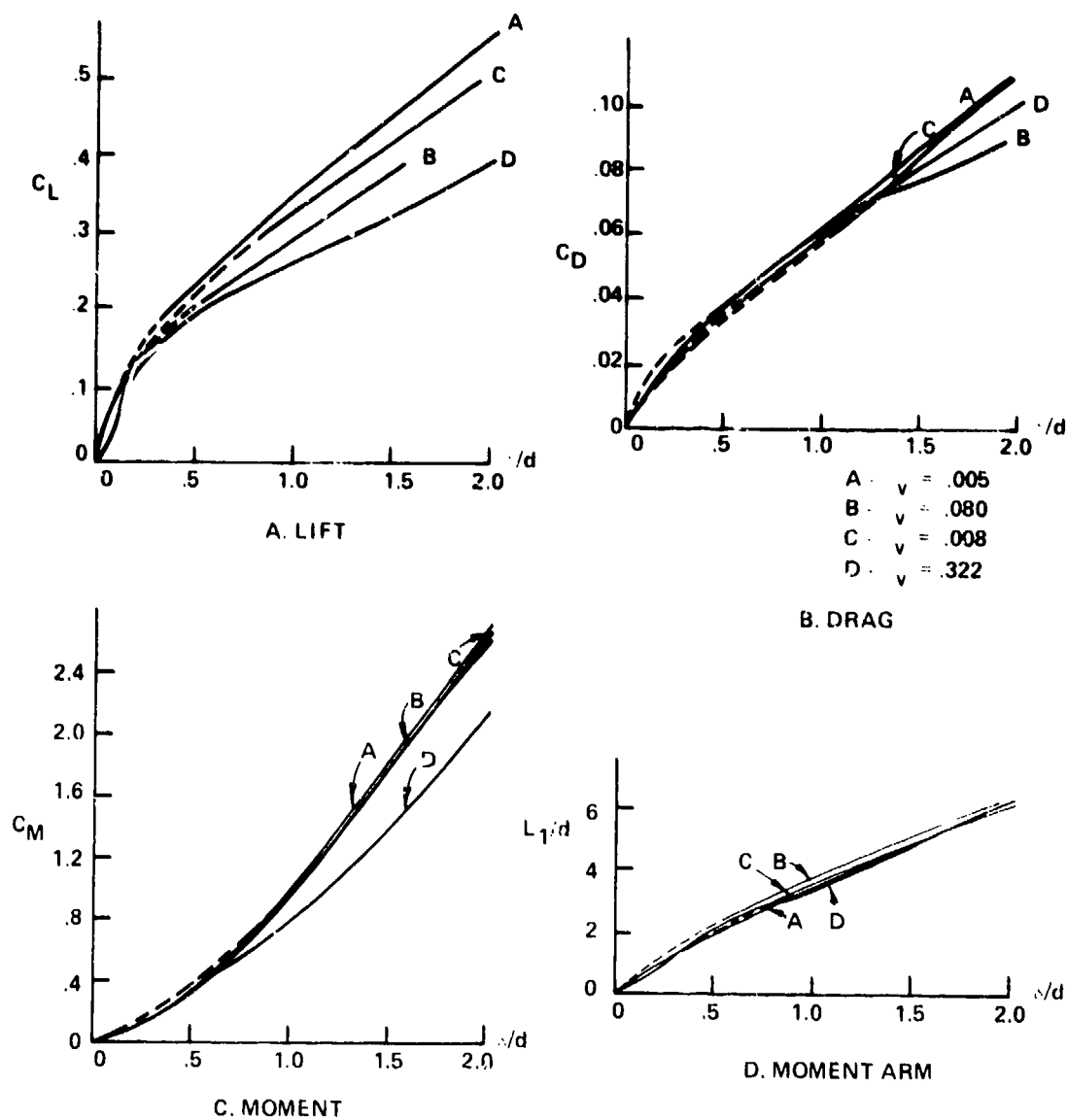
FIG. 2-44 COEFFICIENTS OF CYLINDRICAL AFTERBODY PLANING AT 16-DEGREE ANGLE
OF ATTACK ADAPTED FROM REF (2-57)
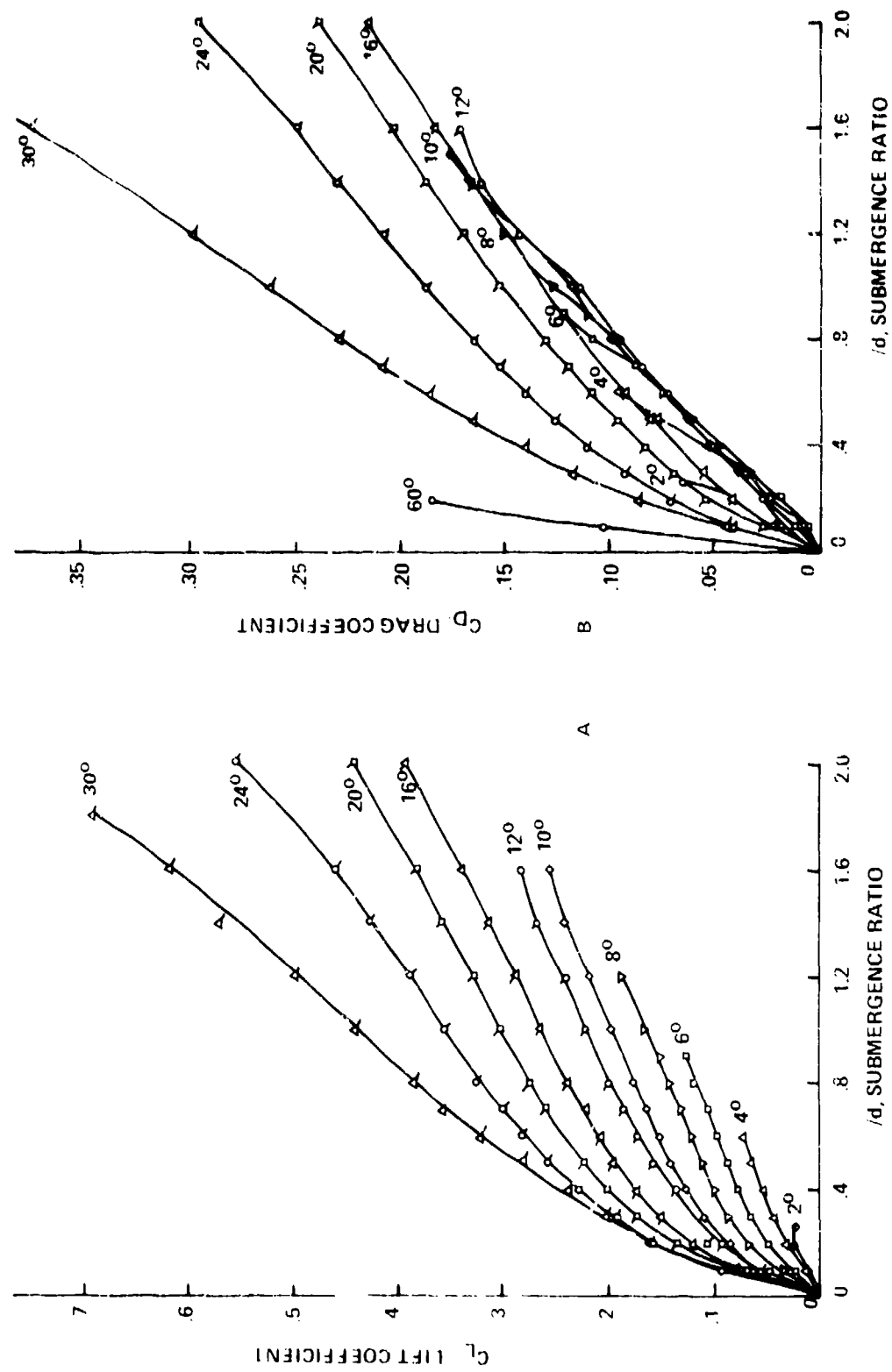
FIG. 2.45 FORCE SYSTEM ON PLANING CYLINDER
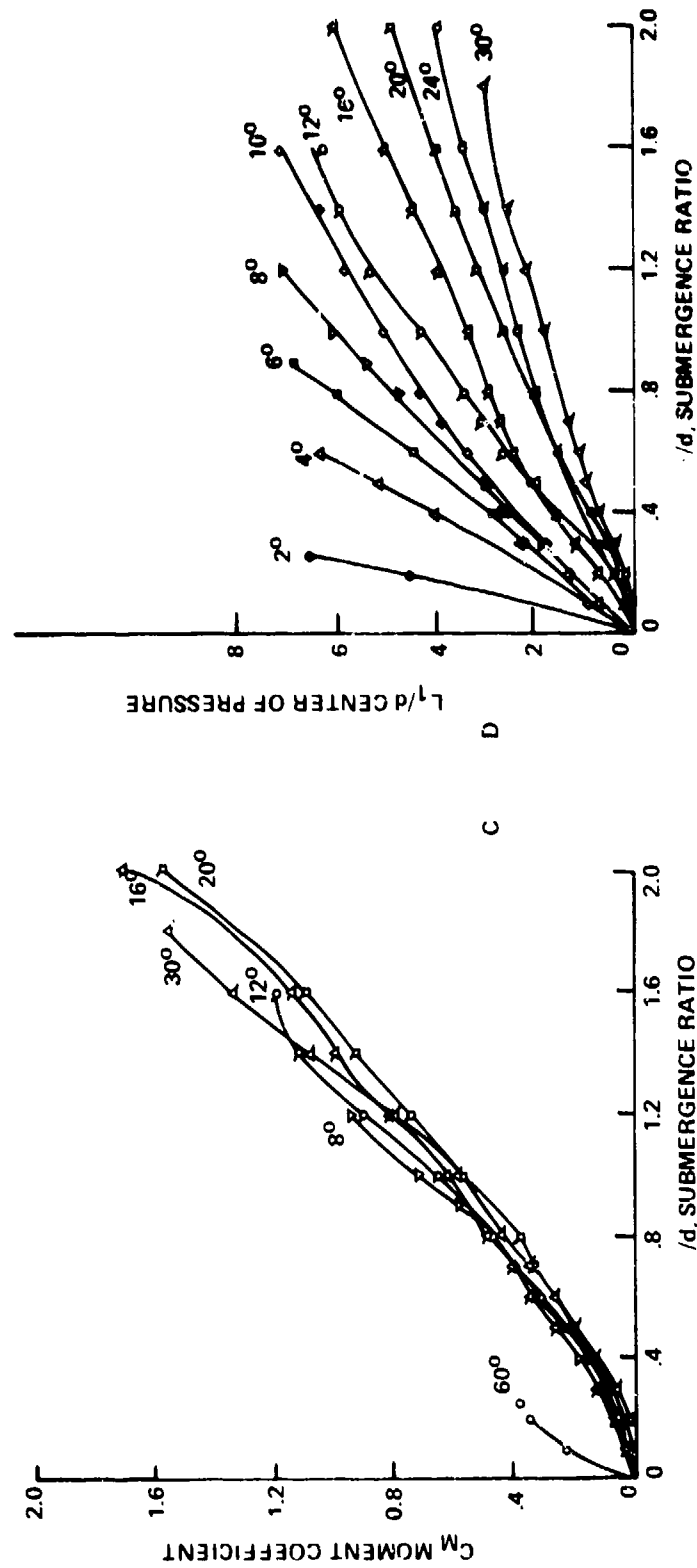
FIG. 2-45 (CONT) FORCE SYSTEM ON PLANING CYLINDER
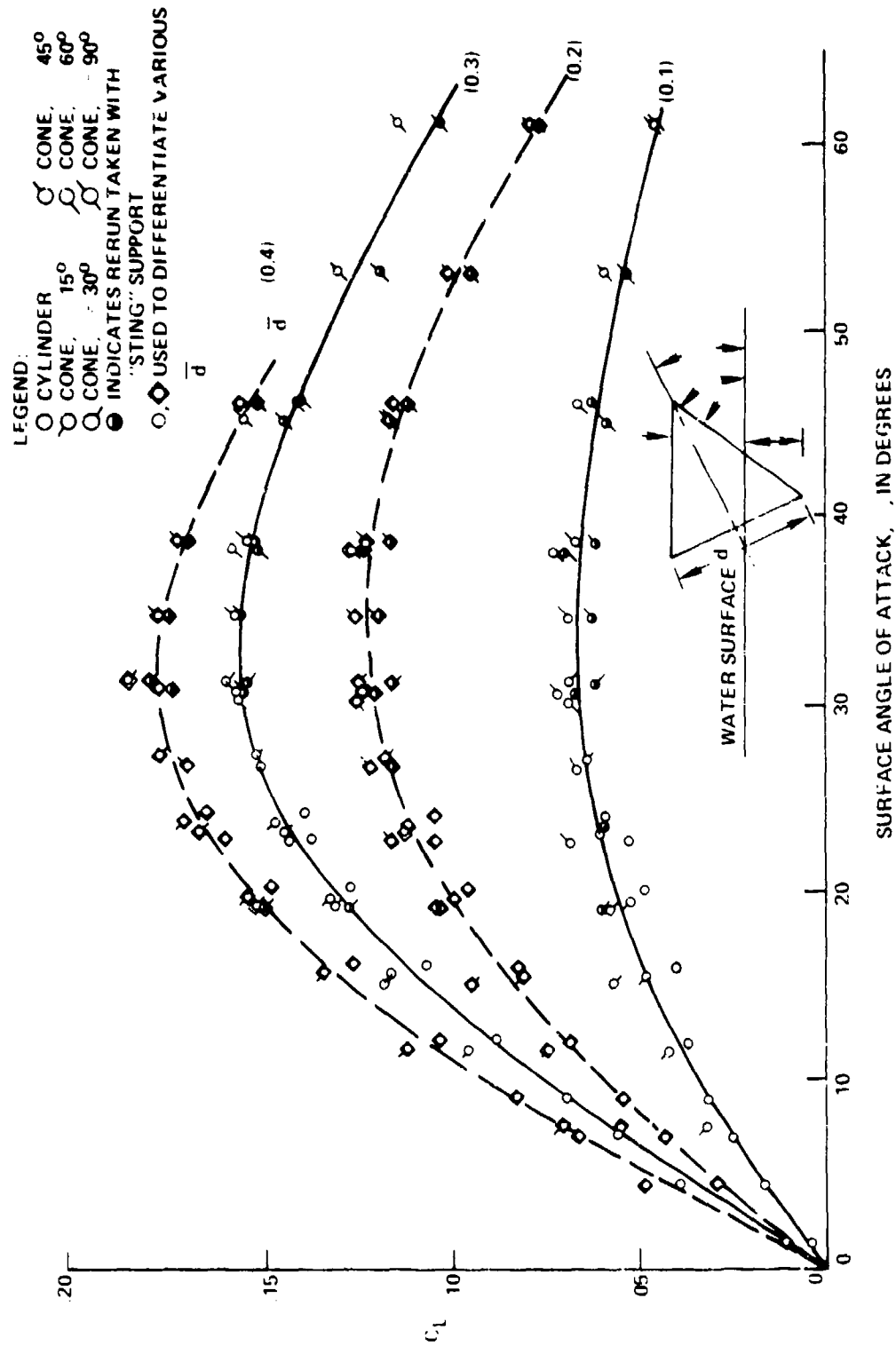
FIG. 2 46 LIFT COEFFICIENT VS. MODEL SURFACE ANGLE OF ATTACK FOR A FAMILY OF 2-IN. BASE DIAMETER CONES FROM REF (2-59)

DEFINITION OF SYMBOLS
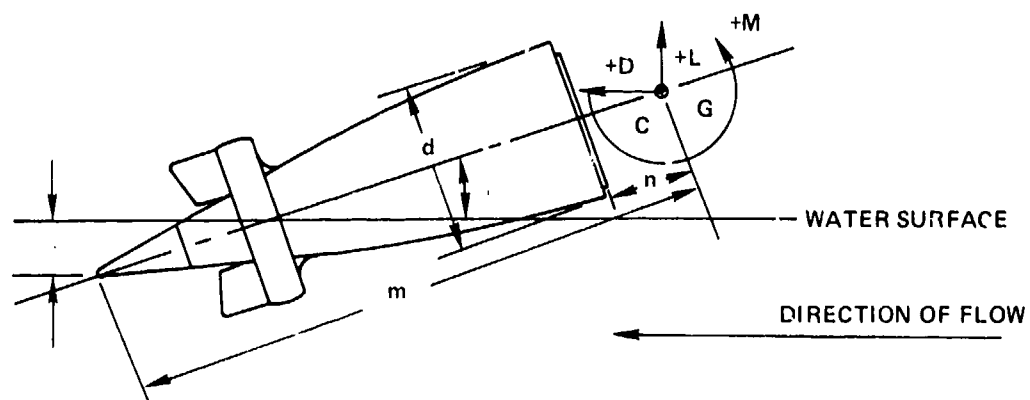
FIG. 2-47 TAIL WITH FINS AND SHROUD REF (2-60)

FIG. 2-48 LIFT COEFFICIENT FOR TORPEDO TAIL REF (2-60)
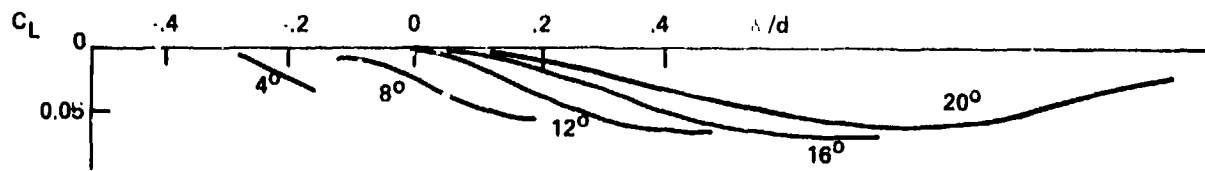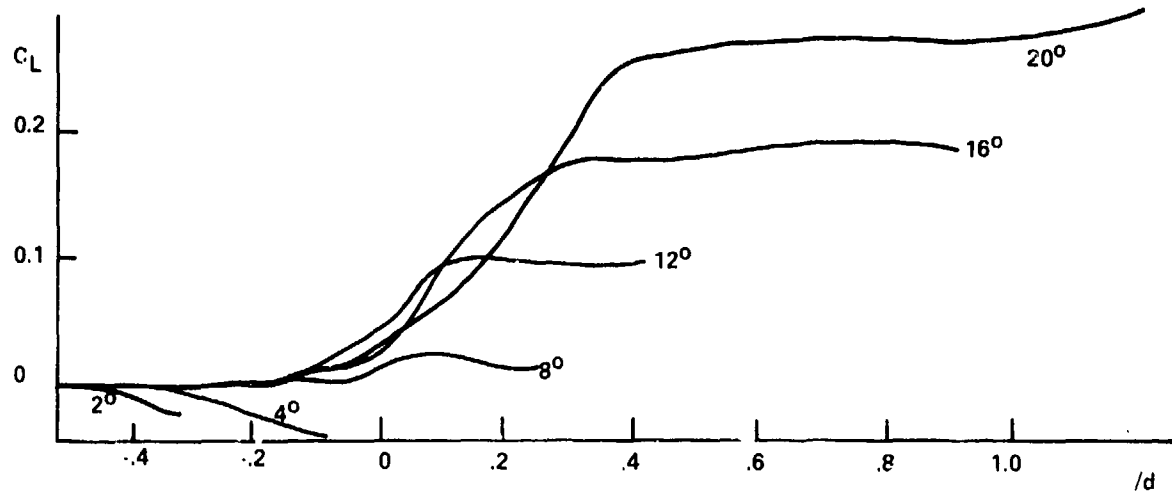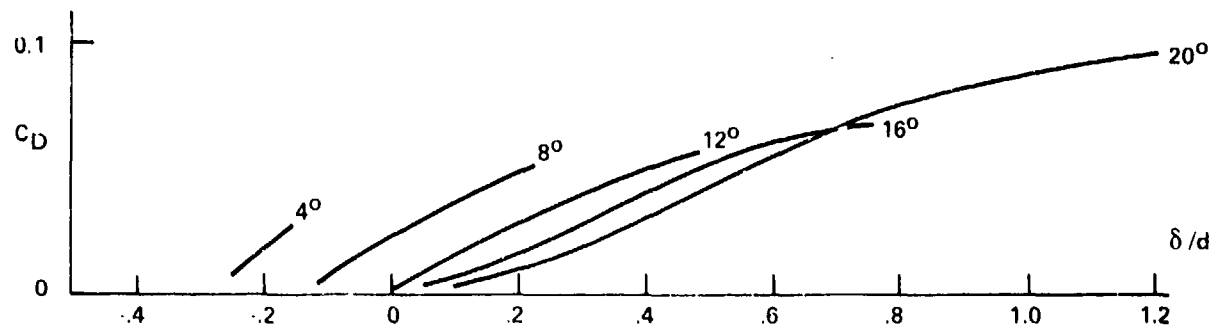
A. BARE BODY
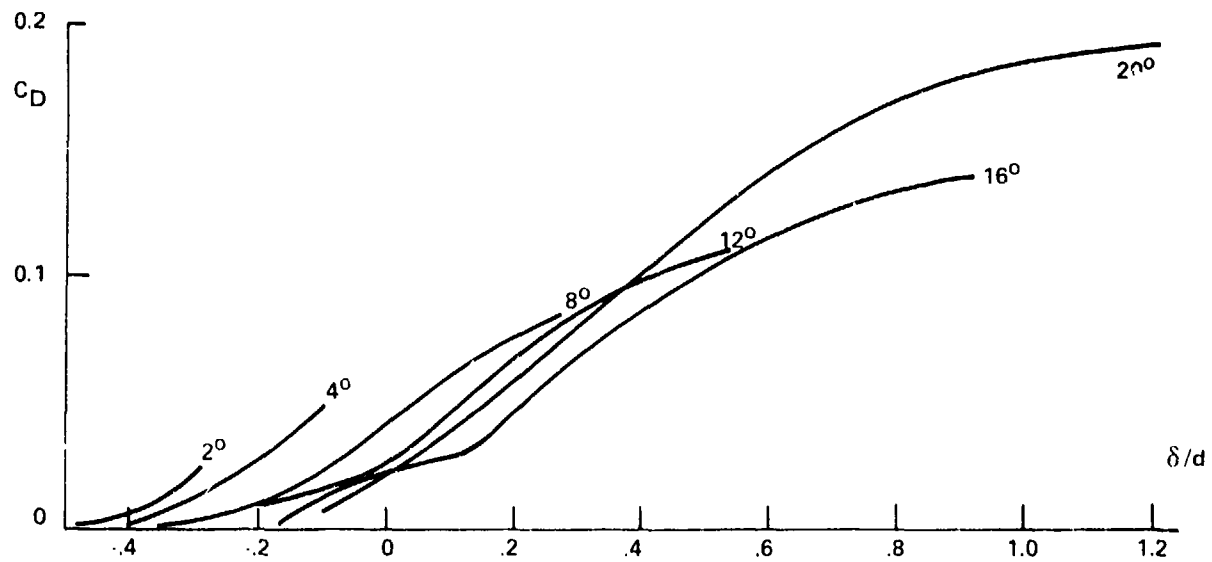
B. FINS AND CONVEX SHROUD
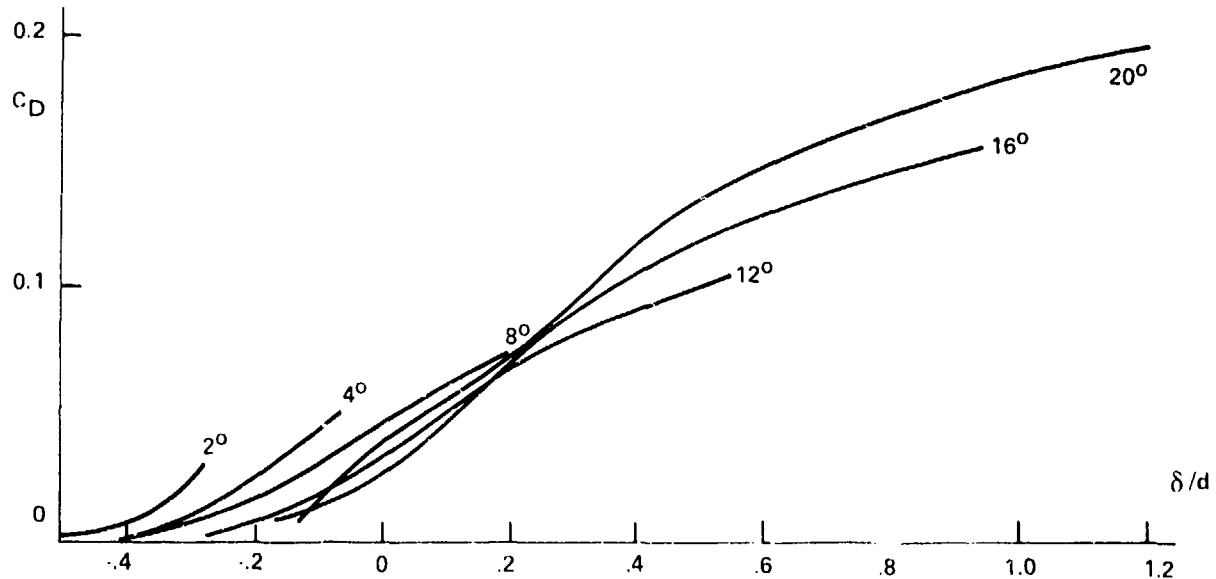
C. FINS AND CONCAVE SHROUD

FIG. 2-49 DRAG COEFFICIENT FOR TORPEDO TAIL REF (2-60)
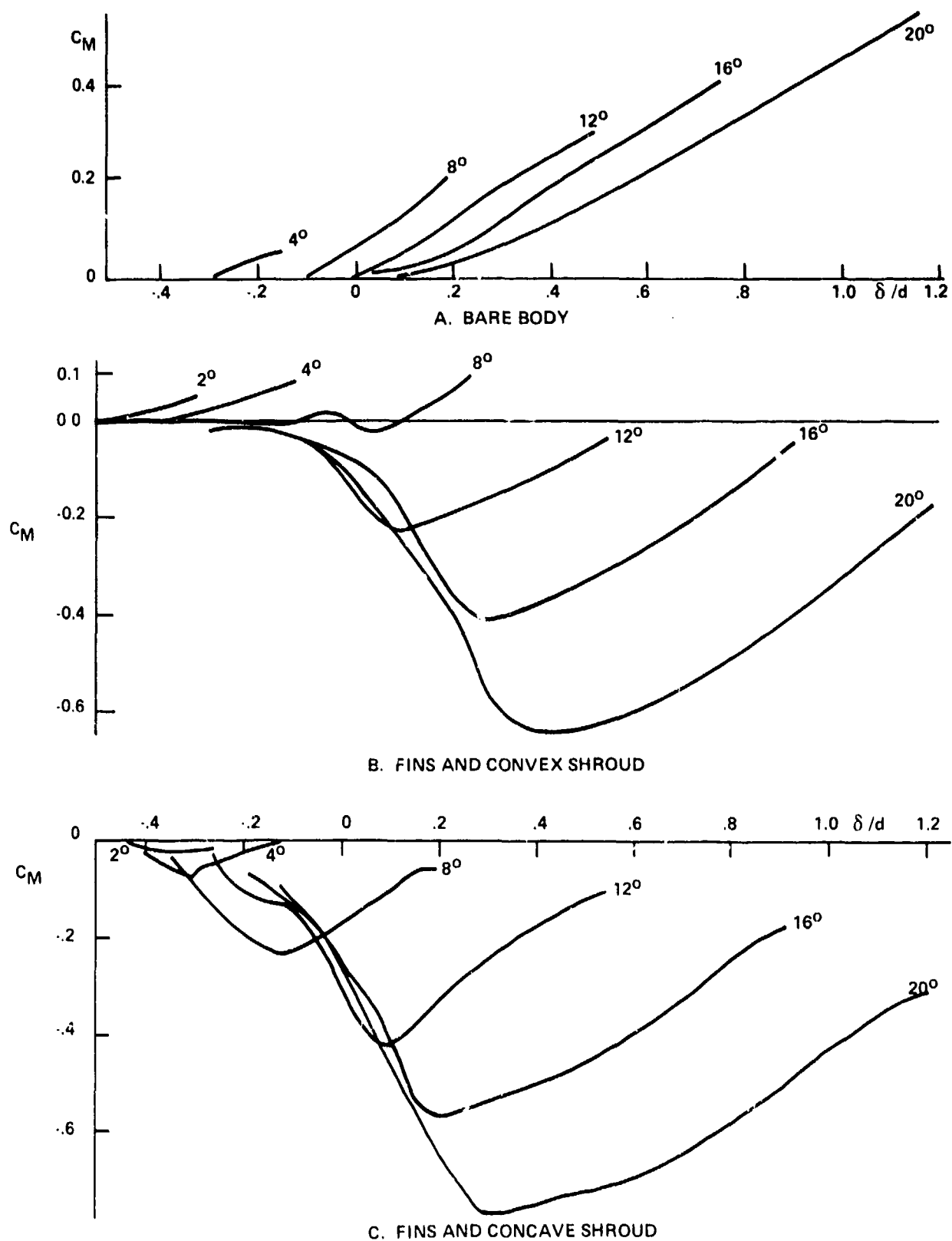
FIG. 2-50 MOMENT COEFFICIENT FOR TORPEDO TAIL REF (2-60)

Chapter 3

CAVITIES

SYMBOLS

A	drag area; usually $\pi d^2/4$
A_1, A_c	cross-sectional areas defined in Appendix A
A_j	cross-sectional area of 3-dimensional jet
a,b	parameters in equations
C_D	drag coefficient = D/qA
C_{Do}	cavity-running drag coefficients for $\sigma = 0$
C_{Dm}	drag coefficient based on maximum cavity cross section
C_p	pressure coefficient = $(p - p_o)/q_o$
C_Q	air entrainment coefficient = $Q/U_o d^2$
c	chord
D	drag force
d	reference diameter; usually maximum missile diameter or width of a 2-dimensional body. Sometimes the missile diameter where flow separation occurs
d_m	maximum cavity diameter
F	Froude number = $U_\infty/\sqrt{gd}$
f	parameter due to Reichardt = C_{Dm}/σ
g	acceleration due to gravity
h	hydrostatic head. Width or diameter of water tunnel.
J	thickness of 2-dimensional jet
J_o	Bessel function of zero order
L	length of cavity (especially without gravity); width of strip (in equation (3-30)
ℓ	length of cavity in a transverse gravity field
M	parameter in equation (3-36)
n	parameter in equations
p	local pressure

p_a partial pressure of air in cavity $= p_c - p_v$

p_c pressure in cavity

p_∞ freestream pressure

p_v saturation vapor pressure (of water)

Q   entrainment or ventilation rate in ft^3/sec.; empirical parameter in equation (3-35)

q   dynamic pressure $= (1/2)\rho U^2$

q_∞ freestream dynamic pressure $= (1/2)\rho U\infty^2$

R   Reynolds number

r   radius $= d/2$

r_e a "unit radius" Defined where used

r_m cavity radius $= d_m/2$

S   empirical parameter in equation (3-35)

t   parameter in equation (3-3)

U   flow velocity

U_c velocity on separation streamline (cavity wall)

U_∞ freestream velocity or missile velocity

W   mass rate of ventilation in lbs/sec.

x,y   longitudinal and transverse coordinates of cavity

α attack angle of projectile

β half angle of cone or wedge

θ angle where flow separates; measured from forward stagnation point

ρ mass density (of water)

σ cavitation number $= (p_\infty - p_c)/q_\infty$

σ_v cavitation number of vapor-filled cavity (or of tunnel condition $= (p_\infty - p_v)/q_\infty$

σ^* critical value of cavitation number for vortex generation

σ_{∞} cavitation number at tunnel blockage

iii

INTRODUCTION

A missile traveling through water is often partially or completely enveloped by an air or vapor-filled cavity. Usually the presence of the air-water interface of this cavity has a major influence on the behavior of the missile. Cavities are usually formed when missiles enter water from the air, and these cavities are filled by air which follows the missile into the water. Similarly any missile traveling through water at sufficiently high speed generates a cavity, but such cavities may contain only water vapor. A missile which generates a cavity as it travels through the water is said to be cavity running. When only its nose is wetted it is sometimes said to be riding on its nose.

This chapter will discuss the cavity and its properties. In another chapter, the water-entry process will be described from water impact to the ultimate fully wetted condition of the missile.

It is important at the start to recognize the equivalence of two situations: the travels of a missile through otherwise still water, and the uniform flow of water past an obstacle at rest. In each case the water is generally regarded as completely at rest or in uniform motion, except for the disturbance due to the missile or obstacle. Principal examples are the cavity-running missile in free flight and the model in the water tunnel.

CAVITIES, CAVITATION AND BUBBLES

When water streams uniformly past a solid body, it will flow faster at some points near the body than in the freestream, and slower at others. The local pressure will be reduced where the speed is greater in accordance with Bernoulli's theorem which, neglecting gravity, may be written

$$(1/2)\rho U^2 + p = \text{constant},$$

where U is the flow speed, p the static pressure at any point on a streamline, and ρ is the fluid density. If, near the body, the pressure drops to about the vapor pressure of the water at the local temperature, the water will tend to boil locally and produce a vapor-filled cavity. The well-known fact that the initiation of such cavities may occur at pressures above or below the vapor pressure of the water (Ref. (3-1)) will not be discussed in this chapter.

When the water is flowing very slowly past a body, it will contact the full surface of the body and the body is said to be fully wetted. At somewhat higher speeds the local pressure will drop to the vapor pressure at various points, and small separate vapor-filled bubbles may form at these points and collapse rapidly when the pressure rises again. This process is called cavitation.

When the cavitation is incipient, the life of the individual voids is extremely short, but as the flow speed increases, larger areas of the surface of the object have a pressure sufficiently low for cavitation, and the voids increase in size and permanence. At high enough speeds they no longer collapse but form large cavities which may be filled almost solely with water vapor. It should be understood that the benavior described is that seen by an observer whose position is fixed relative to the obstacle or missile. For travel with the water there is no such cavitation permanence; the void collapses when the water speed is no longer sufficient to reduce the pressure to that of the vapor.

More or less permanent and extended cavities formed on bodies such as missiles, propeller blades, or hydrofoils, are said to be _fully developed_, and the phenomenon is called _supercavitation_. Such cavities may be filled with air or water vapor.

The term _bubble_ will usually be reserved for cavities which are not attached to fast-moving bodies, but are relatively independent volumes filled with gas or vapor. These may have become detached from water-entry cavities, may be generated by the exhaust of a rocket, from the detonation of explosives, by incipient cavitation, etc.

VENTED AND UNVENTED CAVITIES

If permanent gases enter a cavity, it is said to be _vented_ or _ventilated_. On the other hand an _unvented_ cavity contains only (or almost only) water vapor. Water ordinarily contains air both in the form of very small bubbles and in solution, and venting from this source is to be expected (Ref. (3-1)), but it is probably not significant for large cavities. Venting may come from many sources, intentional and unintentional. The water-entry cavity is always vented through its opening to the atmosphere during its early life; hydrofoils or underwater bodies towed near the water surface frequently are vented from the surface; the cavities following rockets are filled with the exhaust; explosion bubbles are filled with the products of the reaction; and in the water tunnel a gas may be blown into the cavity through a small tube which terminates just behind the generating nose of the body.

CAVITIES AND THEIR GENERATION

Authors have classified cavities in various ways, usually based on the intended manner of treatment. In the present report cavities will be described as _steady_, _almost steady_, and _transient_.

Steady cavities are produced in the cavitation water tunnel where the water may be made to flow past an obstacle at a speed sufficient to cause the nose of the missile to generate a cavity, assisted often by a reduction of freestream pressure or by venting the cavity. Actually, the designation "steady" will be used principally in this chapter to denote a cavity which appears reasonably steady to the eye. It will be shown later that such cavities are usually quite unsteady in their

downstream ends, and that under some conditions the cavity boundaries themselves are more apparent than real.

The term "almost steady" will be applied to cavities which are of a shape which is not quite steady, but is gradually changing (for example, to a smaller size because of the loss of air content).

The water-entry cavity is a good example of the transient cavity. For some time after entry it elongates, grows, divides, etc., in a completely unsteady fashion. The term "transient cavity" has also been used (Ref.(3-2)) to describe the vapor bubbles which characterize incipient cavitation. In the present report the latter regime will not be discussed, so that there will be no confusion in terms.

In Figure 3-1, U_∞ is the freestream velocity of the water in the tunnel. The pressure of the vapor and gas in the cavity is p_C, and p_∞ is the freestream pressure, that is, the pressure in the undisturbed liquid approaching the body.

The local pressure at points in the vicinity of a body immersed in a steady flow can be expressed in terms of the dimensionless <u>pressure coefficient</u>

$$C_p = \frac{p - p_o}{(1/2)\rho U_\infty^2}$$

where p is the local pressure. If gravity effects are negligible, Bernoulli's equation for steady flow can be written

$$p + (1/2)\rho U_\infty^2 = p_\infty + (1/2)\rho U_\infty^2$$

Hence

$$C_p = \frac{p - p_\infty}{(1/2)\rho U_\infty^2} = 1 - (U/U_\infty)^2 \tag{3-1}$$

which is a function only of the ratio of local velocity to freestream velocity.

Cavity behavior is most easily discussed in terms of a dimensionless coefficient called the <u>cavitation number</u> (parameter or index)

$$\sigma = \frac{p_\infty - p_C}{(1/2)\rho U_\infty^2} \tag{3-2}$$

which relates the difference in pressure between the cavity and its surroundings to the dynamic pressure ($q_\infty = (1/2)\rho U_\infty^2$) of the freestream. The pressure in the cavity p_C may be that of water vapor p_V or water vapor plus air. When the cavity is unventilated and thus filled only with vapor, the symbol

$$\sigma_v = \frac{p_\infty - p_v}{q_\infty} \qquad\qquad (3-3)$$

is sometimes used.

From the equations given, σ is closely related to the negative of the pressure coefficient C_p. The maximum (positive) value of $-C_p$ for a given body is called the <u>critical cavitation number</u>. The pressure coefficient has a specific value at each point on the surface of the obstacle, and these values are reasonably independent of U_∞, p_∞, and ρ so long as the flow pattern is steady and the obstacle is fully wetted and at a fixed angle of attack.

There is usually a "stagnation point" on the missile nose where the flow speed is reduced to zero and the pressure coefficient has the value

$$C_p = \frac{p - p_\infty}{q_\infty} = \frac{(p_\infty + q_\infty) - p_\infty}{q_\infty} = +1$$

The value of C_p drops to zero where the flow speed reaches freestream speed and becomes negative where the speed is greater than freestream speed.

To understand cavity initiation and behavior it is useful to consider what happens as the speed of flow past an obstacle in a water tunnel is gradually increased from a low value at any fixed freestream pressure p_∞ (without ventilation). The pressure on the body will be lowest where $-C_p$ has its greatest value (the critical cavitation number). At that point

$$-C_p = (p_\infty - p)/q_\infty$$

will for a time remain fairly fixed in value as U_∞ increases, with p decreasing and q_∞ increasing. When p drops to the vapor pressure of the liquid p_v

$$-C_p = (p_\infty - p_v)/q_\infty = \sigma_v$$

and boiling tends to start at this point of minimum pressure, and cavitation is initiated. As the flow speed of the tunnel continues to increase, it is evident that the local pressure at the point considered cannot continue to drop, since boiling will occur and maintain the pressure at the value p_v once cavitation has started. As the pressure in the flow about the cavitation starts to drop below p_v, the cavity expands by displacing the wall at which the pressure is dropping. This displacement changes the shape of the flow path; the flow speed on the cavity wall is reduced; and the pressure there does not fall below p_v. The flow, instead of being guided by the shape of the obstacle, now travels about the shape of the obstacle-plus-cavity

which is more streamlined than the obstacle and has a lower critical cavitation number.

When cavitation first occurs, it will be seen that the cavitation number of the cavity will equal the negative pressure coefficient at which it occurred. Hence the term "critical cavitation number."

Still another usage should be clarified at this point. It is usual to speak of the cavitation number at which a water tunnel is operated, and this cavitation number is numerically equal to $\sigma_V = (p_\infty - p_V)/(1/2)\rho U_\infty^2$. This is the cavitation number of a vapor cavity produced at the p_∞ and U_∞ of the tunnel. If the critical number of the obstacle is less than this, cavitation will not occur. If the critical cavitation number of the obstacle is higher than the cavitation number of the tunnel, a cavity will be produced with the cavitation number p_V, which is also the cavitation number of the tunnel.

A study of Figure 3-2 may assist in the understanding of the phenomena of cavity development at an obstacle. Taken from Reference (3-3), and based on a water-tunnel cavity study, it shows pressure coefficients on the surface of a model with hemispherical nose, plotted against position along the model surface. Graphs are drawn for a variety of tunnel cavitation numbers which were obtained by changing the ambient pressure with constant freestream velocity. The symbols of the original figure have been changed to agree with those of this report.

A single graph is given for cavitation numbers ≥ 0.80, indicating that the pressure coefficient is independent of the tunnel conditions when cavitation does not occur. The increase of flow speed due to the nose configuration was sufficient to lower the pressure coefficient to about -0.73, and no cavitation or change in the C_p graph would be expected until the cavitation number of the tunnel was reduced to this value. When the tunnel cavitation number was reduced to 0.5, the flow speed somewhere between stations 4 and 5 was sufficient to cause cavitation under the reduced ambient pressure. The local pressure coefficient did not continue to drop because it could not go below the vapor pressure. Instead, p, U, and C_p remained constant along a part of the nose. Finally the flow speed decreased with an increase of C_p.

At $\sigma = 0.2$, cavity initiation occurs slightly sooner (just after station 4). The smallness of the drop in pressure coefficient (to -0.2) is due to the replacement of the relatively bluff shape of the hemisphere by the rather streamlined shape of the large cavity which is produced. The velocities on the cavity surface do not reach values proportionately as high as those found when the whole hemisphere is wetted, but the speed is maintained at an almost constant value for several sphere diameters along the cylindrical afterbody of the model. The length of the cavity is roughly equal to the length of the flat portion of the graph -- the portion with constant cavitation number.

The cavitation number is most suitable in application to steady cavities such as are produced in the water tunnel. When applied to the water-entry cavity, the varying missile speed should, in some way, replace the speed of the freestream. Also the hydrostatic pressure varies along the length of the water-entry cavity and along the cavity due to the surface-piercing strut of a hydrofoil. The treatment of the cavitation number of such cavities will be discussed further when the water-entry cavity is analyzed.

Flow Separation

When a cavity is formed, the flow must separate from the nose of the missile. The position and nature of this separation is of both theoretical and practical importance.

Dependent on the shape of the missile nose, two types of separation are distinguished: abrupt and smooth (Refs. (3-4)(3-5)). The separation is abrupt when the missile nose contains a sharp edge, collar, or shoulder from which the flow must separate; for example from disks or right cylinders, or the bases of cones. The separation is said to be abrupt because theory shows that the free streamline has infinite curvature where it leaves the sharp edge; this streamline has a small angular change at the edge, rather than having a smooth curvature there. Rouse and McNown (Ref. (3-3)) reported that, in many cases of abrupt separation, the cavity seems to start slightly behind the shoulder. This is evident in the drawing of Figure 3-3 which is a part of Figure 52 of Reference (3-3). The same phenomenon was observed by Eisenberg (Ref. (3-6)) at about the same time.

Smooth separation occurs from convex noses whose radii of curvature are sufficiently large that the line of separation can creep along the surface as the experimental flow conditions are slowly modified. Smooth separation occurs from spherical, ellipsoidal, and ogival surfaces.

Attempts to predict the position of smooth separation have been rather unsuccessful since theory has been based on potential flow and separation is strongly influenced by surface forces and the viscous boundary layer (Refs. (3-7) , (3-8)). Calculations have been made for circular and elliptical cylinders and for the sphere. For two dimensions the methods of the complex variable are available (Ref. (3-4)); methods of analogy have been used for the sphere (Refs. (3-4), (3-8)).

The nature of the "smooth separation" from a sphere can be seen from Figure 3-4 (Ref. (3-9)) which shows the cavity following the vertical water entry of a one-inch steel sphere. The flow does not separate at a particular "latitude"; the angle varies so that separation occurs along a very jagged line. As the flow tends to leave the surface along a tangent to the surface, small surface forces change the position of separation by slightly changing the angle of flow.

At low speeds the effect of such surface forces may be sufficient to prevent separation completely (Refs. (3-7), (3-10)). It has been shown (Ref. (3-7)) that a very clean one-inch steel sphere can enter water vertically at 20 ft/sec. without producing a cavity, but that the flow will separate readily if the surface of the sphere is contaminated. It is clear that a definite angle of separation is not to be expected under given conditions unless the experiment is carefully controlled, and that attempts to predict the position of separation should give too ear y separation since viscous and surface-tension forces are neglected. Reference (3-11) states that measured values reported for separation angles refer to the earliest angles at which separation was found.

It might be expected that separation would correlate with surface tension, i.e., with the Weber number, but it does not (Ref. (3-5)). Viscosity limits the flow into the narrow separation slit formed as the flow starts to leave the curved surface. This causes an underpressure in the crevice and a tendency for the flow to reattach. It is this underpressure that has such an important effect on whip at water impact. After a readjustment of flow conditions, it may take several minutes for the separation point to stabilize (Ref. (3-5)).

Separation is sensitive to the condition of the boundary layer and, accordingly, the angle of separation for the sphere changes with Reynolds number. Two experimental investigations have been made of this dependence (Ref. (3-5), (3-11)), and the data were studied by Brennan (Ref. (3-5)). They are replotted in Figure 3-5. It is evident that the data separate into two groups having different separation angles. The upper group had Reynolds numbers (based on diameter) less than 3.4×10^5 and in the lower group they were 4.0×10^5 or greater. This is approximately where the boundary layer on the sphere is known to become turbulent (although it has been reported (Ref. (3-3)) that no pressure change occurs on the spherical surface above $R = 2 \times 10^5$). For fully wetted flow about the sphere it is at the critical Reynolds number that the drag suddenly drops with increasing Reynolds number, as the position of flow separation moves downstream. For cavity running, the position of flow separation moves upstream with increasing Reynolds number.

A further analysis was attempted to determine the dependence on R in each group on Figure 3-5. No systematic dependence could be observed and the straight lines were obtained by least squares. It is probable that there is some dependence on R within the groups and the distribution of the data available has some influence on the regression lines. The graphs show that separation may occur anywhere from 70° to 90°. The lowest graph on Figure 3-5 shows the values predicted by Armstrong and Tadman (Ref. (3-8)). The agreement is quite poor as has been mentioned.

If the body from which separation occurs is not a complete sphere but a cylinder with spherical tip, separation will occur from the spherical surface if the angle of the surface is sufficient, but will separate at the edge of the spherical surface if the angle of flow required before separation exceeds the angle provided. The separation from a convex surface is unaffected by the downstream geometry.

3-7

Little work has been reported for nose shapes other than the sphere. Predictions have been made for the two-dimensional circular cylinder, notably by Armstrong and Tadman (Ref. (3-8)) and by Roshko (Ref. (3-12)). Their predicted values are compared in Figure 3-6 with the range of values obtained by Daily from experiment (Ref. (3-13)). Daily reported merely that the measured values lay in the rectangle shown in the figure. His measurements were made with Reynolds numbers between 2.4 and 2.8 x 10^5. Since this is in the critical range it is probable that the scatter of his data was large although the five degrees reported is only half the scatter for the sphere (Fig. 3-5). As for the sphere, the experimental values of the separation angle are about 20° higher than those predicted.

Brodetsky (Ref. (3-14)) calculated the separation angles at $\sigma = 0$ for elliptic cylinders and the results are shown in Figure 3-7. Since his data show the same angle for the circular cylinder as Armstrong and Tadman, presumably his data for the elliptic cylinder will also be of the order of 20° below experiment.

Reference (3-3) gives the results of experimental measurements of the pressure on one- and two-caliber ogives, and on 2:1 and 1:2 ellipsoids. It is possible to obtain order-of-magnitude separation angle data from that report.

Although potential-flow solutions predict the same curvature for the cavity and the missile nose where separation occurs (Refs. (3-4), (3-15) and (3-16)), experimenters have frequently reported abrupt changes in slope at this point (Refs. (3-3), (3-6), and (3-15)). In fact, Birkhoff stated (Ref. (3-17)) that boundary-layer theory predicts a jump of slope at the separation point, and the details of this jump were discussed by Parkin (Ref. (3-15)).

The separation point moves downstream as the cavitation number increases (Ref. (3-15)). Also, when spheres enter water vertically while spinning rapidly about a vertical axis, the separation moves back to angles of the order of 110° from the forward stagnation point (Ref. (3-18)).

SHAPE OF THE STEADY AXIALLY-SYMMETRIC CAVITY

When the flow in a water tunnel is deflected by a body of revolution and a vapor- or gas-filled cavity is generated, it is reasonable to assume that the cavity will be constant in shape if it is immersed in a steady flow. This may or may not be the case. It will be seen later that cavities sometimes pulsate, especially when re-entrant jets occur at the aft end, and many cavities only appear to be voids, being largely filled with water. The concept of the steady cavity which will be used in this section is based entirely on practical considerations such as whether the shape is sufficiently stable to permit the measurement of its dimensions.

The shape of the cavity is a matter of scientific interest, but it is also of great importance to the designer of underwater missiles

and rockets. The stability of a missile may depend on whether the cavity length is sufficient to envelop the fins, and the diameter may have a great influence on the straightness of the trajectory.

Cavity shape has generally been specified by giving the length L and the maximum diameter d_m of the cavity, the fineness ratio L/d_m, and the overall outline, both by sketch and formula. The length and diameter are written in the dimensionless form L/d and d_m/d, since they scale well with missile size. Because the early work was done with nose shapes having abrupt flow separation, d was taken as the diameter of the nose where separation occurred, the outside of a disk or the base of a cone. Presumably for shapes having smooth separation it is most practicable to use the nominal maximum diameter of the obstacle since the drag coefficient is usually referred to this cross section. For the sphere the maximum diameter is an obvious choice. Usage has not extended to other shapes but the matter seems to have little importance. It will be seen that both the length and diameter of the cavity are dependent on the drag coefficient of the nose, but on the <u>drag area</u> $C_D A$ (where A is the cross-sectional area used in defining C_D) rather than on C_D alone. Hence the quantities $(L/d)/C_d^{1/2}$ and $(d_m/d)^2/C_D$, which will be used in this section, do not require the identification of d.

In discussing the size of the cavity enveloping a traveling missile, there is advantage sometimes in using the cavity volume (Ref. (3-19)) rather than its linear dimensions, because cavity oscillations change its fineness ratio and presumably have much more effect on L and d_m than on the volume.

It has been assumed that the size of the cavity is not dependent on the dry afterbody of the missile, but this may not be quite true. From their measurements in a vertical free-jet tunnel, Self and Ripken reported (Ref. (3-20)) that "the size of the non-clear cavity associated with a certain head form appears to be significantly influenced by the diameter of the afterbody occupying the cavity" with smaller cavities for larger afterbodies. A somewhat similar behavior has also been suspected in vertical water entry.

Reichardt made the first serious study (Ref. (3-21)) of the steady cavity, based on both theory and experiment. He showed that the fineness ratio of the cavity L/d_m is a function only of σ, and that L/d and d_m/d are functions of σ and also are proportional to $C_D^{1/2}$. The present study verifies the validity of these laws within experimental error, and they will be used to guide the investigation of the cavity dimensions. The quantities L/d and d_m/d, apart from their dependence on σ, are not apparently influenced by the values of p_∞, p_C, and U, and are substantially independent of whether the cavity is filled with vapor, or vapor plus large quantities of air and other gases. Even the presence of large amounts of water within the cavity may not have a large influence on the cavity shape. These matters will be discussed later. Attempts to correlate the scatter of cavity-dimension data with Reynolds number or missile size were usually not successful, perhaps because insufficient experimental data were available.

3-9

Unless statements are made to the contrary, the cavity data presented in this report assume that the missile's nose surface is moderately smooth, the angle of attack is zero, the cavity axis is horizontal, and gravity effects are negligible or have been corrected for.

Most experimental determinations of cavity geometry have been made in the water tunnel but at least one program was carried out in a towing basin (Ref. (3-22)). Reichardt (Ref. (3-21)) used inside calipers to measure the maximum cavity diameter but presumably all others made measurements on photographic records. Such variations of method do not seem to have influenced the data but further study might well be made to investigate the causes of differences between the results of various experimenters.

It is impracticable to measure cavity length directly. It will be shown elsewhere that the downstream end of the cavity is a place of inherent instability and of varying conditions. Hence, it is usual to define the cavity length as twice the distance from the line of flow separation to the cross section of maximum diameter. Although this length is reasonably steady in value, its magnitude is not easily measured since the exact position where the cavity diameter is a maximum is difficult to determine.

Length and diameter data have been reported for the cavities due to several simple nose shapes: disks, spheres, cones, and stagnation cups. (Nose shapes will be discussed elsewhere. However, a stagnation cup is an indented nose, the indentation being a cup with moderately thin walls at right angles to the base of the cup.) Sketches have been published (Ref. (3-3)) of cavity outlines for noses of a few other shapes: ogives, disk-ogives, and ellipsoids. Data for these latter are not included in the present report because it is felt that the accuracy is not high and the cavity shapes can be obtained better by prediction methods to be described. A list of the various sources of length and diameter data is given in Table 3-1.

In the following pages, experimental measurements of diameter, length, and fineness ratio, taken from published reports, will be compared, including the scaling for noses of different drag coefficients. The equations which have been suggested in the literature will be considered and compared with experimental data, and formulas will be derived which appear to fit the data best, and which are consistent for d_m/d, L/d, and L/d_m. Cavity length and diameter will be discussed in the forms $(L/d)/C_D^{1/2}$ and $(d_m/d)^2/C_D$. The square was chosen in one case and not in the other for completely practical reasons related to the accuracy of plotting. Log-log coordinates are indicated for the presentation of the data since their use results in almost straight graphs. Since the use of different cycle lengths on the two coordinate axes appeared undesirable the square of d_m/d was chosen to increase the slope of the graphs of cavity diameter and thus fill a two-cycle by two-cycle page. Unsquared L/d permits the same presentation, and $(L/d)^2$ would require four cycles on the ordinate axis.

SEAHAC/TR 75-2

Table 3-1

AVAILABLE EXPERIMENTAL CAVITY-SHAPE DATA

References	Date and Ref.	diam. (inches)	Vented	Unvented	σ	$Rx10^{-5}$	Disk	Spheres	Cones	Stagn. Cups
Reichardt	1945 (3-21)	.08-.6	v		0.26-.100		v		v	v
Gadd-Grant	1965 (3-23)	3	v	v	.085-.12		*		v	v
Rouse-McNown	1948 (3-3)	1		v	.2 - .9		v	v	v	
Oversmith	1959 (3-22)	1	v	?	.1 - .3		v		v	
Self-Ripken øø	1955 (3-20)	1/4-1		v	.04-.3		v	v	v	
Waid	1957 (3-24)	1/2-1	v		.035-.17	.4-1.6	v			
Eisenberg	1947 (3-6)	1		v	.116	prob.≥18	v			
Hicks**	1952 (3-25)	1/2	?	?	.075-.275		v			
Eisenberg-Pond	1948 (3-26)	1-1.5		v	.1 - .6		ø			
Brennan	1969 (3-5)	3		v	.1 - .4			*		

* Length Data Only
** Measured values are quite high and are not plotted in this report
ø Diameter data only
øø These data for vertical cavities will be discussed separately

Cavity length and diameter data for measurements made in vertical tunnels (Ref. (3-20)), have not been included in this section because of the effect of gravity on the cavity length and shape. Although the data have not been included it appears that d_m/d is in reasonable agreement with data from horizontal tunnels.

Cavity Diameter d_m/d

Reichardt (Ref. (3-21)) gave the theoretical formula

$$\frac{d_m}{d} = \left[\frac{c_D}{\sigma - 0.132\sigma^{3/4}} \right]^{1/2} \qquad (3-4)$$

for cavity diameter, which he derived by source-sink methods. It shows the diameter to be a function only of the cavity-running drag coefficient and of the cavitation number. The derivation of this equation is discussed in Appendix A. Reichardt gave a sketch, which is copied in Figure 3-8, to explain why the form of equation (3-4) is possible. The elliptical and flat nose shapes in the figure have different drag coefficients based on wetted area. If, however, the drag areas C_DA of the two noses are designed to be the same, then the cavities they form will have the same maximum diameter even though the cavity shapes differ considerably in the vicinity of the nose.

Measurements of diameter from four experiments are plotted separately against σ on Figures 3-9 to 3-12. The choice of $(d_m/d)^2/C_D$ as the ordinate variable provides a test of the dependence on C_D shown in equation (3-4). Drag data which were required for the plotting of these figures were taken from Reference (3-27).

Figure 3-9 shows data obtained by Waid (Ref. (3-24)) from measurements on cavities due to a circular disk. The graph is based on the equation

$$d_m/d = 0.534 \; \sigma^{-0.568} + 1 \qquad (3-5)$$

which Waid derived for these data. The experimental points are seen to lie slightly above the line defined by his equation.

Figure 3-10 contains data due to Reichardt (Ref. (3-21)) for the cavities due to cones, disks, and a stagnation cup. There is little dependence on nose shape although for cones of small angles the points tend to be a little low. (The half-angle β will be used in specifying cone noses.) This behavior will be discussed later. The graph on Figure 3-10 is based on Reichardt's formula, equation (3-4). It defines somewhat larger cavities than those indicated by the data points.

Data on the cavities due to spheres, disks, and cones given by Rouse and McNown (Ref. (3-3)) are shown in Figure 3-11. A single graph is drawn for the sphere, disk, and 67.5° cone. The finer cones lie below, with the finest (22.5°) cone at the bottom.

Figure 3-12 gives data obtained by Eisenberg and Pond (Ref. (3-26)) for disk cavities and an approximating graph drawn by eye.

Figure 3-13 compares five graphs chosen by the author as good linear (log-log) approximations to the data of various experiments (excluding data for slender cones). Maximum differences amount to about 40 percent in $(d_m/d)^2/C_D$ but are dependent rather on the experimenter than on the nose shapes tested. A straight line gives a good approximation to the data. The two dots at the sides of Figure 3-13 define the straight-line approximation.

$$(d_m/d)^2/C_D = 1.35\sigma^{-0.93} \tag{3-6}$$

This same straight graph is indicated on the individual plots of Figures 3-9 to 3-12 by large dots at or near the extreme right and left sides of the figures.

Because the scaled diameters $(d_m/d)^2/C_D$ of the cavities due to slender cones seemed to be less than those of other nose shapes in the work of several experimenters, a separate study was made for cones of various angles. The results showed a small dependence on cone angle. Since the slope of the graphs seemed to be rather closely the same for all cone angles, a set of least-square straight lines was calculated with all graphs having the same slope. The resulting graphs are shown in Figure 3-14. The equations of these graphs are

$$(d_m/d)^2/C_D = C\sigma^{-0.91} \tag{3-7}$$

with

C	β
1.48	67.5°
1.38	45°
1.31	22 ... 27°
1.28	14°

The dependence on cone angle indicated by these data appears to be real. However, the variation amounts only to 10 percent in $(d_m/d)/C_D^{1/2}$ and may simply represent a failure of the assumed dependence on C_D. It is significant that the common slope found for the cones by least squares and given in equation (3-7) is very close to the slope, shown in equation (3-6), which had previously been chosen by eye as an average for the data of Figure 3-13.

No correlation with Reynolds number was attempted since the data provided in the literature seemed generally insufficient. While Waid's results (Ref. (3-24)) seemed to show no effect of size, a slight effect

may be noted in the data of Eisenberg and Pond (Ref. (3-26)), with cavities for small disks a little larger than those scaled down from large-disk cavities. No investigation was made of the possible effect of tunnel size.

It is interesting to compare the formula of equation (3-6) which was derived in the present report from the study of all available experimental results, with two published formulas which were obtained theoretically. These formulas are: Reichardt's formula which has been given as equation (3-4), and the equation

$$(d_m/d)^2/C_D = 1/\sigma \qquad\qquad (3-8)$$

which was derived by Garabedian (Ref. (3-28)) for small values of σ. The comparison is made in Figure 3-15 where equation (3-6) is shown as a dashed line.

Garabedian's formula in equation (3-8) was actually given by Reichardt (Ref. (3-21)) as an inferior approximation to that which he adopted. Equation (3-8) is easily derived by the following non-rigorous argument. It has been shown (Ref. (3-29)) that the flow leaves the nose of a missile principally in a transverse direction. The energy given to the water while the missile travels unit distance results in an expansion of the cavity until the work done in cavity expansion becomes equal to the initial kinetic energy of the transverse-flowing water. Thus

$$\text{Drag force} \;=\; D \;=\; qC_D\pi d^2/4 = (p_\infty - p_c)\pi d_m^2/4$$

or

$$(d_m/d)^2/C_D = q/(p_\infty - p_c) = 1/\sigma.$$

Cavity Length L/d

The literature contains a relatively large amount of data on the length of the cavity due to a disk and the results are sufficiently interesting that they will be given a separate presentation before the discussion of other nose shapes. Waid (Ref. (3-24)) gave experimental values of L/d for cavities due to 1/2-, 3/4-, and 1-inch disks. A study was made of these data to see whether an effect of size could be detected. None was apparent.

Data for the length of cavities due to disks are plotted from various reports in Figure 3-16, and straight graphs are shown which approximate the data from the separate sources. The overall scatter is rather small. The straight line

$$L/d = \sigma^{-1.15} \qquad\qquad (3-9)$$

was chosen to represent the overall data for the length of the cavity due to a disk. The position of this straight line is indicated in Figure 3-16 by the dots at the two ends of the string of data points.

Four formulas are available which are applicable to the L/d of the disk cavity. Waid (Ref.(3-24)) gave the expression

$$L/d = 1.08\sigma^{-1.118},\tag{3-10}$$

based on his measurements of disk cavities. Reichardt (Ref. (3-21)) derived not only the formula of equation (3-4) for cavity diameter d_m/d but also a formula for L/d_m. From the product of the two an equation for L/d is obtained which should be applicable to any nose shape:

$$\frac{L}{d} = \frac{L}{d_m} \cdot \frac{d_m}{d} = \frac{\sigma+0.008}{\sigma(0.066 + 1.7\sigma)} \cdot \left[\frac{C_D}{\sigma(1-0.132\sigma^{1/7})}\right]^{1/2}\tag{3-11}$$

Campbell and Hilborne gave (Ref. (3-30))

$$L/d = 1/0.7\sigma$$

as a rough approximation to Reichardt's data in the range $0.04<\sigma<0.12$. The approximation is good at the higher part of this range but is 17 percent low at $\sigma = 0.04$.

The expression

$$\left(\frac{L}{d}\right)^2 \frac{1}{C_D} = \frac{1}{\sigma^2} \log_e \frac{1}{\sigma}\tag{3-12}$$

was obtained theoretically by Garabedian (Ref. (3-28)). A fourth relation based on experimental data is given by equation (3-9). These formulas are compared in Figure 3-17. Graphs are drawn for equations (3-9), (3-10), and (3-11) and, to lessen the confusion, equation (3-12) is represented by a series of discrete points. The graphs differ very little until σ becomes close to unity where equation (3-12) gives the value zero.

The evaluation of cavity length for the disk is carried one step further in Figure 3-18 which contains a plot of $(L/d)C_D^{1/2}$ instead of L/d. A straight line is no longer adequate for the representation since C_D approximately doubles in the range of σ values studied. The graph on Figure 3-18 was drawn by eye. The formula

$$(L/d)/C_D^{1/2} = 1.24\sigma^{-1.123} - 0.60\tag{3-13}$$

approximates it roughly.

A corresponding plot for all nose shapes is contained in Figure 3-19. On this figure the study is simplified by the use of the graph of Figure 3-18 for the disk instead of data points. Points have been plotted for cones, spheres, and concave noses such as the stagnation cup.

If points with larger scatter are ignored in Figure 3-19, the agreement with the graph which was obtained from disk data in Figure 3-18, is quite good. This graph and equation (3-13) then appear to represent $(L/d)C_D^{1/2}$ for all axially symmetric noses.

Because of the dependence on cone angle found for $(d_m/d)^2/C_D$, a separate study was made of $(L/d)/C_D^{1/2}$ for various cone angles. Again a set of parallel least-square straight line was calculated, with the resulting equations

$$(L/d)/C_D^{1/2} - C\sigma^{-1.214}$$

with

C	β
0.873	67.5°
0.907	45°
0.949	22-27°
0.915	14°

The behavior of these data is not as systematic as for $(d_m/d)^2/C_D$, and evidence of dependence on cone angle is not conclusive.

Cavity Fineness Ratio L/d_m
_____

In his analysis of the steady cavity Reichardt first stated (Ref. (3-21)), on the basis of theory and observation, that the fineness ratio L/d_m is substantially independent of the shape of the obstacle which causes it, and is given by the formula

$$\frac{L}{d_m} = \frac{\sigma + 0.008}{\sigma(0.066 + 1.70\sigma)} \tag{3-14}$$

as a function only of the cavitation number. He included a graph showing that his experimental data were in good agreement with the formula. The conclusiveness of his agreement was limited in two respects: the maximum value of the cavitation number employed in his tests was about 0.1, and all nose shapes studied were characterized by abrupt separation (stagnation cup, disk, and cones).

In Figure 3-20 values of L/d_m are plotted from all tests found in the literature to contain the necessary data (see Table 3-1), but to avoid confusion not all points are shown. Disks, cones, and spheres are included as well as concave noses such as the stagnation cup. The sphere is the only nose with smooth separation for which data were found.

Over most of the range of σ values in Figure 3-20 the scatter is quite small especially in view of the wide range of nose shapes from which the data were assembled. The scatter increases considerably at higher values of σ where the cavities are smaller and less stable. There is some evidence that the graph for the sphere is more concave downward than the others, but the information is scant.

In the present study equations (3-6) and (3-13) were derived to express the dependence of $(d_m/d)^2/C_D$ and $(L/d)C_D^{1/2}$ on σ. According to these equations the formula

$$L/d_m = 1.067\sigma^{-0.658} - 0.52\sigma^{+0.465} \tag{3-15}$$

should represent the L/d_m data. It is plotted in Figure 3-20 and is seen to fit the data rather well. Several other formulas have been proposed to express the dependence of L/d_m on σ. Reichardt's (Ref. (3-21)) equation has already been given as equation (3-14). Waid (Ref. (3-24)) gave formulas for L/d and d_m/d based on his experimental data, and from these

$$L/d_m = (1.08\sigma^{-1.118})/(0.534\sigma^{-0.568} + 1). \tag{3-16}$$

Equations derived theoretically for small σ have been given by Garabedian (Ref. (3-28)),

$$L/d_m = \left[\frac{1}{\sigma} \log_e \frac{1}{\sigma}\right]^{1/2} \tag{3-17}$$

and by Münzer and Reichardt (Ref. (3-31))

$$L/d_m = 1.261\sigma^{-5/8}. \tag{3-18}$$

The various formulas are compared in Figure 3-21. In order to avoid confusion, graphs are given for only two of the equations: a solid line for the equation of the present study, equation (3-15), and a dashed line for Reichardt's equation (Ref. (3-14)). The position of equation (3-16) of Waid, equation (3-17) of Garabedian, and equation (3-18) of Münzer and Reichardt are shown by a number of plotted points. Equation (3-18) is a straight line on log-log coordinates. It is valid only for very small σ. Otherwise the differences between the graphs is small except that equation (3-17) falls off rapidly at higher values of σ and reaches the value $L/d_m = 0$ at $\sigma = 1$.

Cavity Outline

Thus far the cavity geometry has been discussed in terms of the maximum dimensions: the length, diameter and fineness ratio. Sketches of the cavity outline have, of course, been given in the literature and two authors have described it as a generalized ellipsoid

$$(x/a)^2 + (y/b)^n = 1$$

but in a considerably different fashion. Münzer and Reichardt (Ref. (3-31)) used $a = L/2$ and $b = d_m/2$ as the semi-major and semi-minor axes of the ellipse, and found the value $n = 2.4$ for the exponent. Waid (Ref. (3-24)) applied the ellipsoid formula to the two arms of the cavity outline rather than to the cavity as a whole. The symbols y and b in his definition are the portions of the cavity radius beyond

the radius of the disk which threw the cavity. Waid found the value
n = 1.8.

A study was made to determine how widely these two cavity
representations differ. The result is contained in Figure 3-22 in
which four cavity shapes are compared. Initially the generalized
ellipsoid formula was plotted for three values of the exponent (1.8,
2.0, and 2.4) using the axis ratio a/b = 6 and ignoring the different
interpretation in Waid's paper. When superimposed and properly
positioned the major part of the outlines agreed closely as is shown
in the figure. The graph for the value n = 1.8 is plotted in the
simple form

$$\left(\frac{x-6}{6}\right)^2 + y^{1.8} = 1 \tag{3-19}$$

while the Münzer-Reichardt shape is displaced axially by writing

$$\left(\frac{x-5.65}{6}\right)^2 + y^{2.4} = 1 \tag{3-20}$$

and the third outline is the true ellipse

$$\left(\frac{x-5.875}{6}\right)^2 + y^2 = 1. \tag{3-21}$$

The fourth equation compared in the figure is of the form defined
by Waid

$$\left(\frac{x-5.46}{6}\right)^2 + \left(\frac{y-0.25}{0.75}\right)^{1.8} = 1.$$

It is not possible to draw the four outlines completely in the
figure because they differ little over much of their length. One half
of the elliptical outline of equation (3-19) is drawn completely. The
graphs for equations (3-20) and (3-21) are complete only in the end
portions where they differ, and for the remainder of the length the
position of the outlines is snown by several plotted points. The
fourth outline is indicated by the nose and a set of points which
terminate at x = 0.54, y = 0.25, at the outside of an assumed
generating disk whose radius was arbitrarily chosen as d = 0.5 for
this study. The four outlines are indistinguishable over most of
their length.

It was shown by the sketch in Figure 3-8 that the cavities for
various nose shapes differ especially in the vicinity of the nose,
that is, at the tip of the ellipse. Waid derived his ellipsoid
experimentally from cavities due to a disk while Munzer and Reichardt
obtained theirs from a theoretical constant-pressure surface.
Effectively, the two bases gave different nose shapes and hence led

to different exponents. Until quantitative information is available concerning the portion of the cavity near the generating nose, it appears that the true ellipsoid is the most reasonable choice as a model. A further discussion of the vertex of the cavity will be given in a later section of this chapter.

A comparison was made between several experimentally derived cavity outlines and ellipses with approximately the same L/d_m. The agreement was fair but far from perfect, and not always consistent. In general it may be said that, to agree with the experimental outline, the ellipse appears to have too great a diameter at very small distances from the vertex, and too small a diameter further back. The agreement can be improved in the latter region by sliding the ellipse toward the vertex but only at the cost of greatly increased disparity near the vertex, perhaps over a length $L/4$. The use of the ellipse appears justified until more information is available, with the realization that the principal source of uncertainty is related to the positioning of the ellipse.

SHAPE OF TWO-DIMENSIONAL CAVITIES

While most missile noses generate cavities with axial symmetry, such as those thus far discussed, hydrofoils and struts may produce cavities which are approximately two-dimensional. The two-dimensional cavity is much more amenable to theoretical treatment than is the cavity with axial symmetry, because of the applicability of complex-variable methods, but even in two dimensions only the infinite cavity corresponding to $\sigma = 0$ has a completely rigorous solution (within, of course, the limitations of potential theory).

Although it is natural to think of the flow about a cavity as approximating that about a similar solid, whether of two or three dimensions, the actual flow on the downstream boundary of a cavity differs greatly from that near the base of a fully wetted missile, because the cavity is unable to provide a stagnation pressure at the rear. The Riabouchinsky model for computation of cavity shape and drag assumes that the cavity closes in the rear on a rigid physical surface which is a mirror image of the nose shape, and this is able to provide the stagnation pressure. Another model, which is ascribed to both Wagner and Efros, assumes the presence of a re-entrant jet, a frequently observed cavity phenomenon. In this model the free streamline bounding the cavity continues on the surface of a jet which travels back into the cavity toward its upstream end. Mathematically the jet continues on through the model to infinity, while in nature the jet dissipates rapidly due to turbulent mixing. Detailed discussions of these models are given in References (3-32) and (3-33).

The flow about the cavity near the generating nose is almost entirely independent of the behavior further downstream and the Riabouchinsky and re-entrant-jet models give nearly identical cavity shapes (including length and diameter) in spite of the great flow differences which they predict at the downstream end.

Still another cavity-flow model is due to Roshko (Ref. (3-12)). The numerical agreement between this model and the others is fairly close.

The Riabouchinsky model (Refs. (3-33), (3-34), (3-35), and (3-36)) and that of Wagner and Efros (Refs. (3-33) and (3-35)) are in good agreement and only the predictions of the former will be presented in this report. Calculations were made by Plesset and Shaffer (Ref. (3-34)) using Riabouchinsky's model for the flat plate (which may also be described as an infinite strip) and they extended the use of this model by applying it to the wedge. Their calculations for the flat plate were extended and computed more accurately by Perry (Ref. (3-36)).

Gilbarg (Refs. (3-32) (3-37)) derived formulas ascribed to Zoller (Ref. (3-38)), as approximations for $\sigma \to 0$, to the results of the Riabouchinsky model, for L/d and d_m/d of the cavity due to the flat plate; namely

$$\frac{L}{d} = \frac{4}{4 + \pi} \left[\left(\frac{2 + \sigma}{\sigma} \right)^2 - (1/2) \ln \left(4 \frac{2 + \sigma}{\sigma} \right) - \frac{1}{4} \right] \qquad (3-22)$$

and

$$\frac{d_m}{d} = \frac{4}{4 + \pi} \left(\frac{2 + \sigma}{\sigma} + \frac{\pi}{4} \right) \qquad (3-23)$$

These approximate formulas give values at $\sigma = 1$ which are accurate within 0.7 percent and they increase in accuracy rapidly for smaller σ (Ref. (3-37)).

Other simple approximations have been derived for use where $\sigma > 0$:

$$L/d = 3.5\sigma^{-1.85} \qquad (3-24)$$

due to Gilbarg and Rock (Ref. (3-29)), and

$$L/d = 8C_{DO}/\pi\sigma^2 \qquad (3-25)$$

and

$$d_m/d = 4C_{DO}/\pi\sigma, \qquad (3-26)$$

(where C_{DO} is the value of C_D for $\sigma = 0$),

due to Tulin (Ref. (3-39)). The latter two formulas are applicable to any two-dimensional shape and prescribe a scaling of L/d and d_m/d with C_{DO} rather than with $C_D^{1/2}$ as was found for axially symmetric bodies. This scaling will be investigated in the following sections.

Little information is available concerning the overall shape of the finite two-dimensional cavity. Tulin (Ref. (3-40)) applied a

linearized analysis to the study of this shape and obtained a two-term expression for it. The first term represents an ellipse while the second term gives a small contribution to the diameter at the rear of the cavity but its largest contribution just behind the separation plane. He finds the aft end of the cavity near elliptical at small cavitation numbers.

Cavity Length L/d

In Figure 3-23 the dashed line is a plot of Perry's data (Ref. (3-36)) for the length of the cavity due to a two-dimensional flat plate, based on Riabouchinsky's model. The graph is almost straight on log-log coordinates. As has been stated, values derived from Zoller's approximate formula, equation (3-22), agree closely with the exact formula, and they are shown as an extension to Perry's data at lower values of σ, by a dot-dash line. The approximation of Gilbarg and Rock, equation (3-24), is plotted as a solid straight line on the log-log coordinates, and it agrees closely with the dashed graph in the region $0.05 < \sigma < 0.5$. Tulin's formula, equation (3-25), gives a straight line whose position is indicated by two large dots near the ends of the graphs on Figure 3-23. It is in good agreement with the graphs for small values of σ, for which it was intended.

The data points plotted on Figure 3-23 are from water-tunnel measurements by Waid (Ref. (3-41)). The agreement with theory is good except for the two data points at the lowest values of σ. These points are undoubtedly in error because of the effect of the tunnel walls, which is discussed in another section.

In Figure 3-24 Perry's calculated values of L/d for wedges (Ref. (3-36)) are compared with equation (3-22), Zoller's approximate formula. In this comparison, miscellaneous values of L/dC_{Do} for various wedge angles are plotted as functions of σ, in a test of the scaling indicated in equation (3-22), which is represented by the graph. The values of C_{Do} were taken from Ref. (3-27) and are shown in Table 3-2.

Table 3-2

DRAG COEFFICIENTS FOR WEDGES FOR $\sigma = 0$

Wedge Half-Angle, in Degrees	C_{Do} (Ref. (3-27)
5	.105
15	.283
30	.487
45	.639
60	.744
75	.821
90 (disk)	.880

A graph of L/dC_{Do} based on Zoller's formula, equation (3-22) is given again on Figure 3-25 together with values from the experiments of Waid (Ref. (3-41)). The scoop channel included there is the two-dimensional analog of the stagnation cup, a channel whose cross section is that of a rectangular cup with thin walls. The agreement between theory and experiment is fairly good for $\sigma > 0.7$ and for the 5° wedge, but is poor under other conditions because of the effect of the tunnel walls to be discussed later.

Cavity Diameter d_m/d

Predictions of the maximum width of the cavity due to a flat plate are compared with experiment in Figure 3-26. The solid line is plotted from Perry's data (Ref. (3-36)) based on the Riabouchinsky model; the dashed extensions of this curve are from Zoller's approximation formula, equation (3-23). As already mentioned, Zoller's formula agrees well with the exact calculations. The lower straight graph is from the equation

$$d_m/d = 4C_{Do}/\pi\sigma \qquad\qquad (3-27)$$

given by Tulin (Ref. (3-39)) as an approximation for all two-dimensional shapes as $\sigma \to 0$. The agreement with other predictions is satisfactory for small σ. Data points plotted in Figure 3-26 are from the experiments of Reichardt (Ref. (3-21)) and Waid (Ref. (3-41)). The agreement with theory is satisfactory except that Waid's data are high because of the wall effect, at lower values of σ, as was found for L/d.

Zoller's approximate formula for d_m/dC_{Do} for wedges is compared with values from the exact calculations of Perry in Figure 3-27. The agreement is quite satisfactory.

Theoretical and experimental values of d_m/dC_{Do} are compared in Figure 3-28. The "agreement" is poor, as in Figure 3-25 for L/dC_{Do} with $\sigma < 0.7$, because of tunnel-wall effects.

Fineness Ratio L/d_m

It is reasonable to expect the cavity fineness ratio to be a function only of σ in the two-dimensional case, as it was for axially symmetric noses. For the flat plate, Zoller's formulas for L/d and d_m/d, equations (3-22) and (3-23), can be combined to give L/d_m, as can the corresponding formulas of Tulin, equations (3-25) and (3-26). Since Zoller's formulas give good approximations to the rigorous Riabouchinsky values it is convenient to take their ratio as a basis. A plot of this ratio is given in Figure 3-29. The graph is almost a straight line on log-log coordinates in the region shown and it is almost as straight throughout the range $0.005 < \sigma < 5$.

The data points plotted on Figure 3-29 are taken from the experiments of Waid (Ref. (3-41)). Experimental data for the 5° cone are much lower than theory and some other values are rather high.

3-22

The expression for L/d_m which is given by Tulin's formulas, equations (3-25) and (3-26) is simply

$$L/d_m = 2/\sigma \qquad (3-28)$$

The value $2/\sigma$ is in excellent agreement with Zoller's data, as can be seen from Figure 3-29. The approximate formula

$$L/d_m = (2 + \sigma)/\sigma \qquad (3-29)$$

which Tulin obtained from a linearized analysis (Ref. (3-42)) agrees with Zoller's values only for small values of σ.

Comparison of Two- and Three-Dimensional Cavities

A comparison of the graphs which have been given for two- and three-dimensional cavities shows that the two-dimensional cavities have lengths and diameters which are much larger than those of three dimensions for the same drag coefficient. Usually this difference amounts to an order of magnitude. The fineness ratio, L/d_m, of the flat-plate cavity can be seen from Figures 3-20 and 3-29 to be 3 to 4 times as great as that for the disk.

CAVITY SHAPE FOR $\sigma = 0$

Thus far in this report, geometry has been discussed only for the finite cavities which are produced when the cavitation number is greater than zero. When $\sigma = 0$, theory shows that both the cavity length and diameter become infinite. The cavitation number

$$\sigma = \frac{p_\infty - p_C}{(1/2)\rho U_\infty^2} \qquad (3-2)$$

will be zero if the freestream velocity (or missile velocity) becomes infinite or if the pressure in the cavity is equal to that of its surroundings. In the former case the pressure differential has no time in which to effect a cavity closure and in the latter there is no pressure differential to bring it about. Although these conditions may not be attainable in practice, very large cavities are observed, and many of the aspects of the infinite cavity can be approached especially when the cavities are nted, for example, following water entry.

The equation of the outline of the two-dimensional cavity due to a flat plate (or infinite strip) with $\sigma = 0$, can be calculated exactly for the potential case by use of the methods of the complex variable. The result is given in the parametric form (Ref. (3-32))

$$
\left.
\begin{aligned}
x &= \frac{L}{4 + \pi} \left[t\sqrt{t^2 - 1} - \ln(t + \sqrt{t^2 - 1}) \right], \\
y &= \pm \frac{L}{2} \pm \frac{2L}{4 + \pi}(t - 1) \qquad t > 1
\end{aligned}
\right\} \qquad (3-30)
$$

3-23

where L is the width of the infinitely long flat plate causing the cavity and t is merely a connecting parameter. The equations (3-30) are almost parabolic and the simple parabolic equation

$$x/L + 1.00 = 1.588 \ (y/L)^2 \qquad (3-31)$$

gives (Ref. (3-43)) the radius y of equation (3-30) within 1.0 percent for 1.7<x<23 and within 2.4 percent for 1.3<x<55.

Presumably the width of infinite two-dimensional cavities should scale like d_m/d for the finite cavity in equation (3-27). Accordingly, the diameter is obtained by multiplying the radius y of equation (3-30) or (3-31) by $2C_{Do}$ for the desired two-dimensional "nose," and dividing by 0.88, C_{Do} for the flat plate.

No comparable predictions have been made for cavities due to bodies of revolution. There exists only Levinson's proof (Ref. (3-44)) that for σ = 0 the asymptotic shape of the axially symmetric cavity (that is, the shape as x → ∞) is

$$\left(\frac{y}{C_D^{1/2}d}\right)^2 \doteq \frac{1}{(\ln x)^{1/2}} \left(\frac{x}{C_D^{1/2}d}\right) \qquad (3-32)$$

The scaling shown for x and y in equation (3-32) is contained implicitly, but not explicitly, in Levinson's paper. Unfortunately, the method of derivation of equation (3-32) tells nothing about the length unit to be used in the logarithmic factor. Proceeding from rather cautious inferences of Dr. E. P. Cooper (contained in an informal, unpublished memorandum dated September 19, 1949), Kendrick (Ref. (3-45)) expressed the quantity x in the logarithmic factor in the unit r_e, equal to the radius when a spherical nose is involved, or, in general

$$r_e = (C_D/0.3)^{1/2}r,$$

where r = d/2 is the radius of the body which is generating the cavity. Thus, Kendrick obtained an expression which can be written

$$\left(\frac{y}{C_D^{1/2}d}\right)^2 = \frac{1}{[\ln(0.6x/C_Dd)]^{1/2}} \left(\frac{x}{C_D^{1/2}d}\right) \qquad (3-33)$$

May reported (Ref. (3-43)) an experimental approximation to the portion of the cavity near the generating axially symmetric nose, namely

$$(y/C_D^{1/2}d)^2 = 0.583 \ (x + a)/C_D^{1/2}d \qquad (3-34)$$

where a is a parameter which allows for the fact that the vertex of
the cavity is not at the nose tip of the missile. In equation (3-34)
the distance x along the cavity is measured from the nose tip. The
values of $\underline{a}$ found (Ref. (3-43)) for three nose shapes and the values
assumed for $\overline{C_{D_O}}^{1/2}$ (Ref. (3-27)) are

nose shape	a	$(C_{D_O})^{1/2}$
disk	0.4	0.898
sphere	0.5	0.515
45° cone	-0.2	0.706

The table shows that the vertices of the computed cavities for the
disk and sphere are in front of the nose tip, but that the tip of the
45° cone projects through the vertex of the computed cavity.

The derivation of equation (3-34) was based on the following
reasoning. When $o = 0$ the growth of a cavity is influenced by no
forces, under the usual ideal conditions, except those within the
water itself. When a cavity is being generated, a portion of the
cavity starts to grow with a transverse velocity which is that
originally given to the water, but when the cavitation number has a
significantly positive value, the cavity wall is soon slowed down
measurably by the difference in pressure between the cavity and its
surroundings (and, of course, by the forces within the water). If
the missile has large mass, so that its deceleration can be neglected,
and is traveling at high speed with small differential pressures,
a portion of cavity near the generating nose will reach appreciable
diameters before being perceptibly affected by the external pressures.
The shape of this portion of the cavity should be that of a part of
the cavity of zero cavitation number. The approximate formula given
by equation (3-34) is a pure parabola, and equations (3-33) and (3-34)
differ only in the logarithmic factor.

Equations (3-33) and (3-34) are compared in Figure 3-30 for the
case of a hemispherical nose. The agreement is good except near the
generating nose where equation (3-33) becomes unusable because of a
singularity.

CAVITY SHAPE FOR BODIES AT ANGLES OF ATTACK

The cavities considered so far have all been produced by bodies
at zero angle of attack α, that is, for axially symmetric bodies the
flow was assumed parallel to the axis of symmetry; for two-dimensional
bodies with two-fold symmetry the flow was parallel to the plane of
symmetry and perpendicular to the body's leading edge in this plane.

Little quantitative data have been published on the geometry of
cavities due to bodies at non-zero angles of attack. The information
which is available is outlined in the following sections.

Disks

The most extensive data on cavities due to bodies with $\alpha \neq 0$ were obtained experimentally by Waid (Ref. (3-24)) for the circular disk. His equations for the disk at zero angle of attack have already been discussed:

$$d_m/d = 0.534\sigma^{-0.568} + 1 \qquad (3-5)$$

$$L/d = 1.08\sigma^{-1.118} \qquad (3-10)$$

He measured also the cavities produced in the water tunnel by disks inclined at angles of 10, 20 and 30 degrees to the flow over a cavitation-number range of $0.043 < \sigma < 0.098$. These cavities are asymmetrical, as shown in the sketch on Figure 3-31. Since the maximum lateral displacement of the cavity wall is not at the same position on the two sides, it is impracticable to speak of a cavity width d_m. Instead, separate radii r_m are shown on Figure 3-31, with r_m/r equivalent to d_m/d. Similarly, since the cavity length is taken as twice the distance to the position of maximum width, a length is ascribed to each side of the cavity.

On these bases Waid derived separate empirical formulas for the portions of the cavity associated with the forward and downstream edges of the disk. His formulas may be written separately for each side of the cavity,

$$r_m/r = 2Q/\sigma^S + 1 \qquad (3-35)$$

$$L/d = 2M/\sigma^{1.118} \qquad (3-36)$$

Three empirically determined parameters, M, Q, and S, are included in these formulas. All are functions of α and are plotted against α in Figure 3-31. The parameter M has the analytical description

$$M = 0.54(1 \pm \sin^2\alpha)$$

where the sign of $\sin^2\alpha$ is taken opposite to the sign of the angle α.

Other Axially Symmetric Shapes

No information at $\alpha \neq 0$ appears to have been reported for the geometry of cavities due to axially symmetric shapes other than the disk.

Rouse (Ref. (3-46)) has measured the pressures on the nose and on the cylindrical afterbodies of a variety of nose shapes at angles of attack. Some information as to the extent of the cavities on these bodies at higher values of σ, might be obtained from the values of the pressure which he reported.

Wedges

Cox and Clayden (Ref. (3-47)) obtained interesting results in a mathematical analysis of the cavitating flow past a yawed wedge. The stagnation point which is at the vertex of the wedge when $\alpha = 0$, moves onto the windward face when the wedge is yawed. As the flow separates on the two sides of the stagnation point the dividing streamline going toward the vertex is found to cause a cavity beyond the vertex on the lee side of the wedge, and such a cavity has been photographed by Cox and Clayden. If this dividing streamline merely continues downstream to infinity, the flow is that past a yawed flat plate. Cox and Clayden show that this streamline cannot reattach to the wedge face. Instead it is assumed that after approaching the wedge face this line doubles under and passes up the face toward the vertex (and infinity) as a re-entrant jet. The general subject of re-entrant jets will be discussed in a later section.

EFFECT ON CAVITY SIZE OF TUNNEL WALLS OR FREE SURFACE

While it may be expected that missiles will ordinarily travel in regions where the water expanse is effectively infinite, tests on which analysis is frequently based have walls or free surfaces so placed as to seriously affect the cavity size. A number of studies have been made of this effect, especially as related to two-dimensional flows. The methods of solution of the problem will not be discussed in this report, but some of the results will be presented, principally as they are collected in a paper by Cohen and DiPrima (Ref. (3-48)).

The problem must be divided between two- and three-dimensional flows. Much more has been done in two dimensions because of the availability of the method of complex variables. Even in that case the solutions are almost solely based on linearized models. The treatment is also dependent on whether the effect is due to a wall or a free surface, representing the use of a closed or open-jet water tunnel. In general, single surfaces must also be considered, but this case will not be discussed here.

The concept of choking or blockage must first be considered for the closed tunnel. The constriction of the flow causes an increase of local velocity and a larger cavity. At a certain cavitation number σ_∞, well above zero, the flow may become blocked; the cavity length is effectively infinite and lower cavitation numbers are unattainable.

Values of the cavitation number at blockage, σ_∞, are given in Figure 3-32. Two two-dimensional cases are shown, the flat plate and the 15° half-angle wedge; with the result of approximate calculations for the three-dimensional circular disk in a tunnel of circular cross section. The quantity d/h is the width or diameter of the model divided by the width or diameter of the tunnel. It will be seen that a closed tunnel whose width is 20 times that of a flat plate (d/h = 0.05) can be used only for values of σ greater than 0.6, while a

15° wedge, because of the smaller disturbance of the flow, could possibly be tested at $\sigma > 0.33$. For the corresponding three-dimensional flows the blockage occurs only at somewhat lower cavitation numbers, and for the circular disk $\sigma_\infty < 0.1$ for $d/h = 0.05$.

In Figure 3-26 a graph of d_m/d was given based on Perry's calculations from the Riabouchinsky model with no wall effect, that is, $d/h = 0$. The tunnel in which Waid obtained his data shown in Figure 3-26 had $d/h = 0.027$. Cohen and DiPrima (Ref. (3-48)) calculated two values of the cavity width for the flat plate. Their points, shown by the square symbols in Figure 3-26, are in good agreement with Waid's data. For the upper point $d/h = 0.025$ and for the lower, $d/h = 0.0295$. In Figure 3-33, d_m/d data are given for the 15° half-angle wedge. Graphs are shown for several values of d/h, including $d/h = 0$, and data due to Waid (Ref. (3-41)) are seen to agree well with the graph for $d/h = 0.026$.

The effect of jet free surface is less than that due to solid walls and is of opposite sign, so that cavities are reduced slightly in length and cross section. In addition, in such tunnels the jet is commonly restricted by a plane, transparent plate on one or two sides, to permit better observation. The effect of such a plate is to add a solid-wall effect to that of the free jet and to partially compensate for it. Still another complication arises when the free-jet tunnel is vertical as at the St. Anthony Falls Hydraulic Laboratory of the University of Minnesota. It will be shown in a later section that gravity tends to lengthen cavities in the vertical tunnel.

Length data for cavities due to a flat plate are given in Figure 3-34. Graphs are based on calculations for unbounded flow and for the open-jet tunnel. Waid's measurements in a closed tunnel with $d/h = 0.027$ is seen to be in good agreement with one of the calculated values. Corresponding data for the 15° half-angle wedge are given in Figure 3-35. The agreement between Waid's data in the closed tunnel and the theoretical predictions is only fair. Silberman's measurements (Ref. (3-49)) in the vertical open-jet tunnel show a considerably shorter cavity than that predicted for the same jet-to-model size in spite of the fact that gravity would be expected to lengthen the cavity rather than contribute to its shortening. The reason for this difference is not known.

Because of the greater mathematical difficulty, fewer studies have been made for the axially symmetric case, but cavitation numbers at blockage were compared for circular disks and the flat plate in Figure 3-32. As compared with the two-dimensional case, blockage for the disk does not occur until a much lower cavitation number is reached, but the difference would be considerably reduced if the comparison were based on cross-sectional area rather than on width and diameter.

Armstrong and Tadman (Ref. (3-8)) derived a technique for computing the corrections for circular closed and open-jet tunnels at small σ and small L/h. They found that L and d_m are changed by an

amoun' proportional to $(L/h)^3$ from the values in unbounded flow, with the increase in a closed tunnel about four times the decrease in a free jet.

Wall Effect on Water-Entry Cavities

A test was carried out (Ref. (3-50)) to determine the effect of tank walls on the cavities due to small steel spheres fired vertically into water. Results showed that the effect on the cavity development was negligible when the tank width was at least five times the maximum diameter of the cavity.

CAVITY FLOW PHENOMENA

Flow About the Cavity

The velocity U_C on the "free streamline" bounding a cavity can be determined from Bernoulli's equation, which has the form

$$p_\infty + (1/2)\rho\ U_\infty^2 = p_C + (1/2)\rho\ U_C^2$$

if gravity is neglected, and from the definition of the cavitation number

$$\sigma = (p_\infty - p_C)/(1/2)\rho U_\infty^2 = (U_C/U_\infty)^2 - 1. \qquad (3-2)$$

Hence, the velocity of the free streamline is

$$U_C = U_\infty(1 + \sigma)^{1/2}. \qquad (3-37)$$

For a stable cavity the pressure within the water cannot anywhere be less than the cavity pressure; the velocity on the cavity wall will be greater than the freestream velocity (or equal to it if $\sigma = 0$); and the free streamlines are everywhere convex toward the cavity. Cavity pressure will be discussed in a later section but it should be mentioned here that pressure variations throughout the cavity are small enough that both cavity pressure and the velocity of the bounding streamline may generally be assumed to be uniform, unless variations of these quantities are especially at issue. The constancy of flow on the cavity wall does not extend to the aft end of the cavity, where the flow is generally unstable. This region will be discussed separately.

The cavities discussed in this section are "natural cavities", that is, they are not "ventilated" by blowing air into them. The assumption that the cavities are steady requires some discussion. When flow separation occurs at the nose of a missile the dividing streamlines enclose a wake, an area where the flow velocities are relatively small. When a liquid is flowing at sufficient speed the dividing streamlines enclose a space containing only gas - the wake has been replaced by a cavity. Between the conditions of the gas-filled

cavity and of the water-filled wake there is a flow condition in which the wake region contains both gas and liquid.

If the flow speed over a fully wetted body is slowly increased the incipience of cavitation is seen in the formation of vapor-filled bubbles along separating streamlines. At first these cavities collapse rapidly but at greater flow speed they persist for a longer distance of travel and grow in size and number. As the speed continues to increase, the separation of the flow becomes visible to the eye because of the cavitation. This surface becomes increasingly cavity-like in appearance but the shape of the surface changes little except with changes of σ. In other words, at a given cavitation number there is little change in the "cavity" geometry between the low-speed cavitating condition and the full cavity, although short-duration flash photography will show that in one case the "cavity" is only an appearance due to the passage of small cavitation bubbles. This condition was reported by Eisenberg and Pond (Ref. (3-26)) with the presentation of the photographs of Figure 3-36. Figures 3-36A and 3-36B show photographs taken under the same condition of cavitation incipience, and Figures 3-36C and 3-36D under a condition where the cavity appears rather well-developed. In the latter case the cavity is filled with foam rather than with air alone, but it exhibits the properties of a steady cavity since the average envelope appears steady. Eisenberg reported (Ref. (3-2)) that the water was not all eliminated from their cavities at σ = 0.116, the lowest value of σ reached in their experiments. It is quite remarkable that the cavity shape at a given value of σ seems to have almost no dependence on whether the cavity is gas-filled or filled with a mixture of gas and liquid.

There is some interest in the consideration of the transverse motion of the cavity wall as it would appear to an observer traveling with freestream velocity, that is, the motion of the cavity wall in a transverse plane viewed in a tank, as a missile passes by with constant velocity. This behavior will be discussed later in connection with the water-entry cavity. The kinetic energy represented by the transverse velocity given to the water by the missile nose, is expended in the expansion of the cavity against the pressure difference between the cavity and its surroundings. The cavity reaches its maximum diameter when this energy has been used up, and almost as much energy is developed again during the cavity collapse. The energy is finally dissipated in the turbulent mixing at the rear of the cavity. The cavity outline is, of course, a plot against time of the cavity diameter in a given transverse plane (assuming a constant freestream velocity).

Closure Phenomena of Natural Cavities

In the discussion of cavity shape it was brought out that the steady cavity is approximately ellipsoidal but that the defining measurements are made on the front half of the ellipsoid. It is easily seen that a purely ellipsoidal shape is unacceptable since the free streamlines would converge to the closure point with equal and

opposite velocities, greater than the freestream velocity. The cavity differs from a solid ellipsoidal body in that there is no rear solid surface to support a downstream stagnation pressure and that the pressure exerted by the water on the cavity is substantially constant.

As mentioned earlier, Riabouchinsky suggested a mathematical model of the flow in which the cavity closes on an afterbody which is a mirror image of the wetted portion of the nose. In the absence of the closing surface of the Riabouchinsky model, instead of a pressure build-up at the rear of the cavity, a so-called "re-entrant jet" is formed which travels back into the cavity toward the cavity-generating nose. Mathematically the jet travels past the nose to infinity and the physical difficulties are avoided mathematically by putting the jet on a second Riemann surface. Actually the jet does sometimes hit the missile or plunge through the cavity wall past the generating nose. It is not unusual in an air-containing cavity following a missile in free flight, for the re-entrant jet to strike and apparently enlarge the cavity around the forward end of the missile. Actually the jet, by impacting the cavity wall, has driven air into the water, and the cloud of bubbles remains as an excrescence on the cavity. This cloud does not travel with the missile and the cavity seems to travel through the surrounding envelope and leave it behind in the wake.

The cavity with re-entrant jet is never completely steady. The jet disintegrates by hitting the lower cavity wall when deflected by gravity in a horizontal flow, or by self-flooding when the jet is upward in a vertical water tunnel. By its collapse the jet interferes with its own production and fluctuates in both length and vigor.

The jet is assumed to have the velocity of the bounding streamline of the cavity

$$U_c = U_\infty (1 + \sigma)^{1/2} \tag{3-37}$$

although in a real liquid it may be nearer to the freestream velocity (Ref. (3-51)).

It has been assumed that in the two-dimensional problems of flat plates and wedges, the thickness of the jet can be determined by equating the momentum generated in the jet in unit time to the drag force on the generating nose. The resulting ratio, jet thickness J to thickness d of the wedge, is (Ref. (3-32))

$$J/d = (1 + \sigma + \sqrt{1 + \sigma}) \, C_D/2. \tag{3-38}$$

Swanson and O'Neill suggested (Ref. (3-52)) an approximation to the jet diameter for the case of axially symmetric bodies. For this case the momentum theory gives a relation identical with equation (3-38) except that J/d is replaced by A_j/A, the corresponding areas for the three-dimensional case. With the approximation

$$C_D \doteq C_{Do} (1 + \sigma) \tag{3-39}$$

the result

$$\frac{A_j}{A} \doteq \frac{C_{Do}\sqrt{1 + \sigma}}{2[1 + \sqrt{1+\sigma}]} \doteq \frac{C_{Do}}{4} \left(1 + \frac{\sigma}{4}\right) \tag{3-40}$$

is obtained (Refs. (3-32)(3-53)). If C_D is known it would appear better to use equation (3-38) with J/d replaced by A_j/A or the approximation

$$A_j/A \doteq (C_D/4) (1 + 3\sigma/4) \tag{3-41}$$

which is equivalent to equation (3-40) without the use of equation (3-39).

The re-entrant jet is strong for short cavities (of large σ), and may be very weak when the cavity is long.

Air Entrainment

Streams of small bubbles (or froth or foam) may be seen in the wake of a cavity which contains air. (Presumably a pure vapor cavity leaves no bubbles in its wake (Ref. (3-21)). For the cavities attached to missiles after water entry, such entrainment decreases the air content of the cavity. If the cavity is ventilated, that is, if air is infused into the cavity to create or enlarge the cavity, the entrained air must be replaced if the cavity is to maintain its size.

Although other sources doubtless contribute (Refs. (3-54)(3-55)), most of the air entrainment from the cavity is believed to be due to the re-entrant jet. At some point the air is mixed with the jet during its collapse. It has been shown (Ref. (3-56)) for two-dimensional cavities, that the entrainment is approximately twice as great for the cavity in a vertical tunnel as for the horizontal cavity. This has been ascribed to the fact that the vertical jet strikes both side walls of the cavity while the jet in the horizontal cavity, because of gravity, strikes only the lower wall. The mixing may occur largely where the jet strikes the side wall or, as has been claimed (Ref. (3-54)), further to the rear where the air in the boundary layer is carried backward into the collapsing jet.

The high-speed jet from a rocket, air or steam exhaust, directed backward from the rear of the missile, will increase the entrainment rate if it strikes the downstream mixing region. If it breaks up before reaching this region it will presumably act only to increase the ventilation, and hence the pressure, of the cavity.

Gas Flow Within the Cavity

Whether a cavity contains air or only water vapor, boundary layers form on the cavity wall, representing a flow of the gas or vapor toward the rear of the cavity (Ref. (3-54)). Along the center line of the cavity a reverse flow occurs because of the flow direction of the jet and because the rear of the cavity generally is a region of slightly elevated pressure. Hence there is a circulation of gas within the cavity. When only vapor is present, vapor which is entrained by the flow and therefore lost to the cavity, must be replaced. Because of the flow pattern, evaporation should occur preferentially near the front end of the cavity.

When cavities are ventilated, air is usually introduced just behind the generating nose and, in the steady condition, enough air must be added to replace the air entrained. This results in a flow aft in the cavity. Nevertheless Silberman and Song (Ref. (3-57)) have determined that the mean air velocities within cavities are very small compared with the water velocity on the cavity wall.

EFFECT OF VENTILATION ON CLOSURE PHENOMENA

It was shown in an earlier discussion that the cavity shape depends mainly on cavitation number and cavity size mainly on the drag force and, for a given cavitation number, the size and shape are almost independent of whether the cavity contains air or only water vapor. Cavities are frequently ventilated, especially in the water tunnel, by blowing air into the region at or immediately behind the cavity-generating nose.

Ventilation assists in the production of cavities which are large and of small cavitation number without the use of excessively low freestream pressure or high tunnel speeds. Advantages may accrue from the presence of enveloping cavities on a missile, hydrofoil, or propeller through the reduction of cavitation damage, cavitation noise, and skin friction. Sometimes ventilation is unavoidable as in the case of rocket discharge or the venting to the atmosphere of a shallow-running hydrofoil.

By ventilation a cavity may be created where no cavity was before. If ventilating air is introduced into the flow at the tip or shoulder of a missile nose (or at the leading edge of a hydrofoil), bubbles appear and the flow carries them into the wake. As the ventilation rate increases, the bubble density increases, building up to a froth and, under suitable conditions, a cavity appears and grows to an enveloping size.

If air is vented from a point which is not in or near an existing cavity, a cavity will not form upstream or the point of venting (Refs. (3-55)(3-58)(3-59)) unless the pressure in the water at the ventilating point is very near the vapor pressure. Thus rocket-discharge gases will usually not cause a cavity to form upstream of the base of the rocket, and ventilation will not cause an enveloping

cavity at low speeds unless the discharge is very near the edge at which separation tends to occur. On the other hand, if a missile or the portion of a missile near the venting point, is already enveloped in cavity, the gases discharged will fill the existing cavity space and usually increase its size and pressure, and decrease the cavitation number. The most convenient method of ventilating (Ref. (3-55)) is probably to introduce enough air near the front of the body to cause a cavity to form, and to supply the remainder of the ventilating air near the base of the body.

Lang (Ref. (3-59)) has reported a hysteresis in the development of supercavitation on hydrofoils. As the ventilation increases, the collapse point of the cavity travels back on the foil until it reaches the trailing edge. At a critical ventilation rate this point springs rearward to a point about two chord lengths behind the trailing edge of the foil. During decrease of ventilation a similar discontinuity occurs when the rear of the cavity jumps from a point about one chord length behind the foil to a point just ahead of the trailing edge.

In 1951 Swanson and O'Neill (Ref. (3-52)) made a most interesting experimental study of the behavior of ventilated cavities in a horizontal water tunnel. At higher cavitation numbers they obtained cavities with re-entrant jets but, as the ventilation was increased and σ reached a critical value, the jet tended to be replaced by a pair of trailing vortices, through whose hollow cores it was assumed that the air flowed into the wake. A copy of their entrainment curves is given in Figure 3-37.

They used an entrainment coefficient defined by the equation $C_Q = Q/U_o d^2$, where Q is the entrainment or ventilation rate in cubic feet per second (at NTP, that is, at normal temperature, 0°C, and normal pressure, 760 mm/Hg). To represent the same quantity C_Q, Campbell and Hilborne (Ref. (3-30)) used the symbol C_{Qd} and Cox and Clayden (Ref. (3-59)) used C_{Qd2}. Reports from the St. Anthony Falls Laboratory of the University of Minnesota, who worked with two-dimensional shapes for which C_Q was not designed, use W or W_A, the mass rate of air added, in pounds per second, equivalent to Q rather than C_Q. The quantity C_Q was chosen, of course, on the assumption that the entrainment is proportional to the cross section of the obstacle and to the freestream velocity.

Re-Entrant Jet Cavities

A cavity which is ventilated at a low rate continues to be closed by a re-entrant jet and the general appearance of the cavity is the same as when unventilated. Experimenters show little agreement, however, in the relations which they report between C_Q and σ for ventilation in this region. The varied behavior is surely due in part to the variety of experimental conditions in the tests. Research has been done on axially symmetric bodies, on two-dimensional bodies, and on wing-like plates (usually of rectangular planform). Generally σ_v had too high a value to permit a cavity to form without ventilation.

The facilities used include the horizontal closed-jet tunnel, the free-jet vertical tunnel, and straight and circular towing basins. Gravity causes differences in cavity shape between the horizontal and vertical tunnels, and mixing and entrainment due to the jet striking the cavity wall differ considerably in the two facilities. The jet itself is never quite steady and is involved with the trailing vortices. Sometimes the jet is strong enough to plunge past the generating body into the oncoming flow, with an augmented mixing, and sometimes it strikes the ventilating jets and thus affects the incoming flow and the amount of entrainment (Ref. (3-57)).

In Figure 3-37 the re-entrant jet is associated with the portions of the graphs to the right of the minima. The positive slope in this region indicates that the cavity pressure and size decrease as the ventilation rate increases. The authors explain the behavior by the strengthening of the jet as the cavity shortens, with consequent increase of entrainment due to mixing where the jet strikes the cavity wall. Although this behavior appears anomalous, it was verified by Cox and Clayden (Ref. (3-60)) who reported that, in this region, "a slight increase in air entrainment rate was observed with further decrease in the length of the cavity." Brennan reported measurements (Ref. (3-61)) almost wholly in the jet regime, made during ventilation of the cavity due to a 3-inch sphere. He gave data for only three values of σ, but they show almost throughout, the same qualitative behavior as that found by Swanson and O'Neill.

It might be significant that all of these tests in which a positive slope was found in the re-entrant jet region were made with horizontal cavities due to axially symmetric bodies. Swanson and O'Neill, and Brennan used water tunnels, working with a 1-inch disk and a 3-inch sphere respectively. Cox and Clayden made tests on 1/2-, 3/4-,and 1-inch disks in a towing basin.

Most of this research was carried out under experimental conditions which would not support a cavity without ventilation. Swanson and O'Neill described their re-entrant jet cavities as being on the verge of collapse as the ventilation was changed. This collapse would not occur if σ were sufficiently low, that is, with high velocity and low ambient pressure.

Tests at the St. Anthony Falls Laboratory have shown a negative slope of the W against σ graph in the re-entrant jet region (Refs. (3-55)(3-57)). Qualitatively similar results were obtained in a vertical water tunnel and in a towing basin, but the tests were made on two-dimensional bodies or plates with aspect ratios of 2.5 to 6. The negative slope is much easier to explain and these programs were quite extensive.

Because of the rather complicated nature of the problem of ventilation with re-entrant jet closures, and the incompleteness of available information, little quantitative data will be given here. Silberman and Song (Ref. (3-57)) reported a dependence on the ratio σ/σ_V while Schiebe and Wetzel (Ref. (3-55) used the related quantity

$p_a = p_c - p_v$, the partial pressure of air in the cavity. The latter authors have given a ventilation formula which may be written (Ref. (3-56))

$$Q = (\frac{0.59 - 0.83\sigma}{0.82 + 1.66\sigma})\ (\frac{nAC_D}{1+\sqrt{1+\sigma}})\ (\frac{p_a}{p_{atm}}) \qquad (3\text{-}42)$$

Because this equation was derived for two-dimensional or foil-like bodies of finite span, it is written for Q rather than C_Q, which is related to axially symmetric shapes. The parameter n has the value unity for horizontal cavities and 2 for vertical cavities, representing the number of cavity walls struck by the jet. In the pressure ratio, p_{atm} is the atmosphere pressure related to the volume rate Q.

The Critical Value of the Cavitation Number

At certain values of σ, the re-entrant jets tend to disappear or at least to become weaker and part-time. These are also the maximum values of σ at which the vortex behavior appears. Swanson and O'Neill (Ref. (3-52)) first observed that this critical value of the cavitation number σ^*, approximately obeys the relation

$$F\sigma^* = 1 \qquad (3\text{-}43)$$

where $F = U_\infty/\sqrt{gd}$ is the Froude number based on body diameter.

Figure 3-38, which is copied from Campbell and Hilborne (Ref. (3-30)) shows a plot of the critical cavitation number against F, for small disks. It is evident that the approximation given in equation (3-43) is good over a considerable range, although the product is somewhat higher than unity at the lower Froude numbers.

The Vortex Regime

The trailing vortices observed by Swanson and O'Neill are easily explained. Because of gravity and the uniform pressure in the cavity, the flow speed must be greater below than above the cavity, and the resulting circulation is responsible for the vortices (Ref. (3-60)). This will be discussed further in the section dealing with the effects of gravity.

The steep slope of the entrainment graphs in the vortex region of Figure 3-37 indicates that large increases in the ventilation rate are required to produce small changes in the cavity pressure. The air was supposed to escape through the expanding hollow cores of the vortices but Silberman and Song reported (Ref. (3-57)) that the same rapid loss of gas occurs for non-lifting bodies in a vertical tunnel where there are no trailing vortices. Even when the vortices occur, the flow through them is sometimes into, rather than out of, the cavity. For bodies of large aspect ratio several pairs of vortices may appear (Ref. (3-56)).

Figure 3-39 contains data believed to be significant for the ventilation of small disk cavities (Refs. (3-30)(3-52)(3-60)). The Froude number is shown for each C_Q - versus-σ graph, and the dependence on Froude number is evident. A test of this dependence is made in Figure 3-40 where plots of σ against F are given for data read from Figure 3-39 at C_Q values of 0.2 and 0.4. The data for 3/4-inch and 1-inch disks agree well on Figure 3-40 and a single graph is drawn for them. Data for the 1/2-inch disk lie slightly lower. This lack of scaling was observed by Campbell and Hilbourne (Ref. (3-30)). They reported that tests to detect a dependence on Weber number (surface tension) were unsuccessful, and suggested that the effect may be due to Reynolds number.

Ventilated cavities both with re-entrant jets and with trailing vortices are usually observed to be "steady" although having short-period fluctuations. Obviously from Figure 3-39 it is not possible to obtain cavities which are arbitrarily large and of low cavitation number, by ventilation.

Cavity Pulsations

Silberman and Song (Ref. (3-57)) reported that another phenomenon occurs during the ventilation process. While ventilating the cavity due to a two-dimensional plate in a vertical free-jet tunnel, they obtained the data plotted in Figure 3-41. The graphs appear similar to those already discussed except that the steep portions are presumably vertical. The test showed that when σ had been reduced to a value which depends on the initial cavity conditions, a further increase of the ventilation rate caused a violent vibration of the cavity, with pulsating changes of its length and diameter, as a wave along the cavity deformed the wall. No pulsations occurred unless σ was reduced to less than 0.19 times the initial cavitation number, σ_V. The initial condition may be a fully wetted one, that is, the cavity might not appear until ventilation is begun. Further, they found that the air required at a given σ, depends solely on the initial value, σ_V. In the vibrating cavity, air is apparently not lost from the cavity as a continuous stream of bubbles, but as a mass of air-water mixture discharged periodically from the rear of the cavity.

While the cavity pulsates, the increasing ventilation rate does not increase the average cavity pressure. Instead, σ remains roughly constant while the cavity vibrates at a rather steady rate of 40 to 60 Hz with the production of an audible sound (Ref. (3-55)).

No further changes occur as the ventilation rate increases until, at a high value, the average length and pressure of the cavity suddenly increase, with a decrease of σ. The vibrations are now less vigorous and the deformation of the cavity wall is two waves long. This has been called a second-stage cavity. With further ventilation increases, similar discontinuous changes can occur producing up to six such stages.

The cavity pulsation phenomenon is primarily related to free surfaces (Ref. (3-62)). They have been studied also in the towing basin where one free surface replaces the two of the vertical free-jet tunnel. Calculations of Hsu and Chen (Ref. (3-63)) show that it may be possible to obtain pulsation of cavities without a free surface.

Silberman and Song obtained pulsations (Ref. (3-57)) under all conditions of sufficient ventilation rate because, in the vertical tunnel, vortices were not present. In the towing facility pulsation appears to occur (Ref. (3-56)) in the transition region between the re-entrant jet cavities and the trailing-vortex cavities. On the other hand, for bodies of high aspect-ratio at high angles of attack, vortices tend to appear as the re-entrant jet weakens, without the occurrence of pulsations.

PRESSURE IN THE STEADY CAVITY

The pressure in the steady finite cavity must be less than in the water surrounding it, otherwise there would be no tendency for the cavity to close. On the other hand the cavity pressure must be at least as great as the saturation vapor pressure of the water at the temperature of the cavity walls. If only water vapor were present, this pressure would be attained very rapidly.

The temperature drop of the cavity walls due to evaporation has been studied to determine whether it is large enough to affect the partial pressure of water vapor in the cavity. It appears that the drop will be immeasurably small (Ref. (3-61)), except for minute cavities. Hence, the partial pressure of the water vapor in the cavity, p_v, may be taken as the vapor pressure at the temperature of the surrounding water: 0.042 atmosphere at 30°C (86°F), and 0.006 atmosphere near 0°C (32°F).

Air or other gases may enter a cavity in several ways:

1) by an intentional infusion of gas; for example, from rocket exhaust or from air added in order to maintain a cavity;

2) by venting through an "accidental" channel to the atmosphere. For example, the cavity generated by a shallow-running hydrofoil or a surface-piercing strut may become open to the atmosphere. Such an open-cavity condition can also be caused by excess cavity pressure from rocket exhaust;

3) by diffusion from the surrounding water, through the cavity walls.

In discussing cavity pressure it must be considered whether the so-called cavity is indeed a void, filled only with gases and vapors, or whether it is merely the envelope of a region of froth, a mixture

of bubbles and water, as was shown in Figure 3-36. The following paragraphs will assume, unless the contrary is noted, that the portion of the cavity being discussed is almost empty of froth.

In the cavity the partial pressure of air which results from diffusion is generally taken (Ref. (3-61)) to be proportional to the total air content of the water. Since natural water is generally saturated with air, this condition can usually be assumed. Hence, the total cavity pressure will always be a little above vapor pressure but this is only a few percent (Refs. (3-20)(3-23)), where the cavity is free of water. Diffusion into the cavity is presumably much more rapid when the cavity surface is turbulent (Ref. (3-64)).

The pressure in an unvented cavity tends to increase with σ (Ref. (3-20)), but principally in the froth region where the pressure may be several times p_V (Ref. (3-57)). Because of the pressure fluctuations in this area the pressure measured in the froth is at best an average value, but there is evidence that the results are reproducible and meaningful (Ref. (3-65)).

Plots of σ (based on measured cavity pressure) against σ_V, have been given by Parkin and Kermeen (Ref. (3-65)), and by Silberman and Song (Ref. (3-57)) and the agreement between them is good, although the former was derived from tests in a horizontal closed-jet tunnel and the latter from a vertical open-jet tunnel. Figure 3-42 is a copy of the plot from Reference (3-57). The increase of air pressure with σ can be seen from the figure.

Although methods used in measuring cavity pressure will not be discussed, a few words are pertinent concerning the relation of pressure to cavity shape, and the estimation of the pressure from the shape (Ref. (3-19)).

In the discussion of cavity shape it was shown that the fineness ratio L/d_m of the steady cavity is a function only of σ, and the formula

$$L/d_m = 1.067\sigma^{-0.658} - 0.52\sigma^{+0.465} \qquad (3-15)$$

was derived from reported measurements. Since

$$\sigma = (p_\infty - p_C)/(1/2)\rho U_\infty^2 \qquad (3-2)$$

the total cavity pressure p_C can be determined from the fineness ratio if the experimental parameters p_∞, ρ, and U_∞ are known.

APPEARANCE OF THE CAVITY SURFACE

The surface of the cavity is sometimes observed to be smooth and glassy, at other times milky, rough, striated, and so forth. Commonly, some areas of the surface will be smooth and others rough. A few of the causes of surface roughness are:

1. __Water Content of Cavities__. As shown in Figure 3-36 cavity surfaces observed at higher cavitation numbers are actually only surfaces in which small cavitation bubbles are moving. At somewhat lower values of σ the cavity is still composed of a myriad of small bubbles with a considerable amount of water between them. This cause of cavity roughness disappears only when $\sigma < 0.1$ approximately (Refs. (3-20)(3-21)(3-66)).

2. __Spray from the Re-entrant Jet__, striking the cavity wall, roughens it and produces small bubbles in the surface of the wall. This is a most common cause of surface roughness. The effect is greatest for short cavities where the jet is most energetic. In a long cavity the jet does not reach and disturb the forward end of the cavity.

3. __Irregular Line of Flow Separation__. If a cavity-generating disk has burrs at its edges, lengthwise irregularities or striations will appear in the cavity surface. These are seen also in the case of so-called smooth flow separation where some variation of separation angle is obtained; but presumably the effect would disappear at high speeds. Such striations are shown in Figure 3-4. Recently dilute polymer solutions were reported (Ref. (3-67)) to produce surface effects with both longitudinal and transverse corrugations.

4. __Boundary-Layer Turbulence__. When flow separation occurs with a laminar boundary layer the cavity will be glassy smooth if other causes of roughness are absent. Often the surface becomes rough through turbulence only a short distance from separation. Preceding the roughness of the surface a growing wave pattern may be observable (Refs. (3-49)(3-61)). The cavity surface may be rough at separation if the boundary layer is turbulent at that time.

5. __Body Vibration__. If the cavity-generating body vibrates while producing the cavity, transverse wavefronts may appear on the cavity surface. This is observed especially at water entry where the water impact may cause ringing of the missile (Refs. (3-68)(3-69)).

It appears improbable that vaporization from the cavity wall is an important cause of roughness although it was once so considered (Ref. (3-70)); also it does not appear significant for cavity roughness that the cavity does or does not contain air in addition to water vapor (Ref. (3-1)).

It has been reported (Ref. (3-69)) that aeration of the water beyond equilibrium concentration produces surface roughness. This might be important for laboratory tests but probably not for experiments with natural water.

EFFECTS OF GRAVITY FIELDS ON THE CAVITY

Cavities produced in flows past two- or three-dimensional obstacles are normally in a gravity field which affects the flow about the cavity and distorts it.

In order to understand this behavior it is instructive to compare cavity flow with the fully-wetted flow about a rigid body having the ideal ellipsoidal cavity shape. If such an ellipsoidal body is mounted in a horizontal water tunnel with the axis of the body horizontal and at a considerable depth h, the flow past the body is unaffected by gravity while the body is fully wetted, although the pressure exerted on the body by the water will be greater at the greater depth of submergence.

Since the pressure within a steady cavity is almost uniform, the water must exert a uniform pressure on it. In order that the local pressure may be everywhere the same, the Bernoulli theorem

$$p +(1/2)\rho U^2- \rho gh = C \text{ (constant)}$$

(where C may be related to conditions in the freestream) requires that the flow speed increases with depth.

If the flow were about a steady cavity having the ellipsoidal shape assumed above for the rigid body, the flow distribution would be the same as the flow about that rigid body. This is inconsistent with the requirement of uniform total pressure about the cavity, so the assumed ideal steady-cavity shape is unrealistic. In the gravity field the cavity must be distorted to provide the proper velocity distribution The undistorted ellipsoidal cavity would have the same buoyan force on it as the rigid body, but the distorted steady cavity suffers no buoyant force. The pressure over the surface is uniform and the buoyant force has vanished. The fact that the downstream portion of an almost axially symmetric steady cavity is observed to slope upward in a horizontal flow does not indicate that there is a buoyant force on the steady cavity configuration. A buoyant force would cause the cavity to move upward as the free bubble does. The steady cavity is fixed at the end where it is generated and a buoyant force causes its after portion to float upward until the steady position is reached where the net buoyant force vanishes. This distortion is not ure upward inclination and, as will be described, under some conditions the upward slope is not an apparent part of the deformation. It might be noted that the buoyant force on the horizontal ellipsoidal rigid body could be equilibrated (not eliminated) by a negative lift if the body were given a negative angle of attack. The circulation which results from the variations of flow velocity with depth, produces ie trailing vortices which were described in a previous section.

Waid found (Ref. (3-24)) that, because of gravity, cross sections of cavities attached to disks in the horizontal water tunnel tended

to rise a distance which depended on the distance downstream from the disk. He defined the height of rise as the distance of points on the centerline of the cavity above the center of the disk, although the downstream end of the cavity is considerably distorted from its circular cross section, as may be seen in Figure 3-43. The distortion is due to a greater rise of the bottom than of the top of the cavity near its downstream end. Waid found that tests on 1/2-, 3/4-, and 1-inch disks at tunnel speeds from 12 to 24 feet per second were in reasonable agreement, with an upward acceleration of the cross section equal to 27.2 ft-sec^{-2}, as the cross section moves downstream. Evidently the inclination should become very small at high speed (strictly at high values of the Froude number), and this was found by Brennan (Ref. (3-61)) for cavities due to hemispheres.

The behavior of two-dimensional cavities in a horizontal flow is in surprising contrast to that just described. Parkin (Ref. (3-71)) showed theoretically that no appreciable rise was to be expected in the cavities due to inclined flat plates, and Street (Ref. (3-72)), derived similar predictions for the symmetrical wedge. Kiceniuk and Acosta verified experimentally (Ref. (3-73)) that no inclination was measurable for cavities due to wedges with half angles of 7-1/2 and 15 degrees. Parkin found that gravity effects should disappear almost completely for F>6, where F is based on the plate width.

By a linearized analysis Tulin derived (Ref. (3-74)) an approximate value of the length ℓ of a cavity in a transverse gravity field, in terms of the length L under no-gravity conditions. He found

$$\ell/L = (\cos^2 k)/J_o^2(k) \qquad (3-44)$$

where

$$k = g\ell/2U_o^2. \qquad (3-45)$$

The value of L can be estimated from the earlier-mentioned formula

$$L/d = 8C_{D_o}/\pi\sigma^2, \qquad (3-25)$$

also due to Tulin. From the three equations above, the length of a cavity in a transverse gravity field can be approximated. It will be seen that the cavity is always shortened by the field and is not of infinite length even for $\sigma = 0$.

Figure 3-44 shows the distortion of the cavity thrown by a wedge of 10-degree half angle, as calculated by Street (Ref. (3-72)). (In the upper sketch the ordinate scale is one-fifth that of the abscissa.) The cavity for $\sigma = 0.0865$ has a length which is 30 times the chord length. At F = 4 the center of the ellipsoid sags about 14 percent of the maximum diameter, but the cavity rises again at the downstream end. It is noteworthy that the center of the cavity is deflected downward, in the direction of the gravitational field.

Parkin calculated (Ref. (3-71)) the shapes of cavities due to a flat plate inclined to the flow at 4 degrees in a transverse gravity field. His sketches are reproduced in Figure 3-45. (In the upper sketch the ordinate scale is one-tenth that of the abscissa). There is a small dependence of cavity length on F.

The changes of cavity length are greater in a longitudinal gravity field than in a transverse field and they depend in an interesting fashion on the conditions of the experiment. Two principal types of experimental cavities will be considered: those in the vertical free-jet water tunnel, where the flow speed past the cavity is accelerated by gravity; and those generated by vertical missile motion in an "infinite" fluid (for example, in a large water tank).

It is usual to relate the change of length to the square of the Froude number, $F^2 = U^2/gd$, and F^2 is taken to be positive when the gravity field points upstream (or a missile is traveling downwards), and negative if it points downstream (Ref. (3-74)), (or a missile travels upwards). The velocity U is the freestream velocity at the level of the base (Ref. (3-75)) or the center (Ref. (3-49)) of the test body. Froude number has also been based on cavity length, instead of on missile diameter (Ref. (3-74)).

In the vertical free-jet tunnel the flow is of course in the direction of gravity. The free-stream velocity is accelerated along the cavity and thus causes an effectively smaller σ with a longer cavity. In other words, if the value of the cavitation number is based on the freestream velocity at the position of the missile, the cavity should be longer than is normally produced at that cavitation number. Silberman reported (Ref. (3-49)) that this elongation was not found, perhaps because of the shortening of the cavity due to the walls of the free jet, or the uncertainty in measuring the cavity length. In the vertical free-jet tunnel the total pressure is constant along the cavity because of the acceleration of the flow.

A cavity generated in a tank by a missile traveling vertically upward (F^2 negative) is below the missile, in a region of greater hydrostatic pressure. Hence, the numerator in the expression for the cavitation number

$$\sigma = (p_\infty - p_c)/(1/2)\rho U^2$$

is greater than at the reference level (at the missile) and the effective value of σ is increased, the tendency for the cavity to close is greater, and the cavity is shorter than is usual at the reference value of σ. On the other hand if the missile is traveling downward (F^2 positive), so that the cavity lies above the missile, the tendency to close is less and the cavity is lengthened. While the pressure "at infinity" increases with depth, the flow on the cavity wall is accelerated by gravity and thus a uniform pressure is maintained at the cavity.

The length of cavities due to wedges in longitudinal gravity fields, has been calculated by Acosta (Ref. (3-75)) using a linearized model, and by Lenau and Street (Ref. (3-76)) with a non-linear model. Figures 3-46 and 3-47 contain, from Reference (3-76), curves of cavity length for wedges with half angles of 15 and 45 degrees, for both positive and negative values of F^2. The graph for $1/F^2 = 0$ should agree with data already presented for the gravity-free problem. It is easily shown that the agreement with Zoller's formula, (Fig. 3-25), is good at small values of σ, but not at larger values, where the difference is especially large for wedges of small angle.

Tulin gave (Ref. (3-74)) a formula for the length of vertical two-dimensional cavities due to a "point drag forebody", which can be written

$$\frac{L}{d} = \frac{8C_D}{\pi \; \sigma^2 [\; 1 + \dfrac{L}{2dF^2\sigma}\;]^2} \qquad (3-46)$$

It permits the calculation of cavity length as a function of C_D. For $F^2 = \infty$ equation (3-46) reduces to equation (3-25).

The cavities in longitudinal gravity fields are not symmetrical about their midpoints. For negative values of F^2 the after part of the cavity is blunter than the forward part, and the reverse is true when F^2 is positive (Ref. (3-74)). For negative F^2 there is a minimum value of σ, which is reached when the rear end of the cavity becomes cusped. This occurs when the drag on the missile becomes equal to the buoyant force on the cavity (Ref. (3-74)).

The significance of quantitative length data for cavities in a longitudinal field, may be questioned (Ref. (3-74)). For the cavity due to a missile traveling vertically in an infinite fluid, the ambient pressure on the cavity is continually increasing or decreasing with depth, with corresponding changes in σ, and the cavity configuration cannot be steady. Steady conditions are maintained in the vertical free-jet tunnel but it appears improbable that prototype conditions are simulated.

ABBREVIATIONS   REFERENCES

A. R. E.   Armament Research Establishment, Ministry of Supply,
                  Fort Halstead, Kent, England

ASME   American Society of Mechanical Engineers

CIT Hyd.   California Institute of Technology, Hydrodynamics
                  Laboratory

CIT Eng.   California Institute of Technology, Engineering
                  Division

DTMB   David Taylor Model Basin

NACA   National Advisory Committee for Aeronautics

NOL   Naval Surface Weapons Center, White Oak Laboratory,
                  Silver Spring, Maryland (formerly Naval Ordnance Laboratory

NOTS   Naval Ordnance Test Station, Pasadena

ONR   Office of Naval Research

SAF   St. Anthony Falls Hydraulic Laboratory, U. Minnesota

REFERENCES

3-1.   Eisenberg, P., "On the Mechanism and Prevention of Cavitation,"
       DTMB Rpt 712, 1950

3-2.   Eisenberg, P., "A Brief Survey of Progress on the Mechanics of
       Cavitation," DTMB Rpt. 842, 1953

3-3.   Rouse, H. and McNown, J. S., "Cavitation and Pressure
       Distribution; Head Forms at Zero Angle of Yaw," State U. of Iowa,
       Studies in Eng. Bull. 32, 1948

3-4.   Armstrong, A. H., "Abrupt and Smooth Separation in Plane and
       Axisymmetric Cavity Flow," A.R.E. Memo. 22/53, 1953

3-5.   Brennan, C., "A Numerical Solution of Axisymmetric Cavity
       Flows," J. Fluid Mech. 37, pp 671-688, 1969

3-6.   Eisenberg, P., "A Cavitation Method for the Development of Forms
       Having Specified Critical Cavitation Numbers," DTMB Rpts. C-14
       and 647, 1947

3-7.   May, A., "Effect of Surface Condition of a Sphere on its Water-
       Entry Cavity," J. Appl. Phys., 22, pp 1219-1222, 1951

3-8.   Armstrong, A. H. and Tadman, K. G., "Axisymmetric Cavity Flow
       About Ellipsoids," Proc. Joint Adm. - U. S. Navy Meeting on
       Hydroballistics, ONR, 1954

3-9.   May, A., "Vertical Entry of Missiles into Water,' J. Appl. Phys.
       23, pp 1362-1372, 1952

3-10. Worthington, A. M., "A Study of Splashes," Longmans, Green and
       Company, London, 1908; reprinted, The MacMillan Co., New York,
       N. Y., 1963

3-11. Hsu, E-Y and Perry, B., "Water Tunnel Experiments on Spheres in
       Cavity Flow," CIT Hyd. Rpt. E-24.9, 1954

3-12. Roshko, A., "A New Hodograph for Free-Streamline Theory," NACA
       TN 3168, 1954

3-13. Daily, J. W., "Hydrodynamic Forces Resulting from Cavitation on
       Underwater Bodies," CIT Hyd. Rpt. ND-31.2, 1945

3-14. Brodetsky, S., "Discontinuous Fluid Motion Past Circular and
       Elliptic Cylinders," Proc. Roy. Soc. A102, pp 542-553, 1923

3-15. Tulin, M. P., "New Developments in the Theory of Supercavitating
       Flows," Second Symposium on Naval Hydrodynamics 235-260,
       ONR, 1958. Discussions by B. R. Parkin and W. A. Clayden

3-16. Knapp, R. T., Daily, J. W., and Hammitt, F. G., "Cavitation," McGraw-Hill Book Co., New York, 1970

3-17. Birkhoff, G., "Jets, Wakes and Cavities," Second Symposium on Naval Hydrodynamics, pp 261-275, ONR, 1958

3-18. Wayland, H. and White, F. G., "Boundary Layer Effects on Spinning Spheres," NOTS, NAVORD Report 1190, 1949

3-19. May, A. and Hoover, W. R., "A Study of the Water-Entry Cavity," NOLTR 63-264, 1965

3-20. Self, M. W. and Ripken, J. F., "Steady-State Cavity Studies in a Free-Jet Water Tunnel," SAF Project Rpt. 47, 1955

3-21. Reichardt, H., "The Laws of Cavitation Bubbles at Axially Symmetrical Bodies in a Flow," Ministry of Aircraft Production Volkenrode, MAP-VG, Reports and Translations 766, ONR, 1946

3-22. Oversmith, R. H., "Some Observations on Cavitating Flows," Convair Eng. Dept. Rpt. ZR-659-015, 1959

3-23. Gadd, G. E. and Grant, S., "Some Experiments on Cavities Behind Disks," J. Fluid Mech., 23, pp 645-656, 1965

3-24. Waid, R. L., "Cavity Shapes for Circular Disks at Angles of Attack," CIT Hyd. Rpt. E-73.4, 1957

3-25. Hicks, W. E., "Correlation of Experimental Data on Axially Symmetric Steady-State Cavities," Proc. of the 9th Conf. on Underwater Ballistics, 1945

3-26. Eisenberg, P. and Pond, H. L., "Water Tunnel Investigations of Steady-State Cavities," DTMB Rpt. 668, 1948

3-27. May, A., "The Forces Acting on Cavity-Running Missiles," Chapter 3 of this report

3-28. Garabedian, P. R., "Calculation of Axially Symmetric Cavities and Jets," Pac. J. of Math 6, pp 611-684, 1956

3-29. Birkhoff, G. and Caywood, T. E., "Fluid Flow Patterns," J. Appl. Phys. 20, pp 646-659, 1949

3-30. Campbell, I. J. and Hilborne, D. V., "Air Entrainment behind Artificially Inflated Cavities," Second Symposium on Naval Hydrodynamics, pp 467-482, ONR, 1958; abridged version in Shipbuilding and Shipping Record, 1959

3-31. Münzer, H. and Reichardt, H., "Rotational Symmetrical Source-Sink Bodies with Predominantly Constant Pressure Distributions," A.R.E. Trans. 1/50, 1950

3-32. Gilbarg, D., "Jets and Cavities," Encyclopedia of Physics,
       Vol. IX, Fluid Dynamics III, Springer Verlag, Berlin, 1960

3-33. Gilbarg, D. and Rock, D. H., "On Two Theories of Plane
       Potential Flows with Finite Cavities," 1946

3-34. Plesset, M. S. and Shaffer, P. A., Jr., "Cavity Drag in Two
       and Three Dimensions," J. Appl. Phys. 19, pp 934-939, 1948

3-35. Gurevich, M. I., "Some Remarks on Stationary Schemes for
       Cavitation Flow about a Flat Plate," DTMB Transl. 224
       (Wehausen), 1948

3-36. Perry, B., "Evaluation of the Integrals Occurring in the
       Cavity Theory of Plesset and Shaffer," CIT Hyd. Rpt. 21-11,
       1952

3-37. Gilbarg, D., "Free-Streamline Theory and Steady-State Cavitation,"
       (First) Naval Hydrodynamics Symposium, pp 281-295, ONR, 1956

3-38. Zoller, K., "Widerstand einer ebenen Platte mit Totwassergebiet,"
       Deutsche Luftfahrtforschung, UM 4518, 1943

3-39. Tulin, M. P., "Supercavitating Flow Past Foils and Struts,"
       Cavitation in Hydrodynamics, Philosophical Library, New York,
       1957

3-40. Tulin, M. P., "Steady Two-Dimensional Cavity Flows about Slender
       Bodies," DTMB Rpt. 834, 1953

3-41. Waid, R. L., "Water Tunnel Investigation of Two-Dimensional
       Cavities," CIT Hyd. Rpt. E-73.6, 1957

3-42. Tulin, M. P., "Cavitation," Handbook of Fluid Dynamics,
       McGraw-Hill Book Co., New York, 1961

3-43. May, A., "The Cavity After Vertical Water Entry," NOLTR 68-114,
       1968

3-44. Levinson, N., "On the Asymptotic Shape of the Cavity Behind
       an Axially Symmetric Nose Moving Through an Ideal Fluid,"
       Annals of Math., 47, pp 704-730, 1946

3-45. Kendrick, J. B., "Prediction of Water-Entry Trajectories by a
       Step-by-Step Semigraphical Analysis," NOTS NAVORD Rpt. 1974,
       1952

3-46. Rouse, H., "Cavitation and Pressure Distribution; Head Forms
       at Angles of Yaw," State U. of Iowa, Studies in Eng., Bull. No.
       42, 1962

3-47. Cox, A. D. and Clayden, W. A., "Cavitating Flow About a Wedge
       at Incidence," J. Fluid Mech., 3, pp 615-637, 1958

3-48. Cchen, H. and DiPrima, R. C., "Wall Effects in Cavitating Flows," Second Symposium on Naval Hydrodynamics, pp 367-390, ONR, 1958

3-49. Silberman, E., "Experimental Studies of Supercavitating Flow About Simple Two-Dimensional Bodies in a Jet," J. Fluid Mech., 5, pp 337-354, 1959

3-50. May, A., "The Influence of the Proximity of Tank Walls on the Water-Entry Behavior of Models," NOL NAVORD 2240, 1951

3-51. Knapp, R. T., "Recent Investigations of the Mechanics of Cavitation and Cavitation Damage," ASME Proc. 77, pp 1045-1054, 1955

3-52. Swanson, W. M. and O'Neill, J. P., "The Stability of an Air-Maintained Cavity Behind a Stationary Object in Flowing Water," CIT Hyd. Rpt. M-24.3, 1951

3-53. O'Neill, J. P., "Flow Around Bodies with Attached Open Cavities," CIT Hyd. Rpt. E-24.7, 1954

3-54. Cuthbert, J. W., "An Analysis of Air Entrainment in Cavity Flows," Hydronautics, Inc., Tech. Rpt. 003-1, 1960

3-55. Schiebe, F. R. and Wetzel, J. M., "Ventilated Cavities on Submerged Three-Dimensional Hydrofoils," SAF Tech. Paper 36, Series B, 1961

3-56. Schiebe, F. R. and Wetzel, J. M., "Further Studies of Ventilated Cavities on Submerged Bodies," SAF Proj. Rpt. 73, 1964

3-57. Silberman, E. and Song, C. S., "Instability of Ventilated Cavities," SAF Tech. Paper 29, Series B., 1959

3-58. Wadlin, K. L., "Mechanics of Ventilation Inception," Second Symposium on Naval Hydrodynamics, pp 425-445, ONR, 1958

3-59. Lang, T. G., Daybell, D. A., and Smith, K. E., "Water-Tunnel Tests of Hydrofoils with Forced Ventilation," NOTS NAVORD 7008, 1959

3-60. Ccx, R. N. and Clayden, W. A., "Air Entrainment at the Rear of a Steady Cavity," Cavitation in Hydrodynamics, Philosphical Library, New York, 1957

3-61. Brennan, C., "The Dynamic Balances of Dissolved Air and Heat in Natural Cavity Flows," J. Fluid Mech., 37, pp 115-128, 1969

3-62. Song, C. S., "Pulsation of Ventilated Cavities," SAF Tech. Paper 32, Series B, 1961

3-63. Hsu, C. C. and Chen, C. F., "On the Pulsation of Finite Ventilated Cavities," Hydronautics, Inc. Tec. Rpt. 115-4, 1962

3-64. Brennan, C., "Cavity Surface Wave Patterns and General Appearance," J. Fluid Mech., 44, pp 33-49, 1970

3-65. Parkin, B. R. and Kermeen, R. W., "Water Tunnel Techniques for Force Measurements on Cavitating Hydrofoils," J. Ship Res., 1, pp 36-42, 1957

3-66. Birkhoff, G. and Zarantonello, E. H., Jets, Wakes, and Cavities, Academic Press Inc., New York, 1957

3-67. Brennan, C., "Some Cavitation Experiments with Dilute Polymer Solutions," J. Fluid Mech. 44, pp 51-63, 1970

3-68. McMillen, J. H. and Kramer, R. L., "Shadowgraphic Investigation of Small Spherical Missiles Entering Water Vertically at 7000 Feet per Second," NOL NAVORD Rpt. 2846, 1952

3-69. Waugh, J. G. and Stubstad, G. W., "Water-Entry Cavity Modeling, Part I. Vertical Cavities," NOTS NAVORD Rpt. 5365, 1956

3-70. Knapp, R. T., "Entrance and Cavitation Bubbles," CIT OSRD Section 6 i-sr 207-1900, HML No. ND 31, 1944

3-71. Parkin, B. R., "A Note on the Cavity Flow Past a Hydrofoil in a Liquid with Gravity," CIT Eng. Rpt 47-9, 1957

3-72. Street, R. L., "Supercavitating Flow about a Slender Wedge in a Transverse Gravity Field," J. Ship Res. 7, pp 14-23, 1963

3-73. Kiceniuk, T. and Acosta, A. J., "Experiments on Gravity Effects in Supercavitating Flow," J. Ship Res. 10, pp 119-121, 1966

3-74. Tulin, M. P., "The Shape of Cavities in Supercavitating Flows," Proc. of the Eleventh Intern. Congr. of Appl. Mech., Munich, Germany, 1964

3-75. Acosta, A. J., "The Effect of a Longitudinal Gravitational Field on the Supercavitating Flow Over a Wedge," Transact. ASME, J. Appl. Mech., 28, Series E, pp 188-192, 1961. Also CIT Eng. Rpt. 79.1, 1958

3-76. Lenau, C. W. and Street, R. L., "A Non-Linear Theory for Symmetric, Supercavitating Flow in a Gravity Field," J. Fluid Mech. 21, part 2, pp 257-280, 1965
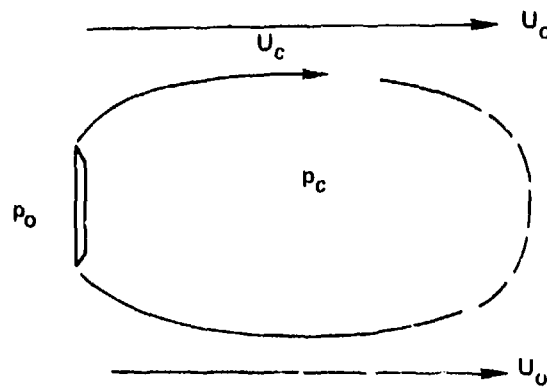
FIG. 3-1. CAVITY NOMENCLATURE
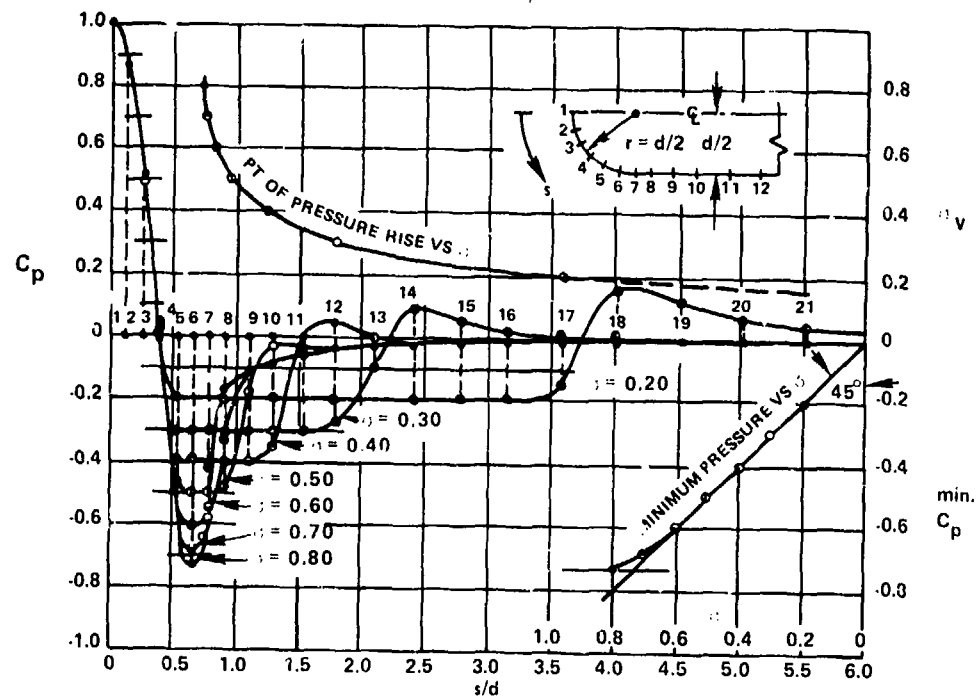
FIG. 3-2. EFFECT OF CAVITATION ON THE PRESSURE
DISTRIBUTION AROUND A CYLINDRICAL BODY WITH
A HEMISPHERICAL HEAD. FROM ROUSE-McNOWN REF (3-3)
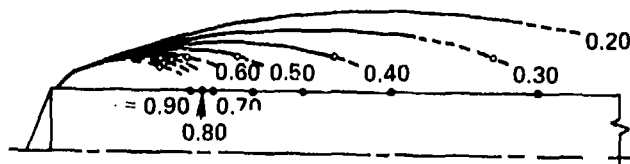
FIG. 3-3 CAVITIES DUE TO A CONE, SHOWING DELAYED
SEPARATION FROM ROUSE-McNOWN REF (3-3)
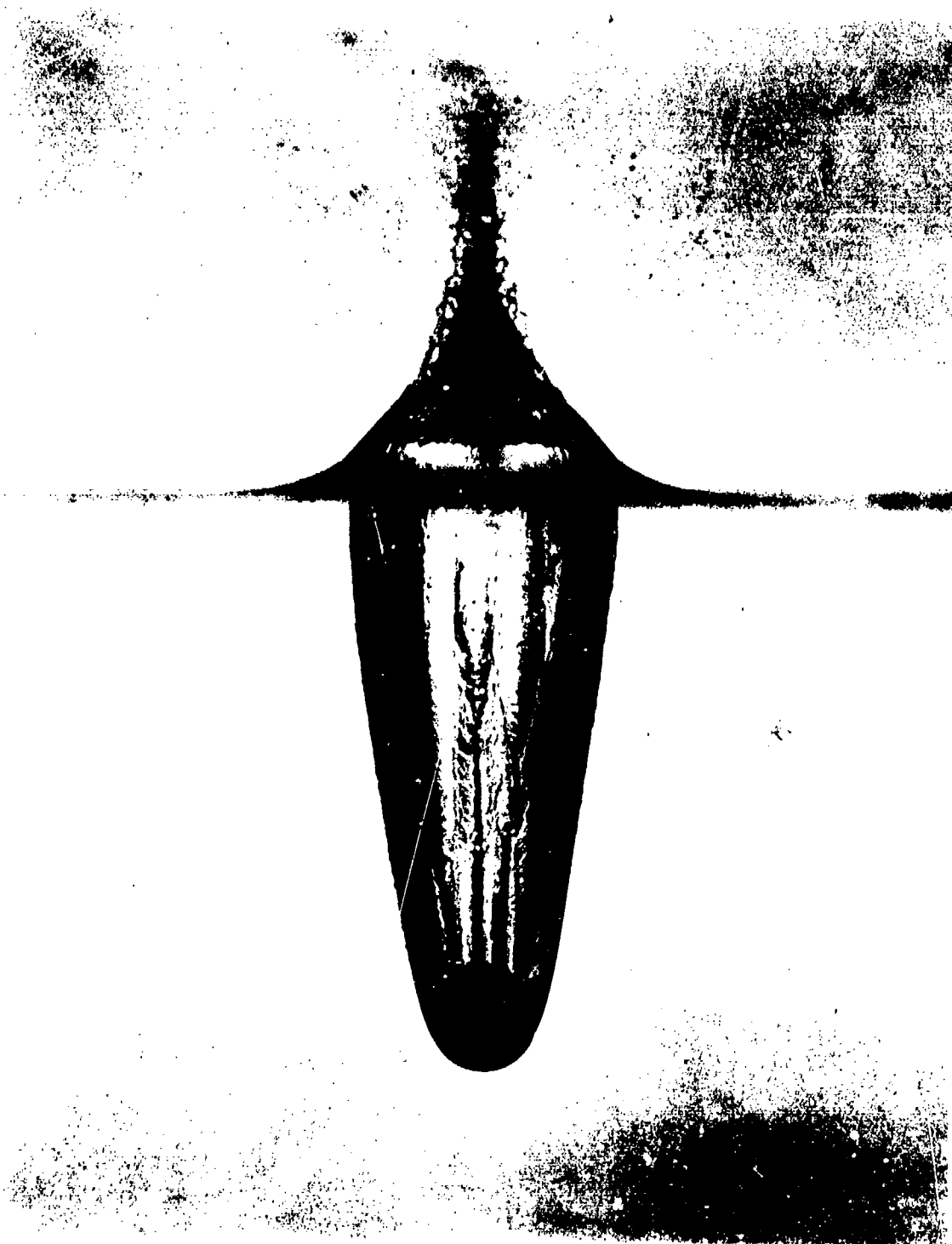
FIG. 3-4   IRREGULAR FLOW SEPARATION FROM A SPHERE REF (3-9)
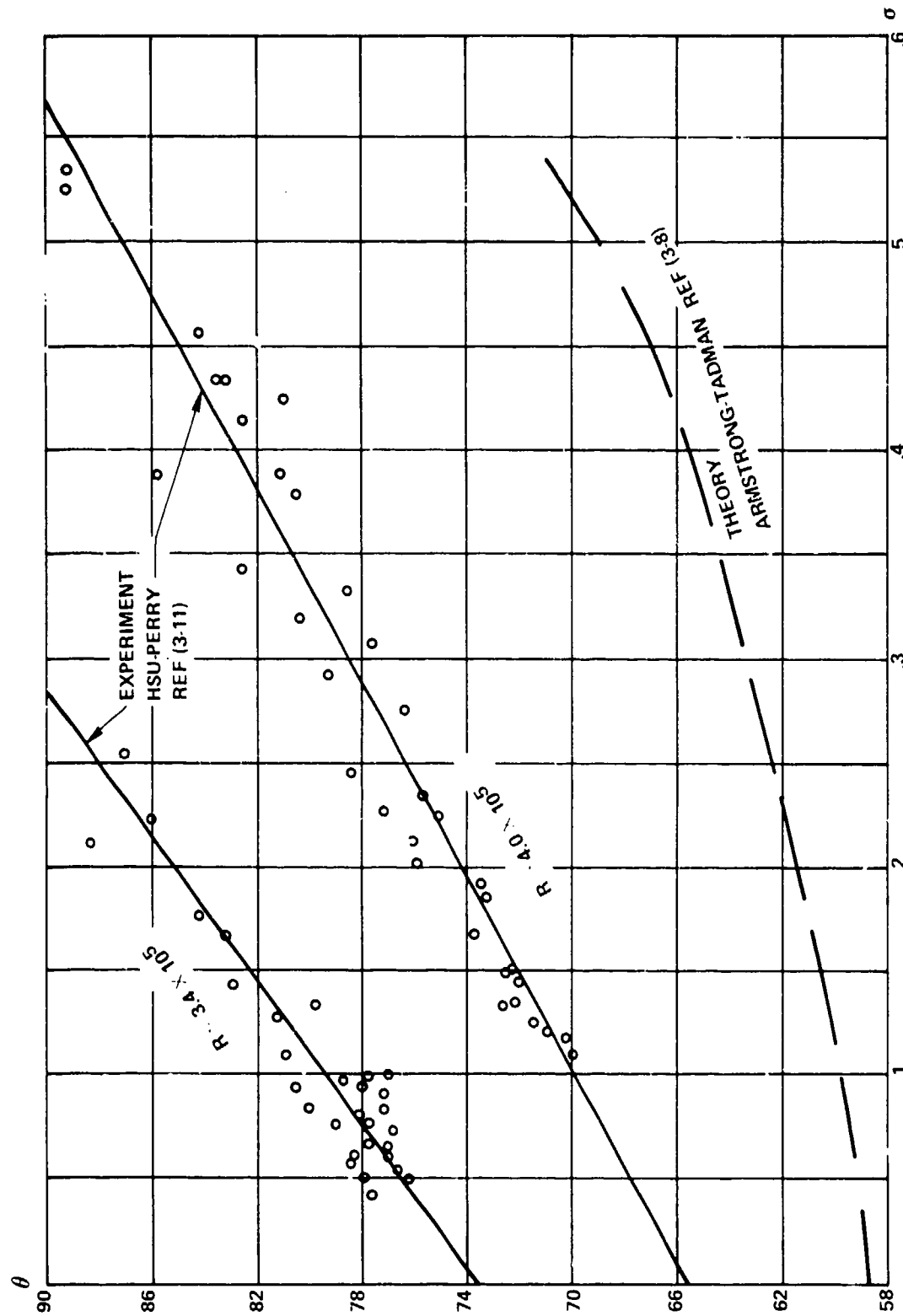
FIG. 3-5 ANGLE OF FLOW SEPARATION FOR SPHERES
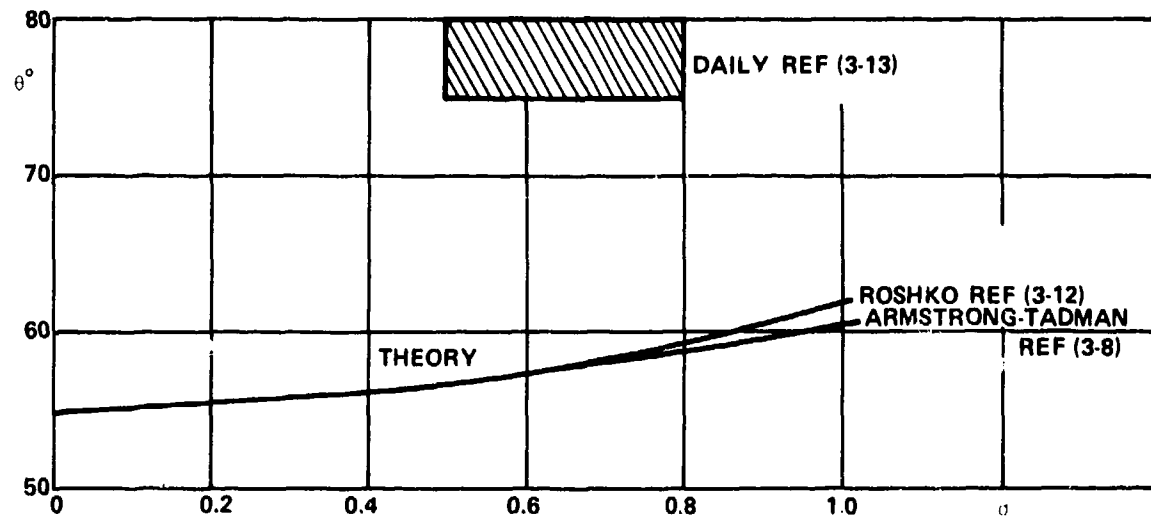
FIG. 3-6 FLOW SEPARATION FOR CIRCULAR CYLINDER
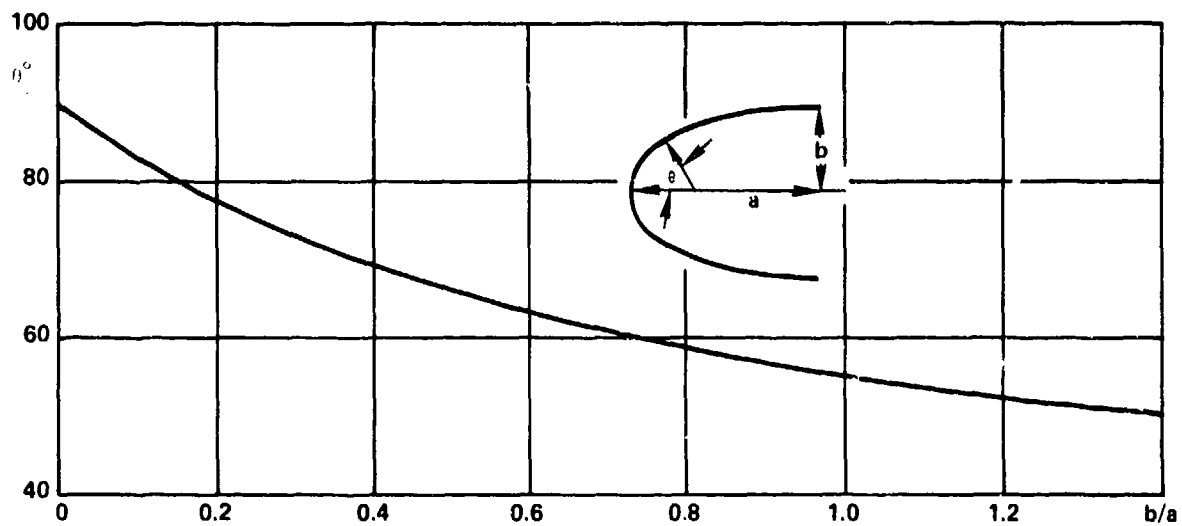
FIG. 3-7 SEPARATION ANGLE FOR THE ELLIPTIC CYLINDER AFTER BRODETSKY REF (3-14)
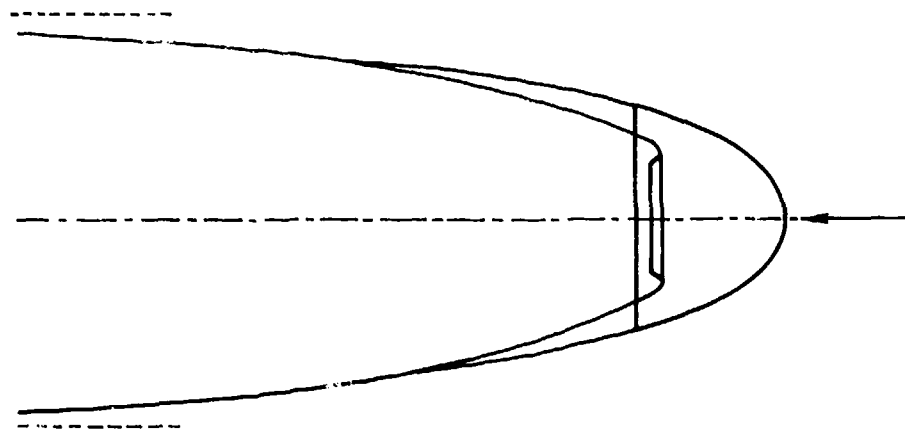
FIG. 3-8 SKETCH OF CAVITIES DUE TO ELLIPSOID AND DISK HAVING THE SAME
DRAG AREA $C_D A$. AFTER REICHARDT REF (3-21)
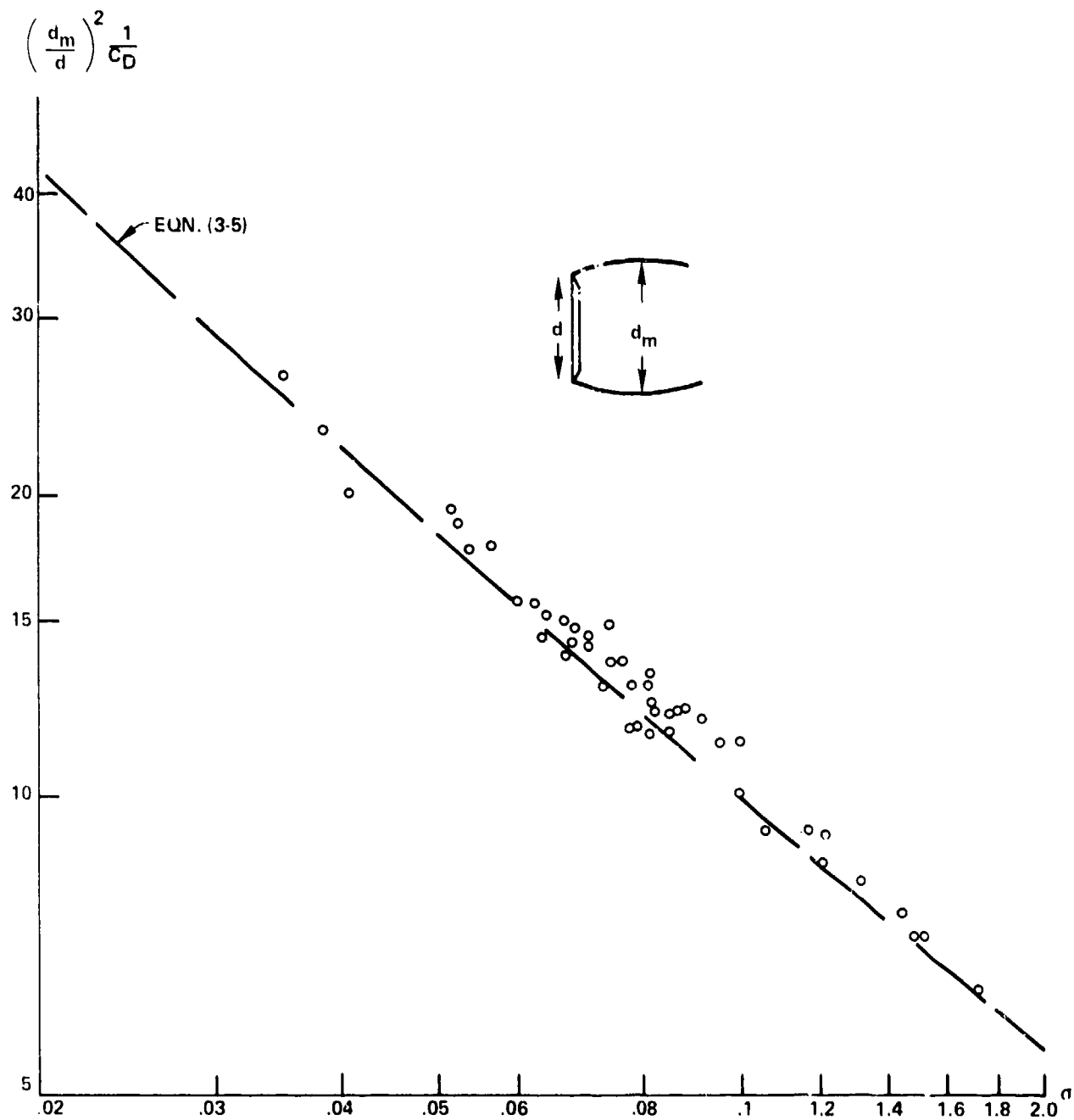
FIG. 3-9 CAVITY DIAMETER DATA FOR DISK — WAID REF (3-24)
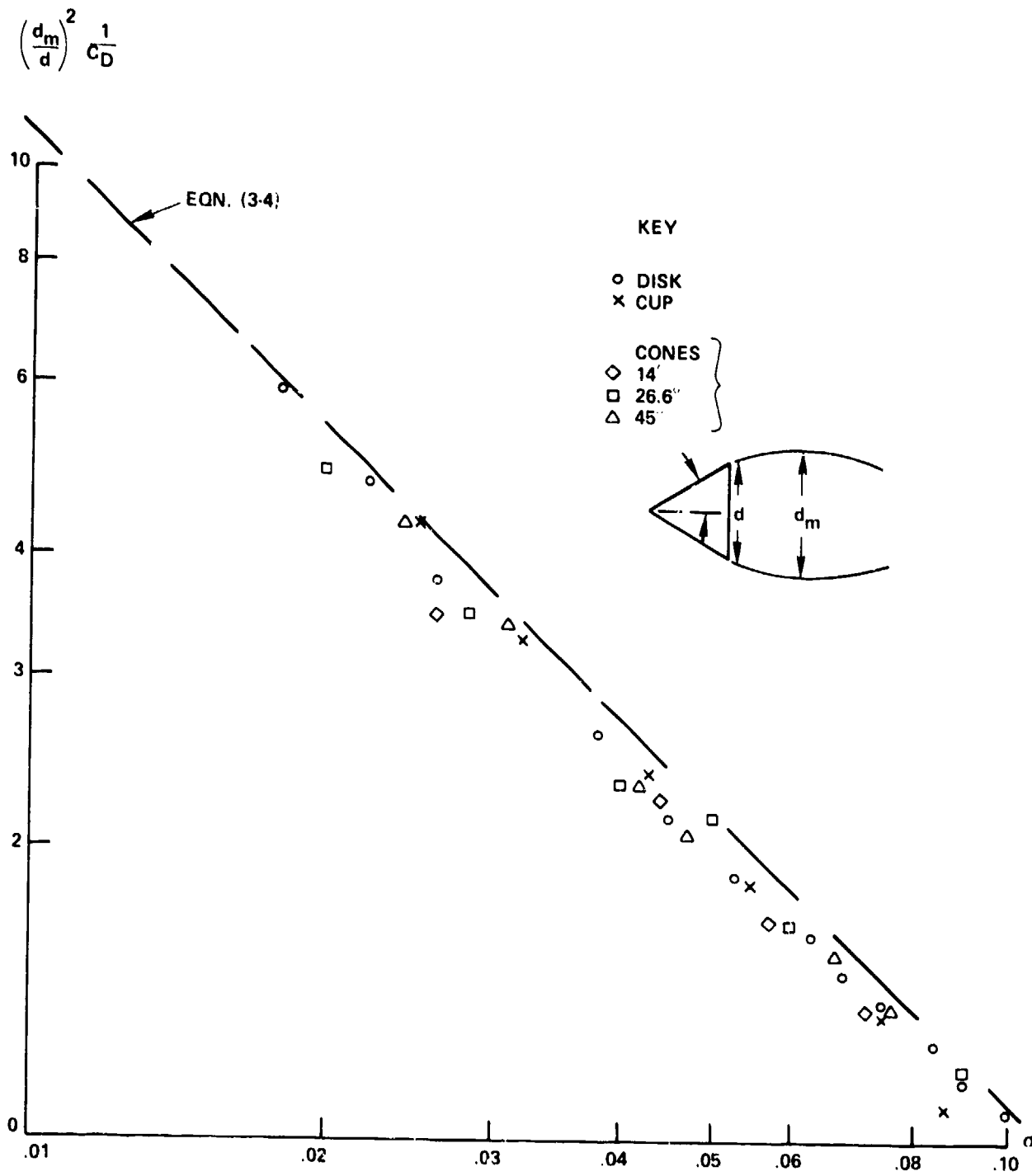
FIG. 3-10 CAVITY DIAMETER DATA — REICHARDT REF (3-21)
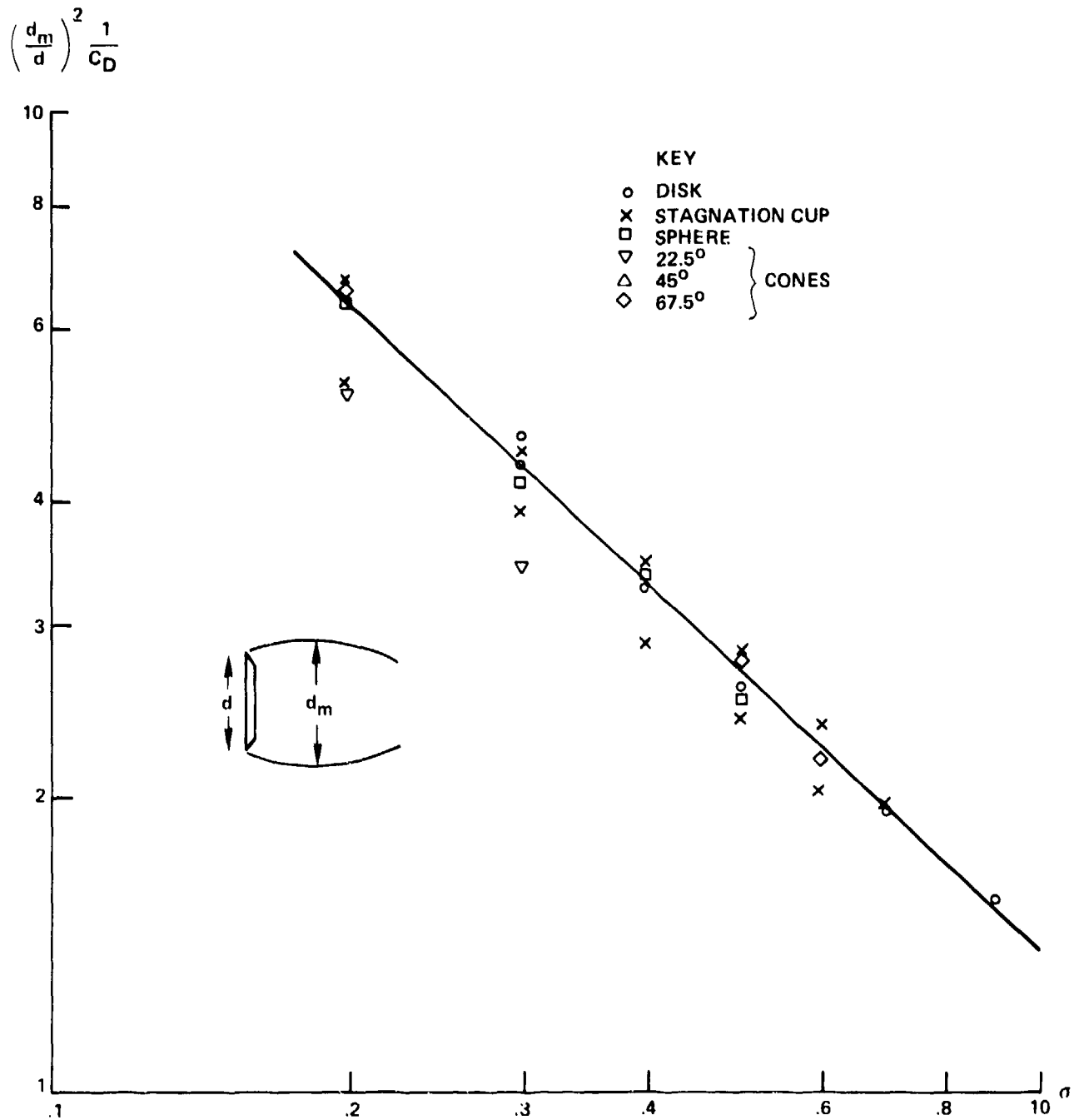
FIG. 3·11 CAVITY DIAMETER DATA – ROUSE AND McNOWN REF (3·3)
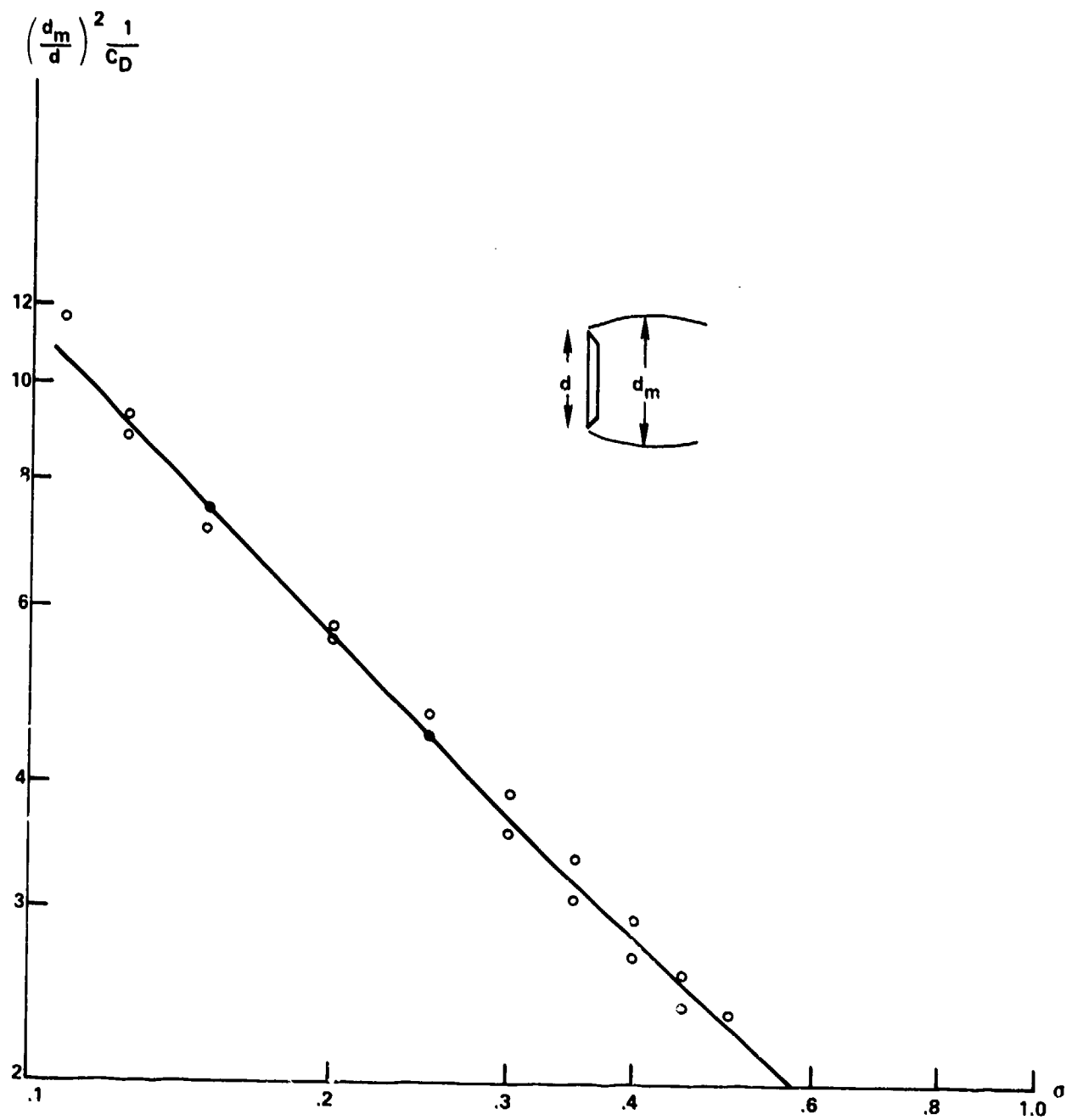
FIG. 3-12 CAVITY DIAMETER DATA FOR DISKS — EISENBERG-POND REF (3-26)
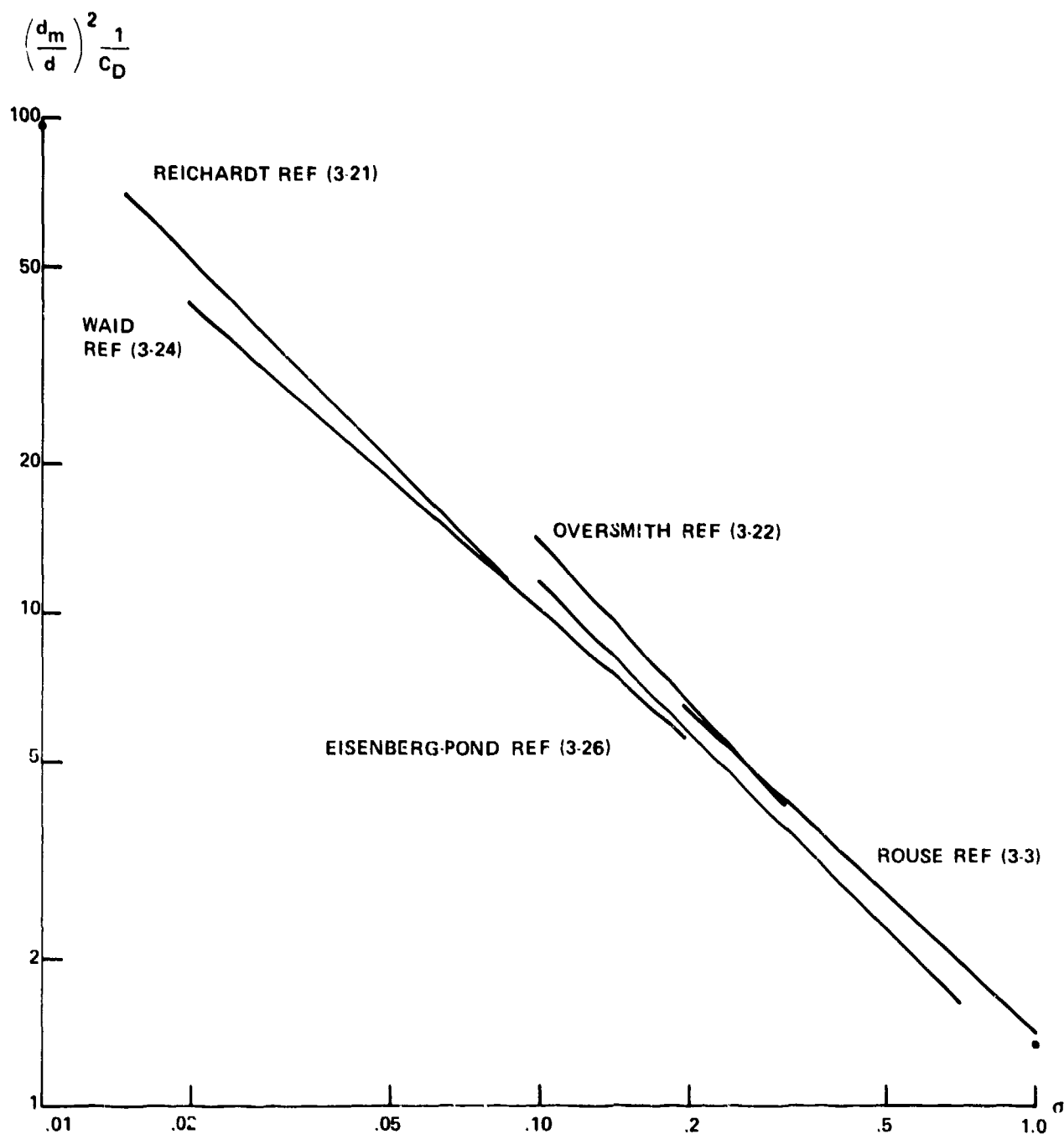
FIG. 3-13 CAVITY DIAMETER RESULTS OF VARIOUS EXPERIMENTERS
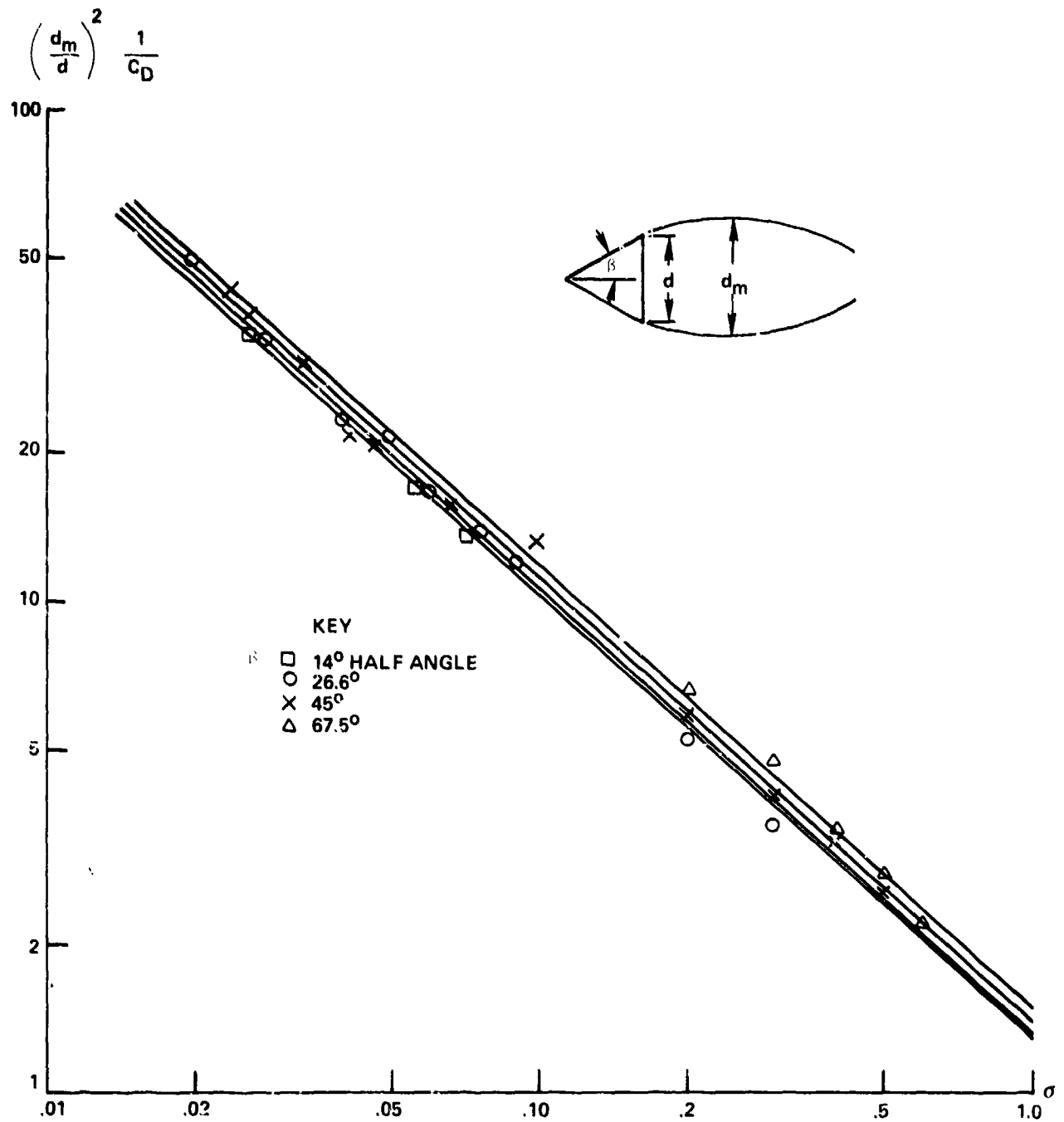
FIG. 3-14 DIAMETERS OF CAVITIES DUE TO CONES
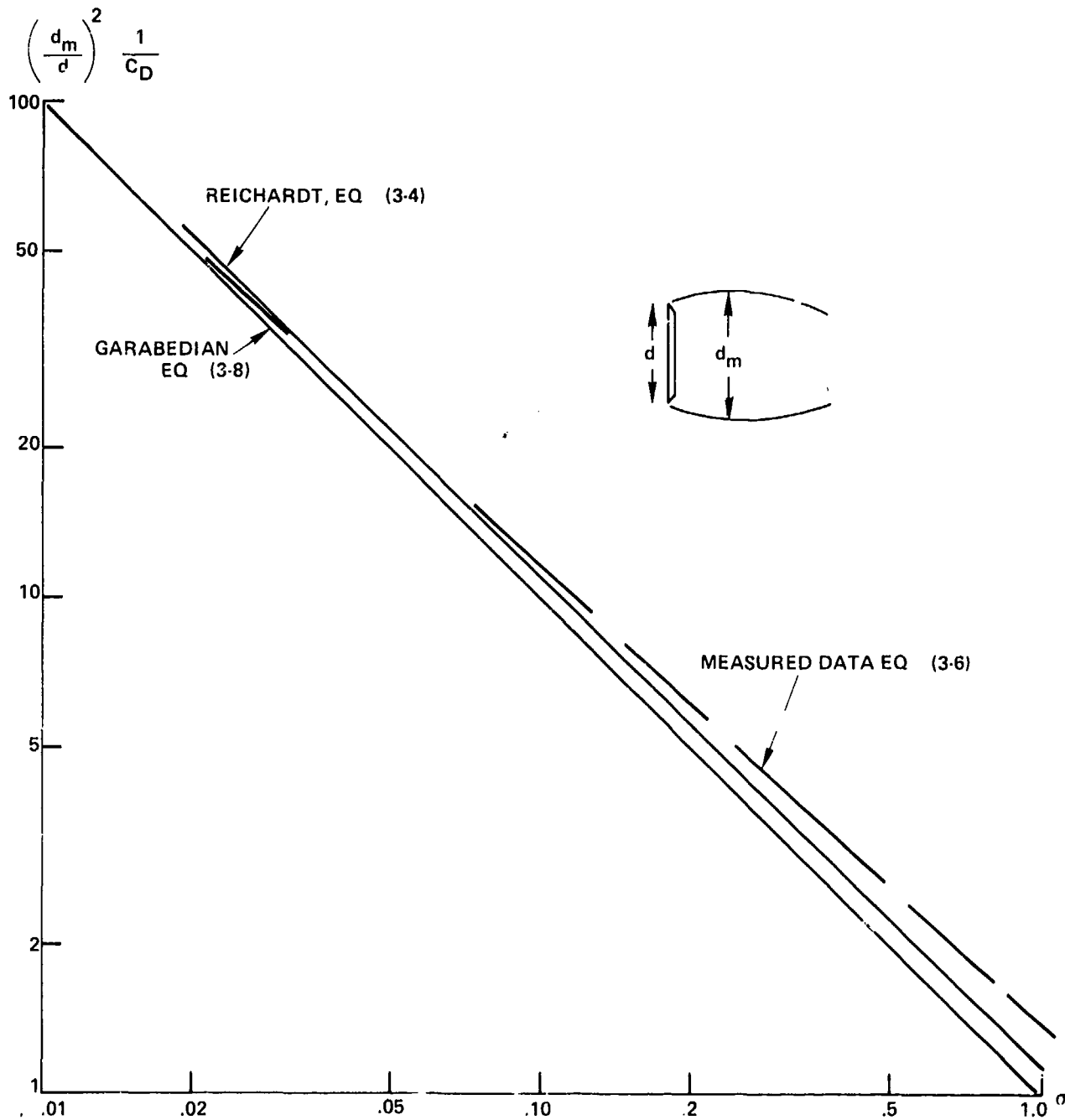
FIG. 3-15 COMPARISON OF PREDICTED AND MEASURED CAVITY DIAMETERS
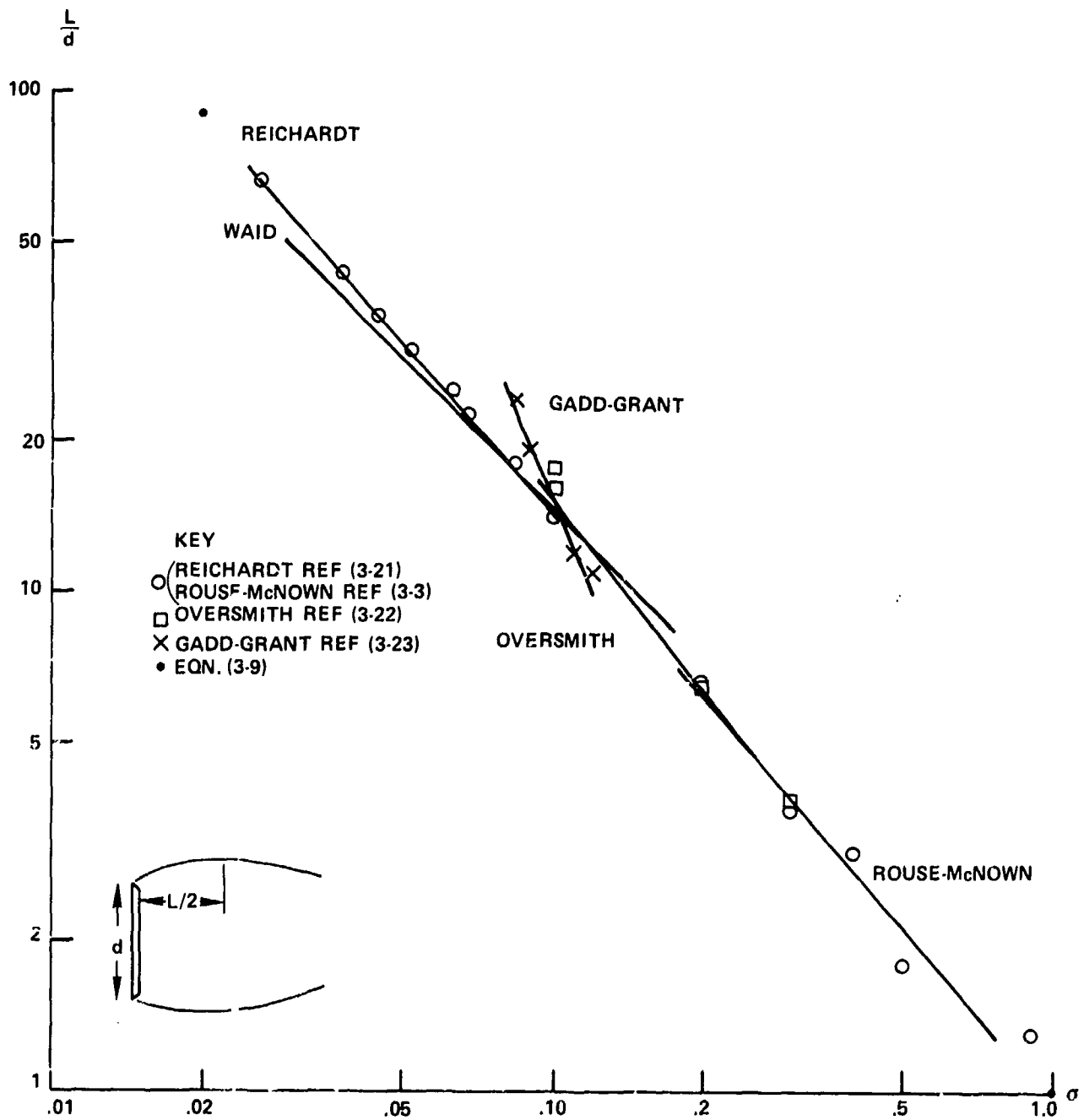
FIG. 3-16 LENGTH OF CAVITIES DUE TO A DISK
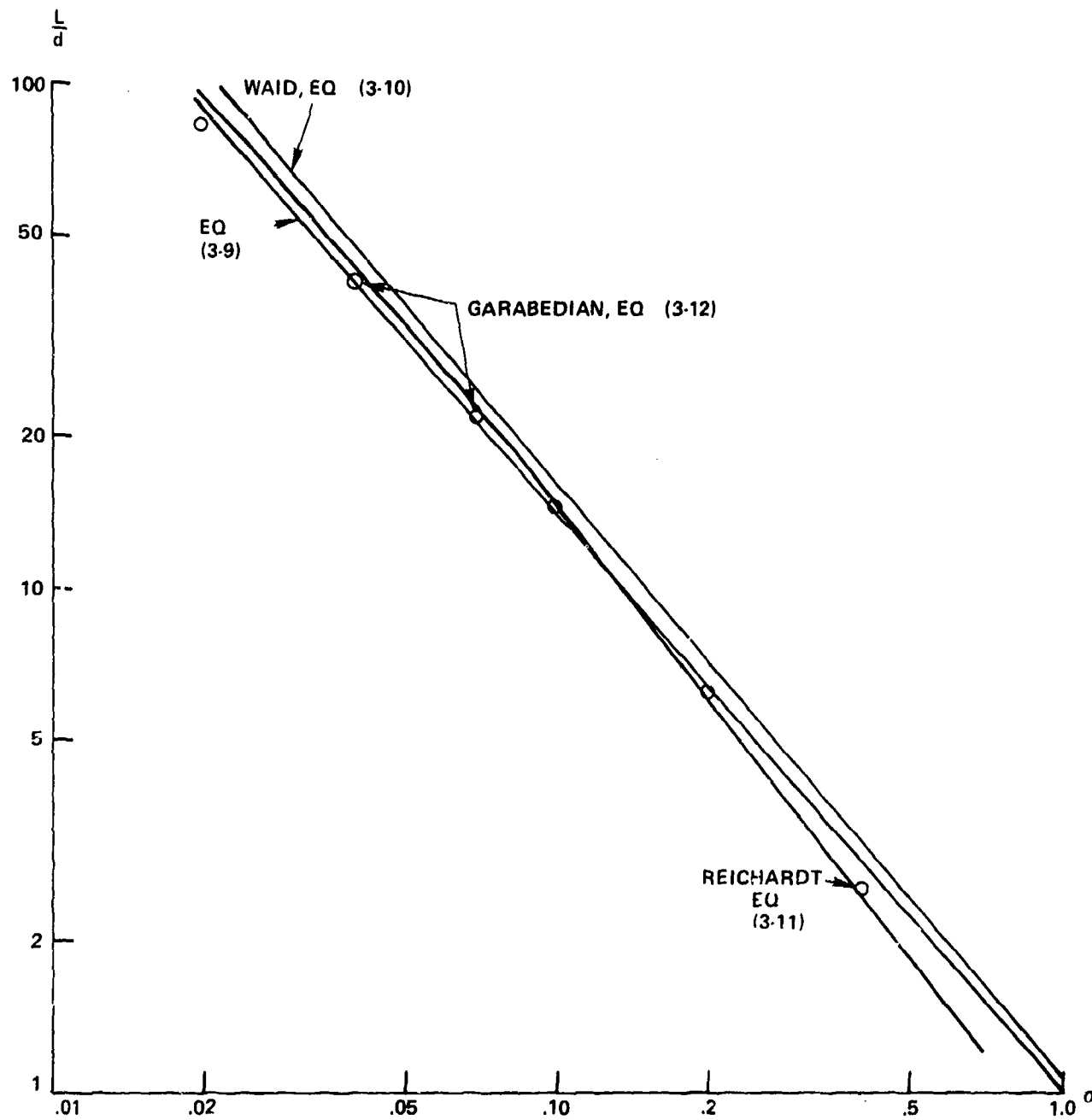
FIG. 3-17 LENGTH OF DISK CAVITY — COMPARISON OF FORMULAS
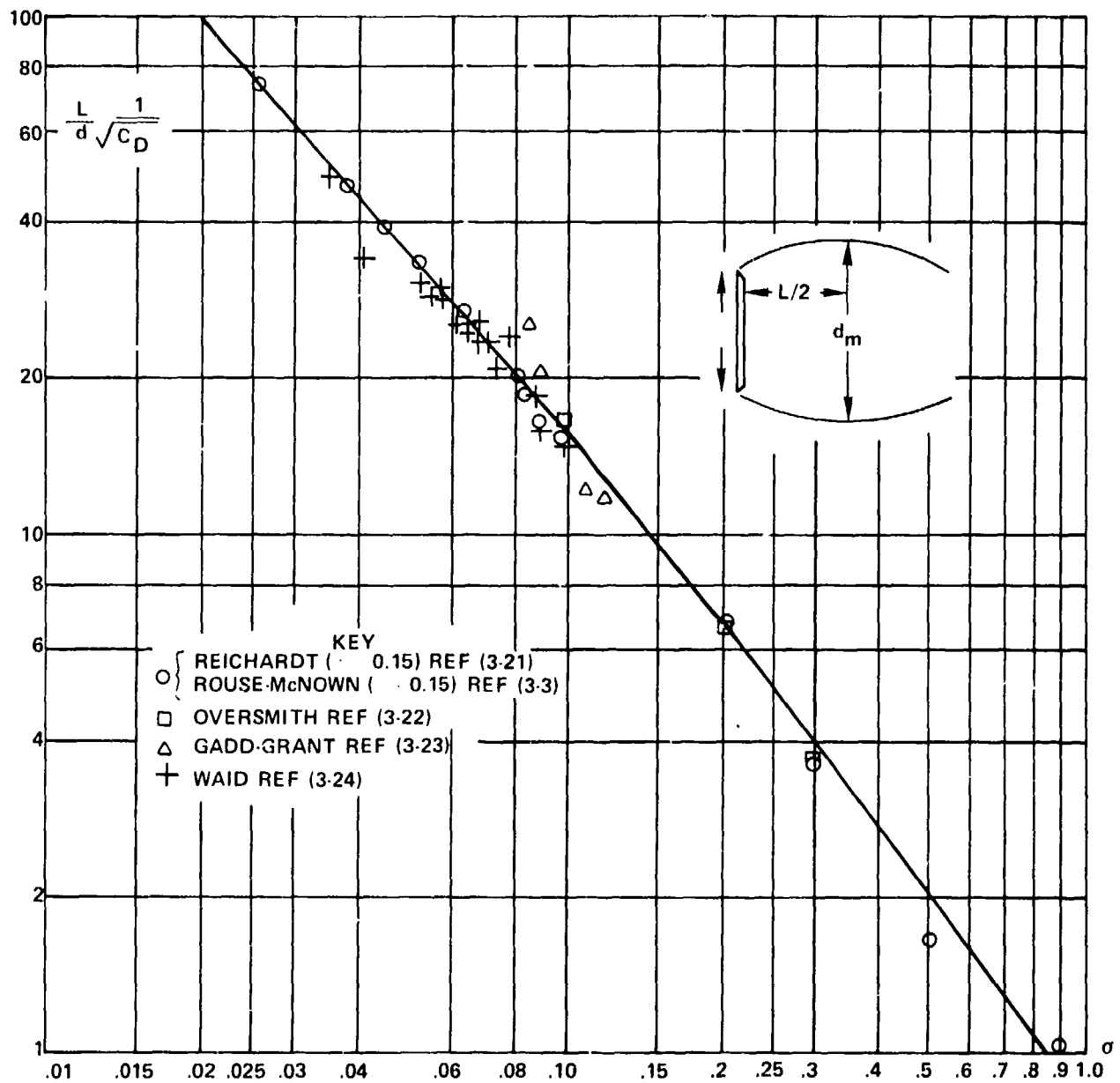
FIG. 3-18 SCALED LENGTH OF CAVITIES DUE TO A DISK
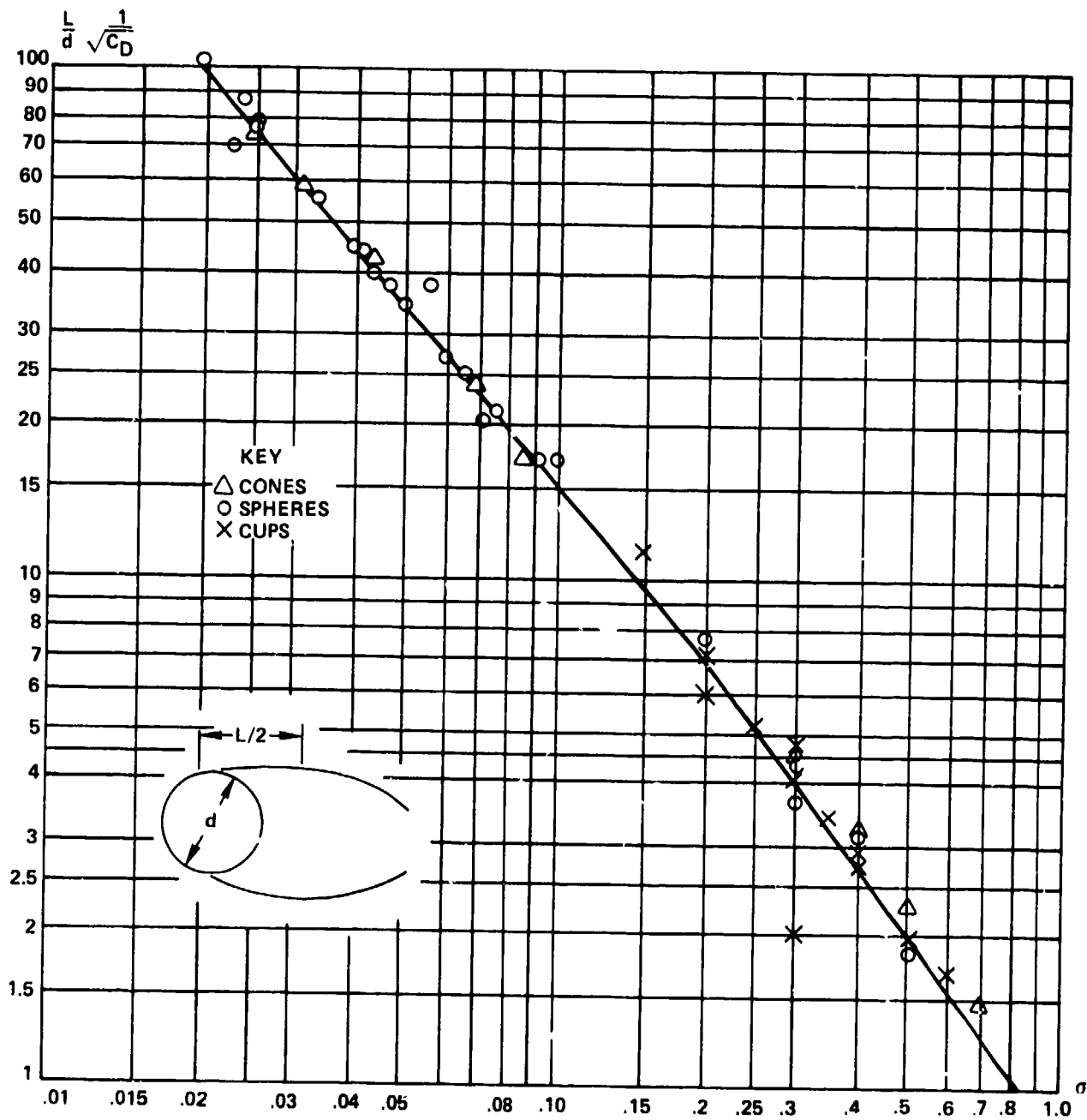
FIG. 3-19 LENGTH OF CAVITIES FOR VARIOUS NOSE SHAPES
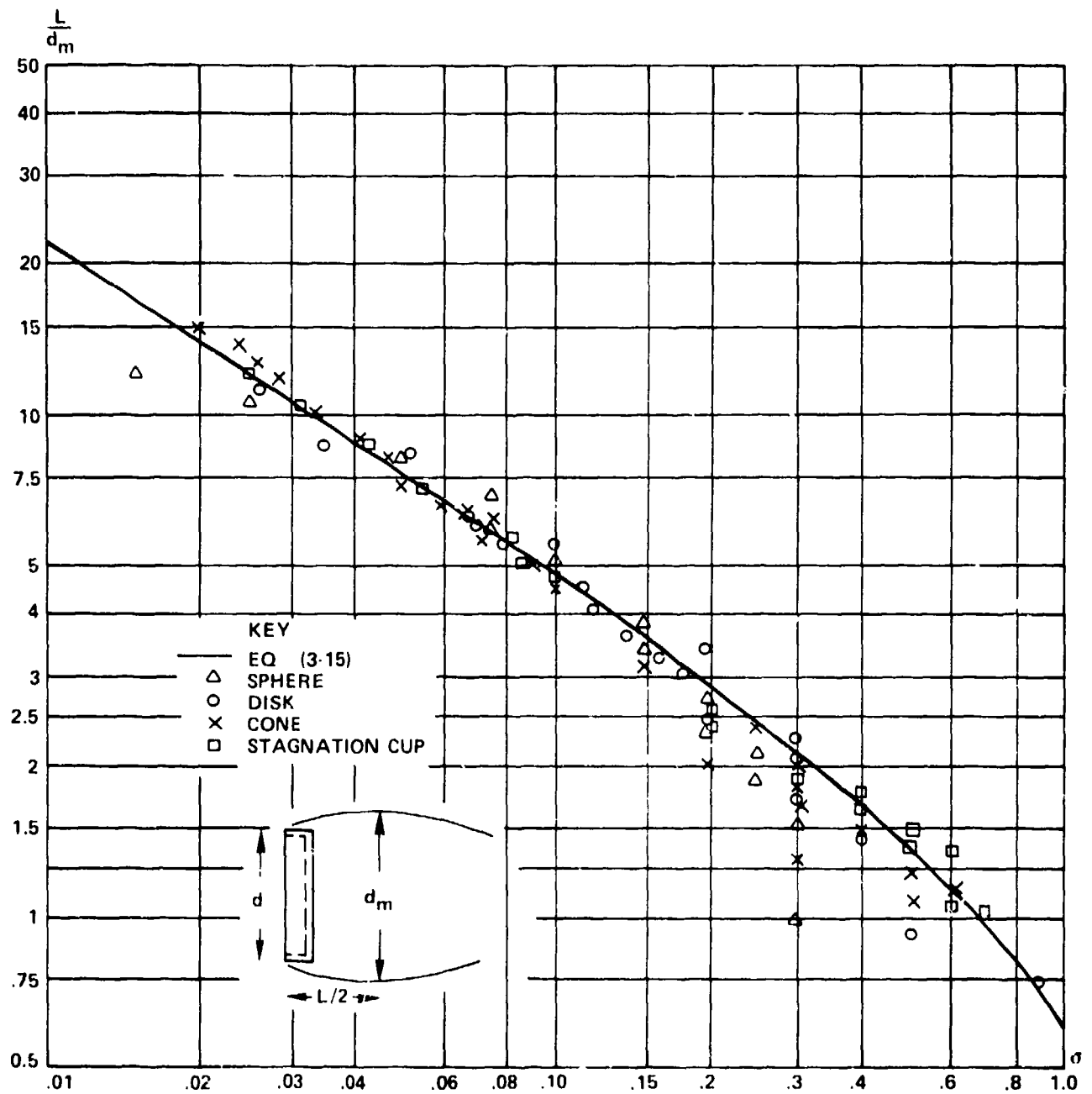
FIG. 3-20 EXPERIMENTAL L/d_m DATA
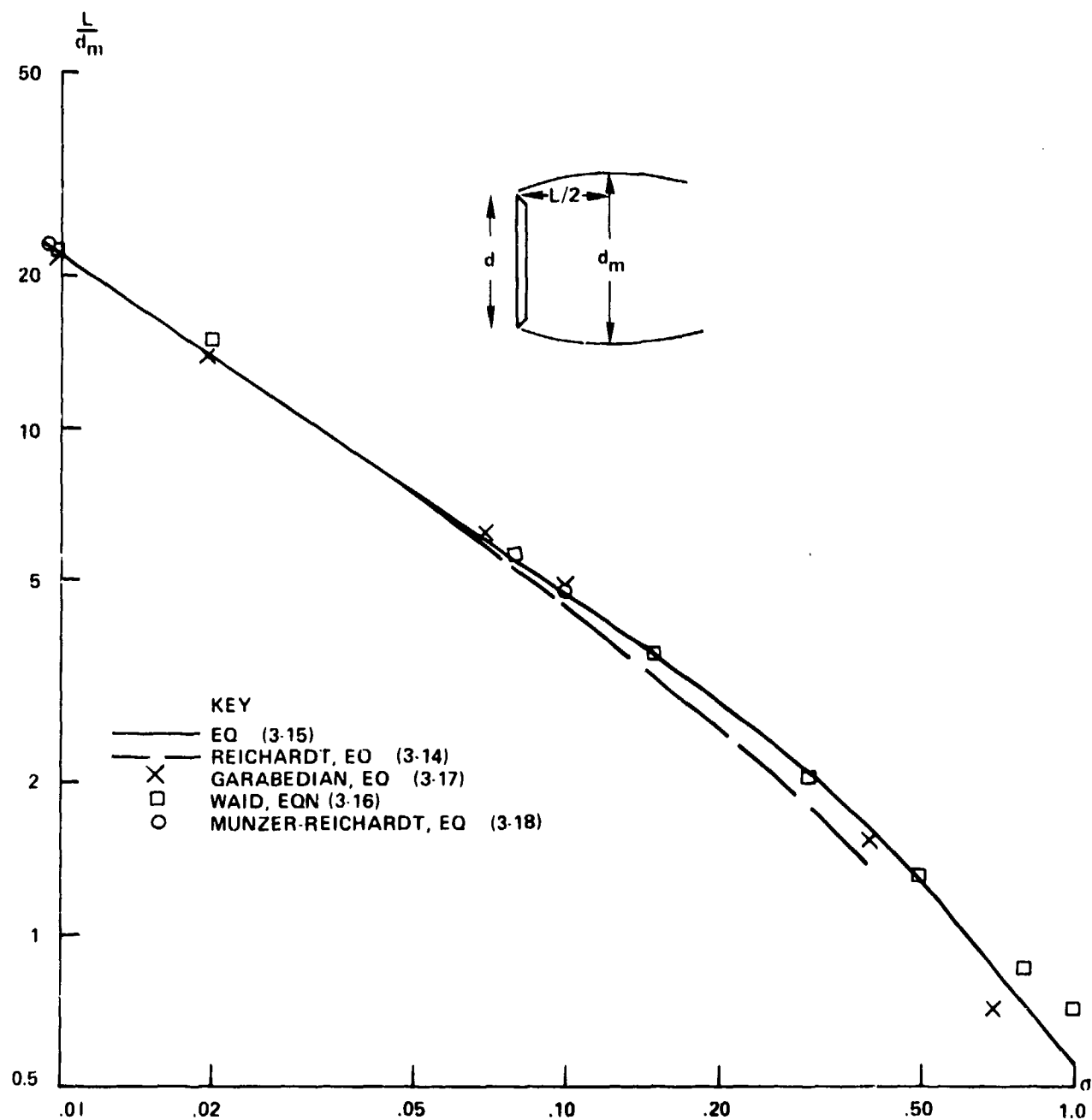
FIG. 3-21 COMPARISON OF FORMULAS FOR L/d_m
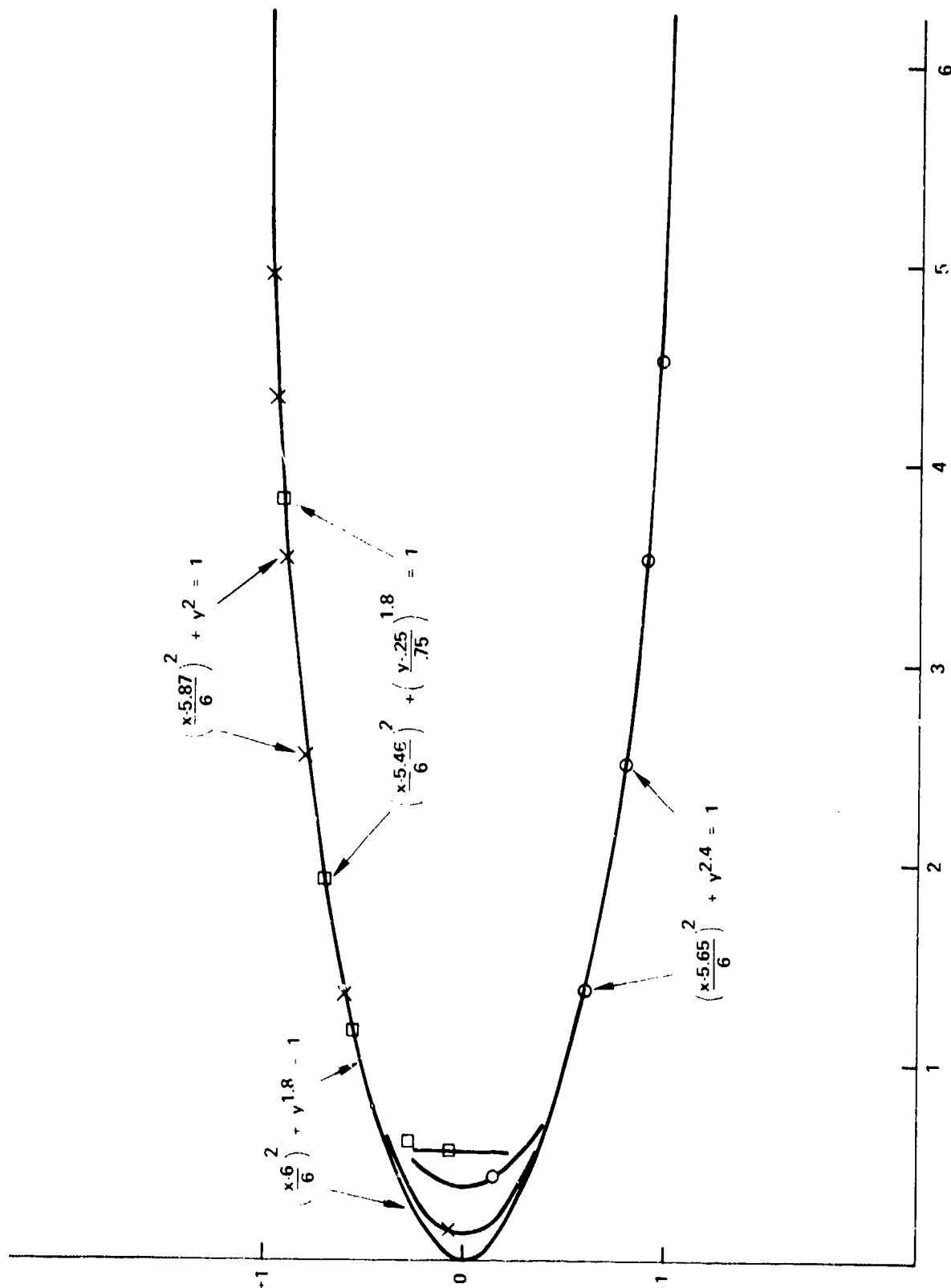
FIG. 3-22 COMPARISON OF PROPOSED CAVITY OUTLINES

$$\left(\frac{x-5.87}{6}\right)^2 + y^2 = 1$$

$$\left(\frac{x-5.46}{6}\right)^2 + \left(\frac{y-.25}{.75}\right)^{1.8} = 1$$

$$\left(\frac{x-5.65}{6}\right)^2 + y^{2.4} = 1$$

$$\left(\frac{x-6}{6}\right)^2 + y^{1.8} = 1$$
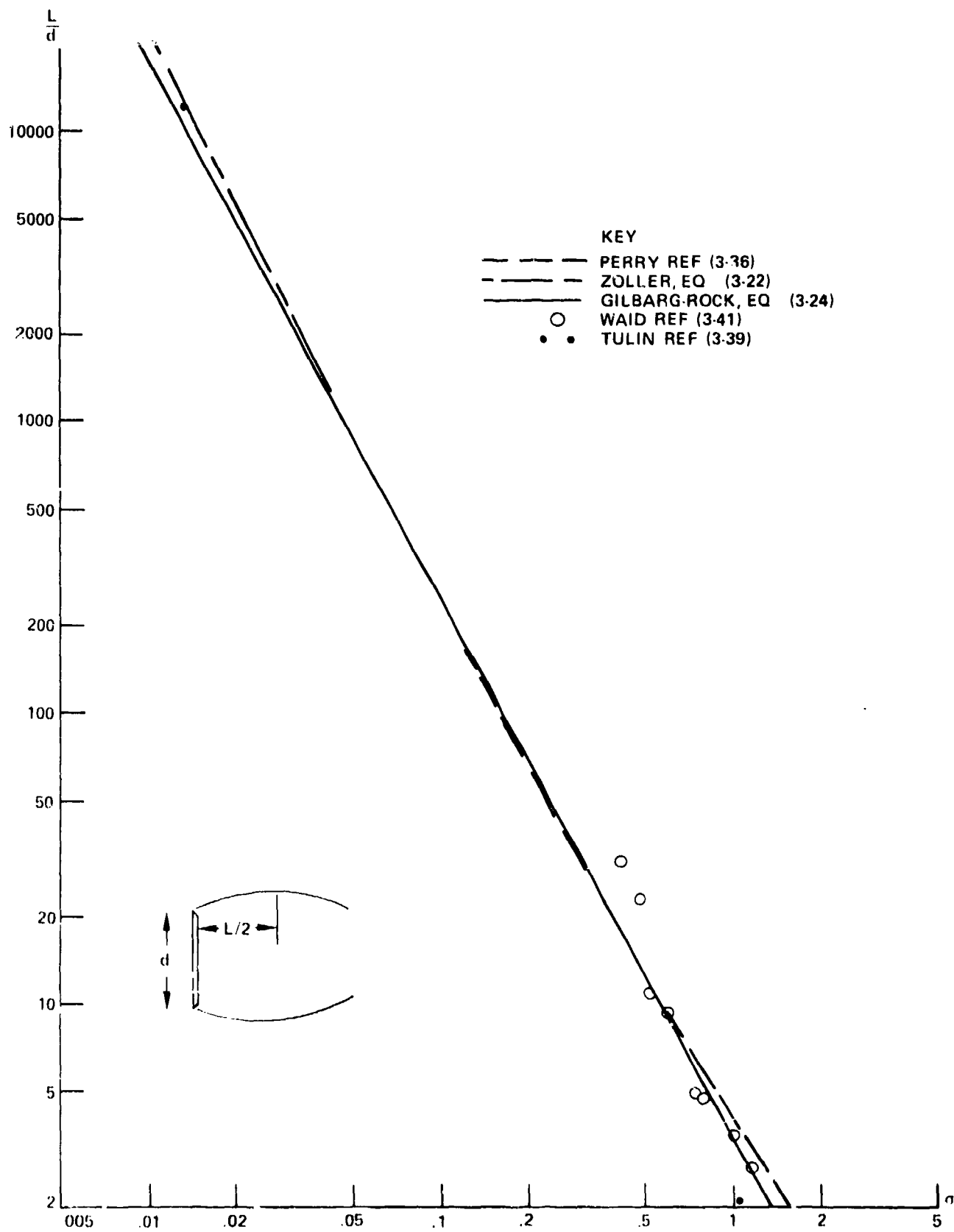
FIG. 3.23 LENGTH OF CAVITY DUE TO FLAT PLATE COMPARISION OF FORMULAS AND TEST
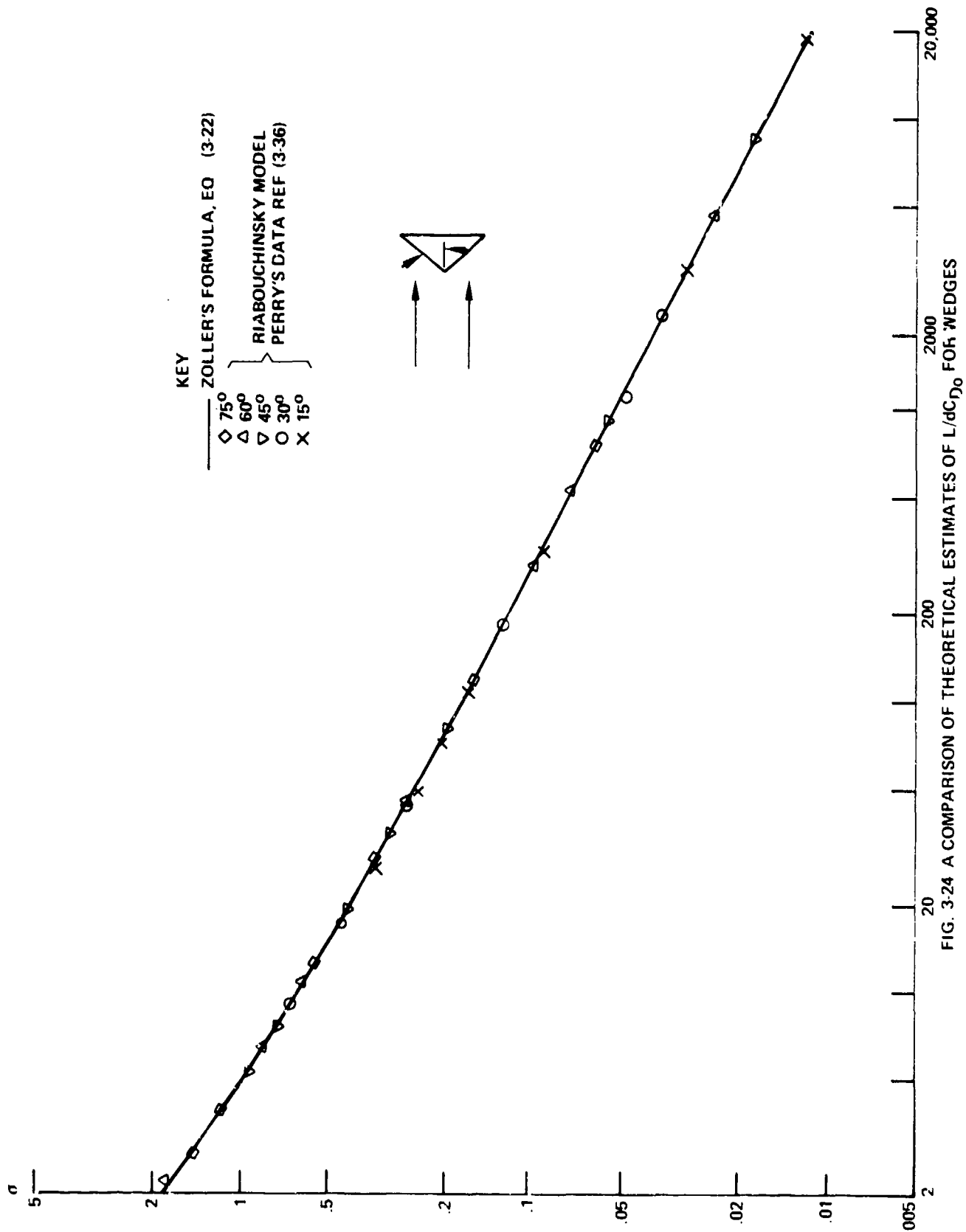
FIG. 3-24 A COMPARISON OF THEORETICAL ESTIMATES OF L/dC_{D_O} FOR WEDGES
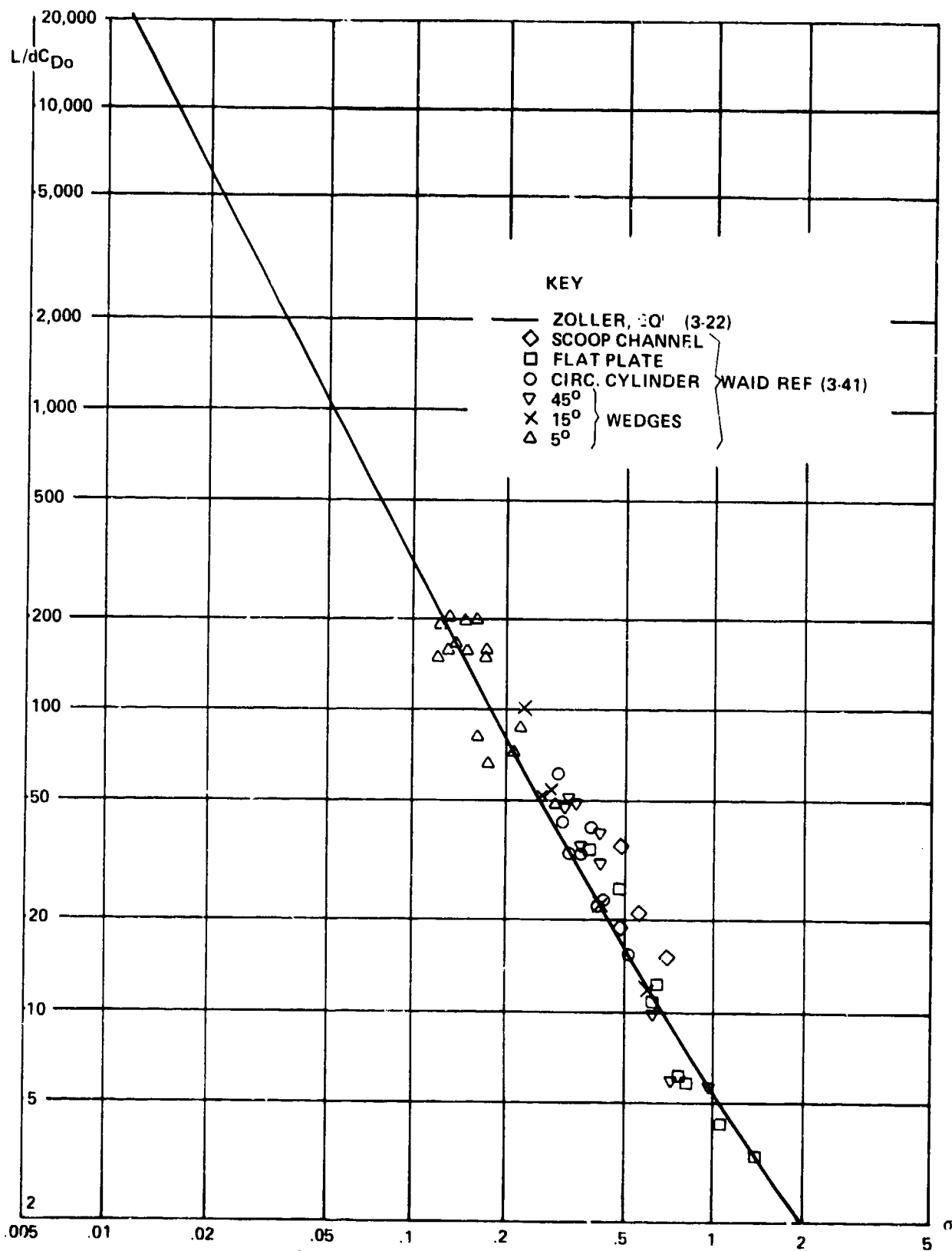
FIG. 3-25 COMPARISON OF THEORETICAL AND EXPERIMENTAL
TWO-DIMENSIONAL CAVITY LENGTHS
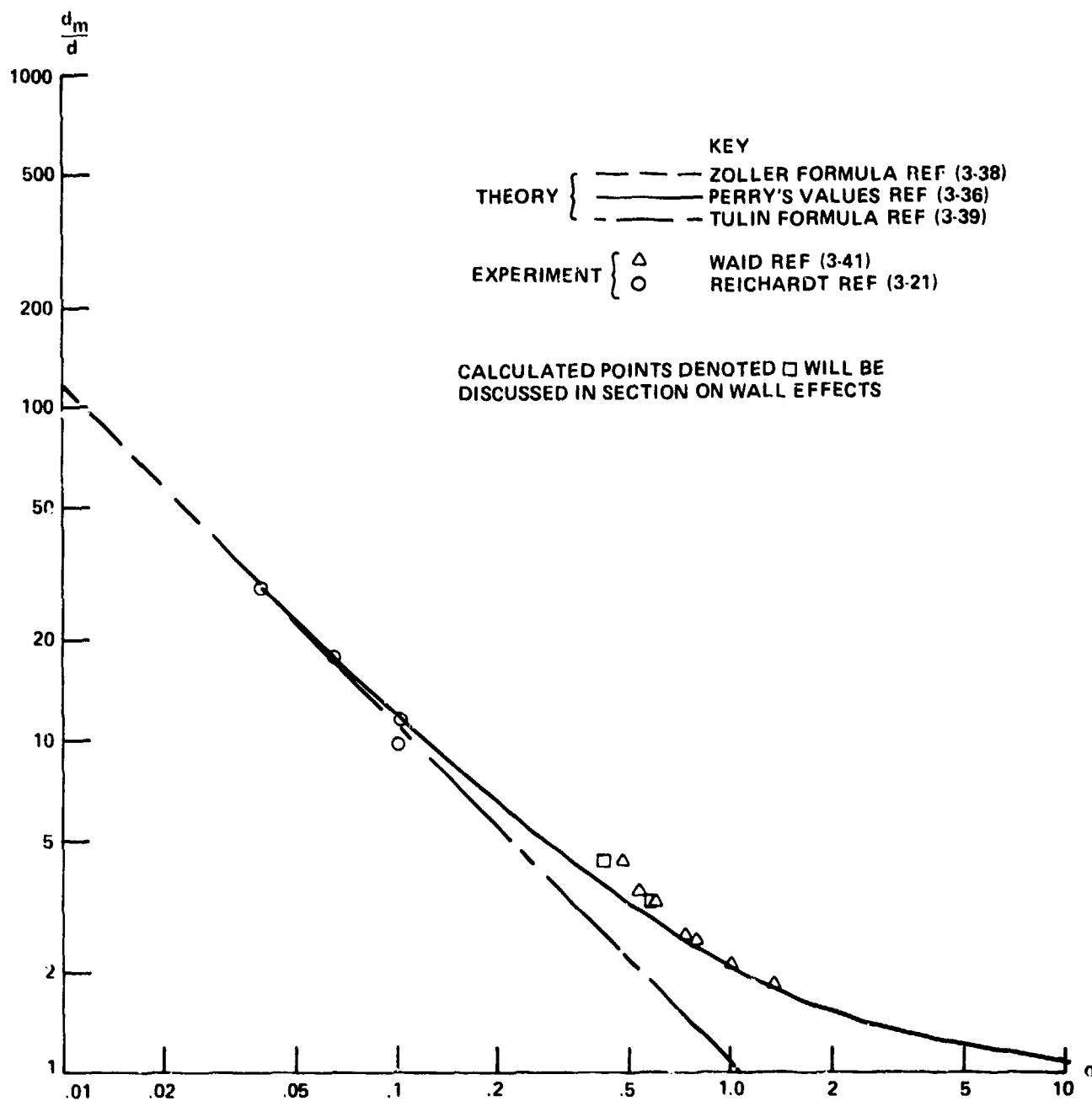
FIG. 3-26 COMPARISON OF d_m/d VALUES FOR FLAT-PLATE CAVITIES FROM THEORY AND EXPERIMENT
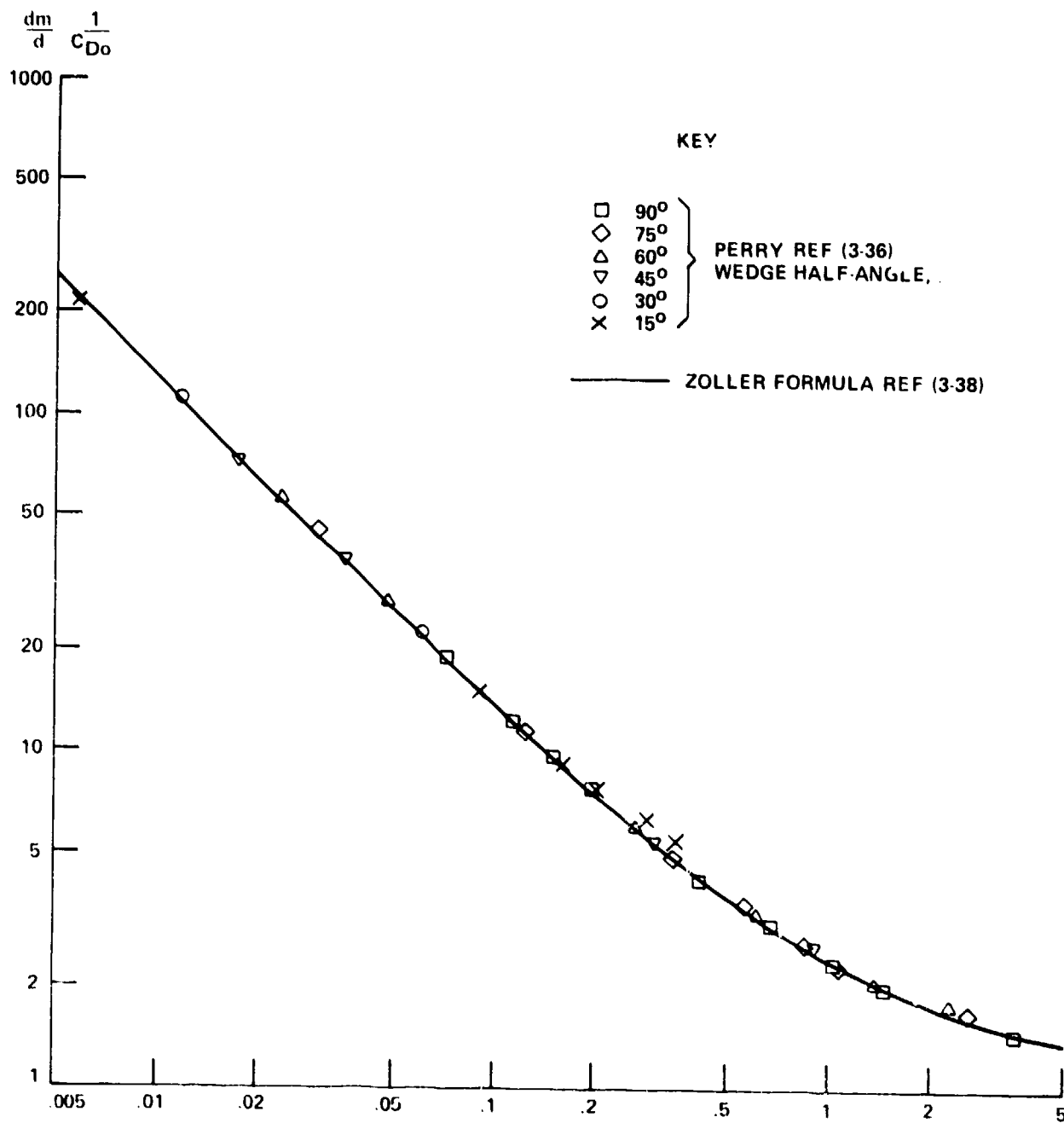
FIG 3 27 COMPARISON OF THEORETICAL ESTIMATES OF d_m/dC_{Do} FOR WEDGES
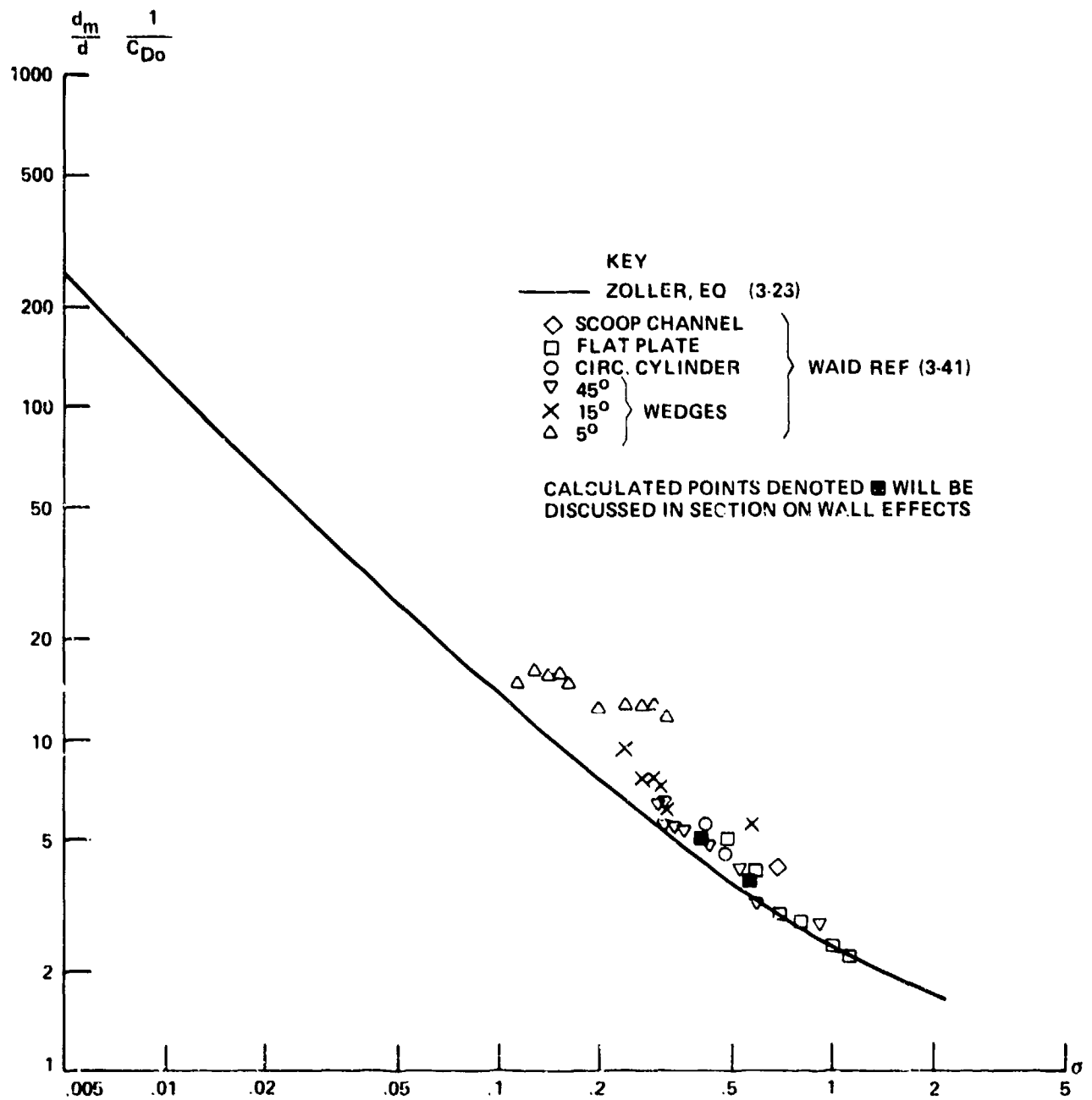
FIG. 3-28 COMPARISON OF THEORETICAL AND EXPERIMENTAL TWO DIMENSIONAL CAVITY DIAMETERS

KEY

ZOLLER, EQ (3-22) AND (3-23)

◇ SCOOP CHANNEL
◻ FLAT PLATE
○ CIRCULAR CYLINDER   } WAID REF (3-41)
▽ 45°
✕ 15°   } WEDGES
△ 5°

FIG. 3-29 COMPARISON OF L/d_m FROM THEORY AND EXPERIMENT FOR TWO-DIMENSIONAL CAVITIES
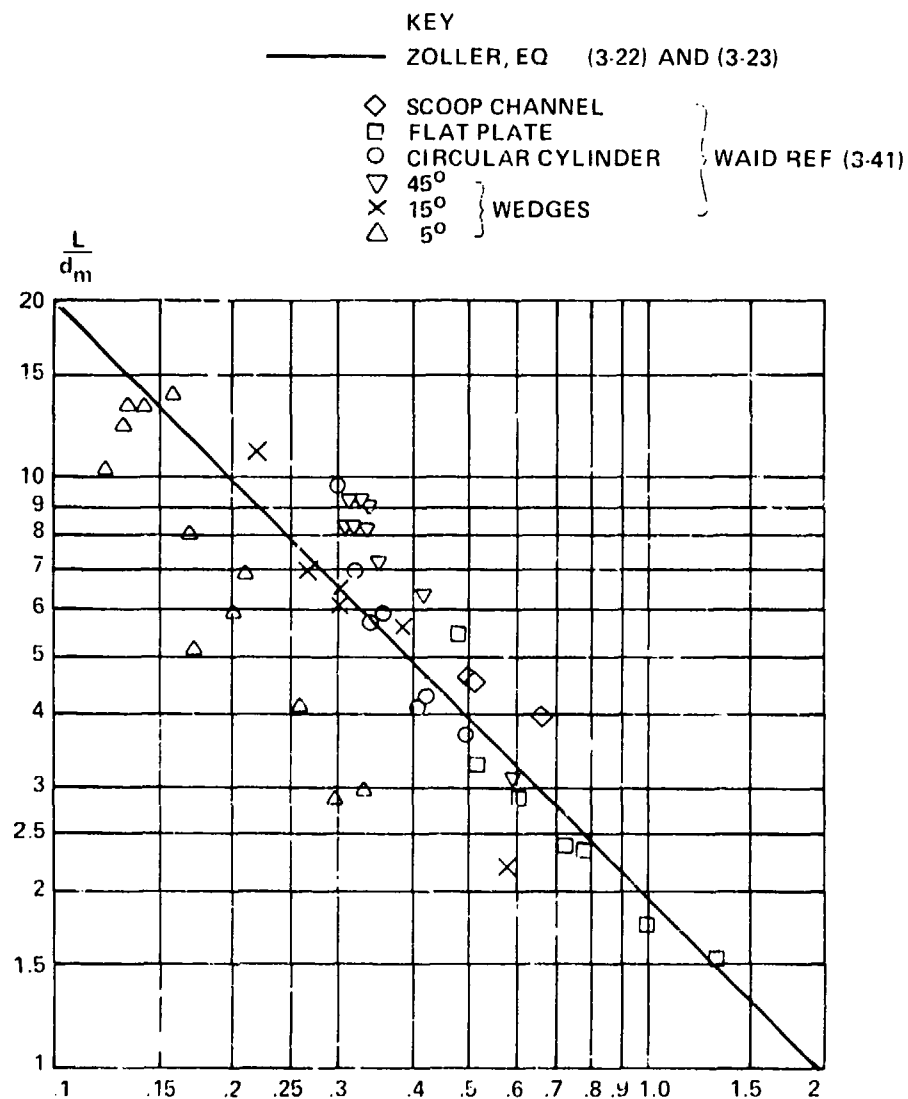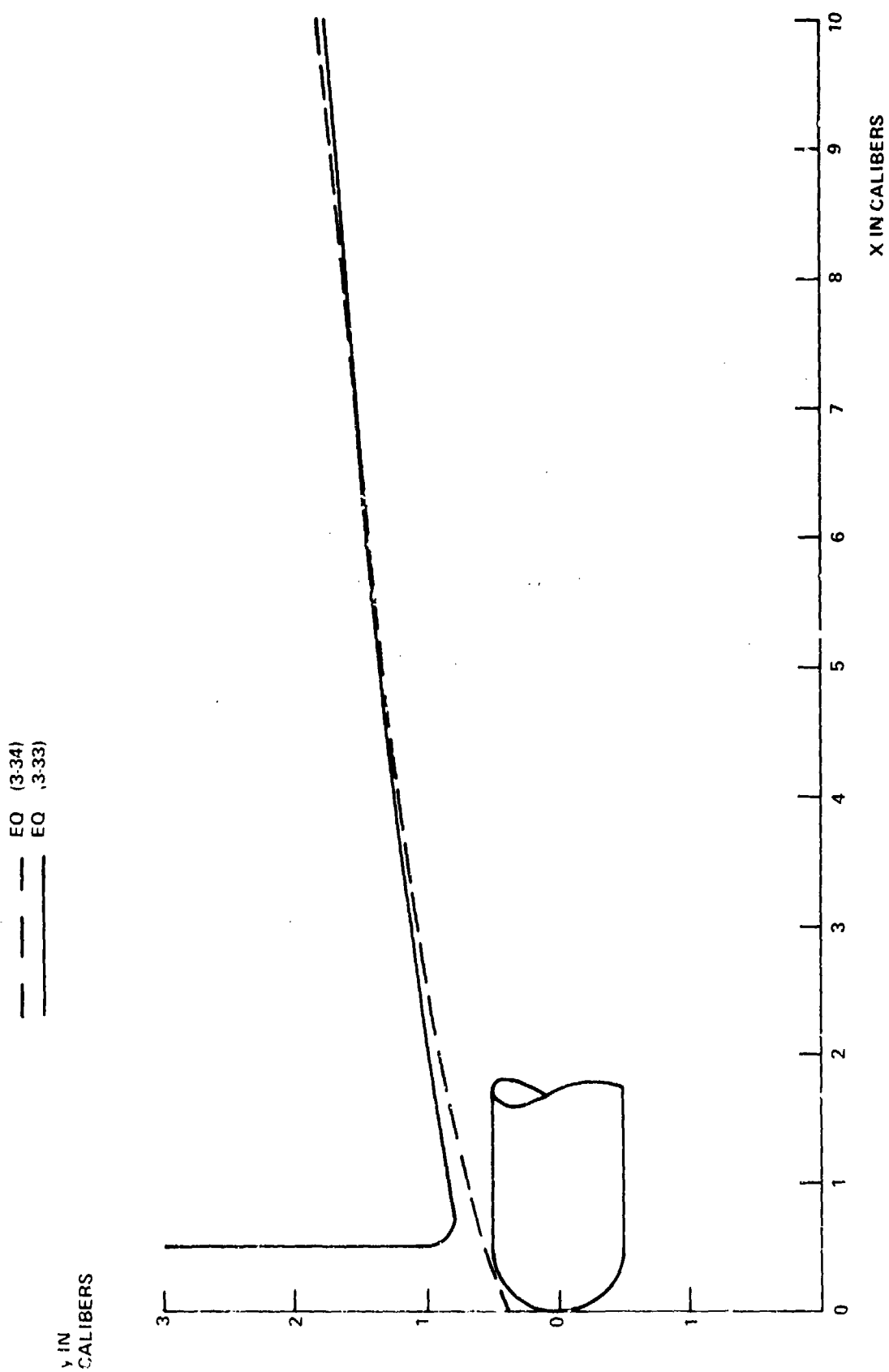
FIG. 3-30 CAVITY DUE TO A SPHERICAL NOSE WITH σ = 0
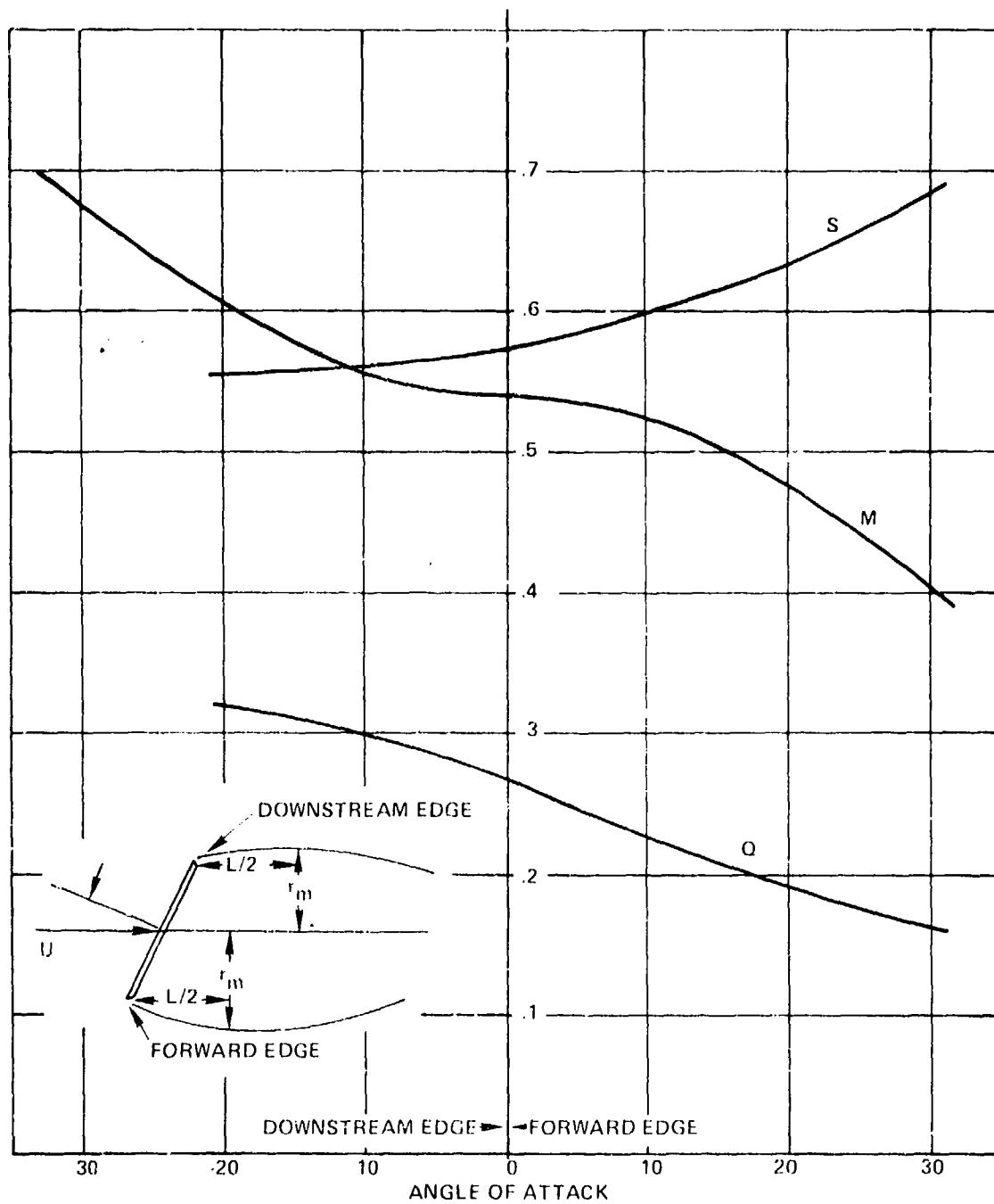
FIG. 3-31 VALUES OF PARAMETERS FOR USE IN EQUATIONS FOR LENGTH AND DIAMETER
OF CAVITIES DUE TO DISKS AT ANGLES OF ATTACK AFTER WAID REF (3.36)
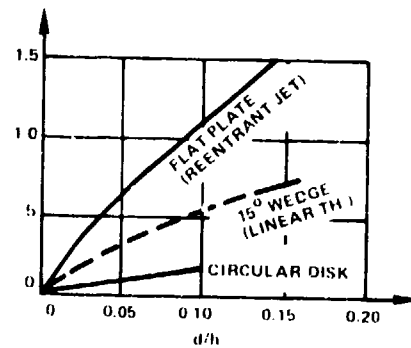
FIG. 3·32 THE DEPENDENCE OF BLOCKAGE
CAVITATION NUMBER ON d/h
AFTER COHEN-DIPRIMA REF (3·48)
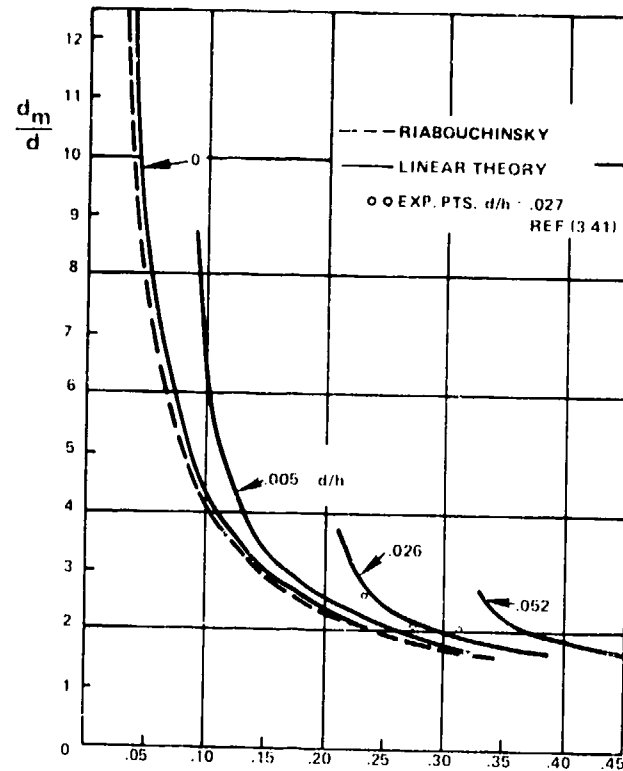
FIG. 3·33 THE DEPENDENCE OF MAXIMUM CAVITY
WIDTH ON CAVITATION NUMBER FOR A
15-DEGREE WEDGE IN A CHANNEL AFTER
COHEN-DIPRIMA REF (3·48)
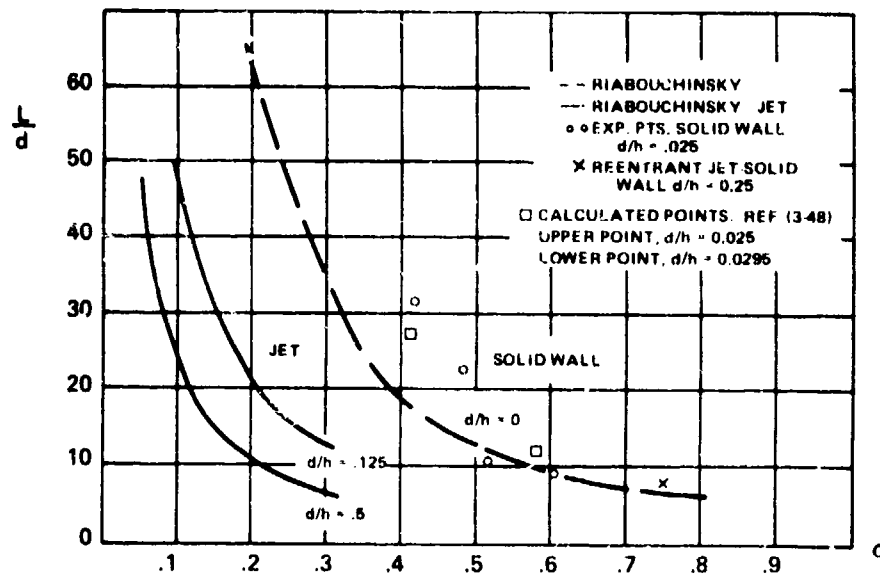
FIG. 3-34 THE DEPENDENCE OF CAVITY LENGTH ON CAVITATION
NUMBER FOR A FLAT PLATE AFTER COHEN-DIPRIMA REF (3-48)
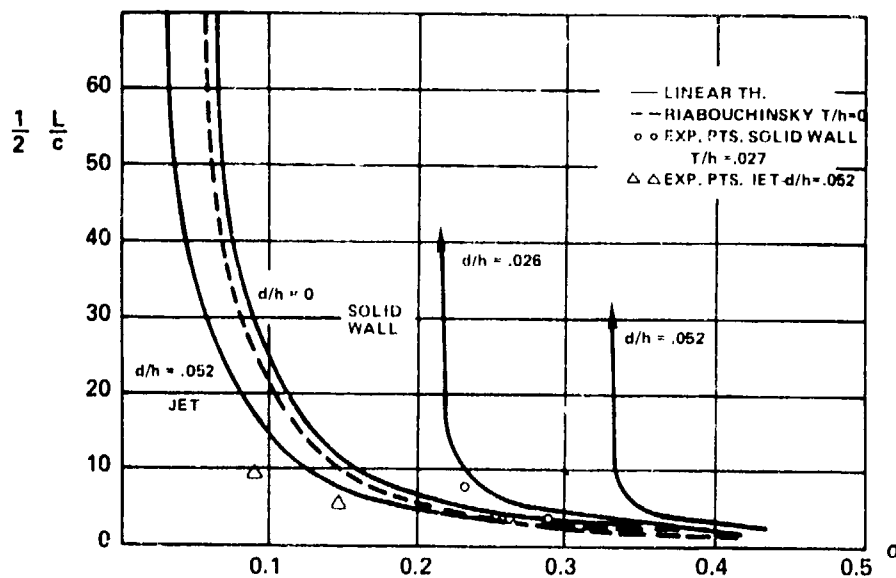
FIG. 3-35 THE DEPENDENCE OF CAVITY LENGTH ON CAVITATION
NUMBER FOR A 15-DEGREE WEDGE AFTER COHEN-DIPRIMA REF (3-48)
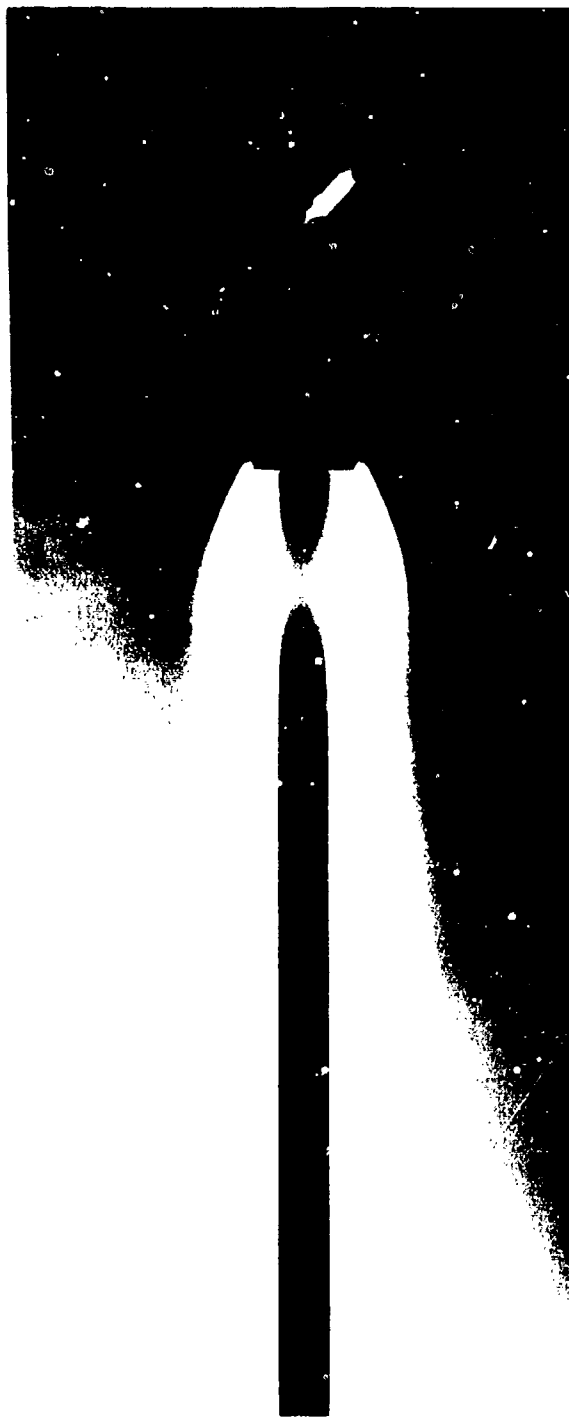
FIG. 3-36A. CAVITY BEHIND A DISK. 0.57, EXP. TIME = 2 SEC.

FIG. 3-36B. CAVITY BEHIND A DISK σ 0.57, EXP. TIME = 1/10000 SEC.
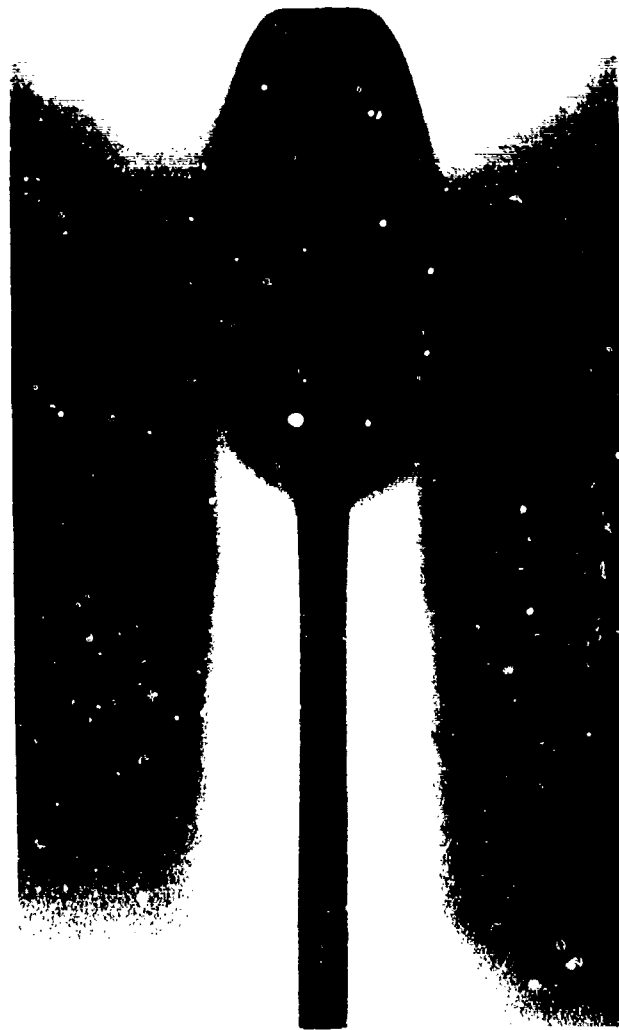
FIG. 3-36C. CAVITY BEHIND A DISK · 0.19, EXP. TIME = 2 SEC.
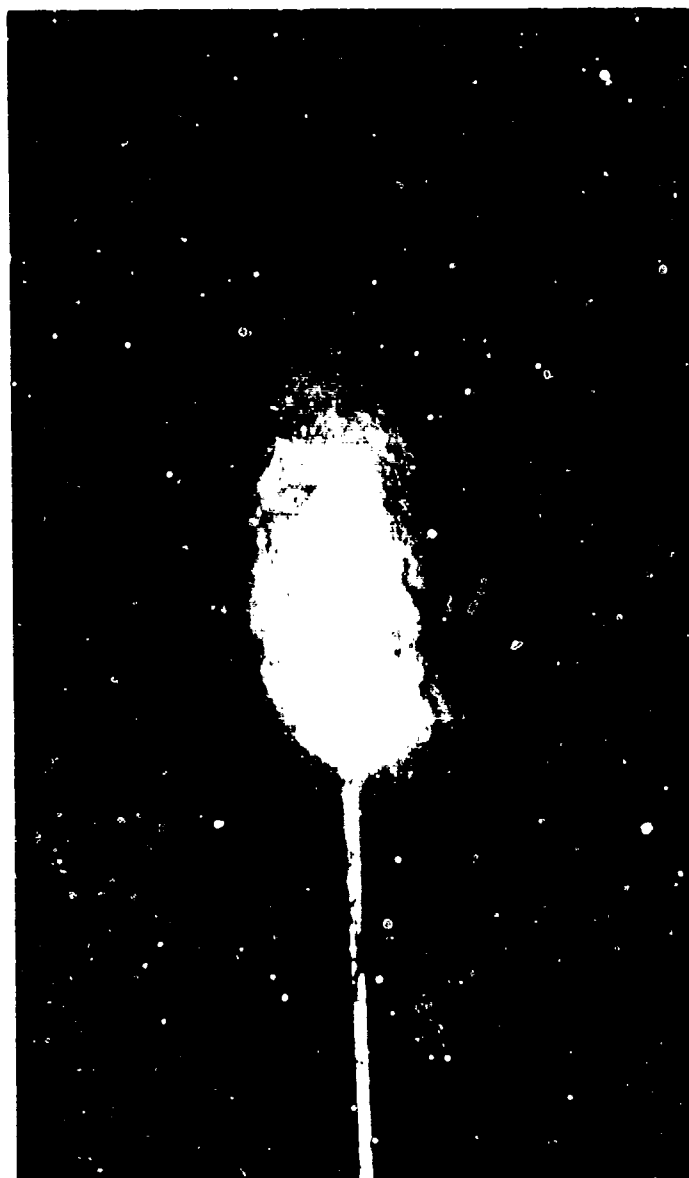
FIG. 3-36D. CAVITY BEHIND A DISK σ 0.19, EXP. TIMES = 1/10,000 SEC.

FIG. 3-38 VARIATION OF MAXIMUM OBTAINABLE CAVITATION NUMBER WITH FROUDE NUMBER (AFTER CAMPBELL-HILBORNE)

FIG. 3-37 ENTRAINMENT FOR A 1-INCH DISK (AFTER SWANSON-O'NEILL)
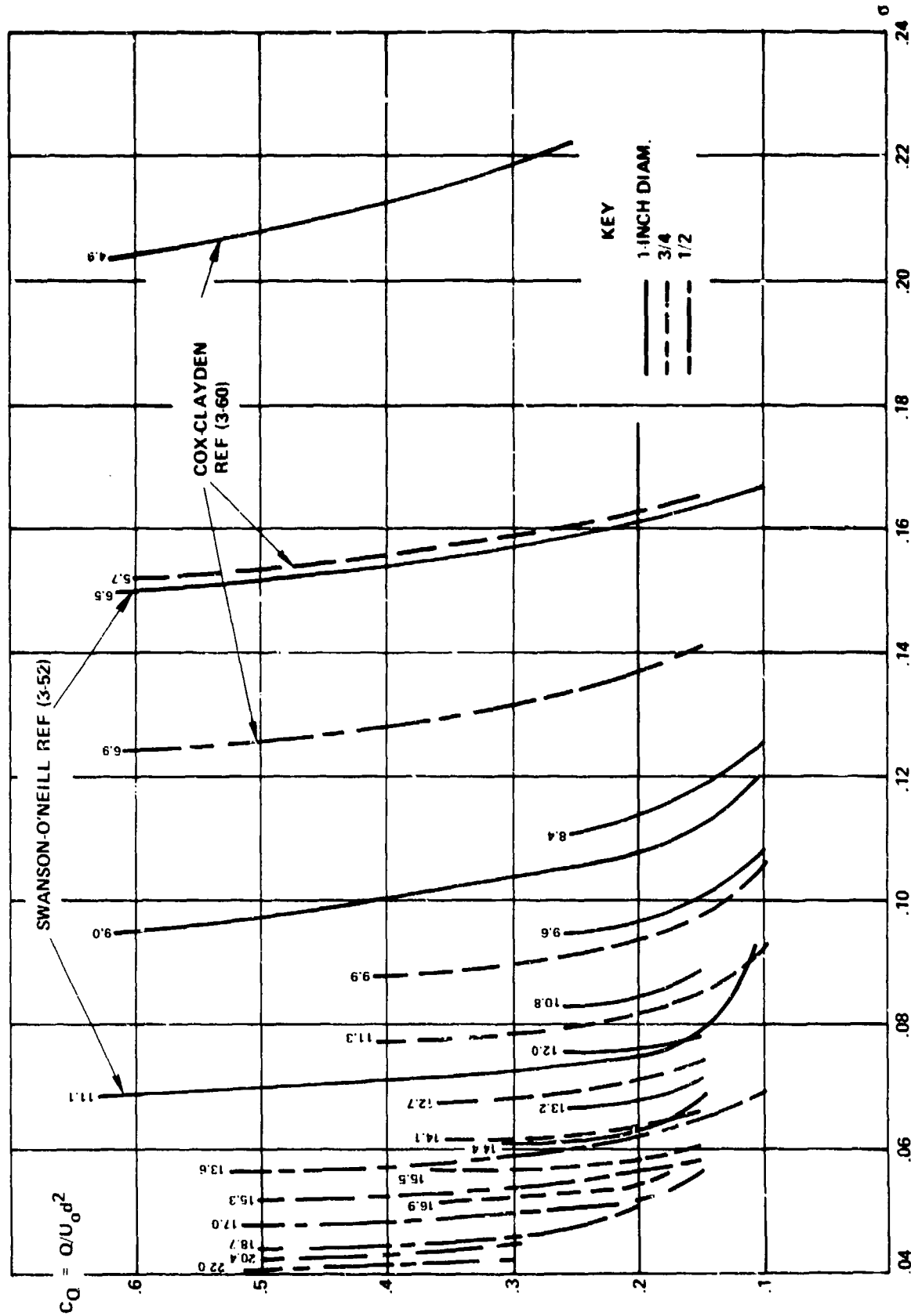
FIG. 3-39 VENTILATION CURVES FOR CAVITIES DUE TO SMALL DISKS DATA FROM CAMPBELL-KILBORNE REF (3-30) EXCEPT WHERE LABELED. FROUDE NUMBERS ARE SHOWN ABOVE THE GRAPHS.
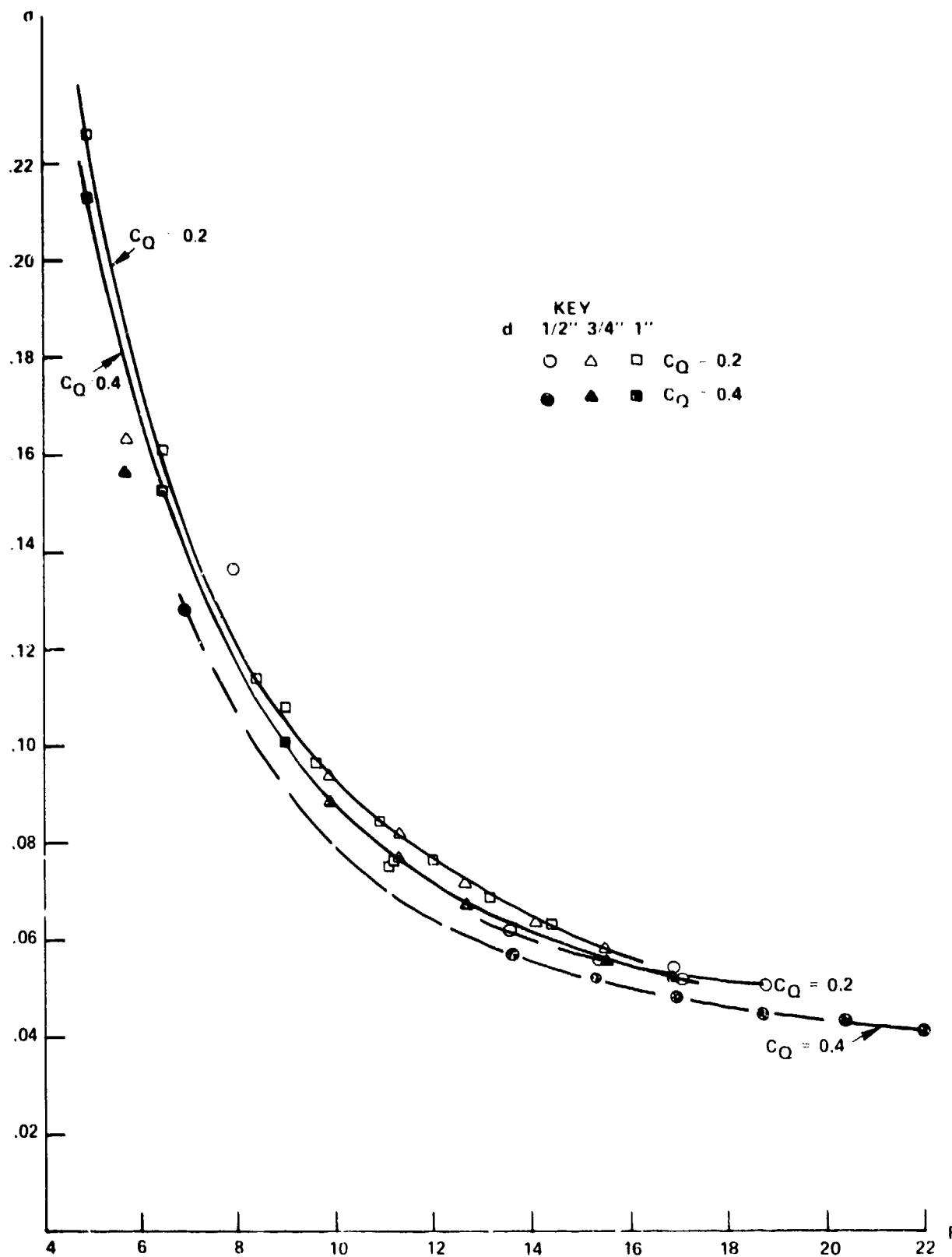
FIG. 3-40 CAVITATION NUMBERS FOR CONSTANT VENTILATION RATES
SMALL DISK CAVITIES
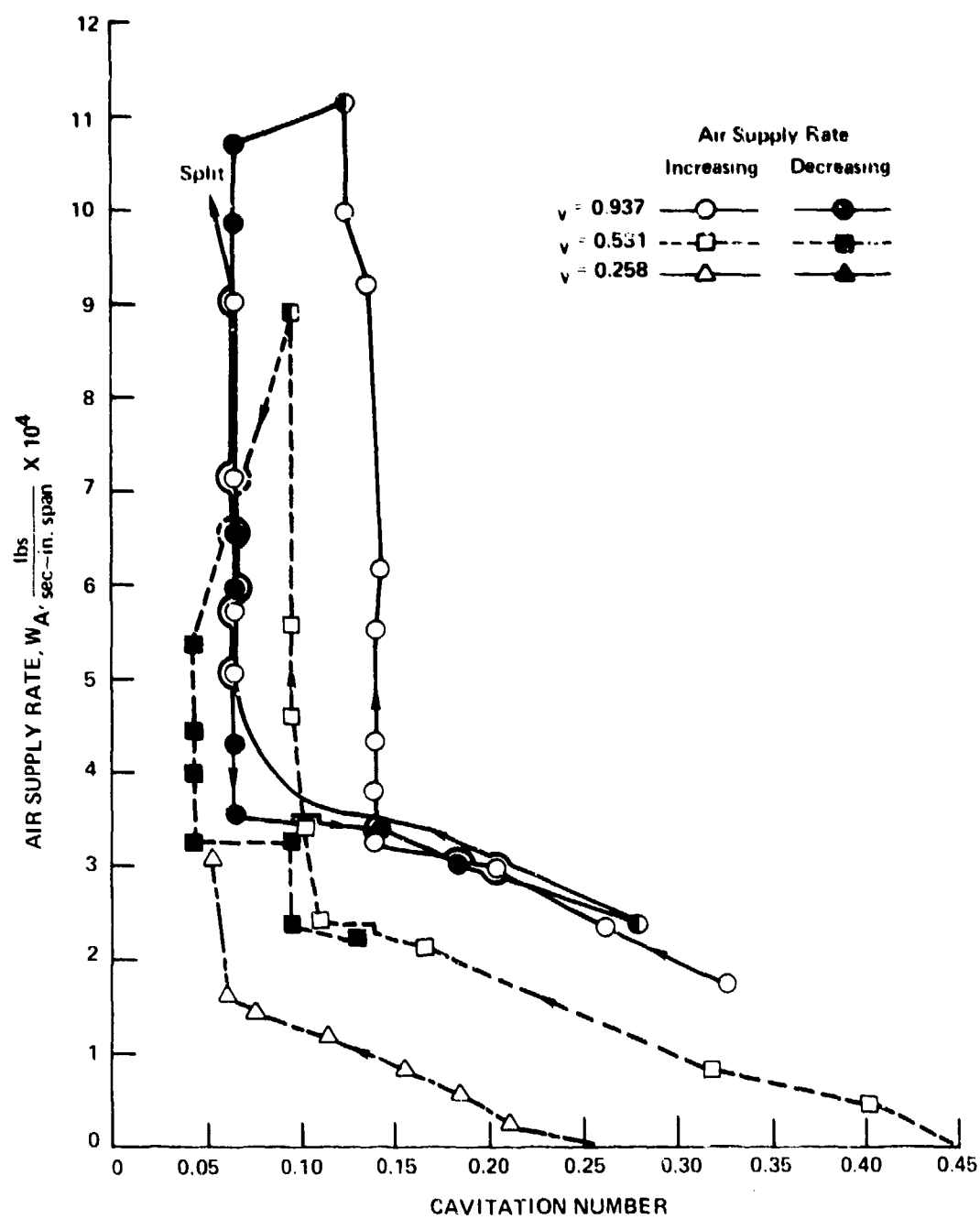
FIG. 3-41 AIR SUPPLY RATE AS A FUNCTION OF CAVITATION NUMBER
(TWO-DIMENSIONAL, 1/8-IN. NORMAL PLATE IN 10-IN. JET)
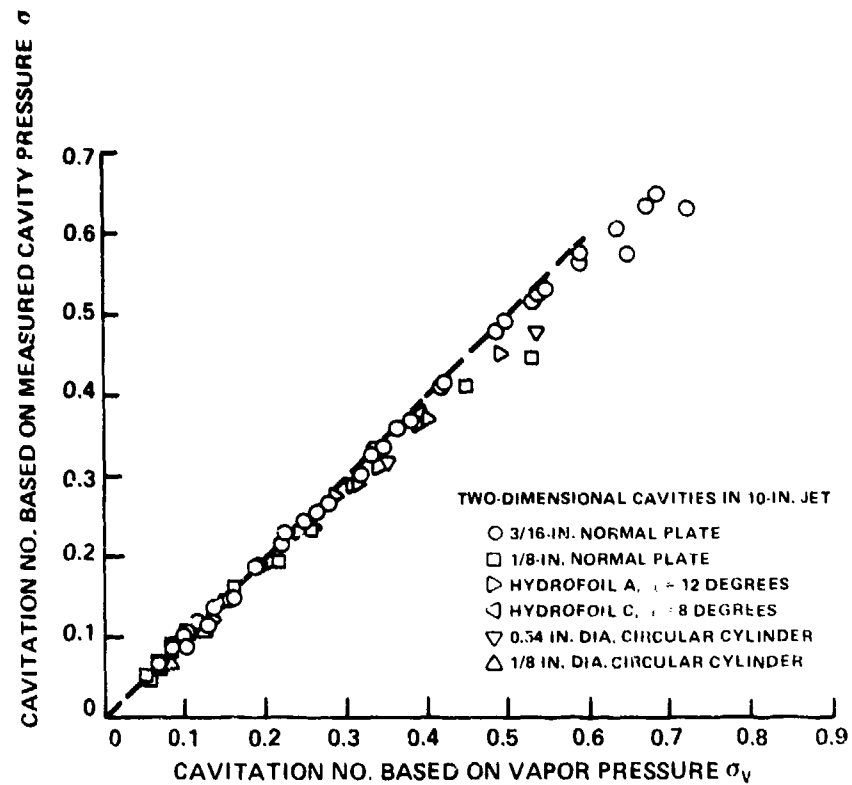
FIG. 3-42 COMPARISION BETWEEN CAVITATION NUMBER BASED ON
VAPOR PRESSURE AND CAVITATION NUMBER BASED ON
MEASURED CAVITY PRESSURE FROM SILBERMAN-SONG REF (3-57)

FIG. 3-43 EFFECT OF GRAVITY ON CAVITY DUE TO A DISK
(COURTESY OF NAVAL SHIP RESEARCH AND
DEVELOPMENT CENTER)

10-DEGREE WEDGE — STREET REF (3-72)
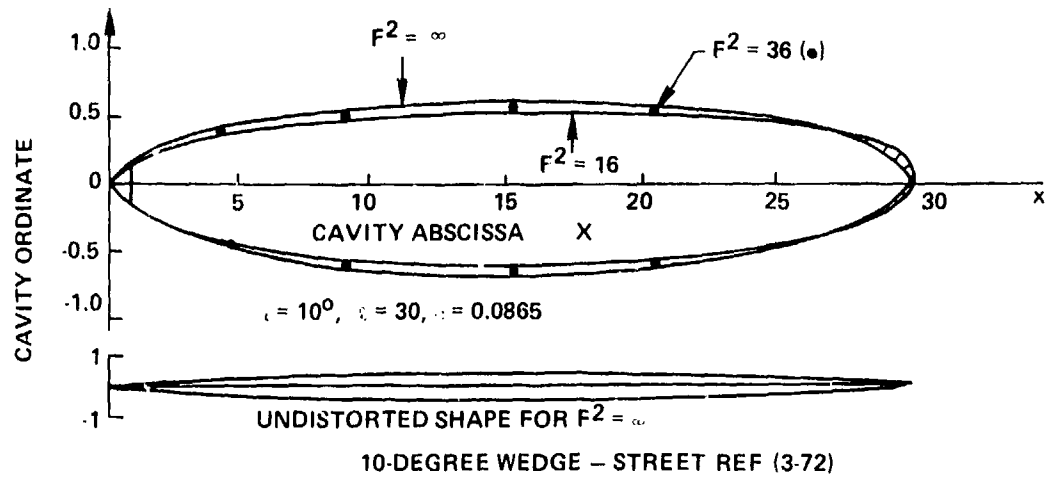
FIG. 3-44 EFFECT OF FROUDE NUMBER ON CAVITY SHAPE
IN TRANSVERSE GRAVITY FIELDS
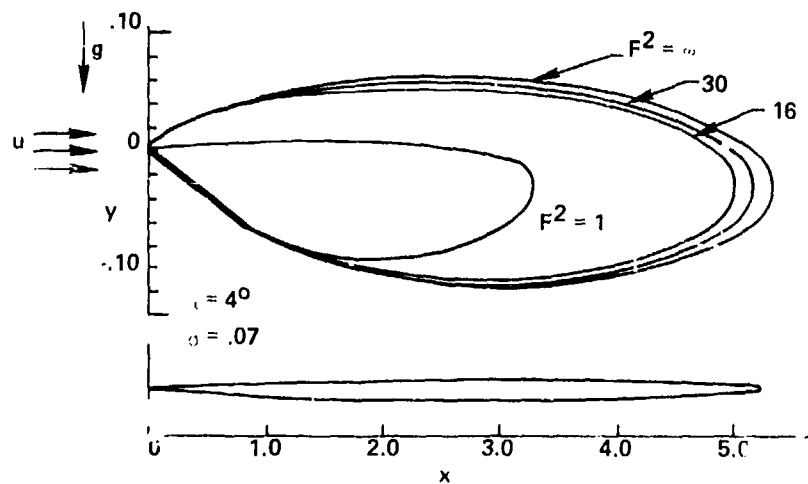
FLAT PLATE INCLINED AT 4 DEGREES — PARKIN REF (3-71)

FIG. 3-45 EFFECT OF FROUDE NUMBER ON CAVITY SHAPE
IN TRANSVERSE GRAVITY FIELDS
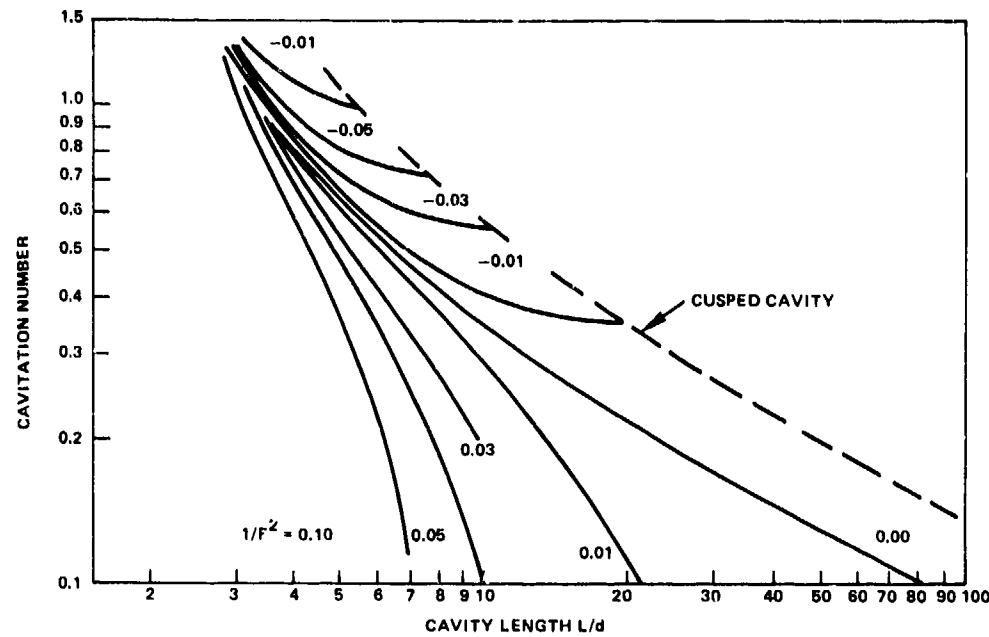
FIG. 3-46 LENGTH OF CAVITY DUE TO 15° HALF-ANGLE WEDGE
IN LONGITUDINAL FIELD REF (3-76)
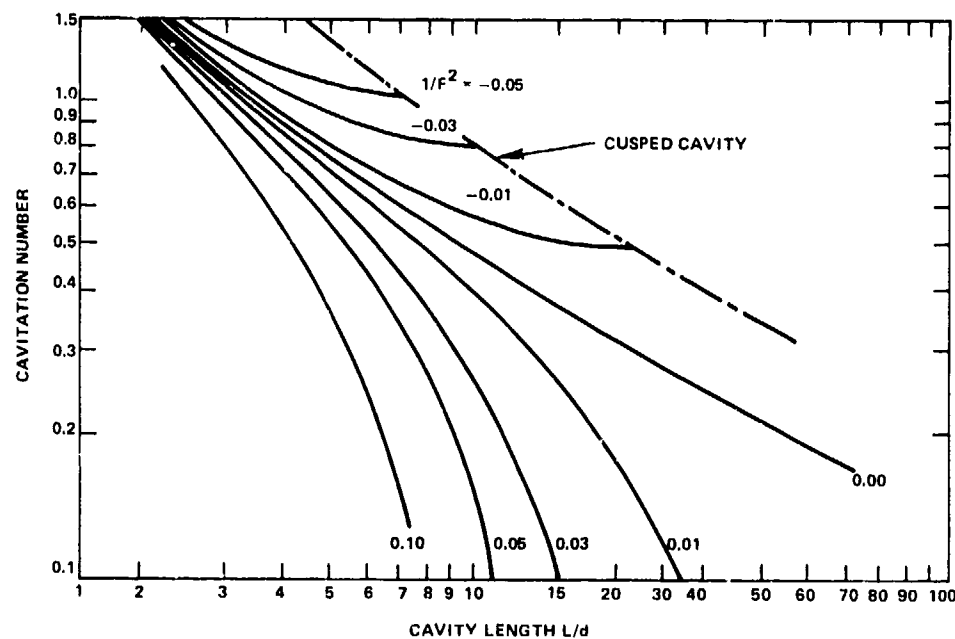
FIG. 3-47 LENGTH OF CAVITY DUE TO 45° HALF-ANGLE EDGE
IN LONGITUDINAL FIELD REF (3-76)

APPENDIX A

DERIVATION OF EQUATION (3-4)

Reichardt (Ref. (3-21)) presented a formula, which is equation (3-4) of this report, for the maximum diameter of the steady cavity as a function only of the drag coefficient and cavitation number. The major part of the general argument underlying this formula is presented below in simplified form.

The obstacle which generates the cavity may be regarded as mounted in a water tunnel of uniform cross section, large enough that the effect of the walls can be ignored. Control surfaces are located across the tunnel at AA and BB in Figure 3-A1. At AA freestream conditions exist with U_∞ and p_∞. The surface BB is at the maximum cross section of the cavity where the pressure is p and the velocity U outside of the cavity. The pressure is p_c within the cavity and the velocity there may be taken as zero since it is the momentum of the flow that is significant. The area of the general cross section is split into two parts based on the cross section BB: A_1 outside of the cavity and A_c within the cavity.

The force acting on the volume of water and reducing the momentum of the flow consists of the pressure force and the drag force D. In general terms

$$\text{rate of change of momentum} = \int (p_\infty - p)\, dA - D = -\rho \int (U_\infty^2 - U^2)\, dA$$

where the integration is over the control surfaces. In detail

$$D = \int_1 (p_\infty - p)\, dA + \int_c (p_\infty - p_c)\, dA + \rho \int_1 (U_\infty^2 - U^2)\, dA \div \rho U_\infty^2 A_c \quad (3\text{-}A1)$$

where $\int_1$ and $\int_c$ are integrals over the areas A_1 and A_c respectively.

Reichardt introduced equation (3-A1) in discussing a wake problem and then applied it to the cavity. For the cavity problem the second integral contains the force on the missile due to cavity pressure. This small component of the drag force is accordingly included erroneously both in this term and in D.

If Bernoulli's equation

$$P_\infty - p = (1/2)\rho\, (U^2 - U_\infty^2)$$

is used in the first integral of equation (3-A1), and the continuity relation

$$\int_1 U dA = \int_1 U_\infty dA + \int_C U_\infty dA = \int_1 U_\infty dA + U_\infty A_C$$

is inserted in the last term:

$$D = (1/2)\rho \int_1 (U_\infty^2 - U^2) dA + \int_C (p_\infty - p_C) dA + \rho \int_1 U_\infty U da - \rho \int_1 U_\infty^2 dA$$

or

$$D = (p_\infty - p_C) A_C - (1/2)\rho \int_1 (U_\infty - U)^2 \,\llcorner \qquad (3\text{-}A2)$$

If

$$C_{Dm} = D/A_C q_\infty = D/A_C (1/2)\rho U_\infty^2$$

is defined as the cavity-running drag coefficient based on the maximum cross-sectional area of the cavity instead of the cross section of the obstacle, then, from equation (3-A2)

$$C_{Dm} = \frac{p_\infty - p_C}{q_\infty} - \frac{1}{A_C} \int_1 \left(\frac{U_\infty - U}{U_\infty}\right)^2 dA = \sigma - \frac{1}{A_C} \int_1 \left(\frac{U_\infty - U}{U_\infty}\right)^2 dA \qquad (3\text{-}A3)$$

Thus the drag coefficient C_{Dm} has a value which is less than σ by an amount which depends on the reduction of speed of the streamlines outside of the cavity.

For convenience, equation (3-A3) can be written

$$C_{Dm} = \sigma f \qquad (3\text{-}A4)$$

where f may be a function of σ. Further, from the definition of the drag coefficient,

$$C_D = (d_m/d)^2 C_{Dm}$$

where C_D and C_{Dm} are the drag coefficients related to the maximum body area $A = \pi d_m^2/4$. Hence

$$C_D = (d_m/d)^2 \sigma f$$

and

$$d_m/d = (C_D/\sigma f)^{1/2}. \qquad\qquad (3\text{-}A5)$$

Reichardt reported the value

$$f = 1 - 0.132\sigma^{1/7} \qquad\qquad (3\text{-}A6)$$

based on a source-sink theoretical determination. This leads to equation (3-4).

If the last term in equation (3-A6) is neglected, equation (3-A5) reduces to equation (3-8), the result obtained by Garabedian (Ref. (3-28)).
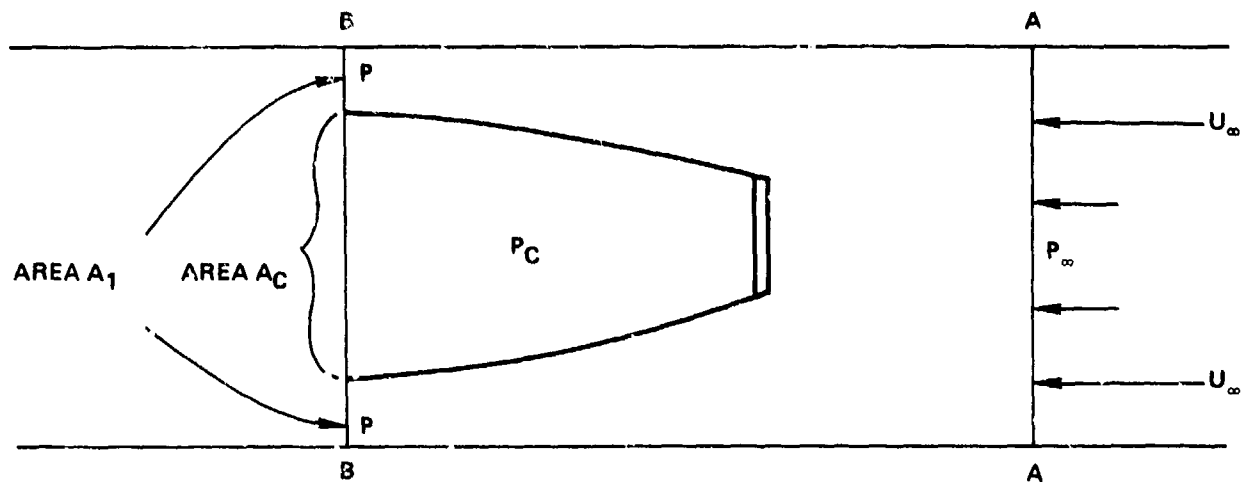
FIG. 3-A1 CONTROL SURFACES FOR CAVITY PROBLEM

Chapter 4

FORCES AT WATER IMPACT

Symbols

A	cross-sectional area of missile used as reference
A_i	cone cross-sectional area at original water surface
A_n	cross-sectional area of wetted portion of missile nose
b	= s/r, nondimensional penetration distance
B	buoyant force
B_1	effective depth of cone
c	speed of sound
C_D	drag coefficient referred to instantaneous velocity
C_D^*	drag coefficient referred to impact velocity
$C_{D\infty}^*$	C_D^* for missile of infinite mass
C_{ds}	steady cavity-running drag coefficient
C_{Ds}	assumed partial C_{ds} during water entry
d	maximum diameter of missile
D	drag force
f	skin-friction force
F	total force on missile
h	drop height before water impact; missile depth; penetration ratio = l/w
I	transverse moment of inertia
k	added-mass constant = $m/\rho s^3 (\tan \beta/2)^3$
K	"total" added-mass constant = $k + \pi C_{ds}/6 \tan (\beta/2)$
ℓ	half width of plate
L	half wetted breadth of wedge
m	added mass
m'	= $2m/\rho$ Ar, dimensionless added mass
M	mass of missile

ii

M'	$= 2M/\rho\ Ar$, dimensionless missile mass
p	pressure
r	maximum radius of missile
r_i	cone radius at original water surface
r_o	ogive radius
R_o	$= r_o/d$, ogive radius in calibers
s	distance along trajectory
t	time
t^*	$= U_o t/r$, dimensionless time
T	half period of pressure pulse
du/dt	acceleration which would exist if W-F-B were zero
U	missile velocity
U_o	velocity of missile at water impact
w	wetting factor
W	weight of missile
W'	impulsive-moment coefficient
x	distance from central plane of wedge
β	half angle of cone or wedge
β'	deadrise angle of wedge $= \pi/2 - \beta$
θ	angle of water entry (measured from horizontal)
λ	dimensionless lever arm
ρ	mass density of water
σ	specific gravity
ϕ	angle between normal to surface element and trajectory
ψ	angle turned through by missile
$\Delta\omega$	whip = transverse angular velocity acquired by missile at water entry

Subscripts

a   quantity in air

m   quantity evaluated when drag of cone is maximum

w   quantity in water

INTRODUCTION

When missiles enter water from air, they commonly experience force systems which not only affect the motion but may cause serious damage. The axial force, in decelerating the missile, may deform the nose or destroy internal instrumentation. The moment of the impact force may seriously affect the straightness of the trajectory and even cause the missile to buckle or break in two.

In this chapter the only forces considered will be those effective while the nose of the missile is being wetted and shortly thereafter. Forces which arise when the tail strikes the cavity, will be discussed in connection with the trajectory, elsewhere.

Forces, especially when derived experimentally, may be of several types. They may be the forces on the missile case, as derived for example, from pressure sensors; they may be based on the readings of accelerometers variously placed in the body of the missile; or they may be derived from the motion of, and about, the center of mass of the missile. In this report the type of force will generally be clear from the discussion, but it is a matter which should be kept in mind.

THE PHASES OF WATER ENTRY

During the entry of a missile into water the successive conditions which exist are commonly divided into a number of "phases", given variously by different authors. The following division is frequently made.

Shock-Wave Phase. During this phase, which is most significant for the vertical entry of blunt bodies, compressibility is important, and a shock wave is generated in the water. Although large forces which may cause damage to the missile are effective during this phase, the time is very short, and the phase is usually of small practical importance.

Flow-Forming Phase. During its entry the missile has to establish a pattern of flow in water which was initially at rest. While this flow is being generated the missile experiences its greatest water-entry deceleration, the forces are most destructive, and have the greatest influence on the trajectory.

Open-Cavity Phase. During this phase the missile is cavity running, that is, it is generating a cavity as it travels. The cavity is open to the atmosphere at its upper end (at the water surface). This, and the later phases are not discussed in this chapter.

Closed-Cavity Phase. In this phase the cavity has closed above the water surface and envelops the missile (when conditions are suitable).

Collapsing-Cavity Phase. The cavity size decreases and later the rear of the cavity collapses onto the tail of the missile.

Fully Wetted Phase.   Finally, the water is in contact with the
complete surface of the missile.

THE SHOCK PHASE

If a plate or disk or the flat end surface of a right cylinder
impacts a level surface of water vertically with zero angle of attack
(Fig. 4-1), a high pressure builds up at the colliding surfaces and
a shock wave travels downward into the water. Until recently it was
assumed that this pressure was relieved only by the compressibility
of the water, and that the duration of the shock would depend on the
travel time of the shock in the water from the center of the disk or
plate to the free edge. It was held that the pressure at the front
surface of the disk would equal $\rho c_w U_o$, where ρ is the mass density
of the water, c_w is the velocity of sound in the water, and U_o is the
impact velocity of the missile. Experiments showed that the pressure
did not attain a value as high as this prediction.

It was demonstrated experimentally and theoretically by Chuang
(Ref. (4-1)) and at approximately the same time by tests of Verhagen
(Ref. (4-2)), Lewison and Maclean (Ref.(4-3)), and Johnson (Ref. (4-4)),
that the lessening of the pressure is due to a layer of air which is
compressed and deforms the water surface below the flat plate
approximately as shown in Figure 4-2. This cushions the impact . As
a result many reports which were written to discuss the effect of
water compressibility on the force of impact, have little significance.
Instead, the compressibility of the air layer is important, and the
duration of the shock is greatly increased because of the different
flow mechanism (the pressure buildup takes as long as the decay), and
the fact that the compressibility of air is involved rather than that
of water. In addition, air which cannot escape from the high-pressure
region is pressed into the water, and the mixture has a considerably
lower sound speed than water alone. Chuang reported that ripples on
the water had little effect on the pressures, but Lewison and Maclean
stated that rough-water performance was not repeatable.

While the shock would be much more intense if air were not
present, it is believed (Ref. (4-1)) that the total impulse is about
the same; the smaller amplitude when air is present is compensated by
the increased duration. It will be shown later that the deceleration
of a missile entering water is associated with the "added mass" of the
flow set up in the water. The total amount of this added mass is not
greatly affected by the presence or absence of air below the missile.
On the other hand the impulse will depend on the mass of the impacting
body. This dependence, as predicted by Verhagen (Ref. (4-2)) for a
two-dimensional falling plate, is shown in Figure 4-3. Figure 4-4
compares his predictions for two masses of the plate with his experi-
mental results and those of Chuang. For Chuang's tests, as is shown,
the effective mass $M/\rho \ell^2 \approx 2$. Since compressibility was neglected
in the predicted values, the theory is not suited to heavier masses,
and Verhagen suggested that the lack of agreement of Chuang's values
with theory may be due to this error in the analysis or to deformability
of Chuang's dropping mass. The three-dimensional nature of his experi-
ment may also have importance.

Chuang found that the maximum pressure is approximately the same over all of his falling plate except at the extreme edges, but the time variation of the pressure varies greatly. He gave the following predictions for the pressures

$$p_{max} = \frac{1}{32 \times 144} \left[\frac{1.4^2 + \pi^2}{e^{-1.4} + 1} \right] \rho c_a U_o \approx 4.5 U_o$$

wit p in psi and U_o in ft/sec. Further

$$p(t) = 2p_{max} e^{1.4t/T} \sin \pi t/T$$

with the half period

$$T = 4\ell/c_a.$$

It appears improbable that these formulas can have wide applicability. The half period T has a value of approximately $\ell/300$ so that if a plate hit the water at 300 ft/sec, it would travel a distance 2ℓ during the full shock duration. By this time, as will be seen later, added-mass effects, which scale with U_o^2 rather than with U_o, must be quite strong, and the force is surely not dependent principally on the shock.

Measured values of the maximum shock pressures for the water entry at 20° of a torpedo with hemispherical nose are shown (Ref. (4-5)) in the polar diagrams of Figures 4-5a and 4-5b. Pressures were measured at the angle shown by the radial lines. The maximum pressure was found to be at an angle somewhat ahead of the angle of entry, presumably because of the piling up of water as sketched in Figure 4-5c. The results appear reasonably consistent with those obtained for flat surfaces.

Denting of the missile nose has often been ascribed to the impact shock but it is improbable that internal damage to the missile is likely because of the shortness of the shock pulse.

THE FLOW-FORMING PHASE

As a missile enters water from air, the water, which may usually be regarded as initially at rest, must be set into a pattern of motion characteristic of the nose and the cavity shape. This flow establishment taker place principally while the nose is being wetted but invariably extends beyond this time. This is especially evident in the vertical entry of a disk. While most of the work of flow establishment is done in a very short time following the contact of the disk with the water, obviously the flow pattern will grow as the penetration of the disk progresses. While the pressures are somewhat less during the flow-forming phase than in the shock phase, the duration is usually much longer. Hence the forces have great influence on the trajectory and have a great potential for damage to the missile.

It might appear that the behavior of a missile could be predicted accurately from the time variation of the pressure distribution on the body of the missile and principally on its nose. This is a great oversimplification because the missile is never a rigid body. The forces acting on and about the center of mass may differ greatly from those measured near the nose tip.

The force acting on the missile is not a simple one. It is combined from pressures distributed in both space and time. However, the time required for the missile to enter the water, even for a missile length, is usually short enough that the force system can be treated as impulsive.

The main constituents of the nose force are an axial or drag force, which causes deceleration and perhaps damage, and a lift or normal force, whose greatest importance is through the transverse angular velocity created by its moment. (It will be shown that axial forces may also produce angular velocity). The angular-velocity change is called "whip."

It is important to be able to predict, on the basis of theory or experiment, what time variation of drag and lift may be expected for an arbitrary body shape under arbitrary entry conditions. This is a problem of considerable difficulty. Theoretically a solution is required of a boundary-value problem in which the boundary varies with time in a fashion which must be determined as a part of the solution. Only primitive solutions have been obtained so far. Almost all productive analytical treatments have used a momentum method which will be discussed in the next chapter. Experimentally the water-entry problem is a very difficult one also, because of the large forces and moments and the brief time during which they act. Instrumentation equal to this assignment has only recently become available and measurements have not yet been extended to high-speed entry.

ADDED MASS

Prediction of drag forces during water entry has been due principally to a method suggested by von Karman (Ref. (4-6)) in 1929. This method assumes that momentum is conserved during the water-entry process; momentum lost by the missile as it slows down is converted into momentum of the added mass of water.

The concept of added mass (or virtual, induced or apparent mass) was first applied to potential flow (Ref. (4-7)). When a body moves through quiet water a flow is induced in the vicinity of the body (and theoretically to infinity), which is dependent on the body shape, and its velocities are proportional to the speed of the body. The "added mass" is that mass which would have the same kinetic energy as that of the flow, if traveling with the missile speed. Some justification of the association of added mass with the momentum rather than the kinetic energy of the induced flow, has been given by Shiffman and Spencer (Ref. (4-8)).

The basic idea of the von Karman method, which was originally applied to the vertical entry of two-dimensional wedges, is the estimation of the added mass during the water entry as a function of the penetration depth, and a calculation of the time variation of the force required for the transfer of momentum.

Many have used the von Karman method for the prediction of the water-entry force but the most elegant use is probably the application of the method to the estimation by Shiffman and Spencer (Ref. (4-8)) of the drag force during the vertical water entry of spheres. The conceptual basis for the method will be discussed in this section, and its application to water-entry scaling will be treated in the next section.

In the absence of other forces (which will be introduced in the next section) the momentum theorem for vertical entry may be written

$$MU_O = (M + m)U \qquad (4-1)$$

where M and m are the masses of the missile and the added mass, and U_O and U are the missile speed at and after impact. The fictitious added water mass m, which changes as the missile penetrates the water, is thought of as having the speed of the missile at each instant. For a given missile at a given entry angle it is assumed that the added mass is a function only of the distance the missile has penetrated the water, and further that m is proportional to ρ and to the cube of the linear scale of the missile; but is not a function of the mass of the missile or of its speed.

In the absence of other forces the drag force could be written

$$D = - MdU/dt = (1/2)\rho U^2 AC_D = (1/2)\rho U^2 AC_D^* \qquad (4-2)$$

where A is the reference cross-sectional area of the missile and C_D is the usual drag coefficient. Generally the drag coefficient C_D^* is used for the water-impact forces. It is referred to the impact velocity U_O which is easily measured, instead of the instantaneous velocity U.

By using equation (4-1) and the relation

$$\frac{d}{dt} = \frac{d}{db} \quad \frac{db}{ds} \quad \frac{ds}{dt} = \frac{U}{r} \quad \frac{d}{db}$$

(where b = s/r is the distance traveled, expressed in radii of cross section of the missile), equation (4-2) can be written

$$D = \frac{U^2 M}{(M + m)r} \quad \frac{dm}{db} = \left(\frac{M}{M + m}\right)^3 \frac{U_O^2}{r} \quad \frac{dm}{db} = \frac{U_O^2 \rho AC_D^*}{2}$$

4-5

or

$$\frac{2}{\rho A r} \frac{dm}{db} = \left(\frac{M + m}{M}\right)^3 C_D^* = C_{D\infty}^* \qquad (4\text{-}3)$$

From equation (4-3) it will be seen that the scaled value of dm/db, the rate of increase of added mass with increase of penetration, is proportional to $C_{D\infty}^*$, the drag coefficient related to the impact velocity for a missile of infinite mass, that is, in the absence of deceleration.

Although it is difficult to predict theoretically the values of added mass for water entry (for example, see Ref. (4-8)), there seems to be no evidence against its adoption as an exact basis. In other words we may hope that drag due to increase of added mass, as measured during water entry, may be ascribed to definite values of m at various water penetration distances, even though these values cannot be justified theoretically.

The goal then will be to determine, where possible, the graphs of m versus b, for various angles of entry. Preferably the graph for dm/db should also be given. although it can be found from the slope of the m graph. Correspondingly the dm/db graph suffices for the determination of the m graph by integration.

After some penetration the added mass should reach a steady value so that no further contribution to the drag will result. The drag will not drop to zero, of course, as the penetration increases, but will reach the steady value of C_D characteristic of cavity running (Ref. (4-9)) although C_D^* will continue to decrease. On the other hand, predictions calculated from added mass will give graphs reaching zero drag after sufficient penetration.

For the experiments that have been performed to study drag at water entry there is no indication that the scaled added mass or the drag due to it, is a function of missile entry speed, or missile size or weight.

THE SCALING OF WATER-IMPACT FORCES

Comparisons of the drag data reported for any single, simple nose shape have shown little agreement among the various determinations, except that the force (or drag coefficient) has a single maximum. This lack of agreement has arisen from two causes: the considerable difficulty in determining the force by either theoretical or experimental means; and the failure, when comparisons are made, to allow properly for the differing experimental conditions under which the measured results were obtained.

The purpose of the present section is to show how such comparisons should be made, how drag force can best be presented, and, as a first example, to apply these methods to the comparison of the drag data

for spheres at vertical water entry. As has been inferred, the method of presenting data will be essentially that used by Shiffman and Spencer (Ref. (4-8)) in their classical analytical work on spheres.

A number of assumptions will be made in the comparison of data:

1. The entry speed is sufficiently high so that an air-filled cavity forms behind the missile but not high enough to make compressibility effects important. Because of the cavity

2. only the forward, wetted part of the missile contributes to the impact forces. Accordingly,

3. missiles whose wetted portions are identical, experience the same water-impact forces if other conditions are the same. For example, a missile with hemispherical nose will experience the same forces as a sphere, if only the hemispherical portion is wetted.

4. The impact force can be used to define a drag coefficient C_D^* by means of the equation

$$D = (1/2)\rho U_o^2 \; A C_D^*.$$

If the drag area $A C_D^*$ is considered, rather than just C_D^*, the value of the product $A C_D^*$ is independent of the area A to which C_D^* is referred.

From equations (4-2) and (4-3) it will be seen that

$$C_D^* = (U/U_o)^2 C_D = (U/U_o)^3 C_{D\infty}^* \qquad (4-4)$$

A great difficulty experienced in the comparison of water-entry force data for a given nose shape, is the variety of coordinate variables used in the presentations. Data for spheres include plots of D, dU/dt, C_D^*, m, and dm/db against s, b, t, and the dimensionless time $t^* = U_o t/r$, as well as some variants of these. In addition, many reports contain only maximum values of quantities, and some give values of the pressure on the wetted surface.

Unfortunately the accelerations of a missile entering water may depend on several forces in addition to those due to added-mass changes, and those of steady cavity running, namely, gravity forces (weight and buoyancy) and skin friction. These can complicate the problem of determining the added mass as a function of penetration, and also the problem of predicting the motion or forces from the added-mass data.

ANALYSIS IN THE ABSENCE OF BODY FORCES AND FRICTION

An analysis will first be carried out for the vertical entry of spheres under the assumption that weight, buoyancy, and skin friction can be neglected. This assumption is good for most reported data on spheres. It is easily shown that the steady drag on a 1.5-inch

4-7

steel sphere will be about 100 times its weight if U_O = 30 ft/sec.
The buoyant force will be negligible except in the case of very
light spheres such as the light wooden shell used by Watanabe
(Ref. (4-10)), and friction is generally small.

The equations already derived are listed with others in
Table 4-1. The quantities M and m have been written in the
dimensionless forms

$$M' = 2M/\rho Ar$$

and

$$m' = 2m/\rho Ar.$$

Multiplying by the naturally recurring quantity $2/\rho Ar$ makes these
masses independent of the liquid density and missile size. Equations
(4-8) and (4-9) in Table 4-1 can be obtained by integrating
equation (4-2)

TABLE 4-1

Water-Impact Formulas
(when gravity and friction are absent)

Equation

(4-1) $M'U_O = (M' + m')U$

(4-2) $\dfrac{2}{\rho Ar} D = -M' \, dU/dt = (U^2/r)C_D = (U_O^2/r)C_D^*$

(4-3) $\dfrac{dm'}{db} = \left(\dfrac{M' + m'}{M'} \right)^3 C_D^* = C_{D\infty}^* = (U_O/U)^3 \, C_D^* = (U_O/U) C_D$

(4-4) $C_D^* = (U/U_O)^2 \, C_D = (U/U_O)^3 \, C_{D\infty}^*$

(4-5) $M' = 2M/\rho \, Ar; \qquad m' = 2m/\rho Ar,$

(4-6) $t = r \int db/U$

(4-7) $b = (1/r) \int U dt$

(4-8) $\int C_D^* \, db = (1/2)M' (1 - U^2/U_O^2)$

(4-9) $-\int dU/U = \ln U_O/U = (1/M') \int C_D \, db$

A single graph of a function against b is sufficient for a
complete data evaluation, and the function may be m', dm'/db, C_D or
C_D^*. Plots of m' and dm'/db are preferable and it is desirable that
both be provided. If either is plotted, the other can be obtained
by graphical differentiation or integration.

It has been assumed that for a given nose shape at a given
angle of entry, m' is a unique function of b, so that the same can
be said about dm'/db, and its equal quantity $C_{D\infty}^*$. From equations

(4-3) and (4-4) then it can be seen that the ordinary drag coefficient C_D depends on both b and U, and therefore on the missile mass.

It will be assumed that M', r, and U_o are known and that plots are given against b or t (or the equivalent s or t*). The problem is to determine any of the quantities m', dm'/db, U, dU/dt or D, or C_D^* for a set of values of b (or t). If plots are against b or t, corresponding values of t or b, respectively, may be found from equations (4-6) or (4-7).

When axial force data are to be presented so as to be useful with a minimum of subsequent calculation, curves of C_D^* should be plotted for a number of values of missile mass, M, or of the specific gravity, σ (Ref. (4-8)). Such curves for the vertical entry of spheres are given in Figure 4-6. Their derivation will be discussed later. The topmost graph of this set is that for $C_{D\infty}^* = dm'/db$ from equation (4-3). The user can interpolate between these curves by reading interpolated values of C_D^* from plots of C_D^* against 1/σ for the b-values of interest. A cross plot for this purpose is provided in Figure 4-7.

Calculations from reported data will usually fall into one of four classes, and Table 4-2 shows how the required data can be obtained in each case.

TABLE 4-2

Procedures for Reducing Data

	Given plots of	against	Procedure
Ia	m' and dm'/db	b or t	U from equation (4-1); C_D^* from equation (4-3); dU/dt from equation (4-2).
Ib	m' or dm'/db	b	dm'/db from graphical differentiation or m' by integration and proceed as in Ia.
Ic	m'	t	U from equation (4-1); dU/dt by graphical differentiation; C_D^* from equation (4-2); dm'/db from equation (4-3);
Id	dm'/db	t	provides insufficient data
IIa	C_D^*	b	dU/dt from equation (4-2); U by integration in equation (4-8); m' from equation (4-1); dm'/db from equation (4-3).
IIb	C_D^*	t	dU/dt from equation (4-2); U from $U = \int (dU/dt)dt$; m' from equation (4-1); dm'/db from equation (4-3).

TABLE 4-2 (Cont'd)

Procedures for Reducing Data

	Given plots of	against	Procedure
III	D or dU/dt	b or t	C_D^* from equation (4-2); proceed as in IIa or IIb.
IVa	C_D	b	U by integration in equation (4-9) m' from equation (4-1); C_D^* and dU/dt from equation (4-2); dm'/db from equation (4-3).
IVb	C_D	t	provides insufficient data

The Vertical Entry of Spheres

This section applies the method just outlined to the vertical entry of spheres for which a relatively large amount of experimental data are available. In addition, the theoretical investigation by Shiffman and Spencer (Ref. (4-8)) of the vertical entry of spheres is probably the best analysis of its kind available.

The data to be compared are taken from References (4-8) and (4-11) to (4-15), as well as unreported data from the Naval Surface Weapons Center. (The latter data were kindly made available by Howard K. Steves, who obtained them as a part of a comprehensive program to be reported later.) Information regarding these sources is listed chronologically in Table 4-3. The missiles used in such tests are rarely complete spheres, but rather cylindrical bodies with hemispherical noses, or weighted spherical shells containing an accelerometer. It is seen from the table that the impact speeds were consistently low, often less than 12 ft/sec; and the (effective) specific gravities were usually quite low. Other theoretical and experimental results might have been included in the comparison, but none were considered sufficiently reliable to justify inclusion. In particular, theoretical methods have generally neglected the splash entirely and it has been shown (Ref. (4-8)) to be far from negligible. Earlier experimental research suffered instrumental limitations which prevent it from competing in accuracy with recent work.

Figure 4-8 shows the variation of the dimensionless added mass, as derived from the sources listed in Table 4-3, by the methods of the previous section. There is reasonable agreement for the sources which were expected to be most reliable: Shiffman-Spencer, Mosteller, Hobbs, and Steves.

Corresponding plots of dm'/db = $C_{D_\infty}^*$ are given in Figure 4-9. Figures 4-8 and 4-9 show that the curves based on the work of Mason-Slichter, Richardson, and Blundell are in poor agreement with

the later determinations. (Only one curve of Richardson--that showing best agreement--was included here.) These sources have self-variations of 20 to 80 percent at the peak of dm'/db, and they will not be considered further. The results furnished by Steves comprise two graphs for $C_{D\infty}^*$. Figure 4-10 shows the small deviation between them. Data obtained from the mean of these curves are given in Figures 4-8 and 4-9.

Based on the evidence of Figures 4-8 to 4-10, it was decided to determine m' and dm'/db from the graphs of Figures 4-10, but the accuracy should be substantiated by further tests.

Using the method of Shiffman-Spencer (Ref. (4-8)) a family of curves for C_D^*, based on Figure 4-10 has already been given as Figure 4-6. The graphs are for four values of the specific gravity, σ, related to the volume of the basic sphere: $\sigma = 0.25, 0.5, 1.0$ (the neutrally buoyant sphere), and $\sigma = \infty$, the sphere of infinite mass and constant speed. This last is the curve for $C_{D\infty}^* = dm'/db$ (equation (4-3)).

TABLE 4-3

Sources of Sphere Data (Vertical Entry)

Source	Ref.	Year	σ	U_0 ft/sec.	r inches	curves used
Watanabe	(4-10)	1934	0.116	10.3	6.3	not used
Blundell	(4-11)	1937	.212-.331	8-11.4	10.0	mean
Shiffman-Spencer	(4-8)	1945	theoretical			
Mason-Slichter	(4-12)	1946	1.082	17-29	9.0	mean (σ=1.082)
Richardson	(4-13)	1948	0.304	9.5	10.0	"best" only
Hobbs	(4-14)	1950	3.19	7.5	3.0	one only
Mosteller	(4-15)	1957	7.95	25.	1.0	one only
Steves	-	1968	4.45	18-24	1.5	two

Curves for the interpolation to intermediate values of σ were contained in Figure 4-7. Here C_D^* is plotted against $1/\sigma$ for various values of b.

Figure 4-11 is a copy of the m' graph based on the data of Figure 4-6.

Drag Not From Added Mass

The behavior of C_D^* for large values of b, requires discussion. Values based entirely on added mass, such as the theoretical estimates of Shiffman-Spencer, approach zero as the added mass becomes nearly constant. Shiffman-Spencer found this condition to be approximated as the penetration of the sphere becomes one radius, that is, when the equator reaches the undisturbed water surface. Actually the flow separates from the sphere at a penetration as little as $0.65r$, although the added mass increases beyond this point.

Of course, the experimental value of C_D approaches not zero but the steady cavity-running drag. If C_D becomes constant, C_D^* approaches zero as U^2, since $C_D^* = (U/U_o)^2 C_D$. How the "steady" component of drag builds up from zero during the early stages of the entry to the full cavity-running value, is not known.

In Figure 4-12 the heavy lines are Shiffman-Spencer's C_D^* curves from graph 1 of Reference (4-8). The two lighter (solid) lines are copied from Figure 4-6. The agreement of theory and experiment is excellent up to the peaks, but the experimental curves then fall as much as 15 percent below the theoretical ones. At about b = 0.5 the experimental curve starts to swing back toward the theoretical curve, presumably because of the incipience i the "steady" drag. The dashed line faired to the $\sigma = \infty$ curve in Figure 4-12 represents a guess as to how the experimental curve would behave if the drag were due only to added mass. Such a change in C_D^* would move the m' curve in Figure 4-11 only to the dashed line.

Since the region above the entering missile is filled with air rather than water, it is generally assumed that the added mass is about half that for fully wetted flow about the immersed shape. For a sphere, for which the fully wetted added mass is $0.5\rho(4\pi r^3/3)$, this would give

$$m' = \frac{2m}{\rho A r} = \frac{2}{\rho \pi r^3} \quad \frac{\rho}{4} \quad \frac{4\pi r^3}{3} = \frac{2}{3}$$

as compared with the asymptote of the dashed graph in Figure 4-11, which is perhaps a little more than m' = 0.45.

Actually the importance of being able to draw graphs of "pure" m' and dm'/db appears questionable, except that failure makes the comparison of theory with experiment difficult. Values of m' and dm'/db obtained directly from experiment contain a false contribution due to the steady drag but, if uncorrected, they may be used to compute the actual drag coefficient, including the steady component.

When weight, buoyancy and friction must be allowed for, the problem is a more difficult one. A more complete momentum equation for vertical entry may be written

$$W - B - f - (1/2)\rho U^2 AC_{Ds} = \frac{d}{dt} U(M + m) = (M + m)dU/dt + Udm/dt$$

$$(4-10)$$

including the weight W, the buoyancy B, and the "steady" drag force. As indicated above, the "steady" drag force, $(1/2)\rho U^2 AC_{Ds}$, is an assumed part of the total drag, which represents a cavity-running drag which is building up toward its full value. The full value will be designated $(1/2)\rho U^2 AC_{ds}$ (Ref. (4-16)).

Usually the total drag is measured through the acceleration which it causes. The term Udm/dt is the part of this force which is effective in increasing the added mass. To help in its evaluation, several of the forces can be calculated and removed from the equation; the weight is assumed to be known; the buoyancy, $B = A_n z$ is the product of the cross section of the wetted part of the nose and its depth; the skin friction is calculated from flat-plate data (but generally is significant only for bodies such as slender cones and ogives). The friction increases with the penetration and may be treated as a part of the increasing "steady" drag force, $(1/2)\rho U^2 AC_{Ds}$. Presumably friction generates added mass proportional to the friction drag, but this is probably not important.

When various forces in equation (4-10) are large enough to be significant, the procedure may be as follows. From a plot of acceleration against time, a graphical integration gives U as a function of t, and a second integration gives values of b. The total force on the missile is given by

$$F = MdU/dt.$$

If the "extra" forces are subtracted from this

$$F + W - f - B = M \, du/dt$$

where du/dt is the fictitious acceleration which would occur in the absence of W, F and B. Then, from equation (4-1)

$$(M' + m')du/dt = -U \, dm'/dt = -(U^2/r)dm'/db. \qquad (4-11)$$

The added mass, m', is calculated in steps starting at impact, by computing successive increment rates, dm'/db, using the values of m' previously found. Because du/dt does not represent the actual acceleration, the true velocity, U, must be used at each step.

Similarly, in working from available dm'/db data, such as those of Figure 4-6, the total force (or acceleration) can be calculated for entries in which W, f, and B are significant, by first finding the force due to dm'/db from equations (4-2) and (4-3), and adding the forces W, f, and B. The corresponding acceleration follows immediately, and values of U are found by a step process.

The Oblique Entry of Spheres

This section will evaluate and compare published drag data for spheres at oblique water entry. The handling of the data differs from that for vertical entry in the previous sections only because each oblique angle of entry yields a distinct graph of m' and dm'/db. The evaluation is assisted however by the fact that the graphs for various angles should form a family with systematic variation as the entry angle is changed.

Only four sources of data were found (Refs. (4-15), (4-17), (4-18) and (4-19)) for spheres at oblique entry. Test conditions are shown in Table 4-4. As can be seen from the table, Norman's data cover the range of entry angles from 15 to 33 degrees at intervals of 3°; the Hydroballistics Design Handbook covers 10 to 40° at 10° intervals; and Mosteller's data range from 15 to 90° with an interval of 15°. The data of Hobbs et al, were obtained at two angles only: approximately 65° and 40°.

Values of dm'/db were calculated for all of the entries listed, using the techniques described for vertical entry. Curves for dm'/db were plotted as shown in Figure 4-13, and from these plots a family of curves for entry angles from 10° to 90°, with an interval of 10°, was deduced as shown in Figure 4-14.

Graphs of m' obtained from Figure 4-14 by integration, are given in Figure 4-15. These curves contain the steady drag and do not approach fixed values but presumably asymptotes which have slopes such that $dm'/db = C_{ds}$. The graphs of Figures 4-14 and 4-15 are based on $C_{D\infty}^*$ and do not contain any effect of change of speed. In using the graphs, data are required for C_D^* at finite rather than infinite mass. A family of curves similar to those of Figure 4-6 can be drawn for any entry angle by application of equation (4-3).

TABLE 4-4
Sources of Sphere Data (Oblique Entry)

Source/Ref.	Year	σ	θ range (deg.)	angle increment	U_o ft/sec	r inches
Hobbs, et al. (4-17)	1951	1.64	37-68	28°	11-17	4
		0.109	36-65	25°	12-17	10
Hydroball. Design Hdbk. (4-18)	1955	7.35*	10-40	10°	?	1.0
Mosteller (4-15)	1957	7.95	15-90	15°	25	1.0
Norman, et al (4-19)	1959	8.57	15-33	3°	225	10

*Value in Reference (4-18) was incorrect

Smoothing of Data

The family of smooth curves in Figure 4-14 for spheres at oblique entry, was obtained from the raw data of Figure 4-13 by a smoothing technique. At any particular value of b (say, b = 0.3) the value of dm'/db was read from each graph of Figure 4-13. These values of dm'/db were then plotted together (for b = 0.3) against the corresponding values of θ, and a smooth curve was drawn through the points. This smoothing was carried out for values of b at intervals of 0.05 for 0 < b < 0.3, and at intervals of 0.1 from 0.3 to 1.0. Judgment was used in drawing the smoothed curves rather than mathematical method because of the inconsistencies evident in Figure 4-13. Values were then read from the smoothed curves at θ intervals of 10°, these values were plotted on coordinates of dm'/db versus b, and graphs were drawn to give the curves of Figure 4-14.

Evaluation and interpretation of tne data for oblique sphere entry meant the taking of liberties with data from each of the references, somewhat as follows.

The Handbook states (Ref. (4-18)) that the drag coefficients which it gives for oblique sphere entry are of questionable accuracy, and Figure 4-13 shows that these graphs have peaks at much lower values of b than the other data. The Handbook data were regarded as less reliable than other data, when the smoothed curves were drawn.

One set of Norman's smoothed curves (Fig. 9 of Ref. (4-19)) are given in Figure 4-16. The initial peaks shown in this figure were not included in data transferred to Figure 4-13 since their geometry appeared questionable. They were removed by fairing the original graphs past the peaks to the origin. The effect on the later results of the deletion of the peaks may be analyzed as follows. In Figure 4-16 the ordinate values of the peaks represent accelerations and these are proportional to the axial force. Equation (4-2) showed that C_D^* is directly proportional to the acceleration, and the removal of peaks from dU/dt will prevent peaks from occurring in C_D^* at the same abscissa values. On the other hand, from equation (4-3), later values of dm'/db will be affected by the removal of the peaks since the peaks decrease U. This effect is small because of the small area under the deleted peaks.

The data of Hobbs, et al (Ref. (4-17)) show scooped-out areas in the peaks which are hardly believable. These have not been allowed to influence the smoothed values.

The Water Entry of Disks

Some discussion of the vertical water entry of disks and plates was given in the treatment of the shock phase of entry. No data were found in the literature from which the added mass for vertical entry could be estimated.

Studies by Mosteller (Ref. (4-15)) and by Norman, Burden and Suter (Ref. (4-20)), have been reported for the oblique water entry of disks. Mosteller used models of 2-inch diameter and entry speeds of 25, 50, and 75 ft/sec. Because of the greater accuracy claimed for his 25 ft/sec. entries, these alone are reported here. In Mosteller's work the angle of entry was varied from 15 to 75 degrees at intervals of 15 degrees. Norman's missiles had a diameter of 20 inches, and his U_0 values were 175 and 325 ft/sec. The angle was varied from 15 to 33 degrees in steps of 3 degrees.

Plots of dm'/db calculated from these reports are given in Figure 4-17. Both tests included entry angles of 15 and 30 degrees. For these entries Mosteller's graphs peaked at somewhat earlier times. A smooth family of graphs was obtained from the data of Figure 4-17 by the method discussed for hemispheres. The result in Figure 4-18 is practically a smoothed version of Mosteller's data, since it was deemed more reliable.

Presumably for all angles of entry the drag coefficient should approach the steady cavity-running value at sufficient penetration. No attempt was made, however, to make all graphs approach the horizontal at 0.8, the cavity-running drag coefficient, because of lack of precision in the data.

Values of m' obtained by integrating the graphs of Figure 4-18 are plotted in Figure 4-19. The resulting graphs are approximately parallel straight lines for a major part of the region plotted. This is, of course, the immediate result of the steady drag values at the right side of Figure 4-18. It might be expected that the time required for m' to reach any percentage of its maximum value (excluding the apparent contribution of the steady drag) would be related to the time at which the front face of the disk becomes fully wetted. The times at which the disk is completely below the original water surface are indicated on Figure 4-19 by small flags on the graphs. For the 15-degree entry the slope is approximately constant some time before the disk is submerged, while the straight portion comes long after this time for the 75-degree entry. Usually the time when the disk starts "pushing on solid water" is regarded as more important than the time of submergence. At the former time the whole region in front of the disk (that is, the volume which will be swept out by the disk itself) is entirely filled with water due in part to the rise of the water surface in front of the disk. The condition is sketched in Figure 4-20.

Entry of the Cone

The cone has a very special characteristic in common with its two-dimensional analog, the wedge: ideally at least, it is self-scaling. In other words when the penetration of a cone is doubled (while its surface is still being wetted), the submerged part becomes effectively a similar cone of double the linear size. This feature has proved attractive to the mathematician.

In the discussion of the entry of a sphere the importance of the splash was mentioned and the fact that analytical methods ignoring it are usually considerably in error. The same is true for the cone. Shiffman and Spencer first discussed (Ref. (4-21)) the effect of the splash on the drag. They used a sketch which is reproduced in Figure 4-21, to show that the effective immersion is increased by the splash from s, the length of the cone beneath the original water surface, to $B_1 = ws$, where w is a <u>Wetting Factor</u>. It is commonly assumed that the wetting factor is constant for a given cone angle, so that the rise of level near the cone is proportional to the length immersed. It is usually reported that the cone behaves as if it were immersed to the length which is "pushing on solid water", and this is the condition sketched in the figure. For vertical entry, Baldwin found (Ref. (4-16)) that the force on the cone reaches a maximum value, for blunt cones when the end of the cone bears on solid water, and somewhat later for slender cones. He defined a "penetration ratio", h, as the ratio of the length of the cone below the original water surface when the drag is a maximum, to the actual length of the cone. Evidently,

$$h = 1/w.$$

Data on the wetting factor for the cone are given in Figure 4-22. The data include a theoretical graph due to Shiffman-Spencer (Ref. (4-21)), a point due to Chuang (Ref. (4-22)), and experimental data of Baldwin (Ref. (4-16)) and Watanabe (Ref. (4-23)). Baldwin found that the drag force was a maximum (and so presumably the full cone was bearing on solid water) when the 70-degree half-angle cone had three quarters of its length (and half its surface) below the original water level. He presented experimental evidence, which he did not regard as conclusive, that the maximum drag for very slender cones occurs after the cone is completely submerged.

Because of the scaling property of the cone, Shiffman and Spencer assumed that the added mass can be written in the form

$$m = K\rho s^3 (\tan \beta)^2 \qquad (4-12)$$

where β is the half angle of the cone and K is a proportionality factor which they called the "dimensionless virtual mass". Hence,

$$C_{D_\infty}^* = \frac{2}{\rho A r} \frac{dm}{db} = \frac{6Ks^2 (\tan \beta)^3}{\pi r^2} = \frac{6Kb^2 (\tan \beta)^3}{\pi} \qquad (4-13)$$

in terms of the quantities defined in the treatment of spheres.

For the cone there is advantage in expressing the drag coefficient in terms of the cross-sectional area at the original water surface rather than relative to the base area of the cone. The notation C_D will be used for drag coefficients referred to the former area, (which will be written $A_i = \pi r_i^2$), instead of C_D. Then

$$C_{D\infty}^{*} = C_{D\infty}^{*} \; r^{2}/r_i^{2} = 6Ks^{2} \; (\tan \beta)^{3}/\pi r_i^{2} = 6K(\tan \beta)/\pi \qquad (4-14)$$

As was discussed for the sphere, the drag force during impact is dependent on more than the increase of added mass. As the added mass approaches a constant value, the drag approaches the steady cavity-running drag. Because of this, Baldwin (Ref. (4-16)) defined the "total mass constant" K, as including the coefficient of the increasing "steady" drag, C_{ds}:

$$K = k + \pi C_{ds}/6 \tan(\beta). \qquad (4-15)$$

He assumed that the "steady" drag reaches its cavity-running value when the impact drag is a maximum, since presumably the cone is completely wetted at that time even though its base has not reached the original water surface. He described the "steady" drag coefficient at any instant, in terms of the maximum drag coefficient as

$$\underline{C_{Ds}} = \underline{C_{Dm}} \; r_i^{2}/r_m^{2} \qquad (4-16)$$

where the subscript m denotes values when the drag is a maximum.

Shiffman and Spencer assumed that K should be constant during the entry of a cone with a particular nose angle, but found it to vary strongly for experimental cone data obtained by Watanabe (Ref. (4-23)). Baldwin (Ref. (4-16)) showed that approximately constant values of K would result from that data if the time of impact assumed by Watanabe was slightly changed.

Friction makes a negligible contribution to the drag of blunt cones, but for slender cones it may form the major portion. This is shown in Figure 4-23 (Ref. (4-16)) where the skin-friction correction to the total added-mass constant, K, is plotted for slender cones. Data presented in this section have been "corrected" for friction. It is interesting that the graph in Figure 4-23 passes through the origin when skin-friction has been removed.

Figure 4-23 shows the graph for the total added-mass constant, K, for cone half angles up to 35 degrees, and the extension of this graph to higher angles (slightly modified from a graph of Reference (4-16)), is given in Figure 4-24 where the lower experimental graph and data points are compared with the (upper) theoretical prediction of Shiffman and Spencer (Ref. (4-21)).

Values of the maximum drag coefficient for the vertical entry of cones are shown in Figure 4-25 (Ref. (4-16)), including Baldwin's experimental results, and theoretical and experimental data quoted by Weible (Ref. (4-24)). The lower graph in Figure 4-25 is a plot of the values of "steady" cavity running drag assumed by Baldwin. It will be seen that the maximum drag coefficient is approximately equal to the steady drag coefficient up to cone half angles of about 23 degrees. This means, of course, that the drag curve has no peak, that the drag increases from zero to the cavity-running drag value.

A graph due to Baldwin is given in Figure 4-26 to show the actual added masses which he calculated for maximum drag of his 3-inch cones. Values here have been corrected for the "steady" drag and, since its increase is known only very roughly, good accuracy cannot be presumed for the values shown. Actually the added masses undoubtedly increase slightly after the time of maximum drag because of the nearness of the cone surface to the water surface (Ref. (4-16)).

The Added-Mass Constant corresponding to the corrected added mass, as given by Baldwin, is shown in Figure 4-27. It is lower than the lower graph of Figure 4-24 by the amount of the apparent added-mass contribution due to the increasing "steady" drag.

Figure 4-28 gives graphs for three cone angles, which Baldwin determined for the "corrected" added masses for his 3-inch cones. The small circles show the times at which the maximum drag coefficient was observed.

Figure 4-29 presents a family of total drag curves for cones of various half angles. These were given as average graphs by Baldwin (Ref. (4-16)), and in Figure 4-30 are corresponding graphs for added mass. The dashed curves show the added mass as derived directly from the graphs of Figure 4-29, containing a contribution of the steady drag; the solid curves give values after removing the estimated contribution of the steady drag.

The Entry of Ogives, Disk Ogives, and Cusps

The ogive and disk-ogive families comprise a broad range of nose shapes. Typical members of the family are shown in Figure 4-31. Starting with the right cylinder the edge may be rounded by a radius of any desired value. The ogive or disk ogive is usually identified by the radius of the arc expressed in calibers (missile diameters). If the radius is small the arc is drawn so that it is tangent to both the cylindrical wall of the missile and the flat surface of the front of the nose. Disk ogives result as at B and C in the figure. If the arc radius is half the body diameter (a half-caliber ogive), the nose is a hemisphere. For greater radii the arc does not become tangent to the front surface but the arcs meet to form typical pointed ogive tips. If the arc is still tangent to the cylindrical body, t' shape is a tangent ogive (sketches E and F); otherwise it . ' a secant ogive. Ogive calibers commonly run from one to six or more.

While it has been usual to specify ogives, especially tangent ogives, in calibers, as on Figure 4-31, Baldwin (Ref. (4-25)) has specified the ogive by two angles, as is seen in Figure 4-32. (The symbols on Figure 4-23 are those of Reference (4-25) and are not used with the same meanings elsewhere in this report.) The two-angle specification has two advantages for the purpose of Reference (4-25); it can be applied equally to cusps as Figure 4-32 shows, and it allows a comparison with related cones. One of the

angles used is the total angle of the related cone, and the second is the arc length (or "swept angle") which generates the ogives or cusps. Whether tangent and secant ogives of the same caliber behave similarly at water impact, depends on whether or not separation occurs (with cavity generation) before the end of the secant ogive. This will not be discussed further in this report.

Values of the maximum total drag coefficient are plotted in Figure 4-33 against the reciprocal of the tangent-ogive radius, R_O (in calibers). The experimental data were given by Baldwin (Ref. (4-25)) and the values from theory were calculated by Hoover and Reardon (Ref. (4-26)) using the von Karman momentum method. The latter data appear much too high, and some further evaluation of the method will be given in connection with data for the ellipsoid (Fig. (4-37)).

Graphs of the drag coefficient $C_{D\infty}^* = dm'/db$ are given in Figure 4-34 for a family of disk ogives, based on smoothed experimental results of Norman, Burden and Suter (Ref. (4-27)) for water entry at an angle of 30°. The data for the extreme members of the family, the disk and hemisphere, have already been presented. Graphs of the dimensionless added mass, m', calculated from the data on Figure 4-34 are given in Figure 4-35. As was discussed for the oblique entry of disks, the graphs for m' become straight after a sufficient penetration, but for the disk-ogive family the slopes differ because of differing cavity-running drags. An interesting comparison is possible for the hemisphere. In Figure 4-11 it appeared that the true added mass reached a maximum value of about 0.45 for vertical entry. It would be expected that the added mass would reach the same limit for oblique entry, and Figure 4-35 shows that the value 0.45 is reached for the hemisphere with 30° entry, at a penetration of about 1.75 radii. The straightness of the remaining portion of the hemisphere graph in Figure 4-35 tends to justify the comparison.

Figure 4-36 gives a comparison of the drag coefficients at vertical entry of various ogives and cusps having the same fineness ratio as the 45° cone (Ref. (4-25)). The shape includes ogives and cusps with 30° swept angles, and the ogive with 90-degree sweep, which is the hemisphere, the bluntest ogive. The graph for the hemisphere has been taken from Figure 4-6 of this report. The drag peak is highest by far for the cusp, lowest for the corresponding ogive, and the related cone is close to the hemisphere.

The Entry of Ellipsoids and Other Projectile Shapes

Hoover and Reardon (Ref. (4-26)) have given graphs of the drag coefficient for the vertical entry of a family of ellipsoids, calculated by simple momentum theory. As already mentioned, such calculations are inaccurate because the splash is neglected, but one may hope that useful information can be drawn from the behavior within a family of shapes. For this reason the ellipsoid graphs are reproduced in Figure 4-37. The hemisphere is a member of both the ogive and ellipsoid families and it has already been discussed.

A second source of error in the application of the momentum method usually occurs because the unknown added mass of the nose shape is approximated by using the known added mass of a simpler shape. The approximation suggested in the original presentation of the method (Ref. (4-6)) and used in computing the data for Figure 4-37, is the added mass of the flat plate or disk at the water surface. Since this is used for all ellipsoids in Figure 4-37, and they have the same caliber, all are found to have the same final value of m', and the areas under all graphs are the same.

The data that have been presented in this report for disks, spheres and disk ogives are believed to be the only oblique-entry data available. Beyond this one may say, in general, that greater obliquity results in smaller and later peak drag coefficients, and with sufficient obliquity the peaks disappear and the drag simply increases to the steady cavity-running value.

Impact of Two-Dimensional Bodies

A relatively large amount of study has been devoted to the water impact of wedges, both because of their mathematical simplicity and their importance in relation to ship slamming. For vertical entry, theory is based on Wagner's classic study (Ref. (4-28)) of the wedge of small deadrise angle, $(\beta' = \pi/2 - \beta)$, and its clarification in a paper of Pierson (Ref. (4-29)). The rather difficult experimental investigation has been carried out by Chuang (Ref. (4-30)) and others.

The geometry of the problem can be seen from the sketch in Figure 4-38, which Chuang adapted from Wagner. Wagner made a careful study of the splash and found that the half width of the wetted portion of the wedge, L, is $\pi/2$ times the half breadth of the wedge at the original water surface. He derived the expression

$$p(x) = (1/2)\rho U^2 \left[\frac{\pi}{\beta'(1 - x^2/L^2)^{\frac{1}{2}}} - \frac{x^2/L^2}{1 - x^2/L^2} + \frac{2L\ddot{z}}{U^2}(1 - x^2/L^2)^{\frac{1}{2}} \right] \tag{4-17}$$

for the pressure at points on a symmetrically entering wedge. According to this equation the pressure at any point is dependent only on β', U, and the position of the point, and is constant in time if the deceleration is negligible. In that case the pressure has a maximum value

$$p_{max} = (1/2)\rho U^2(1 + \pi^2/4 \beta'^2) \tag{4-18}$$

and this occurs at the position

$$x = L(1 - 4\beta'^2/\pi^2)^{\frac{1}{2}} \tag{4-19}$$

rather than at the vertex or keel.

Chuang performed tests (Ref. (4-30)) to determine the importance, for various deadrise angles, of air-trapping which he had found to buffer the normal impacts of the flat plate (Ref. (4-1)). His tests showed the effect is unimportant for angles of 3 degrees or more. Combining information from theory and experiments at low speeds, Chuang concluded that the maximum values of pressure on the wedge may be written, for various deadrise angles, as shown in Table 4-5 (Ref. (4-50)).

TABLE 4-5

Maximum Pressures on Wedges at Vertical Impact

β Deadrise Angle (degrees)	Maximum Pressure	
	At Vertex	Away from Vertex
0	$0.68U_o^2$	$0.68U_o^2$
1	$1.00U_o^2$	$1.00U^2$
3		$1.72U^2$
6		$0.75U^2$
10	$0.68U_o^2\cot\beta$	$0.36U^2$
15		$0.20U^2$
$\geq$ 18		$2.17(1+2.47\cot^2\beta)$

Adapted from Reference (4-50). Values are for fresh water and would be 2.5 percent higher for salt water. Pressures are in psi; and U and U_o are in ft/sec.

Values of the added mass of the impacting wedge have been estimated and values due to Pierson (Ref. (4-31)) are listed in Table 4-6. The values in parentheses are extrapolations to Pierson's data based on comparison of the trend of his calculations with those of other authors.

Some additional two-dimensional solutions have been attempted, but they will not be outlined here. An extensive bibliography is available in a recent review article by Szebehely and Ochi (Ref. 4-32)).

TABLE 4-6

Added Mass of Wedges (per unit length)

β' Degrees	$\dfrac{m}{(1/2)\pi\rho L^2}$
10	(0.69)
20	0.575
30	0.483
40	0.40
50	0.34
60	(0.30)

From calculations of Pierson (Ref. (4-31)), except values in parentheses which are estimates from comparison with other sources.

LIFT FORCES DURING WATER ENTRY

In contrast to the extended treatment which has been given to the drag forces during water impact, only a brief comment will be made about lift forces. There are two reasons why it appears unprofitable to devote much space specifically to lift forces: their importance arises principally from the whip which they generate and this will be discussed in detail in the next section; and the scant data that have been published do not permit a systematic treatment of these forces.

Measurements of lift which have been reported for such simple bodies as the sphere (Refs. (4-12) and (4-17)), show that C_L behaves like C_D, in that it has an early maximum followed by a decrease to relatively small values.

Only primitive studies have been made of the scaling of lift, and even for the sphere it is known that the lift behavior may be expected to change with sphere diameter and entry speed. A principal cause of such dependencies is the "underpressure" which does not scale like the hydrodynamic forces. It will be discussed in the next section.

The study of lift is hindered by the fact that the projectile is never completely rigid, but consists of a deformable body, usually with a quite complicated structure. Values of transverse acceleration vary greatly throughout this structure and make the evaluation and systematizing of lift a matter of great difficulty.

WHIP

Introduction

During oblique water entry the pitching moment is a most important component of the force system acting on the missile. This moment tends to turn the nose of the missile up (positive) or down (negative), giving the missile an angular velocity about a transverse axis and often strongly affecting the subsequent behavior and trajectory. The major contribution to this moment comes during the flow-forming phase, but this is followed frequently by a negative moment due to an underpressure below the nose, then a continuing "cavity-running" moment on the nose, and finally, moments due to slaps of the tail against the cavity wall. In fact, it is reported (Ref. (4-19)) that under some conditions, "the angular velocity is seen to rise in a continuous sweep until practically the whole length of the projectile has entered the water".

The effect of the water-entry moments has been measured by the whip, which is defined as the impulsive change of angular velocity in the pitch plane during water entry. Significant contributions to the knowledge of whip have been made by few laboratories: by the California Institute of Technology during WWII, by the Naval Ordnance Test Station at Pasadena and Morris Dam especially during the following decade, and more recently by the Admiralty Research Laboratory at Teddington, England and Glen Fruin, Scotland. Today some studies are being made by the Naval Surface Weapons Center, White Oak Laboratory (formerly the Naval Ordnance Lab).

The integrated effect of the moments has been discussed rather than the time variation of the moment itself, because the instrumentation available during early studies did not permit the resolution of the moment variation. Later research has given information on this variation but there seems no point in discarding the concept of the integrated effect of the moment since it is usually this which proves useful for subsequent behavior analysis, and the time variation often is not important.

Because of the continuing existence of moments and the different periods during which various components are of importance with various missile shapes, numerous choices have been made for the duration of whip, and this variation of period necessarily affects the angular-velocity change which is measured. The aim is to include all important moments which are especially associated with the water-impact process and to exclude other continuing moments which are related rather to the later phases of the water-entry sequence of events.

Choices which have been given for the whip-producing period include the time (some concepts mentioned are still to be discussed):

1.   during which the full diameter of the projectile is being submerged below the original water surface (Refs. (4-33) and (4-34)),

2.   while the whole missile is being completely immersed beneath the original water surface (Refs. (4-18) and (4-35)),

3.   until the plotted angular-velocity data show a sudden change in slope (Ref. (4-36)). (Such a sudden change is reported for ogive data but not for most other noses.)

4.   until the drag is a maximum (Ref. (4-19)) (because this choice was found suitable for shapes such as the hemisphere),

5.   for unvented disks or right cylinders, until both hydrodynamic entry forces and underpressure forces have ceased (Ref. (4-37)).

No single definition of the time of whip production has been adopted and accordingly the comparison of whip data is difficult. At least, each nose shape should have a whip period associated with it, but for some shapes the choice might prove arbitrary because the moment continues to increase until the missile tail strikes the cavity wall, without significant changes of the increase rate.

It has been mentioned that the largest contribution to the whip is made during the flow-forming phase, or "while the nose is being wetted". It should be noted that shearing forces are very small at this time, so that the force on the surface of the nose is everywhere almost normal to the surface. Tests of the water entry of small spheres at an angle of 19 degrees and a speed of about 95 ft/sec. (Ref. (4-38)), showed that the shearing force was less than one percent of the drag force. It is interesting that the rotation observed for the spheres was retrograde, that is, the front surface moved up. It is believed that this resulted from a higher flow speed upward in front of the sphere, than past its under surface.

Prolate noses such as the hemisphere and ogive, have forces which, in the early entry stage, are predominantly upward, so as to give a positive moment and positive whip. Actually, this is true of practically all noses except right cylinders, disks, or truncated shapes. For the latter noses, the forces initially are parallel to the axis and below the ordinary center of mass, as sketched in Figure 4-39, so that the whip of a disk is slightly negative.

A method of predicting the whip was proposed about 1944 by Birkhoff, although he categorized the method only as "plausible" (Ref. (4-39)). It was assumed that the pressure on the nose of the missile can everywhere be taken equal to $(1/2)\rho U^2 \cos^2\phi$, where ϕ is the angle between the normal to any surface element and the trajectory. The questionable theoretical basis for this has been discussed by Burt (Ref. (4-40)) and by Tate (Ref. (4-41)), and

will not be entered into here. Burt has given the result of applying the method to the whip of disk ogives and the comparison with experiment is shown in Figure 4-40. While the calculations agree with experiment in order of magnitude, the comparison does not suggest that the method may be relied on for other nose shapes without further confirmation.

An important phenomenon known as the "underpressure effect" often occurs just after water entry, with the formation of a thin cavity below the missile nose, as sketched in Figure 4-41. In contrast to earlier opinions, it is believed (Ref. (4-42)) that this is a simple case of cavitation in which the cavity initially has a pressure equal to the saturation vapor pressure of the water. Later the cavity often breaks open to the upper air, is "vented", and the pressure rises approximately to that of the atmosphere.

The earlier interpretation was that the underpressure cavity appeared when a cavity tended to open both above and below the entering missile. Below the missile the greater constraints on the flow made it difficult for the thin cavity to open up, that is, for air to flow into it. Hence, it was interpreted as a Reynolds number effect (Ref. (4-43)). It will be discussed further in the next section.

It has been assumed in the discussion thus far, that the missile strikes the water with zero angle of attack, that is, that the missile axis is parallel to the trajectory. The presence of an angle of attack will tend to change the value of the whip, but this will be discussed in connection with the various nose shapes. Here it is only necessary to state that effect of angle of attack on whip will be small for blunt noses, but will be large in the case of slender ogives.

The variation of whip with angle of attack was described in early work (Ref. (4-36)) as "pitch dependence of whip", but the term "attack sensitivity" was later adopted (Ref. (4-18)) as more appropriate.

The Scaling of Whip

Whip is not a satisfactory quantity for the analysis of missile behavior since it is not dimensionless. It has been customary to report values of whip for a given missile at a given angle of entry as, for example, a whip of 100 degrees per second for a missile with a transverse moment of inertia of 800 slug-ft^2, and a C.G. 71 inches from the nose tip, entering water at 500 ft/sec.

For the hydrodynamic forces at water impact, scaling laws may be derived as follows. The impulsive moment which acts on the missile due to these forces at water entry is the time integral of the moments during the flow-forming phase. The total impulsive moment may be regarded as some total impulse on the nose times some lever arm, λd, from the C.G. to the line of action of the impulse. One may

write the proportional scaling relations

$$\text{force} \propto \rho U^2 d^2$$

$$\text{lever arm} \propto \lambda d,$$

$$\text{duration} \propto d/U.$$

From the product of these proportions

$$\text{impulsive moment} = W'\rho U d^4 \lambda \qquad (4\text{-}20)$$

where W' is a dimensionless "Impulsive Moment Coefficient". If the transverse moment of inertia about the C.G. is I,

$$\text{whip} = \text{impulsive moment}/I = W'\rho U d^4 \lambda/I \qquad (4\text{-}21)$$

It is instructive to calculate the angle that the missile would turn through with constant angular velocity (whip) during a travel of one caliber (or one missile length). Again the duration is proportional to d/U, so that the angle turned through is

$$\text{angle due to hydrodynamic force} \propto \text{whip} \times d/U \propto \rho d^5 \lambda/I. \quad (4\text{-}22)$$

When tests are made with scaled models, that is, models geometrically similar and with the same average density, $I \propto d^5$, so that, from equation (4-22) the angle will be proportional to $\rho\lambda$ for both prototype and model, and independent of size and velocity. This is true for the hydrodynamic forces only.

The situation for the underpressure forces is as follows. The pressure in the cavity below the nose is substantially zero, so that there is a downward pressure equal to that of the atmosphere p_a, and

$$\text{force} \propto p_a d^2,$$

$$\text{lever arm} \propto \lambda d,$$

$$\text{duration} \propto d/U, \text{ and}$$

$$\text{whip due to underpressure} \propto p_a \lambda d^4/IU. \qquad (4\text{-}23)$$

With the same process as before, the angle turned through for scaled models ($I \propto d^5$), will be

$$\text{angle due to underpressure} \propto \lambda p_a/U^2. \qquad (4\text{-}24)$$

If model and prototype are compared at the same Froude number = $U/\sqrt{gd}$, $U^2 \propto d$, and

$$\text{angle due to underpressure} \propto \lambda p_a/d. \qquad (4\text{-}25)$$

4-27

Equation (4-25) shows that underpressure tends to make small missiles turn downward more strongly than large ones, and the prototypes of some missiles are known to come back out of the water (broach) while scaled models of these missiles dive at the same Froude number. It is seen also from equation (4-25) that if the pressure of the atmosphere is made proportional to the scale of the missile, (i.e., 1/10 atmosphere if the model scale is 1/10 that of the prototype) the underpressure effect will be independent of missile size at the same Froude number.

Only one systematic study seems to have been reported of the effect of atmospheric-pressure scaling to produce the same whip in model and prototype (Ref. (4-35)) and the scale factor between model and prototype was 11.2. The model whip data with scaled pressure lay within the scatter of the prototype (d = 22.4 inches) data, except for the 0.1 -caliber disk-ogive which had the least whip of all missiles included. Because of the influence of the air density on cavity-closure phenomena the density of the atmosphere should be maintained constant while the pressure is dropped for model scaling. When this was done in the tests just mentioned, satisfactory scaling was obtained.

It must be emphasized that correction of the scaling by reduction of atmospheric pressure is useful in model tests but does not provide simple scaling relations between prototype missiles. Missiles must travel in normal atmospheres except in laboratory tests, and scaling difficulties therefore are present in the dependence on various experimental parameters, especially size and velocity.

A comment regarding Froude scaling appears appropriate here. Comparison of data at the same Froude number should be made when both hydrodynamic and gravity effects are significant. It has been usual (Refs. (4-37) and (4-45)), to compare whip at the same Froude number. However, gravity plays only a small part during the generation of whip, and it is probable that the importance of Froude scaling has been overemphasized.

Although the use of a relation such as equation (4-20) for the scaling of whip may appear impracticable today, it should not be inferred that scaling attempts are either futile or useless. The aeroballistician would not discard the concept of drag coefficient because C_D is strongly velocity dependent for a bullet in the transonic region. Further study should make possible the scaling of whip at least for particular missiles under restricted conditions. In equation (4-21) all quantities except W' and λ are experimentally accessible, and the product $W'\lambda$, as determined from experiment, will be used in the following sections.

The Disk or Vented Right Cylinder

Although the right cylinder is a simple geometrical shape, its whip is greatly complicated by the existence of underpressure.

Conditions are much simpler for the disk, where an open cavity rather than vapor cavitation, is generated. Primarily, in order to separate out the whip due to underpressure, programs comparing the disk and right cylinder were carried out at the Naval Ordnance Test Station (Refs. (4-34) and (4-45)), and at the Admiralty Research Laboratory (Ref. (4-37)). Figure 4-42 shows models used in one of the NOTS tests (Ref. (4-34)). The model in sketch A is a disk, the presumption being that the cavity formed behind the front edge is completely vented, that is, that air fills the cavity to ambient pressure. For the other models, sleeves of various lengths were provided just behind the disk, to test the value and extent of the underpressure. In the ARL tests models similar to sketches A and F were provided for study of the completely vented and unvented cylinders.

The parameters of the missiles and the entry conditions of the tests are given in Table 4-7. It will be seen that the NOTS tests were carried out at substantially a single entry angle of 20°, using two models with diameters of 2.0 and 22.4 inches, each at, or corrected to, a single speed (but with some variation of impact angle of attack). In the ARL (and AHBRE) tests the diameter ranged from 2 to 6 inches, and the entry angle, entry speed, moment of inertia, C.G. position, weight, and angle of attack were varied systematically.

For the vented disk ARL found that the whip was proportional to the entry speed, to $\cot\theta$, and to the reciprocal of the moment of inertia, but was independent of the distance of the C.G. behind the nose. Tests at NOTS showed it to be independent of p_a (Ref. (4-44)). These very important results may be analyzed as follows.

The fact that the whip was found proportional to the entry speed is a verification of the hydrodynamic-force theory of the previous section and it shows that no appreciable underpressure effect existed. It appears probable that it would be so for all noses in the absence of underpressures. In particular, the whip should be proportional to U if the nose is effectively vented, but there are few nose configurations for which underpressure will be completely absent, even with venting. Presumably the whip may be expected to be proportional to $\cot\theta$ only for the disk.

It is probable that the whip is usually inversely proportional to the moment of inertia; at least this result would be expected if the total impulsive moment (hydrodynamic and underpressure) is not changed by a simple change of I. It should not be changed if the moment is of very short duration so that little rotation of the missile occurs during the development of whip.

In scaling whip with I, the added moment of inertia due to entrained water should be added to that of the missile. The scaling has appeared satisfactory without this refinement.

TABLE 4-7

Missile Parameters and Entry Conditions
(Vented and Unvented Right Cylinders)

Laboratory	Missile Diameter (inches)	Entry Angle (Deg.)	Entry Speed* (ft/sec)	Moment of Inertia	I/d^5** (lb/in³)	Dist from CG to nose (calibers)	Instrumentation	Ref.
NOTS Morris Dam	22.42	20-22	400	800 slug-ft²	0.65	2.69	flare camera	(4-45)
NOTS Pasadena	2.0	20.4	137.5	21 lb-in²	0.66	3.1	optical recorder	(4-34)
AHBRE Glen Fruin	4.0 and 6.0	6°-75°	107-283 130-346	1399-8740 10300-66300 lb-in²	2.15 2.14	2-6 4	strain gage accelerometers	(4-37)
ARL Teddington	2.0 and 4.0	6°-75°	75-200 75-100	43.7-273 lb-in²	2.50 2.15	2-6 2-6	optical recorder	(4-37)

*or corrected to these speeds
**scaled moment of inertia (basic value only)

The constancy of the whip as the C. G. is moved fore and aft, should mean that the force causing the pitching moment has little transverse component. As was shown in Figure 4-39 the hydrodynamic forces are almost completely perpendicular to the disk, that is, parallel to the axis of the missile. The lever arm is therefore transverse and the moment is unchanged by a displacement of the C.G. along the missile axis.

There seems to be little dependence of whip on the mass of the missile (Ref. (4-37)) unless the missile is light enough that the speed changes significantly during entry.

Since the whip of the vented disk is proportional to $\cot\theta$ within experimental accuracy, it is possible to compare values of $W'\lambda \tan\theta$ from various tests, and nine such values are collected in Table 4-8.

The first two values are from NOTS "torpedo" and model entries at about 20 degrees; the next three are values read at 20 degrees from straight graphs obtained at ARL from a series of tests in which θ was varied; and the last four are from ARL tests in which entry speed was varied and in which the entry angle ranged from 6 to 25 degrees.

The variation of the quantity $W'\lambda \tan\theta$ in Table 4-8 appears to be due to experimental error rather than to scaling effects. The low values found for the entries at 6 degrees are probably due to water hitting the afterbody. The value

$$W'\lambda = (I\Delta\omega/\rho U_o d^4) \cot\theta = 0.0162 \cot\theta \qquad (4-26)$$

TABLE 4-8

Compared Values of $W'\lambda\tan\theta$

Missile Diam. (inches)	Entry Angle, θ (degrees)	Impact Velocity (ft/sec)	$-W'\tan\theta$	Reference	Remarks
22.4	21	400	0.0164	(4-45)	NOTS, Morris Dam
2	20.35	137.5	0.0186	(4-34)	NOTS, Pasadena
4	20	107	0.0162		ARL
4	20	283	0.0163	(4-37)	θ-variation
2	20	75	0.0147		series
4	25	100-280	0.0159		
4	8	110-280	0.0174	(4-37)	ARL
4	6	105-290	0.0127		U_o-variation
6	25	135-350	0.0116		series

is a reasonable "best value" from these data. It is expected that this formula will give a fair approximation for most entries of vented disks, where the water strikes only the front face of the disk.

Three reports have included data for the dependence on angle of attack of whip of the vented right cylinder (Refs. (4-34), (4-37), and (4-45)), but the data are not conclusive. There is evidence that the whip at 20 and 25-degree entries decreases with positive (nose-up) pitch angles (Refs. (4-37) and (4-45)), and that the whip may become positive for 25-degree entries at pitch angles of about +8 degrees. It appears that the whip may also become less negative at increasing negative angles of attack.

It was pointed out by Borrows (Ref. (4-46)) that the "underpressure effects are extremely sensitive to small variations in flow, such as those caused by small changes in initial pitch, so making a projectile at model scale appear to be much more sensitive to pitch than in fact is really the case".

The Unvented Right Cylinder

The underpressure effect was first noted on relatively fine noses (Ref. (4-12)) and the initial observation was that the effect is much greater on small than on large missiles. Later it was shown that it may be large even for right cylinders, and for 20-degree entries the effect was found for right cylinders with diameters of 2 inches (Ref. (4-34)) and of 22 inches (Ref. (4-45)).

Measurements of pressure in the cavities beneath right cylinders during entries at angles between 6 and 60 degrees are shown in Figure 4-43 (Ref. (4-37)). The cylinder had a diameter of 4 inches and U_O was 106 ft/sec. The ordinate in the figure is the amount by which the cavity pressure is below atmospheric pressure. The cavity pressure is practically zero at the start, and this is shown at the left of the graphs as a pressure of -14.7 psi. The pressure stays at this value for a time depending on the obliquity of the entry and then the cavity vents to the atmosphere and the pressure difference drops in 2 to 4 milliseconds to a value near zero. The dashed line at the foot of each graph shows by its intersection with the abscissa the estimated effective time at which the underpressure phase disappears. These times are given in Figure 4-44 with the times at which the hydrodynamic forces terminate, both expressed as fractions of the time to submergence of the missile face.

The duration of the underpressure phase is short, of the order of 4 milliseconds, for entry of 25 degrees, and the missile travels about a quarter caliber during this phase. For 8-degree entry the underpressure lasts about twice as long.

Mention has been made of a NOTS test (Ref. (4-34)) in which sleeves of various lengths, on which the underpressure may act, were provided behind a 2-inch disk, and the models used are sketched in Figure 4-42. Values of $-W'\lambda \tan\theta$, obtained from that test are plotted in Figure 4-43 against the length of the sleeve in calibers. As the length is increased from zero (completely vented conditions) at the left of the figure, to a completely unvented condition at a sleeve length of 1.78 calibers, the whip increases by a factor of 2.8. The build-up of whip with sleeve length is complicated by the

varying length of the underpressure cavity and the varying time at
which the cavity vents to the atmosphere.

Two points are shown on Figure 4-45 for the completely vented
and unvented conditions of a 22.42-inch cylinder (Ref. (4-45)). For
this missile the whip of the unvented cylinder is only 37 percent
greater than when vented. While part of the difference between the
performances of the two missiles probably depends on unexplained effects
of missile size, water-impact speed also contributes. The speed was
137.5 ft/sec. for the two-inch cylinder and 500 ft/sec. for the
22.42-inch cylinder. The lack of scaling with speed can be seen from
Figure 4-46 which shows the whip of two 4-inch cylinders which entered
the water at 25 degrees: one completely vented and the other unvented
(Ref. (4-37)). The ratio of vented to unvented whip is 5.5 at 100
ft/sec. and 2.0 at 300 ft/sec. The reason for this is given by
equation (4-23) which shows that the whip due to underpressure varies
as the reciprocal of the impact speed. This reciprocal dependence
assumes that the size of the underpressure cavity does not vary with
the speed but that the duration is inversely proportional to it.
Actually it is probable that the size of the cavity increases with
missile speed so that the whip due to underpressure will not decrease
quite as fast as the reciprocal of the speed. The graphs of Figure
4-46 do indicate that the underpressure contribution is decreasing
with increasing speed, but not as strongly as $1/U_o$.

Mention was made earlier of the effect of atmospheric pressure
on the whip due to underpressure. Tests have showed that the whip
of an unvented 2-inch right cylinder may be five times as great at
$p_a = 1.5$ atmos. as at $p_a = 0.1$ atmos. (Ref. (4-44)).

The possibility of developing scaling laws applicable to the
unvented cylinder, does not appear bright, and the prospect for the
more complicated shapes seems poor indeed.

It has been mentioned that whip of the vented cylinder scales
well with $\cot\theta$. A plot of whip against $\cot\theta$ is given for unvented
cylinders in Figure 4-47 (Ref. (4-37)). Data points are shown for
scaled cylinders ($I \propto d^5$) with diameters of 2, 4, and 6 inches. The
deviation from proportionality with $\cot\theta$ is not large. The tests of
Figure 4-47 were Froude scaled, that is, the velocities were
proportional to $d^{1/2}$. As was stated earlier, this scaling is not
generally indicated for water-impact tests. Equation (4-21) shows
that, for scaled models, better agreement might be expected if the
velocities are proportional to d (rather than $d^{1/2}$) and the data of
Figure 4-47 substantiate this conclusion.

Attack-sensitivity data for the unvented disk cylinder are
somewhat inconsistent. Probably it can be said that the attack
sensitivity is small and positive (increasing upward whip with upward
pitch angle) (Refs. (4-34) and (4-37)), although a negative attack
sensitivity has also been reported (Ref. (4-45)). Tests at ARL
(Ref. (4-37)) indicated that the whip increases with positive and
negative angles of attack, with a minimum whip usually between 0 and
-2 degrees.

4-33

The Hemisphere Cylinder

So far, whip has been discussed for the right cylinder only. In proceeding to other shapes, the rather simple hemisphere cylinder (a cylinder capped by a hemisphere) is considered first because information, although scant, is still more plentiful than for others.

The most extensive program reported for the hemisphere cylinder is that of Norman and others (Ref. (4-19)). Using missiles with diameters of 20 inches, the entry speed, angle, and pitch were varied. A smaller program carried out with 22.4-inch missiles at NOTS, is reported in two papers: one gives the whip and attack sensitivity at 20-degree entry (Ref. (4-36)) and the other (Ref. (4-18)) presents data, for which accuracy is not claimed, for whip at a number of entry angles. In the plot of the latter $W'\lambda$ data against $\cot\theta$ in Figure 4-48, the deviation from linearity is only moderately large. The data were obtained from photographs of tail flares on the missile, and the whip was evaluated when the flares and the tail disappeared into the water.

Figure 4-49 is a plot of the variation of angular velocity with time after entry for the ARL test (Ref. (4-19)) of the hemisphere cylinder at entry angles of 15 to 33 degrees. The graphs are approximately the same shape for all entry angles. An initial peak, which becomes only a shoulder for the smallest angles, occurs just before 10 msec (2.2 ft). The positive whip is then decreased by the underpressure, but subsequently increases steadily until about 130 msec after water impact (30 ft. of travel) when the tail of the missile hits the lower cavity wall. Between 10 and 130 msec there is a rather constant overturning moment which increases the angular velocity of the missile. Presumably the whip is best evaluated at the first peak and ARL (Ref. (4-19)) used approximately this time when they chose the time when the drag is a maximum. The NOTS entries from which Figure 4-48 was obtained, used for whip the angular velocity after a travel of about 6.4d. This distance was reached in about 24 msec for the NOTS entries or 48 msec for the ARL entries of Figure 4-49. At that time, Figure 4-49 gives a whip of about 56 deg/sec for $\theta = 20$ degrees or $W'\lambda = 0.130$, which is in fair agreement with Figure 4-48 at $\cot (20°) = 2.75$.

A comparison of whip and attack-sensitivity values can be made from straight graphs that are given in NOTS and ARL reports. Data are listed in Table 4-9. The values of whip were evaluated at NOTS when the missile completely disappeared into the water and at ARL, 25 msec after entry. In contrast, ARL usually evaluated whip at about 8 msec. The whip given for 8 msec by ARL data was

$$\Delta\omega = 31.1 + 1.64\phi,$$

less than 60 percent of the 25-msec value at zero pitch, and less than 1/3 the attack sensitivity. Considering the different distances at which whip was evaluated, the 25 percent difference in $W'\lambda$ values is not discouraging. The most discouraging feature of the comparison

is in the variation of whip with entry angle. As compared with the
smooth dependence found by NOTS (Figure 4-48) that of Figure 4-49 is
quite irregular.

TABLE 4-9

Data Comparing Whip and Attack Sensitivity

Laboratory	NOTS	ARL
Reference	(4-36) Fig. 4-9	(4-19) Fig. 4-78
θ (degrees)	20	18
d (inches)	22.42	20
I	800 sl-ft^2	14405 lb-ft^2
U_O (ft/sec)	500	225
C.G. to nose tip (calibers)	3.17	2.93
Whip evaluated after	6.4d / 24 msec	3.4d / 25 msec
Whip	133 + 10.2ϕ	54 + 5.6ϕ
W'λ	0.157 + 0.012ϕ	0.125 + 0.013ϕ

A simple study of the variation of whip with velocity (Ref. (4-19))
tends to confirm the elementary theory. If in Figure 4-50 whip is
evaluated for 30-degree entry at the first peak (at about 10 msec),
the values are rather well given by the expression

$$\Delta\omega = 0.249U - 3430/U,$$

where U is in ft/sec. The two terms correspond to the hydrodynamic
contribution of equation (4-21) and of the underpressure in equation
(4-23).

Because of underpressure, p_a causes a large negative contribution
to the whip of the unvented hemisphere cylinder. For example, for a
2-inch model, a whip of 250 deg/sec was reported at $p_a = 0.1$ atmos.
and -400 deg/sec at 1.5 atmos. (Ref. (4-44)). For the higher values
of p_a the contribution of underpressure to the whip was found to be
variable, and a change in angular velocity of comparable magnitude
was sometimes observed in the yaw plane.

Disk Ogives and Spherogives

The programs already mentioned for the hemisphere were extended
at both NOTS (Ref. (4-47)) and ARL (Ref. (4-27)) to other members of
the disk-ogive family and, in addition, tests were made at NOTS for
pure ogives and for spherogives (Ref. (4-36)).

The members of the ogive and disk-ogive families were sketched
in Figure 4-31. Three different methods have been used to specify
members of the family: reports of ARL have given the ogive radius,
r_o, in inches; historically this radius has been given in calibers,
that is, $R_o = r_o/d$; and sometimes the function

$$Q = 1/(1 + 2r_0/d) = 1/(1 + 2R_0),$$

is used. This quantity has the advantage for ogives, where the radius can become very large, that Q has a range only from 0 to 1.

For $R_0 = 0$ the missile is a right cylinder; for $0 < R_0 < 0.5$, a disk ogive; for $R_0 = 0.5$, a hemisphere; and for $0.5 < R_0$, an ogive. Tests at ARL with a missile diameter of 20 inches (Ref. (4-27)) used radii of 0, 1, 2, 4, and 10 inches, or 0, 0.05, 0.1, 0.2, and 0.5 calibers. At NOTS (Ref. (4-47)) the radii were 0, 0.1, 0.25, 0.5, 1.5, and 3.5 calibers. Since the noses were unvented in all of the tests described in this section, whip results will usually be given without attempt at scaling.

In Figure 4-51, graphs of angular velocity are plotted against time for the noses tested by ARL at entry angles of 18 and 30 degrees. Most of the graphs have shoulders which furnish an obvious, if poorly defined, position for the evaluation of whip. From the figure, the whip is evidently near zero for an ogive radius of 0.1 caliber or perhaps between 0.1 and 0.2. The noses contained in Figure 4-51, ranging from the flat to the hemisphere, have a whip which varies monotonically through this range, going from a rather large positive (nose-up) whip for the hemisphere to a rather large negative one for the flat, or right cylinder.

Figure 4-52, based on NOTS data, shows the same qualitative behavior with the whip becoming more positive as the nose is varied from flat to hemisphere, and reaching a maximum at about the 1.5-caliber ogive. The apparent decrease in whip for noses more pointed than the 1.5-caliber ogive requires comment. In the sketch of Figure 4-52 it is, of course, assumed that the missiles differ only in nose shape, and that the C.G. position and transverse moment of inertia are the same for all. Evidently the "needle nose" shown at the extreme left of the figure as having zero whip, is completely impractical, since this nose must have no volume but a large moment of inertia. It is probable that the decreased whip shown for the 3.5-caliber ogive is also misleading in most cases. As the nose becomes more slender it is usually difficult to prevent an aft displacement of the C.G., with increased lever arm and increased whip.

The increase in attack sensitivity with increased sharpness of the nose, is shown by the dashed graph of Figure 4-52.

The missiles with which the data of Figures 4-51 and 4-52 were obtained are similar but the velocity and moment of inertia were roughly half as great for Figure 4-51 as for Figure 4-52. Values of $W'\lambda$ agree fairly well for noses having negative whip (with roughly the same values of λ) but not very well in the region of positive whip where the hydrodynamic and underpressure contributions are of opposite sign and scaling failures become more evident.

Figures 4-53 and 4-54, based on the ARL data, show the dependence of the whip graph on entry velocity and angle. There are several

interesting features in these graphs. From Figure 4-53, the ogive radius for which the whip is zero, varies with the entry speed because of the scaling failure of the underpressure forces. The fact that the whip for noses at the right of Figure 4-53 has values which increase a little more rapidly than the first power of U_o is due to the decreasing importance of the underpressure at higher speeds.

It has generally been accepted that the magnitude of the whip increases as θ decreases, as shown for unvented right cylinders in Figure 4-47, and for hemispheres in Figure 4-48. According to Figure 4-54, however, for disk ogives having positive whip, the whip increases as θ increases from 18 to 30 degrees. If this behavior is correct, it must mean that, as the angle gets flatter, the underpressure contribution to the whip increases more strongly than the hydrodynamic. Evidently the whip must approach zero as θ approaches 90 degrees.

Figure 4-55 contains data obtained at NOTS in a test including spherogives (Ref. (4-36)). An ogive is changed into a spherogive if its tip is replaced by a spherical surface so that the sphere and ogive have common tangents where they meet. As can be seen from the sketches the sphere can be given any radius from zero to that of the missile cylinder, and spherogives form families based on given ogival radii. Two families are shown in Figure 4-55, based on 1.5 and 3.5-caliber ogives. The whip is less for the 3.5-caliber than for the 1.5-caliber ogive family. The hemisphere nose is a member of both families and the point g in the left-hand part of Figure 4-55 must lie on extensions of both solid graphs. Evidently each graph has a minimum, probably between the point g and the points f and c. The straight dashed graph between the origin and point g, is drawn merely to show how close the points f and c lie to it. No theoretical importance is ascribed to this fact. Attack sensitivities for the families are given in the right-hand graphs.

Cone Cylinders

Apparently only one experimental report has been published (Ref. (4-48)) on the whip of cone cylinders, and no theoretical results are available although the problem has been discussed (Ref. (4-49)).

Experiments were reported by Gurney of NOL only for a 10-degree half-angle cone cylinder entering water at 45 degrees at speeds usually 100 to 135 ft/sec. The data were too incomplete to be regarded as dependable. The center of pressure (CP) of the integrated force was found to be far in front of the tip of the cone. This indicates that the principal component of the force system is a positive couple. Such a couple could easily arise from an upward hydrodynamic force on the forward part of the cone and a downward underpressure force further aft. Such a position of the CP would make the whip almost independent of the position of the C.G. except that the CP position might be strongly variable.

The data indicate an average $W'\lambda = 0.54$ approximately for the 10-degree cone. For 3 5-caliber ogive data (Ref. (4-36)), similar calculations show $W'\lambda = 1.43$. The ogive was measured at 20-degree entry and the cone at 45 degrees, and scaling by $\cot\theta$ shows the two $W'\lambda$ values to be very nearly the same. Gurney fou d comparable values of attack sensitivity from the tests of the two shapes. These comparisons are probably only order of magnitude, but the behavior of cones might somewhat resemble that of ogives.

REFERENCES

Abbreviations

AMP   Applied Mathematics Panel, Office of Scientific Research and Development, National Defense Research Committee

ARL   Armament Research Laboratory, Teddington, Middlesex, England

CIT   California Institute of Technology, Pasadena, California

NBS   National Bureau of Standards, Washington, D. C.

NOL   Naval Surface Weapons Center, White Oak Laboratory, Silver Spring, Maryland (formerly the Naval Ordnance Laboratory)

NOTS   Naval Ordnance Test Station, Pasadena, California; now NUC

NUC   Naval Undersea Research and Development Center, Pasadena, California

Sc. Pap. Inst. P. C. Res.

       Scientific Papers of the Institute of Physical and Chemical Research, Tokyo.

       *   *   *

4-1.   Chuang, S. L., "Experiments on Flat-Bottom Slamming," _J. Ship Research_, _10_, pp 10-17, 1966

4-2.   Verhagen, J. H. G., "The Impact of a Flat Plate on a Water Surface," _J. Ship Res._, _11_, pp 211-223, 1967

4-3.   Lewison, G. and Maclean, W. M., "On the Cushioning of Water Impact by Entrapped Air," _J. Ship Res._, _12_, pp 116-130, 1968

4-4.   Johnson, R. S., "The Effect of Air Compressibility in a First Approximation to the Ship Slamming Problem," _J. Ship Res._, _12_, pp 57-68, 1968

4-5. Office of Scientific Research and Development, "Aircraft Torpedo Development and Water-Entry Ballistics," OSRD Rpt. 2550, CIT, 1946

4-6. von Karman, T., "The Impact of Seaplane Floats during Landing," NACA Transl. TN 321, 1929

4-7. Milne-Thomson, L. M., Theoretical Hydrodynamics, The Macmillan Co., New York, Third Edition, 1955

4-8. Shiffman, M. and Spencer, D. C., "The Force of Impact on a Sphere Striking a Water Surface (Second Approximation) NDRC AMP Rpt. 42.2R, 1945

4-9. May, A., "The Forces Acting on Cavity-Running Missiles," Alden Research Laboratories, Chapter 2 of this report

4-10. Watanabe, S., "Resistance of Impact on Water Surface, Part V - Sphere," Sc. Pap. Inst. P.C. Res. 23, pp 202-208, 1934

4-11. Blundell, R. W., "Force Measurements on a Hemisphere when Dropped into Water," Marine Aircraft Exptl. Est., Felixtowe (Min. of Sup.) Rpt F/Res/106, 1937

4-12. Office of Scientific Research and Development, "Water Entry and Underwater Ballistics of Projectiles," OSRD Rpt. 2551, CIT, 1946

4-13. Richardson, E. G., "The Impact of a Solid on a Liquid Surface," Proc. Phys. Soc. (London) 61, pp 352-367, 1948

4-14. Hobbs, E. V., "Experimental Determination of Virtual Water Mass from Measurement of Forces Developed during Entry of a Sphere into Water," NBS Rpt. 6.4/196, Project No. 3518, 1951

4-15. Mosteller, G. G., "Axial Deceleration at Oblique Water Entry of 2-inch Diameter Models with Hemisphere and Disk-Cylinder Noses," NOTS NAVORD Rpt. 5424, 1957

4-16. Baldwin, J. L., "Vertical Water Entry of Cones," NOL TR 71-25 1971

4-17. Hobbs, E. V., Breakstone, H. I., and Woodson, J. B., "Oblique Entry of Spheres into Water," NBS Rpt. 2788, 1951

4-18. Hydroballistics Design Handbook, BuOrd NAVORD Rpt. 3533, 1955

4-19. Norman, J. W., Burden, W. J., and Suter, R. A., "Deceleration of Water Entry-III, Velocity, Entry Angle, and Pitch Effects on a Projectile with a Hemisphere Head," ARL/R4/G/HY/2/3, 1959

4-20. Norman, J. W., Burden, W. J., and Suter, R. A., "Deceleration
       at Water Entry-IV, The Effects of Velocity, Entry Angle and
       Pitch on a Projectile with a Flat Cylindrical Head,"
       ARL/R5/G/HY/2/3, 1960

4-21. Shiffman, M. and Spencer, D. C., "The Force of Impact on a
       Cone Striking a Water Surface (Vertical Entry)," Comm. Pure
       and Appl. Math 4. pp 379-417, 1951

4-22. Chuang, S. L., "Theoretical Investigations on Slamming of Cone-
       Shaped Bodies," J. Ship Res., 13, pp 276-283, 1969

4-23. Watanabe, S., "Resistance of Impact on Water Surface. Parts 1
       and 2-Cone," Sc. Pap. Inst. P.C. Res. Part 1, 12, pp 251-267,
       1929; Part 2, 14, pp 153-168, 1930

4-24. Weible, A., "The Penetration Resistance of Bodies with Various
       Head Forms at Perpendicular Impact on Water," Naval Res.
       Lab. transl. 286, 1952

4-25. Baldwin, J. L., "Vertical Water Entry of Some Ogives, Cones,
       and Cusps," NOLTR 71-155, 1971

4-26. Hoover, W. R. and Reardon, P. J., "Approximate Impact Drag
       Coefficients for the Vertical Water Entry of Families of Cone,
       Ellipsoidal, and Tangent Ogive Nosed Missiles," NOLTR 64-110,
       1965   .

4-27. Norman, J. W., Burden, W. J., and Suter, R. A., "Deceleration
       at Water Entry-V. The Effects of Varying Head Radius,"
       ARL/R6/G/HY/2/3, 1962

4-28. Wagner, H., "Ueber Stoss- und Gleitvorgänge an der Oberfläche
       von Flüssigkeiten (On Impact and Planing at the Surface
       of Liquids)" Z. f. AMM, 12, pp 193-215, 1932

4-29. Pierson, J. D., "On the Pressure Distribution for a Wedge
       Penetrating a Fluid Surface," Stevens Inst. of Tech.,
       Exptl Towing Tank Rpt. pp 336, 1948

4-30. Chuang, S. L., "Experiments on Slamming of Wedge-Shaped Bodies,"
       J. Ship Res., 11, pp 190-198, 1967; and "Impact Pressure
       Distributions on Wedge-Shaped Hull Bottoms of High-Speed
       Craft," Naval Ship Res. and Dev. Center Rpt. 2953, 1969

4-31. Pierson, J. D., "On the Virtual Mass of Water Associated with
       an Immersing Wedge," J. Aero. Sciences 18, pp 430-431, 1951

4-32. Szebehely, V. G. and Ochi, M. K., "Hydrodynamic Impact and
       Water Entry," Applied Mechanics Surveys, Spartan Books,
       Washington, D. C., 1966

4-33. Norman, J. W., and Burden, W. J., "Deceleration at Water
       Entry-Some Preliminary Measurements with Strain Gauge
       Accelerometers," ARL/R2/G/HY/2/3, 1955

4-34. Waugh, J. G., Mosteller, G. G., and Ager, R. W., "Effect of
       Underpressure on the Water-Entry Whip of 2-inch-Diameter
       Missiles with Vented Disk-Cylinder Heads," NOTS NAVORD 3342,
       1954

4-35. Waugh, J. G., "Water-Entry Pitch Modeling," Proc. First BuOrd
       Hydroballistics Symposium, 1957; also J. Hydronautics, 2,
       pp 87-92, 1968

4-36. Waugh, J. G., "Water-Entry Whip and Deceleration of Eight
       Full-Scale Torpedo Models with Ogive and Spherogive Heads,"
       NOTS NAVORD Rpt. 1223, 1950

4-37. Norman, J. W., Macdonald, L. I., Burkett, D. J., and Skelly, M.M.,
       "The Water Entry Whip of Right Circular Cylinders," ARL/G/R12,
       1966

4-38. Mason, M. and Slichter, L. B., "Shearing Stress on Projectiles
       at Water Impact," OSRD Rpt. 2483, 1945

4-39. Birkhoff, G., Birkhoff, G. D., Bleick, W. E., Handler, E. H.,
       Murnaghan, F. D., and Smith, T. L., "Ricochet off Water,"
       AMP Memo. 42.4M, 1944

4-40. Burt, F. S., Advances in Hydroscience, Vol. 1, Academic Press,
       New York, 1964

4-41. Tate, M. B., "The Speculum-Momentum Phase of Water Entry,"
       Proc. NOL Water-Entry Symposium, 1 Dec 1955, NAVORD Rpt. 4180

4-42. Norman, J. S., and Aylott, L. J., "The Correction of Differential
       Pressure Errors in Water Entry Experiments by the Application
       of Volatile Liquids," ARL/G/R15, 1967

4-43. Birkhoff, G., Hydrodynamics, 2nd Ed., Princeton Univ. Press,
       1960

4-44. Waugh, J. G., and Stubstad, G. W., "Hydroballistics Modeling,"
       NUC, San Diego, GPO, 1972

4-45. Waugh, J. G., Mosteller, G. G., and Ager, R. W., "Effect of
       Underpressure on the Water-Entry Whip of a 22.4-inch-Diameter
       Missile with Plate-Cylinder Head," NOTS NAVORD Rpt. 1995,
       1952

4-46. Borrows, W. L., "An Historical Survey of Water-Entry Research
       at the Admiralty Research Laboratory," Jour. Royal Naval
       Scientific Service, 23, pp 147-152, 1968

4-47. Waugh, J. G., and Ager, R. W., "Water-Entry Whip and Deceleration of Six Full-Scale Torpedo Models with Ogive and Plate-Ogive Heads," NOTS NAVORD Rpt. 1308, 1951

4-48. Gurney, J. O., Jr., "A Preliminary Study of the Mechanism of Water-Entry Whip of 20° Cone Nosed Models," NOLTR 66-148, 1966

4-49. Cox, R. N. and Maccoll, J. W., "Recent Contributions to Hydroballistics," (First) Symposium on Naval Hydrodynamics, Sep 24-28, 1956

4-50. Chuang, S. L., "Investigation of Impact of Rigid and Elastic Bodies with Water," NSRDC Report 3248, 1970
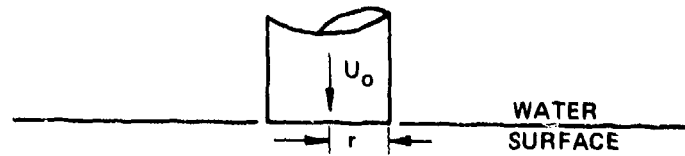
FIG. 4-1 VERTICAL IMPACT OF RIGHT CYLINDER
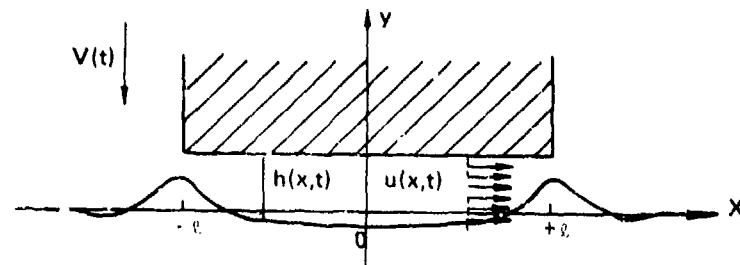
FIG. 4-2 BUFFERING EFFECT OF AIR DURING IMPACT
AFTER REF (4-2)
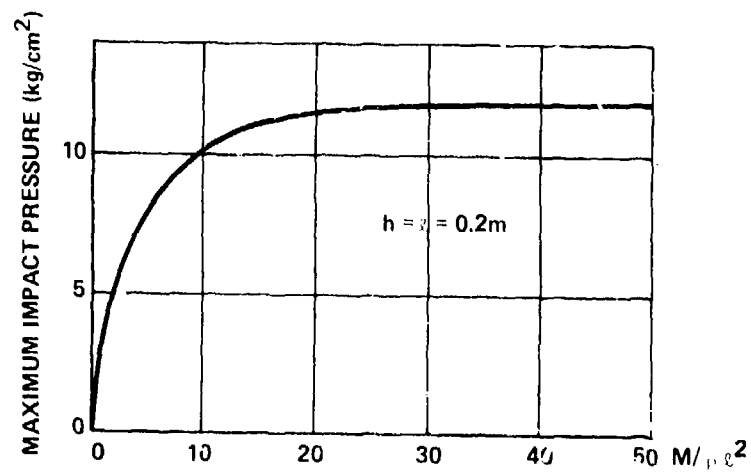
FIG. 4-3 EFFECT OF MASS OF FALLING PLATE ON
MAXIMUM IMPACT PRESSURE AFTER REF (4-2)
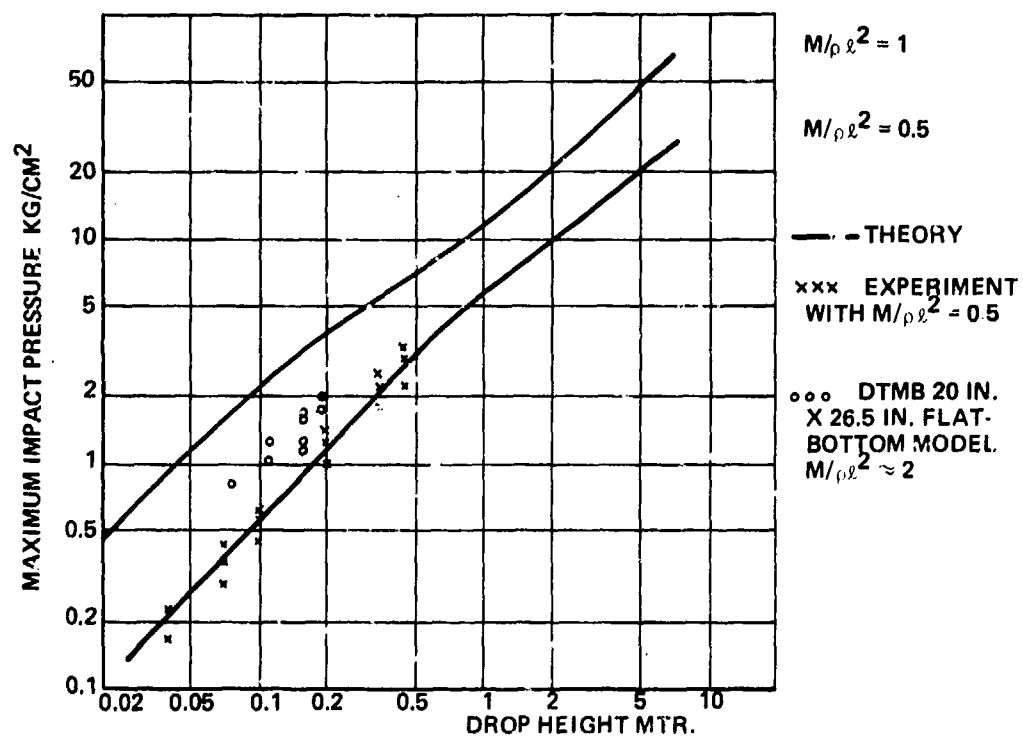
FIG. 4-4 MAXIMUM IMPACT PRESSURE AS A FUNCTION OF DROP HEIGHT
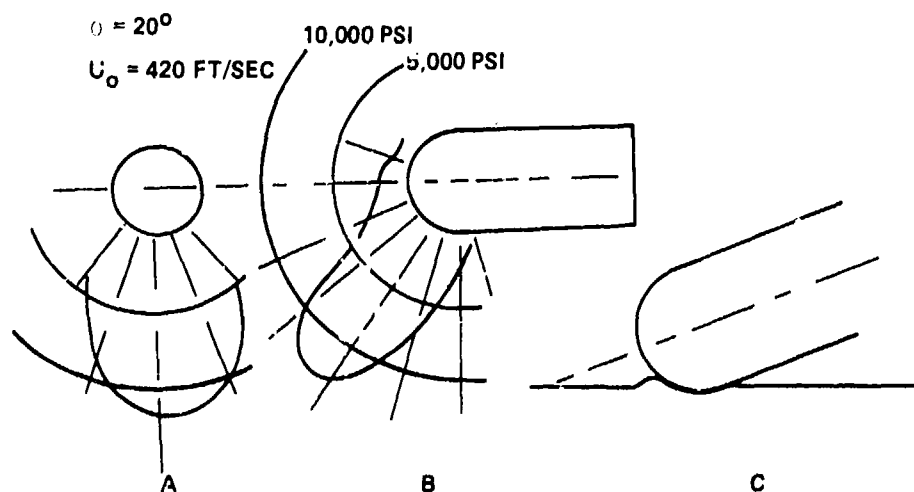
FIG. 4-5 SHOCK PRESSURE AT IMPACT OF HEMISPHERE
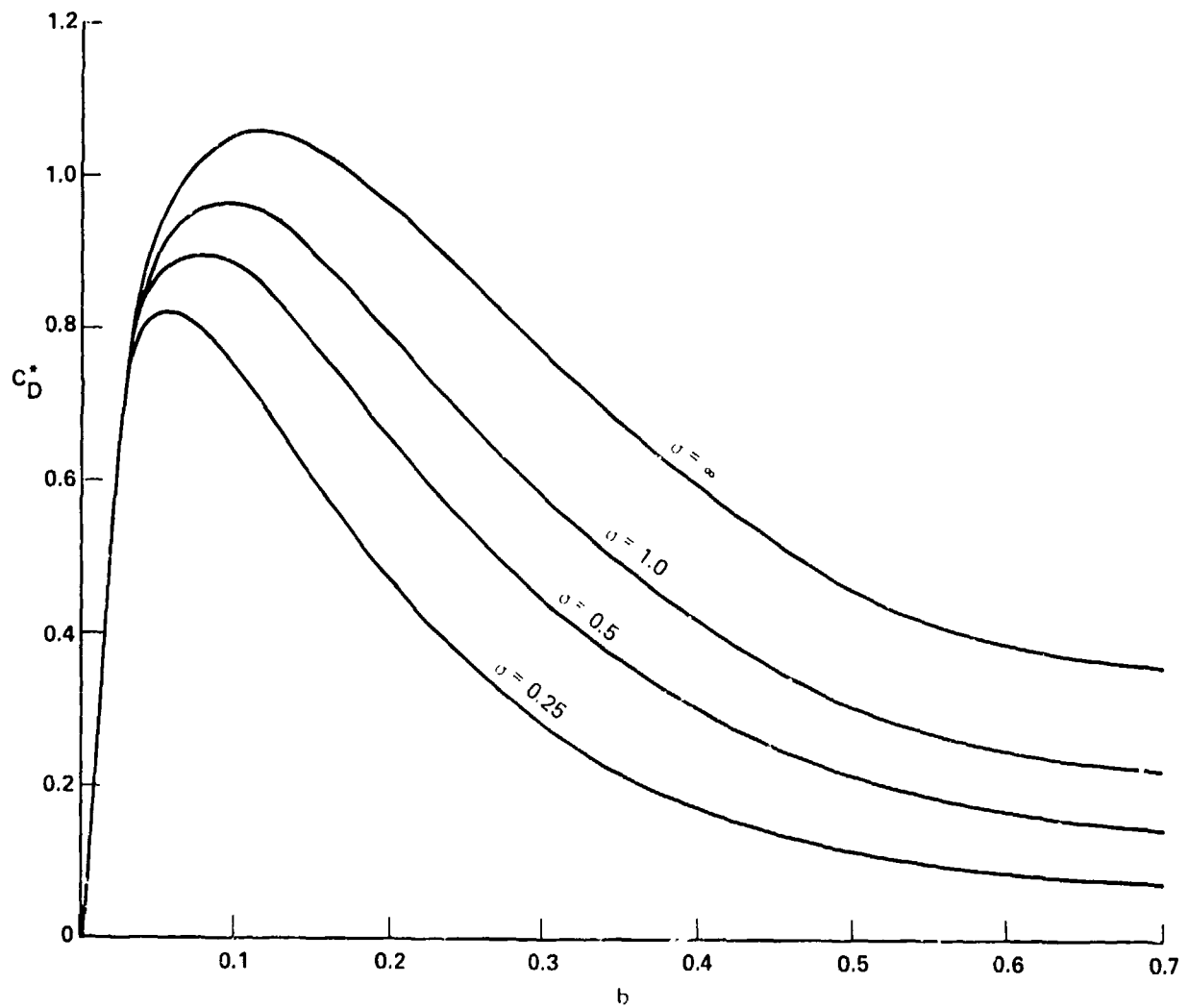
FIG. 4-6 PROPOSED WORKING DRAG CURVES FOR VERTICAL ENTRY OF
SPHERES OF VARIOUS SPECIFIC GRAVITIES
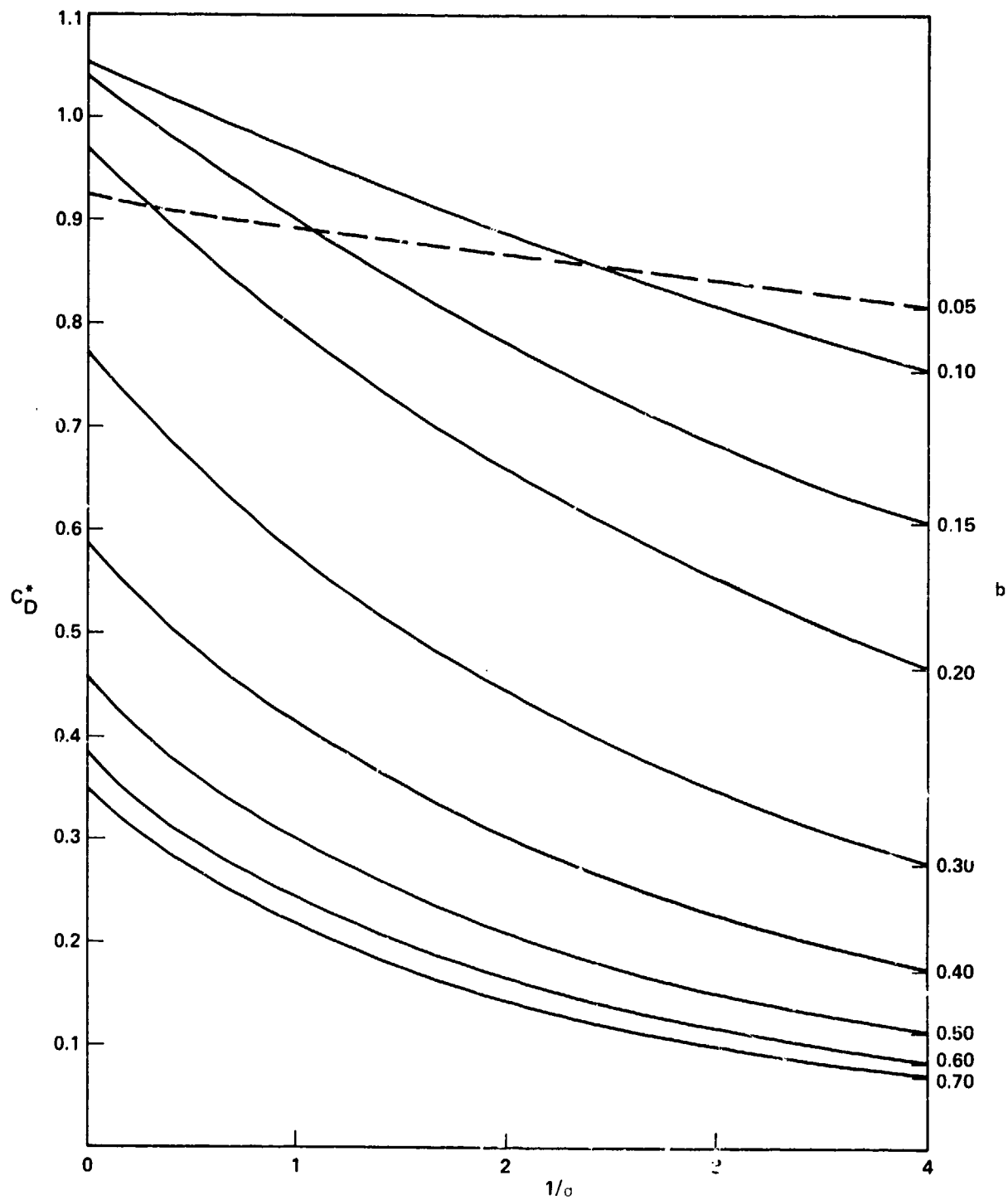
FIG. 4-7 INTERPOLATION CURVES FOR USE WITH FIG. 4-6
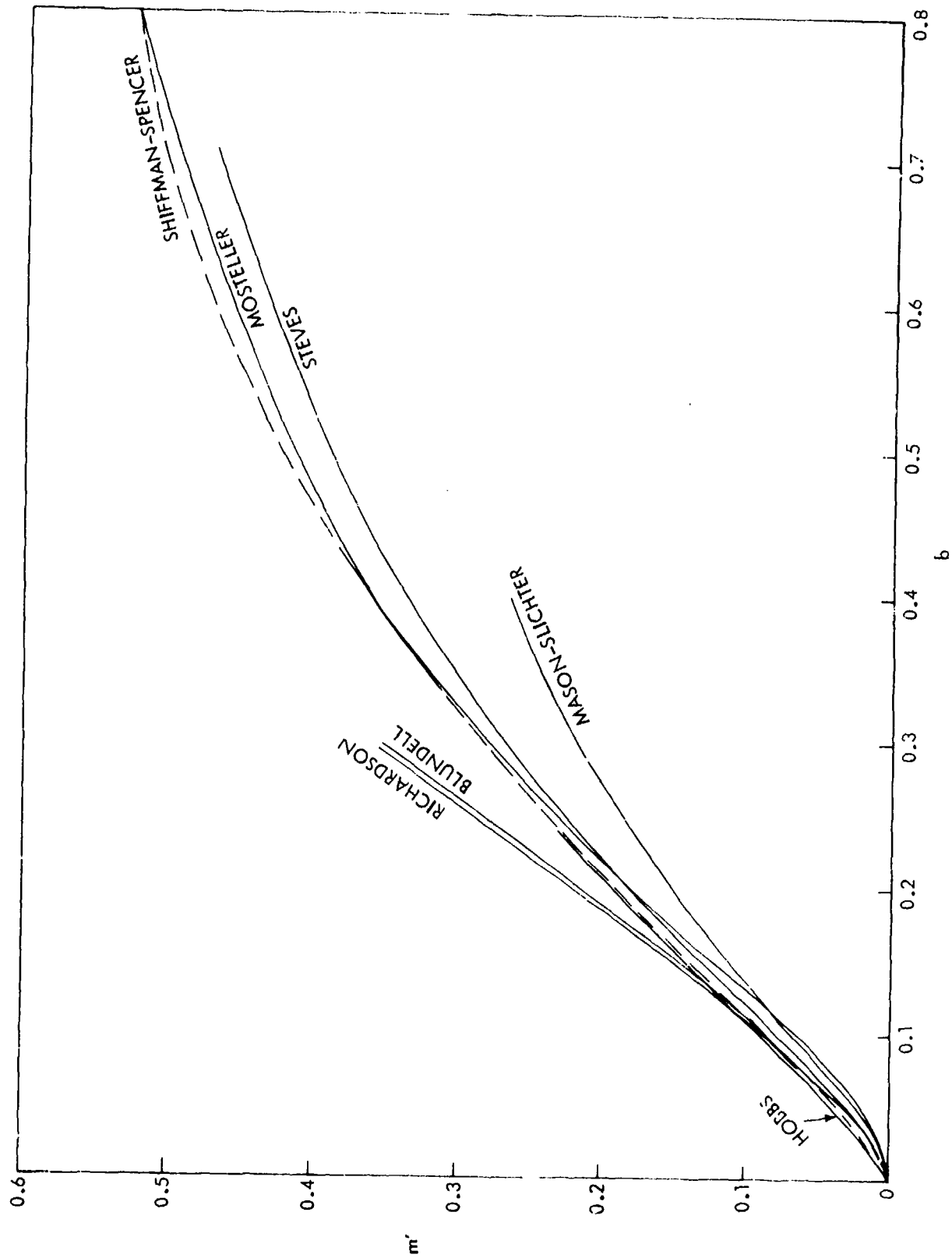
FIG. 4-8 DIMENSIONLESS ADDED MASS DURING THE VERTICAL WATER ENTRY OF SPHERES
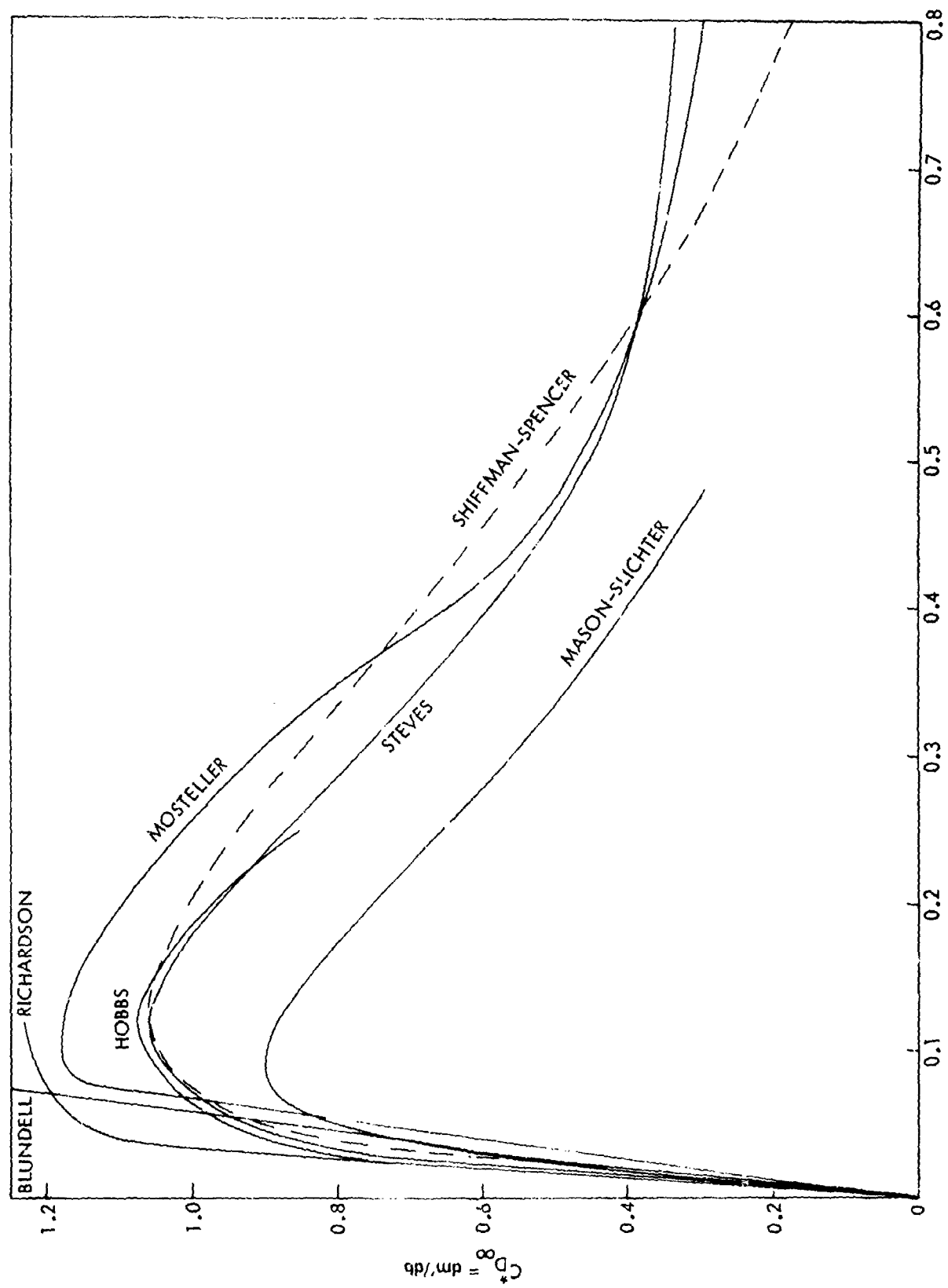
FIG. 4-9 dm'/db DURING THE VERTICAL WATER ENTRY OF SPHERES
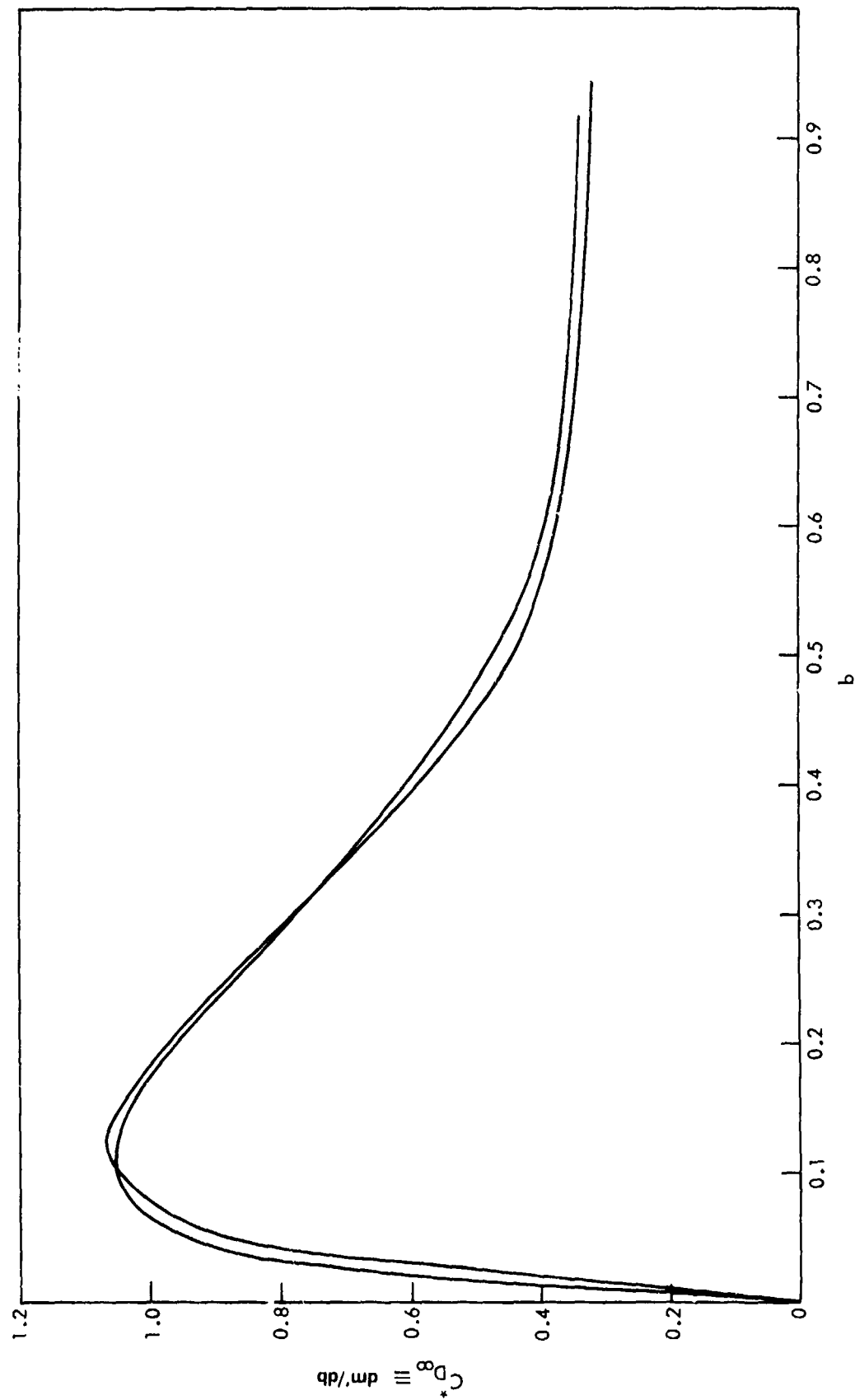
FIG. 4-10 DRAG MEASUREMENTS OF TWO VERTICAL WATER ENTRIES OF SPHERES (NOL—STEVES)
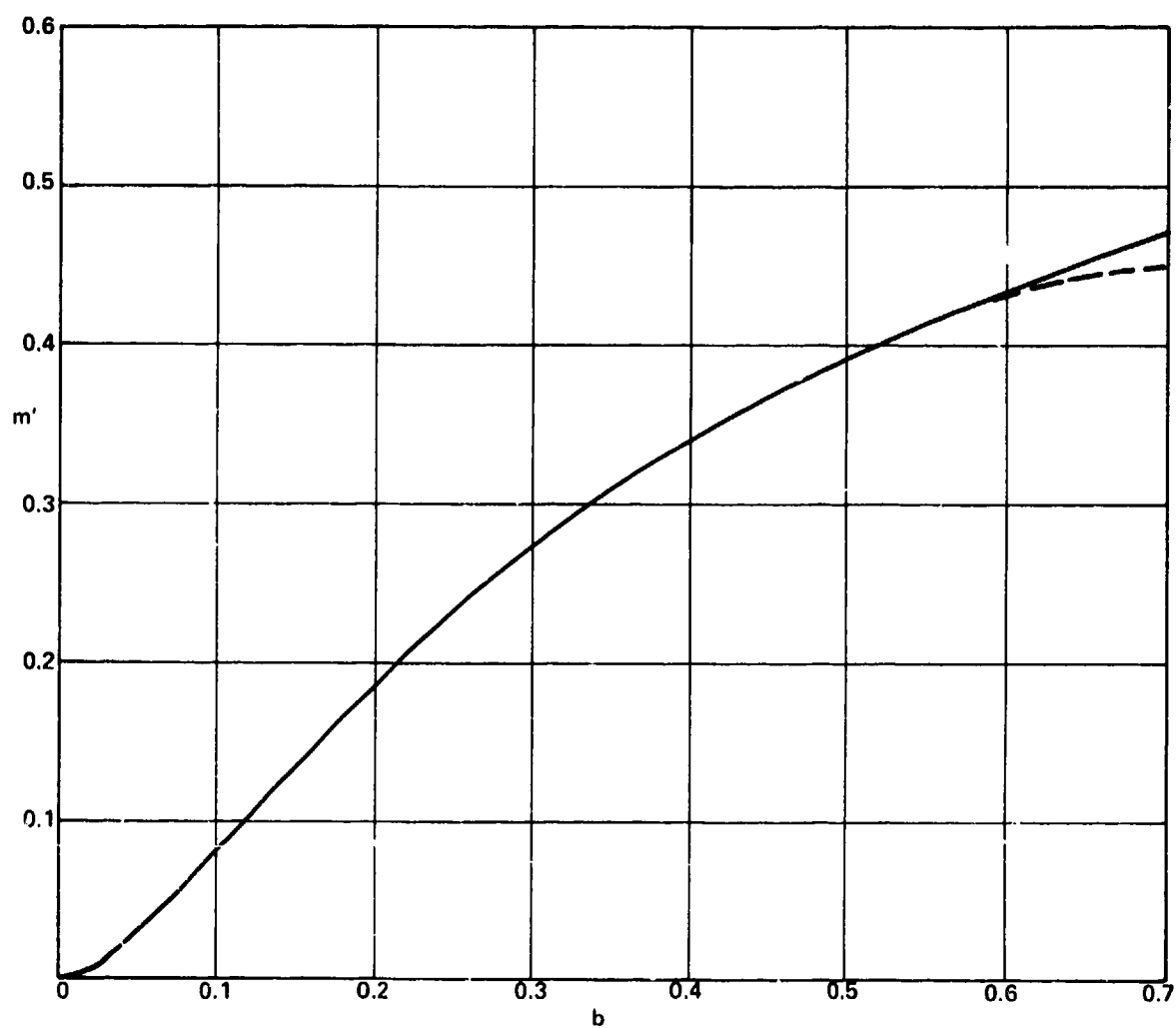
FIG. 4-11 PROPOSED WORKING CURVE OF DIMENSIONLESS
VIRTUAL MASS FOR VERTICAL SPHERE ENTRY
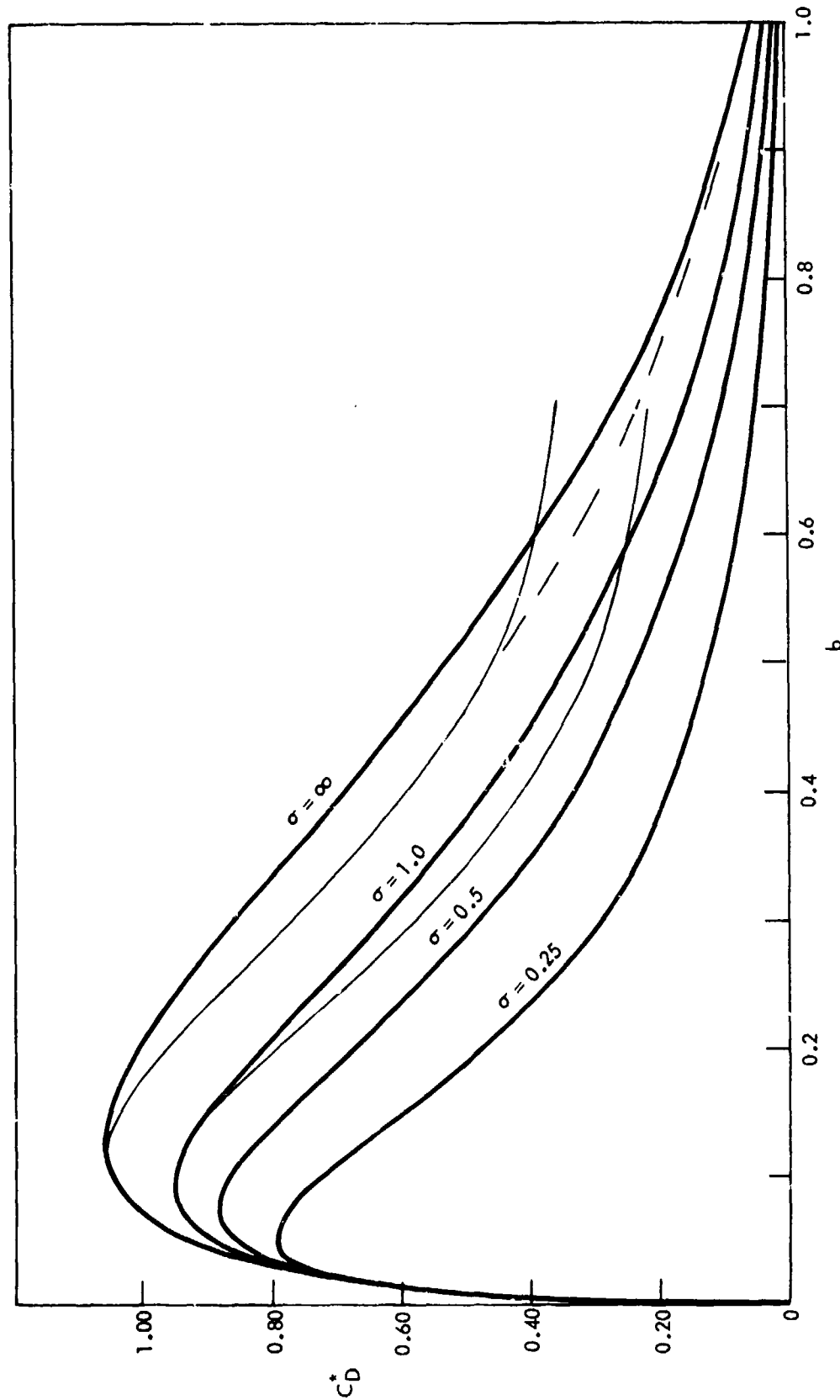
FIG. 4-12 COMPARISON OF THEORETICAL (HEAVY-LINE) AND EXPERIMENTAL (LIGHT-LINE) DETERMINATIONS OF THE DRAG OF A SPHERE DURING VERTICAL WATER ENTRY
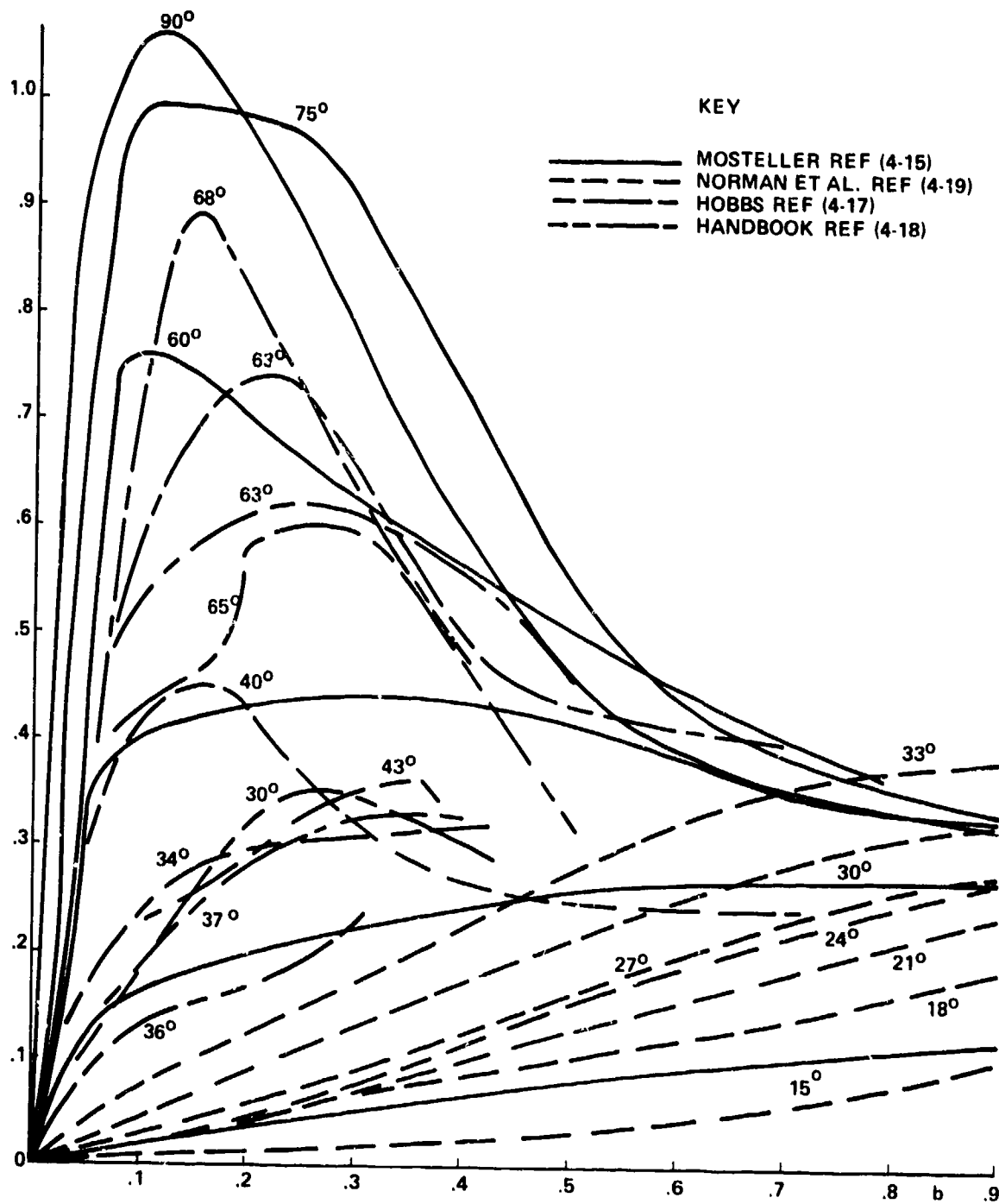
FIG. 4-13 DRAG OF SPHERES AT OBLIQUE WATER IMPACT (TEST DATA)

$$\frac{dm'}{db} = C_{D}^{*}$$
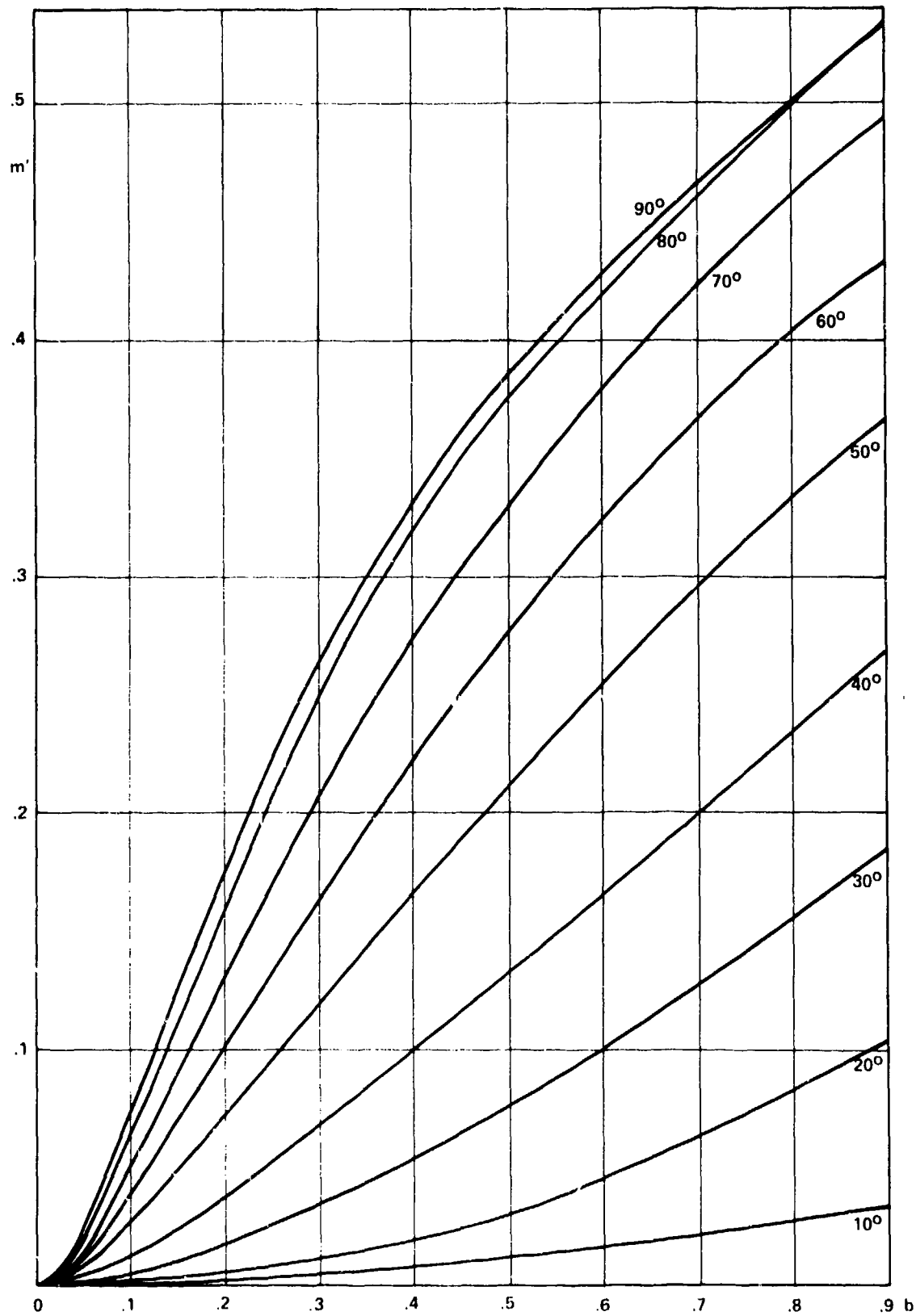

FIG. 4-14 DRAG OF SPHERES AT OBLIQUE WATER IMPACT
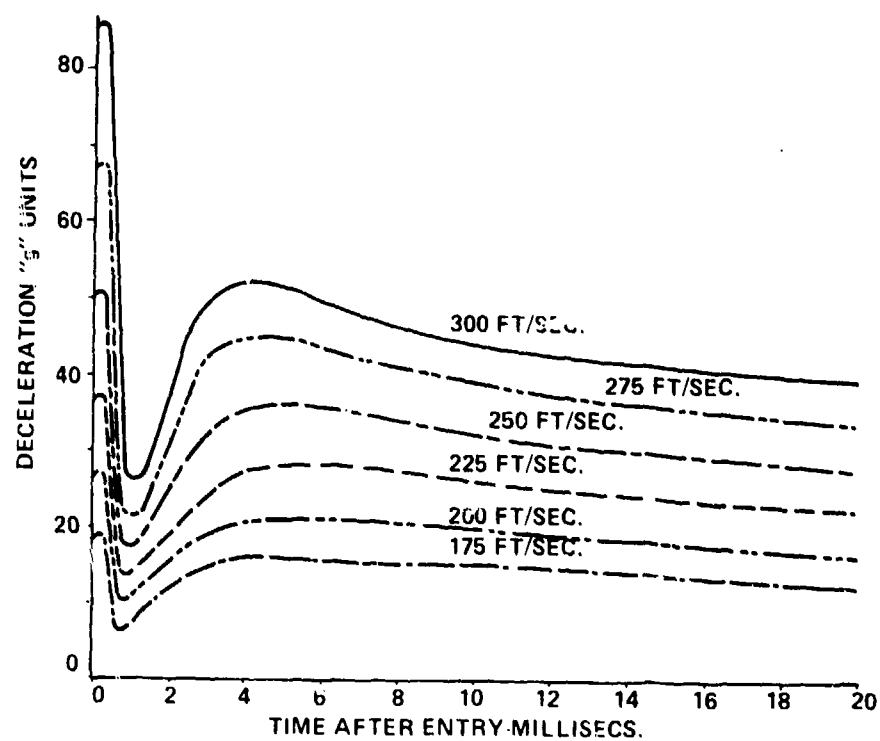
4.5-9

FIG. 4-15 ADDED MASS FOR OBLIQUE ENTRY OF SPHERES

FIG. 4 16 HEAD ACCELERATION—HEMISPHERE; VARIATION WITH
ENTRY VELOCITY; TRAJECTORY ENTRY ANGLE 30°,
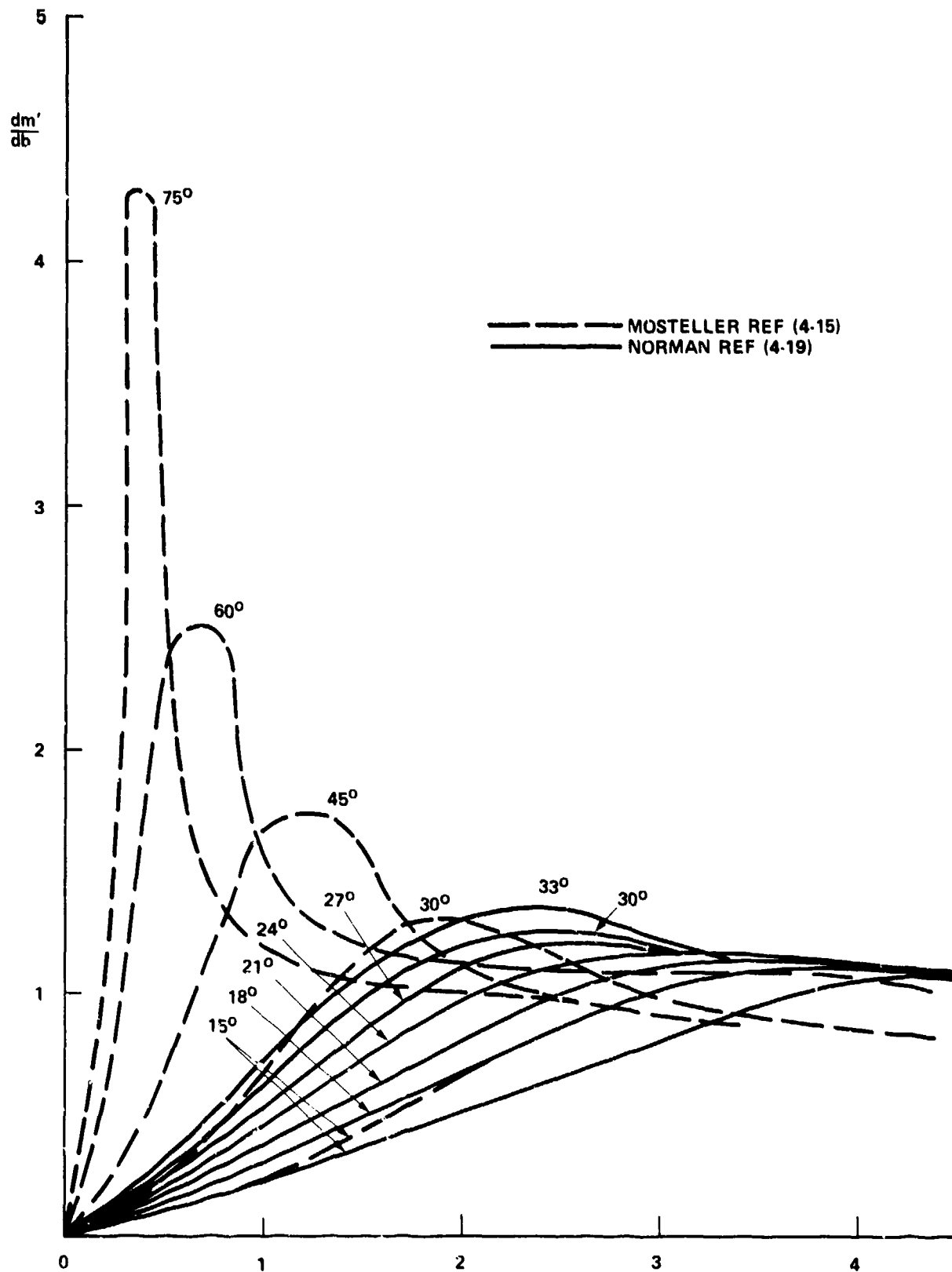PITCH 0° FROM REF (4 19)

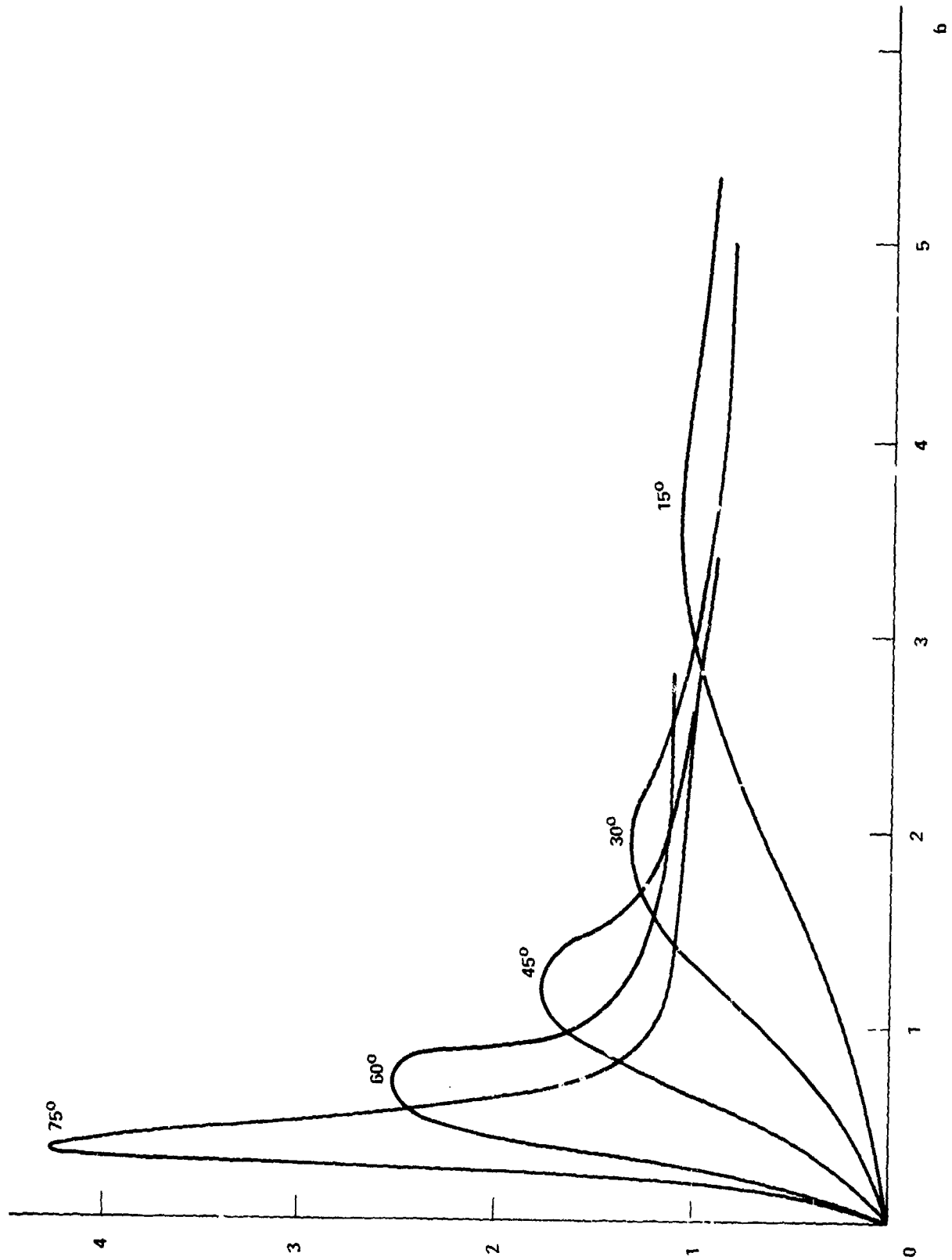FIG. 4-17 DRAG OF DISKS AT OBLIQUE ENTRY (EXPERIMENTAL DATA)
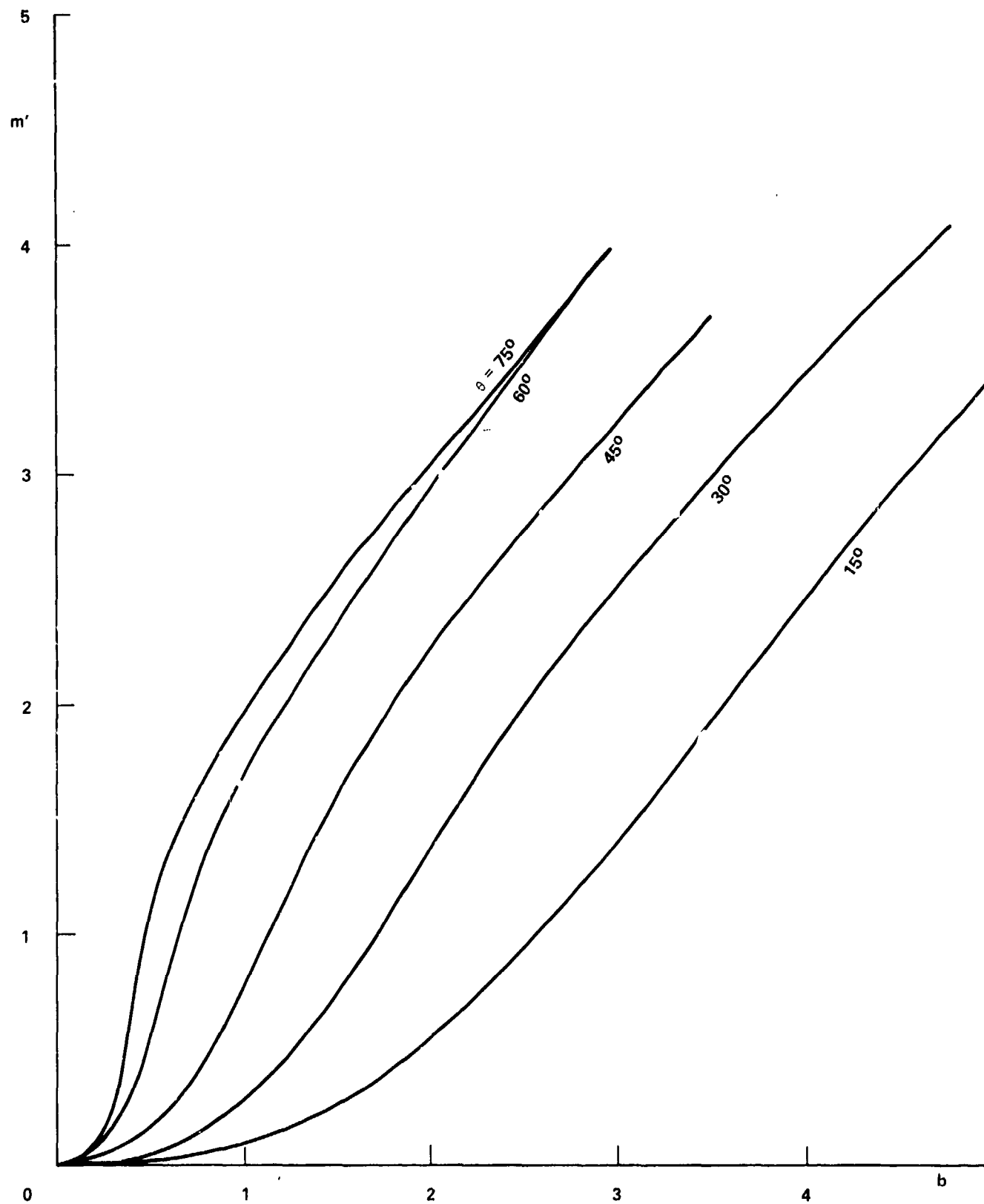
FIG. 4-18 DRAG OF DISKS AT OBLIQUE ENTRY

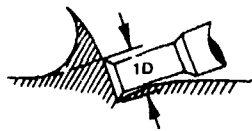FIG. 4-19 ADDED MASS FOR OBLIQUE ENTRY OF DISKS

FIG. 4-20 DISK "PUSHING ON SOLID
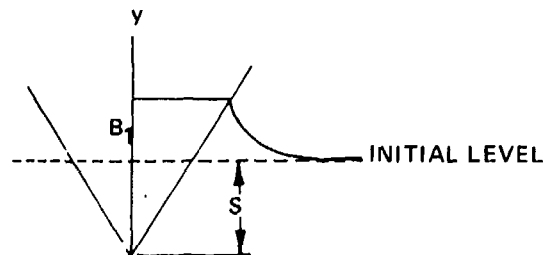WATER" FROM REF (4-20)

FIG. 4-21 WATER SURFACE NEAR CONE DURING
VERTICAL ENTRY FROM REF (4-21)
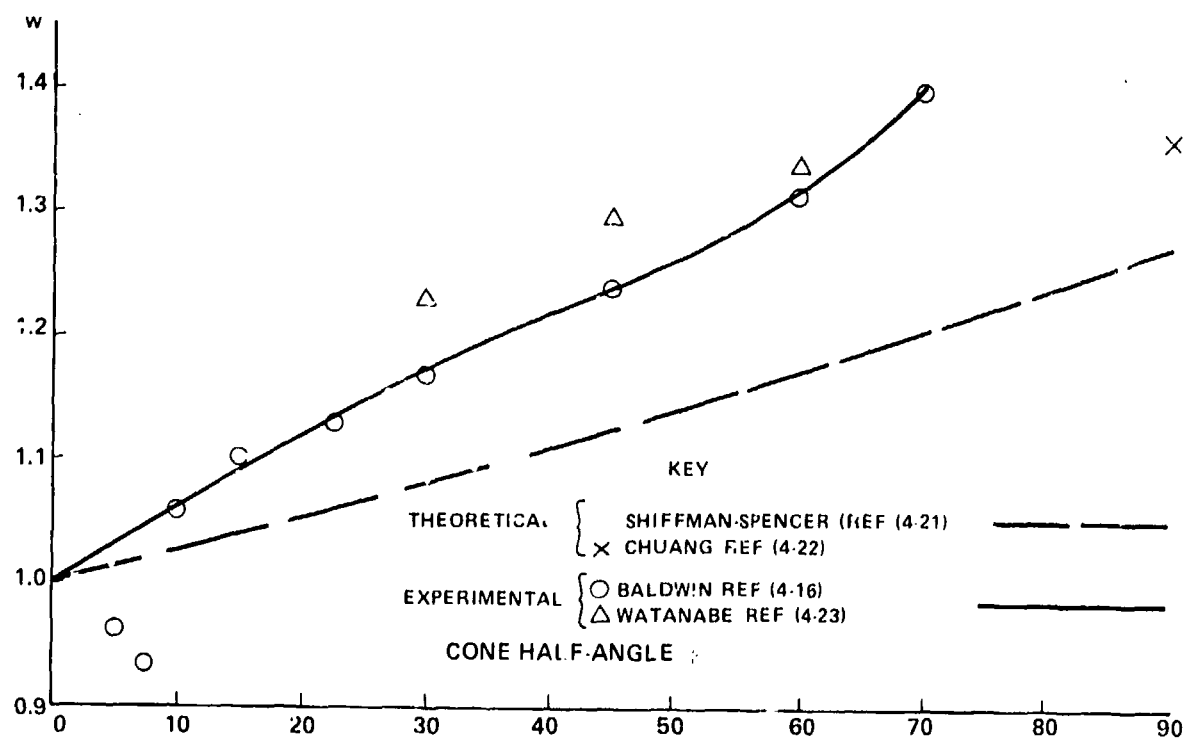
FIG. 4-22 WETTING FACTOR FOR CONES
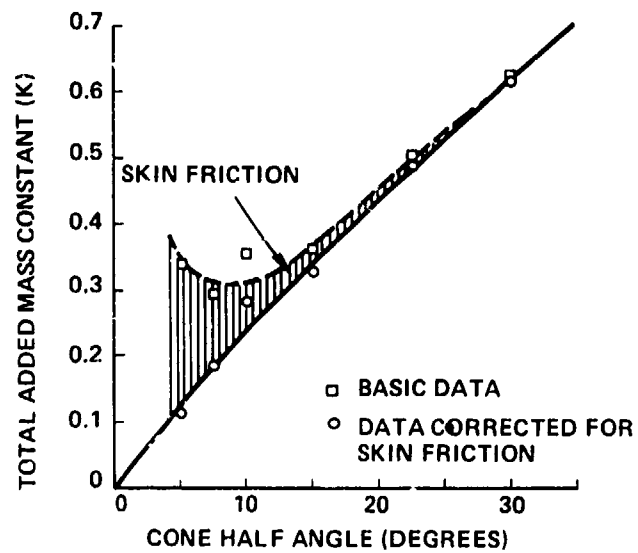
FIG. 4-23 CORRECTION OF TOTAL ADDED MASS
CONSTANT VS CONE ANGLE FROM REF (4-16)
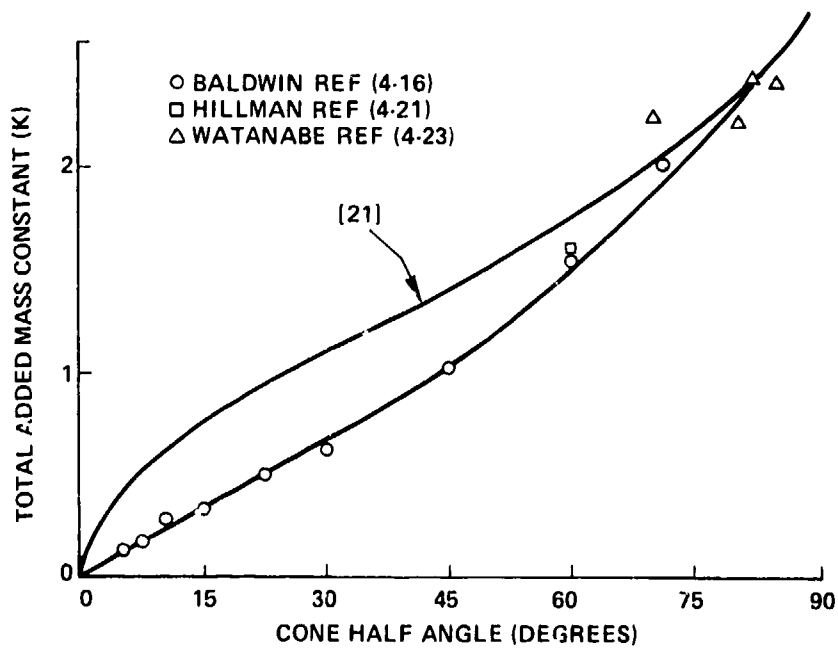
FIG. 4-24 TOTAL ADDED MASS CONSTANT VS CONE ANGLE (ADAPTED
REF (4-16))
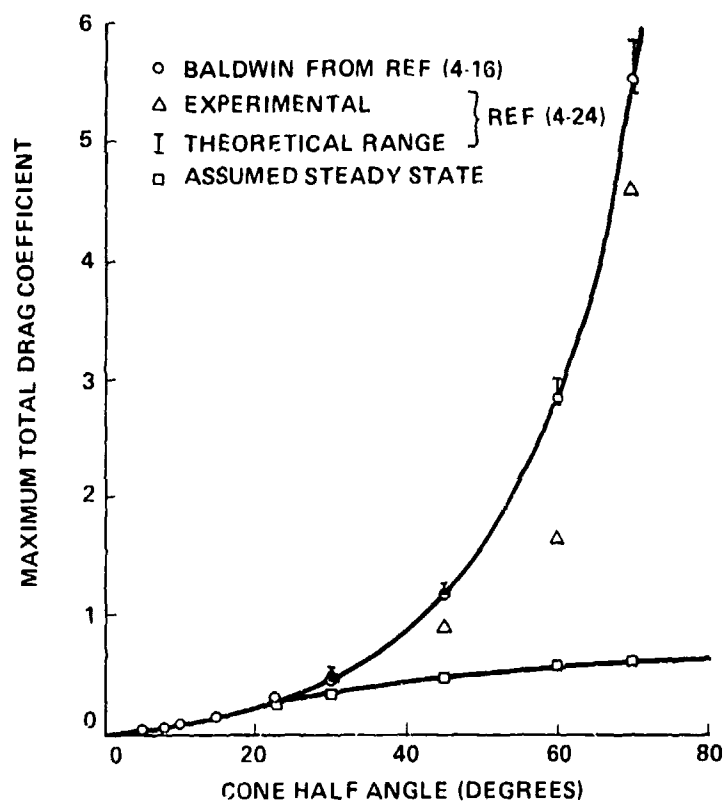
FIG. 4·25 MAXIMUM TOTAL DRAG COEFFICIENT VS CONE
ANGLE REF (4·16)
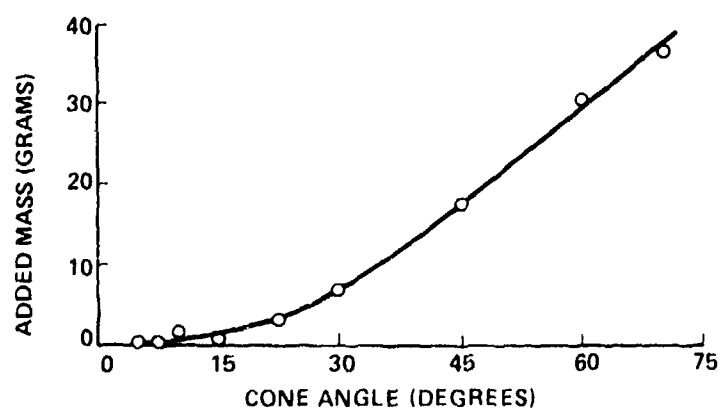
FIG. 4·26 ADDED MASS ASSOCIATED WITH MAXIMUM DRAG
COEFFICIENT VS CONE ANGLE FROM REF (4·16)
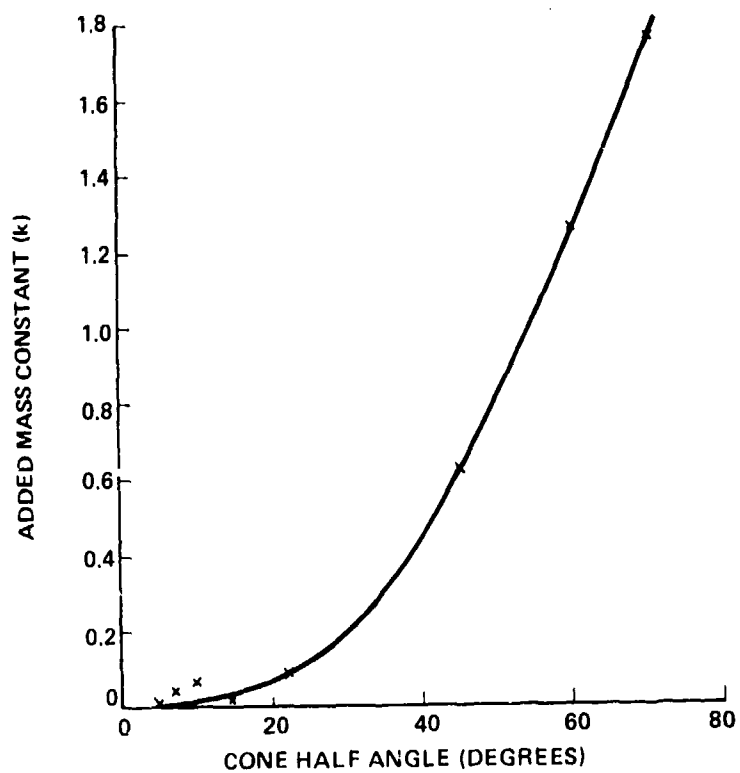
FIG. 4·27 ADDED MASS CONSTANT VS CONE ANGLE
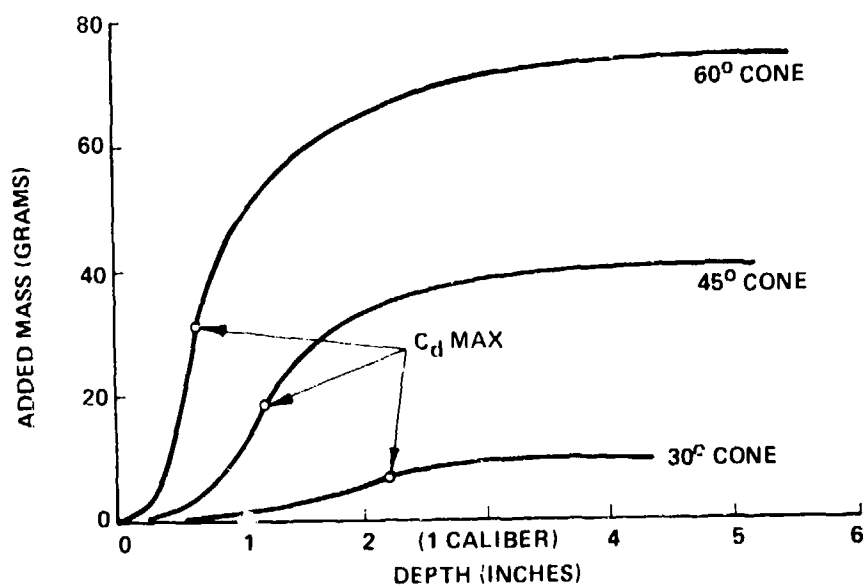
FIG. 4·28 ADDED MASS VS DEPTH FROM REF (4·16)
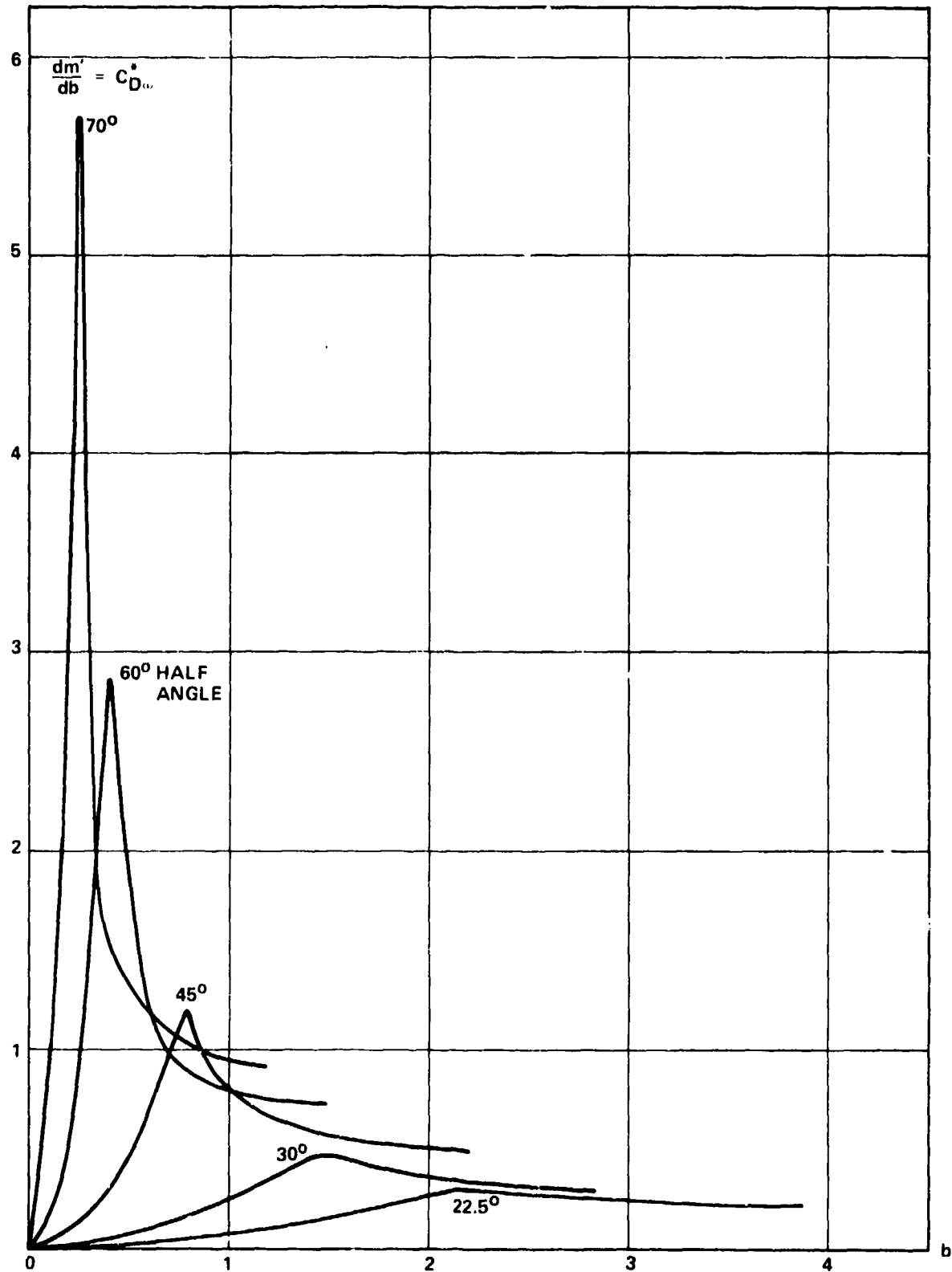
FIG. 4.29 IMPACT DRAG COEFFICIENTS FOR VERTICAL ENTRY OF CONES
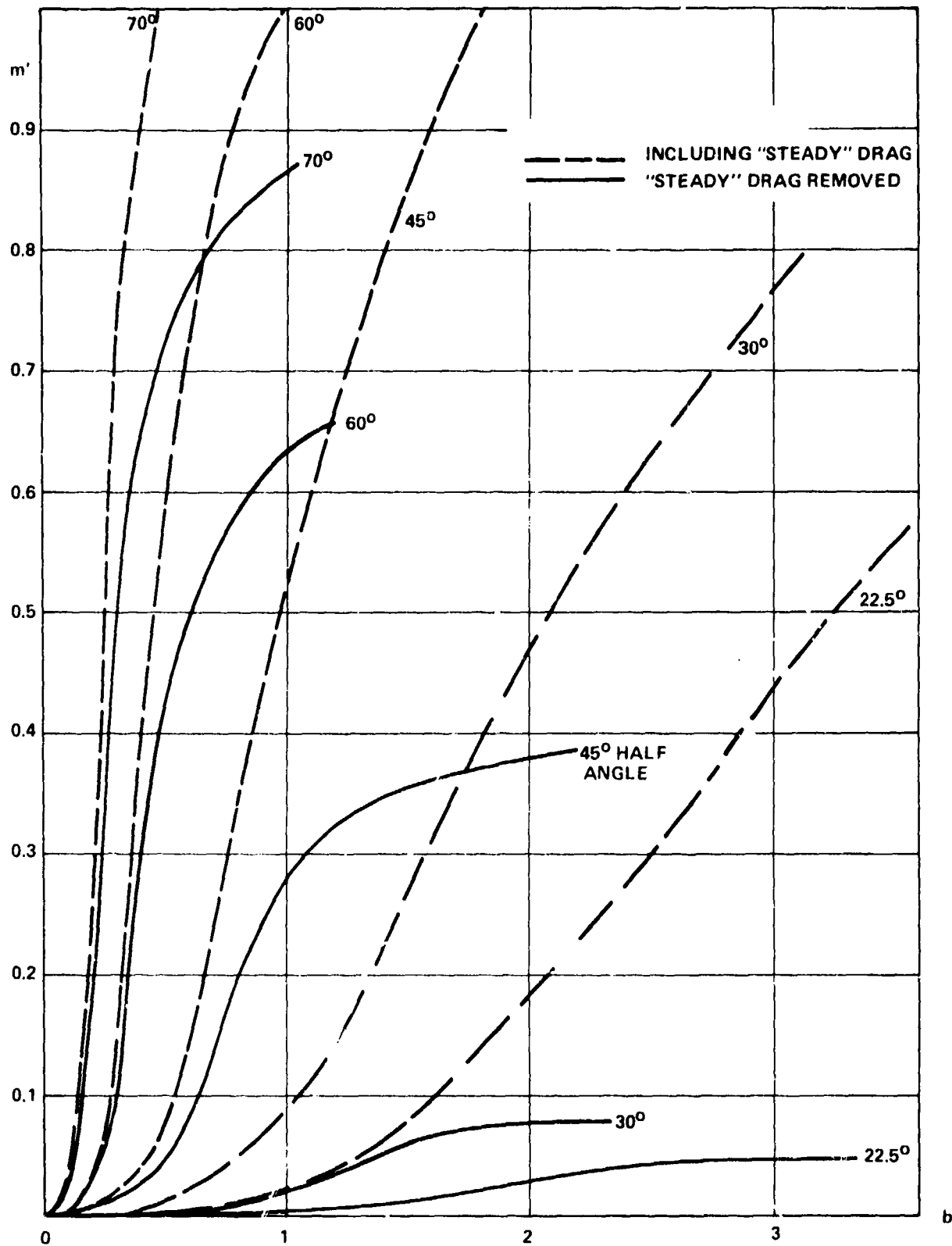
FIG. 4-30 ADDED MASS FOR VERTICAL ENTRY OF CONES

**CALIBER
OF
OGIVE**

A	0	DISK
B	0.1	
C R_o	0.25	DISK OGIVES
D R_o	0.5	HEMISPHERE
E R_o	1.5	OGIVES
F R_o	3.5	
G		
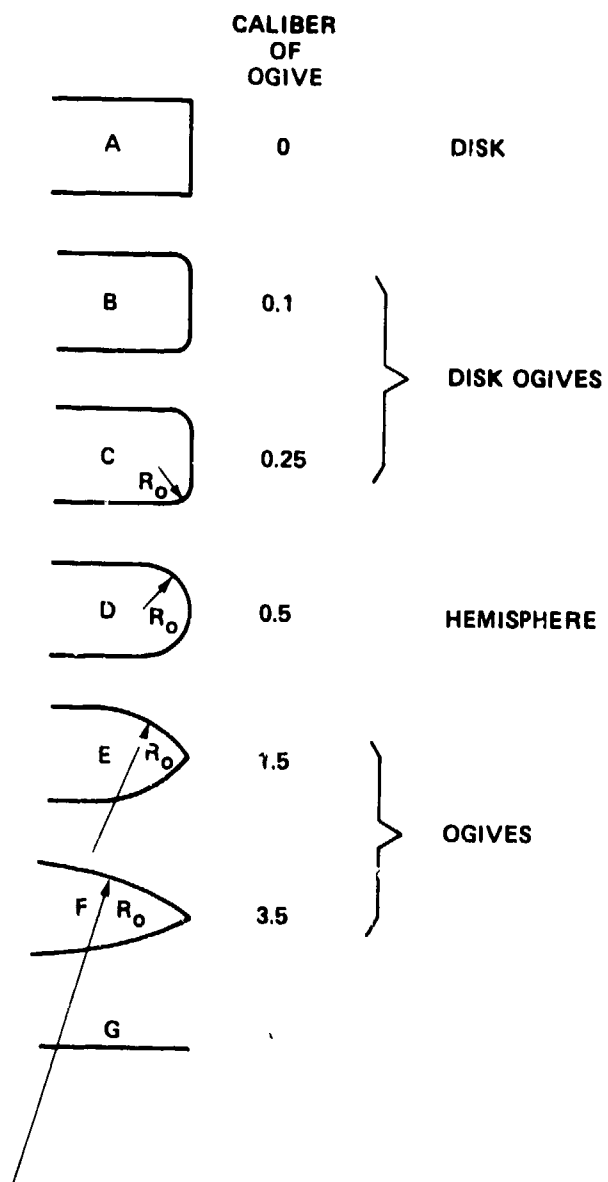
FIG. 4·31 DISK·OGIVE FAMILY
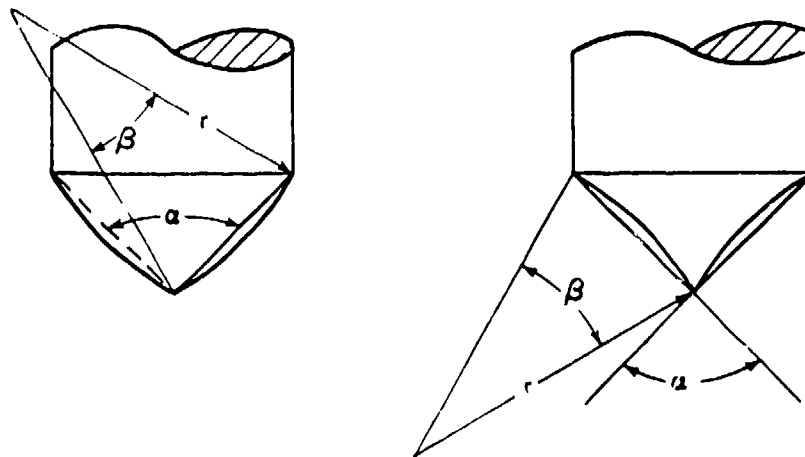
FIG. 4-32 OGIVE GEOMETRY

THE SYMBOLS, WHICH ARE THOSE OF REF (4-25)
ARE USED WITH OTHER MEANINGS
ELSEWHERE IN THIS REPORT
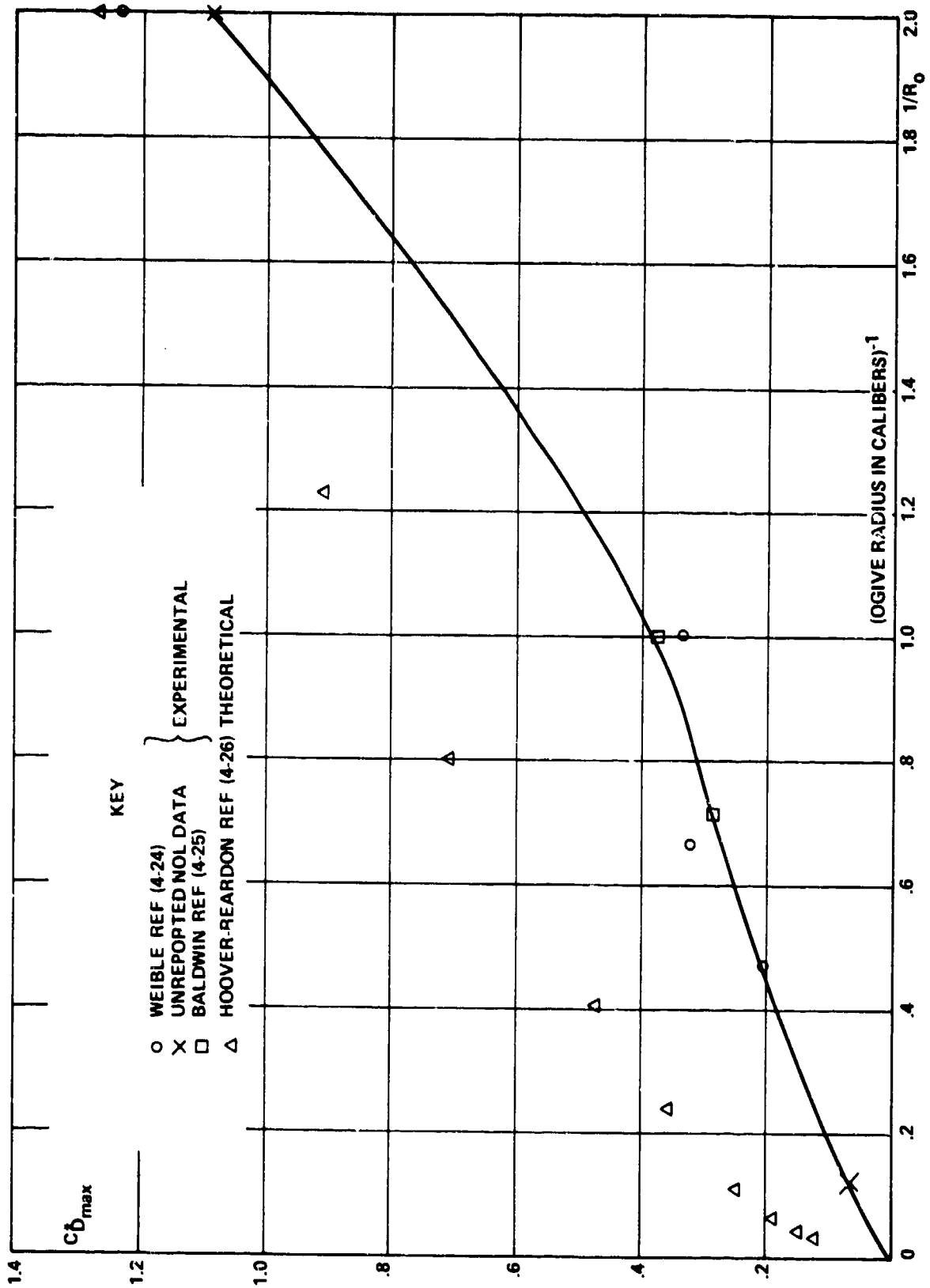
FIG. 4-33 MAXIMUM DRAG COEFFICIENT DURING THE VERTICAL ENTRY OF OGIVES
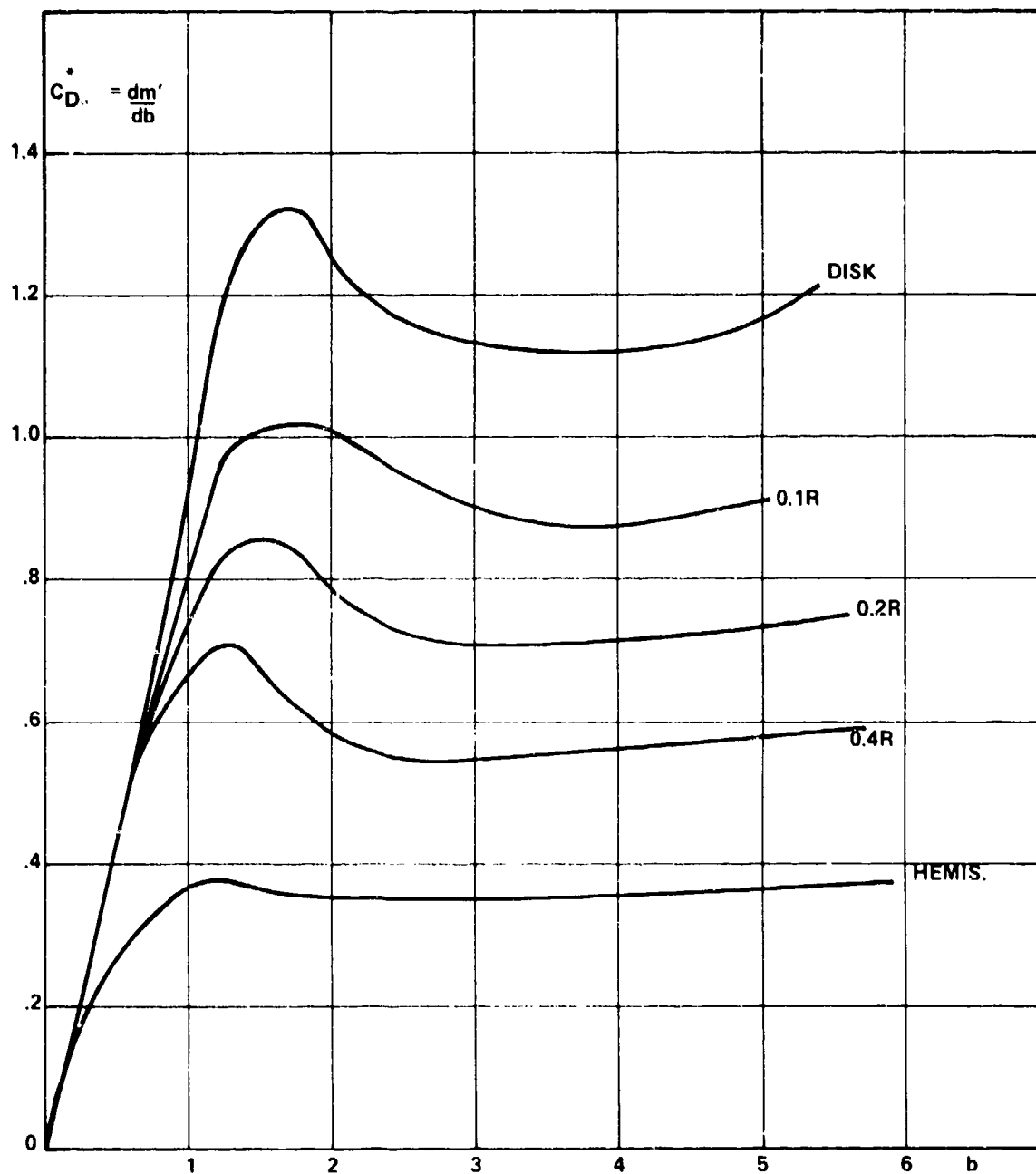
FIG. 4-34 IMPACT DRAG COEFFICIENTS FOR ENTRY OF DISK-OGIVES AT 30°
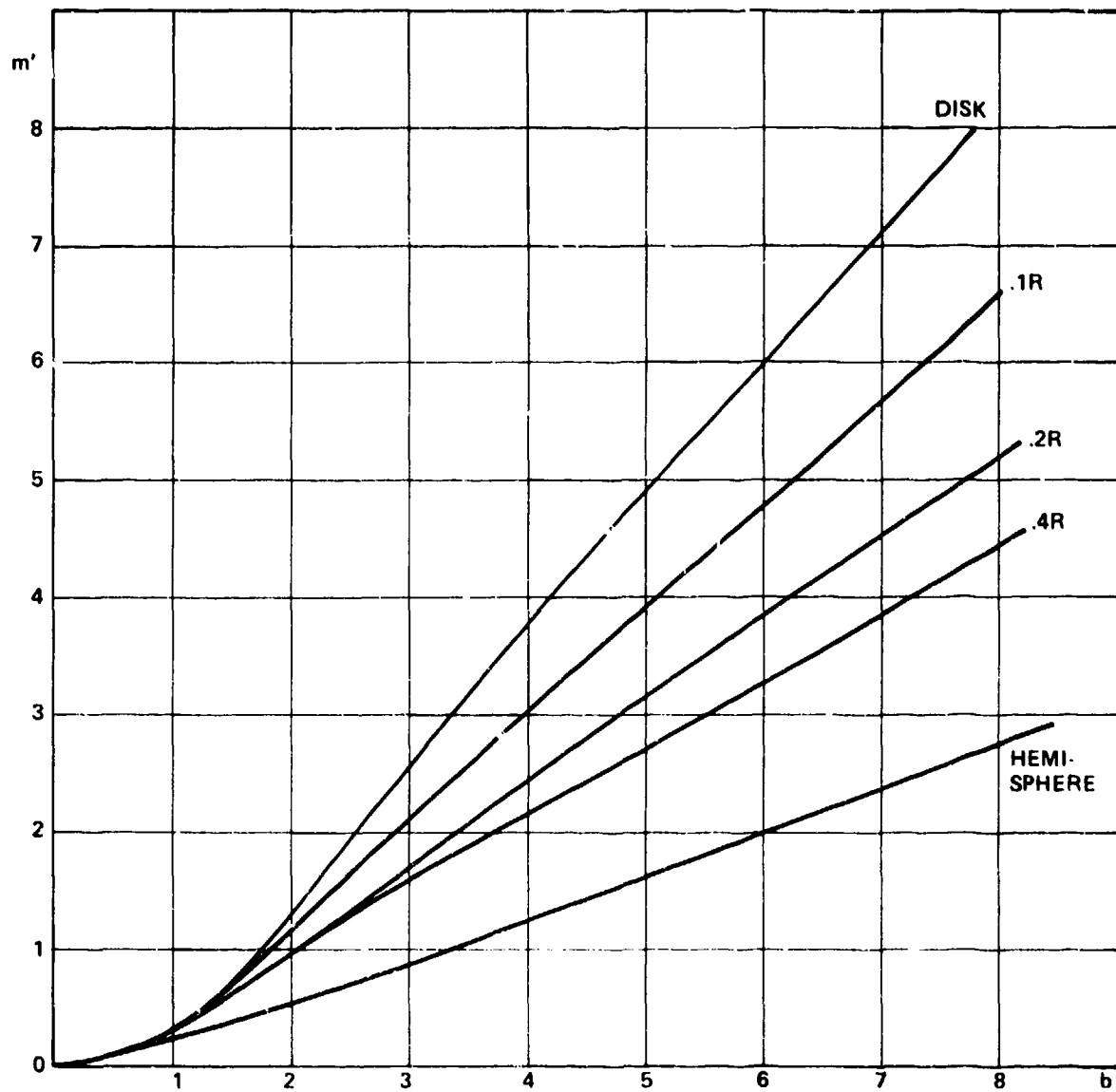
FIG. 4-35 ADDED MASS FOR ENTRY OF DISK OGIVES AT 30° AFTER REF (4-27)
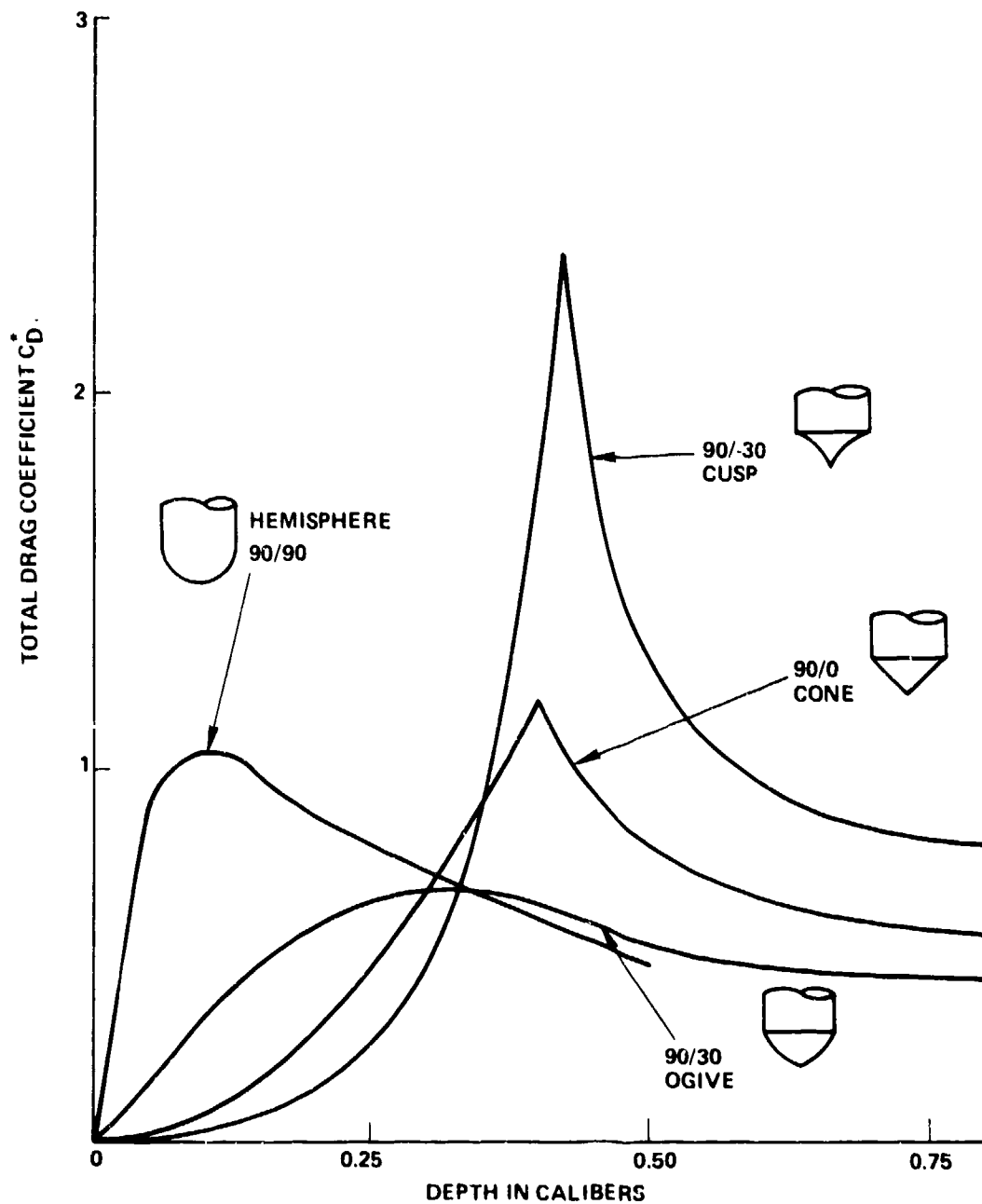
FIG. 4-36 TOTAL DRAG COEFFICIENT VS DEPTH FOR
NOSES OF EQUAL LENGTH AFTER REF (4-25)
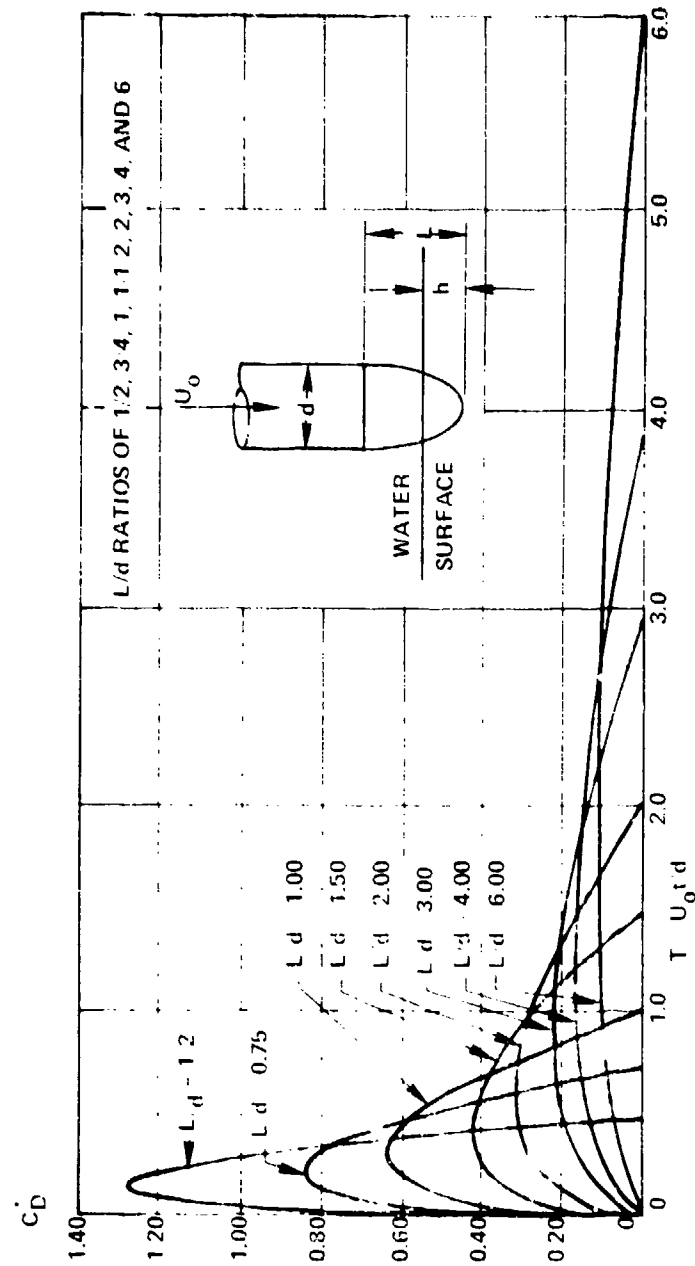
FIG. 4.37 IMPACT DRAG COEFFICIENTS FOR THE VERTICAL WATER-ENTRY
OF MISSILES WITH TANGENT ELLIPSOID NOSES
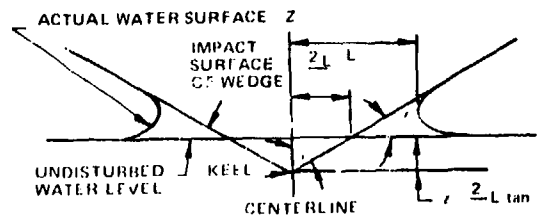
FIG. 4-38 WATER ENTRY OF A WEDGE
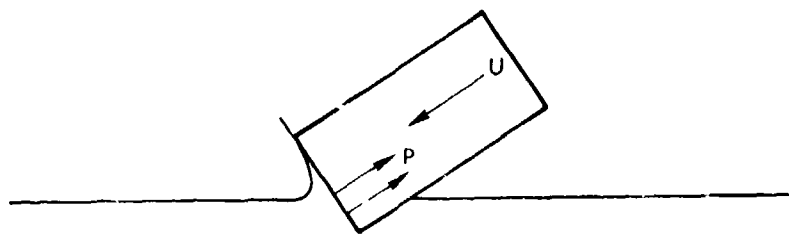
FIG. 4 39 PRESSURE ON A CYLINDER AT WATER ENTRY
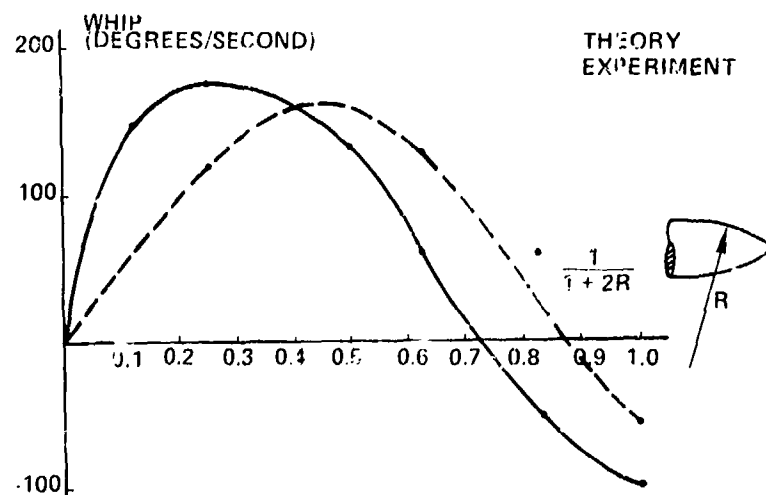
FIG. 4-40 APPLICATION OF BIRKHOFF'S SEMIEMPIRICAL METHOD
TO THE PREDICTION OF "WHIP". FROM REF (4-40)

FIG. 4-41 "UNDERPRESSURE"
CAVITY FROM REF (4-12)
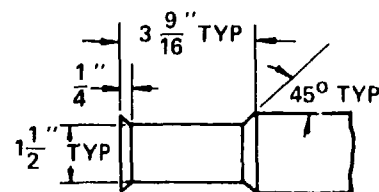
A. FULLY-VENTED DISK
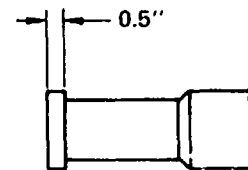
B. DISK 0.5-IN. CYLINDER
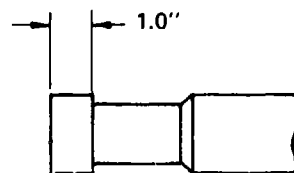
C. DISK 1.0-IN. CYLINDER
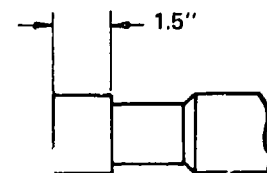
D. DISK 1.5-IN. CYLINDER
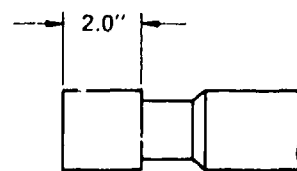
E. DISK 2.0-IN. CYLINDER
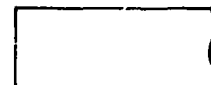
F. UNVENTED DISK CYLINDER

FIG. 4-42 HEAD SHAPES USED IN WATER-ENTRY STUDIES
ON 2-INCH DIAMETER MODELS. (ADAPTED
REF (4-34))
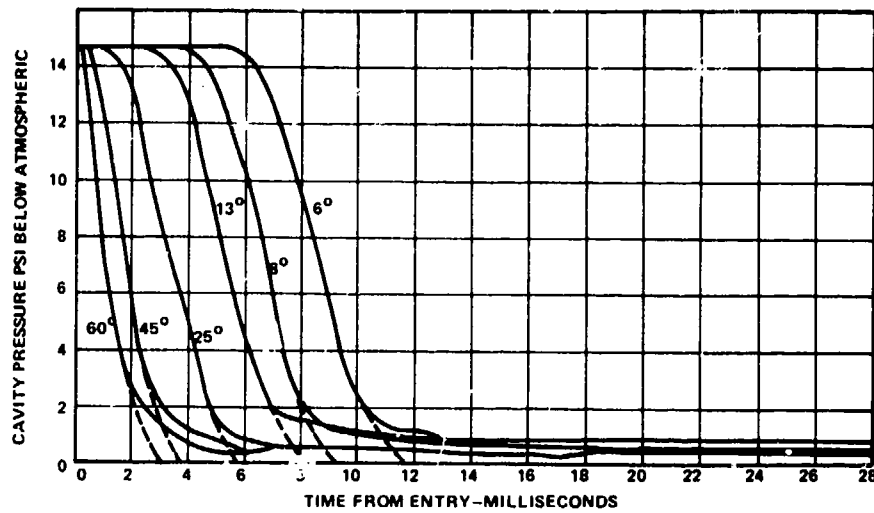
FIG. 4-43 CAVITY PRESSURE-VARIATION WITH ENTRY ANGLE
FROM REF (4-37)
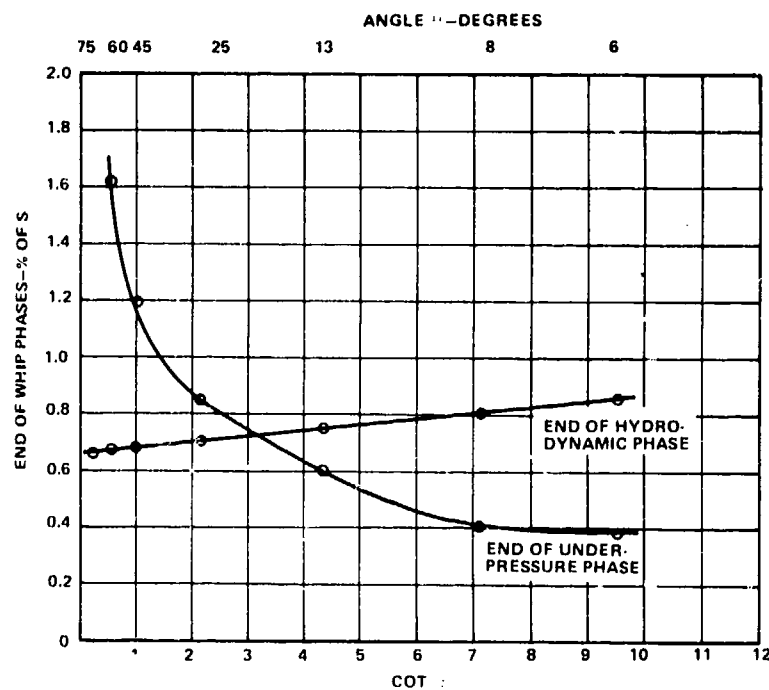
FIG. 4-44 END OF HYDRODYNAMIC & UNDERPRESSURE PHASES—
VARIATION WITH ENTRY ANGLES UNVENTED RIGHT
CYLINDER FROM REF (4-37)

W' · TAN θ

.06

VENTED

UNVENTED

.04

.02

△

0   .25   .50   .7_   1.0   1.25   1.5   1.75

SLEEVE LENGTH IN CALIBERS
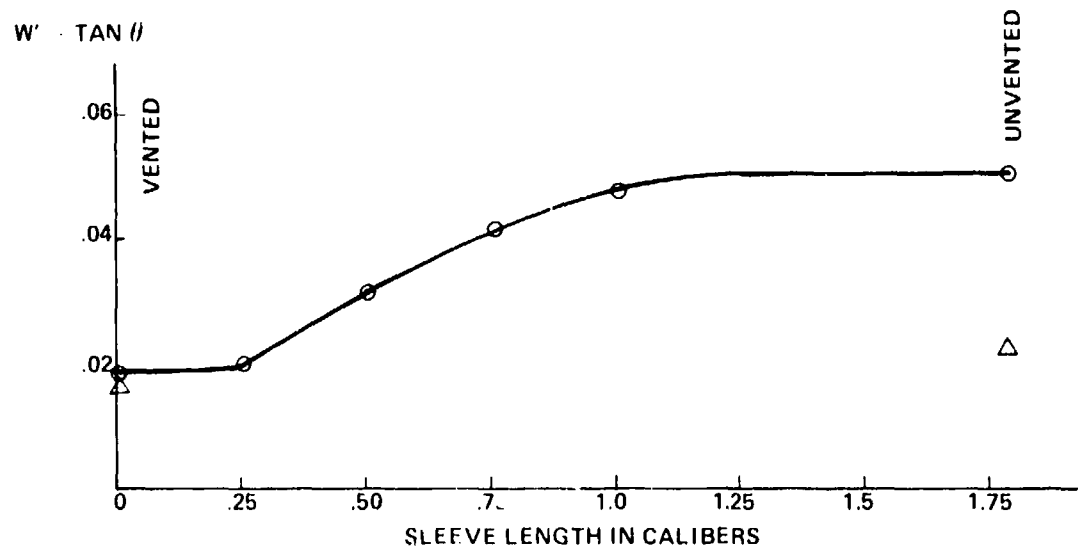
FIG. 4·45 DEPENDENCE OF WHIP ON SLEEVE LENGTH
BASED ON REF (4·34) ○ AND REF (4·45)△

WHIP

·60

·40

UNVENTED

·20

VENTED

0   100   200   300   400 U_o
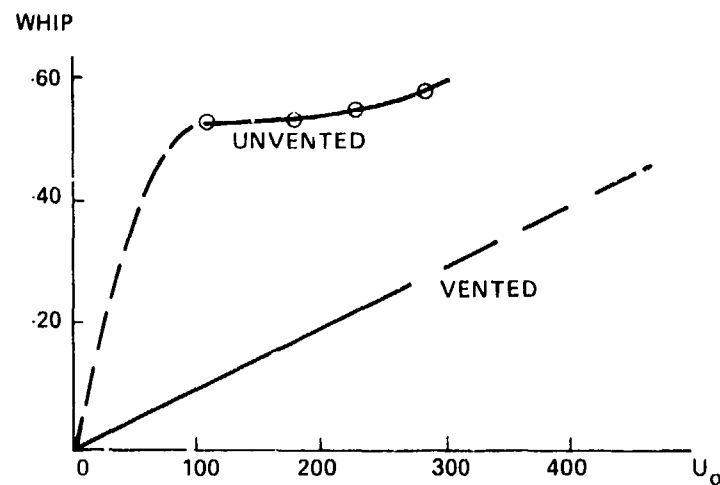
FIG. 4·46 WHIP OF VENTED AND UNVENTED CYLINDERS
ADAPTED FROM REF (4·37)
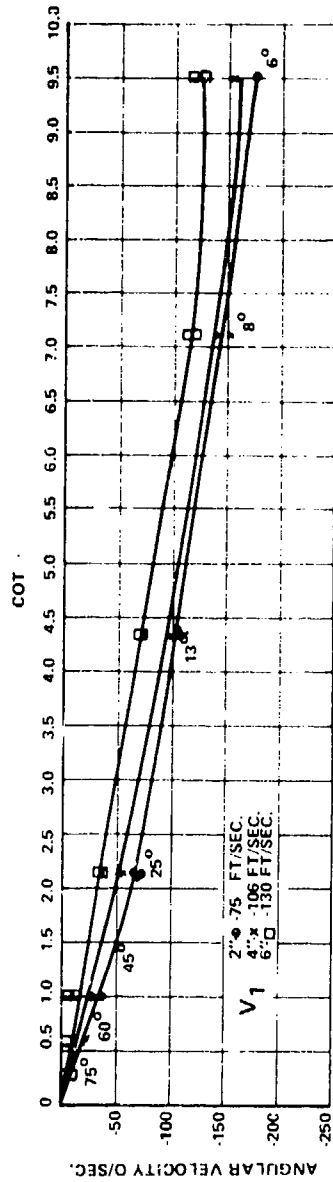
FIG. 4-47 WHIP OF RIGHT CYLINDER; ANGLE SERIES RESULTS
2'', 4'' AND 6'' UNVENTED MODELS FROM REF (4-37)
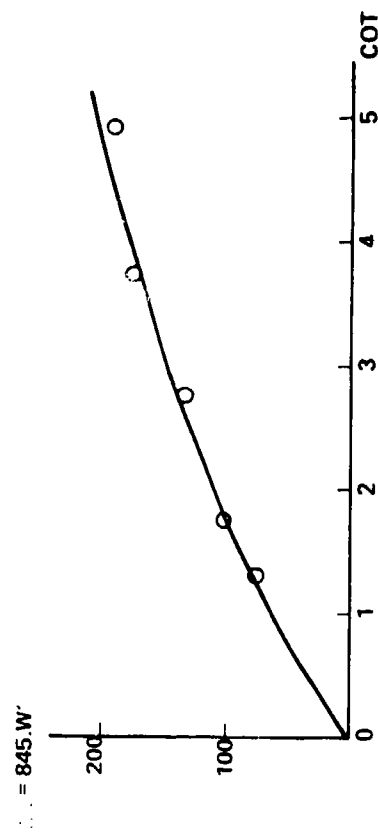
FIG. 4-48 WHIP OF HEMISPHERE CYLINDER DATA FROM REF (4-18)
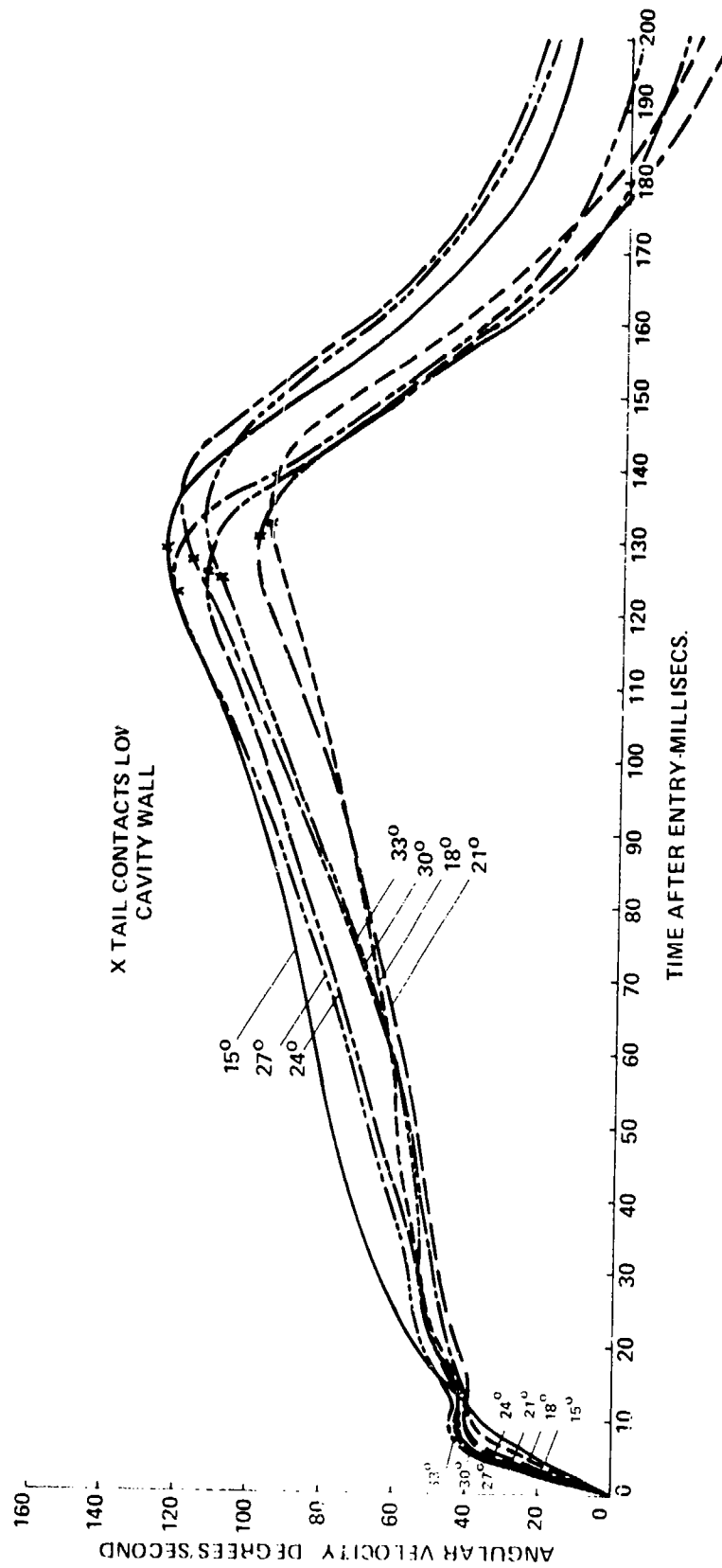
FIG. 4-49 VARIATION OF ANGULAR VELOCITY AT DIFFERENT ENTRY ANGLES HEMISPHERE CYLINDER U_o = 225 FT/SEC. FROM REF (4-19)
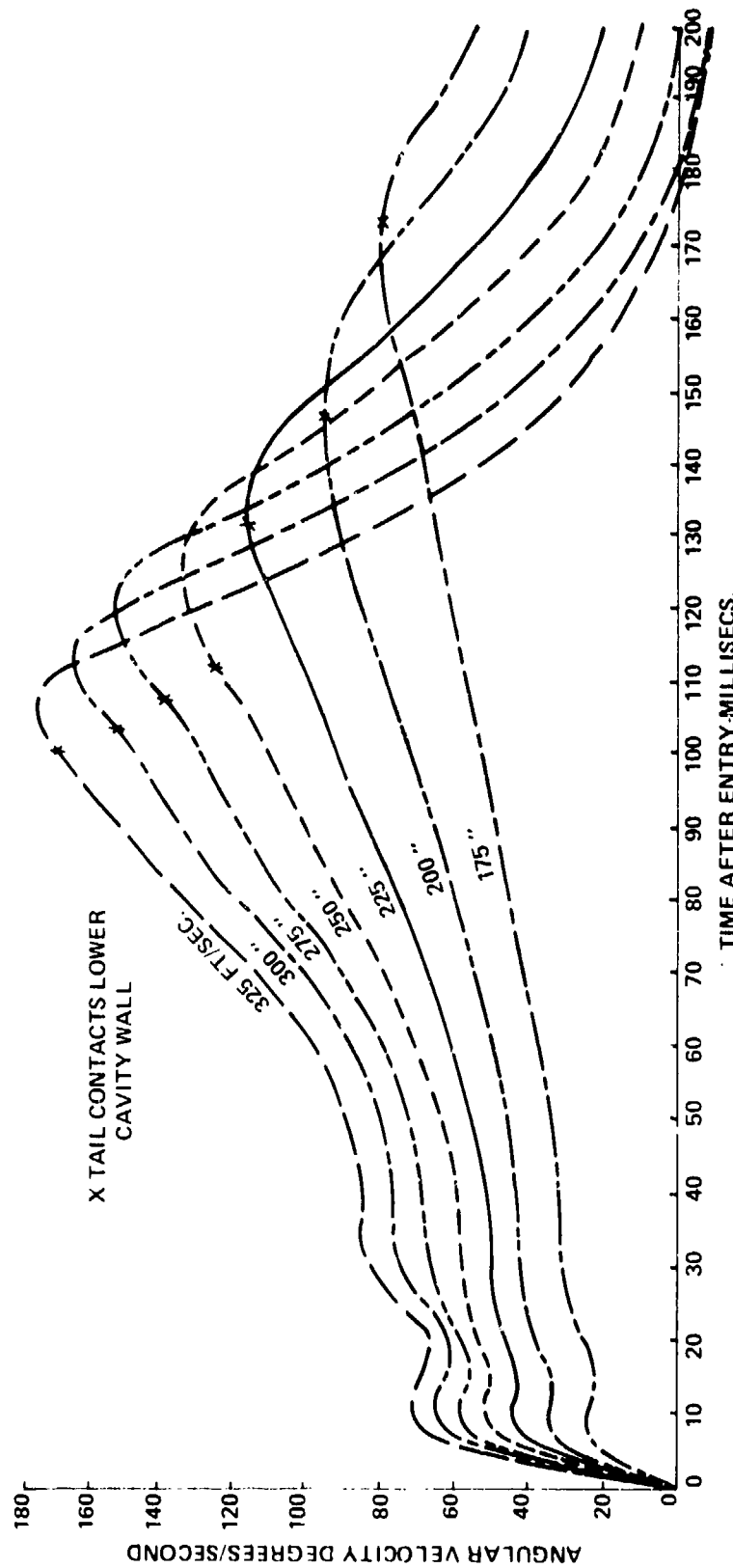
FIG. 4-50 VARIATION OF ANGULAR VELOCITY AFTER ENTRY AT VARIOUS SPEEDS
HEMISPHERE CYLINDER $\theta = 30^o$ PITCH $= 0^o$ FROM REF (4-19)
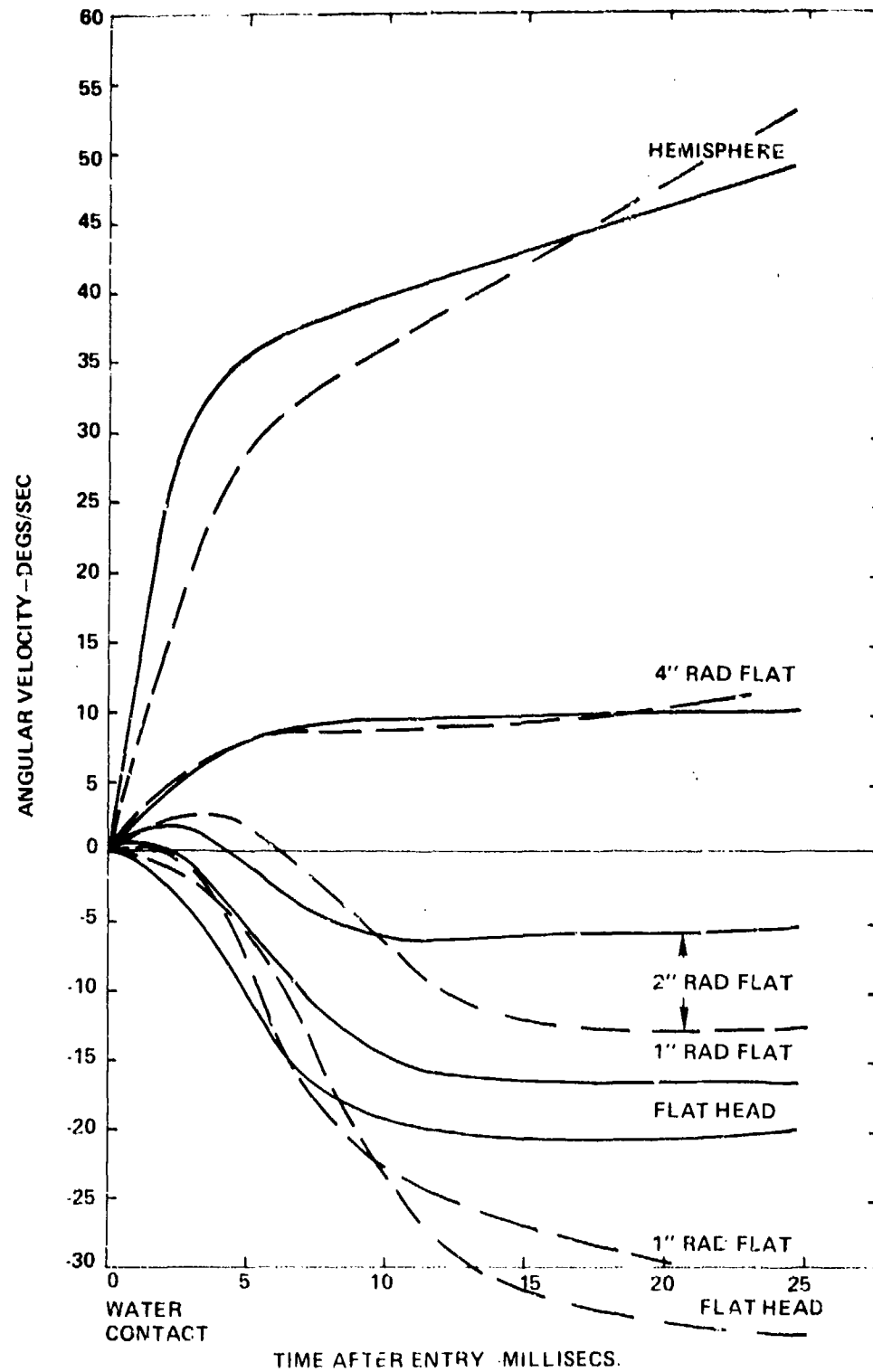
FIG. 4 51 VARIATION OF ANGULAR VELOCITY WITH HEAD RADIUS
U_0 225 FT/SEC θ 30^0 ———— θ · 18^0 — — — —
ADAPTED FROM REF (4 27)
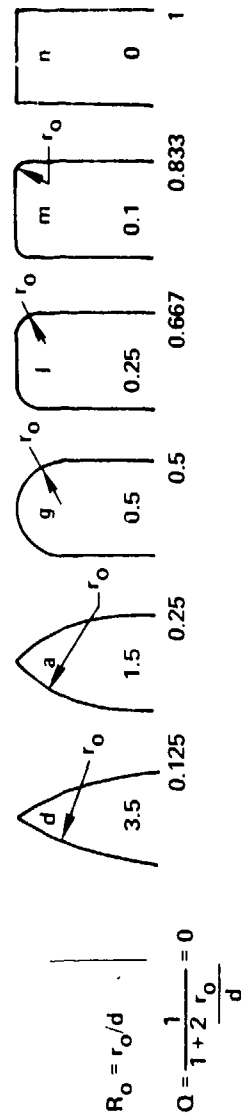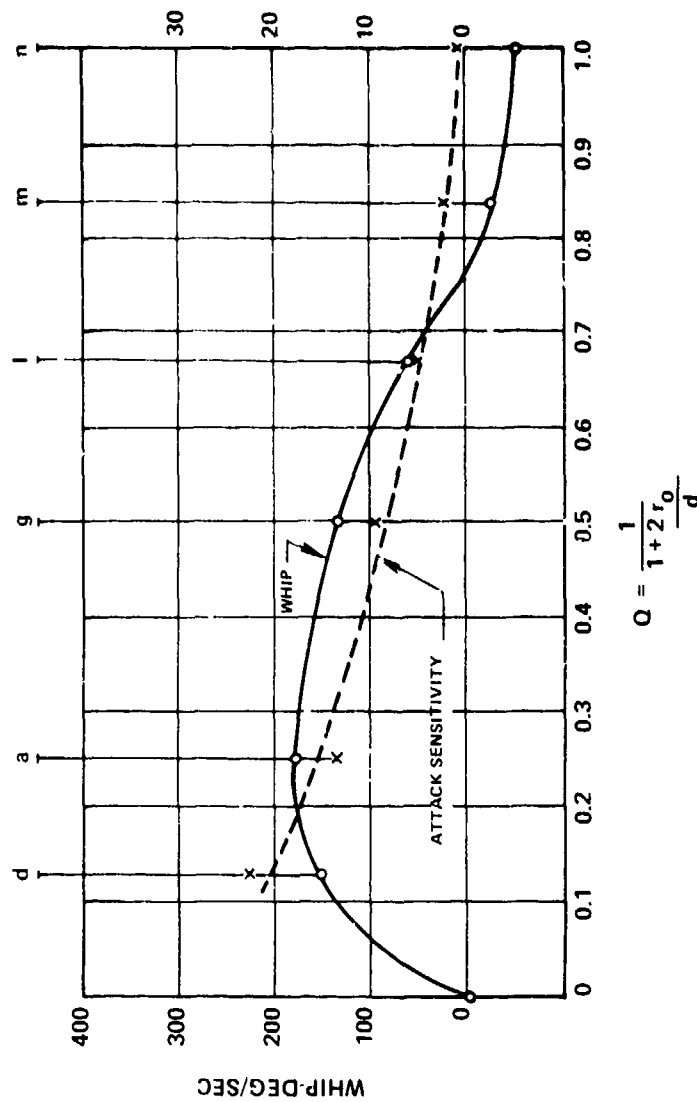
FIG. 4-52 DISK OGIVE WHIP AND ATTACK SENSITIVITY AT
ZERO ANGLE OF ATTACK $U_o = 500$ FT/SEC;
$\theta = 20^\circ$ FROM REF (4-47)
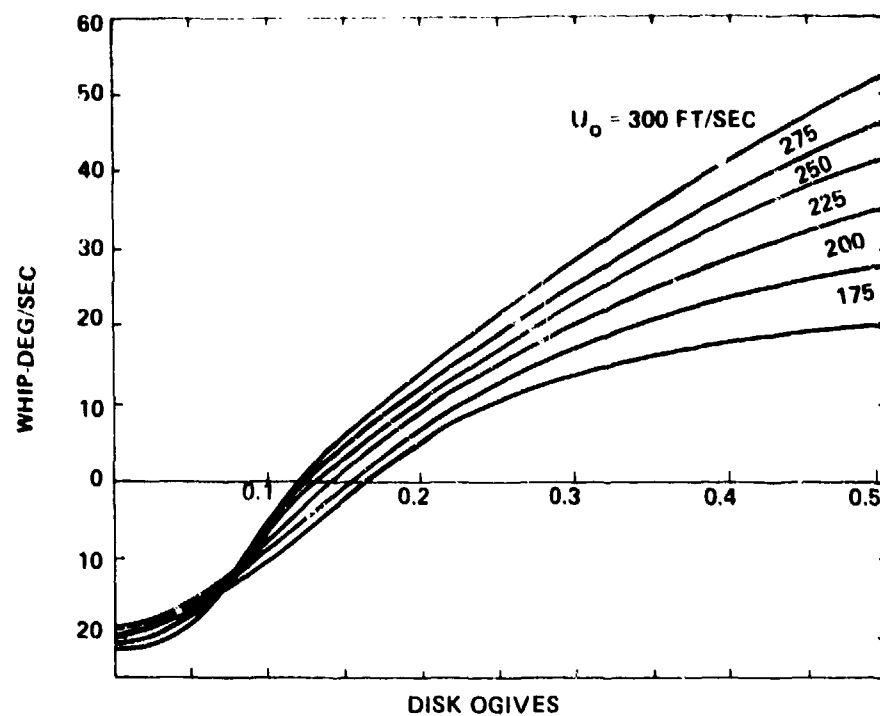
FIG. 4-53 VARIATION OF WHIP WITH ENTRY SPEED FROM REF (4-27)
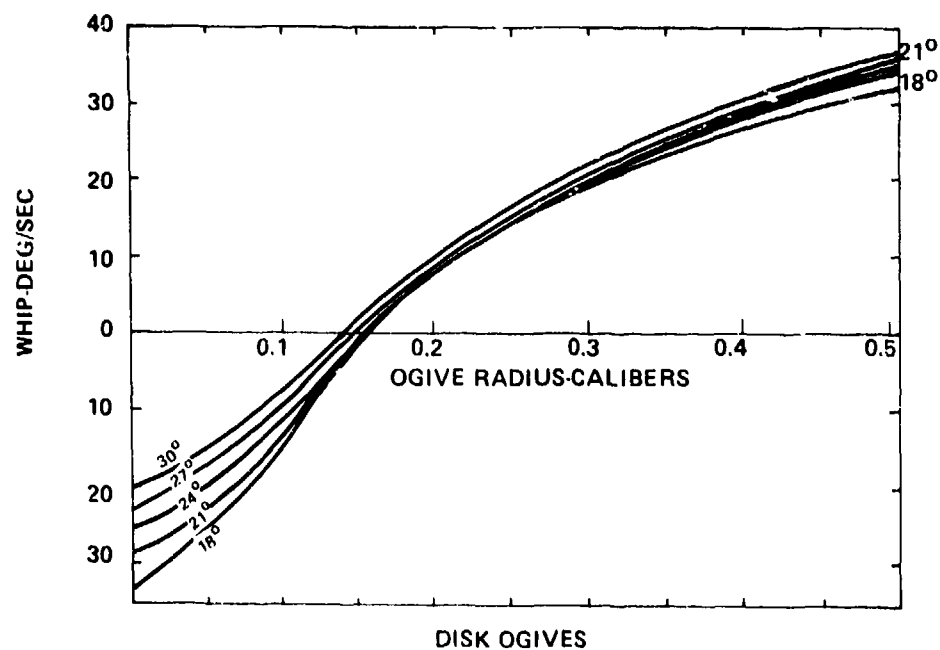
FIG. 4-54 VARIATION OF WHIP WITH ENTRY ANGLE
U_O 225 FT/SEC FROM REF (4-27)
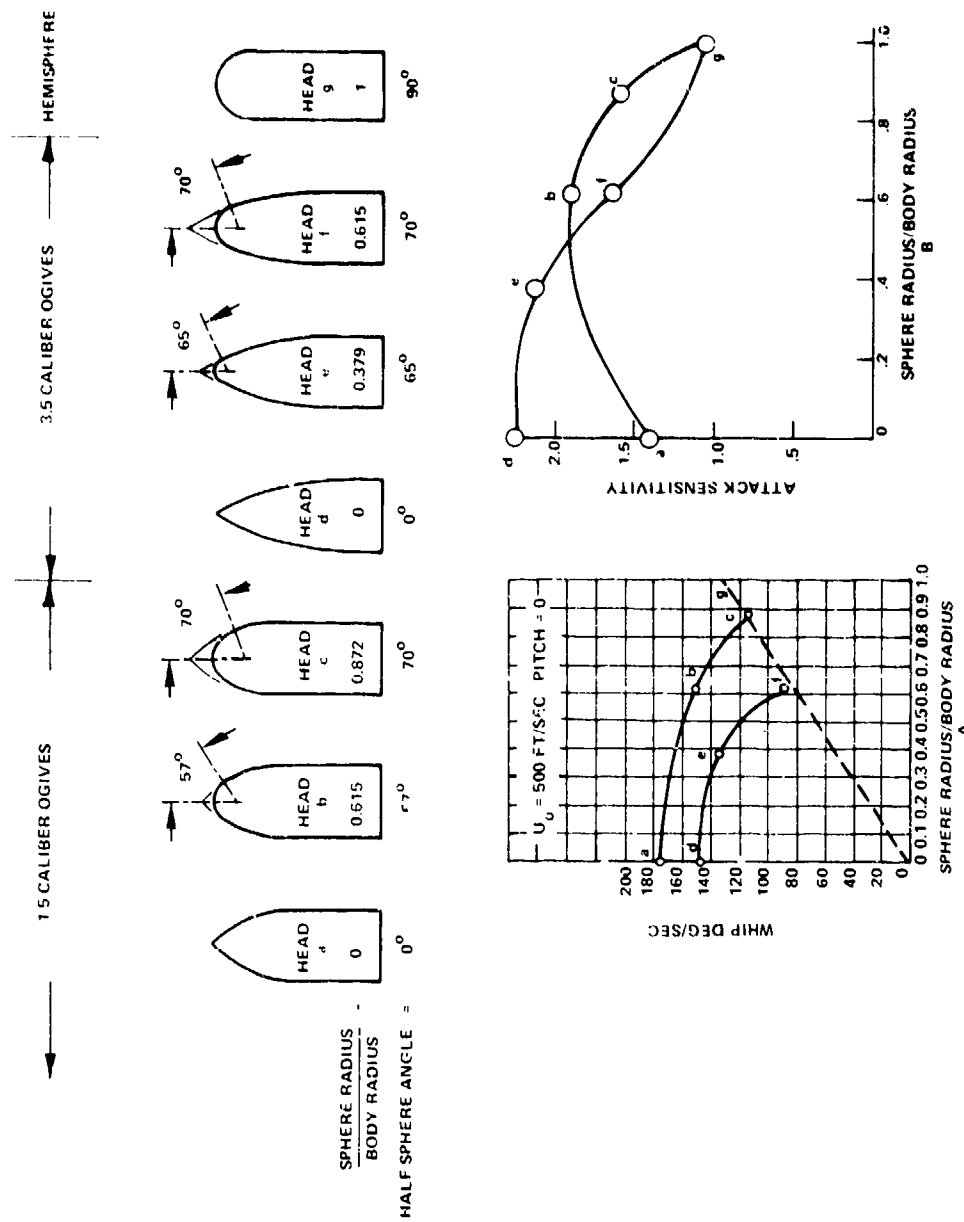
FIG. 4-55 WHIP, PITCH SENSITIVITY, AND DECELERATION AT WATER ENTRY AS FUNCTIONS OF SPHERICAL CAP RADIUS (ADAPTED FROM [36])

Chapter 5

TRAJECTORIES OF MISSILES WHILE CAVITY RUNNING

SYMBOLS

A	maximum cross-sectional area of missile
C_D	drag coefficient $= 2D/\rho U^2 A$
C_D^*	drag coefficient based on water-impact speed $= 2D/\rho U_o^2 A$
C_L	lift coefficient $= 2\Gamma/\rho U^2 A$
C.G.	center of gravity
d	maximum diameter of missile
D	drag force
d_n	diameter of truncation on missile nose
L	length of missile; also, lift force
M	mass of missile; also, hydrodynamic moment
p_a	pressure of air above water
p_c	cavity pressure
p_∞	freestream pressure
Q	correlation parameter for disk ogives $= 1/(1 + 2R_o)$
r_o	ogive radius
r_s	radius of sphere tip of missile nose
R	radius of circular path
R_o	$= r_o/d$, ogive radius in calibers
S	path length
S'	$= S/d$, path length in calibers
t	time after contact with water
t'	$= tU_o/d$, dimensionless time after water contact
U	missile velocity
U'	$= U/U_o$, dimensionless missile velocity
U_1	missile velocity at water entry; also, "first" missile velocity

U_2 missile velocity at water exit; also, "later" missile velocity

U_o missile velocity at water impact

x, y coordinates of cavity outline

α $= \rho C_D A/2M$, retardation coefficient; also, angle of attack in pitch plane

ζ half angle of spherical nose tip

θ_c critical angle for broach or ricochet

θ_1 trajectory angle at water entry, measured from horizontal

θ_2 trajectory angle at water exit, measured from horizontal

ρ mass density of water

σ $= (p_O - p_C)/(1/2)\rho U^2$, cavitation number; also, specific gravity of sphere

ϕ angle of circular path in radians; also, angle of attack in yaw plane

INTRODUCTION

This chapter deals principally with the cavity-running trajectories of inertia-propelled missiles, but after the collapse and disappearance of the cavity, usually these trajectories become those of a fully wetted motion.

The cavity-running condition exists especially after water entry (Ref. (5-1)). Because the water-entry cavity is air-filled, the missile generally travels in full cavity for a considerable time. Later the cavity decreases in size and, when the speed reaches relatively low values, the cavity collapses onto the missile and ultimately disappears. A similar behavior is found when inertia-propelled missiles are launched at high speeds under water, except that the cavity may not contain air and its existence depends principally on missile speed. On the contrary, a rocket-propelled missile may start its travels without a cavity and subsequently be contained in a large cavity created by the increasing speed, and containing the exhausted gases.

The factors which influence the trajectories of missiles while cavity-running and while fully wetted are generally quite different. For cavity running the stability does not depend on the usual hydro-dynamic coefficients but rather on nose moments and on moments of tail forces due to contacts between the tail of the missile and the cavity wall. Missiles which lack stabilizing surfaces may be satisfactorily stable during cavity running but quite unstable when fully wetted.

The different behavior in the two regimes makes it difficult to evaluate tests made on unstable missiles. For example, the plunge bomb (Fig. 5-1A) is designed for short-range attack and is stable only when cavity running, that is, while the cavity persists. If a plunge bomb is found unstable in a test, it may be because of an inherent instability while cavity running, or because the cavity collapsed as a result of too high drag or too low mass or initial speed. In particular, in the evaluation of model tests, trouble may arise because of the use of Froude scaling without cavitation-number scaling. When a trajectory is reported as being "straight" without precise information, one cannot deduce how the behavior would be influenced by change of entry speed, the presence of pitch or pitching at entry, increase of the fineness ratio, L/d, of the missile, and so forth.

Parenthetically it might be mentioned, relative to straightness of trajectory, that all buoyant and nonbuoyant missiles are deflected by gravity and the ultimate part of the trajectory may be expected to be vertically downward (or upward, if the missile is buoyant). As a rule of thumb, it may be said that if gravity would not change a trajectory significantly in air for the same _time_ of flight, it may be neglected for the corresponding trajectory in water.

Before leaving the evaluation of model tests, another difficulty should be mentioned. There is a considerable flexure of torpedo-like missiles when they enter water at a low angle, and results obtained with over-rigid models may be in error. Similar troubles arise when the fins on model and prototype are not equally rugged.

At water impact and for a time thereafter, usually only the nose of the missile is in contact with the water, and the missile is said to be "riding on its nose" (Fig. 5-2A). Almost invariably, however, the afterbody of the missile eventually swings around until the tail strikes the cavity wall (Figs. 5-2B and 5-2C). The force system at impact generates an angular velocity called "whip" (Ref. (5-2)). It is positive or nose-up for slender and streamlined noses. Only for almost totally blunt shapes, such as the disk, is the whip downward. During cavity running the missile continues to rotate about its nose within the cavity. The angular velocity of whip is now augmented by a continuing moment on the nose due to the angle of attack of the missile (Ref. (5-3)). Throughout cavity running this is almost invariably such as to produce instability; the only exception is a weak stability for the disk.

Still another contribution to the angular velocity comes from "underpressure". During water entry there is usually a region below the missile nose in which the pressure is substantially zero (Ref. (5-2)) while above the missile the pressure is that of the atmosphere. The result is a downward force which normally gives a nose-down moment to the missile. A similar moment may arise during cavity running if one side of the nose is wetted and not the other. The result can be a strongly asymmetric force, and instability.

TAIL SLAP AFTER OBLIQUE ENTRY

The first impact of the missile tail on the cavity wall is an event of some importance since it has a considerable influence on the trajectory. How fast it occurs depends on many factors. The general behavior is somewhat as follows for oblique entries.

If a missile with a disk nose (Fig. 5-1B) contacts the water without pitch, it acquires a small negative (nose-downward) whip (Ref. (5-2)), so that the missile tail may be expected to move toward the upper cavity wall (Fig. 5-2C). If the missile is a right-cylinder (Fig. 5-1C), an underpressure may be expected to increase the negative whip and shorten the time to tail slap. A hemispherical nose (Fig. 5-1D) has a moderately large positive whip which will tend to make the tail strike the lower cavity wall (Fig. 5-2B). In this case the under-pressure will give a moment contribution of opposite sign, but probably only large enough to delay the contact. A slender ogive will behave like the hemisphere but the contact will occur sooner. The tail slap can vary greatly in intensity, the higher intensity evidently accompanying a higher angular velocity.

The first tail slap sometimes occurs at the cavity lip, below and behind the missile as in Figure 5-2D. It is at the position of

this lip that the cavity was first generated, and gravity causes the cavity to rise, and the wall to form a cusp and curve inward there (Fig. 5-3). Sometimes the contact at the cavity lip is primarily due to the missile tail traveling downward and sometimes to the splash moving upward. Usually this type of tail slap is of small intensity and importance.

When the tail of the missile strikes the wall, it moves into the wall because of momentum. During this penetration a continuing moment on the nose usually serves to increase the angle of attack but the greater restoring moment resulting from increased tail penetration, tends to reduce the angular velocity to zero. If the impulsive moment on the tail is large enough, the angular velocity decreases to zero and then may grow to an approximately equal maximum value in the opposite sense. It is such behavior that leads to an oscillating motion.

If the tail rebounds from the wall with a small angular velocity, an opposing moment on the nose may reverse the direction of this angular velocity shortly after, or even before, the tail leaves the wall on its first rebound. The missile tail will fall back onto the same wall again, or will not leave the wall but remain buried in it, perhaps after some oscillation, reaching such a depth that the nose and tail moments about the C.G. are equal and opposite.

The failure of the tail to rebound results from damping of the angular velocity, and the continuation of the nose moment. Greater damping may be expected for greater immersion in the wall.

Sometimes at small angles of entry the tail will rebound after striking the upper cavity wall but, because of gravity, cannot rebound from the lower wall. This difference would not occur for steep entry angles.

If the tail moment is insufficient to reduce the angular velocity to zero, the tail continues to penetrate deeper into the wall until broadside results. Often a missile is stable in this broadside mode and travels onward broadside, with large drag and a large cavity.

When the afterbody strikes the cavity wall the missile may be at a small or large angle of attack (Figs. 5-2B and 5-2E). When the angle is large there is usually a large overturning moment on the nose, and a strong curvature of the path results. The angle at wall impact is dependent on:

1. the drag area, $C_D A$, of the nose, where C_D and A are the drag coefficient and cross-sectional area. The cavity width increases with the drag area (Ref. (5-4)) and increased width means larger angle, as in Figure 5-2E.

2. missile length. The longer the missile the smaller the angle.

3. diameter and contour of the afterbody. If the afterbody
is made more slender, the angle will be greater at contact; this is
especially evident when the afterbody is tapered (boat-tailed).

4. shrouds, which effectively increase the afterbody diameter
and decrease the angle at contact. Fins alone do not act in this way.

TYPES OF CAVITY-RUNNING TRAJECTORIES

Nose-Riding Motion

Seldom do missiles, no matter how blunt, "ride on their noses"
(Fig. 5-4A) throughout the trajectory without the tail impacting the
cavity wall. The right cylinder has small whip and a limited
stability when cavity running and may ride on its nose for a
considerable distance. Usually such a blunt body has a rapid
deceleration and short cavity life.

When a missile is riding on its nose, its trajectory is usually
quite straight, and this applies even during the unsteady motion
while the missile is falling toward the cavity wall (Ref. (5-5)).
During this time the tail configuration has no importance.

Oscillatory Motion

If the hydrodynamic moment due to the tail is sufficiently
stabilizing, the missile, after tail-slap, may rebound from the wall.
If it rebounds successively from opposite walls, the missile will
follow a sinuous but almost straight trajectory (Fig. 5-4B).

Circular-Arc Motion

Under most conditions the tail of a missile does not rebound to
the opposite wall after tail slap but remains leaning against, or
partially buried in, the wall which it struck first (Fig. 5-4C). The
lift forces on nose and tail are in the same direction, their moments
about the C.G. are equal and opposite, and a curved trajectory is
produced which is approximately circular.

The greater the lift forces the greater the transverse
acceleration and the smaller the radius of the circular arc. Usually
greater curvature accompanies greater angle of attack.

The nose force on a simple right cylinder is almost completely
along the missile axis. At wall contact in a narrow cavity (Fig. 5-4D)
the angle of attack and the lift force are small, and the moment is
almost zero. Accordingly there is little pressure between the tail
and the wall, and the trajectory is nearly straight even though the
tail leans against the wall as the missile travels.

The circular trajectory does not start at the water surface
but approximately at the point of tail slap (Ref. (5-5)). Hence, the
trajectory appears as an initial straight section blended into a
circular arc (Fig. 5-4E).

The radius, R, of the path may be as short as ten missile lengths for conical and ogival noses, and short projectiles, and as great as 60 lengths for missiles which are less unstable (Ref. (5-6)). For broaching (q.v.), Birkhoff has given the horizontal plow during the circular-arc motion (Fig. 5-4E) as approximately $2R\sin\theta_1$, the maximum depth of submergence as $(1/2)R\sin^2\theta_1$, and the ratio of exit to entrance speed as $U_2/U_1 = R\phi e^{-2\alpha}$. The maximum depth has been given also as approximately $(S/4)\sin\theta_1$ (Ref. (5-7)). (S and ϕ are the length and the angle in radians, of the circular path in water, and $\alpha = \rho C_D A/2M$, with ρ the density of the water, C_D, A, and M the drag coefficient, cross-sectional area, and mass of the missile).

Circular-arc motion is usually undesirable since the path may be far from straight and broaching may result, as described below. It has some potential for underwater attack on surface ships.

Broadsiding Motion

If the moment exerted during tail slap is insufficient to stop the angular motion, the tail penetrates the cavity wall (Fig. 5-4F) and often oscillates about an orientation approximately transverse to the trajectory. This attitude is accompanied by a greatly increased drag. It is usually quite unacceptable, but it has been employed for the rapid deceleration of ordnance to prevent bottom damage and for decrease of dispersion in shallow-water planting.

The broadside mode is stable for many missiles at high speeds. It is especially likely to occur for missiles without stabilizing surfaces, or for bombs whose fins have been stripped or damaged. Typically, broadsiding occurs after 3 to 5 missile lengths of travel (Ref. (5-6)).

Most missiles curve upward at water impact, and when broadsiding occurs the lift force causes a strongly ascending trajectory.

Ricochet

A missile is said to ricochet when it bounces off the water surface without having been completely below water (although any rebound of a sphere is regarded as a ricochet). The skipping stone is the typical example. There is another form called "tail-up ricochet". This occurs especially for very flat entries with negative (nose-down) angle of attack; the tail travels over the nose of the missile, which leaves the water surface. The ricochet of spheres is discussed in a later section.

Broaching

If a missile comes out of the water after entry and complete immersion (Fig. 5-4E), it is said to broach (Ref. (5-6)). Missiles following upward circular-arc trajectories will broach if the speed is adequate to maintain an enveloping cavity during such travel. Both ricochet and broach have been considered as methods for attacking surface ships.

Considerable study of broaching (and ricochet) after circular-arc trajectories, was made in the 1940's and interesting statistics for this condition were given in Reference (5-6). Some of these follow.

The critical angle, θ_c, below which broaching occurs, usually varies between 8 and 25 degrees, but it depends strongly on entry velocity. The critical angle may double (more tendency to broach) for a doubling of entry velocity (say, 100 to 200 ft/sec). Above some speed, the angle no longer increases but reaches a maximum value asymptotically.

The exit angle, θ_2, is greater than the entry angle, θ_1. At shallow angles, θ_2 is often between $2\theta_1$ and $3\theta_1$, but nearer to the critical angle it is rather between θ_1 and $2\theta_1$. As θ_1 approaches θ_c, θ_2 stops increasing and may even decrease. On the average $\theta_2 \approx 2\theta_1$.

The plow, (or plough) (horizontal distance of travel in water) varies from about 15L (missile lengths) down to about 3L. The latter distance might be for $\theta_1 = 4°$, with $\theta_c = 15°$.

The model always turns nearly 45 degrees, and loses at least 25 percent of its speed before broach. The projectile usually emerges with nose vertical or even tilted slightly backwards, and a large nose-forward angular velocity is imparted to the projectile during exit.

The dependence of θ_c on missile speed is easily explained. At low speeds two forces combine to resist the upturning of the trajectory: gravity and the underpressure force. The latter force, arising from a reduced pressure under the entering nose, is present on almost all nose shapes. At high speeds (say 600 to 800 ft/sec) the hydrodynamic force is predominant and causes the missile to follow an arc of relatively small radius.

CAVITY COLLAPSE

If, after water entry, the inertia-propelled missile does not broach, the cavity decreases continually in size until finally it is unable to envelop the missile. When this condition is reached, the rear end of the cavity collapses onto the tail of the missile. The effect of this depends on the nature of the stability. If the missile is without stabilizing surfaces, it will usually become unstable, and broadside. If the missile has stabilizing fins and is stable fully wetted, the collapse of the cavity onto the tail is usually without obvious effect. The collapse does not generally disturb the missile and the fins supply the stabilizing moment provided earlier by the reaction with the cavity wall.

EFFECT OF MISSILE DESIGN ON TRAJECTORY

There are many aspects of missile design that affect the trajectory and behavior of the missile, including nose shape, tail shape, missile length, C.G. location, missile mass, and moment of inertia.

Nose Design

The nose shape influences missile behavior through water-impact drag, whip, cavity-running drag, nose moments while cavity-running, and cavity shape. Force systems at impact and while cavity running have been discussed in other chapters (Refs. (5-2) and (5-3)).

Very roughly, it may be said that the stability is improved by making the nose more blunt, and the drag, by making it more stream-lined. The right cylinder (and the equivalent adequately-truncated nose) and disk ogives with radii less than about one-quarter caliber, have low whip, the highest stability when cavity running, and the greatest drag at impact and while cavity running. Finer noses tend to have large positive (nose up) whip and large upsetting moments when cavity running, but they have smaller drag both at impact and while cavity running.

Noses designed for water entry almost invariably have front surfaces which are completely flat, at least over the central portion. Most often the nose is a truncated ogive or cone, or a disk-ogive with radius of 1/4-caliber or less. The right cylinder has the best stability but the drag is usually excessive, so that the missile travels only a short distance in full cavity.

Because of their large whip and large overturning moment when cavity running, fine noses generally follow circular-arc trajectories. An oscillating motion can be obtained by adding a flared tail or by making the missile quite long. Both of these means (which will be discussed in later paragraphs) will usually result in high drag after the missile becomes fully wetted, and thus the advantage of the fine nose is lessened.

It is shown in another chapter (Ref. (5-4)) that the diameter of the steady cavity is proportional to the square root of the drag area, $C_D A$, and the same relation holds for the forward part of the water-entry cavity. The small diameter for the low-drag missile means that the angle of attack of the missile is small when tail slap occurs. This condition favors an oscillatory motion, but the advantage is often negated by a strong upsetting nose moment.

If a truncated nose is used to provide stability, the diameter of the truncation will generally be made as small as practicable, to minimize the drag. If the nose is adequately truncated, its drag will be that of a disk of the truncation diameter. The drag coefficient of the disk is 0.81 (Ref. (5-3)), so the truncated nose will have $C_D = (d_n/d)^2 0.81$, if d_n is the truncation diameter.

The diameter of the truncation is adequate only if the flow leaves the edge with a clean separation from the rest of the nose. If the flow, under unfavorable conditions, wets part of the nose behind the nose tip, an underpressure generally results, with great instability. The smallest truncation diameter can be used if the portion of the nose aft of the truncation is made quite slender

(a slender cone or ogive, for example) preferably with a sharply reduced diameter just behind the tip. Slender noses tend to displace the C.G. toward the tail, however, and make less room for explosives near the nose of the missile.

Tail Design

The forces arising when a bare, uniform cylindrical afterbody planes on the cavity wall as in Figure 5-5, have been discussed in another chapter (Ref. (5-3)). If the missile is long enough, these forces may be sufficient to make the tail rebound from the cavity wall and to produce an oscillatory motion. If the missile diameter is large, the angle of attack when the tail hits the wall tends to be small and the cylinder offers a large surface to the wall. Both of these conditions increase the probability that the tail will rebound. When fully wetted, the missile with uniform cylindrical afterbody is almost never stable, and its form drag is large because of base pressure. The tapered afterbody shown in Figure 5-6B has a lower form drag when fully wetted, but, without fins and shroud, would provide little moment to aid rebound.

To assure the rebound of the tail, appendages such as fins and shroud, or conical tails (Fig. 5-6C), are generally used when a missile must have a straight trajectory while cavity running. Any of these devices may produce stability and all will increase the fully wetted drag more or less directly with the increase in stability. The shroud is especially effective because it meets the wall before the missile body does.

A cone tail is quite effective in aiding rebound, but it causes considerable increase in drag. If the cone is made too large, the missile has excess activity in the cavity, bouncing back and forth rapidly between the walls, and increasing the cavity-running drag. The cone should be of small angle (say, 15 degrees) and small area.

The recessed flare shown in Figure 5-6D, has two major advantages. Fully wetted it offers less drag then the projecting cone, and it can be launched from a smooth tube without saboting.

Missile Length

Increased length generally improves the stability of cavity-running missiles; the angle of attack and the angular velocity are smaller when the tail hits the cavity wall; and the tail presents a larger area to the wall. These conditions favor a rebound of the tail.

Great length can provide cavity-running stability with a low-drag nose. For example, a missile with a 20-degree half-angle cone nose and a cylindrical afterbody with a fineness ratio of 30 would be stable cavity running because of the small angle and large surface presented at tail slap. However, the cavity is large enough to envelop the missile only at high speeds and the skin-friction drag when the missile is fully wetted, is very high.

Even if the oscillating motion is not attained, the long missile has a circular-arc motion with large radius (absolutely or when measured in model lengths) because of the small missile angle of attack. Conversely, the very short missile gives a trajectory with small radius, and favors broadsiding.

Increased missile length tends to be accompanied by increased mass and moment of inertia, and a displacement of the C.G. away from the nose (but not necessarily as a percentage of missile length). These influences will be discussed in other paragraphs.

Moment of Inertia

Large transverse moment of inertia is generally desirable in a missile at water entry, principally because it prevents appreciable rotation while the missile is subjected to large moments at impact. An important example is the entry at almost grazing angles, where the nose meets resistance but the tail can turn freely about the nose. The missile tends to stand on its nose and ricochet. A large moment of inertia resists rotation during the early entry moments, and the angle of attack is still moderate when the unbalance of forces on the nose has lessened.

Mass

The mass of the missile is principally of importance in its effect on the maintenance of missile speed and therefore of cavity-generating power. The rapid deceleration of light missiles results in an early approach of the partial cavity phase with wetted tail. The wetting may cause an unstable missile to lose its cavity-running stability, or allow the tail surfaces to create stability during cavity disappearance.

Center-of-Gravity Location

For cavity-running, as for fully-wetted behavior, it is usually advantageous to have the C.G. as far forward as practicable, since this tends to decrease the overturning nose moment and to increase the moment of the tail forces. Thus, the tail is more likely to rebound from the cavity wall and produce an oscillating motion. If a circular-arc motion is established, the curvature will be less for forward C.G., because of small wall penetration and smaller angle of attack. A broadside motion may occur if the C.G. is too far aft.

As the tail sinks to greater depth in the wall in attempting to produce a greater restoring moment, the center of pressure of the lift force on the tail moves forward (Ref. (5-3)), and this increases the probability of instability due to an aft position of the C.G.

Axial Spin

Spin of the missile about its axis is introduced here among design criteria since it necessarily must be considered in missile

design, if at all. For fully wetted motion through water it is well known that missiles cannot he stabilized by spin as they can in air because the greater density of water makes the hydrodynamic forces more than 800 times those in air. On the other hand, slow spin, usually produced by a canting of the fins, is effective in reducing the scatter due to missile asymmetries.

Better behavior as the result of missile spin has been reported (Refs. (5-6) and (5-8)) principally in the prevention of ricochet and broaching. The improvement is caused by the gyroscopic resistance to rotation about the axis of the applied torque. The spin axis of the projectile tends toward the applied-torque axis. A nose-up moment causes the usual spinning shell to turn slightly toward the right, but not to nose-up further and thus leading to broaching. When the tail of a spinning shell hits the cavity wall, it tends to follow around the wall instead of bouncing away. The resulting helical motion has been reported to increase the dispersion (Ref. (5-8)).

DEPENDENCE OF TRAJECTORY ON WATER-ENTRY CONDITIONS

The trajectory of a missile after water entry depends not only on the design of the missile, as has been described, but also on the experimental conditions of the entry. These conditions include:

1. entry angle,

2. entry velocity,

3. angle of attack at water impact, including both pitch (in the vertical plane), and yaw (transverse to this plane),

4. pitch velocity and yaw velocity, that is, the angular velocities about the transverse axes,

5. pressure and density of the atmosphere above the water. This atmosphere is substantially fixed for prototype use, but not in the laboratory. The density and other properties of the liquid might also be treated. The use of liquids other than water is quite unusual and will not be discussed here.

Only general aspects of the influence of the experimental parameters will be outlined in this introduction. Specific applications will be described in connection with the various nose shapes.

Entry Angle

Whip and underpressure are of great importance in determining the trajectory of a missile after water entry, and both have their strongest effect when the entry is at a relatively small angle to the horizontal.

At grazing incidence, noses such as the sphere (Fig. 5-7A) experience an early force which is principally vertical. Hence, there is little retardation of the missile, but a large lift force tends to cause ricochet. If the overall configuration is a cylinder with hemispherical nose, the missile may experience a large whip, and tumbling may occur. In Figure 5-7B, it will be seen that the cone experiences a similar force if the entry angle is less than the half angle of the cone. For the ogive (Fig. 5-7C) the side force is present when the entry angle is less than half the angle at the ogive tip, but the effect becomes small when this angle is approached.

The behavior of the missiles sketched in Figure 5-7 depends greatly on the transverse moment of inertia. If this is small, the whip will be very large and the missile may ricochet. A long missile with large moment of inertia acquires only a small whip and turns through a small angle before the strongly asymmetric force on the nose is relieved.

In general, if the moment of inertia is not large, ricochet is probable for grazing entries except for right cylinders or adequately truncated noses.

As the entry angle increases, the chance of ricochet becomes smaller but a broach may still occur. If the trajectory is a nose-up circular-arc trajectory the missile will leave the water if the missile retains sufficient velocity for cavity generation until water exit.

At steep entry broach is improbable if the missile has stability when fully wetted. On the other hand, an unstable nose such as a slender cone or ogive on a short cylindrical body without fins, may broach with high exit velocity, when fired into the water vertically.

Entry Velocity

High entry speed is most likely to affect the trajectory because of missile damage; nose or fin deformation results in asymmetric forces, and fin-stripping causes later instability. As for direct influence, high speed tends to simplify the trajectory problem by lessening the importance of gravity and underpressure forces. These, however, are downward forces, and their ineffectiveness at high speeds makes the missile more likely to veer upward and to broach. This effect is aggravated by the fact that at high speeds the cavity generation continues for a longer time, and frequently until the circular-arc trajectory has carried the missile out of the water.

At entry velocities high enough that gravity and underpressure are unimportant, whip is proportional to the velocity, but the angle through which the missile rotates while it is becoming submerged, is independent of the speed. The shape of the front part of the cavity which surrounds the missile, is almost independent of speed when the cavity is well developed, that is, if the cavity does not close too

near the missile tail. Hence, at various speeds the tail will strike
the wall at roughly the same position and while at the same angle
of attack. Both the angular velocity at tail slap and the planing
speed of the tail at that time are proportional to the missile entry
speed, so that the hydrodynamic forces will increase as the square
of the speed.

Pitch and Yaw

Pitch, or angle of attack in the vertical plane, may have a
large influence on the trajectory. Since the forces on most nose
shapes are destabilizing during cavity running, the presence of
positive or negative pitch tends to curve the trajectory up or down,
respectively. There is usually a critical angle of attack, a value
of pitch for which the missile, at least initially, tends to follow
a trajectory curving neither up nor down. The behavior when an
initial angle is present in the yaw plane is similar to that described
for the pitch plane, except that at zero yaw angle the missile does
not tend to swerve. A prolate nose generally swerves in the direction
of the pitch or yaw, and the flat nose, in the opposite direction.

Pitch and Yaw Velocities

Pitch and yaw velocities at water impact (that is, angular
velocities of pitch and yaw) have little direct influence on the
forces and moments acting on a missile. For example, the fact that
a missile has a pitch velocity at impact does not change the whip
appreciably, but the angular velocity attained will equal the whip
plus the initial pitch velocity.

Atmosphere Above the Water, and Missile Size

In the service use of ordnance no changes can be made in the
pressure and density of the atmosphere, but for laboratory testing
there is importance which requires discussion.

It has been shown in another chapter (Ref. (5-2)) that the downward
moment due to underpressure is proportionately stronger for small
missiles than for large ones. In particular, if model and prototype
are compared at the same Froude number, the angle they will turn
through due to underpressure alone is proportional to p_a/d, the
pressure of the atmosphere divided by the missile linear scale. The
technique of testing small models with the atmosphere reduced in
pressure by the scale factor, is well known (Ref. (5-9)). The purpose,
of course, is to produce the same trajectory for model and prototype.
In using this reduced pressure technique it is important, in general,
that the atmospheric density be the same for model and prototype
(although this may not be required in some cases of oblique water
entry where the cavity surface closure is very slow (Ref. (5-10)).

Evidently, if air is used above the water, the pressure cannot
be reduced without reducing the density also, and heavy gases are
required for this scaling (Ref. (5-9)).

If the gas density is reduced, the time of surface closure is delayed and the cavity grows to a larger size (Ref. (5-1)). This has small effect on the early trajectory, but is important because it results in a cavity which persists longer before collapsing onto the missile.

The designer of missiles must consider the possibility of variation of behavior with missile size because of underpressure. This effect should vanish at high speeds where underpressure becomes unimportant.

Underpressure can be prevented by venting (Ref. (5-5)), that is, by providing a path for air to flow from above the missile into the region below it, where underpressure would exist. An adequately vented missile should suffer no changes of trajectory due to underpressure effects.

THE DRAG EQUATION

In addition to the trajectory or path of a missile in its travels after water entry, it is important to consider its speed along this path. For the momentum-propelled missile the speed continually decreases in a fairly steady fashion. During the earlier part of the trajectory, at least while the missile is cavity running in an open cavity, the drag coefficient does not change greatly.

The drag force can be written

$$D = -M dU/dt = M\alpha U^2 = (1/2)\rho U^2 C_D A \qquad (5-1)$$

The quantity

$$\alpha = \rho C_D A/2M \qquad (5-2)$$

is known as the retardation coefficient.

If the variation of C_D and the presence of other forces can be neglected, solutions of equation (5-1) can be written

$$\alpha S = \ln(U_o \alpha t + 1), \text{ and} \qquad (5-3)$$

$$U = U_o e^{-\alpha S}, \text{ or} \qquad (5-4)$$

$$1/U = 1/U_o + \alpha t, \qquad (5-5)$$

where S and t are distance traveled and time measured from water impact; and U_o is the velocity at impact.

The quantities U, α, S and t can be nondimensionalized, using U_o and d, the maximum diameter of the missile (Ref. (5-10));

$$U' = U/U_o \qquad \alpha' = \alpha d; \qquad S' = S/d; \qquad t' = tU_o/d, \qquad (5-6)$$

and equations (5-3), (5-4), and (5-5) become

$$1/U´ = 1 + α´t´ = e^{α´S´} \qquad (5-7)$$

The three equations (5-7) are "universal equations" (Ref. (5-10)) in the sense that each can be represented by a single graph of U´ versus α´S´, U´ versus α´t´, or α´S´ versus α´t´. These equations do not hold when C_D changes appreciably or when other forces, such as gravity, become significant.

After water entry, as the velocity along the trajectory varies with the drag force, the cavity development can be divided into several phases: impact, open-cavity, closed cavity, travel with a collapsing cavity, and fully wetted.

During the impact phase, C_D varies strongly with time and with nose shape and angle of entry as is discussed in another chapter (Ref. (5-2)). For vertical entry the average C_D following first water contact is greater than the steady cavity-running drag because of the force needed to accelerate the added mass of water. The change of missile speed during the entry is significant, however, only for light missiles, and it can be estimated by reference to the graphs in Reference (5-2). For entry at low angles the average C_D after entry is less than the steady value because, for a time, the missile nose is only partially immersed.

During the open-cavity phase, that is, while the cavity is open to the atmosphere, the drag can usually be based on the assumption that the cavitation number (Ref. (5-4))

$$σ = (p_a - p_c)/(1/2)ρU^2 \qquad (5-8)$$

is equal to zero. In equation (5-8) p_a and p_c are the pressure of the atmosphere above the water and the pressure in the water-entry cavity. If U is very large, σ is small, and if U is small p_c is very nearly equal to p_a during the open-cavity phase, so that σ is again small.

After surface closure of the water-entry cavity, p_c normally drops as the cavity expands, thus increasing the values of σ and of C_D. Quantitative data for this phase are not available (Refs. (5-10) and (5-11)). Even less is known about the drag coefficient while the cavity is collapsing on the missile, but some approximation might be attempted if the size of the cavity were known (Ref. (5-10)).

If equation (5-4) is written in the form

$$U_1/U_2 = e^{αS},$$

it will be seen that for any fixed drag coefficient (or α) travel over any given distance S, causes the velocity to drop by a fixed ratio U_1/U_2. For example, the distance in which the speed drops to half of its initial value is

$$U_1/U_2 = 2 = e^{\alpha S},$$

so that $S = 0.69/\alpha$. After each distance of this magnitude the speed will have dropped by another factor $1/2$, provided that changes in the drag coefficient may be ignored.

TRAJECTORIES FOR VARIOUS NOSE SHAPES

The Right Cylinder

Much can be learned about the early behavior of a right cylinder after water entry, from a detailed study due to Norman and his associates (Ref. (5-12)). Figure 5-8 shows a family of angular-velocity graphs for a right cylinder after water entry at angles between 15 and 33 degrees to the horizontal. The missile was torpedo-like with a diameter of 20 inches and a length of 148 inches, and the boat-tail on the aft end was provided with fins and shroud. Since the study extended only slightly past the time of first tail slap, the makeup of the tail seems unimportant.

During the first two calibers or so of entry, a negative angular velocity (whip) was acquired which was greater (but attained more slowly) for the flatter entries. The whip produced a negative angle of attack and, because the disk is weakly stable, the angular velocity subsequently decreased. For the 15-degree entry the negative angular velocity did not decrease appreciably, and it remained negative. For the 33-degree entry the negative angular velocity decreased so strongly that it became positive after 16 feet of travel. At about 27 feet for the 15-degree entry and 34 feet for 33 degrees, the missile tail struck the cavity wall, with a change of angular velocity. It should be noted that, under the conditions of the test, even when the angular velocity was continually negative, the tail of the missile always struck the bottom of the cavity so that the angular velocity became more negative. It struck the bottom because the impact between the tail of the missile and the cavity was not due primarily to the motion of the missile, but to the collapse of the cavity upward onto the missile. It appears probable that the influence of the collapsing cavity on the missile is usually not as significant as that seen in the figure but that this rather large influence is due to the asymmetrical conditions accompanying the shallow entries.

The tail contact is due in this case to cavity collapse because the rapid deceleration of the missile makes it unable to throw a wide cavity. The missile was light (slightly buoyant) and with its high-drag nose its velocity had dropped to about one-fourth of the entry speed when the tail contact occurred. As is shown in Figure 5-9B, the missile had a negative pitch at all speeds and would have tended to strike the top of the cavity if the cavity were straight and noncollapsing.

For 30-degree entry the angle of the missile changed very little (Fig. 5-9A). It did not rotate in space, but the trajectory turned about 30 degrees (Fig. 5-9C) so that the travel then was almost horizontal and the pitch angle (Fig. 5-9B) was about -30 degrees. Nevertheless, the cavity collapsed upward onto the missile tail.

Figure 5-10 gives the effect of changing the entry speed for 30-degree entries. A comparison of Figures 5-8 and 5-10 shows that qualitatively the trajectory varied in the same manner with speed as with angle, with the maximum negative angular velocity at the lowest speed. Figure 5-10 shows that contact of the missile tail with the cavity wall occurred after about 32 feet of travel for the 175 ft/sec entry, and at about 36 feet for 300 ft/sec. Since this contact is primarily due to cavity collapse, the slight variation resulted from greater cavity persistence at the higher speeds.

It is shown in Figure 5-11 that the presence of a pitch angle at water impact of a right cylinder, produces an angular velocity which is inversely related to the entry pitch. In spite of these angular velocities, Figures 5-12A and 5-12B show that the missile's angle in space and its pitch were not greatly affected for some two missile lengths of travel. Figure 5-12C shows that the trajectory angle or direction of travel varied inversely with the entry pitch but the effect was large only for negative angles of pitch. For a pitch of -4 degrees at 30-degree entry, the trajectory is horizontal 36 feet after entry.

In Figure 5-11 both entries with positive pitch showed an impact with the cusp at the cavity entrance and a subsequent increase of negative angular velocity. The entry with +4-degree pitch was given sufficient negative angular velocity to make the tail hit the upper cavity wall, with the change of pitch angle seen in Figures 5-11 and 5-12B.

For the flat-nosed missile that has just been discussed, a continuing well-behaved trajectory might be expected if the missile is stable fully wetted; but if it is completely unstable, it would start to broadside at the end point of the trajectories discussed.

Numerous tests have been reported on the trajectory after water entry of the plunge bomb (Fig. 5-1A) (Refs. (5-13), (5-14) and (5-15)). Because of the complete instability of these rounds when fully wetted, it is difficult to evaluate the tests and to determine whether, in general, instabilities are due to the behavior cavity running, or to the absence of a cavity.

Curved Noses

Although trajectories have been reported for many missile configurations, it is difficult to draw general conclusions from them. Comparisons are available from tests carried out by the Naval Ordnance Test Station at Morris Dam on a full-sized mock-up of a torpedo

provided with 14 different nose shapes (Ref. (5-16)). Trajectories
from these tests are plotted in Figure 5-13 (Ref. (5-17)) for 20-
degree entries. Three representative nose shapes are included: a
spherogive made up of a 57-degree spherical cap of 0.30d radius on
a 1.5-caliber ogive; a hemisphere; and a 1/4-caliber disk ogive.
Trajectories are given for three values of the pitch at impact;
about +0.5° and ±5°.

All of the vehicles were slightly buoyant and the disk ogive,
for example, was moving only 18 ft/sec after traveling 160 ft. At
that time the vehicle was not cavity running and some upward effect
of buoyancy might be expected.

The spherogive and hemisphere curved upward strongly except when
there was several degrees of negative pitch at impact. With a pitch
of -6° both missiles tended to dive. Under all the conditions of
pitch, the disk ogive traveled rather well along the line of fire for
about 80 ft, and for positive pitch it apparently deviated from the
straight line only because of buoyancy.

Ricochet of Spheres

The ricochet of spheres has some interest and importance as a
rather special and simple case. For grazing angles of impact the
depth of penetration is extremely small. The plow, or distance
that the sphere is in contact with the water during the ricochet, has
been reported (Ref. (5-6)) as about 10 to 50 sphere diameters, but
Ramsauer cited (Ref. (5-18)) a firing in which an 11-mm ball ricocheted
after complete immersion and a plow of 86 diameters.

The energy lost in a ricochet may be very small. de Jonquieres,
who first made a study of sphere ricochet in 1883, described the
horizontal firing of 6-inch spheres at a speed of 1500 ft/sec
(Ref. (5-19)) With an initial impact angle of about one degree
these rounds executed an average of 22 ricochets in a flight of 1.5
miles. The average deceleration per ricochet was estimated as about
7 ft/sec, and the water penetration must have been very small.

For each sphere there is a critical angle, θ_c, below which
ricochet occurs from smooth water. A lighter sphere is more easily
deviated from a straight line and therefore ricochets at a larger
angle. Simple theory shows that θ_c should have little dependence
on the speed of the sphere and Birkhoff reported (Ref. (5-20)) an
observed increase of 20 percent as the speed increased from 200 to
2000 ft/sec. The formula derived by Birkhoff

$$\theta_c = 18°/\sqrt{\sigma} \tag{5-9}$$

where σ is the specific gravity of the sphere, is in reasonable
agreement with various measurements (Refs. (5-6), (5-18), (5-19),
(5-20) and (5-21)) although the sphere diameters varied between 0.43
and 6.2 inches.

There are several forces which arise because of the asymmetry
of the flow about the sphere. There is a main lift force due to the
gliding behavior; a lift, even when the sphere is completely submerged,
because of the nearness to the free surface; and a downward force due
to underpressure below the sphere (Ref. (5-7)). And, of course,
gravity. The downward forces are important only at low speeds, and
a downward "refraction" has been reported at less than 50 ft/sec
(Ref. (5-6)).

The attraction toward the free surface is generally unimportant
(Ref. (5-20)). Ramsauer computed the lift force due to incomplete
immersion during the plow (Ref. (5-18)) and his data, following
Birkhoff (Ref. (5-6)), are presented as a lift coefficient, C_L,
against fractional immersion, in Figure 5-14. Initially, the coef-
ficient increases with immersion depth and reaches its maximum when
the sphere is half submerged. Its value then is about one-quarter
of the drag coefficient.

The angle θ_2 at which the sphere leaves the water is reported
(Refs. (5-6) and (5-21)) to be always less than the impact angle
θ_1. The ratio θ_2/θ_1 is largest when θ_1 is much less than θ_c, and U_o
is high, while in general, $0.8 \leq \theta_2/\theta_1 \leq 1.0$ (Ref. (5-6)). de Jonquieres
found (Ref. (5-19)) θ_2 to be larger than θ_1 by about 8'.

Presumably the underwater path of the sphere depends little on
the size of the sphere or on its speed (Ref. (5-18)). For the same
value of θ_1/θ_c, theory and experiment show (Ref. (5-20)) that the
maximum penetration depth (in diameters) is approximately the same
for all spheres. The sphere will just submerge when $\theta_1/\theta_c \approx 0.9$ and
the maximum depth compatible with ricochet is about two diameters.
For $\theta_1 = 1°$, Ramsauer (Ref. (5-18)) found the maximum depth about
one-sixteenth the diameter.

MISSILE DESIGN

Design criteria for missiles depend strongly on the intended use.
It will be assumed here that the missile is not to be used solely for
fully wetted travel, but rather for water entry at various angles,
for short runs in full cavity or long runs ending up fully wetted,
for inertia or rocket-propelled applications, and so forth.

Water Entry

There are two casualities which especially must be guarded
against in designing for water entry: instability arising from whip
at water impact, and missile damage resulting from the high stresses
during high-speed entry.

Noses on missiles designed for water entry almost invariably are
flat or truncated, with the truncations usually on cones or ogives
(Figs. 5-15A and 5-15B), or are disk ogives (Fig. 5-15C). The
diameter of the truncation is usually 0.5 or 0.6 of the body diameter.
Diameters less than 0.5d may be used, as in the plunge bomb, where the

afterbody is a slender cone. If the truncation is too small, one side of the nose will be wetted when conditions are unfavorable, such as when the missile has an appreciable angle of attack, and this will generally make the missile quite unstable. With sufficient truncation, missiles can be designed to enter water reliably at angles as low as 2 degrees without ricochet or broaching. The objection to a large truncation is the large water-entry shock and cavity-running drag.

At one time the probe or spigot (Fig. 5-15D) was a popular design idea. It is a cylinder of diameter less than the missile diameter and a length up to about one caliber. If the flow hits the blunt surface behind the spigot, the behavior is generally unsatisfactory; if not, the behavior is like that of the truncated nose.

In the design of the plunge bomb (Fig. 5-15B) for short-range attack after water entry, the drag was kept low by using a small truncation on a slender cone. The stability is optimized by making the bomb longer and moving the C.G. as far forward as possible. The plunge bomb is unstable except in full cavity. Hence, the range is effective only while the bomb speed is sufficient to generate an adequate cavity.

It is possible to use an untruncated slender ogival or conical nose on a water-entry missile if the body is a cylinder 20 calibers or more long (Fig. 5-15E). The transverse moment of inertia should be so high that the missile will resist turning during the short entry time of large upsetting moment. Such a body will travel nearly in a straight line so long as the velocity is high because the tail will be guided by the very narrow cavity. When fully wetted the missile has excessive drag.

In some respects the disk ogive is an optimum nose for water entry since its whip can be made almost zero for specific conditions of entry. Its advantage over the flat are small especially since whip varies with angle of entry, velocity, and missile size.

Various "fixes" have been used with slender noses such as the ogive to prevent large whip at entry. The most popular of these has been the kopfring, sketched in Figure 5-15F. It is a narrow ring of approximately triangular form which projects from the ogival surface. When the lower edge of the kopfring strikes the water during oblique entry, it gives a strong downward moment to counteract the nose-up moment characteristic of fine noses. The ring works well but it increases the drag considerably when the missile is cavity running or fully wetted. There are variants of this stabilizing device. Sometimes more than one kopfring has been proposed; the ring can be replaced by separate projecting fingers, called spades (Fig. 5-15G); and an appendage, aptly called a "pickle barrel", was tested on the ogive nose, with the idea that it would be removed by the entry forces (Fig. 5-15H). It has some potential also for shock mitigation. In most applications adequate truncation appears to be the best way of providing water-entry stability.

The high air speed before water entry, of recently designed missiles has required that means be provided for slowing up the missile before entry, or of mitigating the entry shock so that the missile case will not be deformed or the internal instrumentation severely damaged.

Parachutes and retro-rockets are effective in slowing up the missile for water entry but this solution has the disadvantages that the deceleration makes the missile a better target prior to entry, and considerably increases the time to depth for the missile.

Shock mitigation at entry has been accomplished by providing means on the nose for lessening the maximum stress experienced by the missile during entry. This is effected by an energy-absorbing device during the time of maximum stress. The most usual approach is to mount a fairing on the truncated nose, which completes the ogival shape and lessens the drag during air travel. If the fairing is made of a frangible plastic, energy taken up in breaking and removing it is taken from the drag force (Refs. (5-22) and (5-23)). Other shock mitigators have employed the compression of trapped air or of spring devices (Ref. (5-24)).

Cavity Running

Design features suitable for cavity running are similar to those for water entry and include adequate, but small, truncations or other blunt noses, in general; C.G. far forward; and long cylindrical after-body. In addition, it is usually desirable to have tail-stabilizing surfaces which will cause rebound of the tail from the cavity wall and will furnish stability during the fully-wetted phase. Fins may furnish adequate stability but the addition of a shroud ring is generally advisable; its additional drag when fully wetted is usually more than compensated by improved stability and better cavity-running behavior.

The disk ogive seems to have no advantage over the truncated nose for cavity running. The cavity size is the same for two noses if they have the same drag, and cavity separation is cleaner at the sharp edge of a truncation.

A bare afterbody will behave better when cavity running if it is a uniform cylinder without taper or "boat-tail". On the other hand, the fully wetted drag is lower if it is boat-tailed. Boat-tailing increases the need for a shroud during cavity running.

If an up-curving trajectory is desired after water entry, the tail surfaces should generally be made only large enough to provide the stability needed when fully wetted. The radius of the curved path can be lessened by shortening the body of the missile.

An almost straight path can be obtained by making the missile very long so that rebounding from the cavity wall is hardly needed,

or by adding a conical tail or flared skirt (Fig. 5-6C) to produce positive rebound. If the cone is added, it should be made quite narrow and of moderate angle, so that rebound is obtained but not excessive activity within the cavity. There is advantage in providing the cone on a recessed region (Fig. 5-6D), but none of these means are likely to provide stability after the cavity is gone.

Successful Designs

In Figure 5-16 are sketched a number of projectile designs which have proved satisfactory, especially for water entry. All are either truncated ogives or disk ogives, stabilized by fins and shroud. Figures 5-16A to 5-16C, (Refs. (5-25), (5-26) and (5-27)) give designs of truncated ogives with considerably different fineness ratios and main body lengths. The EX-30 Projectile in Figure 5-16A has an L/d of 10.5 and the body of the missile extends to the shroud. This design has the advantage of large volume and moment of inertia. The missiles of both Figures 5-16A and 5-16C enter the water stably at angles of 2.5 degrees or less although at the smaller angles the side of the nose, instead of the flat, first strikes the water. They have oscillating trajectories which are satisfactorily straight. Tests showed that the presence of a fuze on the nose, lessened the straightness of the path, probably causing a circular-arc trajectory.

The sketches of Figures 5-16D and 5-16E show similar configurations with the truncated ogive replaced by a 0.2-caliber disk ogive (Refs. (5-28) and (5-29)). These configurations were designed for water entry at angles of about 15 degrees or more. They give good entry stability at these angles and probably at somewhat smaller angles.

Usually the fins on these missiles are given a cant of 5 to 10 degrees to produce a slow rotation with the purpose of reducing the dispersion due to asymmetries in manufacture.

PREDICTION OF TRAJECTORIES AFTER WATER ENTRY

It is of obvious importance to the missile designer to be able to predict the trajectory of a missile for various experimental conditions. Several reports have proposed methods for such computations (Refs. (5-30), (5-31) and (5-32)) and many investigations listed earlier in this report have discussed parts of the problem and have derived data needed for the predictions. The descriptions given here will pertain primarily to unpowered (or inertia-propelled) missiles, but the extension to rockets is rather obvious.

Trajectory prediction after water entry, is complicated by the facts that the missile is traveling in a gas-filled cavity and the variation of the forces is strongly nonlinear or even discontinuous. The most practicable method is a step-by-step analysis, in which the trajectory is divided into a number of intervals, in each of which initial velocities and position of the missile lead to final velocities and position, usually by graphical integration.

Divisions of the trajectory must be made in an ad hoc manner, but
should proceed somewhat as follows. In the first, or impact phase,
there are drag and lift forces on the nose of the missile, and whip,
and these have been discussed elsewhere (Ref. (5-2)). After impact
the missile travels for a while with only the nose in contact with the
water, so that only nose forces and moments need be considered (Ref.
(5-3)). The tail of the missile commonly strikes the cavity wall and
may rebound or ride on the wall. The time of wall impact depends on
the cavity shape and size (Refs. (5-1) and (5-4)), and the forces
depend on conditions at the missile tail (Ref. (5-3)). Later the
missile travels in partial cavity, and finally, and outside the extent
of this discussion, the missile is fully wetted.

It is convenient to use an inertial coordinate system with origin
at the position of the C.G. at the time of water contact, as shown in
Figure 5-17; the x axis is in the direction of the velocity at water
contact, with z in the vertical (pitch) plane. The trajectory is at
an angle θ with the horizontal. The analysis requires the value of
the linear and angular accelerations during each step. In general,
these accelerations are known very imperfectly.

Before Water Contact

The initial conditions are those at first water impact. These
include the position in space of the coordinate origin, x_i and z_i;
the direction of the trajectory, θ_i (or $\dot{x}_i$ and $\dot{z}_i$); the orientation of
the missile axis (its angle of attack, α in pitch and ϕ in yaw); and
the components of angular velocity of the missile. The trajectory is
frequently quite sensitive to the initial pitch angle, and the change
from a few degrees of positive pitch to a few degrees of negative
pitch can change the trajectory completely (Ref. (5-16)).

Water-Impact Phase

A missile usually experiences very strong forces during a few
calibers of travel just after water contact. Published drag and whip
data for impact are collected and analyzed in Reference (5-2), with
drag given as graphs of

$$C_D^* = 2D/\rho U_o^2 A \tag{5-10}$$

(drag coefficients referred to the impact velocity) plotted against
penetration into the water. These drag coefficients can be averaged
graphically over the early penetration, but must be adjusted for the
mass of the missile by a method given in Reference (5-2).

The change of speed is usually small during the short entry phase.
It can be calculated from the equation

$$\Delta U = \Delta \dot{x} = \rho U_o \overline{C_D^* A} \Delta S/2M, \tag{5-11}$$

where $\overline{C_D^*}$ is the average C_D^* over the displacement ΔS, which extends through the period when the drag is varying rapidly.

Few data are available for the lift force during entry. For missiles with flat noses it can be assumed that the total nose force is along the missile axis so that the ratio of lift to drag force is the sine of the pitch angle. Data are available for the spherical nose (Ref. (5-2)); for many others the effect of lift may be neglected. The transverse velocity at the end of the impact phase can be obtained from the relation

$$\dot{z} = \rho U_o \overline{C_L} A \Delta S / 2M \tag{5-12}$$

if lift data are available. The new values of $\dot{x}$ and $\dot{z}$ define the value of θ from

$$\tan(\theta - \theta_c) = \dot{z}/\dot{x} \tag{5-13}$$

The most important change at impact is generally the whip. Available whip data are given in Reference (5-2). While the scaling of whip is poorly understood, estimates are possible from the published data. The whip is a change in the angular velocity in the pitch plane; changes in angular velocity in the yaw plane can usually be neglected. The angular velocity in the pitch plane at the end of the impact phase is the sum of the whip and angular velocity assumed at first water contact. The impact phase for bluff shapes at steep entry is too short to permit significant changes in the missile attitude. For entries at low angles the impact phase may be long, and the angular change must be calculated by the method of a later section. The total change of angle of attack in the pitch plane is the sum of this angular change and the change of the trajectory direction, $\Delta\theta$.

Estimate of Cavity Shape

The tail of the missile usually strikes the cavity wall and the position of the tail slap depends on the cavity shape. Shape has been discussed in detail for the water-entry cavity (Ref. (5-1)) and for the steady cavity (Ref. (5-4)). Although the overall size of the water-entry cavity increases greatly with entry speed, its size and shape near the forward end, which contains the missile, is almost independent of missile speed, if this speed is reasonably high.

It has been shown (Ref. (5-4)) that this part of the cavity would always be of the same shape for missiles of constant speed if there were no pressures acting, such as hydrostatic pressure, which tend to restrict the cavity development. If these pressures are present, there will still be a portion of the cavity whose shape has not been observably affected by them. The shape of the cavity which has suffered no collapsing effects of this sort (substantially a part of the cavity of zero cavitation number) was found experimentally to have the shape (Ref. (5-4)).

$$(y/C_D d)^2 = 0.583(x/C_D d)^{1/2} \tag{5-14}$$

with the vertex of the cavity slightly displaced from the nose tip of
the missile. This so-called "Ideal Cavity", corresponding to constant
missile speed, is shown by the solid-line graph in Figure 5-18

(with $C_D^{1/2} d = 0.685$). It will be seen from equation (5-14) that all
Ideal Cavities are geometrically similar.

Although some forward part of a large cavity is almost independent
of missile speed if that speed is constant, the shape is considerably
different if the speed decreases or increases rapidly, that is, while
the portion of the cavity being viewed, was being generated. In a
cavity photograph such as Figure 5-3, the cavity, at each cross section,
developed at a rate which was proportional to the missile speed when
the nose was at that cross section, and the photograph shows the
cavity growth at each cross section in the time required for the missile
to travel to the vertex of the cavity shown, from the position of the
cross section.

The two broken lines in Figure 5-18 give calculated cavity shapes
for cases in which the missile doubles or halves its speed in traveling
from A to B in the figure. These are merely examples of the "lag
effect" because of which the cavity width at the tail depends on an
earlier velocity of the missile. The angle of attack of the missile
also has an effect on cavity shape (Ref. (5-4)).

The cavity size, given by equation (5-14), is a limiting size in
the sense that any part of the actual cavity will not be larger than
this, and will tend to be narrower because of the effect of the
pressure difference between the cavity and its surroundings. The
deviation from equation (5-14) is smaller, the shorter the section
of the cavity being considered, and can be neglected when the missile
is traveling at high speed and shallow water depth.

Considerable study has been given to the steady cavity such as
that produced by a uniform flow about an obstacle in the water tunnel.
The geometry which has been observed for such cavities under constant
hydrostatic conditions cannot be ascribed to the transient water-entry
cavity with its strong gravity gradient. Moreover, the cavitation
number is generally not known for the water-entry cavity, although it
will be near zero while the cavity is still open to the atmosphere.
After it closes, the amount of air in the cavity gradually decreases,
but σ cannot be higher than about 0.2 if the cavity is large enough
to envelop a missile. Outlines have been reported for the steady
cavity long after water entry (Ref. (5-4)) and these may be used as
approximations from which σ can be estimated. Even for the steady
cavity, some portion nearest the generating nose (perhaps a very
small portion) will approximate the Ideal Cavity.

Before Tail Slap

Unless a missile nose is almost completely flat it has a nose-up
whip at oblique water entry and is unstable when cavity running. There
is a critical angle of pitch for rounded noses at which the missile,

at least initially, does not terd to rotate either nose-up or nose-down. For pitch greater or less than this value the missile tail tends to hit the bottom or top of the cavity, respectively.

Since the trajectory is approximately straight between water-impact and tail slap, it is not the shape of this part of the trajectory which is at issue, but the time and conditions of tail slap, since these determine the subsequent behavior.

For the estimation of the time of tail slap it is necessary to calculate the probable angle of the missile as a function of time and, from a series of sketches of the cavity outline, to determine when the tail will reach the cavity wall.

During the impact on the water surface, the angular velocity (whip) acquired by the missile is added to any which existed at water contact. After the impact phase the angular velocity usually changes further because of a nose moment exerted on the missile while cavity running, and this moment depends on the instantaneous value of the angle of attack. Underpressure, the low pressure which may exist in a region below the nose of the entering missile, makes another contribution to the nose moment.

First, a determination should be made of the maximum angle of attack at which tail slap may occur. This can be approximated by drawing an outline of the Ideal Cavity based on equation (5-14), and sketching the missile on a transparent overlay.

For steep entry, the missile, immediately after the impact phase, has substantially the angle of attack of its airflight. The nose moment during cavity running must be based, for the given angles of attack, on the little experimental data available (Ref. (5-3)). Since the dependence of moment on angle of attack will not generally be a simple one, it may be necessary at first to assume the moment to be constant at some "average" value over a small time interval and to calculate the change of angle during this interval, adding a contribution of underpressure if necessary. Some estimate of the latter may be possible from the experimental data in Reference (5-2). Other small increments should then be chosen until a sufficient angle is reached, as indicated by the Ideal Cavity outline.

Because the Ideal Cavity is larger than the actual cavity, an estimate is made of cavity length and volume from experimental data (Ref. (5-1)), and this information is used to modify the Ideal Cavity width, and thus to determine the time of tail slap.

For flat angles of entry it cannot be assumed that the angle of attack at the end of the impact phase is nearly that in air, since the impact (or nose-wetting) phase may persist through a considerable part of the trajectory. For some simple nose shapes experimental data are available (Ref. (5-2)) from which estimates can be made of the variation of the whip-producing moment with time during entry.

The variation of missile speed during this phase (and the phase after tail slap) can be calculated by use of cavity-running drag coefficients (Ref. (5-3)). To the accuracy of the trajectory calculation, these may be assumed to be independent of angle of attack. If the drag coefficient can be taken as constant, the relations of velocity, distance, and time can be determined from equations (5-3) to (5-5). If C_D must be treated as variable, it may be necessary to divide the trajectory into sections in each of which C_D is then assumed to be constant.

A different type of tail slap was mentioned earlier -- a type in which the tail strikes the under lip of the cavity at the water surface rather than a side wall of the cavity. Such slaps appear in the trajectory data of Figure 5-11 for entries of a right cylinder at 30 degrees. It is not easy to predict when such tail slaps will occur nor how much effect they will have on the subsequent trajectory. In the tests of Figure 5-11 the slaps occur because of the flatness of the entries and the presence of positive (nose-up) pitch at water contact.

During and After Tail Slap

Because most missiles are unstable when cavity running, the tail of the missile usually does not rebound from the cavity wall after tail slap but remains against the wall and slightly imbedded in it. At tail slap the angle of attack will always be large enough to ensure an unstable moment, and a rebound would have to take place in the presence of a continuing and often large overturning moment. This moment accelerates the tail toward the wall before tail slap, and afterwards, also, if rebound occurs. Often the tail is observed to bound away from the wall and then fall back onto it.

The depth to which the tail will penetrate into the wall can be calculated by combining the angular velocity at tail slap with tail forces measured for various depths of penetration, for similar tails during planing (Ref. (5-3)). The correctness of the result may be seriously affected by neglect of energy loss at tail impact and of the effect of underpressure forces. Underpressures arise when the tail leans against the wall just as when the underside of the nose is producing a cavity. This force, which attracts the tail to the wall, is especially evident when a simple right cylinder remains leaning against a cavity wall.

There is an increase of drag coefficient during tail slap whether the tail leaves the wall or not, and its magnitude is probably at least as large as the calculable contribution of skin friction on the wetted portion of the tail and its appendages.

If the missile is provided with a conical tail (Fig. 6-6C) of sufficient angle and width, rebound will occur, but in most other cases it may be assumed that the tail remains against the wall.

When the tail rebounds alternately from opposite sides of the cavity wall, the oscillating motion is sinuous but deviations from a straight line can usually be neglected. As has been mentioned, the drag is greater than it would be if the missile were "riding on its nose". If the rebounds are very vigorous, this increase may be very large.

The straight trajectory just discussed was based, of course, on the absence of gravity. Generally, the effect of gravity is negligible during the early part of a trajectory, but becomes of great importance when the velocity is small. The trajectories of inertia-propelled missiles usually approach the vertical (downward or upward) when the velocity has become small, and the gravity force can usually be simply superimposed on the cavity-induced forces. In these later stages of the trajectory, as the cavity collapses on the body, the behavior will depend on whether the missile is stable fully wetted. Plunge bombs, which may be adequately stable when cavity running become completely unstable, and broadside. Re-entrant jets often occur intermittently in the later stages of cavity travel, and these, traveling forward in the cavity, can seriously affect the missile motion. Such interference is not common, however; the effect of the jet more often is merely to hasten the disintegration of the cavity.

In the case of a rocket, the thrust must also be introduced into the calculations. The effect is primarily to oppose the drag, but the thrust is along the missile axis rather than along the trajectory.

Circular-Arc Trajectory

The circular-arc trajectory is given a separate section at this point, since it is the mode of travel of most missiles after water entry. The curvature is usually upward unless there is negative pitch. Even when there is a rebound from the upper cavity wall, gravity often prevents a rebound from the lower wall, and this leads to an upward-curving trajectory.

When a circular trajectory is assumed, the radius of curvature may be found as follows, using force data available from Reference (5-3)). As before, a probable cavity shape is derived from the Ideal Cavity and the size of cavities observed experimentally after water entry, plus a curvature of the cavity due to the trajectory shape. The angle of attack at which the tail will bear on the cavity wall is estimated as already described (with allowance for curvature and for penetration into the cavity wall). For this angle of attack the moment of the nose force about the C.G. can be estimated from experimental data. If the trajectory is a circular arc, the tail and nose moments must be equal, and the tail penetration needed to produce the necessary moment may again be available from experimental data. The sum of the lift forces on nose and tail must equal the centrifugal force of the missile in its circular trajectory, $F = MU^2/R$, and the radius of the path is given by this relation.

As the cavity decreases in size and collapses onto the missile tail, the discussion above loses meaning and, depending on the stability of the missile, it tends to broadside or to travel off on a tangent, influenced, of course, by gravity. Such collapse of the cavity can be most important in determining whether a missile in a circular arc trajectory, will broach.

EFFECT OF SURFACE WAVES ON WATER ENTRY

In treatment of water entry, whether discussion involves the impact forces, the cavity behavior, or the subsequent trajectory, the water surface is usually taken as horizontal and undisturbed. It is of some importance to consider the probable effect of surface roughness on missile behavior. Little of the quantitative experimental information available for waves is useful for this evaluation, and most data are derived from analytical calculations based on simple models. Frequently consideration is restricted to the "steady-wind wave" (Ref. (5-33)), which is uniform and two dimensional with an infinite, straight wave front. For analysis this wave is usually taken to be trochoidal, based on observations of Stokes (Ref. (5-34)). He found that instability occurs when the maximum slope exceeds 30 degrees, corresponding to a ratio of wave height to length of 1/7. Greater slopes are possible especially in the vicinity of breakers, but the probability of a missile striking in such an area is so small that these conditions may be neglected.

From experimental observation Boeckel estimated (Ref. (5-33)) that the wave slope does not exceed 14 degrees 98 percent of the time, or 12 degrees 90 percent of the time. The radius of curvature of the principal wave surface is generally large compared with the missile caliber so that locally the surface can be regarded as plane. Small-scale variations of slope are probably important only because they tend to prevent the trapping of air, or slamming over large areas, in the case of very blunt noses.

On the basis of the facts just enumerated, it is usually only necessary to recognize that the water-entry angle may effectively be a little more than 10 degrees greater or less than the angle between the trajectory and the horizontal. It appears unlikely that the probability of ricochet is significantly increased by grazing contacts with wave slopes, since the effect tends to be canceled by the presence of the next wave.

Local flow velocities are generally small compared with missile velocities, and can be neglected. Some special consideration is necessary in the case of the missile which is decelerated by a parachute before water impact (Ref. (5-33)). In a steady wind the parachute and its load tend to move with the wind. If the wind is effective for a considerable time the attitude of the parachute and its load will be the same as if the wind were absent. At low entry speeds it may be necessary to consider the horizontal component of velocity due to the wind, and this may result in an angle of attack if the load is hanging vertically.

REFERENCES

Abbreviations

AHL   Alden Hydraulic Laboratory, Worcester Polytechnic Institute

ARL (US)   Alden Research Laboratories, Worcester Polytechnic Institute

ARL   Armanent Research Laboratory, England

CIT   California Institute of Technology, Pasadena, California

NOL   Naval Surface Weapons Center, White Oak Laboratory, Silver Spring, Maryland (formerly the Naval Ordnance Laboratory)

NOTS   Naval Ordnance Test Station, Pasadena, California

NSRDC   Naval Ship Research and Development Center, Carderock, Bethesda, Maryland

5-1. May, A., "Water Entry," Chapter 1 of this report

5-2. May, A., "Forces at Water Impact," Chapter 4 of this report

5-3. May, A., "Forces Acting on Cavity-Running Missiles," Chapter 2 of this report

5-4. May, A., "Cavities and the Cavity-Running Behavior of Missiles," Chapter 3 of this report

5-5. Mason, M., et al., "Water Entry and Underwater Ballistics of Projectiles," CIT, 1946

5-6. Summary Technical Report of the National Defense Research Committee, Mathematical Studies Relating to Military Physical Research," Vol. 1, 1946

5-7. Bowen, I. S., "Underwater Behavior of 3.5-Inch Aircraft Rockets," OSRD CIT JPC 23, 1943

5-8. Yost, H. C., "Water-Entry Performance of a 5-Inch Flat-Nose Spinning Missile (Model SM-1)," NOTS NAVORD Rpt 1951, 1952

5-9. Waugh, J. G. and Stubstad, G. W., "Hydroballistics Modeling," NUC, San Diego, GPO, 1972

5-10. May, A. and Hoover, W. R., "A Study of the Water-Entry Cavity," NOLTR 63-264, 1965

5-11. Abelson, H. I., "Pressure Measurements in the Water-Entry Cavity," J. Fluid Mech., 44, pp 51-63, 1970

5-12. Norman, J. W., Burden, W. J., and Suter, R. A., "Deceleration at Water Entry IV. The Effects of Velocity, Entry Angle, and Pitch on a Projectile with a Flat Cylindrical Head," ARL/R5/G/HY/2/3, 1960

5-13. Mosteller, G. G., "Plunge Bomb Warhead for Kingfisher 'F'," NOTS NAVORD Rpt 1232, 1950

5-14. Hooper, L. J., "Water Entry and Underwater Performance Tests of Modified Plunge Bomb Models," AHL Rpt 27, 1952

5-15. Hooper, L. J., "Effect of Spin on Water Entry and Underwater Performance of 1-1/2" Model Plunge Bomb," AHL Rpt 29, 1953

5-16. Waugh, J. G., "Underwater Trajectories of Fourteen Full-Scale Unpowered Torpedo Models with Ogive, Spherogive, Plate-Ogive, and Modified Cone Heads," NOTS NAVORD 3012, 1953

5-17. Fabula, A. G., Perry, B., and Neale, L. C., "Underwater Cavity Missile Performance," Chap. 11, Hydroballistics Design Handbook, BuOrd NAVORD Rpt 3533, 1955

5-18. Ramsauer, C., Beeck, O., and Dobke, G., "The Influence of Free Surface and Solid Walls on Fast Moving Spheres in Water," (Der Einfluss freier Oberflächen und fester Wände auf schnell bewegte Kugeln im Wasser)", Ann. d. Physik 4F, 84, pp 721-746, 1927

5-19. de Jonquieres, E., "On the Ricochet of Spherical Projectiles at the Water Surface (Sur le ricochet des projectiles sphérique à la surface de l'eau)", Contes Rendus 97, pp 1278-1281, 1883

5-20. Birkhoff, G. et al, "Ricochet Off Water," NDRC AMP Memo 42.4M, 1944

5-21. Richardson, E. G., "The Impact of a Solid on a Liquid Surface," Proc. Phys. Soc., 61, pp 352-367, 1948

5-22. Dooley, W. F., Jr., "Evaluation of the Fairing, Nose, Shock-Mitigating, Mk18 Mod 0, A Component of the SUBROC Missile," NOLTR 67-158, 1967

5-23. Norman, J. W., "Frangible Water-Entry Heads for Underwater Weapons," ARL/G/R18, 1968

5-24. Mosteller, G. G., "A Retractable-Nose Missile for Low Whip and Low Drag," NOTS NAVORD Rpt 4991, 1955

5-25. Hooper, L. J., "Underwater Performance of 1-1/4-Inch Model of the 5" A.S. Projectile EX 30," AHL Rpt 21, 1951

5-26. Hooper, L. J., "Underwater Flight Characteristics of the Model 3" Vertical Fall Depth Bomb with Conical Shroud Ring," AHL Rpt 31, 1953

5-27. Hooper, L. J., "Water Entry and Underwater Performance Characteristics of the 1-1/4" Model of the 6" Projector Charge Ex. 1," AHL Rpt 23, 1951

5-28. Neale, L. C., and Steves, H. K., "Characteristics of Water Entry and Underwater Travel; Signal Depth Bomb Ex-1ₐ Model O," AHL Rpt 50, 1960

5-29. Hooper, L. J., "Water Entry and Underwater Flight Characteristics of the 1-1/4" Model of the Depth Bomb Mark 101 Mod. ," AHL Rpt 43, 1957

5-30. Kendrick, J. B., "Prediction of Water-Entry Trajectories by a Step-by-Step Semigraphical Analysis," NOTS NAVORD Rpt 1974, 1952

5-31. Berger, H. M., "A Step-by-Step Numerical Analysis of the Underwater Travel of Stable Missiles," NOTS NAVORD Rpt 1303, 1951

5-32. Kendrick, J. B., Fabula, A. G., and Schliestett, G. V., "Prediction of Water-Entry Trajectories," Proc. Joint Admiralty-U.S. Navy Mtg. on Hydroballistics, 1954

5-33. Boeckel, J. H., "A Statistical Study of Ocean Conditions for Missile Water Entry," NOL NAVORD Rpt 4180, Proc. NOL Water-Entry Symposium, 1 Dec 1955, pp 30-75

5-34. Mason, M. and Slichter, L. B., "The Effect of Roughness of the Sea on the Entry and Ricochet Angles of a Projectile," CIT 10C 31 Revised, OSRD Rpt 2374, 1945

5-35. Halbmillion, V. and Kulishek, C. J., "Geometric and Aerodynamic Data on Ogives," NOL NAVORD Rpt 2239, 1952

5-36. Baldwin, J. L., "Vertical Water Entry of Some Ogives, Cones and Cusps," NOLTR 75-49, 1975

5-37. Rouse, H. and McNown, J. S., "Cavitation and Pressure Distributions: Head Forms at Zero Angle of Yaw," State U. of Iowa, Studies in Eng., Bull. 32, 1948

5-38. Johnson, V. E. and Rasnick, T. A., "The Drag Coefficient of Parabolic Bodies of Revolution Operating at Zero Cavitation Number and Zero Angle of Yaw," NACA TR R-86, 1960

5-39. Granville, P. S., "Geometrical Characteristics of Streamlined Bodies," NSRDC Rpt 2962, 1969

5-40.   Granville, P. S., "Geometrical Characteristics of Flat-Faced Bodies of Revolution," NSRDC Rpt 3710, 1971
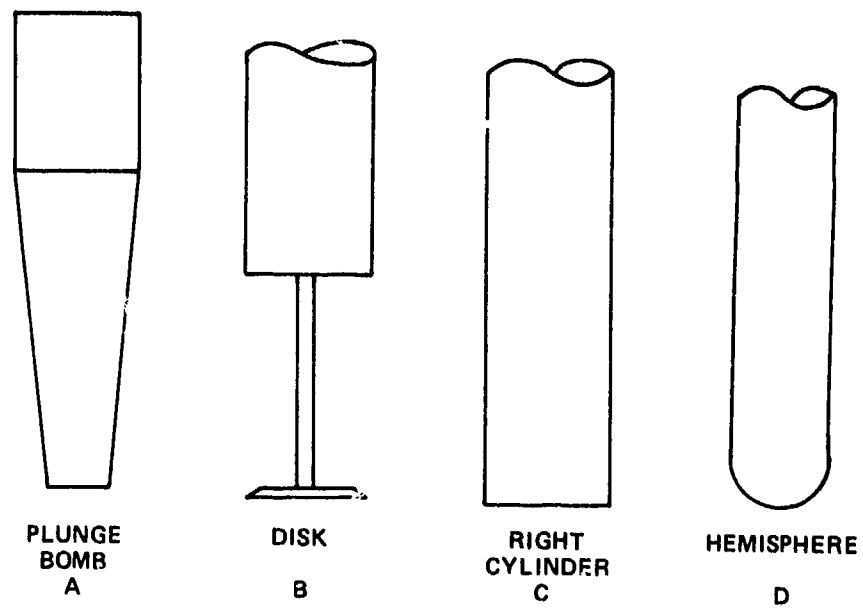
FIG. 5-1 SIMPLE NOSE SHAPES
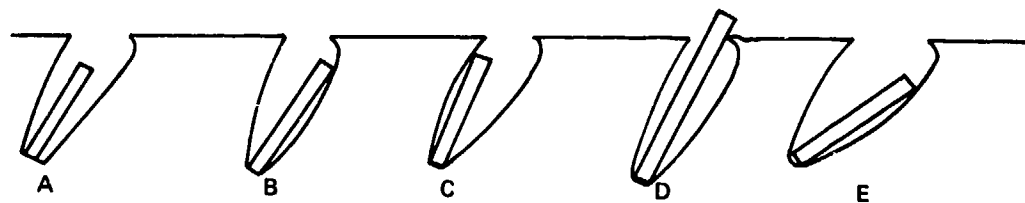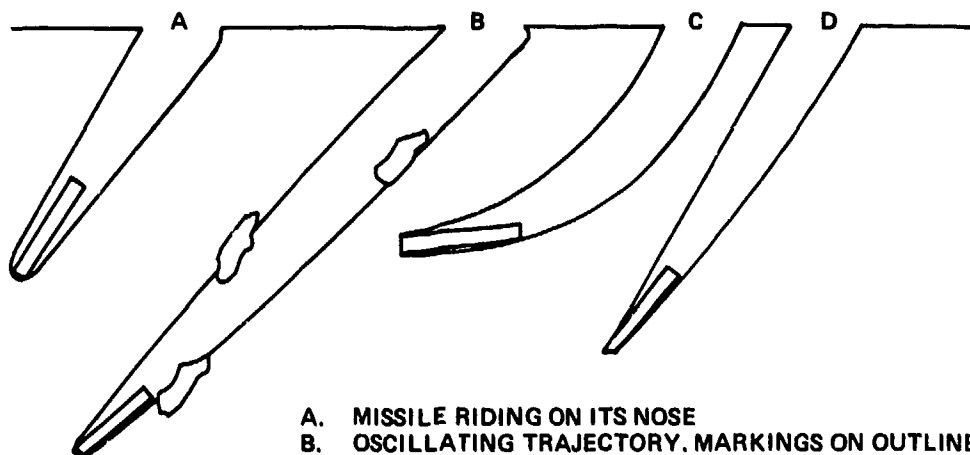

FIG. 5-2 MISSILE POSITIONS IN CAVITY
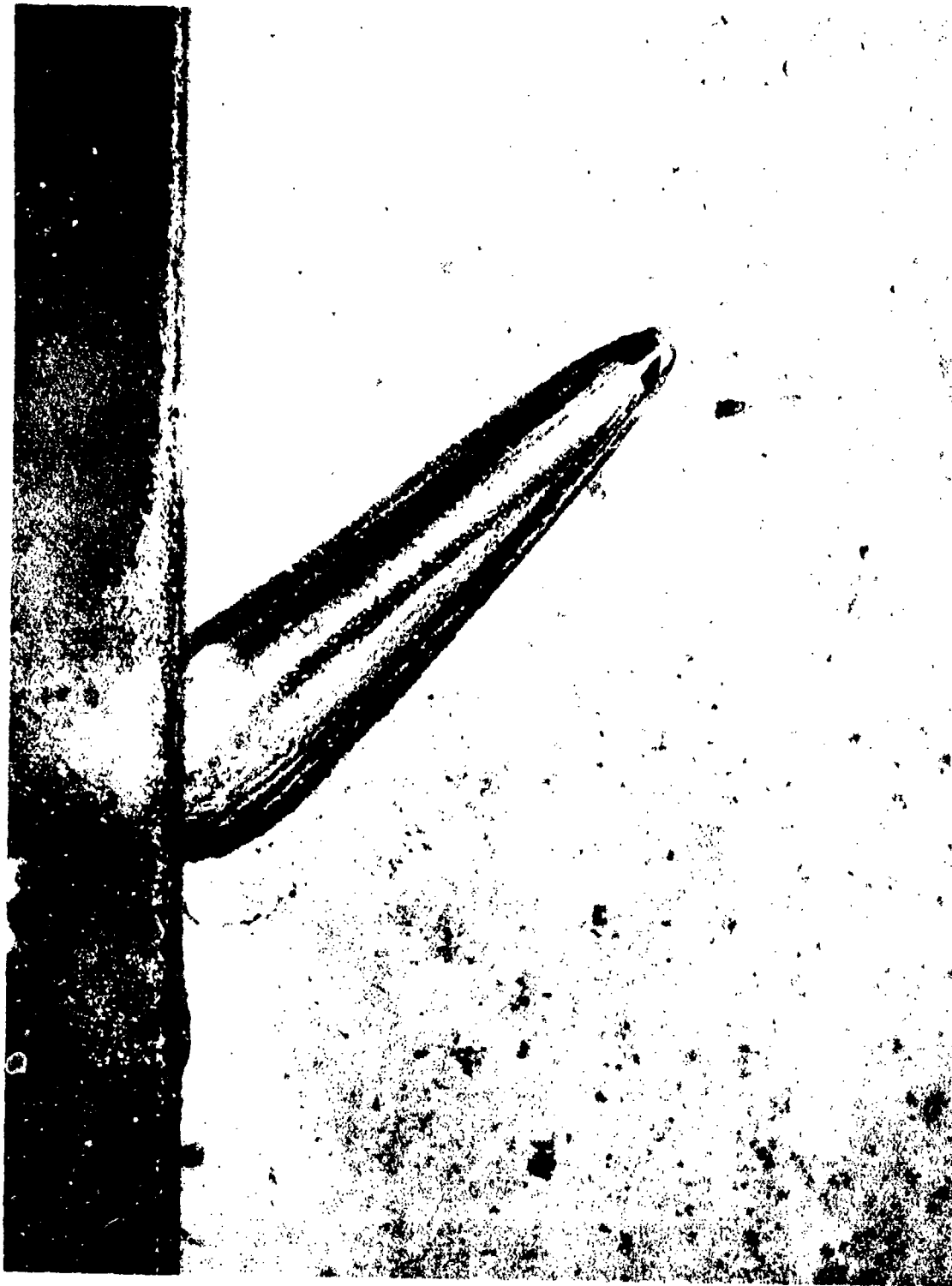
FIG. 5-3 CAVITY AFTER WATER ENTR.

A. MISSILE RIDING ON ITS NOSE
B. OSCILLATING TRAJECTORY. MARKINGS ON OUTLINE
   ARE GOUGES OR BUBBLES DUE TO TAIL SLAP
C. AND D. CIRCULAR-ARC TRAJECTORIES
E. CIRCULAR-ARC TRAJECTORIES SHOWING STRAIGHT
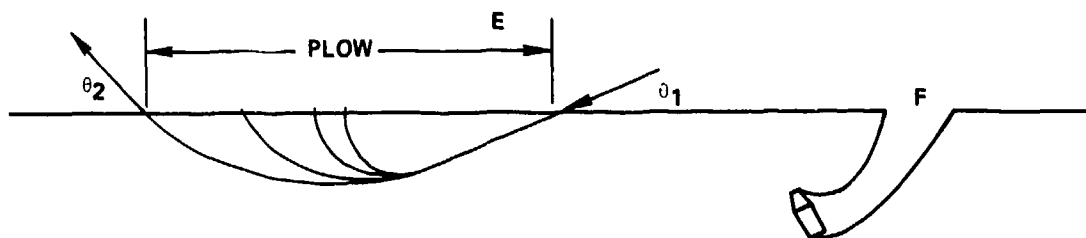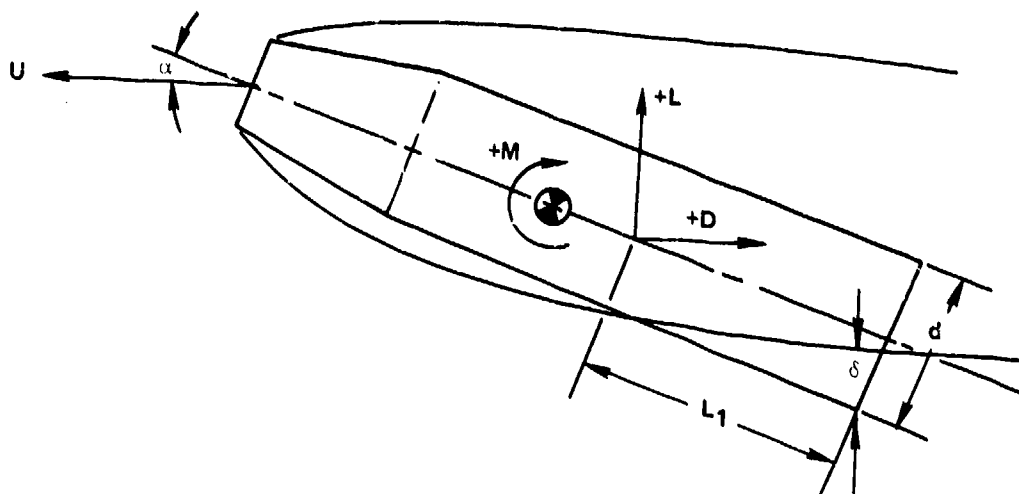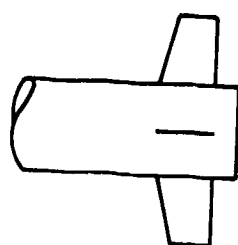   SECTION BEFORE TAIL SLAP
F. BROADSIDING MISSILE

FIG. 5-4 TRAJECTORIES WHILE CAVITY RUNNING

FIG. 5-5 TAIL IMMERSION SCHEMATIC

A. FINS

B. FINS AND SHROUD
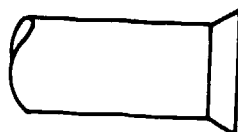
C. CONE TAIL

D. RECESSED FLARE

FIG. 5-6 TAIL CONFIGURATIONS
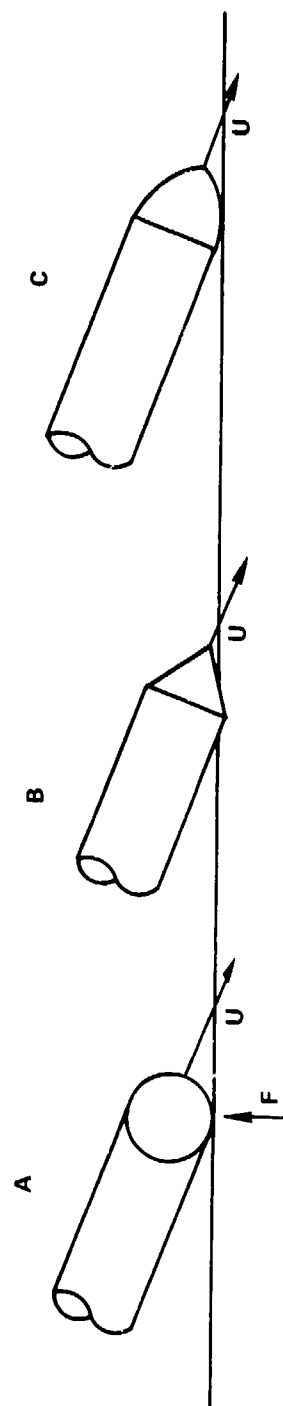
FIG. 5-7 ENTRY AT SMALL ANGLES
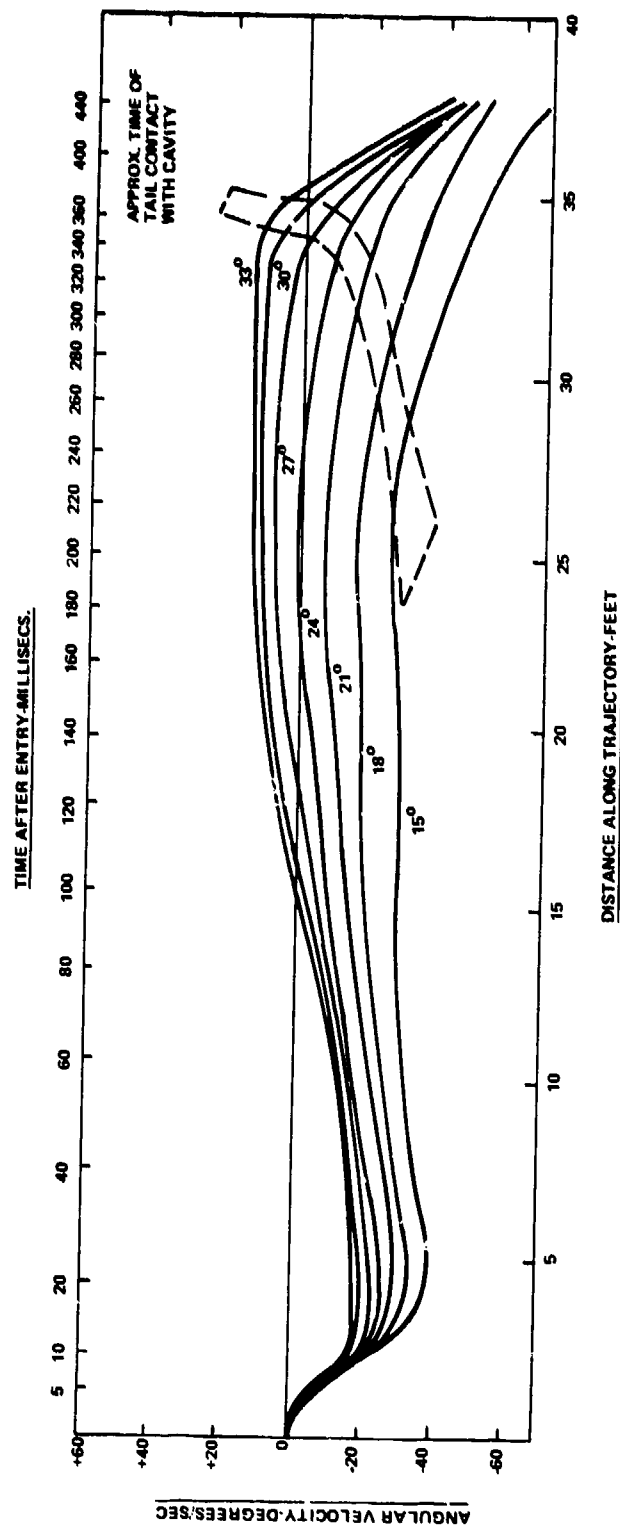
FIG. 5-8 ANGULAR VELOCITY VARIATION WITH ENTRY TRAJECTORY ANGLE U_0 = 225 FT/SEC. PITCH 0^0 FROM REF (5-12)

FIG. 5-9 TRAJECTORY DATA VARIATION WITH ENTRY ANGLE
ENTRY VELOCITY 225 FT/SEC. PITCH 0° FROM REF (5-12)
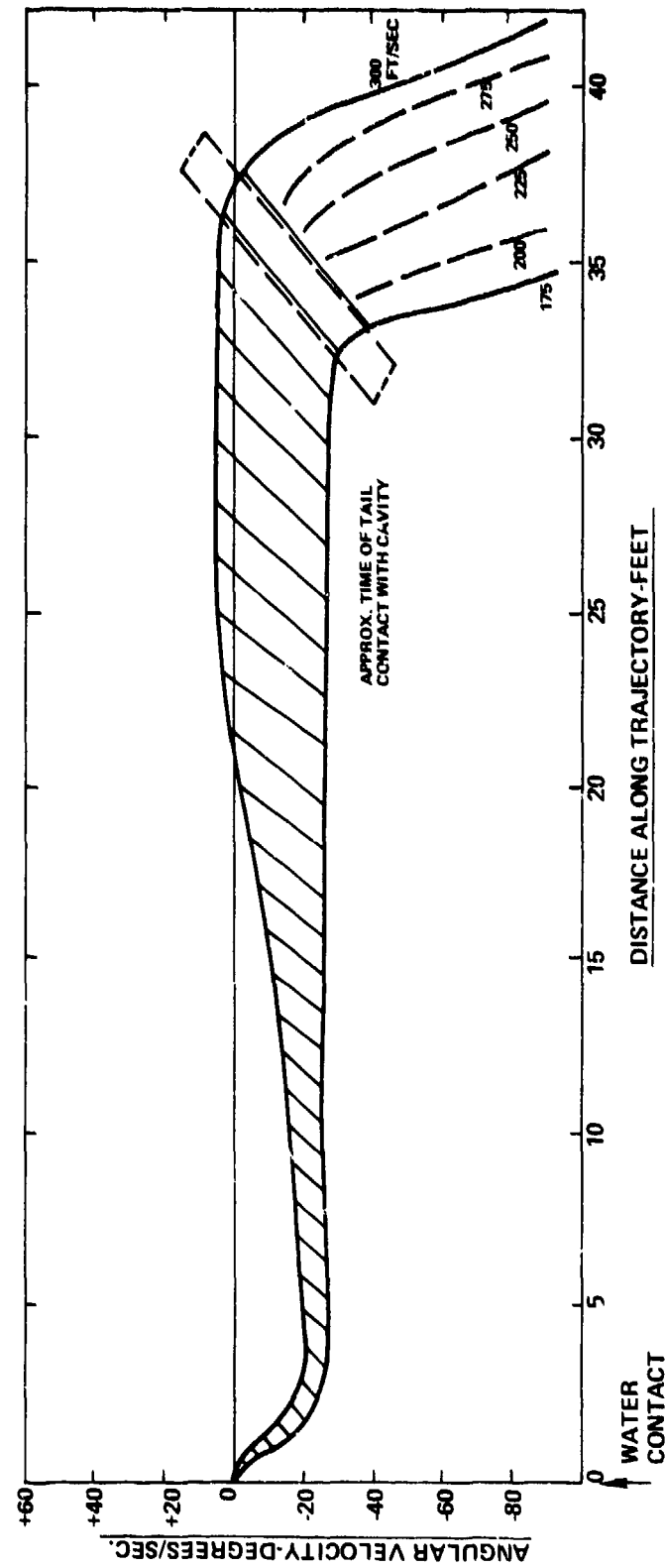
FIG. 5-10 ANGULAR VELOCITY-DISTANCE ALONG TRAJECTORY-VARIATION WITH ENTRY
VELOCITY; ENTRY ANGLE 30°, PITCH 0° FROM REF (5-12)
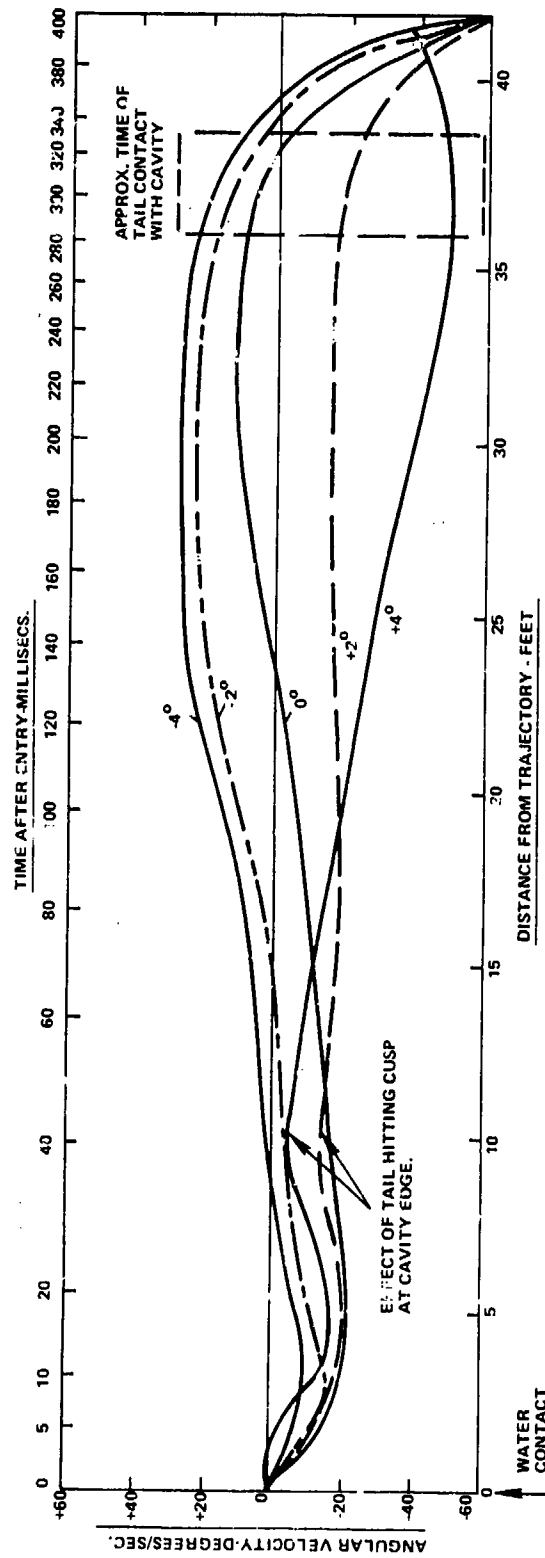
FIG. 5-11 ANGULAR VELOCITY-VARIATION WITH ENTRY PITCH U_o = 300 FT/SEC; θ = 30° FROM REF (5-12)
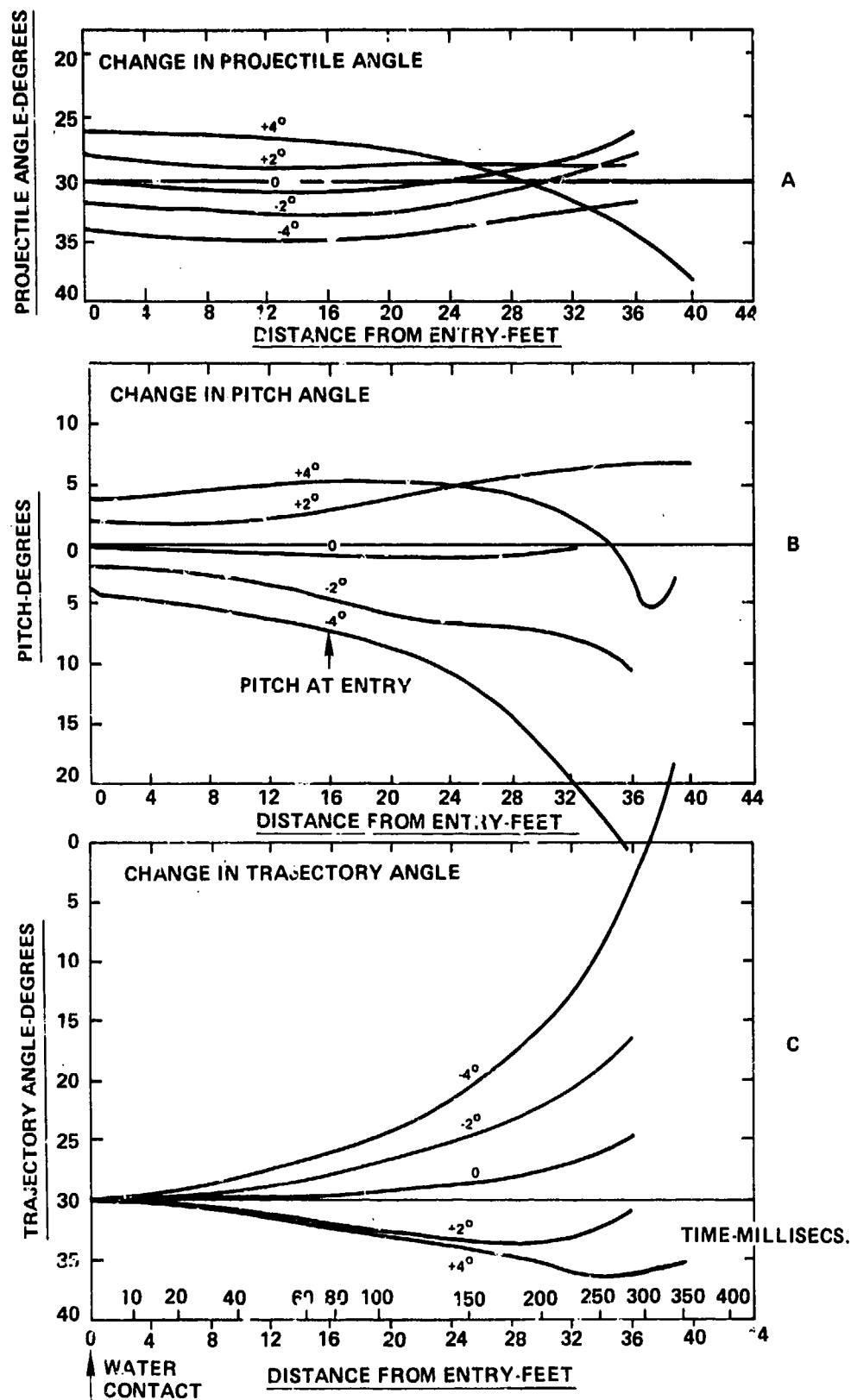
FIG. 5-12 TRAJECTORY DATA-VARIATION WITH ENTRY PITCH U_o = 300 FT/SEC, θ = 30° FROM REF (5-12)
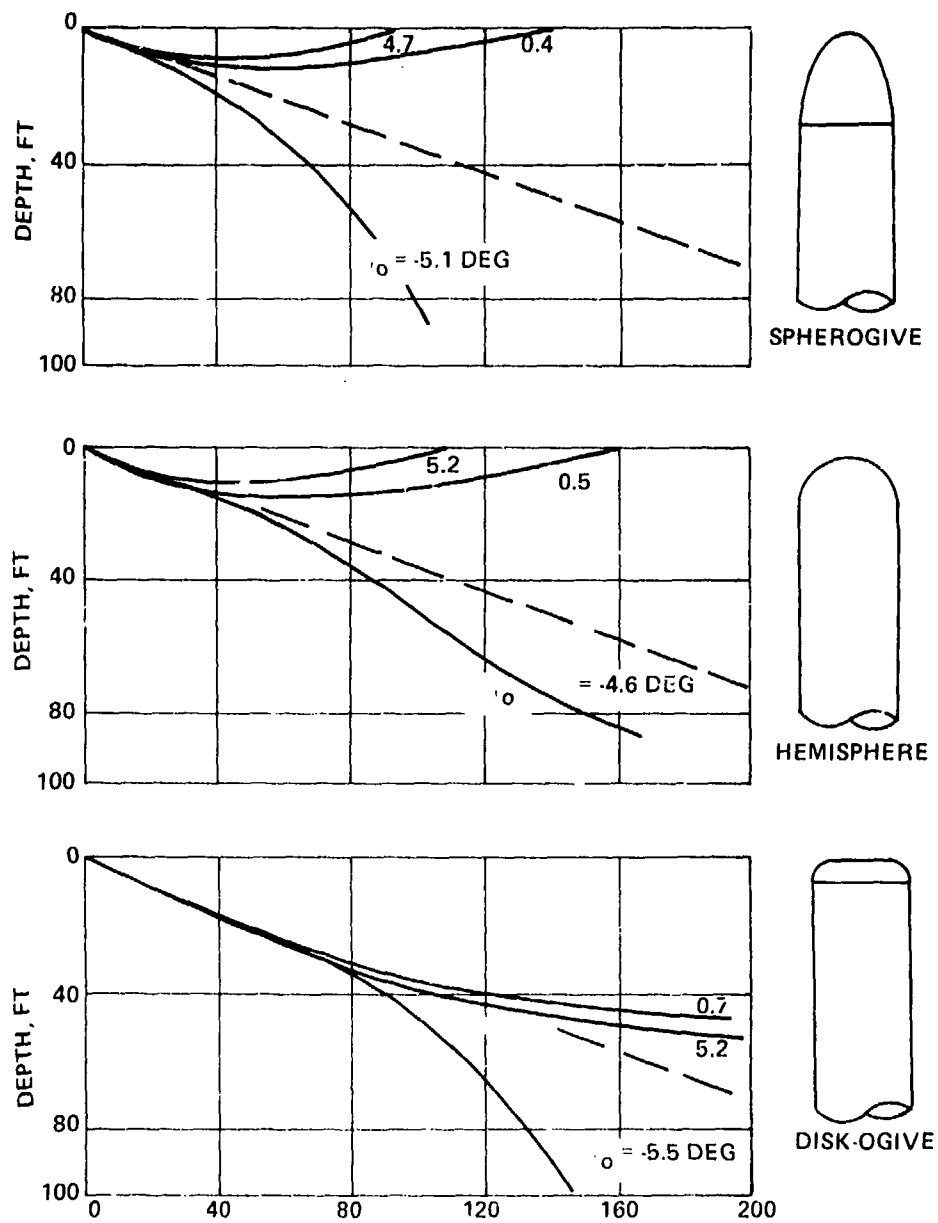
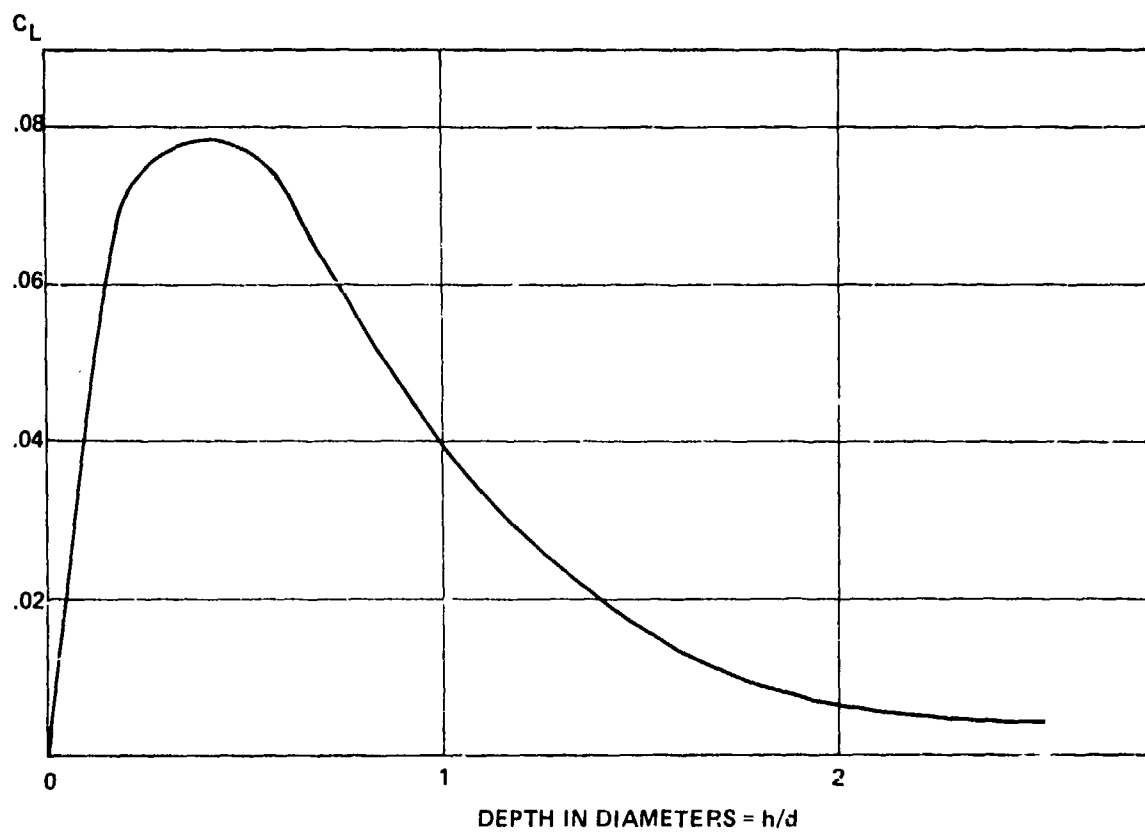FIG. 5-13 TRAJECTORIES AFTER 20-DEGREE ENTRY OF
TORPEDO WITH SEVERAL NOSE SHAPES

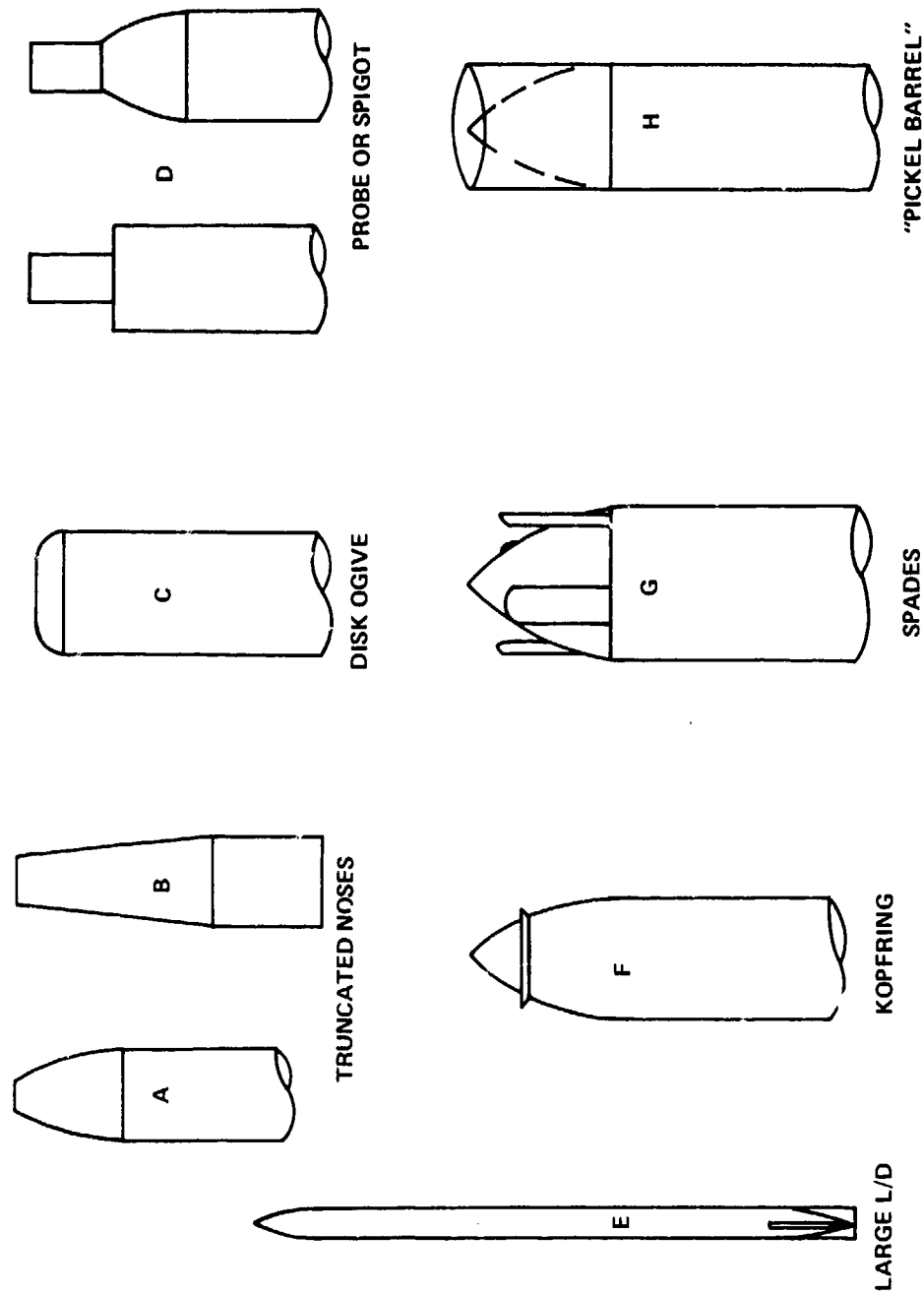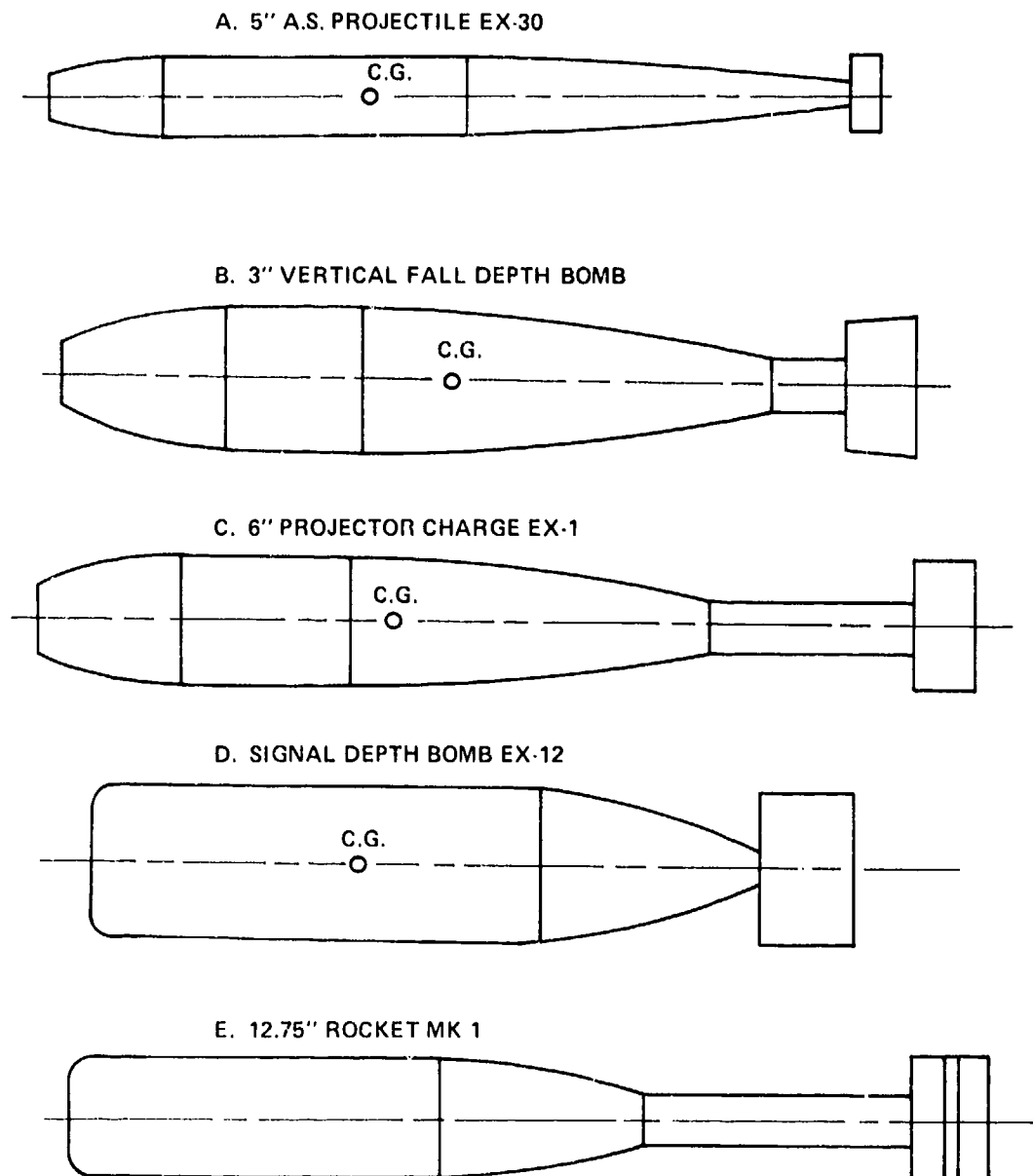FIG. 5-14 LIFT COEFFICIENT FOR A PLANING SPHERE AFTER RAMSAUER REF (5-18, 6)

A — TRUNCATED NOSES

B — TRUNCATED NOSES

C — DISK OGIVE

D — PROBE OR SPIGOT

E — LARGE L/D

F — KOPFRING

G — SPADES

H — "PICKEL BARREL"

FIG. 5-15 DESIGNS FOR WATER ENTRY

A. 5" A.S. PROJECTILE EX-30

B. 3" VERTICAL FALL DEPTH BOMB

C. 6" PROJECTOR CHARGE EX-1

D. SIGNAL DEPTH BOMB EX-12

E. 12.75" ROCKET MK 1

FIG. 5-16 PROJECTILE AND ROCKET CONFIGURATIONS
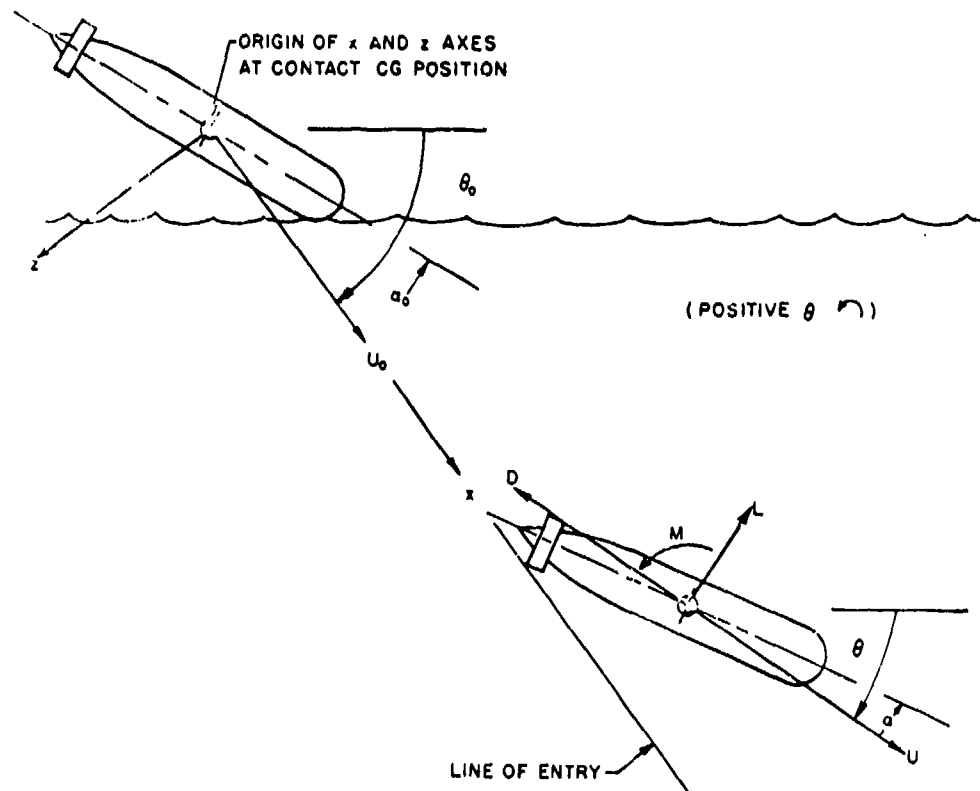
FIG. 5-17 COORDINATES FOR TRAJECTORY PREDICTION ADAPTED FROM REF (5-17)

A ⊢ ⊢— UNIT LENGTH

———————— IDEAL CAVITY (CONSTANT MISSILE SPEED)

— — — — MISSILE SPEED HALVES IN TRAVELING FROM A TO B
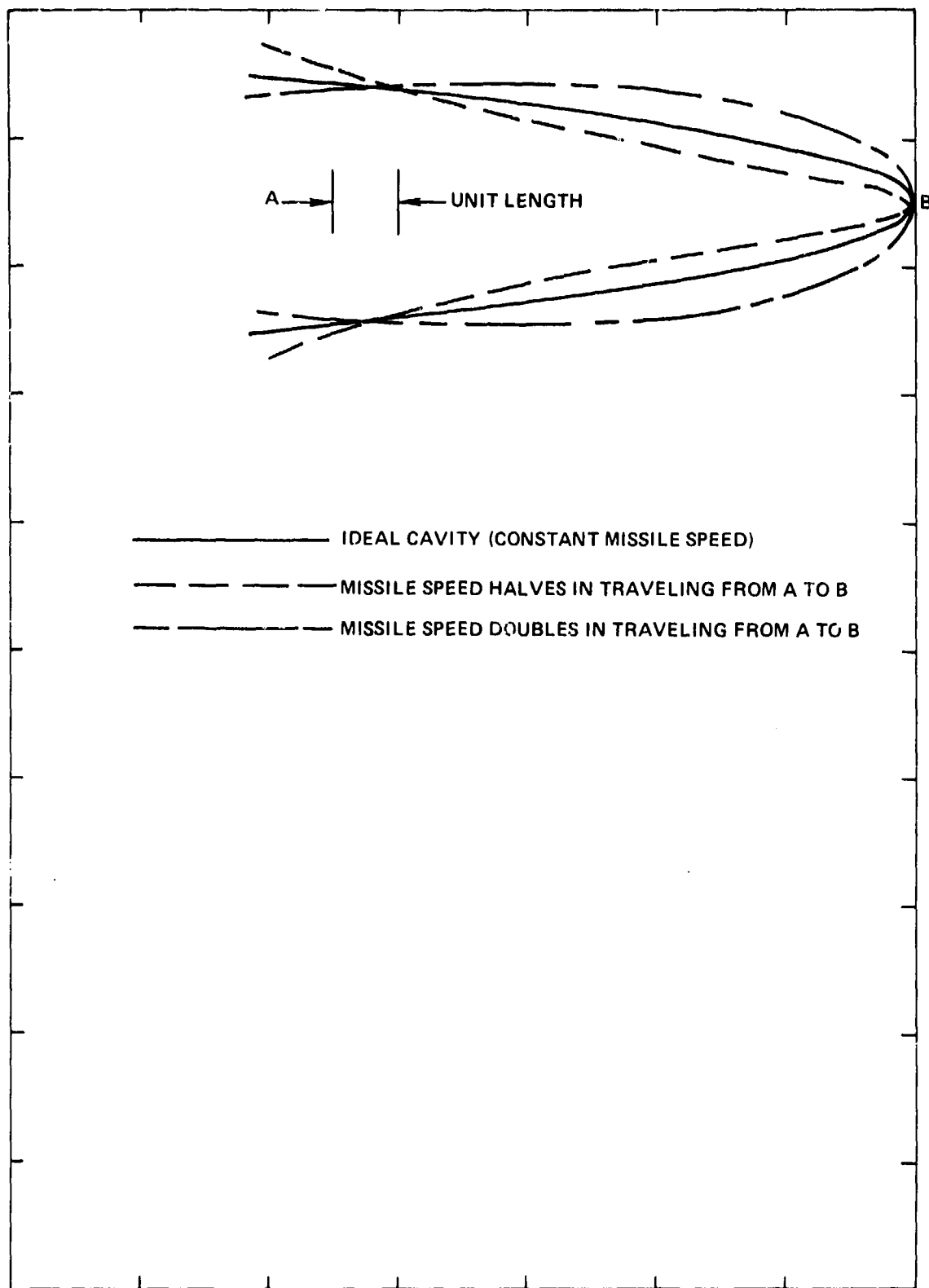
— —— — MISSILE SPEED DOUBLES IN TRAVELING FROM A TO B

FIG. 5-18 EFFECT OF MISSILE ACCELERATION ON CAVITY SHAPE

APPENDIX A

THE NOSE SHAPES OF MISSILES

This appendix defines the various nose shapes used on missiles designed for water entry and underwater travel. All of the shapes listed have axial symmetry, and nearly all are bodies of revolution. Some have been much used; some have rarely been tried and are included principally for definition. Samples of the various types are sketched in Figure 5-A1.

SIMPLE GEOMETRICAL SHAPES

Right Cylinder or Disk. (Also called blunt, disk-cylinder, plate-cylinder, or flat cylinder). Some behavior (for example, whip) may be dependent on the shape behind the front flat surface. In discussions of behavior which is not so influenced, the designation "disk" may be used for convenience.

The Ogive and Disk-Ogive Families. The ogive and disk-ogive families include the right cylinder, disk ogives, ogives, and the hemisphere. They are generated geometrically by rotating a circular arc about the missile axis to form part or the whole of the forward section of the nose. On a lathe, any of them might be generated from a right cylinder by sweeping the cutting tool in a circular arc of suitable radius. The arc is rotated about the missile axis but the center of the arc is usually not on the axis.

It has sometimes been found convenient to identify members of these families by means of the parameter.

$$Q = 1/(1 + 2R_O),$$

where $R_O = r_O/d$ is the ogive radius in calibers. The parameter Q has the advantage that its value varies only from 0 to 1 as the ogive radius goes from infinity to zero.

Disk Ogives. (Formerly called Plate Ogives)(Ref. (5-16)). For the disk ogive the radius of the generating arc is less than the radius of the cylinder, that is $R_O<1/2$; and 0.20 to 0.25-caliber disk ogives are most common. In the disk ogive, the arc is tangent to both the cylindrical wall of the missile and the flat surface on its front. A family of disk ogives is sketched in Figure 5-A2.

Hemisphere. The hemisphere is a half-caliber disk ogive. When flows separate from a sphere, it is usually on the windward side. If so, the presence of a lee surface may be unimportant and the hemisphere-cylinder may behave like a sphere.

Ogives. (Refs. (5-35) and (5-36)). For the ogive the radius of the circular arc is greater than a half caliber, and the arcs do not become tangent to the front surface of the nose, but meet to form a typical pointed ogive tip (Fig. 5-A1). If the arc is still

tangent to the cylindrical body, the shape is a tangent ogive;
otherwise it is a secant ogive, (Ref. (5-36)). Usual ogive calibers
run from one to six or more. If the half angle subtended by a
spherical nose is less than 90 degrees, the nose will be related to
the secant ogive rather than the tangent ogive, as shown in Figure
5-A1.

A family of ogives is sketched in Figure 5-A3, with R_o ranging
from 8.12 to 0.5 caliber. If the missile's cylindrical wall meets
these curves at their common right-hand point in the figure, they are
tangent ogives. If the missile body is a cylinder of smaller diameter,
so that it intersects each curve, the ogives are secant ogives.

Cones. Cones will be specified by their half angles in this report,
but the total angle is often found in the literature. It is
important to note which is employed.

The disk may be regarded as a cone of 90-degree half angle.
Cones with half angles greater than 90 degrees appear also in
reports (Ref. (5-37)). These represent heads with a conical cavity
in the nose surface (Fig. 5-A1).

Ellipsoids. (Also called Spheroids). This family is made up of
ellipsoids of revolution - usually prolate. The hemisphere and disk
may be regarded as members of this family. Ellipsoids with axis
ratios of 1, 2, and 4 are shown in Figure 5-A4.

Truncated Noses. Truncated ogives and cones are the most popular
noses for water entry, and the diameter of the truncation is usually
from 0.5 to 0.6 times the body diameter. Other nose shapes have also
been truncated.

Sphere-Tipped Noses. Families of sphere-tipped shapes were developed
at the Hydrodynamics Laboratory of the California Institute of
Technology during WWII in the attempt to produce configurations with
improved water-entry and cavity-running behavior. These included
sphere-cones, spherogives, and spherellipsoids. Where the sphere
tips meet the "transition section", their tangents are the same. The
sphere tip can be specified by its radius, but the half angle of the
spherical tip, ζ, has usually been given.

A family of spherogives has been sketched in Figure 5-A5. The
upper envelope in the figure is the outline of a 5-caliber ogive, and
the individual curves are spherical nose tips which might be used
with this ogive, specified by the half angle, ζ.

Concave Heads. Noses with a concave front surface have been tested
in the expectation that they would mitigate the water-entry shock
and decrease the whip, but they have received little acceptance. The
stagnation cup has been suggested as a standardizing test nose for
water tunnels. In addition to the stagnation cup, with the wall of
the concavity parallel to the missile wall, conical and ellipsoidal
(or spherical) concavities have been tested (Ref. (5-37)).

Other Geometrical Noses. A modified ellipsoidal nose was introduced
by the Iowa Institute of Hydraulic Research (Ref. (5-37)), as relatively
cavitation free. As shown in Figure 5-A1, it is generated by an
elliptical arc which is rotated, not about the centerline of the missile
as is the case for the simple ellipsoid of revolution, but about a
right-cylindrical center section of the missile. Figure 5-A6 shows
the meridian plane of two families of modified ellipsoids with
different axis ratios.

The cusp, (Ref. (5-36)), is created like the ogive by the
rotation of a circular arc about the axis of the missile, but the
arc is concave outward. Presumably the cusp has not been found to be
an advantageous shape.

The paraboloid has low form drag when cavity running (Ref. (5-38)).
Other power laws may be used also, as well as polynomials, (Refs. (5-39)
and (5-40)).

Special Water-Entry Heads. Special nose designs have been developed
to improve the behavior at water entry. Some were sketched in
Figure 5-15. It is intended that they reduce the shock at water
impact and the whip at entry.

Effect of the After Part of the Nose. It was mentioned that noses
which are hemispheres and complete spheres may behave the same.
Generally, it is assumed that a forward part of the nose is wetted
and that the shape behind this wetted area is not of importance.
This is true if the flow separation is unquestionable, but often
conditions are such that some part, and sometimes a major part, of
the body of the missile is involved. This is especially important
with fine noses, but appears even in the comparison of the performance
of such shapes as the disk and the right cylinder, when underpressure
effects (Ref. (5-2)), have importance because of incomplete flow
separation or flow reattachment. The underpressure may make the
moments acting on these shapes very different, although the drag
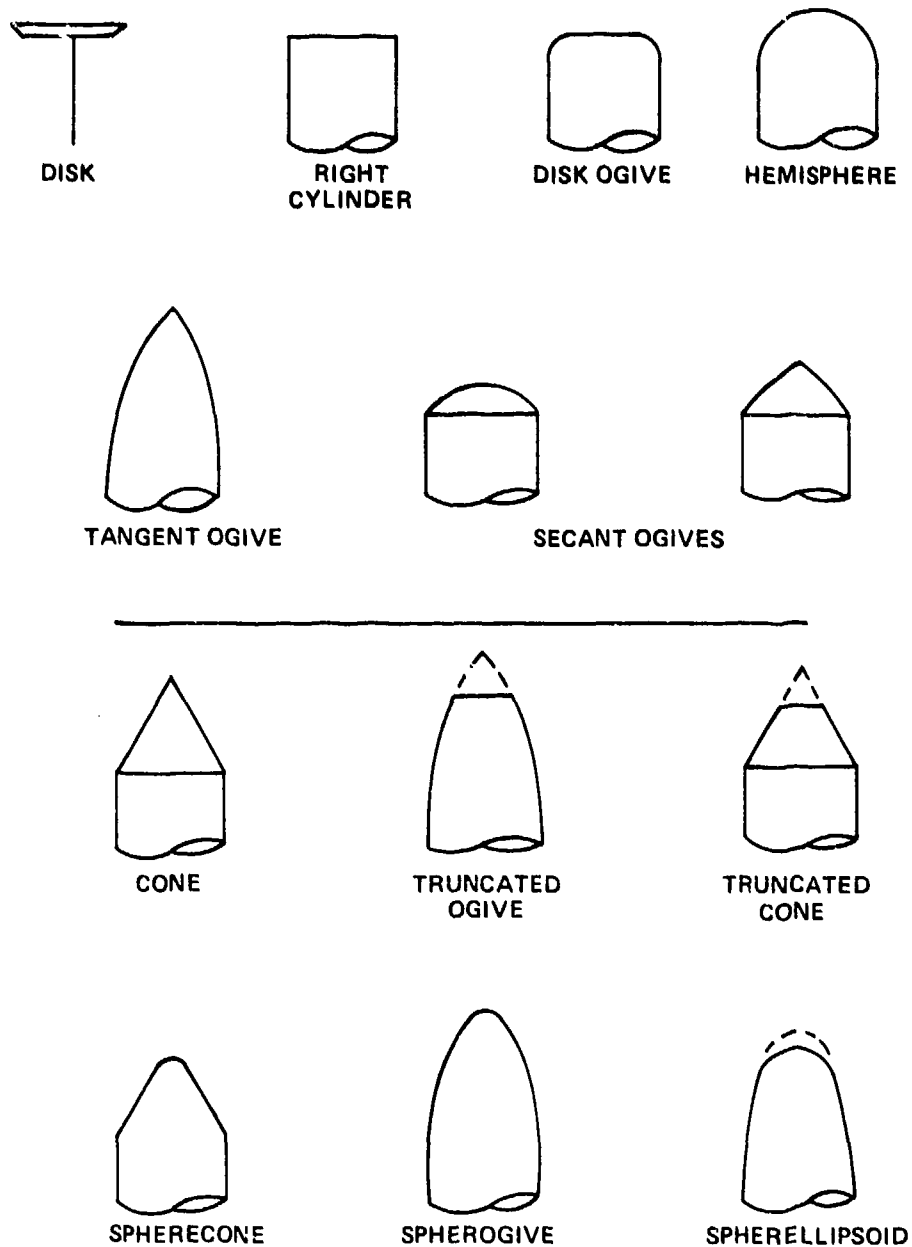forces are the same.

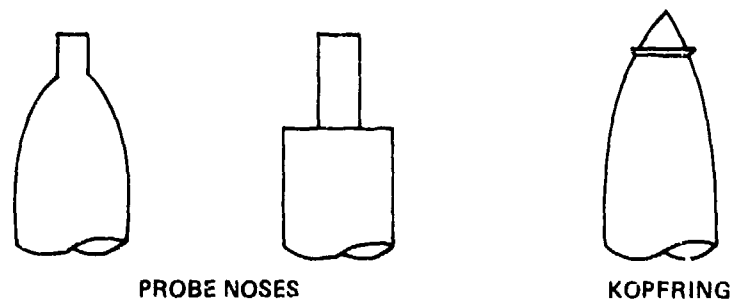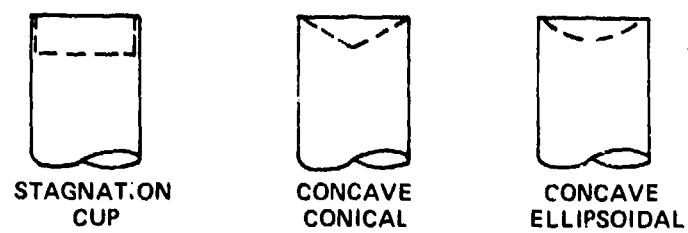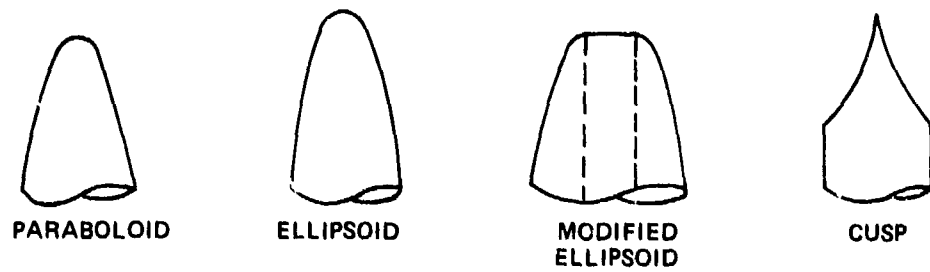FIG. 5-A1 TYPES OF MISSILE NOSES, OGIVE AND DISK-OGIVE FAMILIES

PARABOLOID   ELLIPSOID   MODIFIED ELLIPSOID   CUSP

STAGNATION CUP   CONCAVE CONICAL   CONCAVE ELLIPSOIDAL

PROBE NOSES   KOPFRING

FIG. 5-A1 TYPES OF MISSILE NOSES (CONT.)

R_o
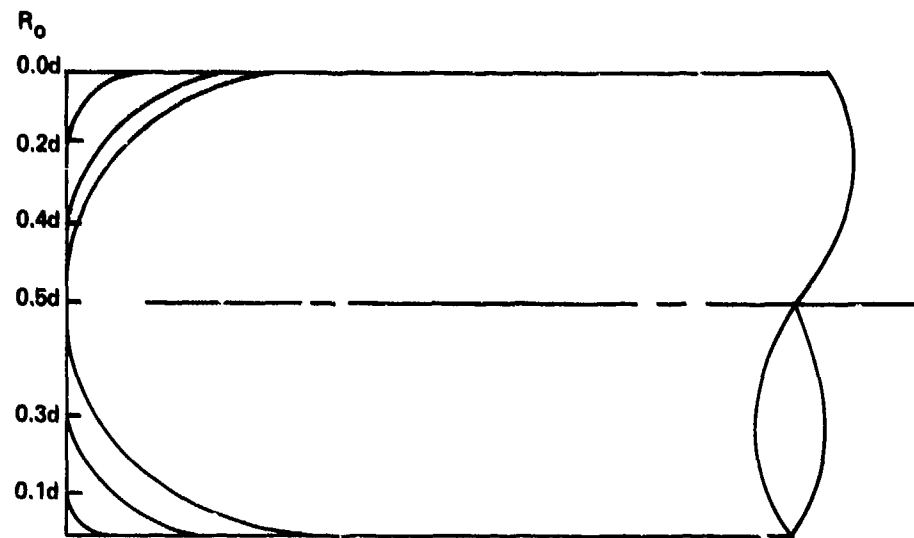
FIG. 5-A2 FAMILY OF DISK OGIVES
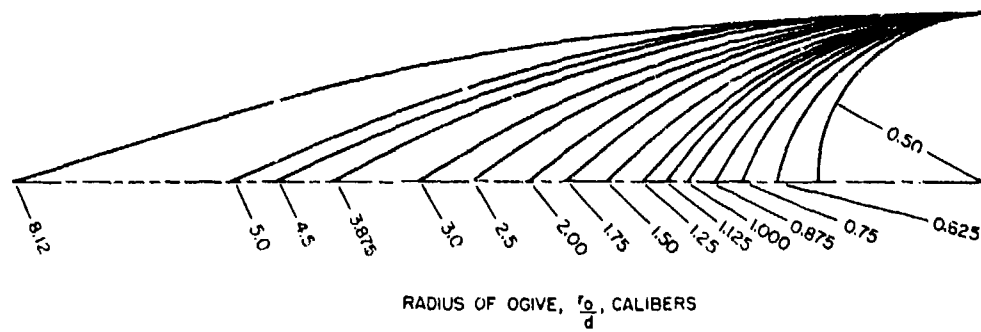

RADIUS OF OGIVE, $\frac{r_o}{d}$, CALIBERS
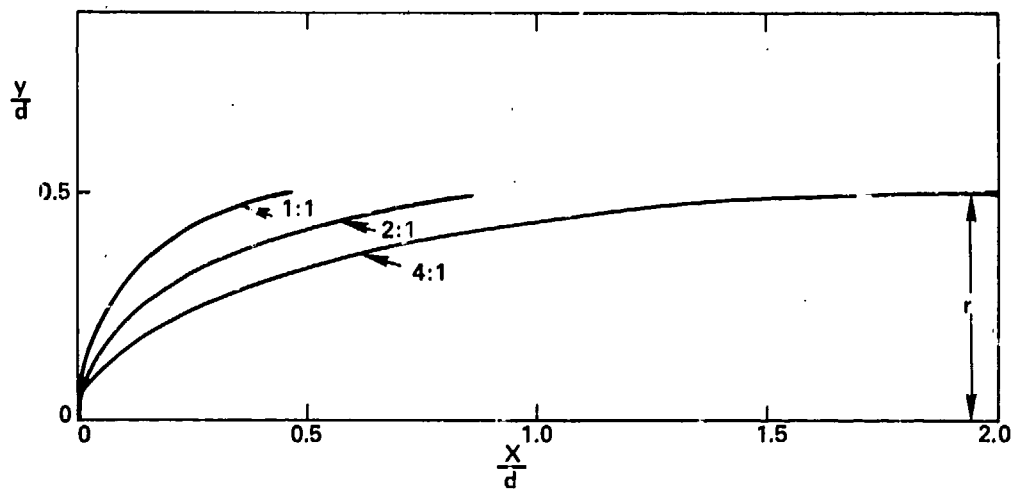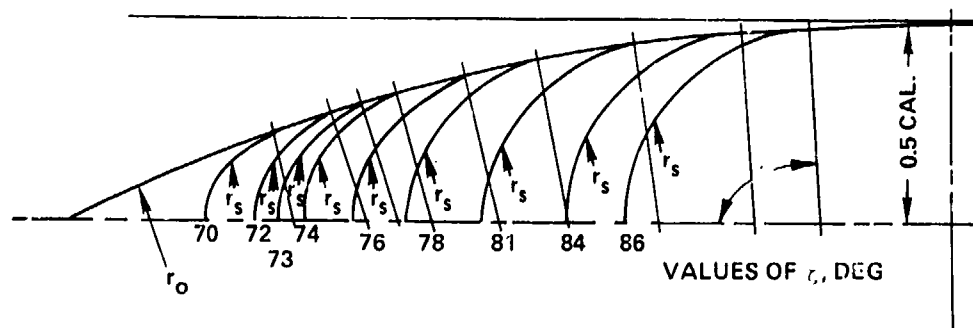
FIG. 5-A3 FAMILY OF OGIVES

FIG. 5-A4 FAMILY OF ELLIPSOIDS
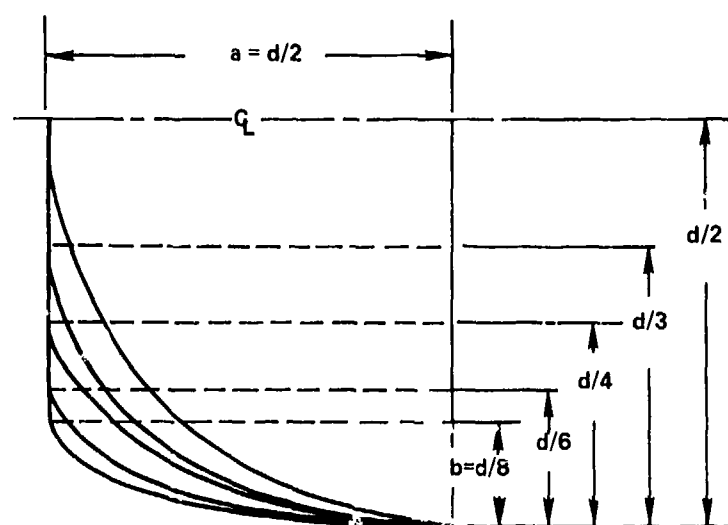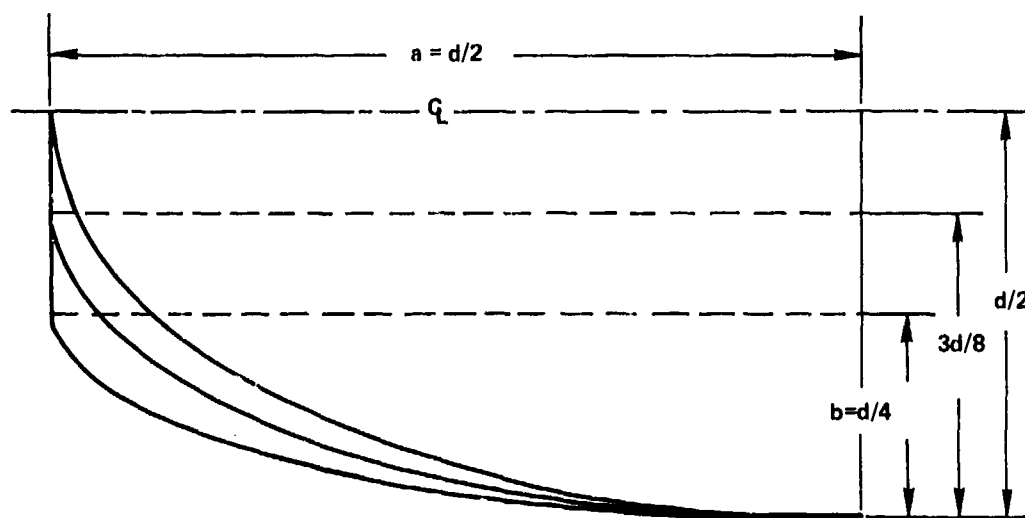

FIG. 5-A5 FAMILY OF 5.0-CAL SPHEROGIVE PROFILES

FIG. 5-A6 FAMILIES OF MODIFIED ELLIPSOIDS

Chapter 6

OPTICS IN EXPERIMENTAL HYDROBALLISTICS

SYMBOLS

h	depth in water of object point P
h'	depth in water of image point P'
n	index of refraction of water relative to air
P, Q	positions of object points
P', Q'	positions of image points
r	radius of missile
R	radius of cavity
y	ray separation, defined by Figure 6-8
θ_a	angle with normal of ray in air
θ_w	angle with normal of ray in water

INTRODUCTION

When tanks of water are used for water-entry, water-exit, and trajectory research, especially when cavities are involved, conditions exist which cause optical distortion for visual observation or for photographic recording. A number of these conditions are discussed in this report. Most of the phenomena are well known and only elementary principles of optics will be employed; reflection and refraction. The purpose is to draw attention to certain optical effects and to provide numerical data concerning them.

When a ray of light passes obliquely from air into water, the ray is bent or refracted at the water surface because light travels with a different velocity in the two media. This is shown in Figure 6-1A, where the light travels along a broken line from A to B. The process is reversible; the ray might be going from B to A in the figure, at the same angles.

The angles which the rays make with the normal to the interface of the two media (and all angles will be so specified), are related by Snell's law:

$$n = \sin\theta_a/\sin\theta_w. \tag{6-1}$$

In the equation, θ_a is the angle with the normal in air (the "less dense optical medium") and θ_w is the angle in water (the "denser optical medium"). Introductory discussions commonly refer to these as the angles of incidence and refraction but such designations become confused when the direction of travel of the light beam is reversed. The nomenclature of equation (6-1) applies to passage in either direction. The index of refraction, n, is the ratio of the speed of light in the two media:

$$n = \text{velocity in air/velocity in water.}$$

The index of refraction in water (relative to air) may be taken as 1.333. This value is for pure water at room temperature and yellow sodium light, but variations from the value 4/3 are negligible for the purposes of this paper. For oblique travel the angle will always be greater in air.

For a ray traveling from water into air, as θ_w increases, θ_a increases until θ_a becomes equal to 90 degrees when $\theta_w = 48° 35'$, the angle of total internal reflection. For this angle the refracted ray proceeds along the water surface, as shown in Figure 6-1B. For $\theta_w > 48° 35'$ the ray reflects from the water surface at the same angle, as shown in Figure 6-1C.

Although Figure 6-1A represents the refraction of a ray originating either in air or in water, it must not be assumed that there is no reflected ray. Specular reflection occurs in air or water at all incident angles, including normal incidence, but the

fraction of the light that is reflected is small unless the angle of the incident ray is nearly glancing, for a ray originating in air, or nearly equal to the angle of total reflection for the ray in water.

APPARENT DEPTH

The apparent depth of an underwater object when viewed through the surface is less than its true depth. When one looks directly downward into the water, any rays which enter the eye make a very small angle with the vertical, so that angles with the vertical can be set equal to their sines, and (for these rays) Snell's law can be written $\theta_a/\theta_w = n$. From Figure 6-2, it is easily seen that the depth appears to be only 3/4 as great as it actually is; since

$$h' = h/n,$$

where h and h' are the real and apparent depths of the point P.

The problem of the apparent depths of objects viewed obliquely through the water surface is much more difficult, but it is easily seen that the apparent depth becomes less as the obliquity is increased. The approximate apparent depth is shown by the curve in Figure 6-3. A number of object points on the bottom of the tank are represented by the circles on the abscissa. It is assumed that the water has unit depth and that the eye is located at unit distance above the water, as shown in the sketch. The broken lines show the apparent light paths from the objects since the images of these objects appear to be on the rays entering the eye. The distances are roughly at the positions where the dashed continuation of the rays in air, meet the curve. The apparent depth is seen to be very small when the obliquity is great.

VIEWING THROUGH A SIDE WINDOW

Windows are usually provided in the vertical side walls of tanks for viewing and photography. Since these windows have plane parallel surfaces their optical effects are small. Refraction occurs at both surfaces, but there is little bending at the inner surface, between glass and water.

The field of view of a camera is decreased when pictures are taken through the water surface. The effect can be seen from the light paths in Figure 6-3. If the lens is placed right at the air-water interface the normal angle of view of the camera is decreased in accordance with Snell's law. If the camera is further from the tank, as in Figure 6-3, the field covered is less restricted, and the narrowing of the field tends to vanish as the object approaches the air-water interface.

When photographing through a side window below the water surface, light totally reflected from the surface will cause a double image of objects near the water surface if this region is included in the field of view. The two images are at an easily identifiable angle

in the case of oblique entry, and this permits a determination of the position of the water surface.

A camera may be located outside a window with the camera lens at water level so that the camera field extends above and below the water surface. In this case the camera can photograph events in air and water simultaneously. Several complications arise in this type of photography.

If an object is photographed above and below the surface (e.g. the nose and tail of a missile in vertical entry) the two halves will not be in focus at the same time. The object below water appears to be only 3/4 as far from the camera as it actually is. This applies only to paths in water, and if the camera is not near the tank, only the water path will contribute to this effect. The object in water not only appears nearer than in air, but correspondingly larger -- as much as 4/3 times as large when the path to the camera is entirely in water.

An angular distortion is shown in the photograph of Figure 6-4. The camera was directly opposite the position of water entry so that the splash and the cavity are in line. The stadia rod which was located to one side appears to be broken at the water surface. The light paths are shown in Figure 6-5. In air the ray comes direct to the eye from the object point P, but in water the ray is refracted at the side of the tank and appears to come from the point P'.

While looking through a vertical side window, it would be impossible to see through the upper surface of the liquid if its index of refraction were greater than $\sqrt{2}$. Since the index for water is a little less than this, a ray can pass through both the side and water surfaces but the line of sight must be at an angle more than 62° to the normal and the image is extremely distorted.

Refraction difficulties at the windows can be obviated by the use of spherical windows such as those sketched in Figure 6-6. Unfortunately, the camera lens must be designed to include the window as a part of the lens system, and the front nodal point of the lens must be at the center of the spherical surfaces.

The camera may, of course, be immersed in the water. If it is mounted in a box with viewing through a window, it does not differ from observations through a tank side window except for the change of location. A camera may also be designed for use directly in the water, with the water wetting the front lens surface. This requires special design since the direct contact of water and glass destroys the focusing of the lens.

ILLUMINATION

The illumination of tests is a matter of importance and difficulty. Only a few comments will be made here. Details of techniques and equipment can be found in the literature (Ref. (6-1)). Color photography will not be discussed since it has generally proved disappointing in hydroballistics work.

Light Duration

Illumination is either continuous (steady) or it is intermittent (stroboscopic). Continuous illumination is provided by incandescent bulbs or glow-discharge lamps. Incandescent lamps usually contain iodine to permit higher filament temperatures. Glow-discharge lamps contain a vapor such as mercury. Steady lighting has the advantage of basic simplicity, but it has a number of serious disadvantages. These include a large power requirement; great heat development when large areas are lighted; and the need for a high-speed "shutter" on the camera so that the motion will be "stopped." Stroboscopic illumination requires expensive power and control equipment, but it develops less heat and the shortness of the flash duration may be effective in stopping the motion. The flash may be triggered by and synchronized with the motion-picture camera.

Flash bulbs designed for photographic use, provide a light source which is somewhat intermediate between the steady and stroboscopic sources. Such bulbs are made with great light intensity and of suitable duration to light a rapidly occurring event, such as the passage of a projectile.

Placing of the Lights

The lights may be placed so that they illuminate the front or sides of the object, or so that the object intercepts the light. The former method is obvious in application and is simpler, but the photographs which it yields are not as sharp in outline as those of good shadow photography.

Methods based on the intercepting of the light include silhouette lighting, shadowgraphs, and schlieren. Excellent pictures for quantitative data-retrieval are possible by means of silhouette lighting. A bank of lights is mounted on the side of the object away from the camera and some translucent material is placed as a diffuser, in front of the lights. The outline of underwater cavities is sharply defined in silhouette since, as will be described later, the outer portions of the cavity are opaque. In Figure 6-4 (which is an enlargement of a high-speed 16-mm motion-picture frame made by silhouette photography), the outline of the missile, the cavity, and the jet may be clearly seen. The principal disadvantage of silhouette lighting in large-scale experiments is the large light bank required in the background. The illumination can be provided either by

continuous or stroboscopic lighting. Stroboscopic lights mounted along a trajectory can be triggered electronically so that only one, or a few, lights in the vicinity of the missile are lighted at any one instant. Photographic flash lights can be operated similarly.

Shadowgraphic and schlieren arrangements in either air or water, are primarily useful for showing variations of local fluid density due to thermal effects, shock waves, and the like (Refs. (6-2) and (6-3)).

There is considerable scattering of light in water, even when it is very clear, and when this scattered light enters the camera lens, the contrast and sharpness of the photography are impaired (Ref. (6-4)). For photography in turbid water, front lighting is especially bad because much of the light intended for the missile is scattered before it reaches it and some returns to the lens. Side lighting can be advantageous under such conditions as is brought out by the comparison of the irradiated regions of the water in Figure 6-7. Back-lighting, such as the silhouette, is quite effective since the scattering of light before it reaches the object creates no problem.

CAVITY OPTICS

The cavities caused by the water entry of missiles are often roughly cylindrical with a taper at the front end as in Figure 6-4. The cavity walls may be transparent or opaque and they may be lighted from any direction.

Figure 6-8 represents the cross section of a circular transparent cavity of radius R, with silhouette lighting. This lighting is supposed to come from a diffusing screen at the top of the figure. Several rays have been traced through the cavity. The observer (camera or eye) is at the bottom of the figure. It is assumed that the observer is far enough away from the cavity so that light rays which enter the lens from the vicinity of the cavity are nearly parallel.

The ray AB passes through the center of the cavity and is undeviated. The ray CD passes through obliquely and is deviated; the angle change is the same at each cavity wall. The deviation becomes quite large as the rays become more oblique, such as the ray EF. The ray GH strikes the cavity wall at the critical angle for water (48°35') and is totally reflected. Obviously the illumination of the cavity depends on the size of the diffusing screen. For example, the ray EF will be lacking if the screen does not extend as far as the point E. In general, the angle which the screen subtends determines the fraction of the cavity width that is lighted from in back. If light comes from the side of the cavity, rays such as GH may cause the rim of the cavity to be front-lighted.

The marginal ray GH travels toward the camera at a distance $R/n = 0.75R$ from the central ray AB. In the photograph of Figure 6-4, the dark outer portions of the cavity add up to a little more than one-quarter of the cavity width.

In shadowgraphs of regions containing cavities, the cavities are observed to be completely dark. The reason is apparent from the sketch in Figure 6-9, where a point source of light forms a shadowgraph on a photographic film. If the cavity is the only optical obstacle, the region outside the cavity will appear bright, as shown by the rays which are indicated by heavy lines. Rays which pass through the cavity (dashed lines) are bent over a wide region. They are so dispersed that no effect of the light is generally observed, except possibly in the center of the pattern where a ray should be undeviated.

Appearance of Body Within Cavity

In Figure 6-8, the right side of the cavity contains a circularly cylindrical obstacle of radius r (the missile), concentric with the cavity. With silhouette lighting this obstacle appears dark and the edge of the missile is marked by the marginal ray JK, which is at a distance y from the central ray AB as it approaches the observer. The ray JK is chosen parallel to the other rays approaching the observer.

From the sketch, $\sin\theta_w = y/R$ and $\sin\theta_a = r/R$. By Snell's law

$$\sin\theta_a = \frac{4}{3} \sin\theta_w = \frac{4}{3} \frac{y}{R} = \frac{r}{R}$$

and

$$y = \frac{3}{4} r.$$

Hence, the missile appears to be three-fourths of its actual diameter. This applies for any ratio of missile diameter to cavity diameter (assuming it is less than one), but requires that both have circular cross sections and be coaxial.

The cavity acts like a cylindrical lens producing a virtual image of reduced size of an object within the cavity. The decrease in apparent size is most obvious when a photograph is taken of a truncated nose which is generating a cavity. The front diameter of the truncation appears to be only three-quarters the diameter of the flat front of the cavity which it generates. This optical effect is seen in Figure 6-10.

In Figures 6-11 and 6-12 circular cavity cross sections are drawn to permit a study of the image formation of objects within cavities. In Figure 6-11 the object is beyond the center of the cavity, and in Figure 6-12, it is nearer than the center. The observer is at the left, and his line of sight is referred to as the

cavity axis. This line, transverse to the cavity is regarded as the axis of a cylindrical lens. The arrows PQ represent objects which are seen, and the arrows P'Q' are their images.

A focus will be found by ray tracing, assuming that all rays from a particular point have the same focus, that is, that they appear to diverge from the same image point. This assumption is good for rays which cross the cavity wall near the axis. Two rays are traced, as is usual in thin-lens analysis. One ray leaves the point P parallel to the line of observation (toward the left), and strikes the cavity wall at point E. The line EF, along which the refracted ray travels, is calculated from the geometry of the figure and Snell's law. The line EF intersects the axis of the figure at point F, the virtual focal point.

The second ray which is traced, is that which passes without deviation from P through the center of the cavity. The image point P' is at the intersection of the two rays. The figures show that the image is nearer to the center of the cavity than is the object, for both locations of the object.

Calculations were made for object points at various distances from the axis and these gave focal points at the positions plotted in Figure 6-13. These distances, measured from the center of the cavity, are the same for the object positions of Figures 6-11 and 6-12. The variation of focal distance is due to cylindrical aberration.

When two rays are traced, as was done above, there is a presumption that both of them contribute to the viewing of the object, and it is obvious in Figures 6-11 and 6-12 that the rays through the cavity center do not go near the observer. The justification for the procedure lies in the assumption that all rays from a point P appear to come from a single point after refraction. While this is not quite true, spot checks show that the "virtual" object points are reasonably well defined.

The location of an image point at the intersection of rays through the center and through the principal focus, is generalized in Figure 6-14. In this figure two rays are drawn parallel to the axis at distances R/4 and 3R/4 from the center. Object points, shown as dots, are situated on these lines, and any two points, one on either line, may be taken as the ends of an object line. The corresponding image points are at the barbs of the arrows on the lines which pass through the foci to the right of the figure.

The results of this analysis may be summarized as follows:

1. Image points lie nearer the axis than object points, representing a reduced image size. The displacements (distance from object to image point) are greater the further the object point is from the axis.

2. The displacement increases as the object point is moved away from the camera (within the cavity) and goes to zero as the object approaches the nearer cavity wall.

3. Reduction in size is three-quarter size at the center of the cavity, and of the order of half size when the object reaches the far wall.

4. All bodies of circular cross section, on the axis, are reduced to three-qua' .er size.

Longitudinal curvature of the cavity may be expected to cause some lengthwise distortion of the image of a body in the cavity, and a similar effect will result if the observer is not directly opposite the missile. The application of Snell's law to this problem is straightforward, and will not be discussed here.

REFERENCES

6-1. Hyser, W. G., "Photographic Instrumentation Science and Engineering: Its Military Equipments, Techniques, and Applications," Gov't. Printing Off., 1965; and "Engineering and Scientific High-Speed Photography," Macmillan and Co., New York, 1962

6-2. May, A. and Williams, T. J., "Free-Flight Ranges at the Naval Ordnance Laboratory," NOL NAVORD Rpt 4063, 1955

6-3. McMillen, J. H. and Harvey, E. N., "A Spark Shadowgraph Study of Body Waves in Water," J. Appl. Phys. 17, pp 541-555, 1946

6-4. May, A., "Research for Design of a Hydroballistics Tank," NOLTR 63-119, 1963
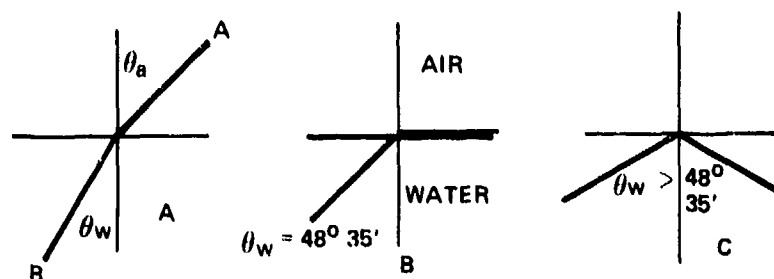
FIG. 6-1 REFRACTION AT AIR-WATER INTERFACE
RAY MAY BE TRAVELING IN EITHER DIRECTION
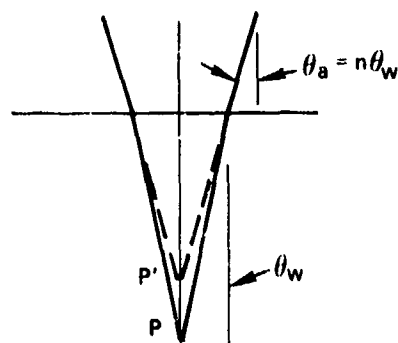
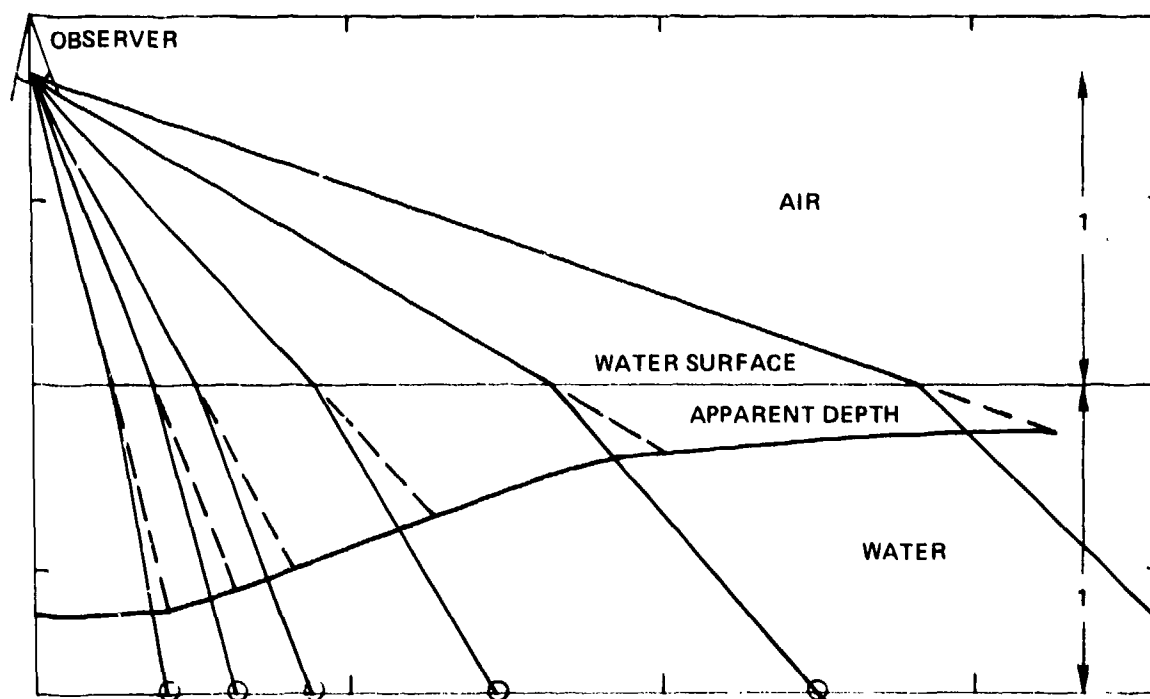FIG. 6-2 APPARENT DEPTH REDUCTION (VERTICAL VIEWING)

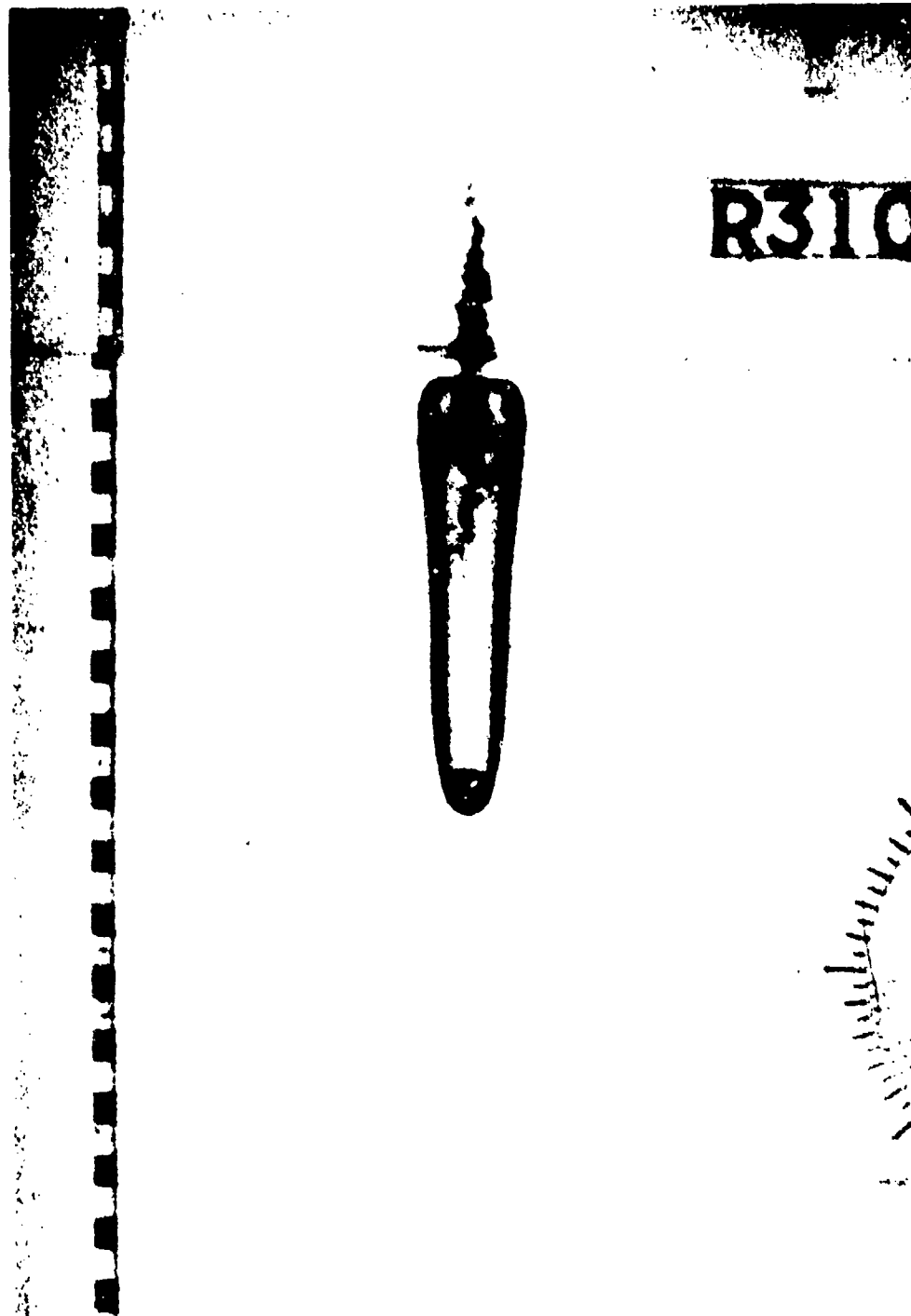FIG. 6-3 APPARENT DEPTH REDUCTION (OBLIQUE VIEWING)

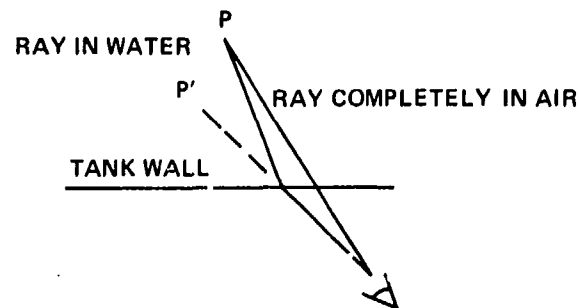FIG. 6-4 CAVITY PHOTOGRAPH AFTER VERTICAL WATER ENTRY
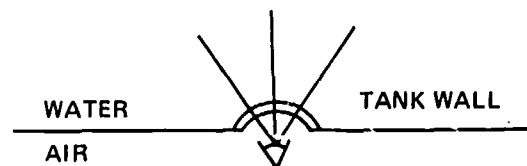
FIG. 6-5 DISTORTION OCCURRING AT THE WATER SURFACE

FIG. 6-6 USE OF SPHERICAL WINDOW TO LESSEN DISTORTION

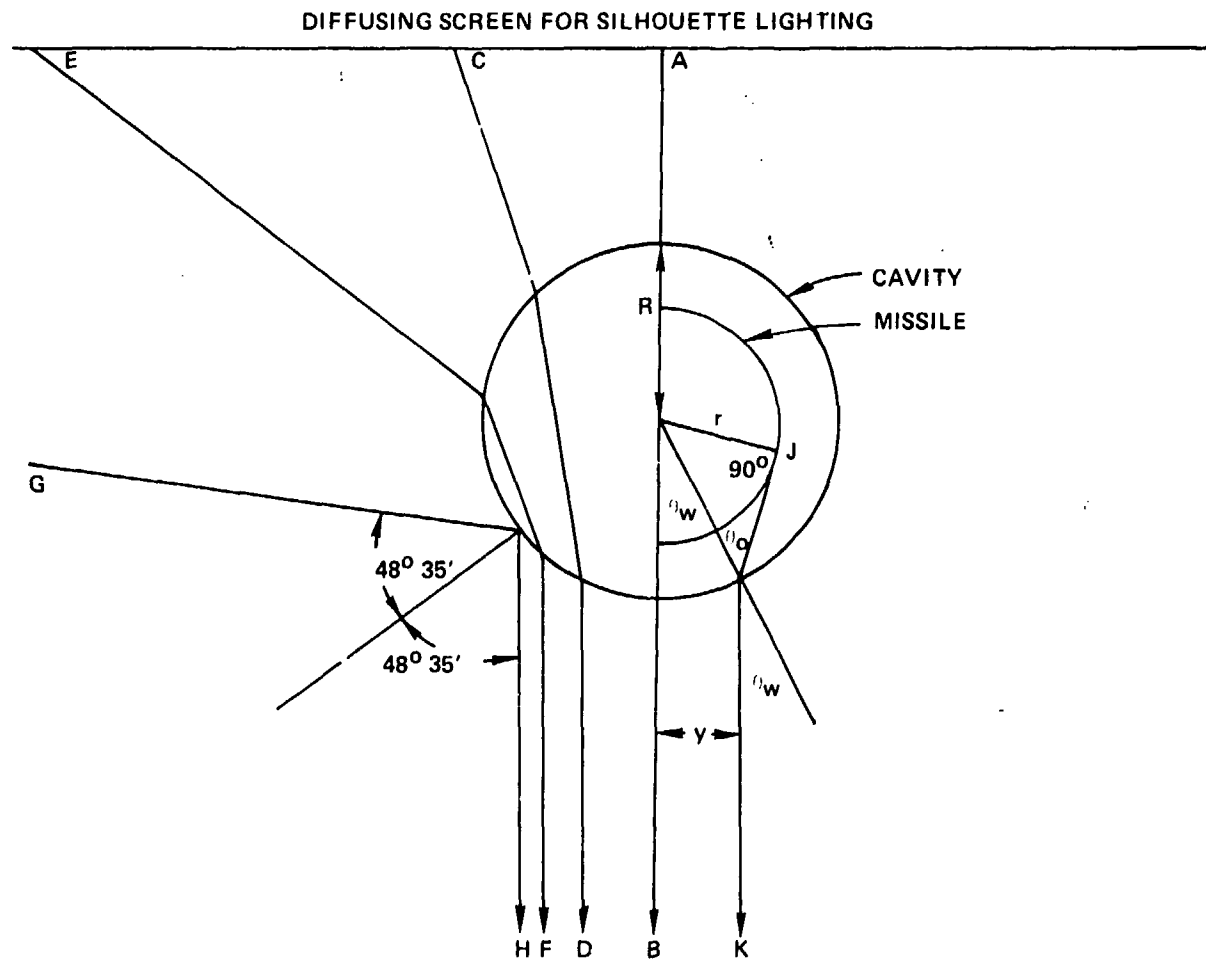FIG. 6-7 REGIONS WHERE SCATTERING OCCURS FOR SIDE AND FRONT LIGHTING
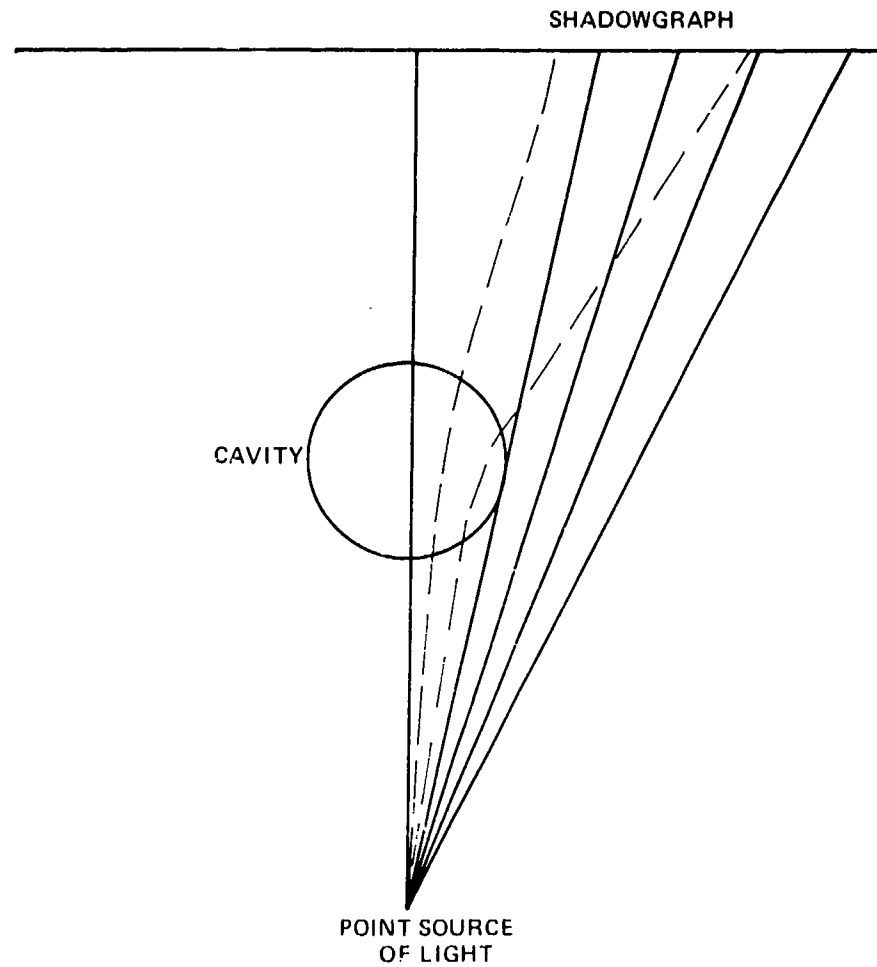
DIFFUSING SCREEN FOR SILHOUETTE LIGHTING

FIG. 6·8 PASSAGE OF LIGHT THROUGH CAVITY

FIG. 6-9 LIGHT PATHS OF SHADOWGRAPH
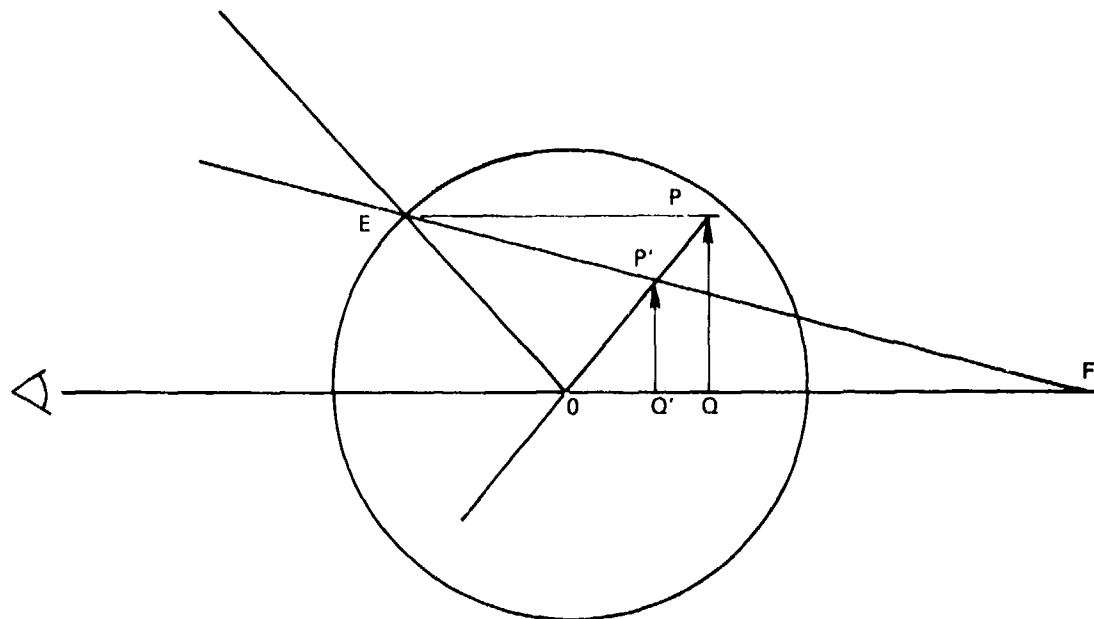
FIG. 6-10 APPARENT REDUCTION IN MISSILE SIZE IN CAVITY

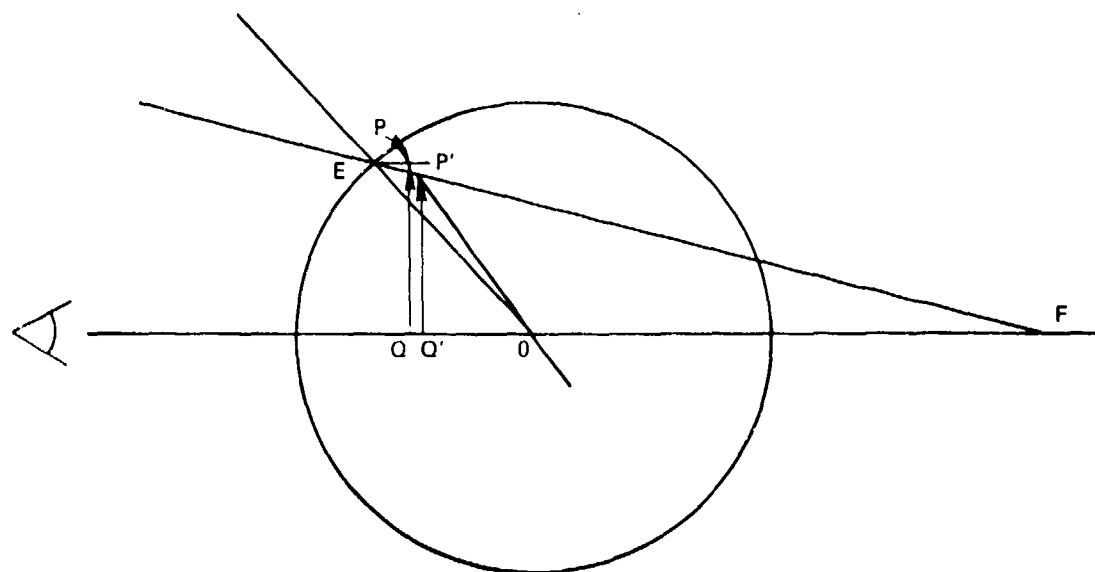FIG. 6-11 IMAGE OF OBJECT WITHIN CAVITY (OBJECT BEYOND CENTER)

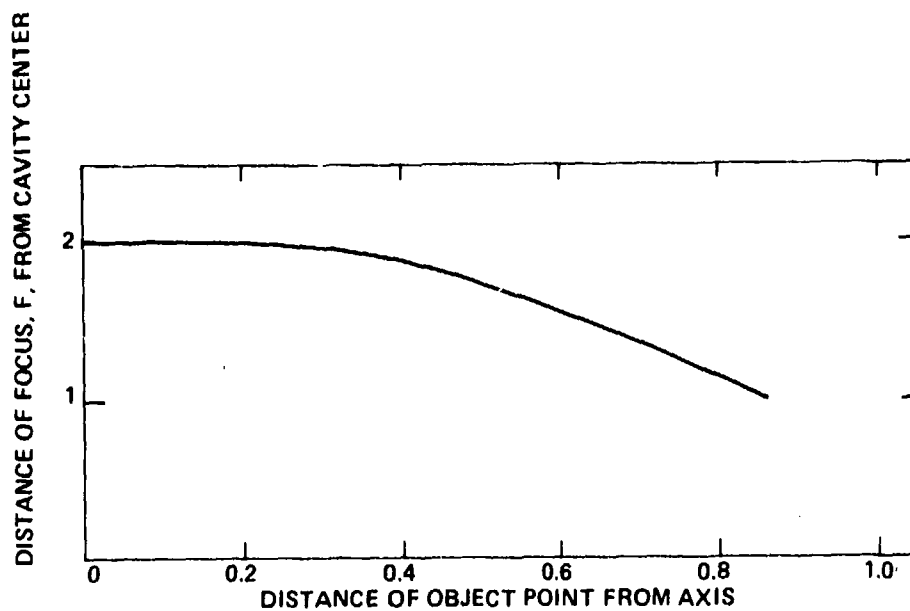FIG. 6-12 IMAGE OF OBJECT WITHIN CAVITY (OBJECT NEARER THAN CENTER)

FIG. 6·13 VARIATION OF FOCAL DISTANCE WITH OBJECT POSITION
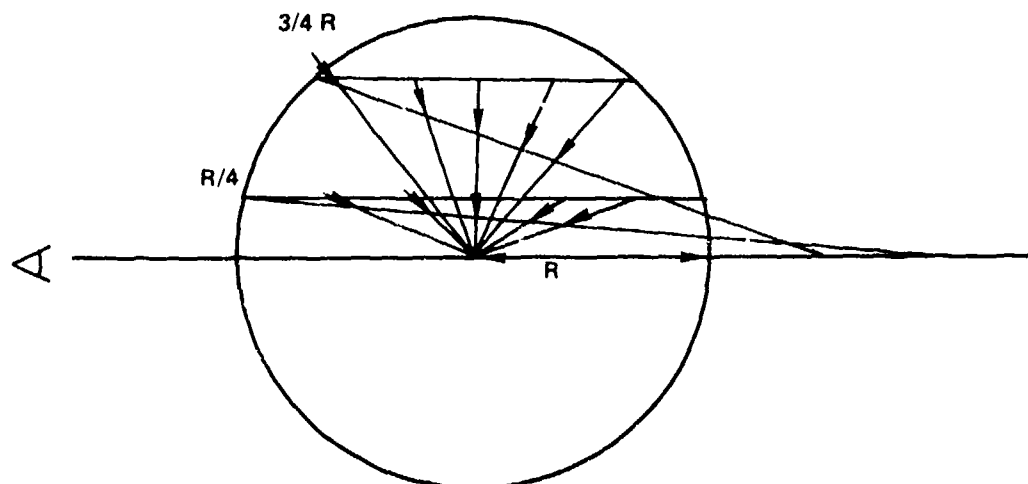(DISTANCES ARE IN CAVITY RADII)

FIG. 6·14 IMAGE FORMATION WITHIN THE CAVITY